Fusion partielle, transfert de magma et partitionnement de la déformation au cours de l'orogénèse Varisque : Exemple des massifs des Aiguilles-Rouges (Alpes) et de l'Agly (Pyrénées)

Jonas Vanardois

Jonas Vanardois. Fusion partielle, transfert de magma et partitionnement de la déformation au cours de l'orogénèse Varisque : Exemple des massifs des Aiguilles-Rouges (Alpes) et de l'Agly (Pyrénées). Stratigraphie. Université Bourgogne Franche-Comté, 2021. Français. NNT : 2021UBFCD067 . tel-03828085

HAL Id: tel-03828085
https://theses.hal.science/tel-03828085v1

Submitted on 25 Oct 2022

THESE DE DOCTORAT DE L'ETABLISSEMENT UNIVERSITE BOURGOGNE FRANCHE-COMTE

PREPAREE A L'UNIVERISTE DE FRANCHE-COMTE

Ecole doctorale n°554

Ecole doctorale Environnement-Santé

Doctorat de Géologie

Par

M. Jonas Vanardois

Fusion partielle, transfert de magma et partitionnement de la déformation au cours de l'orogénèse Varisque.

Exemple des massifs des Aiguilles-Rouges (Alpes) et de l'Agly (Pyrénées).

Thèse présentée et soutenue à Besançon, le 8 décembre 2021

Composition du Jury :

M. GUILLOT Stéphane	Directeur de recherche CNRS, Univ. Grenoble Alpes	Président
M. de SAINT-BLANQUAT Michel	Directeur de recherche CNRS, Univ. Paul Sabatier Toulouse 3	Rapporteur
M. ROLLAND Yann	Maître de conférences à l'Université de Savoie	Rapporteur
Mme GERBAULT Muriel	Chercheure à l'IRD, Univ. Paul Sabatier Toulouse 3	Examinatrice
Mme CAGNARD Florence	Géologue au BRGM à Orléans	Examinatrice
Mme ROGER Françoise	Chercheure au CNRS à l'Université de Montpellier	Invitée
M. MARQUER Didier	Professeur à l'UBFC	Directeur de thèse
M. TRAP Pierre	Maître de conférences à l'UBFC	Codirecteur de thèse

Résumé

A l'échelle des orogénèses, la déformation et la rhéologie de la lithosphère continentale sont fortement contrôlées par les processus de migmatisation et les phénomènes magmatiques au cours de l'évolution des grandes chaines continentales. La déformation de la croûte moyenne assistée par les mécanismes de fusion partielle et la présence de liquides silicatés joue un rôle majeur dans l'accommodation de grands déplacements horizontaux et verticaux au sein de l'orogenèse en construction. Ces fluages de la croûte partiellement fondue sont décrits dans les grands systèmes orogéniques actuels (e.g. Himalaya-Tibet et Andes) et anciens (Chaîne Varisque). Dans le détail, la déformation syn-orogénique, les processus de ségrégation des liquides silicatés et leur migration dans la croûte orogénique sont des phénomènes inter-opérant de manière complexe, à plusieurs échelles de temps et d'espace.

Par l'étude structurale, pétrologique et géochronologique des massifs Varisques de l'Agly (Zone Nord Pyrénéenne) et des Aiguilles-Rouges (Alpes occidentales), nous abordons cette problématique scientifique en ciblant la question des interactions entre partitionnement de la déformation et fusion partielle dans une croûte orogénique en déséquilibre à haute-température. En parallèle, nous proposons de repositionner ces massifs dans leur cadre tectonique Varisque afin d'améliorer la compréhension des processus de fluage à l'origine de leur construction et leur structuration.

L'analyse structurale du massif de l'Agly et la datation des déformations indiquent que la fusion partielle commence dès 325-320 Ma et se termine aux alentours de 300 Ma. Cette migmatisation est contemporaine du développement d'une fabrique planaire subhorizontale interprétée comme le fluage horizontal gravitaire de la croûte partiellement fondue. Ce fluage est localement perturbé par une zone de cisaillement dextre kilométrique drainant les liquides magmatiques et permettant le transfert et l'emplacement de plutons dans la croûte supérieure. Cette déformation dextre est interprétée comme une des branches nord d'une zone de cisaillement d'échelle crustale représentée par la zone axiale des Pyrénées.

Dans les Aiguilles-Rouges, la reconstitution du trajet P-T-t-D des éclogites et de métapélites de moyen grade indiquent un enfouissement en conditions de MP/MT jusqu'à des conditions de haut grade atteignant des conditions de pression-température maximales de l'ordre de 1.75 GPa et 710 °C à 340-330 Ma. L'existence d'une ancienne zone de subduction océanique dans les Massifs Cristallins Externes (ECMs) potentiellement associée à ces conditions de HP-HT est questionnée et discutée. Nos données indiquent qu'entre 340 et 330 Ma, la croûte inférieure est exhumée à la faveur d'un fluage horizontal de la croûte partiellement fondue pendant que la croûte moyenne/supérieure subit un enfouissement, dans un régime global en transpression dextre. Ces deux unités sont ensuite juxtaposées et exhumées par les mouvements transcurrents dextres le long de la Eastern Variscan Shear Zone (EVSZ). Nos données suggèrent que la nucléation des zones de cisaillement verticales composant l'EVSZ s'opère dès les premiers stades de migmatisation et préférentiellement dans les orthogneiss subissant une fusion hydratée. La EVSZ évolue ensuite sous la forme d'un large réseau de zones de cisaillement anastomosées, actif entre 340 et 300 Ma. Le développement de ce réseau vertical favorise le drainage des fluides aqueux, augmentant la production de liquides silicatés à l'origine de la formation de plutons syn-cinématiques, mis en place dans les zones de dilatance d'échelle crustale. Dans la croûte supérieure, ces mouvements transcurrents déforment un bassin antérieur à la collision continentale, formé entre 370 et 350 Ma lors d'une phase de rifting en contexte d'arrière-arc lié à la subduction de l'océan Saxothuringien sous la zone Moldanubienne. Ce bassin est réactivé en pull-apart entre 330 et 310 Ma.

La synthèse de nos résultats nous permet de proposer une évolution géodynamique des ECMs s'intégrant dans l'évolution de la chaîne Varisque Européenne et nous conduisent à présenter une nouvelle reconstitution paléogéographique de la branche Sud-Est Varisque à la fin du Carbonifère. Cette nouvelle vision du positionnement des ECMs, et la comparaison avec le massif de l'Agly nous permettent de discuter de l'évolution spatiale et temporelle du fluage de la croûte partiellement fondue au cours du Carbonifère.

Abstract

During late orogenic evolution, deformation of the continental lithosphere is highly influenced by partial melting and magmatic processes. Melt-assisted deformation of the partially-molten middle crust plays a major role in the accommodation of large horizontal and vertical displacements of molten crustal domains during the building of the orogenic plateaus as described in actual and ancient orogenic systems (e.g. Himalayan-Tibetan, Andean and Variscan belts). In detail, syn-orogenic deformation, melts segregation and melt migration in the orogenic crust are complex phenomena, which interact at several time and space scales.

Through structural, petrological and geochronological studies of the Variscan Agly and Aiguilles-Rouges massifs (North Pyrenean Zone and Western Alps, respectively), the interplay between deformation partitioning, partial melting and magmatic processes in the hot orogenic crust is investigated. Meanwhile, the geodynamic setting and evolution of these massifs are replaced in the global Variscan tectonic framework in order to improve the understanding of late-orogenic crustal flow.

The structural analysis of the Agly massif and U-Th-Pb dating highlight that crustal partial melting started at ca. 325-320 Ma and ended at ca. 300 Ma in this part of the Variscan belt. Partial melting was synchronous with the development of a sub-horizontal planar fabric interpreted as the horizontal gravity-driven flow of the partially molten crust. This flow is locally disturbed by a kilometre-wide dextral shear zone along which melts are transferred upwards with plutons emplacement in the upper crust. This dextral deformation is interpreted as one of the northern branches of a crustal-scale shear zone represented by the Pyrenean Axial Zone.

In the Aiguilles-Rouges massif, the reconstruction of the P-T-t-D paths of the eclogites and metapelites indicates a burial in MP/MT conditions reaching high-pressure high-temperature conditions at ca. 1.75 GPa and 710 °C at 340-330 Ma. The existence of an ancient oceanic subduction zone in the External Crystallin Massifs (ECMs) potentially associated with these HP-HT conditions is questioned and discussed. Our results indicate that between 340 and 330 Ma, the lower crust was exhumed by a horizontal flow of the partially molten crust while the middle/upper crust was buried during a dextral transpressive regime. These two crustal units are then juxtaposed and exhumed by dextral transcurrent movements along the continental scale Eastern Variscan Shear Zone (EVSZ). Our data suggest that the nucleation of the vertical shear zones composing the EVSZ started together with the onset of water-present melting of orthogneiss. The EVSZ then evolved into a large anastomosed network of shear zones, mainly active between 340 and 300 Ma. The development of the anastomosed network enhanced aqueous fluid drainage, which increased the production of melt at the origin of syn-kinematic plutons that emplaced within crustal-scale dilation structures. In the upper crust, these transcurrent movements deformed a detrital basin formed between 370 and 350 Ma during a rifting stage in a back-arc setting related to the subduction of the Saxothuringian ocean beneath the Moldanubian Zone. This basin was later reactivated in a pull-apart basin between 330 and 310 Ma.

Our results allow to propose a tectonic model of the ECMs that fits in the bulk evolution of the European Variscan belt. We also present a reappraisal of the paleogeographic location of the ECMs in the Variscan belt during Carboniferous time. This new vision of the position of the ECMs and the comparison with the Agly massif allow to discuss and to propose a new spatial and temporal evolution of the flow of the partially molten crust during the Variscan late-orogenic evolution.

Remerciements

Et c'est parti pour la fameuse section remerciements que je vais essayer de ne pas trop faire durer !

Je tiens dans un premier temps à remercier Michel de Saint-Blanquat, Yann Rolland, Murielle Gerbault, Stéphane Guillot, Florence Cagnard et Françoise Roger d'avoir accepté d'examiner ce travail de thèse. Je remercie aussi Stéphane Guillot et Christian Sue pour m'avoir suivi et conseillé durant mes comités de suivi de thèse.

Je remercie bien entendu Pierre qui a décidé de me faire confiance il y a de ça déjà 5 ans. Merci beaucoup Pierre, c'est grâce à toi que ce travail à pu aboutir et aller aussi loin, et ce, toujours dans une bonne ambiance. Merci. Infiniment. Il est temps pour toi de voler de tes propres ailes (est-ce que tu sens le souffle de l'HDR sur ta nuque ?).

Continuons sur la lancée académique puisque nous y sommes engagés ! Merci beaucoup à Didier qui a toujours su stimuler ma curiosité scientifique sans parler du fait de s'être toujours rendu dispo pour parler de mon travail. Enfin le troisième mousquetaire : merci Philippe pour m'avoir encadré non officiellement pendant toutes ces années, toujours avec subtilité et finesse soit dit en passant. Merci aussi à toute l'équipe de Géologie de Besançon pour ce qu'elle m'a apporté en connaissance géologique mais aussi beaucoup plus que ça, même si j'ai dû mettre votre patience à l'épreuve quelques fois !

Merci à tous les gens avec qui j'ai collaboré durant ce travail et qui ont toujours été bienveillants avec moi et m'ont permis de progresser : Françoise, Pierre L, Abdeltif, Brice, Jérem', Ben, Flo, Kévin, Guillaume, Thierry, Nico, Sylvia, Stéphane, JB, Emilie, Fabrice, Jean-Louis et Laurent.

Merci aux réserves naturelles de Savoie qui m'ont autorisé à venir crapahuter avec mon marteau au grand dam de la faune et des randonneurs. Merci au RGF et au BRGM de nous avoir soutenu et accompagné dans ce travail.

Et tout ce travail, c'est aussi grâce à l'ensemble du labo qui m'a mis dans un super environnement pour bosser, en particulier grâce aux pauses café et leurs conversations toujours subtiles (ah ironie quand tu nous tiens…). Un merci spécial à mes collègues de bureau : Cyril, Thomas, José, Hugo, Méline, Benjamin, Marion, Pierre, Alexandre, Anthony, Jordan et Mathieu ; merci aussi aux autres doctorants, ATER et autres contractuels pour les parties de tarot, soirée et autres : Charles, Corentin, Marine, Anne-Lise, Valentin, Daniel, Amandine, Céline, Marion et tous les autres. Tous ensemble dans la même galère !

Un grand merci à mes parents, mes sœurs, ma famille et mes amis qui ont toujours été une source de soutien. Mention spéciale aux colocs qui m'ont vécu au quotidien : Mathieu, Louise, Valentin, Eléonore, Clément et Maxime.

Enfin, un immense merci à Fanny pour tout.

Cadeau de moi à moi,

Comment me remercier ?

Kuzco

Sommaire

Chapitre 1. Problématique scientifique : Les relations entre fusion partielle, déformation et transferts de matière au cours de l'orogénèse.

Au sein des zones orogéniques, les transferts de chaleur liés à l'épaississement crustal, la mise en place de magmas et les interactions croûte/manteau sont à l'origine de températures élevées dans la croûte moyenne et inférieure qui atteint alors un état partiellement fondu formant des migmatites, roches contenant une certaine quantité de liquide silicaté (e.g. Thompson and Connolly, 1995 ; Brown, 2006). Deux conséquences majeures de ce phénomène sont : (1) la ségrégation et le transfert de liquide silicaté modifiant la nature des enveloppes crustales et (2) la chute de viscosité des roches contenant du liquide silicaté impactant très fortement le comportement rhéologique et la redistribution des masses crustales soumises aux forces tectoniques et gravitaires. Ci-après, ces deux processus sont décrits plus en détail après avoir discuté des paramètres contrôlant la fusion partielle et la ségrégation des liquides silicatés.

1. Production et ségrégation du liquide silicaté au cours de la fusion partielle de la croûte continentale, un phénomène multi-paramètres :

La fusion partielle des roches de la croûte continentale est à l'origine de migmatites dont les caractères minéralogiques nous renseignent sur les nombreuses réactions de fusion possiblement impliquées. Les réactions de fusion partielle sont dépendantes de plusieurs paramètres physico-chimiques que sont : la nature du protolithe (assemblage minéralogique), les conditions de pression et de température ainsi que la teneur en eau du système (e.g. Weinberg & Hasalová, 2015).

Deux principaux types de réactions de fusion partielle sont distinguées en fonction de la présence de fluides libres (V) ou pas :

-FP fluide-présent : exemple : Ms + Sil+ Qtz + V= L

-FP fluide-absent : Ms + Qtz = Kfs+ Sil+ L

Les réactions fluides-présents sont des réactions congruentes qui produisent exclusivement du liquide silicaté (Weinberg & Hasalová, 2015 et références associées). Les réactions fluides-absents sont non congruentes produisent des minéraux péritectiques tels que le grenat ou l'orthopyroxène par exemple. Il s'agit de réactions de déshydratation parmi lesquelles les réactions de déshydratation de la muscovite, de la biotite ou des amphiboles sont les principales (Figure 1 ; e.g. Weinberg & Hasalová, 2015 et références contenues).

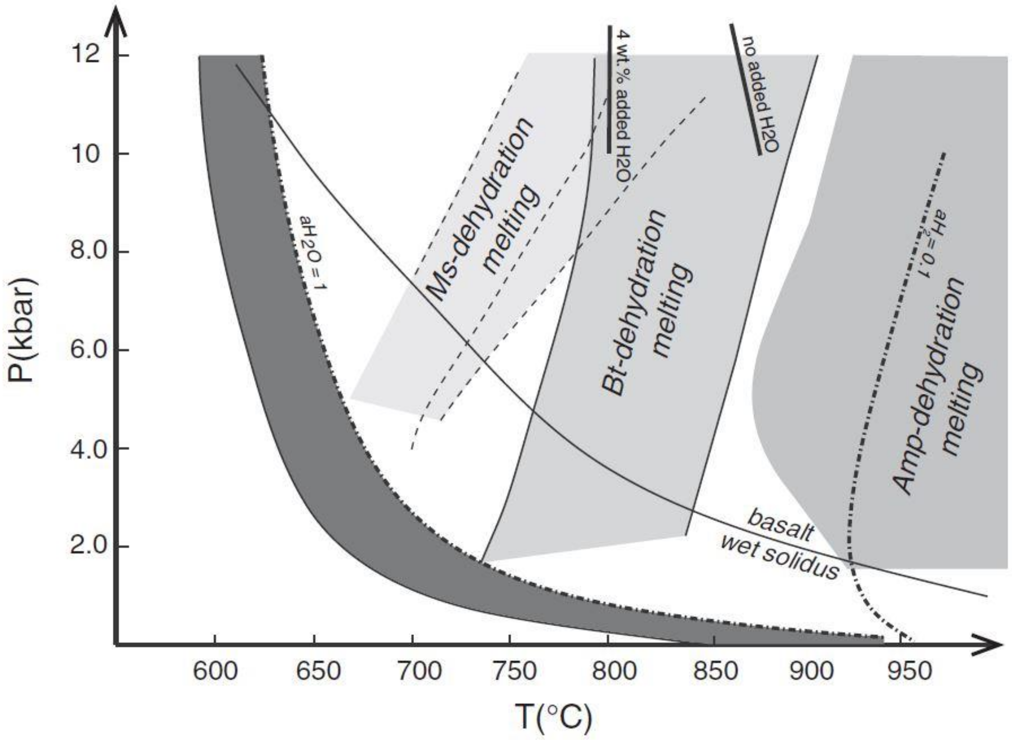

Figure 1 : Diagramme P-T illustrant les principales réactions impliquées dans la fusion partielle de la croûte continentale. L'impact de la quantité d'eau est représenté modifiant la position des ractions dans l'espace P-T (d'après Weinberg & Hasalová 2015).

Selon le type de réaction impliquée dans le processus de migmatisation, la fraction de liquide produite sera différente. Dans les roches riches en micas telles que les métapélites, les réactions fluides-absents peuvent générer d'importantes fractions de liquides atteignant 30 à 50 vol% si les roches atteignent des températures de l'ordre de 850-900 °C (Waters and Whales, 1984; Otamendi and Patiño Douce, 2001; White et al., 2003; Guernina and Sawyer, 2003). En revanche, dans des lithologies granitique, granodioritique ou métagranitique, la fraction de liquide produite par ces réactions de déshydrations sera seulement de quelques pourcents même à des températures supérieures à 800 °C (Berger et al., 2008 ; Schulmann et al., 2008 ; Sawyer, 2010). La fraction de liquide générée par les réactions fluides-présents dépendront directement du volume de fluides disponibles et peuvent atteindre des fractions volumiques de plus de 30% à des températures de 700°C (White et al., 2005 ; Sawyer, 2010 ; Wienberg and Hasalová, 2015). En outre, la quantité de liquide présent dans une migmatite et estimée par le volume de s par exemple, peut être représentée par une partie produite in-situ (réactions décrites ci-dessus) et par une proportion de liquide ayant migré depuis d'autres zones sources, possiblement plus profondes (Sawyer, 2001 ; Hasalová et al., 2008a, 2008b, 2008c ; Stipská et al., 2019).

A partir des années 1980, la majeure partie de la communauté scientifique considérait que la porosité dans les roches de haut-grade était très faible et que les roches de la croûte profonde ne pouvaient contenir que de très faibles volumes d'H2O et donc que la fusion partielle hydratée était un processus minoritaire dans la croûte (Clemens and Vielzeuf, 1987 ; Powell, 1983 ; Thompson, 1983 ; Brown, 2007). Récemment, les études démontrant au contraire l'importance des réactions fluides-présents dans la croûte se sont multipliées (e.g. Burri et al., 2005 ; White et al., 2005 ; Berger et al., 2008 ; Sawyer, 2010 ; Wienberg and Hasalová, 2015 ; Couzinié et al., 2021). La production de larges volumes de liquide par la fusion hydratée nécessite un apport important d'eau dans la croûte qui peut être fourni par la déshydratation de métapélites (e.g. White et al., 2005), par la cristallisation de magmas riches en K2O (Wienberg and Hasalová, 2015 ; Couzinié et al., 2021) ou par la cristallisation de liquides silicatées (e.g. Villaros et al., 2018). Dans la croûte profonde, ces apports importants d'H2O sont généralement drainés par les zones de cisaillement (e.g. Berger et al., 2008 ; Weinberg and Hasalová, 2015).

A partir d'un certain pourcentage de liquide silicaté dans la roche, la collecte et la migration du liquide va s'opérer. Selon les études, le liquide produit au cours de la fusion partielle serait susceptible de bouger librement dès qu'un seuil de percolation serait atteint pour une fraction de liquide de 4% (Laporte et al., 1997) à 7% (Rosenberg & Handy, 2005). On parle de "Melt Connectivity Threshold" (MCT) qui pourrait s'accompagner d'une chute brutale de l'ordre de deux à trois ordres de grandeur de la résistance des roches. Ces résultats sur ces proportions critiques de liquides de 7% (MCT) et ~30% (RCMP) ont été obtenus via des études expérimentales réalisées sur des échantillons centimétriques soumis à des vitesses de bien plus grandes que celles observées dans la nature et provoquant une fracturation de la roche (Rosenberg & Handy, 2005). Cette fracturation induit, par définition, une rupture dans le squelette minéral de la migmatite et donc une chute dramatique de la compétence de cette dernière. Les conditions expérimentales pourraient donc surestimer l'impact du liquide sur la perte de viscosité. Cependant, de nombreuses études documentent l'initiation et la propagation de fractures dans des migmatites en raison du changement de volume positif qui accompagne réactions de fusion (vapeur absente) (Bons et al., 2004, 2008 ; Brown, 2004, 2013 ; Brown & Solar, 1998, 1999 ; Clemens & Mawer, 1992 ; Clemens et al., 1997 ; Petford et al., 2000 ; Yakymchuk et al., 2013). Lorsque la quantité de liquide dans la roche atteint 20 à 40% (RCMP, « Rheological Critical Melt Percentage ») une autre chute brutale de près de dix ordre de grandeur est observée qui correspond à la perte du réseau solide, on passe alors des métatexite au diatexites (Sawyer et al., 2011) lesquelles ont un comportement rhéologique proche de celui des magmas (Arzi, 1978 ; Rosenberg & Handy, 2005). La présence de liquide dans la croûte continentale entraine une chute drastique de la viscosité des roches (Arzi, 1978 ; van der Molen & Paterson, 1979 ; Cruden, 1990 ; Rutter and Neumann, 1995 ; Lejeune & Richet, 1995) mais le concept de seuil rhéologique en lien avec le seuil de percolation est encore très discuté (e.g. Mecklenburgh & Rutter, 2003).

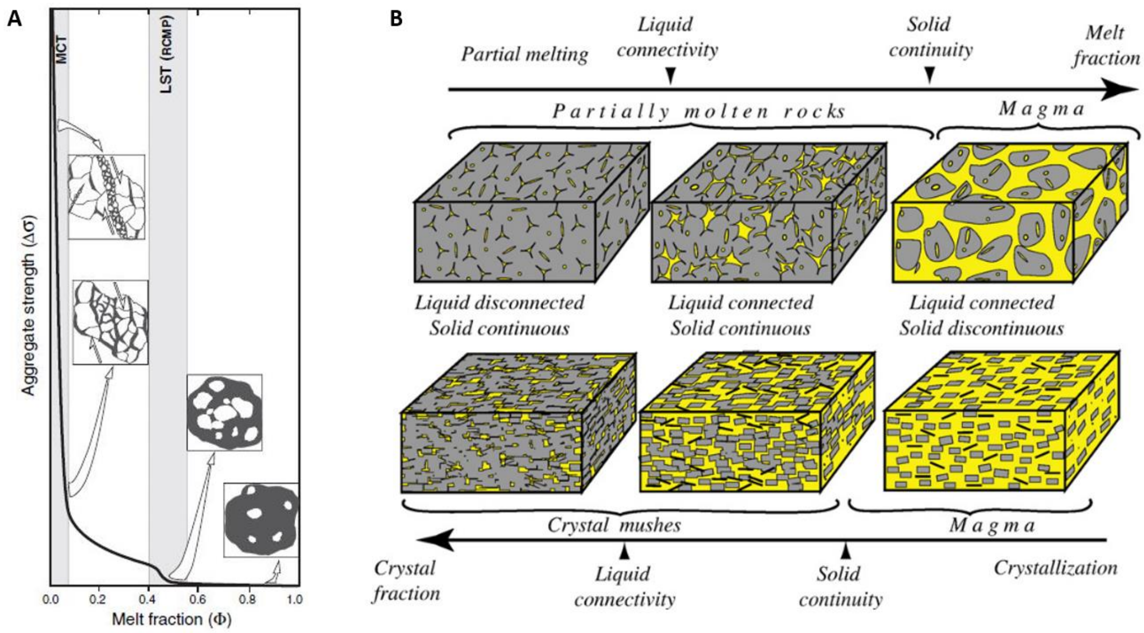

Figure 2 : A : Graphique illustrant la de viscosité en fonction de la proportion de liquide silicaté. La « MCT » correspond à la transition où le liquide devient interconnecté, la « LST » ou « Liquid Solid Transition » est la proportion de liquide à partir de laquelle le solide ne forme plus un réseau connecté (dans Rosenberg & Handy (2005). B : Evolution des limites géométriques entre phase solide et phase liquide en fonction de la quantité de liquide en présence (dans Vanderhaeghe, 2009).

La taille du grain de la roche subissant une fusion partielle est un paramètre supplémentaire, en lien directe avec la nature du protolithe et l'histoire métamorphique subsolidus. L'histoire thermique prolongée au cours de l'évolution métamorphique prograde est à l'origine d'une augmentation de la taille des grains qui va entrainer une augmentation significative de la perméabilité au cours des premiers stade d'apparition du liquide (e.g. Scaillet & Searle, 2006). En raison des forces gravitaires et tectoniques, le drainage du liquide silicaté via des processus de compaction ou de cisaillement est inévitable et peut s'opérer à des échelles de temps très courtes (Fig. 3 ; Jackson et al., 2003 ; Scaillet & Searle, 2006). La fusion partielle et la déformation sont des mécanismes intimement liés (Hollister 1993 ; Brown & Solar, 1998) et des périodes au cours desquelles les taux de déformation sont faibles pourraient correspondre à des périodes d'accumulation de liquide, lequel serait facilement drainé pour des périodes de déformation forte.

L'effet du paramètre temps sur la production et la ségrégation de liquide peut aussi dépendre de la tectonique à grande échelle. Plus la roche va stagner longtemps aux conditions P-T favorables, plus la quantité de liquide produit sera grande. Dans ce cas, la tectonique et les mouvement verticaux associés jouent un rôle majeur puisqu'ils contrôlent les durées et vitesses d'enfouissement et d'exhumation.

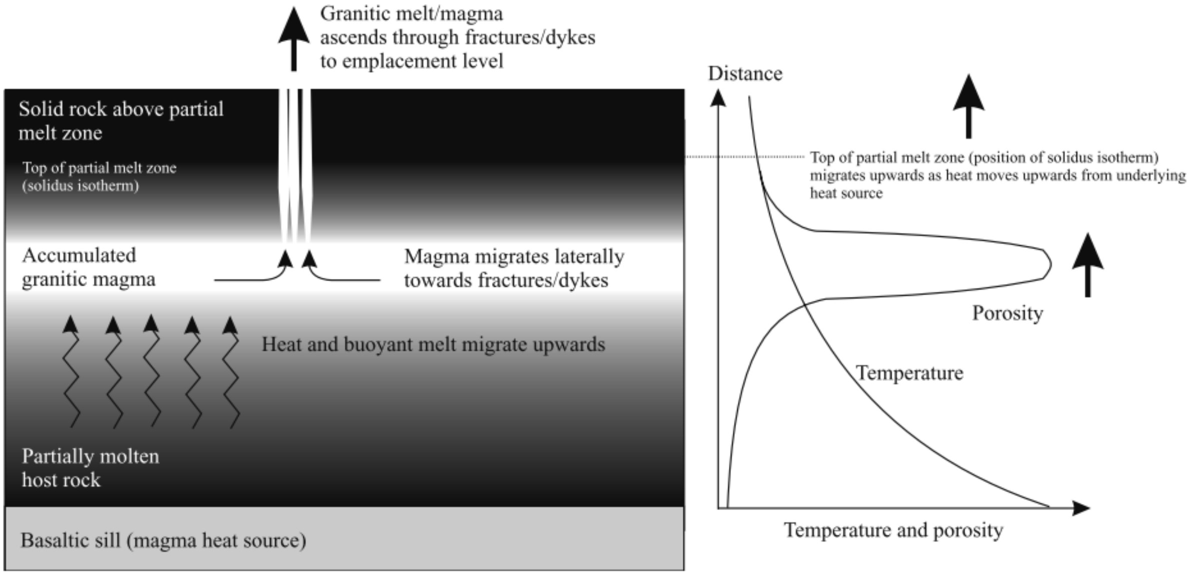

Figure 3 : A : Schéma d'une portion de croûte partiellement fondue et de la migration de liquide silicaté suite à un apport de chaleur lié à un sous-placage basaltique. L'épaisseur de la zone de fusion partielle augmente avec le temps à mesure que la chaleur migre du magma basaltique sous-jacent vers la roche mère sus-jacente. La distribution de la porosité dans la zone de fusion partielle est régie par les taux de transport ascendant relatifs de la chaleur et de la masse fondue ; si la masse fondue migre vers le haut plus rapidement que le sommet de la zone partiellement fondue (défini par la position de l'isotherme solidus), alors elle s'accumule au sommet de la zone partiellement fondue. Ceci augmente localement la porosité et la perméabilité permettant l'expulsion des magmas au travers de dykes (dans Jackson et al., 2003)

2. Stratification de la croûte orogénique partiellement fondue et fluage à grande échelle.

Avec l'augmentation de l'interconnectivité des liquides anatectiques (Melt Connectivity Transition (MCT)) puis la perte de la cohérence des composants non fondus (Solid to Liquid Transition (SLT)) (Rosenberg and Handy, 2005), les liquides silicatés vont donc pouvoir migrer depuis la croûte inférieure vers la croûte supérieure. Il en résulte une structuration à grande échelle de la croûte orogénique mature en couches horizontales. Vanderhaeghe (2009) propose de distinguer quatre principales couches : (i) la zone d'intrusion caractérisée par la mise en place de granites et l'absence de fusion partielle, (ii) la zone partiellement fondue composée de métatexites, (iii) la zone magmatique formée de diatexites et de granites hétérogènes, et (iv) la zone d'accumulation de cumulats granulitiques et de roches non fertiles (Fig. 4a). De ce transfert de matière résulte un nouveau profil rhéologique formé d'une couche faiblement résistante encadrée par deux couches fortement résistantes (Fig. 4a).

En raison de ce contraste rhéologie entre différents niveaux structuraux, la croûte partiellement fondue, mécaniquement affaiblie, va alors fluer horizontalement sous l'effet de la pression lithostatique (e.g. Vanderhaeghe and Teyssier, 2001 ; Beaumont et al., 2001, 2004 ; Rey et al., 2010) (Fig. 4b). Un tel fluage gravitaire est décrit dans les plateaux orogéniques actuels avec la chaîne Himalayenne-Tibétaine (e.g. Beaumont et al., 2001 ; Grujic, 2006 ; Godin et al., 2006 ; Jamieson et al., 2011, 2013) et le plateau de l'Altiplano-Puña (Fig. 5). Dans ce dernier par exemple, le plateau orogénique s'est développé dans un contexte d'arc magmatique continental et les résultats issus d'études géophysiques et de modélisations numériques suggèrent que ce plateau se serait formé par un fluage de la croûte inférieure en réponse à des variations latérales des forces gravitaires : certains proposent un fluage provenant des Cordillères bordant le plateau sous la forme d'un chenal perpendiculaire à la chaîne (Fig. 5a ; Husson & Sempere, 2003 ; Ouimet & Cook, 2010). D'autres proposent un fluage longitudinal, parallèle à la chaîne (Gerbault et al., 2005) supporté par une étude paléotopographique ayant révélé une surrection progressive du plateau depuis les reliefs Sud du Puña vers le Nord (Schildgen & Hoke, 2018) (Fig. 5b). Le fluage gravitaire est aussi décrit dans des analogues anciens comme la chaîne Varisque (Vanderhaeghe et al., 2020; Schulmann et al., 2008; Roger et al., 2020 ; Bento dos Santos et al., 2021).

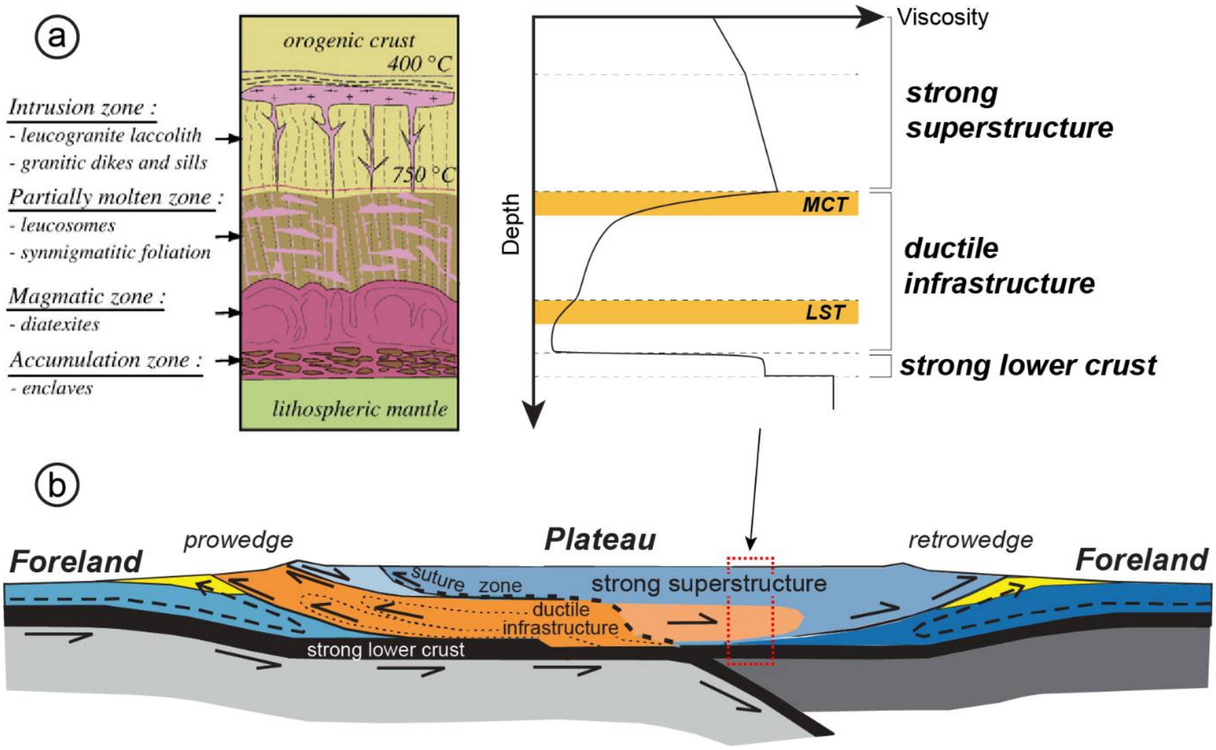

Figure 4 : (a) Structuration à grande échelle de la croûte orogénique mature en couches horizontales d'après Vanderhaeghe (2009) et l'évolution schématique de la rhéologie associée. (b) Modèle conceptuel du fluage latéral induit par la gravité, proposé en chaîne Himalayienne (dans Jamieson et al. (2013) avec l'exhumation de la croûte partiellement fondue en bordure du plateau orogénique.

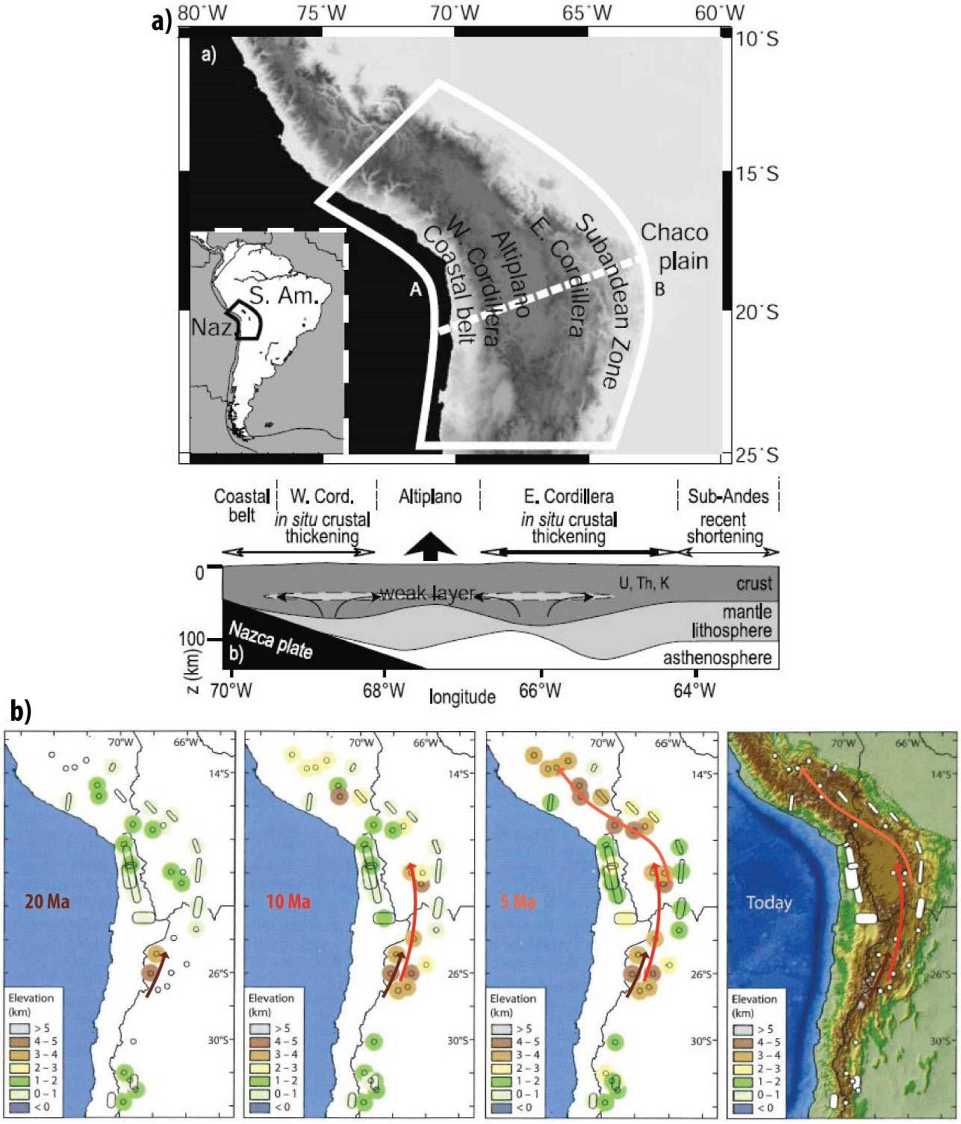

Figure 5 : a) Modèle de fluage gravitaire dans le plateau de l'Altiplano-Puña depuis les cordillères Est et Ouest (dans Husson & Sempere, 2003) ; b) Evolution paléotopographique du plateau de l'Altiplano-Puña depuis 20 Ma (modifié d'après Schildgen & Hoke, 2017) supportant un fluage gravitaire longitudinal comme proposé par Gerbault et al. (2005). Modifié d'après Lobjoie (2018).

3. Le partitionnement de la déformation dans une croûte orogénique partiellement fondue

En plus de la force de gravité, les forces aux limites vont contribuer au contrôle des caractères géométriques et cinématiques du fluage de la croûte partiellement fondue. De nombreuse études montrent un lien étroit entre des failles transcurrentes et le fluage horizontal de la croûte orogénique (Fig. 6) (Gapais et al., 2005 ; Chardon et al., 2009, Yin and Taylor, 2011 ; Liu et al., 2014 ; Xu et al., 2015 ; Cochelin et al., 2017, 2021). Ce partitionnement s'observe dans la croûte inférieure mais aussi dans la croûte supérieure (e.g. Tikoff and Teyssier, 1994 ; Chardon et al., 2009, 2011). Il peut être induit par des changements de contraintes locales (e.g. Rey et al., 2011, 2017), ou éloignées, liées au caractère de la convergence, en particulier si elle est oblique (Tikoff et al., 2004 ; Tikoff and Teyssier, 1994 ; Gapais et al., 2005 ; Chardon et al., 2009, 2011 ; Cochelin et al., 2017, 2021) (Fig. 6). Ce partitionnement résulte en une déformation hétérogène à l'échelle régionale avec la formation de zones de cisaillement verticales et horizontales qui fonctionnent de manière synchrone (e.g. Tikoff et al., 2002). Cependant, au sein d'une croûte partiellement fondue qui caractérisent les orogènes chauds ou ultra-chauds (Chardon et al., 2009) la faible résistance mécanique devrait plutôt favoriser une déformation homogène (Cagnard et al., 2006) à l'échelle crustale.

Dans les chaînes Himalayenne-Tibétaine et Varisque, les croûtes profondes sont partiellement fondues durant la formation des plateaux continentaux et fluent latéralement (e.g. Beaumont et al., 2001 ; Grujic, 2006 ; Godin et al., 2006 ; Jamieson et al., 2011, 2013 ; Vanderhaeghe et al., 2020 ; Schulmann et al., 2008 ; Roger et al., 2020 ; Bento dos Santos et al., 2021). Or, ces deux chaînes orogéniques sont structurées par de nombreuses failles et zones de cisaillement décrochantes (e.g. Edel et al., 2018 ; Styron et al., 2010) qui pourraient rendre compte de ce partitionnement de la déformation entre des structures horizontales et verticales. Néanmoins, ces zones de cisaillement verticales sont peu intégrées dans ces modèles de fluage latéral, en particulier dans la croûte profonde (Fig. 7).

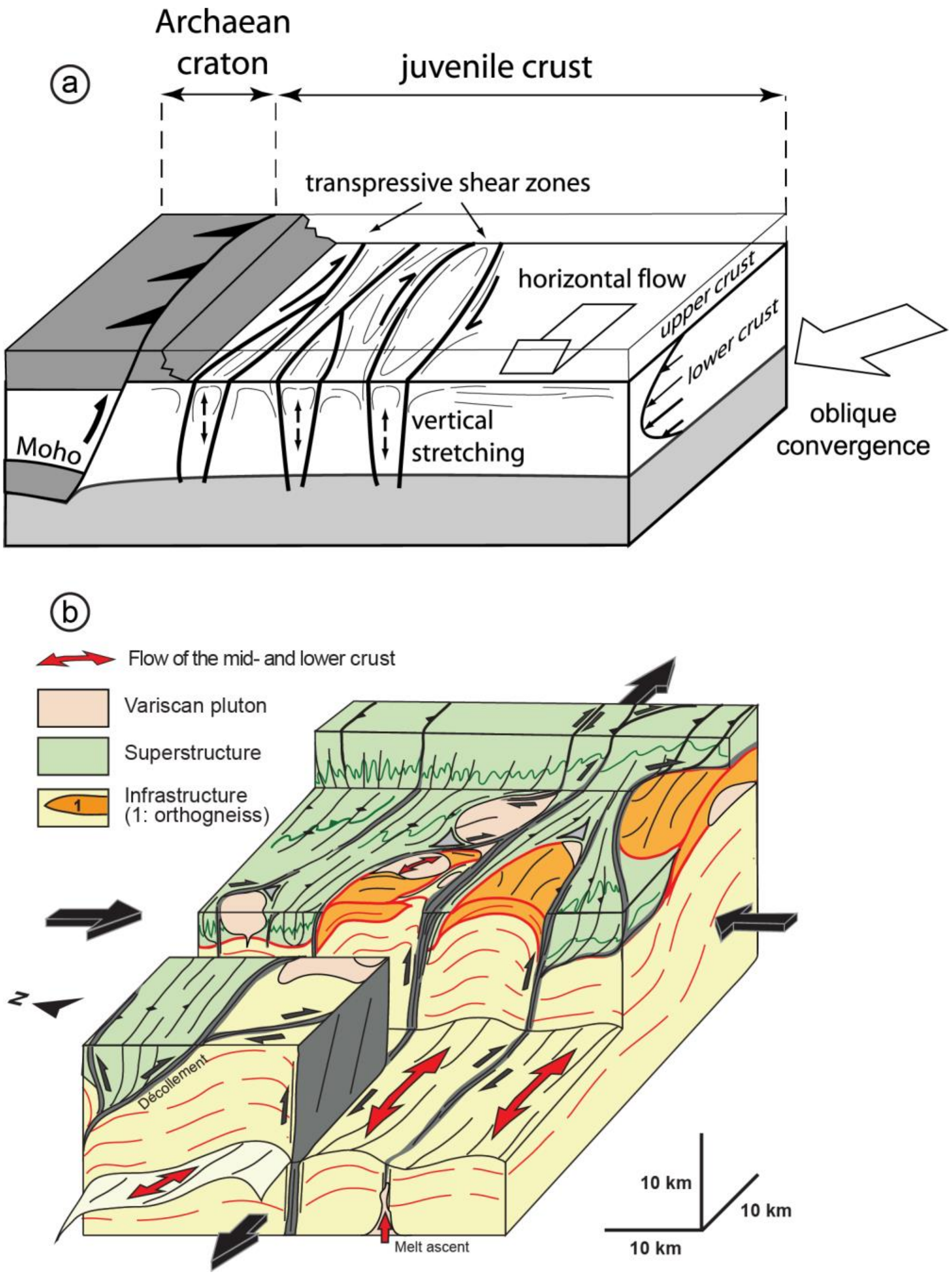

Figure 6 : Partitionnement de la déformation dans la croûte orogénique entre le fluage horizontale de la croûte partiellement fondue et des zones de cisaillement verticales dans (a) la chaîne canadienne Thompson Nickel Belt (d'après Gapais et al., 2005) et dans les Pyrénées Varisques (d'après Cochelin et al., 2017).

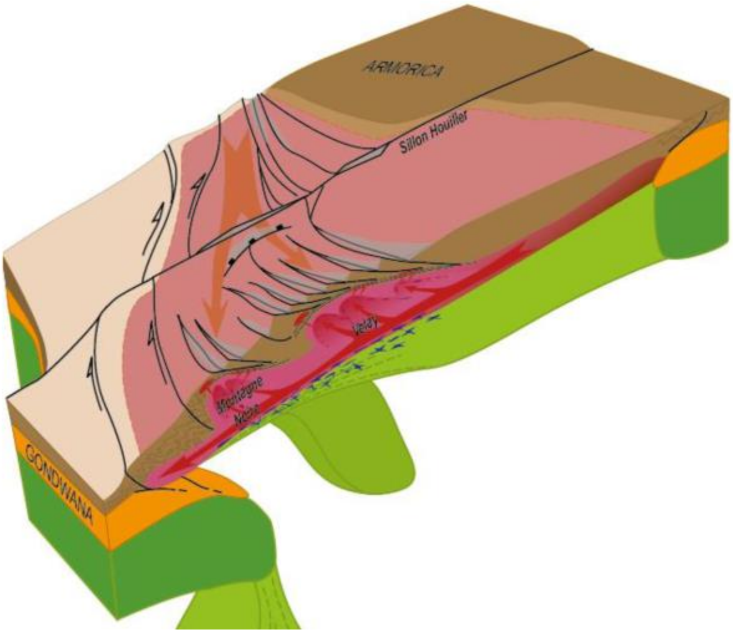

Figure 7 : Modèle 3D de Vanderhaeghe et al. (2020) du fluage latéral de la croûte orogénique du Massif Central au Carbonifère Supérieur durant l'effondrement de la chaîne Varisque. Des failles transcurrentes dextres sont représentées dans la croûte supérieure mais pas dans la croûte inférieure partiellement fondue

La nucléation des grandes zones de cisaillement verticales au sein d'une croûte chaude et partiellement fondue est encore un phénomène mal compris. Les études de terrains conduites sur des zones de cisaillement exhumées et les travaux numérique et expérimentaux mettent en lumière plusieurs processus d'affaiblissement de la rhéologie qui sont responsables de la localisation de la déformation tels que le développement d'une fabrique planaire, le *shear heanting* (chaleur produite par la friction), les réactions métamorphiques, la réduction de taille des grains, la présence de liquides ou de fluides (voir Fossen and Calvante, 2017 pour une synthèse). Les rôles et contributions de chacun de ces processus sont facilement identifiés de l'échelle millimétrique à métrique. En revanche, ils sont beaucoup plus difficiles à définir à l'échelle de la croûte continentale ou celle de la lithosphère qui sont caractérisées par des variations rhéologiques en raison de structures héritées et de leurs complexités lithologiques. Au premier ordre, un contraste rhéologique, entre une phase faible et l'autre forte, est nécessaire pour nucléer une zone de cisaillement quelle que soit l'échelle (e.g. Tommasi et al., 1995 ; Holyoke and Tullis, 2006 ; Cao et al., 2016 ; Gardner et al., 2017). A tout ceci s'ajoute aussi la possibilité que ces failles verticales soient héritées et forment alors des hétérogénéités favorisant leur réactivations (e.g. Calignano et al., 2017).

Au sein de la croûte orogénique profonde, la présence de liquide est donc un processus formant des hétérogénéités rhéologiques majeures entre les roches fondues et celles non-fondues (e.g. Handy et al., 2001 ; Rosenberg and Handy, 2005 ; Rosenberg et al., 2007). Le contrôle à petite échelle de la localisation de la déformation par la fusion partielle a été démontrée par des observations de terrains (e.g. Piazzolo et al., 2020), des expériences analogiques (Grujic and Mancktelow, 1998 ; Druguet and Carreras, 2006) et des modélisations numériques (e.g. Mancktelow, 2002). Cependant, à grande échelle ce processus reste mal compris. Il faut aussi prendre en compte que les temps de résidence relativement court (<2Ma) des liquides dans ces failles peuvent aboutir à un processus épisodique avec de longues périodes de déformation subsolidus entre-coupées de périodes de transfert de liquide impliquant une déformation plus rapide (Handy et al., 2001).

4. Relation entre magmatisme et zones de cisaillement

La formation de plutons dans la croûte supérieure nécessite que les liquides générés dans la croûte inférieure soient séparés de la phase solide résiduelle et soient ensuite collectés dans des conduits ascendants à forte perméabilité pour alimenter (Brown, 2013). De nombreuses études ont décrit la migration de liquides anatectiques au sein de zones de cisaillement (e.g. Brown, 2007, 2010, 2013) alimentant des plutons se mettant en place au niveau de la transition ductile-fragile de la croûte (e.g. Handy et al., 2001 ; Rosenberg et al., 2007 ; Brown, 2013). Les zones de cisaillement peuvent aussi former localement des zones de dilatance collectant les liquides anatectiques et permettant la formation de pluton syn-cinématiques au sein de ces cisaillements (e.g. D'Lemos et al., 1992 ; Brown, 1994). Néanmoins, cette relation entre zones de cisaillement et plutons et parfois inversée et c'est la localisation de pluton dans la croûte supérieure qui va localiser la formation de zones de cisaillement à leur bordure (e.g. Neves et al., 1996). De plus, comme discuté dans le paragraphe précédent, la fusion partielle de la croûte a un impact majeur sur la localisation et de la déformation. Il existe donc une rétroaction entre les zones de cisaillement et la formation de pluton au sein de croûte (e.g. Brown and Solar, 1988 ; Brown, 2007, 2013). Il faut aussi noter que la collecte des liquides anatectiques de la croûte inférieure et leur migration vers la croûte supérieure résulte en une croûte inférieure infertile et appauvrie en liquide caractérisée par une forte rhéologie (e.g. Brown, 2013 ; Diener and Fagerend, 2014).

Il apparaît donc que le partitionnement de la déformation au sein de la croûte orogénique, influencé par la présence de liquides, contrôle les transferts de fluides et de magmas au sein de la croûte (Brown, 2013). Cette advection de fluides et de liquides chauds a elle-même un impact majeur sur l'évolution des géothermes au sein de la croûte orogénique (e.g. Annen and Sparks, 2002 ; Depine et al., 2008). En plus de ce contrôle de l'advection dans la croûte, des études expérimentales ont montré que les fabriques planaires et linéaires des roches ont une influence sur la conductivité thermique (Popov and Mandel, 1997 ; Vosteen and Schellschmidt, 2003 ; Nebalek et al., 2010). Des zones de cisaillement crustales pourraient donc influencer la conductivité thermique de la croûte.

Objectifs de l'étude :

Au regard des points (non exhaustifs) présentés ci-dessus, il apparait que la présence de liquide silicaté a un impact rhéologique fort sur les processus orogéniques et que la fusion partielle et la déformation des roches sont étroitement liées, à plusieurs échelles de temps et d'espace. Il apparait aussi clairement que les processus de fluage de la croûte partiellement fondue, de partitionnement de la déformation en son sein et le transfert des liquides anatectiques sont indissociables du cadre tectonique régional dans lequel ils s'opèrent.

Dans cette thèse, nous étudierons deux massifs de la chaîne Varisque, le massif de l'Agly dans la Zone Nord-Pyrénéenne et le massif des Aiguilles-Rouges dans les Alpes occidentales (Fig. 8). Dans ces deux massifs, la croûte migmatitique affleure largement ainsi qu'une partie de la croûte supérieure peu à pas métamorphique (e.g. Siron et al., 2020 ; von Raumer and Bussy, 2004), permettant d'étudier le partitionnement sur l'ensemble de la croûte orogénique.

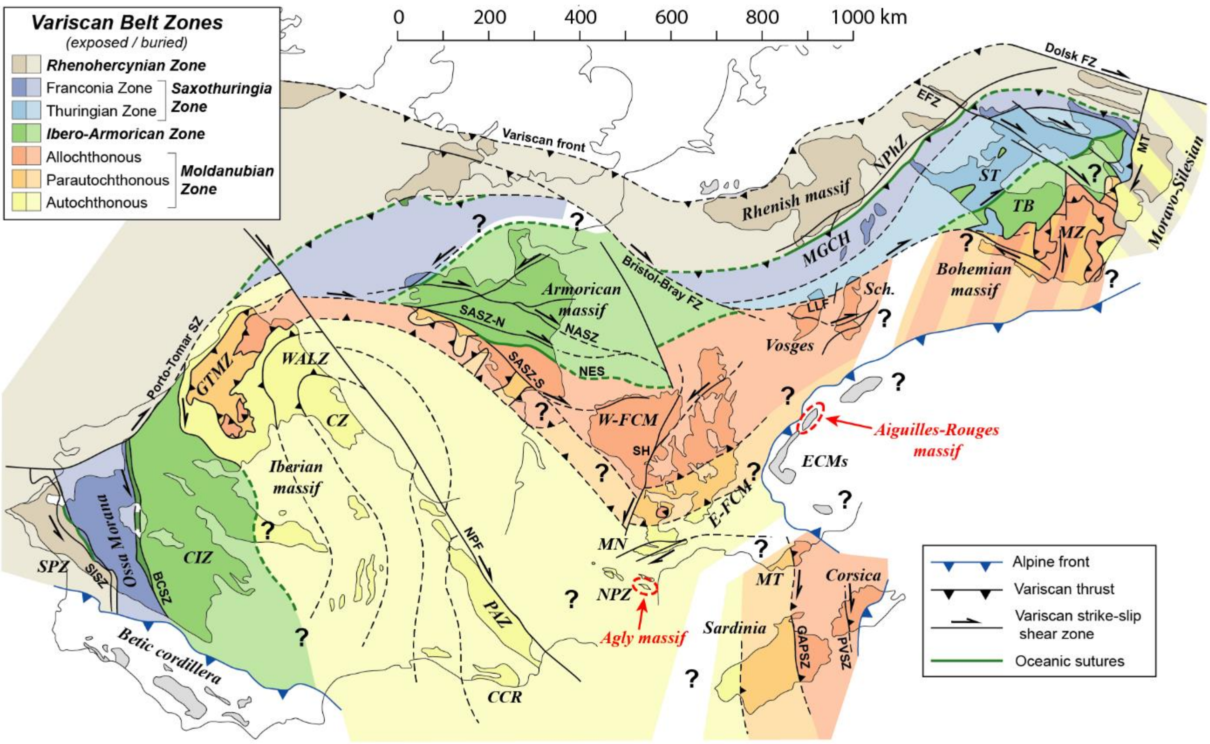

Figure 8: Reconstitution paléogéographique de la chaîne Varisque au début du Permien à la fin de l'orogène Varisque, d'après on Martinez-Catalan et al. (2021), Franke et al., (2017), Edel et al., (2018) et Lardeaux et al. (2014). Zones (Z): CCR: Catalan Coastal Ranges; CIZ: Central Iberian; CZ: Cantabrian; ECMs: External Crystalline Massifs; E-FCM and W-FCM: French Central Massif (East and West); GTMZ: Galicia-Trás-os-Montes; MGCH: Mid German Crystalline High; MN: Montagne Noire; MZ: Moldanubian; NPhZ: Northern Phyllite; NPZ: North Pyrenean; PAZ: Pyrenean Axial; Sch: Schwarzwald; SPZ: South-Portugese; ST: Saxo-Thuringia; TB: Teplá-Barrandian block; WALZ: West Asturian-Leonese. Shear Zones (SZ), Fault Zones (FZ) and Fault (F): BCSZ: Badajoz-Corboda; EFZ: Elbe; GAPSZ: Grimaud-Asinara-Posada; LLF: Lalaye-Lubine; MT: Moldanubian Thrust; NASZ: Northern Armorican; NES: Nort-sur-Erdre segment; NPF: North Pyrenean; PVSZ: Porto Vecchio; SH: Sillon Houiller; SASZ: Southern Armorican (North and South); SISZ: Southern Iberian.

Ces deux massifs ont des positions différentes au sein de l'orogène : Le massif de l'Agly est positionné dans l'avant pays sud de la chaîne (Fig. 8) et est principalement structuré par des zones de cisaillement subhorizontales (Bouhallier et al., 1991 ; Olivier et al., 2004). Le massif des Aiguilles-Rouges est plus proche des zones internes (Fig. 8) et est principalement structuré par des grandes zones de cisaillement verticales (Bellière, 1958 ; Joye, 1989 ; Simonetti et al., 2020a).

Les massifs des Aiguilles-Rouge et de l'Agly montrent aussi beaucoup de similitude telles que la fusion partielle de leurs croûte profonde au Carbonifère supérieur (Bussy et al., 2000 ; Siron et al., 2020), l'intrusion de granites à ca. 305 Ma durant un régime transpressif (von

Raumer and Bussy, 2004 ; Olivier et al., 2008) ou des conditions métamorphiques de haute-température – basse-pression (Genier et al., 2008 ; Siron et al., 2020).

Quatre principales questions guident ce travail de thèse :

Comment s'effectue le partitionnement de la déformation dans la croûte orogénique partiellement fondue des massifs de l'Agly et des Aiguilles-Rouges ?

Quels sont les paramètres ayant contrôlés la nucléation et la propagation des grandes zones de cisaillement dextre observées dans ces massifs, notamment celui des Aiguilles-Rouges ?

Quels rôles jouent ces grandes zones de cisaillement dextre sur les déplacements horizontaux et verticaux des différents niveaux structuraux de la croûte orogénique ?

Peut-on préciser les relations entre la fusion partielle de la croûte, la déformation régionale et le transfert de magma aboutissant à l'emplacement de granites syn-tectoniques dans le massif de l'Agly et le massif des Aiguilles-Rouges ?

Chapitre 2. La chaîne Varisque en Europe.

Ce chapitre a pour but dans un premier temps de faire une présentation non-exhaustive des connaissances actuelles sur l'orogénèse Varisque et son évolution géodynamique. Puis, nous présenterons l'état de l'art sur les Pyrénées Varisques avant de présenter le socle Varisque des Alpes avec un focus particulier sur les Massifs Cristallins Externes. Enfin, nous présenterons succinctement les modèles actuels proposés de corrélations entre les massifs de la branche Sud-Est Varisque et nous terminerons ce chapitre par les questions régionales auxquelles nous tenterons de répondre dans cette thèse.

1. The Variscan belt

The Variscan belt outcrops in the Central and Western Europe and belongs to a long orogenic belt extending from the Appalachian and Ouachita mountains of North America to the Caucasus (Fig. 1) (Matte, 1986; Kroner and Romer, 2013). The Variscan belt results from the collision between the Laurussia and Gondwana mega-continents and occurred during the Devonian to Permian times (e.g. Matte, 2001). The evolution of the Variscan orogeny is summarized in broad terms in the following.

Before the Variscan orogeny, the terranes forming the future Variscan domains were located in the Northern margin of the Gondwana and were westerly bounded by the Iapetus and Tornquist oceans (Fig. 2a) (von Raumer et al., 2002; Stampfli et al., 2013). The Cambrian-Ordovician period is characterized by a broad extensional setting inducing rifting and subsidence in the northern Gondwana (von Raumer and Stampfli, 2008) and resulting in a thin margin associated to a bimodal magmatism, with numerous intrusions of alkaline and tholeiitic mafic rocks, that was associated with alkaline and peralkaline rhyolite (e.g., Pin and Marini, 1993; Crowley et al., 2000). Between ca. 500 – 480 Ma, continental rifting formed the Rheic ocean (Fig. 2b) (Linnemann et al., 2007; von Raumer and Stampfli, 2008; Nance et al., 2010; Kroner and Romer, 2013). The opening and spreading of the Rheic ocean detached a part of the northern Gondwana margin forming two microcontinents named Avalonia and Hun terranes (Fig. 2b) (e.g. Matte, 2001; von Raumer and Stampfli, 2008; Stampfli et al., 2013; Jacob et al., 2020). The drifting of Avalonia towards the North induced the closure of the Iapetus and Tornquist oceans (Fig. 2c) and a continental collision between the Laurentia and Baltica continents (Fig. 2d) during the Upper Silurian (Matte, 2001; Stampfli et al., 2013) formed together the Laurussia continent and were responsible of the Caledonian orogeny (McKerrow et al., 2000).

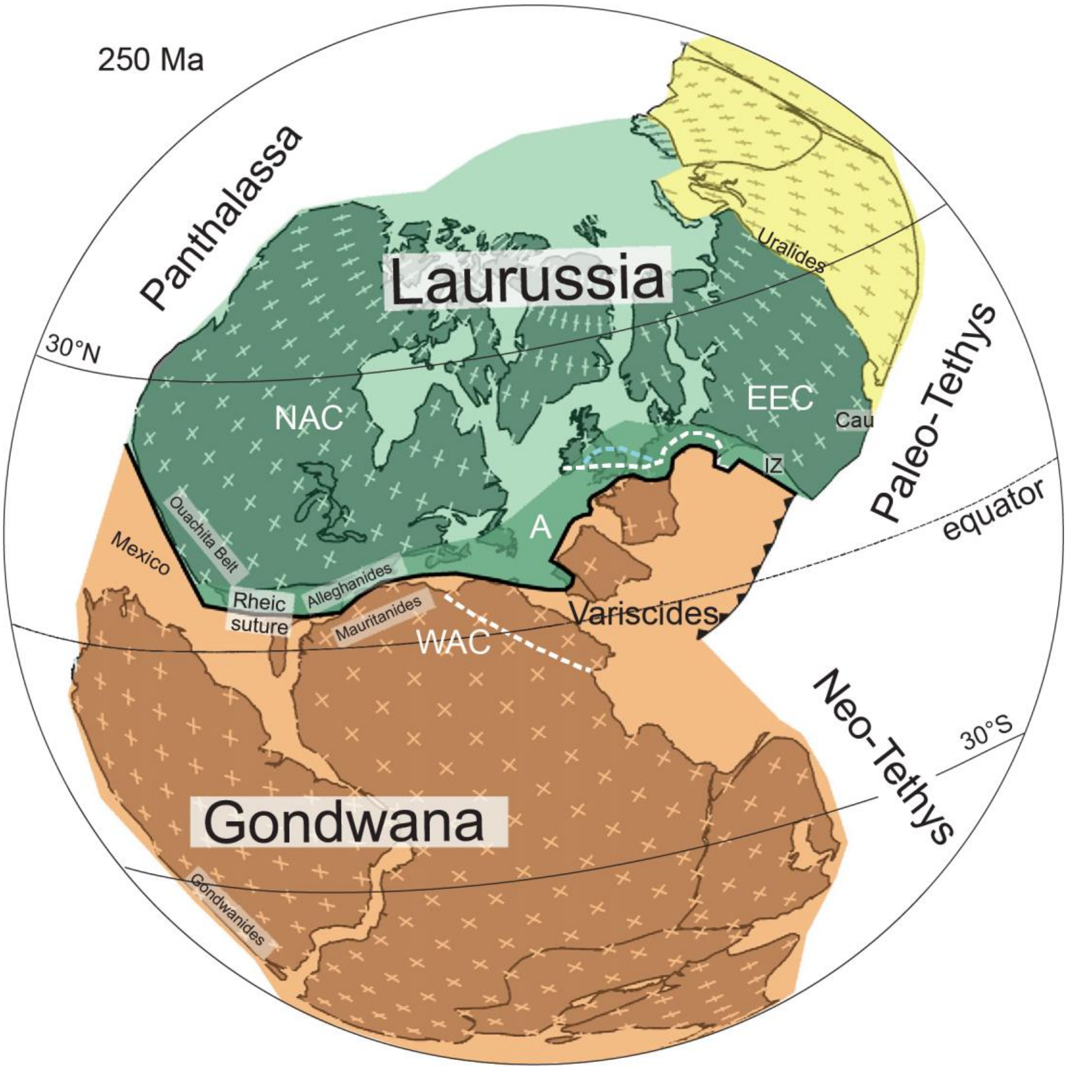

Figure 1: The Variscan orogen in the context of "Wegenerian" Pangea A at 250 Ma, from Kroner and Romer (2013). The orogen encompasses an area of c. 2500 by 2000 km. Stippled blue line: Early Devonian deformation front to the north of the Anglo-Brabant Massif. Stippled white lines: External limit of Late Variscan deformation on the Laurussian and Gondwana plates. NAC: North American Craton; EEC: East European Craton; WAC: West African Craton; A: Avalonia; IZ: Istanbul Zone; Cau: Caucasus.

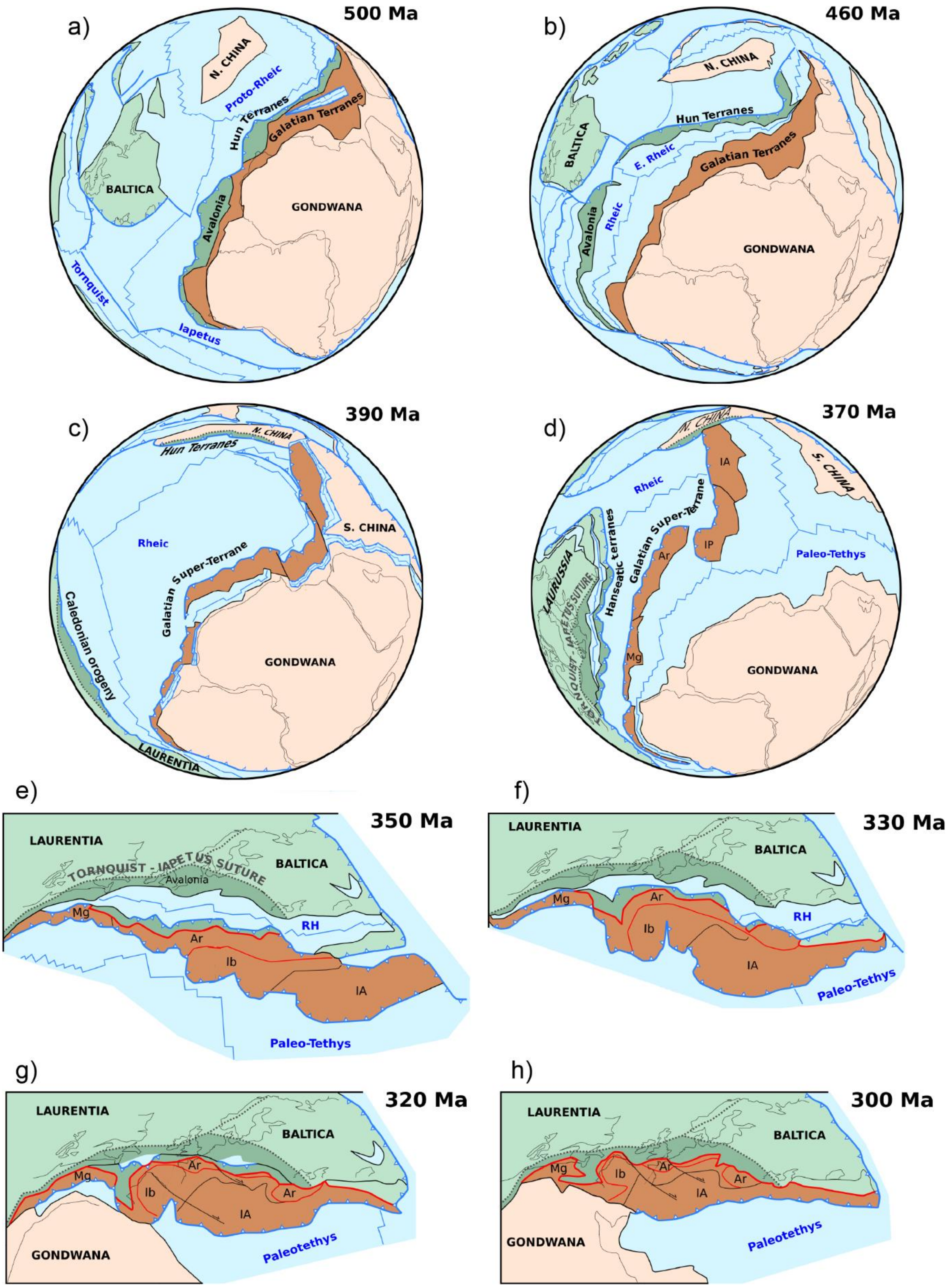

Figure 2: Reconstruction showing the evolution of North Gondwana from the Cambrian to the Late Carboniferous. This period records the progressive opening of the Rheic domain and the drifting of Avalonia during the Ordovician, followed by the rifting of Paleo-Tethys during the Silurian and the Devonian, and the progressive closure of Rheic Ocean and other smaller basins leading to the polyphasic collision between Laurussia, Galatian

Terranes, and Gondwana. It was followed by extension and lateral extrusion of material accommodated by the lithospheric-scale strike–slip faults. Mg, Meguma; Ib, Iberia; Ar, Armorica; IA, Intra–Alpine. light green, Laurentia–Baltica; dark green, Avalonia and Hun Terrane; light brown, Gondwana; dark brown, Galatian Terranes. Modified from Jacob et al. (2020).

During the Late-Silurian, the extension of the northern Gondwana margin leads to the formation of one or several microcontinents drifting from the northern Gondwana margin and that were separated from the Gondwana by an oceanic domain (Fig. 2d) (Stampfli et al., 2013; Jacob et al., 2020; Matte, 2001). However, the exact paleogeographic reconstitutions during this time period is still highly debated in recent studies (e.g. Kroner and Romer, 2013; Stampfli et al., 2002, 2013; Franke et al., 2017; Stephan et al., 2019; Regorda et al., 2020). Depending on the study, the number of microcontinents varies as the number of oceans (Fig. 3) (Stephan et al., 2019). For example, Franke et al. (2017) proposed the existence of two microcontinents separated by the Saxothuringian and the Galacian-Moldanubian oceans (Fig. 3b), whereas the other models suggest that these terranes never drift apart from the Gondwana margin or that there was no creation of oceanic domain (Fig. 3c) (Kroner and Romer, 2013; Stephan et al., 2019). The most used palinspastic reconstruction consists in the formation of one microcontinent (i.e. Armorica or Galacian terranes) separated of the Gondwana by an ocean (Paleotethys, Medio-European or Galacia-Brittany ocean) (e.g. Matte, 2001; Stampfli et al., 2002, 2013; Vanderhaeghe et al., 2020; Martinez-Catalan et al., 2021) (Fig. 3a, b and d).

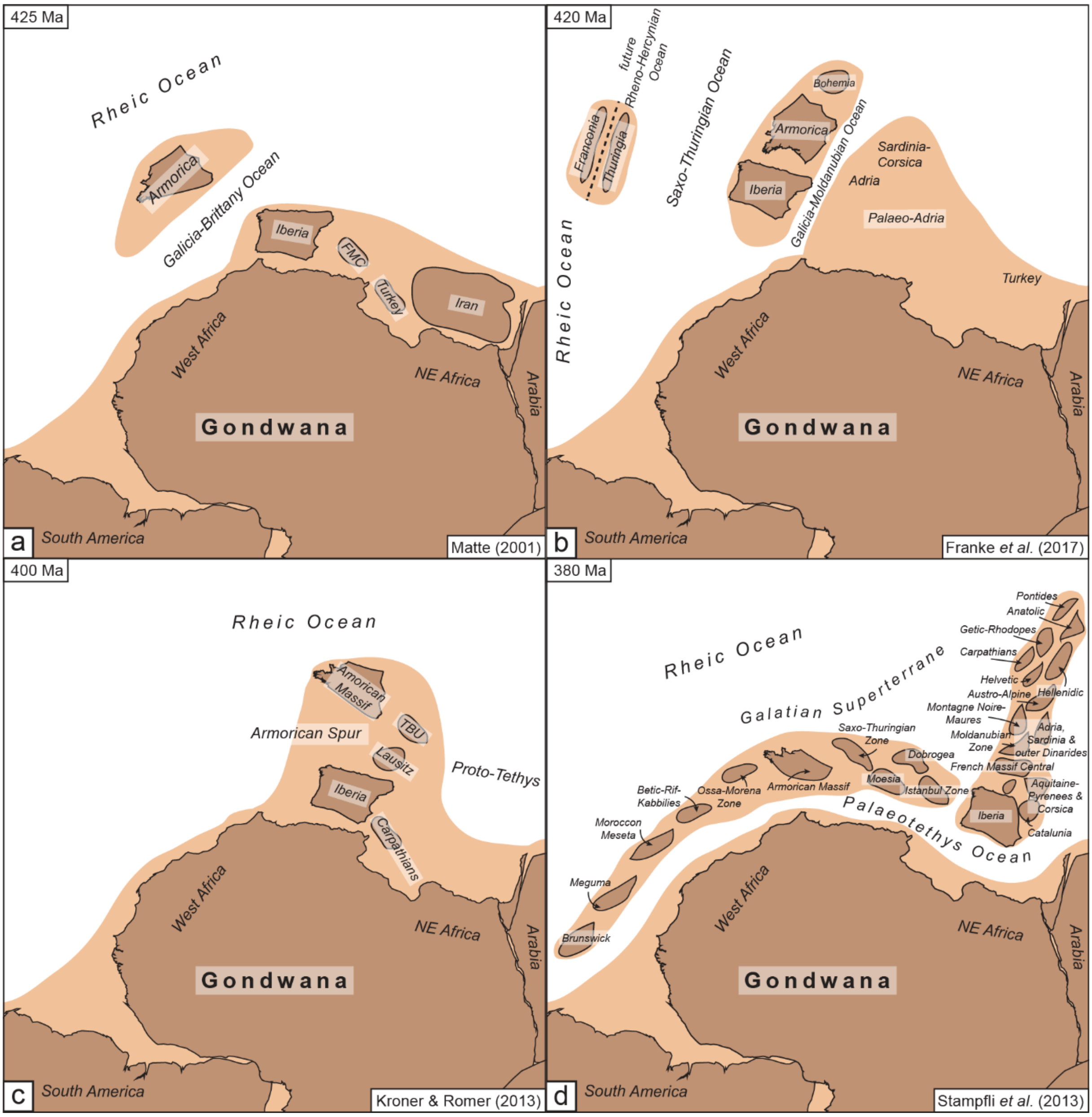

Figure 3: Tectonic models of pre-Pangean paleogeography and architecture of Peri-Gondwana from Matte (2001), Franke et al. (2017), Kroner & Romer (2013) and Stampfli et al. (2013). Note the different number of involved plates and oceans. Review from Stephan et al. (2019).

During the Devonian, the Rheic ocean is progressively closed and subducted beneath Laurussia in the North and beneath the Gondwana derived terranes in the South (Fig. 2d and e) (von Raumer and Stampfli, 2008; Stampfli et al., 2013; Franke et al., 2017). The subduction of the Rheic ocean beneath Laurussia yields to the formation of a back-arc basin evolving into an oceanic domain named Rhenohercynian ocean (Fig. 2d-e) (e.g. Zeh and Gerdes, 2010; Franke et al., 2017). The amplitude of the Rhenohercynian ocean is either differently considered as a narrow basin (e.g. Stampfli et al., 2013) or a large oceanic domain (e.g. Martinez Catalan et al., 2021). During the Late-Devonian and Early-Carboniferous times, the subduction of oceanic domains beneath the Gondwana derived terranes formed small back-arc basins (Lardeaux et al., 2014) (Fig. 2f). The continental collision between Laurentia, Gondwana and potential microcontinents (Fig. 2g) occurred during Carboniferous times and formed a Himalayan-Tibetan-like orogenic system (Maierova et al., 2016), followed by extension and lateral extrusion of material accommodated by the lithospheric-scale strike–slip faults (Fig. 2h) (e.g. Kroner and Romer, 2013; Stampfli et al., 2013; Ballèvre et al., 2018; Edel et al., 2018).

Despite the uncertainties about the numbers of oceans, sutures, microcontinents and discussed paleogeographic reconstructions, most of the geological community agrees on a current subdivision of the European Variscan belt into several domains. These domains are recognized from the Bohemian massif to the Northern Morocco and are named the Rhenohercynian, Saxothuringian, Ibero-Armorican and the Moldanubian zones (e.g. Matte, 1991; Lardeaux et al., 2014; Franke et al., 2017; Ballèvre et al., 2018; Martinez-Catalan et al., 2021) (Fig. 4). However, the exact limits of these domains, the location of sutures and the oceanic domain corresponding to the relictual sutures are still currently under the scientific discussion and widely debated.

The Rhenohercynian zone corresponds to the northern front of the Variscan belt and is formed of allochthonous Avalonian terranes thrusted on autochthonous Laurentia continent located in the North. It is characterized by low-grade rocks structured by folds and thrusts with kinematics towards the North. Its southern boundary corresponds to the Rhenohercynian and/or the Rheic oceanic sutures (e.g. Franke et al., 2017). The Moldanubian zone corresponds to the northern Gondwana margin and the Ibero-Armorica and Saxothuringian zones correspond to microcontinents separated by hypothetical oceanic sutures (e.g. Kroner and Romer, 2013; Schulmann et al., 2014; Paquette et al., 2017; Franke et al., 2017). The Moldanubian zone is often subdivided into Autochthonous and Allochthonous units (e.g. Franke et al., 2017), representing the northern Gondwana margin and the lower crust thrusted on it, respectively. The Ibero-Armorican, Saxothuringian and northern Moldanubian zones form the core of the orogen with numerous eclogitic occurrences and partially molten rocks (e.g. Vanderhaeghe et al., 2020; Paquette et al., 2017). The southern part of the Moldanubian zone is the southern foreland of the Variscan belt with folds and thrusts structures. At a large scale, the Variscan belt forms fan-like shape (Fig. 5) (e.g. Matte, 1991, 2001; Vanderhaeghe et al., 2020; Martinez-Catalan et al., 2021).

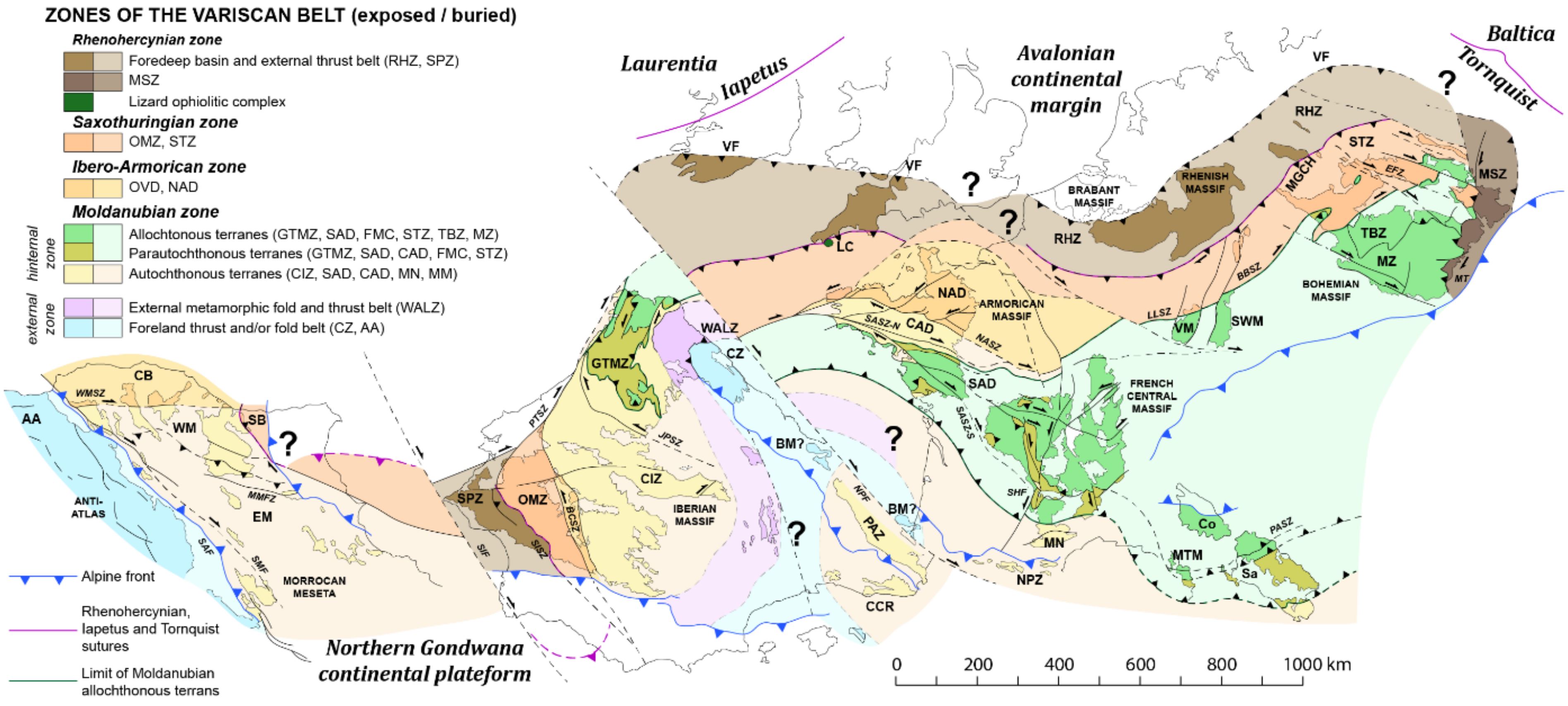
ZONES OF THE VARISCAN BELT (exposed / buried)
Rhenohercynian zone
Foredeep basin and external thrust belt (RHZ, SPZ)
MSZ
Lizard ophiolitic complex
Saxothuringian zone
OMZ, STZ
Ibero-Armorican zone
OVD, NAD
Moldanubian zone
hinternal zone
Allochtonous terranes (GTMZ, SAD, FMC, STZ, TBZ, MZ)
Parautochthonous terranes (GTMZ, SAD, CAD, FMC, STZ)
Autochthonous terranes (CIZ, SAD, CAD, MN, MM)
external zone
External metamorphic fold and thrust belt (WALZ)
Foreland thrust and/or fold belt (CZ, AA)
Alpine front
Rhenohercynian, Iapetus and Tornquist sutures
Limit of Moldanubian allochthonous terrans
Laurentia
Iapetus
Avalonian continental margin
Baltica
Tornquist
Northern Gondwana continental plateform
VF
VF
VF
?
?
?
?
?
?
RHZ
RHZ
STZ
MGCH
EFZ
MSZ
MT
TBZ
MZ
BOHEMIAN MASSIF
RHENISH MASSIF
BRABANT MASSIF
LC
NAD
ARMORICAN MASSIF
SASZ-N
CAD
NASZ
LLSZ
BBSZ
VM
SWM
SAD
SASZ-S
FRENCH CENTRAL MASSIF
SHF
WALZ
CZ
GTMZ
PTSZ
JPSZ
CIZ
IBERIAN MASSIF
SPZ
OMZ
BCSZ
SISZ
SIF
BM?
BM?
NPF
PAZ
CCR
MN
NPZ
Co
MTM
Sa
PASZ
AA
WMSZ
CB
WM
SB
ANTI-ATLAS
MMFZ
EM
SAF
SMF
MORROCAN MESETA
0
200
400
600
800
1000 km

Figure 4: Sketch of the Variscan belt in an early Permian reconstruction that postdates ductile and brittle transcurrence modified after Martinez-Catalan et al. (2021). ***Zones (Z) and massifs****: AA, Anti- Atlas; Armorican Domains (AD): CAD, Central; NAD, North; SAD, South; BAU, Beja-Acebuches Unit; BM, Basque Massifs; Bu, Buçaco; CB, Coastal Block; CIZ, Central Iberian; Co, Corsica; Cr, Crozon; CZ, Cantabrian; EM, Eastern Meseta; FMC, French Massif Central; GTMZ, Galicia-Trásos-Montes; LC, Lizard Complex; MGCH, Mid-German Crystalline High; MM: Moroccan Meseta; MN, Montagne Noire; MTM, Maures-Tanneron Massif; MSZ, Moravo-Silesian; MZ, Moldanubian; OMZ, Ossa-Morena; OVD, Obejo-Valsequillo Domain; RHZ, Rhenohercynian; Sa, Sardinia; SB, Sehoul Block; SPZ, South Portuguese; STZ, Saxo-Thuringian; SWM, Schwarzwald Massif; TBZ, Teplá-Barrandian; VM, Vosges Massif; WALZ, West Asturian-Leonese; WM, Western Meseta.* ***Shear zones (SZ), faults (F) and fault zones (FZ)****: BBSZ, Baden-Baden; BCSZ, Badajoz-Córdoba; BrF: Bray; EFZ, Elbe; JPSZ, Juzbado-Penalva; LLSZ, Lalaye-Lubine; MMFZ, Middle Meseta; MT, Moldanubian Thrust; NASZ, North Armorican; NEF, Nort-sur-Erdre; NPF, North Pyrenean; PASZ, Posada-Asinara; PTSZ, Porto-Tomar; SAF, South Atlas; SASZ, South Armorican (N and S, northern and southern branches); SHF, Sillon Houiller; SIF, South Iberia; SISZ, Southern Iberian; SMF, South Meseta; TTZ, Teisseyre-Tornquist Zone; VF, Variscan Front; WMSZ, Western Meseta.*

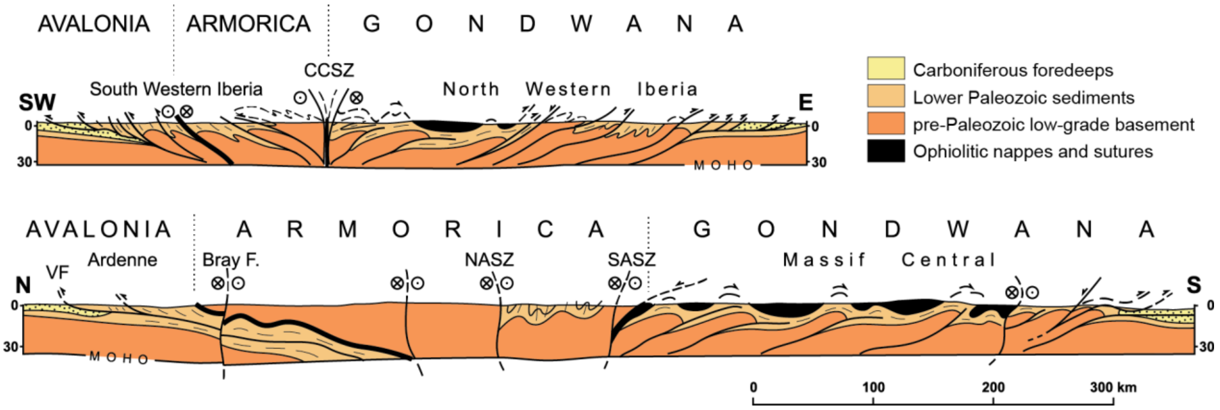

Figure 5: Two ultra-simplified cross-sections at crustal scale through the Variscan belt in Iberian Peninsula and France, without granites, showing the fan-like shape of the belt modified after Matte (2001). CCSZ, Coïmbra-Cordoba left-lateral Shear Zone; Bray SZ, NASZ and SASZ, Bray, North Armorican and South Armorican dextral Shear Zones; VF, Variscan Front.

2. The Variscan Pyrenees

The Variscan Pyrenees are located in the southern external domain of the Variscan belt (Fig. 4) and are considered as the southern orogenic foreland (Druguet, 2001; Laurent et al., 2017; Aguilar et al., 2013) based on Devonian to mid-Carboniferous deep-sea to platform sedimentation (Garcia-Sansegundo et al., 2011, and references therein) and lately turbiditic deposition (Delvolve and Perret, 1989). They are composed of the Pyrenean Axial Zone (PAZ) and the North Pyrenean Zone (NPZ) that are separated by the Variscan EW-striking North

Pyrenean Fault (NPF) (Fig. 4 and 6). These two zones are composed of Proterozoic to Paleozoic sedimentary rocks deformed and metamorphosed during the Variscan orogeny between middle Carboniferous to early Permian (Mezger and Gerdes, 2016; Denèle et al., 2014; Aguilar et al., 2013; Schnaperelle et al., 2020; Vacherat et al., 2017; Cochelin et al., 2021).

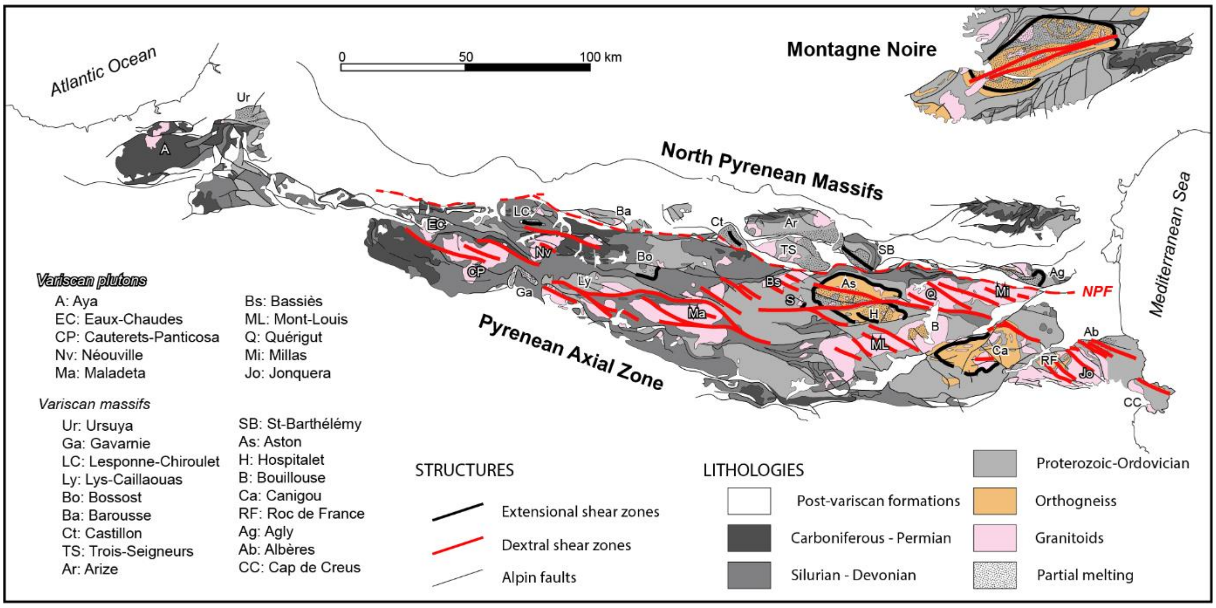

Figure 6: Map of the Variscan Pyrenees and of the Montagne Noire massif with main Variscan shear zones. NPF: North Pyrenean Fault.

In both PAZ and NPZ, the Variscan metamorphism is characterized by a high-temperature and low-pressure (HT-LP) gradient inducing the partial melting of the lower and middle crust in the amphibolitic facies in the PAZ and in the granulitic facies in the NPZ following a typical melt enhanced geotherm (Cochelin et al., 2021 and references therein). This thermal anomaly, dated at ca. 305-300 Ma (Denèle et al., 2014; Siron et al., 2020), is attributed to a high mantle flux associated with emplacements of numerous plutons (Guitard et al., 1996 and references therein), to a rifting stage (Wickham and Oxburgh, 1985, 1986, 1987) or two a slight crustal thickening with a thermal anomaly (Cochelin et al., 2021). This magmatism is characterized by numerous large calk-alkaline plutons in the upper crust, and mainly leucogranites and mafic sills in the middle crust (Denele et al., 2014; Kilzi et al., 2016; Vielzeuf et al., 2021) with hybrid to mantle sources (Debon et al., 1996; Lemirre et al., 2019) dated between ca. 305 and 290 Ma (Denele et al., 2014; Druguet et al., 2014; Kilzi et al., 2016; Lemirre et al., 2019; Vielzeuf et al., 2021). Visean-Serpukhovian magmatism is described in the PAZ (Mezger and Gerdes, 2016; Lopez-Sanchez et al., 2018; Schnapperelle et al., 2020). Permian magmatism at ca. 270 Ma is also documented in the NPZ (Denèle et al., 2012; Kilzi, 2014; Vacherat et al., 2017).

Two main variscan deformation phases are described in the PAZ. Firstly, a nappe stacking toward the south-west or the west responsible for moderate crustal thickening (de Höym de Marien et al., 2019) forming flat-lying foliations and recumbent or overturned folds (e.g. Carreras and Capella, 1994; Matte, 2002; Vilà et al., 2007; Denèle et al., 2009, 2014; Laumonier et al., 2010; Aguilar et al., 2015; Cochelin et al., 2017) (Fig. 7A). This age of this deformation is not constrained but is often interpreted as mid-Carboniferous (e.g. Denèle et al., 2014; Cochelin et al., 2021). This deformation is followed by a dextral transpressive regime D2 inducing a lateral flow of the molten crust toward the east (Fig. 7B) (Denèle et al., 2009; Cochelin et al., 2017, 2021) decoupling the orogenic crust between an Infrastructure and a Suprastructure, molten and unmolten respectively (de Sitter & Zwart, 1960). The continuation of the transpression formed several gneiss-domes in the infrastructure and vertical foliations in the suprastructure (Cochelin et al., 2017) (Fig. 7C). The transpression also formed dextral reverse shear zones allowing emplacement of large plutons in the upper crust (Fig. 6; Gleizes et al., 1997, 1998a, 2001; Denèle et al., 2009, 2014; Laumonier et al., 2010; Cochelin et al., 2017, 2021). Several flat extensional shear zones are also described (Fig. 6; Gibson, 1991; Vissers, 1992; Mezger and Passchier, 2003; Le Bayon and Cochelin, 2020) that are interpreted as evidence for transtensional exhumation of migmatitic dome in a global transpressional regime (Cochelin et al., 2017).

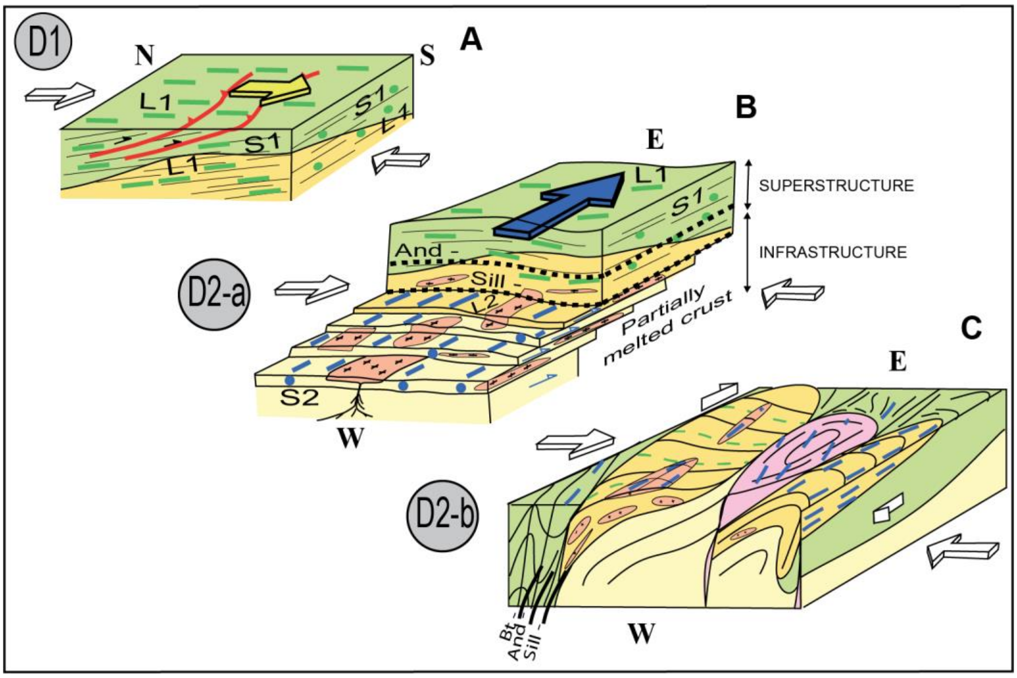

Figure 7: Reconstitution of the Variscan tectonic and magmatic events in the Aston and Hospitalet domes located in the Pyrenean Axial Zone from Denèle et al. (2014).

In the NPZ, the main fabric is a penetrative flat-lying foliation that developed during retrogressive metamorphism during a continuous extensional event (de Saint Blanquat et al., 1990; Bouhallier et al., 1991). This deformation also formed extensive shear zones accommodating important crustal thinning (Delay, 1989; Siron et al., 2020) with top-to-the-north and top-to-the-south kinematics (Bouhallier et al., 1991; de Saint-Blanquat et al., 1993; Olivier et al., 2004). A transpressional setting is also proposed in some massifs (Leblanc et al., 1996; Gleizes et al., 1998; Olivier et al., 2004, 2008). Nevertheless, some authors consider that these flat-lying shear zones do not belong to the Variscan orogeny but were formed during the Cretaceous rifting affecting the NPZ (e.g. Paquet and Mansy, 1991, 1992; Vauchez et al., 2013a) and that this extension could have (re)granulitized the lower Variscan crust (Clerc and Lagabrielle, 2015).

3. The Variscan basement of the Alps

3.1.Subdivision of the Alpine Paleozoic basement

The Paleozoic basement outcrops heterogeneously in the Alps but it represents half of the Alpine domain (Fig. 8a) (von Raumer et al., 2013). Due to the alpine tectonics obliterating the former Variscan tectono-metamorphic events and their relationship geometry, the Variscan basement of the Alps is not included in most of precise Variscan paleogeographic reconstitutions (Fig. 4) (e.g. Martinez-Catalan et al., 2021; Franke et al., 2017; Lardeaux et al., 2014; Faure et al., 2014b). In larger reconstitutions, it is commonly assumed that this basement was a part of the Northern Gondwana and therefore belongs intrinsically to the Moldanubian zone (Fig. 2) (von Raumer et al., 2002, 2015; Stampfli et al., 2002, 2013; Ballèvre et al., 2018). However, the Paleozoic basement of the Alps is subdivided into four lithotectonic domains (e.g. Schmid et al., 2017) that have been defined at the lithospheric scale for the Alpine belt (Fig. 8a): the Helvetic, the Penninic, the Austroalpine and the South Alpine domains. The Helvetic domain represents the autochthonous European margin (e.g. Lemoine et al., 1986; Ballèvre et al., 2018; van Hinsbergen et al., 2019) (Fig. 9). The Penninic domain is composed of various allochthonous nappes that derived from the distal European margin (e.g. the Tauern Window basement nappes; Schmid et al., 2013), the Valaisan basin and the Briançonnais microplate in the western and central Alps (e.g. Manzotti et al., 2014, 2016; Jacob et al., 2020) (Fig. 9). The Austroalpine domain is composed of allochthonous nappes (e.g. Sesia-Dent-Blanche zone, Schmid et al., 2017, and in the Austrian part, Kurz and Fritz, 2003) that form the remnants of the southern margin of Piemonte–Liguria Ocean along the Apulian plate, under which the Penninic nappes have been under-thrusted (Fig. 9). Finally, the south Alpine domain forms the autochthonous part of the Apulia plate (Ballèvre et al., 2018; Schmid et al., 2017) (Fig. 9).

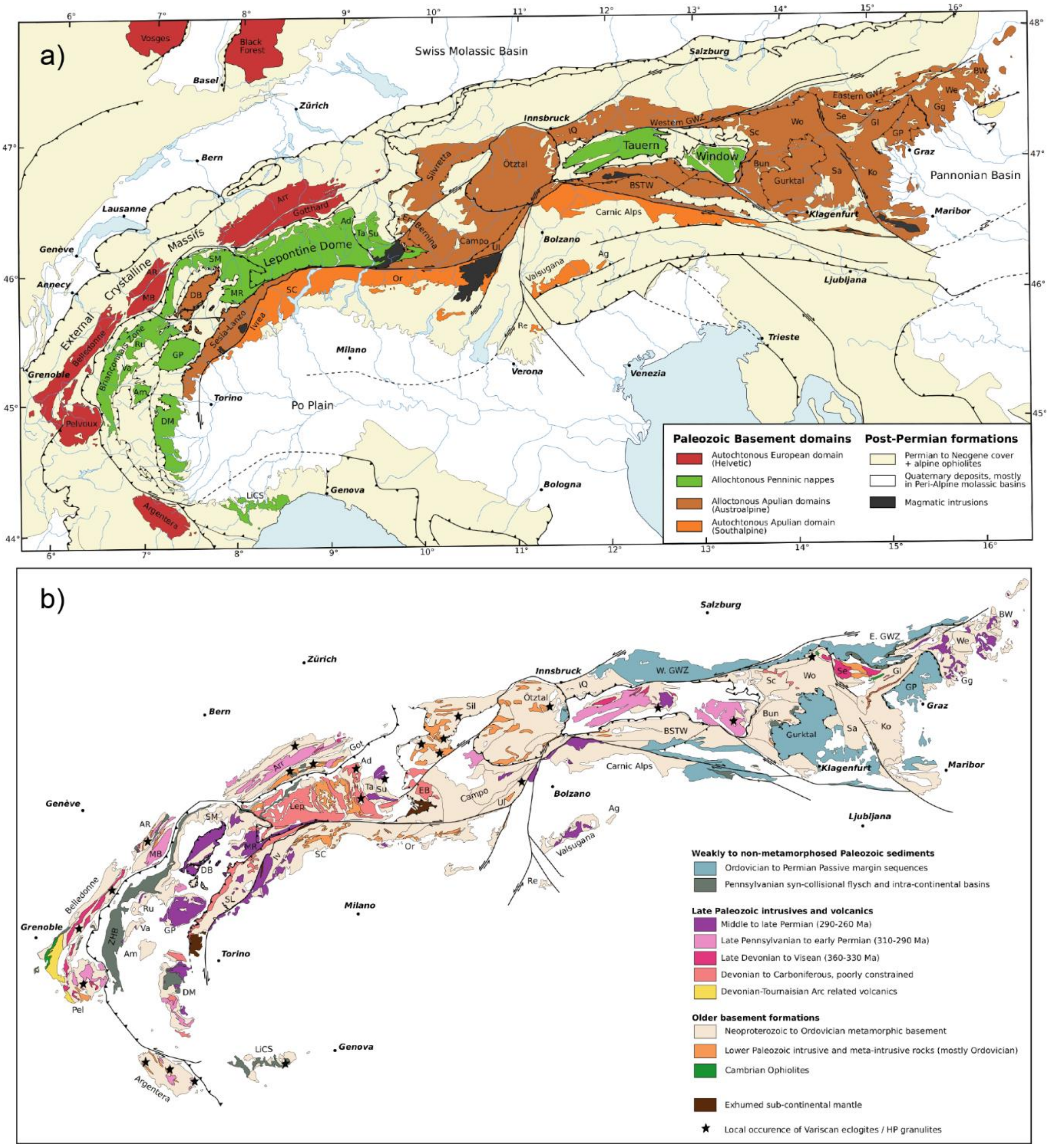

Figure 8: (a) Paleozoic basement units in the Alps in their current tectonic setting and classified according to the Alpine lithotectonic domain to which they belong (i.e., Helvetic, Penninic, Austroalpine, south Alpine) from Jacob et al. (2020). For clarity, no distinction of the lithotectonic domains is made for the post-Permian units, which group the Permian to Neogene sedimentary sequences and the Alpine ophiolites. (b) Simplified geological map of the lithological units within the pre-Mesozoic basement of the Alps from Jacob et al. (2020). From southwest to northeast: LiCS, Ligurian, Calizzano–Savona; DM, Dora–Maira; Pel, Pelvoux; Am, Ambin massif; ZHB, Zone Houillère Briançonnaise; Va, Vanoise; GP, Gran Paradiso; SL, Sesia–Lanzo; Ru, Ruitor; AR, Aiguilles Rouges;

MB, Mont Blanc; DB, Dent Blanche; SM, Siviez–Mischabel; MR, Monte Rosa; Iv, Ivrea Zone; SC, Strona–Ceneri zone; Lep, Lepontine dome; Ad, Adula nappe; Ta, Tambo nappe; Su, Suretta nappe; Got, Gotthard massif; Or, Orobic Alps; EB, Err–Bernina nappe; Sil, Silvretta nappe; Ul, Ulten zone; Re, Recoaro; Ag, Agordo; IQ, Innsbruck Quartzite; BSTW, Basement units south of the Tauern Window; Sc, Schladming nappe; Bun, Bundschuh nappe; Wo, Wölz nappe; Sa, Saualpe; Ko, Koralpe; Se, Seckau nappe; Gl, Gleinalm; GWZ, Grauwacken Zone; GP, Graz Paleozoic; Gg, Grobgneiss; We, Wechsel; BW, Bucklige Welt.

These four different Paleozoic domains have been variously overprinted by Alpine tectono-metamorphic events (Fig. 9) (Bousquet et al., 2004; Schmid et al., 2004). In the Helvetic Zone, the pre-Mesozoic basement crops out in several massifs named the External Crystalline Massifs (ECMs). These ECMs consist of tilted basement blocks bounded by Jurassic high-angle normal faults (Lemoine, 1985; Lemoine & Trümpy, 1987; Lemoine et al., 1986, 1981) perhaps reactivated during the Alpine collision (Bellahsen et al., 2012, 2014; Gidon, 2001; Gillcrist et al., 1987). The Alpine deformation in these basement windows is weak and heterogeneous, and is localized in subgreenschist- to greenschist-facies shear zones (e.g. Marshall et al., 1998; Rossi et al., 2003; Rolland et al., 2005; Filippi et al., 2020) of Oligocene age (Egli et al., 2016, 2017). The Alpine metamorphism is slightly higher in the eastern Helvetic basement (i.e. the Aar – Gothard massif) where it reaches upper greenschist- to lower amphibolite-facies (see references in Goncalves et al., 2012; Girault et al., 2020). Because the Alpine ductile deformation and associated metamorphism are not pervasive, the Variscan or pre-Variscan geodynamic evolution can easily be investigated (von Raumer and Bussy, 2004; Ballèvre et al., 2018).

Between the Penninic thrust and the Periadriatic fault, the Penninic and Austroalpine domains are composed of allochthonous nappes that show various degrees of Alpine metamorphic overprint. In the Western part of the Penninic zone comprising the former Briançonnais microcontinent, metamorphism ranges from lower greenschist in the more external units, to high-pressure–ultrahigh-pressure eclogite facies in the internal units (Ganne et al., 2007; Le Bayon & Ballèvre, 2006; Manzotti et al., 2015, 2016). The Sesia – Dent-Blanche zone, belonging to the western Austroalpine domain, also recorded an Alpine eclogitic metamorphism (Manzotti et al., 2014 and references therein). However, some part of the Dent Blanche domain was mainly preserved of the alpine metamorphism and shows a large cross-section of the pristine Variscan continental crust (Gardien et al., 1994). Re-equilibration along a Barrovian gradient occurred in the Central and Eastern Alps in the Penninic domain, that led to the development of metamorphic assemblages of amphibolite facies associated with migmatization (Bousquet et al., 2004). Due to the pervasive and polyphased Alpine deformation in these areas, undeformed Variscan volumes are relatively modest in size and allow only limited deductions about the large-scale structure of the Paleozoic basement of the Penninic and Austroalpine domain. At last, the South-Alpine basement has been only locally reworked during the Alpine orogeny, and pre-Alpine structures are well preserved (e.g. Siletto et al., 1993; di Paola and Spalla, 2000).

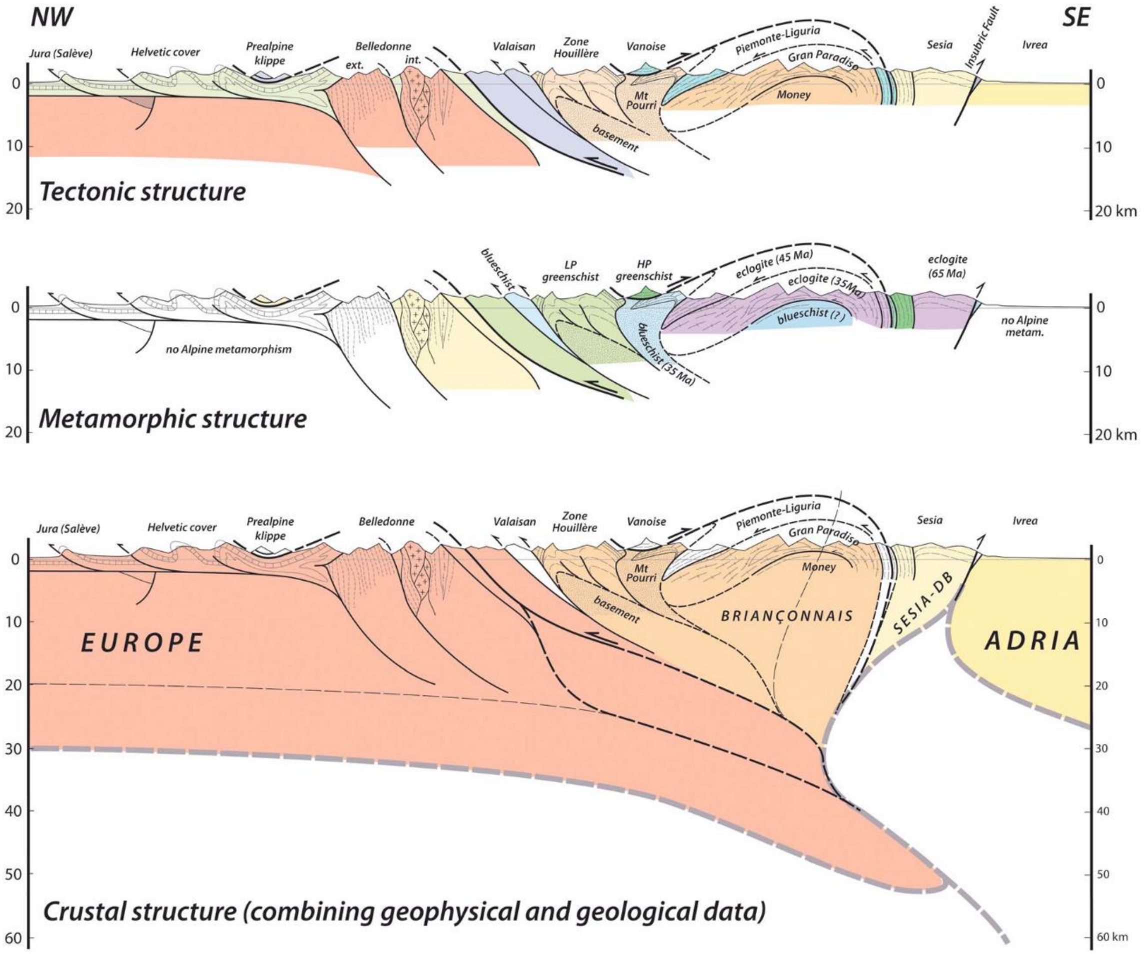

Figure 9: Schematic cross sections from Ballèvre et al. (2018) illustrating the key tectonic features of the Western Alps. Emphasis is put on the four main domains of continental crust, namely, Europe (Helvetic domain), Briançonnais (Penninic domain), Sesia-Dent Blanche (DB) (Austroalpine domain), and Adria (South Alpine domain). LP = low pressure; HP = high pressure.

The pre-Alpine tectono-metamorphic events also differ from an alpine domain to another one. The pre-Alpine basement from the Helvetic Zone is mainly composed of Neoproterozoic – Cambrian sedimentary rocks intruded by large granitic orthogneisses (Bussy et al., 2011). An eclogite-facies (or high-pressure (HP) granulite-facies) event is recorded in mafic bodies from the ECMs (Colombo et al., 1994; Ferrando et al., 2008; Latouche & Bogdanoff, 1987; Paquette et al., 1989; Liégeois & Duchesne, 1981; Jacob et al., 2021; Jouffray et al., 2020). The age of the HP metamorphism is still rather uncertain and has been thought to occur during Ordovician (Abrecht et al., 1991; Abrecht & Biino, 1994; Biino, 1994, 1997; Berger et al., 2017; Gebauer, 1990, 1993; Gebauer et al., 1988; Oberli et al., 1994) or Silurian – Devonian times (Paquette et al., 1989). Recent data also suggest a Carboniferous age (340-330 Ma) for this HP event (Rubatto et al., 2001, 2010; Jacob et al., 2020). The metamorphic evolution then proceeds toward lower pressure, with extensive development of partial melting in appropriate lithologies (Bussy et al., 2000; Genier et al., 2008; Schulz & von Raumer, 1993, 2011; Fréville et al., in review). Local domains from the western part of ECMs display low-grade metasedimentary rocks, probably Visean in age (Fréville et al., 2018). They are associated with Late-Devonian – Early Carboniferous bimodal magmatic suites (Ménot et al., 1987; Ménot, 1986, 1987; Pin and Carme, 1987; Dobmeier et al., 1999; Guillot and Ménot, 2009; Fréville et al., 2018, in review) and an ophiolite complex (Bodinier et al., 1981; Guillot et al., 1992; Ménot et al., 1988a, 1988b). The ECMs are intruded by numerous Late Carboniferous granitic rocks (Fig. 8b) (Bussien Grosjean et al., 2017; Bussy et al., 2000; Debon & Lemmet, 1999; Schaltegger, 1990, 1993, 1994; Schaltegger & Corfu, 1992; Schaltegger & von Quadt, 1990; Rubatto et al., 2001; Fréville, 2016).

In the Penninic zone, the pre-Alpine history is recognized in several outcrops displaying various tectono-metamorphic grade. In the Briançonnais Zone, some units do not show evidence of Variscan metamorphism and tectonics (Mosca et al., 2008; Ballèvre et al., 2018). These Cambro-Ordovician formations do not show, or preserve, relics of a pre-Alpine metamorphism, probably because it has taken place at low grade. Other pre-Triassic basement complexes in the Penninic Zone are polycyclic and recorded pre-Alpine amphibolite facies conditions. These highest metamorphic grades being defined by garnet-staurolite-biotite (± sillimanite, ± feldspar) assemblages (e.g. Le Bayon et al., 2006; Compagnoni & Rolfo, 2003; Ballèvre et al., 2018 and references therein). They were dated between 350-300 Ma (Monié, 1990; Giorgis et al., 1999; Bussy et al., 1996). Several occurrences of eclogite relicts are described all along the Penninic zone (Fig. 8b) (Droop, 1983; Nussbaum et al., 1998; Biino et al., 1997; Eisele et al., 1997; Rahn, 1991; Sartori, 1990; Thélin et al., 1990; Cortesogno et al., 1997; Gaggero et al., 2004; Giacomini et al., 2007; Messiga et al., 1992; Dale and Holland, 2003). Their ages are estimated at 330-340 Ma and 370 Ma (Liati et al., 2009), or 390-375 Ma (Giacomini et al., 2007). The last stages of the regional metamorphism are recorded by the late development of cordierite-rich partial melts. Despite the numerous occurrences of pre-Alpine metamorphism, P-T estimations and geochronological data on these metamorphic events in the

Penninic zone remain scarce. This zone contains several magmatic intrusions emplaced during Cambrian (Guillot et al., 1991; Bertrand et al., 2000), Ordovician (Bertrand & Leterrier, 1997; Guillot et al., 2002; Liati et al., 2009; Gauthiez et al., 2011) and Late-Devonian (Bertrand et al., 1998). Furthermore, a post-Variscan widespread magmatism took place in this domain during Permian times (Fig. 8b) (see review in Ballèvre et al., 2018).

In the Austroalpine zone, the pre-Mesozoic basement consists of crustal units displaying a HT-LP (amphibolite- to granulite-facies) metamorphism (Gardien et al., 1994; Pennachioni & Cesare, 1997; Lardeaux et al., 1982; Lardeaux and Spalla, 1991; Schuster et al., 2001; Manzotti & Zucali, 2013; Manzotti, et al., 2014) of Permian age (Kunz et al., 2018), and of granitoids and few gabbros, also of Permian age (Bussy et al., 1998; Paquette et al., 1989; Rubatto et al., 1999; Manzotti et al., 2017a, 2017b; Monjoie et al., 2007). The identification of pre-Permian events in the Austroalpine domain is still a matter of debate. However, Cambrian, Silurian and Early-Carboniferous igneous rocks have been dated in the pre-Alpine basement (Müller et al., 1996; Liermann et al., 2002; Rubatto et al., 1998, 1999). Few eclogitic lenses have been identified (Godard et al., 1996; Hauzenberger et al., 1996) and are thought to be Variscan (i.e. between 370 and 330 Ma) (Miller and Thöni, 1995; Thöni, 2002; Tumiati et al., 2003; Konzett et al., 2005) or pre-Variscan in age (Faryad et al., 2002). Some paragneisses display HT-LP parageneses dated at 345-330 Ma (Thöni, 2002).

South-Alpine domain constitutes a well-preserved section of the Late-Permian tectono-metamorphic evolution (e.g., Henk et al., 1997; Pistone et al., 2017; Zingg, 1990). The Ivrea-Verbano Zone, in the western South-Alpine domain, displays a tilted metamorphic sequence ranging from amphibolite to granulite facies (Hunziker & Zingg, 1980; Zingg, 1990), intruded by a large Permian mafic body (Garuti et al., 2001; Pin, 1986; Peressini et al., 2007). Further east, the South-Alpine domain essentially consists of Early Paleozoic protoliths metamorphosed and deformed into amphibolite-facies orthogneisses and paragneisses (Zurbriggen et al., 1997). An Early Paleozoic age is proposed for this deformation event (Franz & Romer, 2007; Zurbriggen, 2015). This domain is intruded by nearly undeformed Permian granitoids (Bakos et al., 1990; Klötzli et al., 2014; Pinarelli et al., 1988; Pinarelli & Boriani, 2007; Quick et al., 2009; Pohl et al., 2018). The Permian high-thermal event recorded in the Penninic, Austroalpine and South-Alpine domains is attributed to a lithospheric thinning accompanied by magmatic underplating induced by the opening of future Alpine oceanic domains (Bertotti et al., 1993; Marquer et al., 1998; Schuster et al., 2001; Schuster and Stüwe, 2008; Ballèvre et al., 2018; Casini et al., 2015).

These various pre-Alpine histories recorded in the four tectonic domains of the Alps highlight a late or post-Variscan juxtaposition of various Variscan tectono-metamorphic domains that may be the results of late-Variscan, Permian, Mesozoic and Tertiary Alpine tectonics (e.g. von Raumer et al., 2015; Schmid et al., 2017; Pohl et al., 2018; Haas et al., 2020). In this study, we focus on the zone that was the less affected by these post-Variscan deformation and displacements, i.e. the autochthonous Helvetic domain, where the Alpine overprint is limited to the greenschist facies and the deformation is restricted in local shear zones easily depicted in the field, enabling the study of the pre-Alpine history.

3.2.The Helvetic domain of the Alps

The Helvetic domain outcrops in the External Crystalline Massifs of the Alps (ECMs)and is composed from North to South of the Aar – Gothard, Aiguilles-Rouges – Mont-Blanc, Belledonne, Grandes-Rousses, Pelvoux and Argentera massifs (Fig. 10). These massifs can be subdivided into three main domains, i.e. western, central and eastern domains (Guillot and Ménot, 2009).

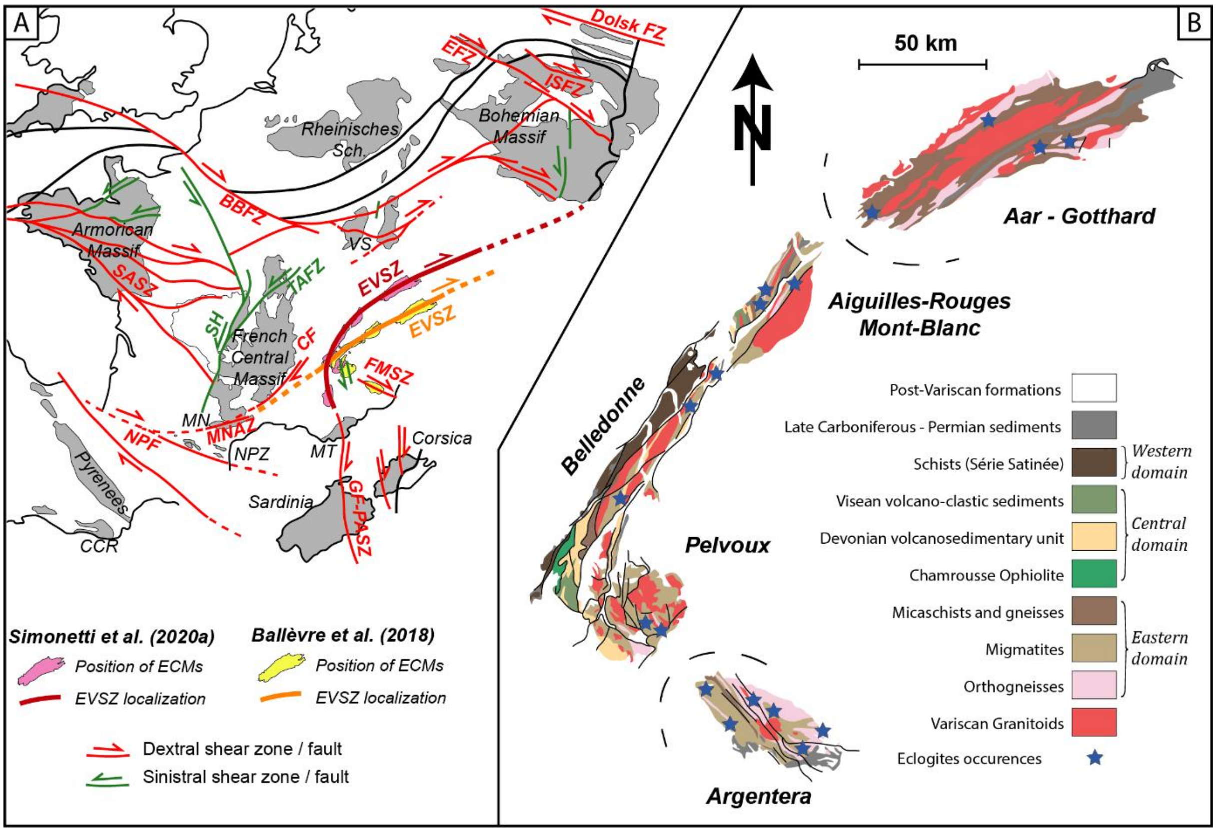

Figure 10: (A) Paleogeographic reconstitution of the European Variscan Belt at the end of the Variscan orogeny modified from Franke et al. (2017). Sardinia and Corsica have the same position as the one used in Simonetti et al. (2020a, 2020b). Models of the EVSZ are after Simonetti et al. (2020a) and Ballèvre et al. (2018). The position

of ECMs is after Bellahsen et al. (2014) in the Ballèvre et al. (2018) model. ***Massifs****: CCR: Catalan Coastal Ranges; MN: Montagne Noire; NPZ: North Pyrenean Zone; VS: Vosges-Schwarzwald;* ***Fault (F), Fault Zone (FZ) and Shear Zone (SZ)****: BBFZ: Bristol Bray; CF: Cévennes; EFZ: Elbe; EVSZ: Eastern Variscan; FMSZ: Ferrière-Mollière; GF-PASZ: Grimault - Posada-Asinara; ISFZ: Intra-Sudetic; MNAZ: Montagne Noire Axial Zone; NPF: North Pyrenean; SASZ: South Armorican; SH: Sillon Houiller; TAFZ: Taure-Aigueperse. (B) Geological map of the Variscan basement of the External Crystalline Massifs in the French and Swiss Alps with eclogitic occurrences*

3.2.1. The western domain

The western domain crops out in the Western part of the Belledonne massif (Fig. 10 and 11). It is composed of low metamorphic grade quartz-feldspar sandstones and two-mica bearing micaschists, considered as an ancient turbiditic formation (Bordet and Bordet, 1963), with rare intercalations of basic layers (Ménot, 1988a), named the Série Satinée. It is separated from the rest of the Belledonne massif by the Synclinal Median dextral strike-slip Fault (SMF) (Bordet and Bordet, 1963; Simeon, 1979) (Fig. 11). Recent U-Pb geochronology on detrital zircon from a sandstone highlights that this series is younger than ca. 460 Ma (Fréville et al., 2018), and does not record any Variscan age (i.e. 380-300 Ma) suggesting an Ordovician-Silurian age for this formation. Carboniferous granitoid intrusions are absent in this domain.

3.2.2. The central domain

The central domain outcrops in the western Pelvoux ("Cortical Pelvoux"), the SW Belledonne, the western Grandes-Rousses and the SW Aiguilles-Rouges massifs (Fig. 10) (Guillot and Ménot, 2009; Fréville et al., in prep). It is best described in the SW Belledonne massif and in the Cortical Pelvoux where it is composed of a pre-Alpine nappe pile (Fig. 11) (Fréville et al., 2018) detailed as follows:

The ophiolitic complex of Chamrousse is a kilometre-scale slab of an oceanic lithosphere (Guillot et al., 1992) that may have formed in a back-arc basin (Pin and Carme, 1987; Ménot et al., 1988a; Guillot and Ménot, 2009; Guillot et al., 2009). The ophiolite succession is tectonically inversed with gabbros and a leptyno-amphibolitic complex at the bottom and serpentinized ultramafic rocks at the top (Bodinier et al., 1981; Ménot et al., 1988b). The leptyno-amphibolitic complex has been dated at 497 ± 24 Ma and 496 ± 6 Ma by Sm-Nd on garnet (Pin and Carme, 1987) and U-Pb on zircon (Ménot et al., 1988b), respectively. The Chamrousse complex is affected by a metamorphism estimated at 0.3–0.4 GPa and 500–600 °C and associated to the initial rifting stage (Guillot et al., 1992), whereas Fréville et al. (2018) calculated a low-temperature – medium-pressure metamorphism around 0.55 GPa and 430 °C that they attributed to the thrusting of the ophiolite during Devonian time. Ultramafites rocks are also found in the others ECMs but they occur as meter-scale lenses included in quartzo-feldspathic migmatitic gneisses (Pfeiffer et al., 1993). They are interpreted as metamorphic differentiation phenomena related to the mobilization of quartzo-feldspatic gneisses under intense deformation (“Schollenamphibolite”, Abrecht, 1980) or could be related to mafic-ultramafic layers of a lower crust calc-alkaline intrusion (Abrecht et al., 1991; Pfeiffer et al., 1993). A larger occurrence of ultramafic rock crops out in the Gothard massif and is interpreted as a remnant of an ophiolite (Abrecht et al., 1991) of Ordovician age (Grauert & Arnold, 1968).

The Rioupéroux-Livet unit consists of bimodal suites of volcanic and plutonic rocks and of volcano-sedimentary rocks (Ménot, 1988a) composed of an alternation of plagioclase-rich leucocratic beds, felsic metavolcanics, metapelites and rare marbles (Fréville et al., 2018) (Fig. 11). Similar rocks are described in the Cortical Pelvoux (Fréville et al., in review), in the Grandes-Rousses massif (Guillot and Ménot, 2009) and in the SW Aiguilles-Rouges (Dobmeier et al., 1999). The magmatic suites include basic and felsic magmas. The metagreywackes from the volcano-sedimentary rocks are intruded by trondhjemitic sills dated at 367-362 Ma by K/Ar on amphibole (Ménot et al., 1985, 1987; Ménot, 1986), and at 367± 17 Ma, 352 ± 55 Ma and 352 ± 1 Ma by U-Pb on zircon (Ménot et al., 1985; Ménot, 1988b; Fréville et al., in review). The origin of this bimodal magmatism of the Rioupéroux-Livet has been interpret as an active continental margin such a back-arc basin (Carme and Pin, 1987; Guillot and Ménot, 2009; Guillot et al., 2009) or as a continental extensional setting (Vivier et al., 1987; Ménot, 1988b).

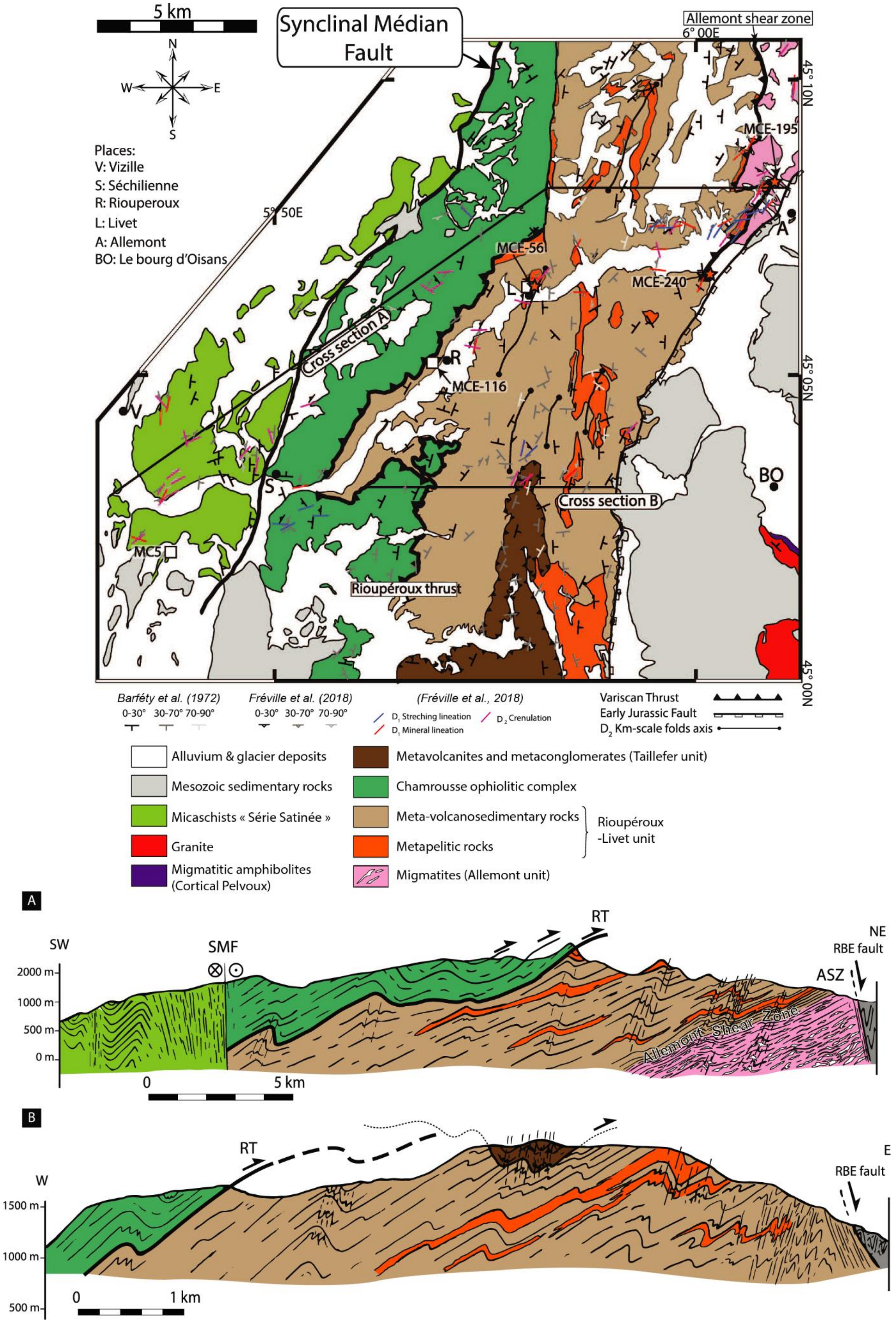
5 km
Synclinal Médian Fault
Allemont shear zone
6° 00E
N
W
E
S
Places:
V: Vizille
S: Séchilienne
R: Riouperoux
L: Livet
A: Allemont
BO: Le bourg d'Oisans
5° 50E
45° 10N
45° 05N
45° 00N
MCE-195
MCE-56
MCE-240
MCE-116
MC5
A
A'
V
S
R
L
BO
Cross section A
Cross section B
Rioupéroux thrust
Barféty et al. (1972)
0-30° 30-70° 70-90°
Fréville et al. (2018)
0-30° 30-70° 70-90°
(Fréville et al., 2018)
D1 Streching lineation
D1 Mineral lineation
D2 Crenulation
Variscan Thrust
Early Jurassic Fault
D2 Km-scale folds axis
Alluvium & glacier deposits
Mesozoic sedimentary rocks
Micaschists « Série Satinée »
Granite
Migmatitic amphibolites (Cortical Pelvoux)
Metavolcanites and metaconglomerates (Taillefer unit)
Chamrousse ophiolitic complex
Meta-volcanosedimentary rocks
Metapelitic rocks
Rioupéroux -Livet unit
Migmatites (Allemont unit)
A
SW
SMF
RT
NE
RBE fault
ASZ
Allemont Shear Zone
2000 m
1000 m
500 m
0 m
0
5 km
B
W
RT
E
RBE fault
1500 m
1000 m
500 m
0
1 km

Figure 11: Geological map and cross-sections of the Southwestern part of the Belledonne Massif from Fréville et al. (2018). The cross-sections are shown by lines A and B. SMF: Synclinal Median Fault; ASZ: Allemont Shear Zone; RBE: Rivier Belle Etoile fault; RT: Rioupéroux Thrust.

In the Cortical Pelvoux and SW of the Belledonne massif, the peak of metamorphic conditions induced by the nappe stacking in the central domain has been estimated at 0.8 ± 0.2 GPa and 590 ± 60 °C (Fernandez et al., 2002; Guillot and Ménot, 1999) and ca. 0.6 GPa and 600 °C (Fréville et al., 2018). This metamorphic event was followed by strike-slip shearing under near isothermal decompression from 0.7 ± 0.2 GPa and 590 ± 60 °C (Fernandez et al., 2002; Guillot and Ménot, 1999) to ca. 0.45 GPa and 550 °C (Fréville et al., in review) before reaching a late retrogression under greenschist facies conditions (Fernandez et al., 2002; Guillot and Ménot, 1999; Fréville et al., in review). The Rioupéroux-Livet unit is underlain by the Allemont migmatitic unit (Fig. 11) composed of garnet-bearing metatexites and migmatitic gneisses (Guillot and Ménot, 1999). The two units are separated by the Allemont shear zone resulting from the Variscan nappe stacking (Fréville et al., 2018). The anatectic event has been firstly interpreted as a late-orogenic collapse setting (Fernandez et al., 2002; Guillot and Ménot, 1999), but have been reinterpreted recently as resulting from the nappe stacking stage inducing a peak of metamorphic conditions at 0.8 GPa and 680 °C (Fréville et al., 2018, in review). Based on K-Ar dating on amphibole (Ménot et al., 1987), granitoid emplacement ages (Debon et al., 1998) and U-Pb dating on monazites (Fréville et al., 2018, in review), the peak of metamorphism induced by the nappe stacking is estimated between 340 and 330 Ma (Guillot et al., 2009; Fréville et al., 2018, in review). The metamorphic gap observed between the Chamrousse ophiolitic complex and the Rioupéroux-Livet unit is explained by the thrusting of the former upon the latter.

The Taillefer unit is composed of siltstones, sandstones, conglomerates and bimodal volcanic rocks (Ménot, 1988a; Fréville et al., 2018). Based on plant fossil fragments, an upper Visean age (i.e. 335-325 Ma) is proposed (Gibergy, 1968). U-Pb geochronology on detrital zircon from a microconglomerate yield a maximum age of 395 ca. Ma (Fréville et al., 2018). The Taillefer unit is affected by a greenschist facies metamorphism coeval with ductile deformation (Barfety et al., 1972). The Taillefer unit tectonically overlies the Rioupéroux-Livet unit (Carme, 1965), and both units were involved in the same tectonic-metamorphic event (Fréville et al., 2018) (Fig. 11). On the basis of the geochemical tholeiitic signature with evidence for crustal contamination of the magmatic rocks, the Taillefer unit was interpreted as emplaced in a continental extensional setting (Vivier et al., 1987). On the same line, Ménot

(1988b) proposed on intraplate origin associated to the opening of pull-apart basin. Similar bimodal magmatic suite and Visean metasedimentary rocks are also described in the SW Aiguilles-Rouges massif (Laurent, 1967; Bellière and Streel, 1980; Dobmeier et al., 1999) which has been interpreted as a continental volcanic arc related to subduction process and associated with continental extension (Dobmeier et al., 1999).

3.2.3. The eastern domain

The Eastern domain is the most represented one and forms the Argentera, the eastern Pelvoux ("Inner Pelvoux"), the eastern Grandes-Rousses, the NE Belledonne, the NE Aiguilles-Rouges, the Mont-Blanc and the Aar – Gothard massifs (Fig. 10).

This domain is mainly composed of Ediacarian sedimentary rocks (metapelites, metagreywackes and few marbles layers) and volcano-sedimentary rocks intruded by Ordovician laccoliths (Bussy and von Raumer, 1994; von Raumer et al., 2002; Bussy et al., 2011). These sedimentary and igneous rocks have strongly been affected by the Variscan orogeny. The most common orthogneiss facies is represented by the augengneisses displaying a peraluminous granodioritic or monzonitic geochemistry and bearing large K-feldspar megacrystals. Some orthogneisses show amphibole-biotite parageneses with metaluminous granodioritic to tonalitic geochemistry (von Raumer and Bussy, 2004). These orthogneisses have alkaline to calc-alkaline geochemical signatures (see references in Guillot et al., 2009).

In addition, several meter-scale to hectometre-scale lenses of metabasic rocks are described in all the ECMs (Pfeiffer et al., 1993; Paquette et al., 1989; Ménot & Paquette, 1993). In the most of the ECMs, these metabasites mostly display a MORB-type geochemical signature. Their protoliths are interpreted as tholeiitic intrusions emplaced within a thin continental crust during continental rifting (Paquette et al., 1989; von Raumer et al., 1990; Ménot & Paquette, 1993; Rubatto et al., 2010; Liégeois & Duchesne, 1981) or as MORBs contaminated by continental crust components (Jouffray et al., 2020). In the Aar-Gothard massifs, mafic protoliths have been interpreted as metabasalts with ophiolitic affinity while metagabbros show an island arc affinity (Biino & Meisel, 1993; Pfeiffer et al., 1993). Their protolith ages have been determined by U-Pb on zircon dating (ID-TIMS and LA-ICPMS) between ca. 483 Ma and 453 Ma (Paquette et al., 1989; Oberli et al., 1994; Rubatto et al., 2001; Schaltegger et al., 2003; Rubatto et al., 2010; Bussy et al., 2011; Fréville et al., in review). Bussy et al. (2011) proposed that both mafic and felsic Ordovician magmatism occurred simultaneously but emplaced away from each other and were juxtaposed by the Variscan tectonics. They also related this bimodal magmatism to an active continental margin induced by the subduction of the Iapetus or Prototethys ocean beneath the northern Gondwana margin (Fig. 2a-b) (e.g. von Raumer and Stampfli, 2008; Guillot and Ménot, 2009).

The metasedimentary rocks, orthogneisses and metabasites are variously metamorphosed by a polyphase Variscan metamorphism (Barféty et al., 1984; Bogdanoff et al., 1991; von Raumer and Bussy, 2004; Guillot and Ménot, 2009). Metasedimentary rocks are metamorphosed either in unmolten micaschists, in metatexites or in diatexites within the same massif (e.g. Aiguilles-Rouges massif: Schulz and von Raumer, 1993, 2011; Krummenacher, 1959). The metabasic lenses are metamorphosed into amphibolite or eclogite and reach high-pressure conditions at ca. 700 °C and 1.5 GPa (Latouche and Bogdanoff, 1987; Schulz and von Raumer, 1993, 2011; Abrecht et al., 1991; Biino, 1994; Ferrando et al., 2008; Jouffray et al., 2020; Jacob et al., 2021) (Fig. 12a). The age of this high-pressure event has been thought as Ordovician (Abrecht et al., 1991), as Silurian-Devonian (Paquette et al., 1989) or more recently as Visean (Jacob et al., 2021; Rubatto et al., 2010; Bussy et al., 2011). The high-pressure stage is also recorded in the metasedimentary rocks with Ky-St assemblages (Guillot et al., 2009) and HP granulitic facies (Ferrando et al., 2008). This metamorphic stage induced a first partial melting event in the middle and lower crust (Barféty et al., 1984; Bogdanoff et al., 1991; Guillot and Ménot, 2009; Fréville et al., in review). The origin of the high-pressure stage has been mainly interpreted as related to a subduction zone (Ferrando et al., 2008; Rubatto et al., 2010; Bussy et al., 2011) resulting in a dismembered suture zone (Abrecht et al., 1991; Jouffray et al., 2020). On the other hand, Jacob et al. (2021) proposed that the high-pressure in the Belledonne massif might be the result of a crustal thickening during the Variscan continental collision.

The high-pressure stage is followed by a near isothermal decompression until ca. 600-650 °C and 0.2-0.6 GPa (Schulz and von Raumer, 1993; 2011; Ferrando et al., 2008; Jacob et al., 2021) (Fig. 12a). In several places, a late high-temperature – low-pressure event is estimated at ca. 800 °C and 0.3-0.7 GPa (Grandjean et al., 1996; Fréville et al., in review) (Fig. 12a) leading to a second anatexis forming Crd-bearing migmatites and Crd-diatexites in the gneisses (Bogdanoff et al., 1991; Krummenacher, 1969; Krummenacher et al., 1965; Fréville et al., in review). This second event occurred during the Late-Carboniferous time around 305 Ma (Fréville et al., in review).

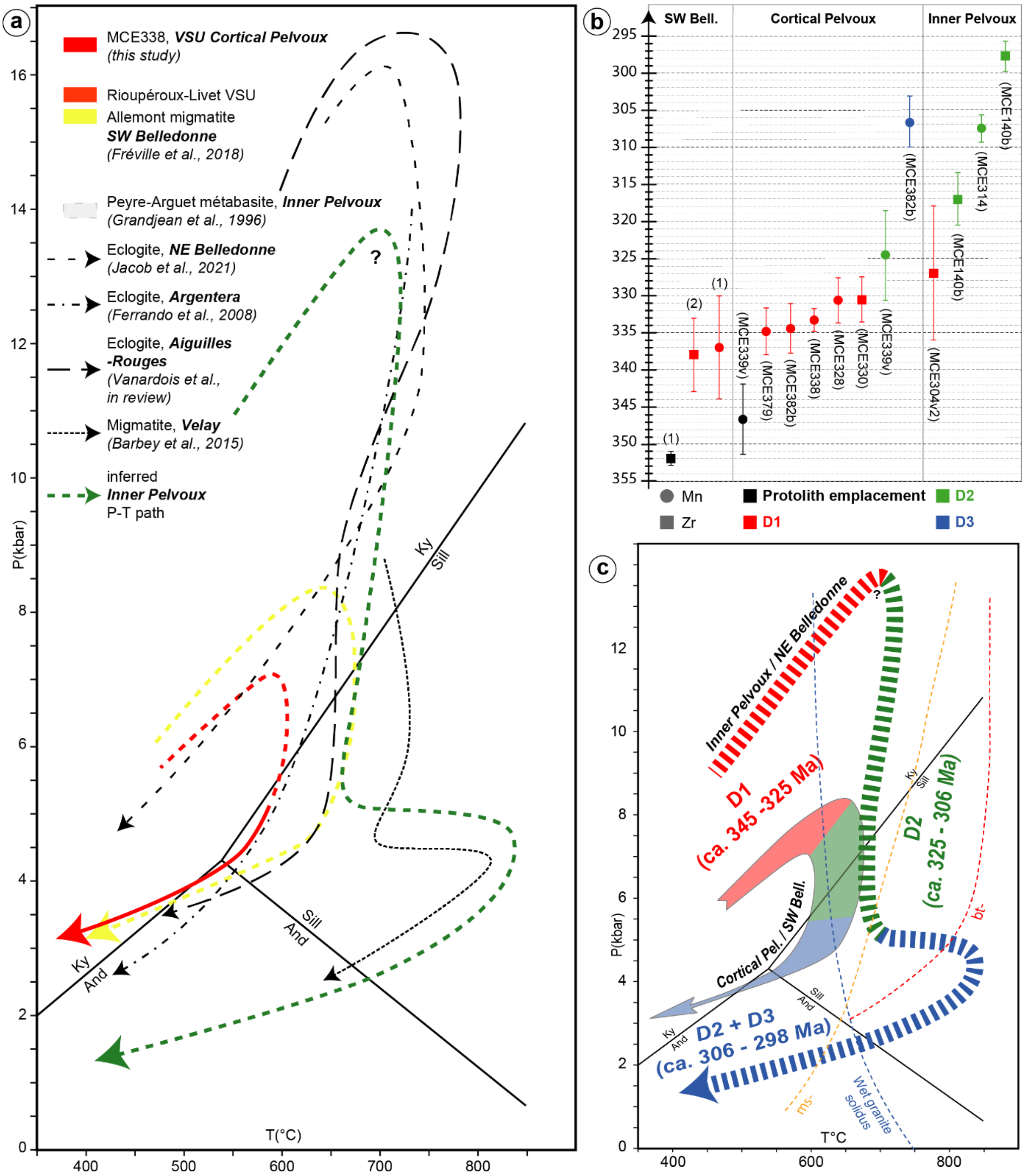

Figure 12: Geochronological and tectono-metamorphic interpretations for the Belledonne and Pelvoux massifs from Fréville et al. (in review). (a) P-T paths of the Cortical Pelvoux / SW Belledonne and of the Inner Pelvoux / NE Belledonne inferred from petrological and thermobarometric results from this study, Fréville et al. (2018), Grandjean et al. (1996), Ferrando et al. (2008), Jacob et al. (2021), Vanardois et al. (in review) and Barbey et al. (2015). (b) Geochronological results constraining the ages of D1, D2 and D3 from this study, (Fréville et al., 2018; Fréville, 2016). (c) Inferred tectono-metamorphic evolutions of the external and internal domains of the Belledonne and Pelvoux areas.

3.2.4. Variscan deformations

Two main Variscan deformation phases are described in the ECMs: (i) an early crustal thickening often attributed to a nappe stacking (D1) and (ii) a bulk dextral or sinistral strike-slip shearing (D2) (Fig. 12b-c) (Dobmeier, 1998; Fréville et al., 2018). The nappe stacking phase is best observed in the central domain, especially in the SW Belledonne where it forms low dipping foliations with kinematic criteria toward the East (Guillot et al., 2009; Fréville et al., 2018) (Fig. 11). This deformation is posterior to the Devonian-Tournaisian magmatism of the central domain dated at around 370-350 Ma and its end is dated by the peak of metamorphism at ca. 330 Ma, defining a potential activity from 350 to 330 Ma (Guillot et al., 2009; Fréville et al., 2018).

All of the ECMs, except the Pelvoux massif, are then affected by a high dextral shearing event forming vertical foliations and wide continental scale shear zones (e.g. Ménot, 1988b; von Raumer and Bussy, 2004; Guillot et al., 2009; Simonetti et al., 2018, 2020a, 2021; Jouffray et al., 2020). In the Pelvoux massif, shear criteria indicate a sinistral shearing, potentially corresponding to conjugate shear zones with the dextral ones (Strzerzynski et al., 2005; Fréville et al., in review). This dextral shearing occurred during the retrogression metamorphic path and its period of activity is broadly estimated occurring during Late-Carboniferous and has been dated by U-Th-Pb EPMA on monazite at 320-300 in the Aiguilles-Rouges massif (Simonetti et al., 2020a) and at 340-300 Ma in the Argentera massif.

Finally, a third deformation (D3) is described in the Belledonne and Pelvoux area and correspond to sub-horizontal planar fabrics. This deformation is interpreted, by several authors, as late detachments during an extensional setting (Guillot et al., 1999; Fernandez et al., 2002; Guillot et al., 2009). Alternatively, Fréville et al. (in review) highlighted that this deformation is located at the anatectic front of the Pelvoux massif and interpreted it as an accommodation of the flow of the anatectic lower crust. Fréville et al. (in review) estimated the P-T conditions at 560 °C and 0.45 GPa in the Cortical Pelvoux and dated this tectonic activity by U-Pb LA-ICPMS on monazite at 306 ± 3.5 Ma.

3.2.5. Carboniferous magmatism

A complete review on Carboniferous granitoids from the ECMs was performed by Debon and Lemmet (1999) combining mineralogical, geochemical and geochronological data. Plutonic bodies in the ECMs display various shapes, various sizes (550 km^2 to <1 km^2) and sharp crosscutting or conformable contacts with their host rocks. They mainly consist of massive or foliated monzo-syenogranites and biotite-amphibole bearing granites. Mafic igneous enclaves are present in variable proportion. They are chemically subdivided in two groups (Debon and Lemmet, 1999): the Magnesian group (MgG) and the Ferriferous-Magnesian group (FeMgG). The MgG emplaced during Visean (343-332 Ma) whereas FeMgG is mainly Stephanian in age (310-292 Ma) (Debon and Lemmet, 1999 and references therein). The MgG suite is interpreted as a hybrid magmatism formed by a mantellic source contaminated by a crustal source. Then, the mantellic component decreased over time and crustal source mainly formed the FeMgG suite (Debon and Lemmet, 1999; Bussy et al., 2000). Granites exposed in Grandes-Rousses and NE Belledonne massifs belong to the MgG suite. In the Pelvoux massif, both suites are recognized (Debon and Lemmet, 1999 and reference therein). Since the review of Debon and Lemmet (1999), only few studies have brought new geochronological data on the ECMs magmatism in the Aiguilles-Rouges (Bussy et al., 2000; Bussien Grosjean et al., 2017) and Argentera massifs (Rubatto et al., 2001). However, recent U-Pb LA-ICPMS analyses on zircon from thirteen plutons from the Belledonne, Grandes-Rousses and Pelvoux massifs highlights the meaningless of the MgG and FeMgG suites but confirm the two magmatic pulses at 340-330 Ma and at 310-300 Ma (Fréville, 2016; Fréville et al., in prep). Alternatively, these analyses emphasize a spatio-temporal evolution of the magmatism in function of the central and western domains. Indeed, Visean magmatism is mainly located in the central domain, whereas Stephanian magmatism are located in the eastern domain.

The Visean putons emplaced in the middle and upper crust through vertical D2 shear zones (Guillot et al., 2009; Guillot and Ménot, 2009; Bussy et al., 2000; Dobmeier, 1996, 1998). These magmatic and structural relationships suggest that the dextral wrenching was already active at ca. 340 Ma. These plutons are often highly deformed by the Late-Carboniferous deformations. On the contrary, two Visean plutons of the Cortical Pelvoux (i.e. Rochail and Entraigues granites) are weakly deformed despite the posterior deformations affecting the area (Fréville, 2016; Fréville et al., in prep).

The Stephanian pluton also emplaced within the vertical shear zones but are weakly deformed and show vertical magmatic foliations suggesting a late-orogenic magmatic emplacement during at the end of the dextral shearing (e.g. Joye, 1989; Bussy et al., 2000; Guillot and Ménot, 2009). Nevertheless, Simonetti et al. (2020a) report that the granite of Vallorcine (Aiguilles-Rouges massif) dated at 306 Ma (Bussy et al., 2000) is crosscut by a dextral shear zone emphasizing a syn-kinematic emplacement.

3.2.6. Late-orogenic Stephanian basins

Several Stephanian basins are known from the Argentera to the Aar Massif (Haudour & Sarrot-Reynauld, 1964; Guillot et al., 2009; Ballèvre et al., 2018). Most of them have underwent the Alpine deformation, with the occurrence of moderate folding to folding with schistosity like the Salvan-Dorénaz Basin (Aiguilles-Rouges massif; Badertscher & Burkhard, 1998; Pilloud, 1991). Sedimentological studies in these basins have provided evidences for syntectonic sedimentation derived from a local source mainly consisting of the exhumed gneissic basement of the ECMs (Capuzzo & Wetzel, 2004; Capuzzo et al., 2003; Dobmeier and von Raumer, 1995). Some of these basins show minor amounts of acid volcanic flows or aerial ash falls (e.g. Salvan-Dorénaz basin), or a huge, thick lavas flows, and pyroclastics interbedded into the coal-bearing sediments in the Grandes-Rousses massif (Banzet et al., 1984, 1985). Theses basins have provided wide paleontological evidences for a late Westphalian D-Stephanian age in the Argentera massif, in the Belledonne, Grandes Rousses, Aiguilles Rouges and Aar massifs (review in Ballèvre et al., 2018). These ages, often determined with biostratigraphy, were confirmed by U-Pb geochronological analyses on zircon from volcanic flow and tuffs located at the bottom and at the top of the Salvan-Dorenaz stratigraphic pile displaying ages at 308 ± 3 Ma and 295+3/-4 Ma (Capuzzo & Bussy, 2000), respectively. The opening of these basins is interpreted as a late and slight orogenic collapse marking the end of the Variscan orogeny (Guillot et al., 2009).

3.2.7. A model of geodynamic evolution of the ECMs

Due to partial deficiency of the Variscan history knowledge on the ECMs, geodynamic reconstitutions remain scarce or are englobed in reconstitutions at the scale of the European Variscan belt which does not allow detailed comparison between the different models (e.g. von Raumer et al., 1998, 2002, 2009, 2013; von Raumer and Stampfli, 2008; Stampfli et al., 2002, 2013). A general geodynamic evolution is proposed by Guillot et al. (2009) (Fig. 13) and is summarized in the followings:

- During the Early Paleozoic, the subduction of the Iapetus ocean beneath the northern Gondwana margin leads to the opening of a narrow back-arc basin forming the Chamrousse oceanic domain at ca. 500 Ma (Fig. 13a).
- The extensional setting in the northern Gondwana margin during the Late-Cambrian – Early-Ordovician induced a widespread magmatic event forming numerous alkaline and calc-alkaline laccoliths and continental MORB tholeiites. The extension

finally formed an oceanic domain (Medio-European ocean) between the Gondwana and the Moldanubian zone preserved in the eclogitic metabasites of the ECMs (Fig. 13b).

- During the Late-Silurian – Early-Devonian, the Medio-European ocean is subducted beneath the Moldanubian zone forming eclogites (Fig. 13c). The collision following the subduction exhumed the eclogites by back-thrusting and formed the eo-Variscan suture zone. It also closed the Chamrousse ocean and induced its obduction. The collision formed a widespread migmatisation and amphibolitisation dated around 380-360 Ma.
- During the Late-Devonian – Early-Carboniferous, the Saxothuringian ocean was subducted towards the South beneath the Moldanubian zone (Fig. 13d). This subduction opened a back-arc basin forming the bimodal magmatism of the Taillefer and Rioupéroux-Livet units.
- The Saxothuringian ocean was closed during the Visean time (Fig. 13e). The collision induced a nappe stacking phase in the central domain, coeval with dextral strike-slip shearing and magmatism with the emplacement of MgG granites.
- Finally, during the Late-Carboniferous – Early-Permian, the western, central and eastern domains were juxtaposed by normal strike-slip faults forming Late-Carboniferous basins during the orogenic collapse (Fig. 13f). In the eastern domain, this collapse induced a low-pressure – high-temperature metamorphism leading to a widespread anatexis and the formation of Crd-migmatites. This thermal event was goings along with the emplacement of numerous granites of the FeMgG suite.

However, recent works (Fréville et al., 2018, in review; Fréville, 2016) highlights that the three domains recorded the same deformations after 350 Ma, suggesting that these three domains of the ECMs where already close together before the Visean collision. In addition, U-Pb geochronological analyses on monazite and zircon dated two anatectic events at ca. 330 Ma and ca. 305 Ma (Fréville et al., in review), and do not record the Late-Devonian – Early-Carboniferous widespread proposed anatexis in Guillot et al. (2009).

Furthermore, the proposed paleogeodynamics of Guillot et al. (2009) is highly dependent on ages of high-pressure stages in the ECMs and in the bulk Variscan belt and strongly related to the recognition and the emplacement of the ancient oceanic domains and their subductions. Recently, Silurian – Early-Devonian ages of the high-pressure event in the ECMs (Paquette et al., 1989) and in the French Central Massif (FCM) (Ducrot et al., 1983; Pin and Lancelot, 1982;

Paquette et al., 1995; Berger et al., 2010) have been criticized (e.g. Paquette et al., 2017) and recent works proposed a Late-Devonian age in the FCM (Lotout, 2017; Lotout et al., 2018, 2020; de Höym de Marien, 2020) and an Early-Carboniferous age in the ECMs (Rubatto et al., 2010; Jacob et al., 2021). Moreover, eclogitic metabasites occurrences are not always the remnants of an ancient suture zone, as in the Montagne Noire (Whitney et al., 2015, 2020). So, the existence of the Medio-European ocean in the ECMs and its timing of subduction remain controversial.

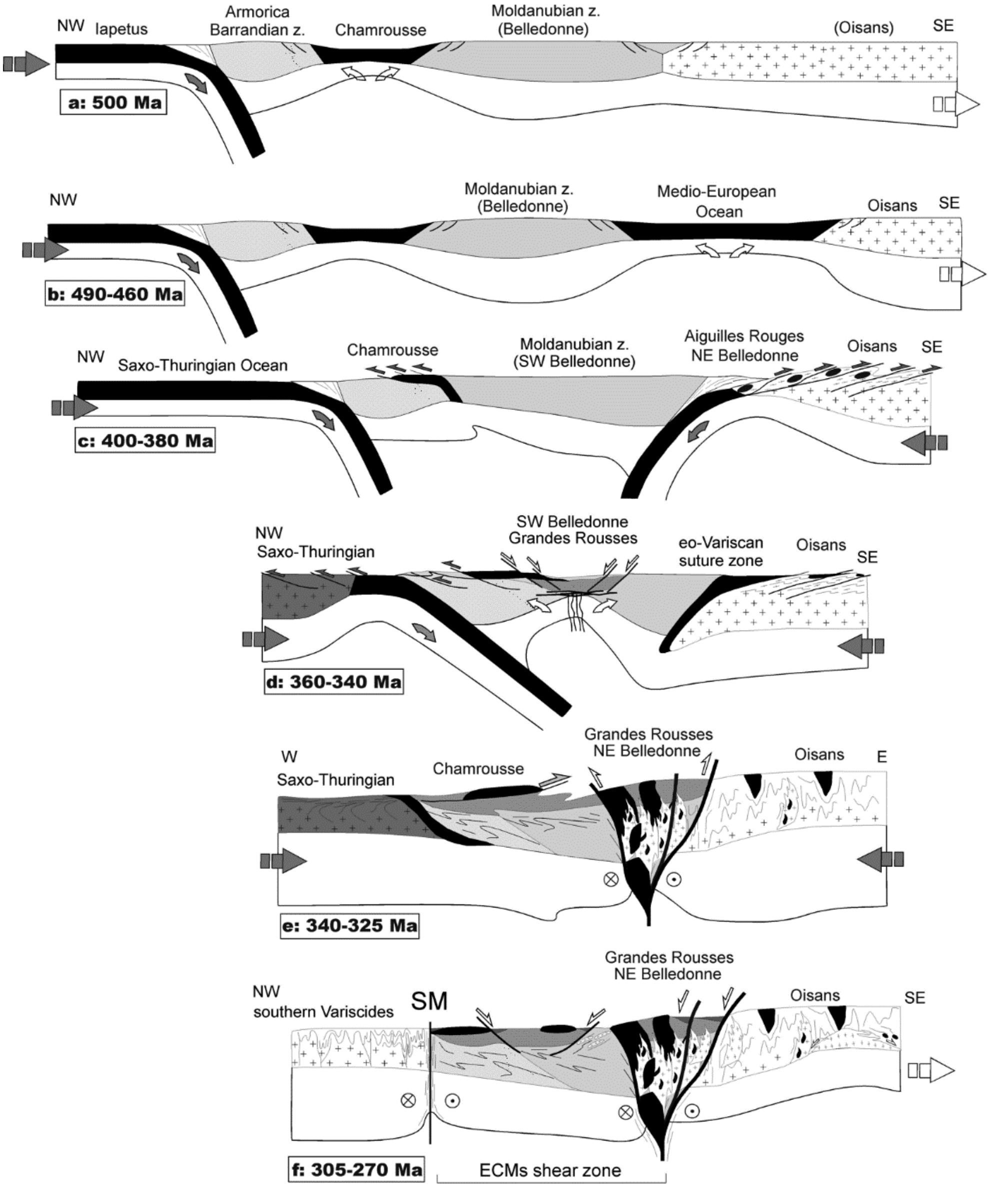

Figure 13: Schematic evolution of the Belledonne, Grandes Rousses and Pelvoux massifs in six steps during the Paleozoic Era from Guillot et al. (2009) (see text for explanation). SM: Synclinal Median fault.

4. The SE branch of the Variscan belt

Thanks to numerous studies, the paleogeographic localisation and the evolution of the northern flank and the southwestern part (i.e. Iberian massif) of the Variscan belt are well-documented and allow precise paleogeographic reconstitutions (e.g. Lardeaux et al., 2014; Franke et al., 2017; Martinez-Catalan et al., 2021). On the other hand, the ancient position of the southeastern branch of the Variscan belt, composed of Corsica, Sardinia, Maures-Tanneron massif and the Paleozoic Alpine basement, is poorly constrained and widely changes from a model to another one (e.g. Fig. 14) (e.g. von Raumer et al., 2002, 2013; Guillot et al., 2009; Edel et al., 2018; Martinez-Catalan et al., 2021). Most of the authors agree to associate the SE branch with the Moldanubian zone (e.g. Franke et al., 2017; Ballèvre et al., 2018; Martinez-Catalan et al., 2021). Few studies propose to correlate the northern part of Corsica with the Teplá-Barrandian zone of the Bohemian massif (Ibero-Armorican zone; Rossi et al., 2009) or with the Saxothuringian zone (Faure et al., 2014a).

4.1.The Moldanubian zone

As already stated, the Moldanubian zone is usually subdivided into allochthonous, para-autochthonous and autochthonous terranes (Fig. 4) based on the stacking of high-grade rocks on lower grade terranes in the French Central Massif (Faure et al., 2009; Lardeaux et al., 2014; Vanderhaeghe et al., 2020) and in the Iberic massif (Martinez-Catalan et al., 2009; Ballèvre et al., 2014; Arenas et al., 2016). The allochthonous terranes are mainly localized in the northern part of the Moldanubian zone while the autochthonous terranes form the southern part of the Moldanubian zone (Fig. 4). The para-autochthonous terranes are inserted between them. In the French Central Massif, the allochthonous terranes (Upper Gneiss Unit (UPU) and Lower Gneiss Unit (LPU)) are composed of metapelites, metagreywackes and metarhyolites associated with bimodal magmatism (« leptynite-amphibolite complex » (LAC)) affected by high or low temperature – high-pressure metamorphism (e.g. Lotout et al., 2018, 2020). Pressure conditions are mainly comprised between 1.5 and 2.0 GPa with rare ultra-high-pressure conditions occurrences (Lardeaux et al., 2001; Berger et al., 2010). LAC are either interpreted as relicts of an oceanic suture (Vanderhaeghe et al., 2020) or as the northern hyper-extended margin of the Gondwana (Lardeaux et al., 2014). Para-autochthonous terranes (Para-Autochthonous Unit (PAU)) are essentially composed of metapelites affected by amphibolitic-facies metamorphism. Finally, in the French Central Massif the autochthonous terranes, outcropping near the Montagne Noire, formed folds and thrusts structures toward the South. These terranes are mainly composed of low-grade metapelites, excepted in the core of the Montagne Noire dome that is formed by migmatites embedding few relicts of eclogites (Faure et al., 2014b; Trap et al., 2017; Whitney et al., 2015, 2020; Pitra et al., 2021). The allochthonous and para-autochthonous terranes form an orogenic plateau further to the continental collision during Early-Carboniferous times whereas the autochtonous terranes exposed in the Montagne Noire are considered as the southern border of the plateau (Whitney et al., 2015; Vanderhaeghe et al., 2020).

4.2.Models and relationships between massifs of the SE branch

Interpretation concerning the position of the ECMs in the Variscan belt are scarce. Guillot et al. (2009) proposed to attributed the ECMs to the Moldanubian Zone of the Bohemian massif, usually interpreted as Moldanubian allochtonous or para-autochthonous terranes (Martinez-Catalan et al., 2021). Several studies proposed to align the ECMs with the Maures-Tanneron massifs and the Corsica-Sardinia bloc along a crustal-scale dextral shear zone named the Eastern Variscan Shear Zone joining the Bohemian (Guillot et al., 2009; Rossi et al., 2009; Duchesne et al., 2013; Padovano et al., 2012; Simonetti et al., 2020a) (Fig. 14a). Other authors proposed to linked this crustal-scale shear zone with the dextral shear zone of the Montagne Noire (Ballèvre et al., 2018; Chardon et al., 2020).

Several reviews and studies highlight the correlation between the Maures-Tanneron massifs and the Corsica-Sardinia bloc and emphasize that these massifs were a coherent bloc before the opening of the Lion Gulf (Elter et al., 2004; Elter and Pandeli, 2005; Bellot, 2005; Rossi et al., 2009; Schneider et al., 2014) (Fig. 14b). These massifs are composed of three zones (Internal, Central and External in Rossi et al., 2009; Schneider et al., 2014) separated by dextral transcurrent shear zones (Rolland et al., 2009; Elter et al., 2004). The Internal zone is composed of migmatitic paragneiss and Ordovician orthogneiss containing eclogitic lenses. The Central Zone is also composed of paragneiss and orthogneiss but they are rarely migmatitic. It also contained few eclogitic lenses and a LAC is described in the Central zone of the Maures massif (Schneider et al., 2014). The Central zone formed nappes that stack uppon the External zone (Rossi et al., 2009; Carmignani et al., 2016). The External zone is composed of low-grade rocks deformed by folds and thrusts. Several authors propose to link the Internal, Central and External zones to the allochthonous, para-autochthonous and autochthonous terranes, respectively (e.g. Edel et al., 2018; Martinez-Catalan et al., 2021; Cochelin et al., 2021).

Recent paleomagnetic data highlighted major rotations of the Maures-Tanneron, Corsica and Sardinia massifs during Permian (Edel et al., 2000, 2014, 2018; Aubele et al., 2012; Bachtasde et al., 2018) that replaced these massifs in a position incompatible with the EVSZ model (Fig. 14b). Furthermore, the EVSZ model suggests that the Argentera massif underwent important anticlockwise rotation after the Variscan orogeny, whereas paleomagnetic data (Bogdanoff et al., 1977; Cogné and Perroud, 1985; Collombet et al., 2002; Kruiver et al., 2000; Sonnette et al., 2014) testify that the Argentera massif did not significantly rotate after the Variscan orogeny.

The Pyrenees are interpreted as the forelands of the Variscan belt (Druguet, 2001; Pereira et al., 2015) and thus are interpreted as autochthonous terranes (Martinez-Catalan et al., 2021). Some paleogeographic reconstructions proposed that the Maures-Tanneron-Corsica-Sardinia bloc was initially next to the Pyrenees and the Catalan Coastal Ranges (Edel et al., 2015; Carreras and Druguet, 2014). Even if the Pyrenees are usually interpreted as the forelands of the French Central Massif (e.g. Laurent et al., 2017; Vanderhaeghe et al., 2020), some paleomagnetic results suggest that the Pyrenees and the Catalan Coastal Ranges have suffered important Permian movements and rotations and that they could have been more to the East during the Variscan orogeny (Edel et al., 2015, 2018).

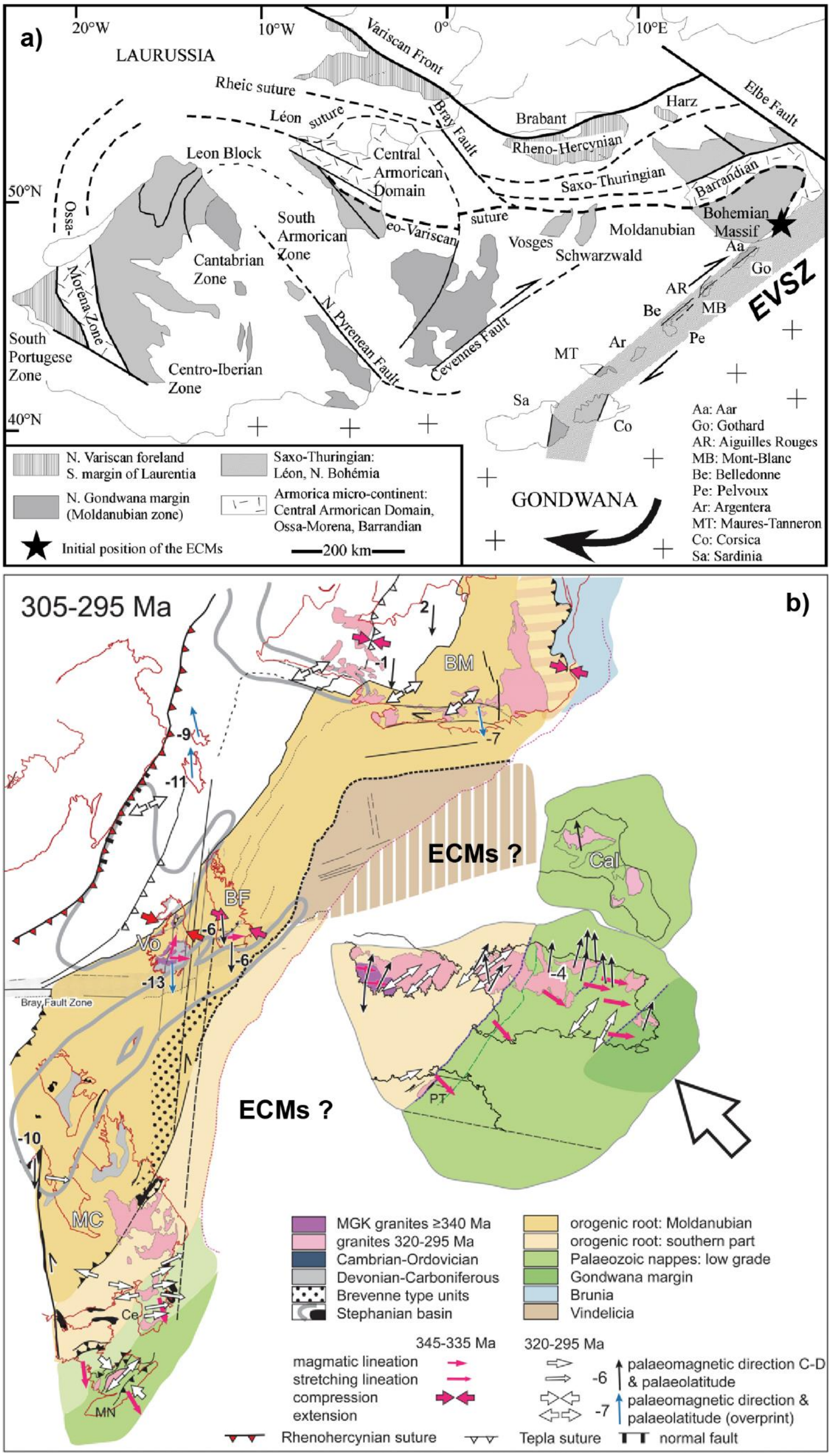
a)
20°W
10°W
0°
10°E
50°N
40°N
LAURUSSIA
Variscan Front
Rheic suture
Léon suture
Bray Fault
Elbe Fault
Harz
Brabant
Rheno-Hercynian
Saxo-Thuringian
Barrandian
Leon Block
Central Armorican Domain
South Armorican Zone
eo-Variscan suture
Bohemian Massif
Moldanubian
Vosges
Schwarzwald
Ossa-Morena Zone
Cantabrian Zone
South Portugese Zone
Centro-Iberian Zone
N. Pyrenean Fault
Cevennes Fault
EVSZ
Aa
Go
AR
MB
Be
Pe
Ar
MT
Sa
Co
N. Variscan foreland S. margin of Laurentia
N. Gondwana margin (Moldanubian zone)
Initial position of the ECMs
Saxo-Thuringian: Léon, N. Bohémia
Armorica micro-continent: Central Armorican Domain, Ossa-Morena, Barrandian
200 km
GONDWANA
Aa: Aar
Go: Gothard
AR: Aiguilles Rouges
MB: Mont-Blanc
Be: Belledonne
Pe: Pelvoux
Ar: Argentera
MT: Maures-Tanneron
Co: Corsica
Sa: Sardinia
305-295 Ma
b)
BM
2
-1
-7
-9
-11
BF
Vo
-6
-6
-13
Bray Fault Zone
ECMs ?
Cal
-4
PT
ECMs ?
-10
MC
Ce
MN
MGK granites ≥340 Ma
granites 320-295 Ma
Cambrian-Ordovician
Devonian-Carboniferous
Brevenne type units
Stephanian basin
orogenic root: Moldanubian
orogenic root: southern part
Palaeozoic nappes: low grade
Gondwana margin
Brunia
Vindelicia
345-335 Ma
320-295 Ma
magmatic lineation
stretching lineation
compression
extension
-6
palaeomagnetic direction C-D & palaeolatitude
-7
palaeomagnetic direction & palaeolatitude (overprint)
Rhenohercynian suture
Tepla suture
normal fault

Figure 14: Possible configurations of the Variscan belt of western Europe in Late Carboniferous times from (a) Guillot et al. (2009) and (b) Edel et al. (2014).

5. Regional problematic and goals

In the light of this global overview on the Variscan belt, the Paleozoic basement of the Alps, the External Crystalline Massifs and the Variscan Pyrenees, it appears that the geodynamic evolution of the southeastern branch of the Variscan belt is poorly constrained and is still discussed. The ECMs, are rarely integrated in the paleogeographic reconstruction of the Variscan belt (e.g. Martinez-Catalan et al., 2021; Franke et al., 2017; Edel et al., 2018). Their geodynamic evolution is still debated, especially about the significance of their eclogites interpreted as an ancient suture (e.g. Rubatto et al., 2010; Jouffray et al., 2020) or as pieces of the lower crust (Jacob et al., 2021), but alos about the geometry and impact of the EVSZ (e.g. Guillot et al., 2009; Padovano et al., 2012; Ballèvre et al., 2018; Simonetti et al., 2020a).

As for the NPZ, it is usually interpreted as the southern forelands of the Variscan belt (e.g. Druguet, 2001; Aguilar et al., 2013; Laurent et al., 2017; Vanderhaeghe et al., 2020), nonetheless the origin of the thermal anomaly inducing HT-LP metamorphism and a widespread magmatism at the end of the Variscan orogeny is poorly understood (e.g. Siron et al., 2020; Lemirre, 2016). Recently, a lateral flow from the French Central Massif has been proposed (Vanderhaeghe et al., 2020) and could be associated to the high thermal conditions in the Variscan Pyrenees. Furthermore, the Cretaceous impact affecting the NPZ is still debated and structures initially considered as Variscan are now reinterpreted as Cretaceous by some authors without a clear consensus (Clerc and Lagabrielle, 2014; Olivier et al., 2013, 2015; Vauchez et al., 2013a, 2013b).

Finally, at the scale of the Variscan belt, the entire south-eastern branch forming the south-eastern border of the orogenic plateau is poorly integrated in paleogeographic models. This area contains numerous eclogitic lenses often interpreted as relicts of ancient sutures (e.g. Rossi et al., 2009; Faure et al., 201a4; Schneider et al., 2014), but also crustal-scale shear zones (e.g. Rolland et al., 2009; Elter et al., 2010; Carosi et al., 2012; Simonetti et al., 2018, 2020b) and partial melting in the lower crust (e.g. Bogdanoff et al., 1991; Giacomini et al., 2008; Cochelin et al., 2021; Fréville et al., in review).

In this study, we investigate in details the Aiguilles-Rouges – Mont-Blanc massifs, two of these ECMs, and the Agly massif from the NPZ. Our results should enable us to better constrain the Variscan tectonic, magmatic and metamorphic evolutions of the ECMs and NPZ, and also to discriminate Variscan and Alpine tectono-metamorphic impacts. Beside allowing us to discuss geological processes, this study should bring new elements to reconstruct the paleogeography of the SE branch of the Variscan belt. Precise overview of the literature on the Agly and Aiguilles-Rouges – Mont-Blanc massifs will be presented in each chapter in function of the developed thematic studies.

Chapitre 3. Partitionnement de la déformation dans le massif de l’Agly. Evidence d’un fluage latéral ?

Cette thèse s'inscrit dans le projet Référentiel Géologique de la France (RGF) conduit par le Bureau de Recherches Géologiques et Minières (BRGM) et mené dans un premier temps sur le Chantier Pyrénées qui s'est terminé en 2018 puis sur le Chantier Alpes qui a commencé en 2019. Les résultats présentés dans ce chapitre sont en partie le fruit de mon travail de Master Recherche dans le cadre du chantier RGF Pyrénées. Des nouvelles observations et des analyses complémentaires ont été faites au cours de la 1ère année de thèse.

Ce chapitre s'intéresse au partitionnement de la déformation au sein du massif de l'Agly qui est localisé dans la Zone Nord-Pyrénéenne. Ce massif présente une section complète depuis le faciès schiste vert jusqu'au faciès granulitique et est structuré majoritairement par des foliations et des zones de cisaillement horizontales. Ces structures, initialement attribuées à l'orogénèse Varisque, ont récemment été réinterprétées comme étant induites par le rifting Crétacé. Une première partie de ce chapitre présente une étude structurale du massif identifiant les différentes fabriques planaires du massif de l'Agly et leurs relations avec les corps magmatiques et le métamorphisme. Cette section, présentée sous forme d'un article publié au *Bulletin de la Société Géologique Française*, nous permet de confirmer l'âge Varisque de ces structures horizontales et illustre pour la première fois un couloir transcurrent dextre au sein de ce massif.

Dans une seconde partie, nous nous sommes attachés à contraindre l'âge de ces événements tectoniques en datant par LA-ICPMS U-Pb sur monazite et zircon des petits corps magmatiques montrant des relations avec ces déformations. Nos résultats indiquent que la fusion partielle était initiée à 325-320 Ma et qu'elle s'est poursuivie jusqu'à 300 Ma et qu'elle est synchrone du développement des structures subhorizontales. A partir de 308 Ma, la déformation locale transcurrente commence et la déformation est alors partitionnée entre les structures horizontales et verticales. Ces résultats nous permettent de discuter du fluage de la croûte partiellement fondues dans l'avant-pays du massif Central. Cette seconde partie est présentée sous la forme d'un article en préparation pour une soumission à *International Journal of Earth Science*.

BSGF - Earth Sciences Bulletin 2020, 191, 15
© J. Vanardois *et al.*, Published by EDP Sciences 2020
https://doi.org/10.1051/bsgf/2020009

Chaîne varisque

Available online at:
www.bsgf.fr

OPEN ACCESS

Kinematics, deformation partitioning and late Variscan magmatism in the Agly massif, Eastern Pyrenees, France

Jonas Vanardois[1,*,a], Pierre Trap[1], Philippe Goncalves[1], Didier Marquer[1], Josselin Gremmel[1], Guillaume Siron[2] and Thierry Baudin[3]

[1] UMR 6249 Chrono-environnement, Université de Bourgogne-Franche-Comté, 25030Besançon, France
[2] WiscSIMS Laboratory, University of Wisconsin-Madison, Madison, Wisconsin 53706, USA
[3] BRGM-French Geological Survey, 3 Avenue Claude Guillemin, 45100 Orléans, France

Received: 20 August 2019 / Accepted: 14 April 2020

Abstract – In order to constrain the finite deformation pattern of the Variscan basement of the Agly massif, a detailed structural analysis over the whole Agly massif was performed. Our investigation combined geological mapping, reappraisal of published and unpublished data completed with our own structural work. Results are provided in the form of new tectonic maps and series of regional cross-sections through the Agly massif. At variance from previous studies, we identified three deformation fabrics named D1, D2 and D3. The D1 deformation is only relictual and characterized by a broadly northwest-southeast striking and eastward dipping foliation without any clear mineral and stretching lineation direction. D1 might be attributed to thickening of the Variscan crust in a possible orogenic plateau edge position. The D2 deformation is a heterogeneous non-coaxial deformation, affecting the whole massif, that produced a shallowly dipping S2 foliation, and an anastomosed network of C2 shear zones that accommodated vertical thinning and N20 directed extension. D2 is coeval with LP-HT metamorphism and plutonism at ca. 315–295 Ma. D2 corresponds to the extensional collapse of the partially molten orogenic crust in a global dextral strike-slip at the scale of the whole Variscan belt. The D2 fabrics are folded and steepened along a D3 east-west trending corridor, called Tournefort Deformation Zone (TDZ), where the Saint-Arnac and Tournefort intrusives and surrounding rocks share the same NE-SW to E-W subvertical S3 foliation. Along the D3 corridor, the asymmetrical schistosity pattern and kinematic criteria suggest a D3 dextral kinematics. The D3 deformation is a record of E-W striking dextral shearing that facilitated and localized the ascent and emplacement of the diorite and granitic sheet-shaped plutons. D3 outlasted D2 and turned compressional-dominated in response to the closure of the Ibero-Armorican arc in a transpressional regime. The progressive switch from D2 thinning to D3 transpression is attributed to the lessening of gravitational forces at an advanced stage of extensional collapse that became overcome by ongoing compressional tectonic forces at the southern edge of the Variscan orogenic plateau.

Keywords: Crustal thinning / Variscan orogen / Gneiss dome / Agly Massif / Eastern Pyrenees

Résumé – Cinématiques, partitionnement de la déformation et magmatisme tardi-Varisque dans le massif de l'Agly, Pyrénées Orientales, France. Afin d'améliorer la compréhension du partitionnement de la déformation tardi-varisque dans le socle du massif de l'Agly, une nouvelle étude structurale a été menée. Elle a combiné un travail cartographique détaillé, la synthèse et l'harmonisation des données de la littérature complétées par notre propre analyse. Les résultats sont retransmis sous la forme de nouvelles cartes structurales et coupes géologiques à travers tout le massif. À la différence des études précédentes, nous avons clairement identifié trois fabriques de déformation nommées D1, D2 et D3. La déformation D1 est à l'état de relique et est caractérisée par une foliation S1 de direction générale NE-SW avec un pendage important vers l'Est, sans linéation minérale ou d'étirement clairement identifiable. D1 est interprétée comme témoignant de l'épaississement de la croûte Varisque au front d'un plateau orogénique. La

---

*Corresponding author: jonas.vanardois@univ-fcomte.fr

[a] Present address: 16 route de Gray, 25030 Besançon, France.

déformation D2 est une déformation hétérogène et non coaxiale, affectant le massif entier, qui engendre une foliation S2 faiblement pentée et un réseau anastomosé de shear zones C2 accommodant un amincissement crustal et une extension vers le N20. D2 est contemporaine d'un métamorphisme de HT-BP et un épisode magmatique entre ca. 315 et 295 Ma. D2 correspond à une extension liée à l'effondrement gravitaire de la croûte orogénique partiellement fondue dans un contexte global décrochant dextre à l'échelle de la chaîne Varisque. La foliation S2 est plissée et verticalisée le long d'un couloir E-W D3, appelé Zone de Déformation de Tournefort (TDZ), où les intrusions de Saint-Arnac et de Tournefort et leurs encaissants partagent la même foliation S3 sub-verticale de direction NE-SW à E-W. Dans la TDZ, l'agencement asymétrique des schistosités et les critères cinématiques indiquent une cinématique D3 dextre. La déformation D3 correspond à un cisaillement transcurent E-W dextre qui localise l'ascension et l'emplacement des plutons dioritiques et granitiques. La D3 s'initie dans l'infrastructure au cours de l'amincissement D2, elle perdure et reprend les fabriques D2 dans un régime transpressif dextre dominant en réponse probable à la fermeture de l'Arc Ibéro-Armoricain. Le passage progressif de l'amincissement D2 à la transpression D3 est attribué à la diminution des forces gravitaires à un stade avancé de l'effondrement gravitaire suivi par la reprise les forces tectoniques compressives en bordure de plateau orogénique. Nos résultats confirment aussi que le rifting Crétacé ne provoque pas de déformation ductile mylonitique dans les roches métamorphiques du massif de l'Agly.

Mots clés : amincissement crustal / orogénèse Varisque / dôme gneissique / massif de l'Agly / Pyrénées Orientales

1 Introduction

In hot and mature orogens, the dynamic nature of late-orogenic evolution results in the preservation of a complex set of spatially and temporally partitioned deformational, metamorphic and magmatic events. Feedback relationships in time and space between those events control the balance of gravitational *vs.* boundary forces that drive the crustal flow, especially within orogenic plateaus featuring a large, hot and weak crust.

Mechanical re-equilibration of the orogenic plateau lead to crustal thinning in its inner part and lower crustal flow toward the foreland where compression and thickening occur (*e.g.* Dewey, 1988; Rey *et al.*, 2010). With ongoing orogenic collapse, further extension and thinning move toward the plateau edges and interact with the deep crust that is continuously subjected to compression, lateral flow and exhumation. On these particular external domains, late orogenic gravitational collapse is responsible for superimposition, in time and space, of contractional and extensional structures the depiction of which is not straightforward but essential to unraveled in order to fully understand lateral and horizontal crustal flow and exhumation of deep crust.

The aforementioned tectonic evolution is well exemplified in the European Variscides where a Tibetan-style orogenic plateau is proposed to have collapsed during the middle Carboniferous-early Permian period (*e.g.* Dörr and Zulauf, 2010; Whitney *et al.*, 2015; Maierová *et al.*, 2016). In France, the French Massif Central (FMC) has been proposed as an example of plateau internal zone, and the Variscan Pyrenees as the plateau edge or foreland with, in between, the Montagne Noire massif (MN) located at the plateau-foreland transition (Whitney *et al.*, 2015). The eastern FMC recorded regional scale extensional collapse and exhumation of the deep partially molten crust (*e.g.* Malavieille *et al.*, 1990; Burg *et al.*, 1994; Vanderhaeghe *et al.*, 1999; Ledru *et al.*, 2001). The MN gneiss dome is considered to have formed at the edge of the collapsing Variscan orogen during Late Carboniferous time (Franke *et al.*, 2011; Whitney *et al.*, 2015). More to the south, the Variscan Pyrenean belt would represent the outer border of the orogenic plateau that share similar structural, metamorphic and magmatic features with the Montagne Noire gneiss dome located at the plateau-foreland transition (Whitney *et al.*, 2015). However, uncertainties still exist about the relative position of Variscan Pyrenean massifs located south of the North Pyrenean Fault, *i.e.* in the Pyrenean Axial Zones, with respect to the FMC and MN. Conversely, the eastern North Pyrenean Massif and in particular the Agly massif may represent a direct southward prolongation of the southern FMC massifs. Unfortunately, this external domain still lacks detailed structural constrains on late-Variscan history in order to understand the complex three-dimensional internal deformations in the Variscan orogen edge that interlinked gravity-driven extensional collapse, voluminous partial melting, magma emplacements, thermal softening and plate-boundary forces under wrench tectonic.

The present study investigates the three-dimensional deformation of the Agly massif as an example of the orogenic plateau foreland during late-Carboniferous-early Permian time. We have identified a detail geometry of the structures with a polyphased deformation history. The structural analysis of macro and microstructures has been linked to metamorphic and magmatic events for which accurate P-T and geochronological constraints are available from the literature. The finite strain pattern of the Agly massif is discussed and replaced in the tectonic framework of the Variscan orogeny considering a progressive switch from gravitational collapse to dextral transpression in a syn-plate convergence context.

As part of the Pyrenean mountain range, the Agly massif recorded both the Variscan and Alpine orogenic cycles. The complex polyphased nature of the Pyrenees is exposed in the North Pyrenean Zone (NPZ, Figs. 1 and 2A), where Paleozoic high-grade metamorphic massifs of Variscan basement, the North Pyrenean massifs (NPMs), are tectonically juxtaposed with fragments of subcontinental mantle and metamorphic Mesozoic sediments in response to Cretaceous extension (*e.g.* Clerc *et al.*, 2015, 2016; Clerc and Lagabrielle, 2014; Lagabrielle *et al.*, 2016; Ducoux, 2017). Most of the NPMs are characterized by numerous shallowly dipping extensional ductile shear zones and an anomalous HT-LP metamorphic gradient (*e.g.* Thiébaut, 1964; Roux, 1977; de Saint Blanquat, 1989, 1993; de Saint Blanquat *et al.*, 1990; Paquet and Mansy, 1991; Guitard *et al.*, 1996). Although these structures and

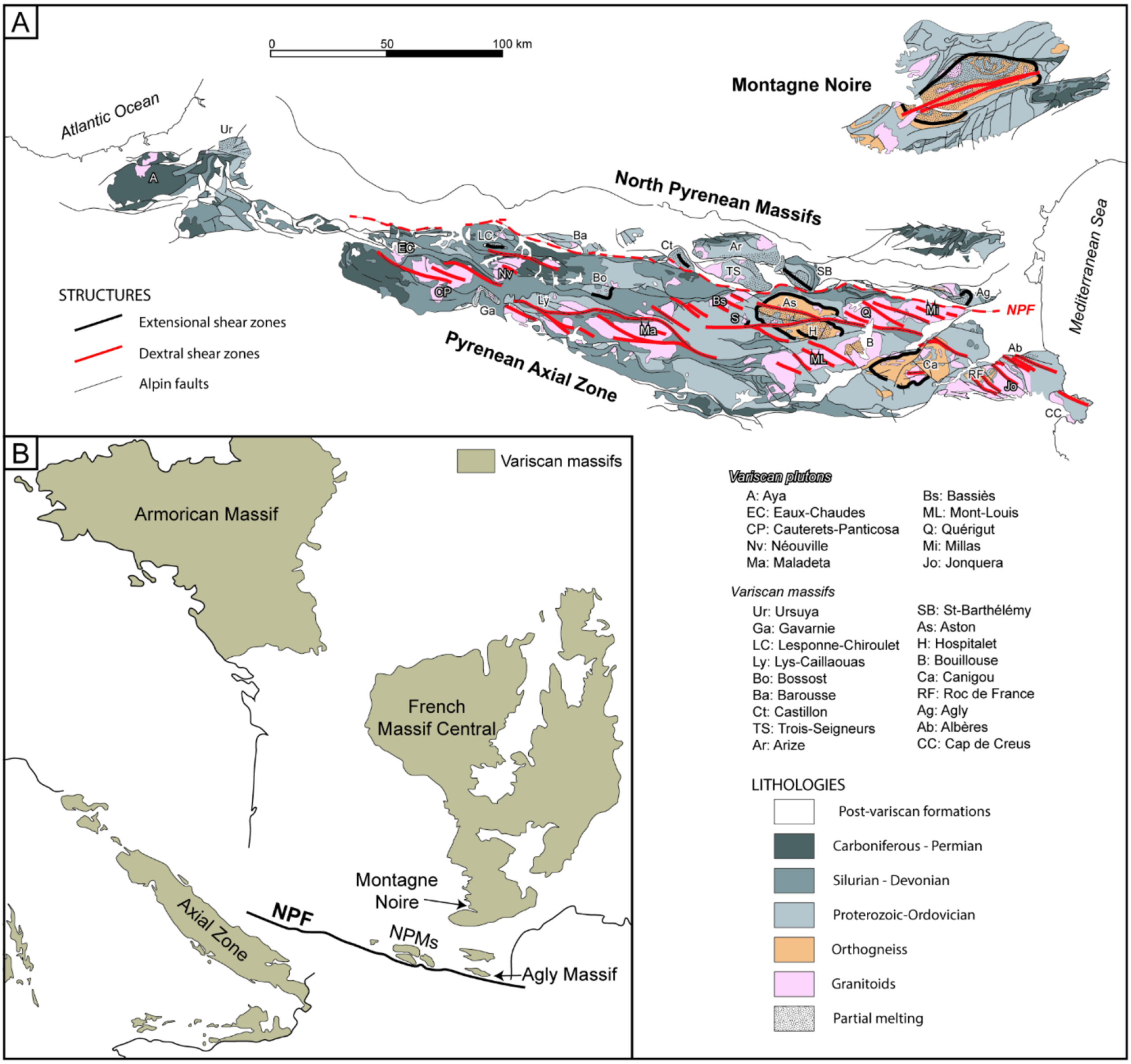

Fig. 1. (A) Map of the Variscan Pyrenees and of the Montagne Noire massif with main Variscan shear zones. (B) Probable position of the Variscan massif at the end of the Variscan orogeny, modified from Carreras and Druguet (2014).

metamorphism have been related to the Paleozoic Variscan orogeny (*e.g.* de Saint Blanquat, 1989, 1993; de Saint Blanquat *et al.*, 1990), some studies highlight the possible impact of Cretaceous extension on the structuration on the Variscan Agly massif basement (Delay, 1989; Vauchez *et al.*, 2013; Odlum and Stockli, 2019). We further discuss this secondary point in the light of our new structural data.

2 Geological Setting

2.1 The Variscan Pyrenees in the Western European Variscan Belt

Within the Western European Variscan Belt, the Variscan Pyrenees, *i.e.*, the Pyrenean Axial Zone (AZ) and the North Pyrenean Zone (NPZ), belong to the external domain corresponding to the southern orogenic foreland (*e.g.* Burg *et al.*, 1994; Edel *et al.*, 2018). The Variscan Pyrenees are composed of Proterozoic to Paleozoic sediments that were metamorphosed and deformed from middle Carboniferous to early Permian time (*e.g.* Aguilar *et al.*, 2013; Denèle *et al.*, 2014; Mezger and Gerdes, 2016). The Variscan metamorphism is characterized by a high temperature and low pressure HT/LP gradient conducing to intense partial melting of the lower and middle crust. It is attributed to a high mantle flux and to emplacements of numerous basic and acid plutons (Guitard *et al.*, 1996 and references therein; Lemirre, 2016). Two main deformation events are described in the Pyrenean Axial Zone: (i) a nappe stacking toward the south D1 responsible for moderate crustal thickening (*e.g.* Carreras and Capella, 1994; Matte, 2002; Vilà *et al.*, 2007; Denèle *et al.*, 2009, 2014; Laumonier *et al.*, 2010; Aguilar *et al.*, 2015), followed by (ii) a

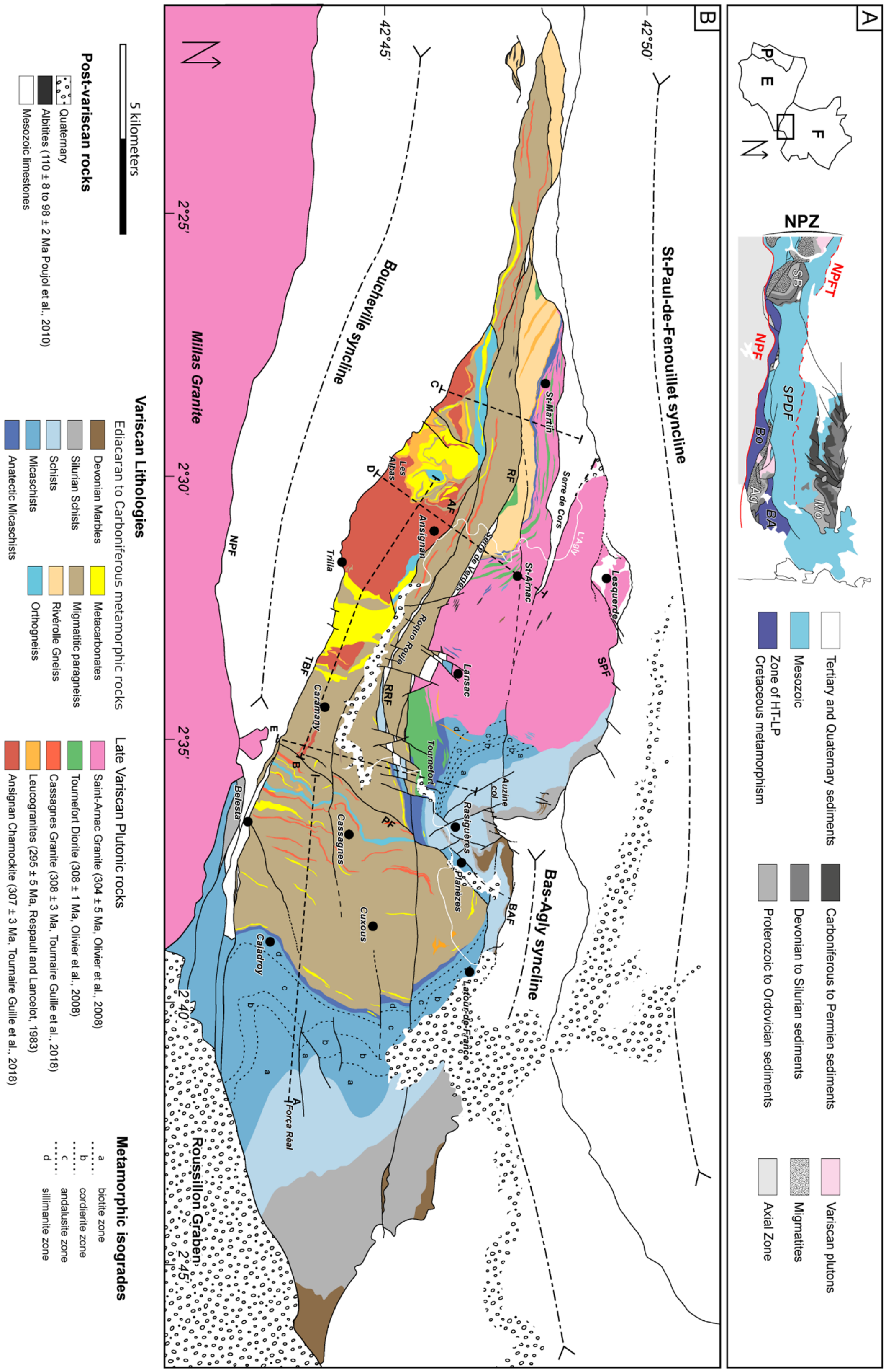

Fig. 2. (A) Location of the North Pyrenean Zone and map of the principal geological formations of the area. (B) Geological map of the Agly Massif modified from Fonteilles *et al.* (1993) and Delay (1989). The location of cross-sections of Figures 4 and 10 is indicated. NPF: North Pyrenean Zone; TBF: Trilla-Bélesta Fault; AF: Ansignan Fault; RF: Rentadou Fault; RRF: Roquo Roujo Fault; PF: Planèzes Fault; BAF: Bas-Agly Fault; SPF: Saint-Paul Fault.

dextral transpressive regime D2 forming several gneiss-domes and dextral reverse shear zones allowing emplacement of large plutons (Fig. 1; Gleizes *et al.*, 1997, 1998a, 2001; Denèle *et al.*, 2009, 2014; Laumonier *et al.*, 2010; Cochelin *et al.*, 2017). Several flat extensional shear zones are also described (Fig. 1; Gibson, 1991; Vissers, 1992; Mezger and Passchier, 2003) that are interpreted as evidence for transtensional exhumation of migmatitic dome in a global transpressional regime (Cochelin *et al.*, 2017). North of the North Pyrenean Fault (NPF), the North Pyrenean Zone mainly also recorded the same HT/LP metamorphism. Conversely to the AZ, the main fabric is defined by a penetrative flat-lying foliation that developed during retrogressive metamorphism during a continous extensional event (de Saint Blanquat *et al.*, 1990; Bouhallier *et al.*, 1991). A full and detail review of the geodynamic evolution of the Western European Variscan belt during Late Palaeozoic times can be found in recent contributions (Cochelin *et al.*, 2017; Ballèvre *et al.*, 2018; Edel *et al.*, 2018).

2.2 Geological outline of the Agly Massif (AM)

The Agly massif is the easternmost NPMs (Fig. 1). It is a 30 km-long and 10 km-wide Variscan massif bounded by three Mesozoic basins: the Boucheville syncline to the south, the Bas-Agly syncline to the Northeast, and the St-Paul-de-Fenouillet to the North (Fig. 2). The Cenozoic (Pliocene) Roussillon Graben sedimentary infilling delimits the south-eastern border of the massif. The Paleozoic and Mesozoic structural domains are separated by E-W trending vertical Alpine faults (Fig. 2B).

The Variscan basement consists of a 6 km-thick metamorphosed Ediacarian to Devonian sedimentary sequence (Fonteilles, 1970; Berger *et al.*, 1993; Casas and Palacios, 2012). The deepest part of the sequence also contains abundant meter to decameter-thick sheets of orthogneisses that correspond to former granitic sills emplaced at ca. 540 Ma (Tournaire Guille *et al.*, 2018). The para- and ortho-derived sequence has been metamorphosed and deformed during the late Variscan orogeny between ca. 305 and 295 Ma (Siron *et al.*, 2012, 2020). Considering structural depths and metamorphic grade, Delay (1989) made a two-fold subdivision of the AM basement into an infrastructure and a suprastructure, separated by the anatectic front. The infrastructure consists of partially molten orthogneisses and paragneisses hosting layers of marbles and calc-silicates. The suprastructure consists of the upper part of the metasedimentary series with Cambrian to early Ordovician micaschists and schists (the so-called Jujols group, Laumonier, 1998), thin and discontinuous late Ordovician volcano-clastic rocks, Silurian black-schists and Devonian marbles (Fig. 2B).

Both the supra- and infrastructure are intruded by late Variscan (308–304 Ma) magmatic bodies. The Ansignan charnockite is a 600 meter-thick laccolith that has intruded the deepest part of the infrastructure, in the southwestern part of the massif, at 307 ± 3 Ma (Tournaire Guille *et al.*, 2018). This magmatic complex is made of two main magmatic rocks (1) a porphyric K-feldspar, garnet and orthopyroxene-bearing granodiorite and (2) a garnet-bearing leucogranite best observed in the intrusion roof (*e.g.* Albas locality). Norite and diorite bodies are also reported within the charnockite (Delay, 1989; Berger *et al.*, 1993; Althoff *et al.*, 1994, Olivier *et al.*, 2008). The Cassagnes granite occurs as several metric to decametric sills in the upper part of the infrastructure (Fig. 2B). It is very similar in composition to the charnockite, except that orthopyroxene is very rarely observed, but was emplaced at the same time at 308 ± 3 Ma (Tournaire Guille *et al.*, 2018). Older ages have been proposed for the emplacements of the Ansignan and Cassagnes sills at ca. 315 Ma (Postaire, 1982; Respaut and Lancelot, 1983; Olivier *et al.*, 2004), The Tournefort diorite and the Saint-Arnac granite intruded the schists and micaschists of the suprastructure (Fig. 2B). Olivier *et al.* (2008) proposed that these two plutons were cogenetic and that they emplaced between 308 ± 1 and 304 ± 5 Ma respectively. The Saint-Arnac pluton is also composed of several acid intrusions (Fonteilles *et al.*, 1993; Olivier *et al.*, 2008). The diorite induced local contact metamorphism responsible for limited partial melting of the surrounding micaschists (Delay, 1989; Fig. 2).

Heat advection associated with the upward transfer of the large volume of magmatic bodies may have contributed to the regional HT/LP metamorphism during the late-Variscan orogeny (Vielzeuf, 1984; Delay, 1989; Guitard *et al.*, 1996; Olivier *et al.*, 2004; Siron *et al.*, 2012, 2020). This is consistent with the recent temporal constraints of the HT-LP peak temperature dated at ca. 305 Ma with *in situ* LA-ICP-MS on monazite and zircon (Siron *et al.*, 2012, 2020; Tournaire Guille *et al.*, 2018). The suprastructure is characterized by a HT-LP metamorphism recorded with the successive apparition of biotite, cordierite, andalusite and sillimanite as index minerals (Fonteilles *et al.*, 1993). Here, the geothermal gradient in the suprastructure has been recently reconstructed at 55 °C/km (Siron *et al.*, 2012). Temperature reached up to 680 °C at the base of the suprastructure (Delay, 1989; Bouhallier *et al.*, 1991; Siron *et al.*, 2012, 2020), triggering the onset of partial melting outside the stability field of muscovite. Below the anatectic front, the infrastructure is characterized by a nearly isothermal geothermal gradient (~ 8 °C/km) during late Variscan event, with temperatures comprised between 730–800 °C (Andrieux, 1982a, b; Vielzeuf, 1984; Delay, 1989; Bouhallier *et al.*, 1991). This has been interpreted as the consequence of thermal buffering due to the highly endothermic behavior of the biotite dehydration-melting reaction (Delay, 1989; Siron *et al.*, 2012, 2020).

Comparison between thermobarometric estimations and present-day thickness suggests that between 3 and 5 km of the crust were subtracted during thinning (Andrieux, 1982a, b; Vielzeuf, 1984; Delay, 1989; Bouhallier *et al.*, 1991; Paquet and Mansy, 1991; Siron *et al.*, 2012, 2020) responsible for tightening of metamorphic isograds closer and the apparent strong metamorphic gradient between 80 °C and 125 °C/km (Guitard *et al.*, 1996 and references therein; Siron *et al.*, 2012, 2020).

The HT/LP metamorphism is related to main strain pattern observed over the AM that corresponds to a pervasive flat-lying foliation and localized mylonites holding an NNE-SSW trending stretching lineation. The foliation is flat-lying in the southern part of the massif, and is very steep and E-W striking in the northwestern part of the massif (Figs. 2 and 3; Berger *et al.*, 1993; Fonteilles *et al.*, 1993). It is synchronous with high-grade metamorphism, partial melting and sheet-shaped granitoid intrusions, the latter showing a magmatic foliation concordant with the gneissic surrounding main foliation

(Delay, 1989; Bouhallier *et al.*, 1991; Paquet and Mansy, 1991; Althoff *et al.*, 1994).

Mylontic to ultramylonitic ductile shear zones are distributed over the whole structural pile. Delay (1989) and Paquet and Mansy (1991) have identified about ten gently dipping mylonitic shear zones of various thicknesses (meter to decameter) that are parallel to the main foliation with a very conspicuous N20 stretching direction. Based on the kinematics of these shear zones (top-to-the-north in the northern part and top-to-the-south in the southern part), Olivier *et al.* (2004, 2008) suggested that these shear zones were localized at the top of the dome roof at ca. 300 Ma as the final stage of a doming under transpressional evolution. In contrast, Bouhallier *et al.* (1991) proposed that top-the-north shear zones are linked to an extensional detachment at the boundary between anatectic micaschists and gneisses, likely responsible for the juxtaposition of the infrastructure and suprastructure during a late-Variscan extension. Based on *in situ* LA-ICP-MS on monazite of mylonitic gneisses, Siron *et al.* (2012, 2020) proposed that this thinning occurred at ca. 300–296 Ma. Olivier *et al.* (2004) have suggested instead that the subtraction and thinning did not occur *via* a single shear zone and proposed that the material was subtracted by many small shear zones at the top of a late Variscan diapiric dome in both the infrastructure and suprastructure.

An earlier tectonic phase is attributed to crustal thickening with relics of kyanite (Fonteilles, 1970; Fonteilles and Guitard, 1971) and moderately dipping relictual foliation with south verging sheath folds interpreted as top-to-the-south shearing and nappe stacking (Bouhallier *et al.*, 1991; Olivier *et al.*, 2004).

In the Mesozoic sediments of the Bas-Agly and Boucheville synclines, the impact of Cretacous extension is supported by HT-LP metamorphism in (Golberg and Leyreloup, 1990) and highlighted by Raman Spectrometry on Carbonaceous Matter (RSCM) studies that reported temperatures up to 550 °C (Clerc, 2012; Chelalou, 2015; Chelalou *et al.*, 2016; Ducoux, 2017) as a result of the Cretaceous crustal thinning and mantle uplift (Clerc and Lagabrielle, 2014; Clerc *et al.*, 2015, 2016; Chelalou *et al.*, 2016; Lagabrielle *et al.*, 2016; Ducoux, 2017). In that context, the late Variscan age of the ultramylonitic shear zones has been questioned since the 1990’s (Delay, 1989; Paquet and Mansy, 1991; Vauchez *et al.*, 2013; Odlum and Stockli, 2019). Mylonitic deformation of Mesozoic limestone at the base of the Bas-Agly syncline, with a N20 stretching direction similar to that affecting the metamorphic basement led Delay (1989) and Vauchez *et al.* (2013) to suggest that part of the ductile shear in the Agly basement may be attributed to Cretaceous extension. More recently, Odlum and Stockli (2019) have shown that U-Pb apatite ages from the southern side and deepest part of the Agly massif were reset between 113 and 123 Ma while those located to the north still preserved late Variscan ages. This difference in thermal history led them to suggest that the high-grade gneisses of the southern part of the massif are part of the lower crust and were exhumed and juxtaposed to the micaschists of the northern part of the massif, interpreted as the upper crust, during early Cretaceous extension.

The Paleozoic basement is cut by steeply dipping E-W to NW-SE trending faults interpreted as ancient sinistral faults formed during the opening of pull-apart basins infilled with Mesozoic carbonates (*e.g.* the Serre de Verges, Roquo Roujo, the Serre de Cors; Fig. 2B; Fonteilles, 1970, 1976). These major faults drain hydrothermal fluids with temperatures between 300 and 550 °C (Fallourd *et al.*, 2014; Boulvais, 2016). Hydrothermalism locally resulted in an almost complete albitization of the Paleozoic rocks, like de Saint Arnac granite and surrounding gneisses between 110 and 95 Ma (Poujol *et al.*, 2010). Recently, using (U-Th)/He method on apatite and zircon in the Agly Massif’s Paleozoic rocks, Ternois *et al.* (2019) estimated the temperature of the Cretaceous thermal event related to fluid circulation along the E-W brittle structures at a maximum of 300 °C. Using RSCM, Ducoux (2017) reported a temperature of 420 °C in the Serre de Verges Mesozoic limestones.

The Mesozoic basins fringing the Agly Massif together with the small pull-apart basins were inverted during Tertiary collision, and pinched between steep reverse faults and overthrusted towards the North. The main reverse faults cutting the Paleozoic basement are from north to south, the Serre de Cors, the Rentadou and the Roquo Roujo (Fig. 2B) delimiting ribbons of NPMs. The faults show top-to-the-north kinematics and exhumed the southern blocks (Delay, 1989). The last stage of the brittle deformation is manifested by N20 and N150 striking conjugate strike-slip faults that accommodated the N-S directed Pyrenean shortening. Among these strike-slip faults, the sinistral NE-SW trending Planèzes Fault (Fig. 2B) may have accommodate a large displacement already during late Variscan and may have been reactivated during Pyrenean Tertiary Tectonics.

In the following, we present the results of a detailed structural analysis focused on Variscan deformation, and performed over the whole Agly massif, with a reappraisal geological mapping, new tectonic maps and series of detailed cross-sections. At variance from previous studies, we clearly identified three Variscan deformation fabrics named D1, D2 and D3 deformations responsible for the present finite strain pattern of the AM. The deformation history in order to correlate new and existing structural, metamorphic, magmatic and geochronological datasets.

3 Overall geometry and deformation partitioning in the Agly massif

The structural maps on Figure 3 present the dataset of more than 3000 foliation and lineation measurements from our own field surveys and from published mapping of Delay (1989). Two main areas are defined: (i) a southern domain, that extends south of a line going from Ansignan to Latour-de-France villages, where the foliation is moderately to gently dipping and the stretching and mineral stretching lineation trends consistently N20; (ii) a northern domain where the foliations are steeply dipping to vertical and generally E-W directed (Figs. 3A–3C). However, microstructural observations and the structural data suggest that the overall finite strain pattern of the Agly massif resulted from the superposition of three major ductile deformations, named D1, D2 and D3, and a local D4 deformation that is only present in the vicinity of the Eastern margin of the Saint-Arnac granite (*cf.* section 4.2). In this scheme, the southern and northern domains are mostly dominated by the S2 foliation and the steeply dipping S3

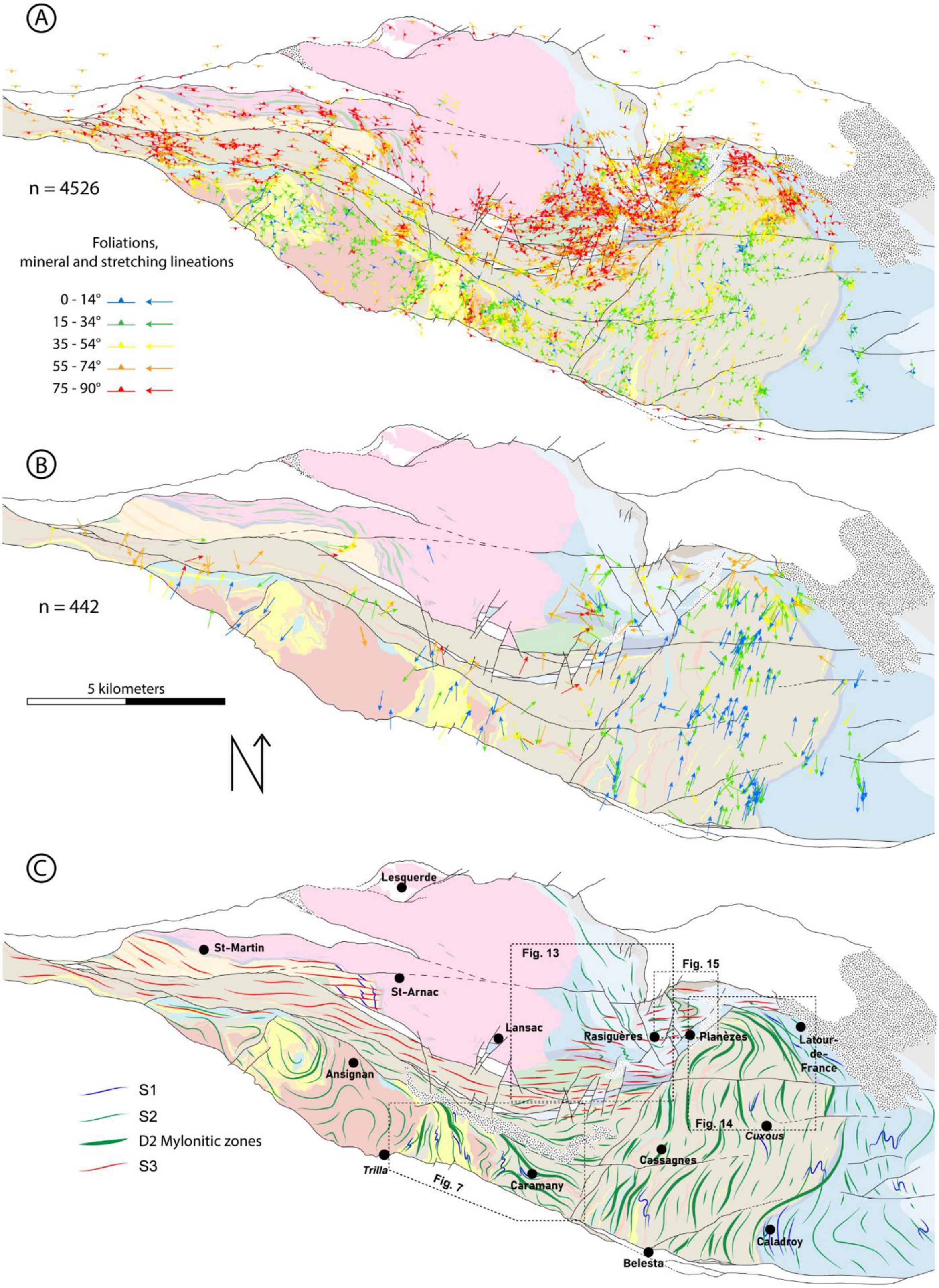

Fig. 3. Maps of the Agly massif showing (A) foliations and (B) lineations measurements from this study and Delay (1989). (C) Synthetic map showing the foliation simplified trajectories of D1, D2 and D3 deformation. Zoom areas of Figures 6, 12, 13 and 14 are indicated.

foliation, respectively (Fig. 3). We further document the geometrical relationships between D1, D2, D3 and D4 and their kinematics in key areas with detailed structural mapping and deformation analyses, focusing on the relationships between deformation, metamorphism, partial melting and magma emplacement.

3.1 D1 deformation

The D1 fabrics are observed in the whole massif as a relictual deformation preserved from D2 or D3 reworking. In the eastern part of the southern domain, where low-grade schists are exposed east of Caladroy and Latour de France, the D1 planar fabrics correspond to a S1, mainly parallel to the sedimentary bedding, that is mostly concordant to the flat lying S2 (Fig. 4 stereograms 1 and 2). The S0-1/S2 relationship is best observed on centimeter- to meter-scale F2 fold hinges in the low grade schist (Figs. 6A–6C) and the Devonian marbles (Fig. 6D). In the gneissic and migmatitic part of the massif, S1 is preserved in ten to hundred meter scale lense-shaped low-D2 strain domains as a moderately to steeply dipping and NE-SW to NW-SE-trending relict S1 foliation (Figs. 5 and 7). In these lenticular domains, the flat lying S2 foliation is pervasive but remains weak.

The S1 enveloping surface is NW-SE (mostly N150E) trending and dips steeply to moderately toward the NE with a stretching and mineral lineation L1 gently plunging SE. S1 is commonly folded and transposed by S2 (Figs. 4, 6 and 7). In the low grade schist of the eastern part of the southern domain, both S1 and S2 are defined by preferential alignment of chlorite, white mica and biotite (Fig. 6B). In the infrastructure, S1 and S2 foliations are outlined by biotite and elongated quartzo-feldspathic aggregates or peritectic minerals like cordierite or garnet (Figs. 6F and 6G). The mineralogical assemblages that define the D1 planar and linear fabrics are similar to the D2 parageneses, preventing any D1/D2 distinction based on metamorphic characters.

The large-scale S1-S2 geometrical pattern is best observed along an E–W trending cross-section (Figs. 5 and 7B) making a foliation envelope that undulates with two predominant orientations. This pattern is well marked in the southern part of the massif where several authors mentioned or represented map-scale folds with N-S trending axis (Delay, 1989; Berger *et al.*, 1993; Tournaire Guille *et al.*, 2018). Delay (1989) proposed that these folds were formed by the emplacement of the Ansignan charnockite, at odds with the concordance between the magmatic foliation and the foliation of country-rock (*cf.* section 4.1). In this area, the low-D2 strain lens are larger and more numerous (Fig. 7), forming alternations between steep S1 and nearly horizontal S2 (Figs. 5 and 7). Relicts of D1 preserved in the D3 domain are observed in the easternmost termination of the D3 deformation corridor and southwest of the Saint-Arnac pluton.

3.2 D2 deformation

Throughout the whole massif, D2 is defined by a pervasive flat lying S2 foliation that holds a N10-20 trending stretching and mineral lineation L2 (Figs. 4, 5 and 8). As originally described by Pascal *et al.* (1976), numerous F2 folds reworking S1 with an S2 axial plane as schistosity and fold axis that commonly parallel L2 are observed in the gneisses and micaschists. In the eastern part of the massif, S2 foliation is parallel to the metamorphic isograds that are characteristic of the HT-LP metamorphic gradients (biotite-in, cordierite-in, andalusite-in, sillimanite-in, muscovite-out and melt-in isograds). The L2 is outlined by preferential alignment of biotite, pressure shadow around sulfides or elongated cordierite and andalusite porphyroblasts (Fig. 8). In the infrastructure, S2 is defined by a gneissic and migmatitic layering. Numerous granitic leucosomes are parallel to S2 or intrude along F2 fold axial plane, but without any internal plastic deformation, arguing for a syn-migmatitic D2 deformation. The migmatitic foliation holds a L2 lineation marked by preferential alignment of biotite +/− sillimanite aggregates. These observations indicates that D2 were coeval with the HT-LP metamorphism (M2).

Shear criteria along L2 is consistent with a bulk top-to-the-north shearing. Localized high-D2-strain zones (C2) are observed as centimeters to ten meters wide mylonitic to ultramylonitic shear zones in the whole structural pile. They lie parallel or slightly oblique to the main S2 foliation (Fig. 9). These C2 shear zones form an anastomosing network of that separates lense-shaped D2-moderate strain domains. In the infrastructure, we have observed major C2 shear zones that form high strain corridors of anastomosed 20–30 meter-thick mylonites called Cuxous, Caramany, western Ansignan and eastern Ansignan shear zones (Figs. 3 and 5). Another major shear zone (Caladroy shear zone, Bouhallier *et al.*, 1991) is located at the interface between the infrastructure and the suprastructure. C2 shear zones bear a well-defined L2 mineral stretching lineation parallel to that of the lower-strain domains formed by elongate and recrystallized Bt + Qtz + Kfs aggregates, with a conspicuous N20 direction (Fig. 8). Kinematic indicators suggest a main top-to-the north shearing observed either in the infrastusture or in the suprastructure (Fig. 9). C2 mylonitic shear zones are often internally affected by C' shear bands that show a similar top-to-the north sense of shear. Although top-to-the-north shearing is the most conspicuous kinematics, top-to-the-south shearing is also reported at different places in the massif and is interpreted as conjugate faults (*e.g.* Bouhallier *et al.*, 1991; Olivier *et al.*, 2004).

Within the deepest rocks of the infrastructure, strain gradients across C2 shear zones show that mylonitic texture developed progressively from the migmatitic foliation without significant changes in the metamorphic assemblages (Fig. 10). Dynamic recrystallization of migmatitic phases produced layers of very fine grained Qtz + Kfs + Bt + Grt ± Sil ± Crd ± Opx assemblage. Plastic flow is accompanied by brittle fracturing of large K-feldspars, garnets and orthopyroxenes (when present). Brittle fracturing and boudinage of the porphyroblasts developed in the presence of water and are responsible for local high-temperature retrogression with the crystallization of syn-kinematic Bt + Sil + Qtz assemblage. Although localized, the mylonitic deformation is homogeneously distributed over the entire gneissic and migmatitic domain.

Within higher structural levels of the infrastructure, along the Cassagnes, Cuxous and Caladroy high-strain zones, mylonitic fabrics are characterized by a fine grained matrix of plastically-deformed quartz aggregates that mantles cataclased feldspars (Fig. 10). Quartz deforms plastically whereas cataclasis of feldspar megacryst, imbrication and boudinage is common. Boudin necks show syn-kinematic growth of biotite. Within the ultramylonitic foliation, the quartz-feldspar grain-size is very low (5–10 µm) and trails of fractured garnets show rare and weak retromorphosis with Bt + Chl + Qtz assemblage. In some samples, chlorite seems to be post-kinematic as related to late alteration of biotite.

3.3 The D3 “Tournefort Deformation Zone” (TDZ)

In the Northern part of the massif, the S2 foliation is affected by a D3 deformation localized along an E-W trending and 4 km-wide strain zone, named the Tournefort Deformation Zone (TDZ). The TDZ crosscuts the whole massif from west to east (Figs. 3 and 11) forming subvertical D3 planar fabrics with strikes ranging from ENE-WSW to ESE-WNW (Fig. 4). The Tournefort dioritic intrusion is also affected by this D3 deformation. The TDZ is cut by the Late Variscan Planèzes fault system that induces a bulk sinistral offset of about 3 km in map view (Figs. 2B and 3).

A gradient of deformation can be observed from the margins to the core of the TDZ (Fig. 11). The D3 TDZ margins are characterized by a progressive folding of the initially shallowly and eastward dipping S2 foliation into a NE-SW direction with a steeper dip (Fig. 11). The margins of the D3 TDZ show F3 folds with a steep NE-SW striking axial surface and weakly plunging axes (Figs. 12A–12C and 13C). F3 axial planes can be associated with the development of a NE-SW subvertical S3 cleavage, like in the Devonian limestone (Fig. 12B).

With increasing D3 deformation towards the core of the TDZ, F3 folds become tighter leading to the intensification of S3 cleavage with an E-W strike. L3 mineral stretching lineations are very scarce and have variable plunge (Fig. 12D). In sections parallel to the stretching lineation (XZ deformation principal plane) where it is horizontal, D3 dextral kinematic criteria are recognized in the micaschists in the form of S-C fabrics and sigma feldspar-clasts in the gneisses (Fig. 12C).

Within the TDZ, two sets of centimeter to decametric subvertical dextral shear zones are observed with N120 and few N90 directions (Fig. 13C). The N120 shear zones are located mainly in the core of the TDZ. The inflexion of S2-S3/C3 observed along these shear zones is consistent with apparent dextral shearing. East of Tournefort diorite and west to the Saint-Arnac granite, the E-W striking S3 is transposed into a NW-SE trend (~ N120) shear zones and also emphasizes an apparent dextral shearing (Fig. 3). The NE-SW to NW-SE spread of poles of D3 planar fabrics (*i.e.* S2-S3/C3) on stereograms from (Figs. 4 and 13) is explained by the D3 gradient of deformation (Fig. 13C).

Between Planèze and Latour-de-France village, the gently eastward dipping S2 foliation progressively rotates at a kilometer scale towards an E-W and sub-vertical orientation and forms a kilometer F3 fold (Fig. 14). The S3 foliation is scarce and not pervasive in this area (not represented on the Fig. 14), whereas it is penetrative in the western part of the dome (Figs. 14C and 14D). It is worth noting that together with the D2 anastomosing network, the S2 and L2 mylonites and ultramylonites are also affected by the D3 folding (Fig. 14).

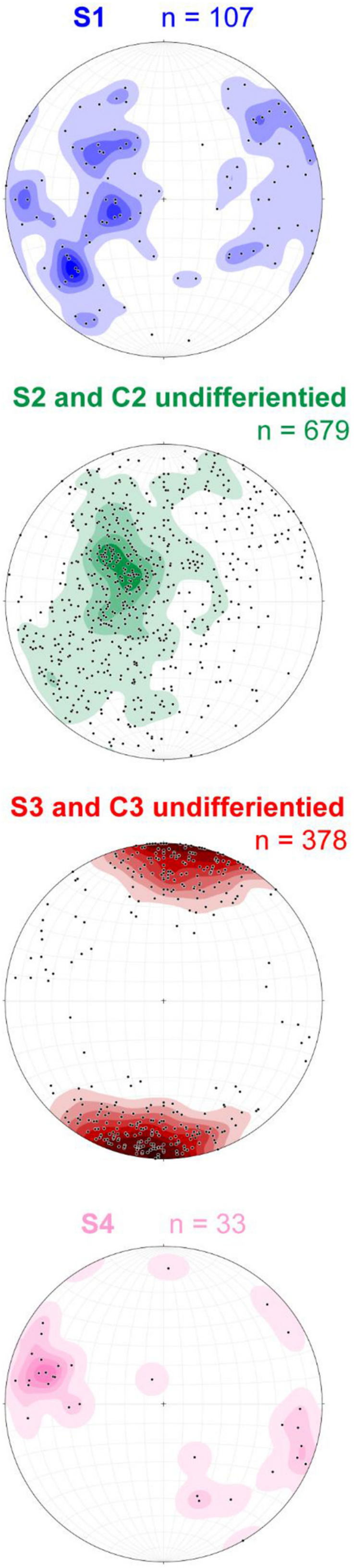

Fig. 4. Poles of planar fabrics of each deformation (D1, D2, D3 and D4) plotted in lower hemisphere Wulf stereograms. Only data with a clear affiliation to one of the four deformations are represented.

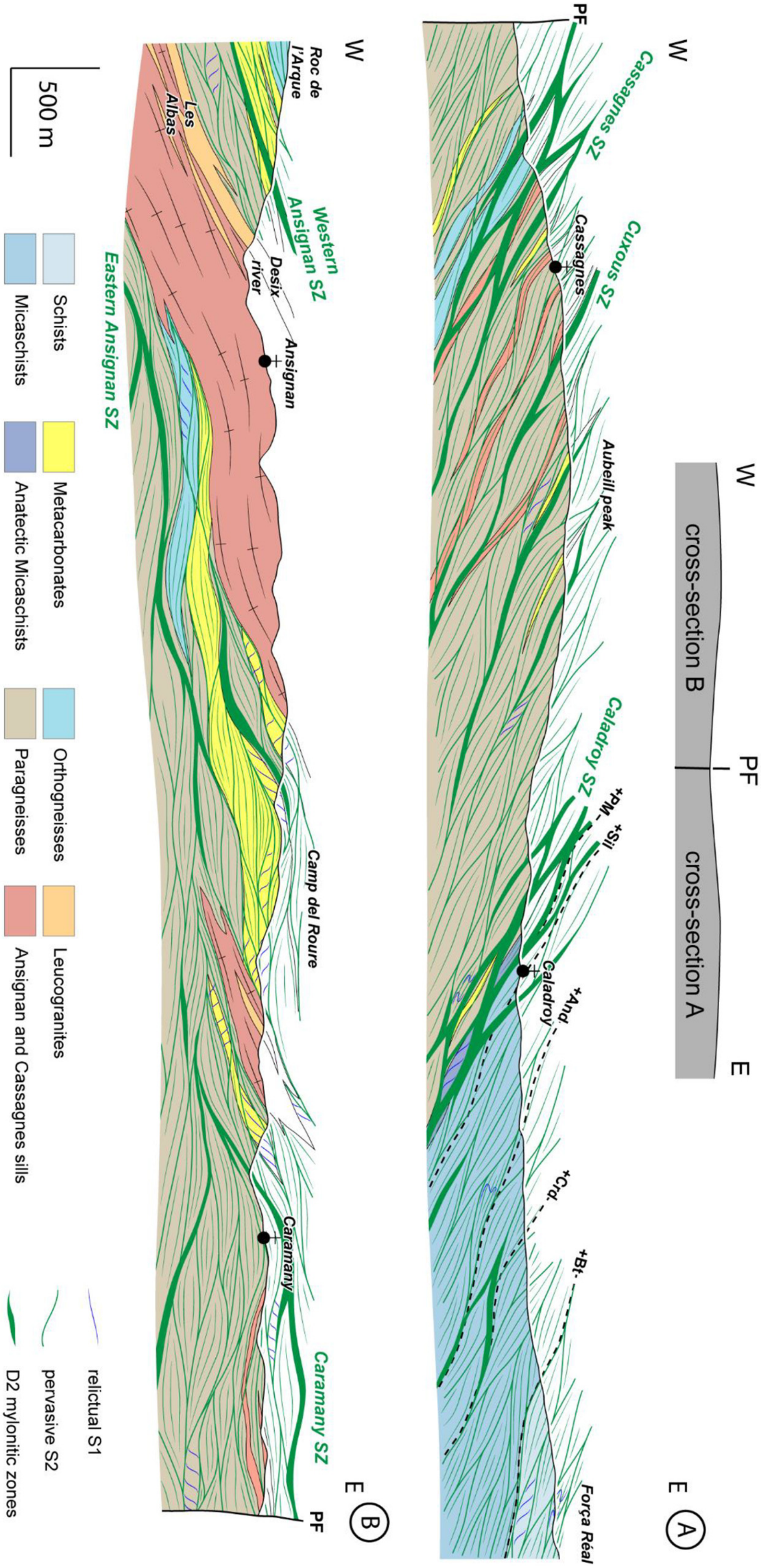

Fig. 5. E-W Cross-sections through the Agly massif. (A) eastern side of Planèzes fault. (B) Southern part of the Agly Massif, in the western side of Planèzes fault. (PM: partial melting).

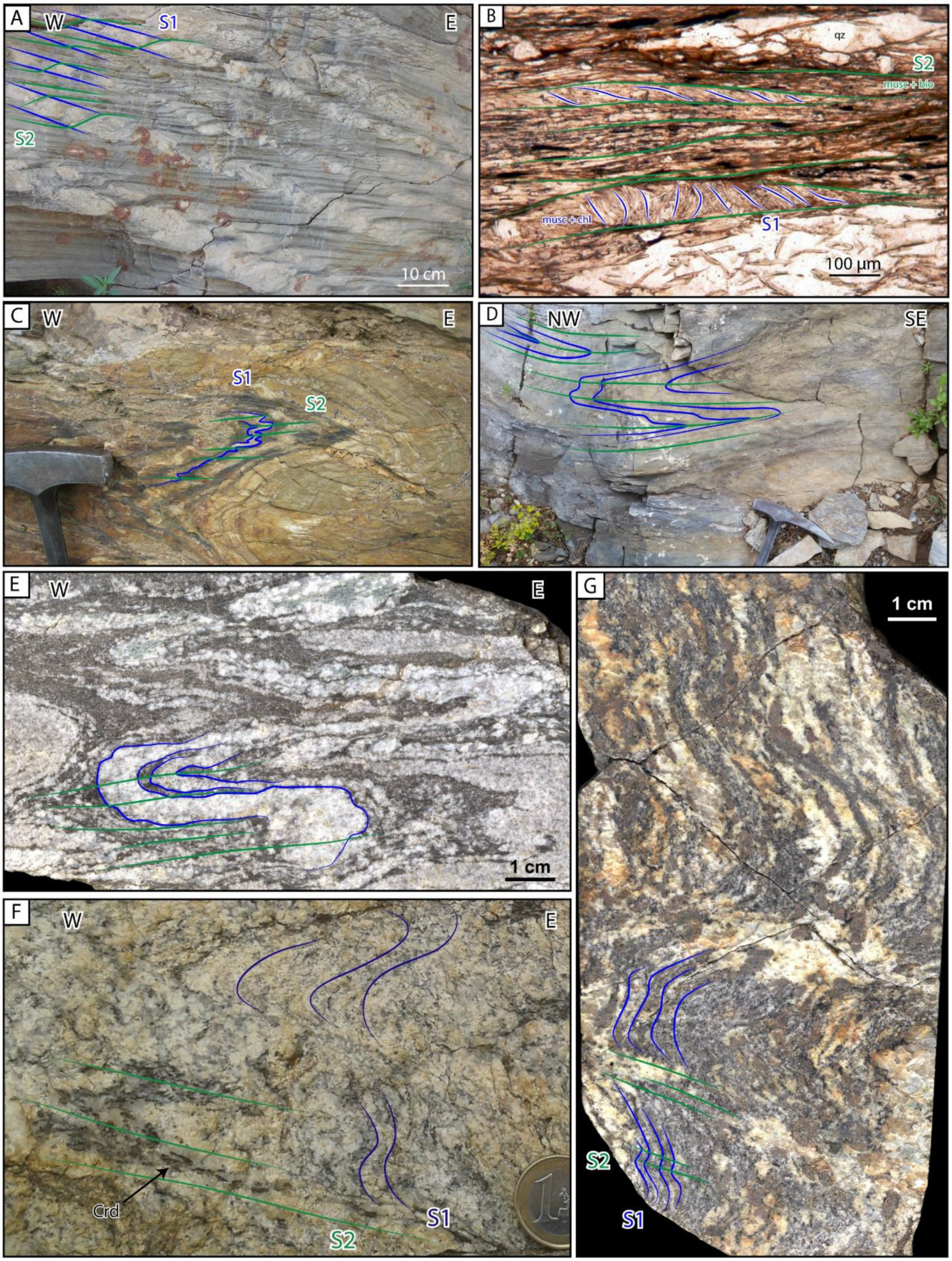

Fig. 6. Outcrop and microphotographs showing D1/D2 relationships. In Força Réal schists, (A) S2 in S0-1 quarzitic layers; (B) remnants of S1 in thin-section, S1 bears chlorites and muscovites, and S2 muscovites and biotites; F2 foldsin (C) Força Réal schists, (D) devonian marbles, (E) migmatitic paragneiss. (F) F2 folds in migmatitic paragneiss, cordierites are crystallized parallel to S2 inside leucosomes coeval with D2 deformation. (G) F2 folds in migmatitic paragneiss with injections of melts parallel to S2.

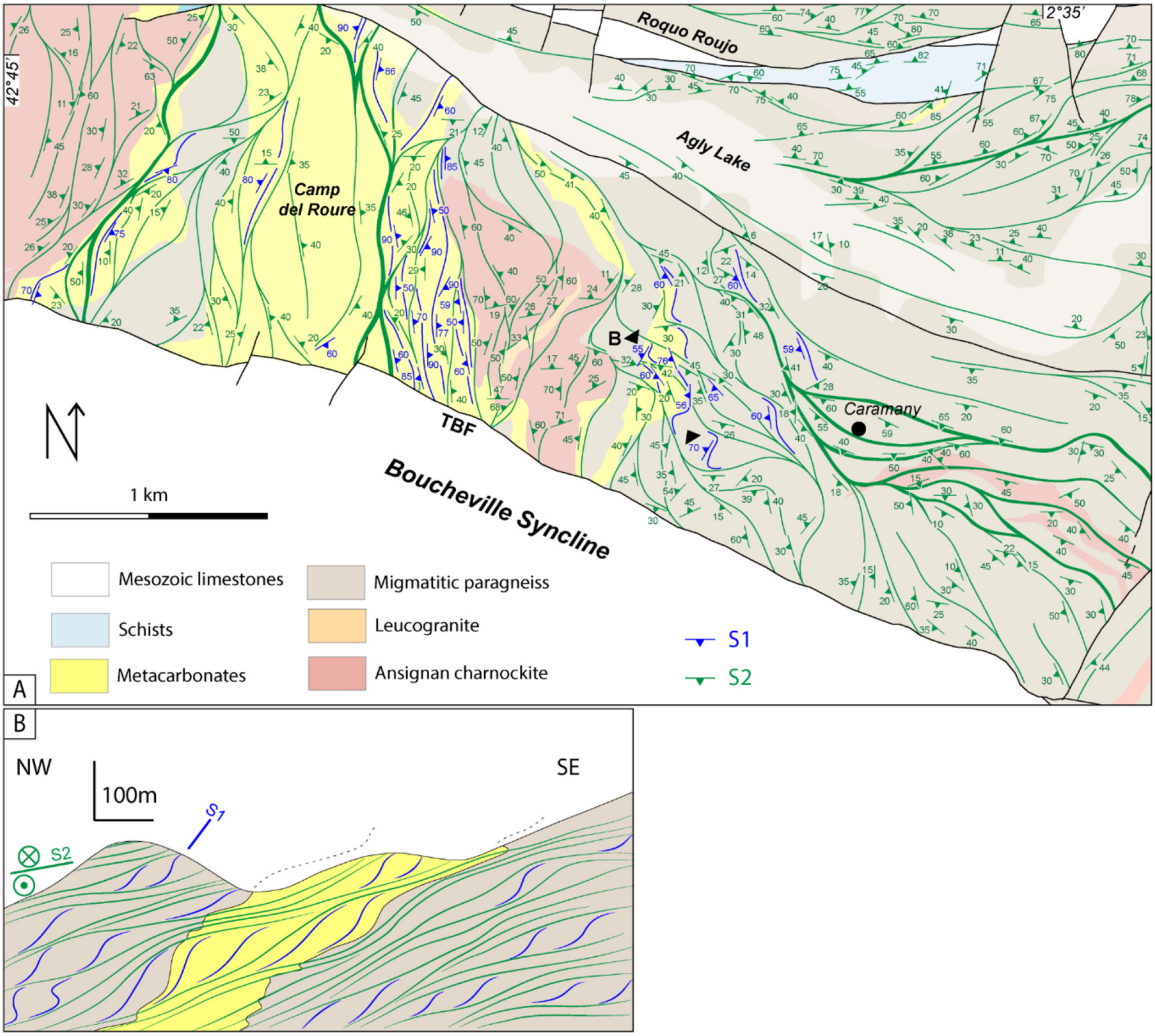

Fig. 7. Detailed structure of the southern part of the massif of the surroundings Caramany village. (A) Map of the foliations and their trajectories. (B) Cross-section.

A widening and intensification of D3 is observed from upper domain, *i.e.* LaTour-de-Fance area, toward the lower domain, *i.e.* Saint Martin village surroundings where all the planar fabrics transposed into S3

A vertical gradient of deformation is also observed in the TDZ. Indeed, D3 is more developed in the infrastructure in the western part of the massif than in the suprastructure in the eastern part. In the infrastructure between Ansignan and Saint-Martin villages, all the planar fabrics are transposed into S3. In the upper structural levels of the suprastructure (*i.e.* Devonian marbles and Silurian schists), the D3 is less pervasive and form kilometer folds (*cf.* next section). Along the TDZ south of the Tournefort diorite, D3 create a pinched synform that open as a fan-like structure to the east.

3.4 D2/D3 interference in the Roque Courbe area

North of Planèzes and Rasiguères villages, at the "Roque Courbe" area (literally "the curved rock" in English), the Devonian marbles and the Silurian-Ordovician schists present reversed polarity, with Ordovician schists on top of the Devonian marbles, observed on the southern side of the Roque Courbe near Planèzes and in the La Peyriere D3 Syncline (Fig. 15B and 15D). Relics of centimetre to decimetre synfolial F2 fold hinges are well preserved in the marbles (Fig. 6D). D2 deformation also resulted in the local boudinage of dolomitic layers of the Devonian marbles along a N-S trending direction, as well as shearing and thinning of the upper part of the metasedimentary pile resulting in a greatly reduced thickness

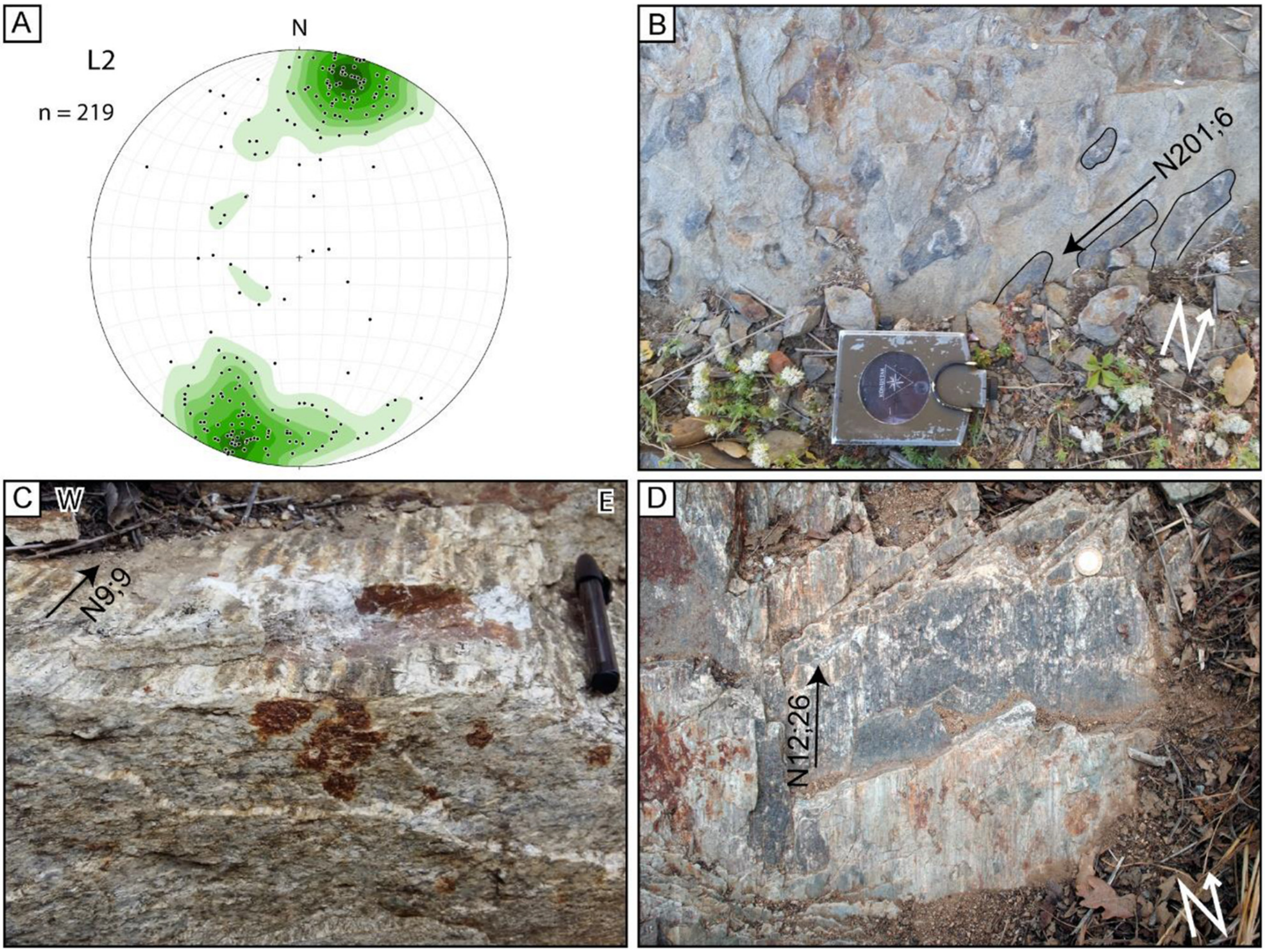

Fig. 8. Characteristics of the L2 stretching and mineral lineation. (A) L2 lineations plotted in lower hemisphere Wulf stereogram. (B) L2 marked by andalusites in micaschists. L2 in mylonitic paragneisses of (C) Caladroy and (D) Cuxous shear zones. Field measurements are given as N direction; plunge on the pictures.

of the sequence (< 20 m) and the scarcity or even absence of the Silurian schist (see Berger *et al.*, 1993). The Roque Courbe area first formed during D2 shearing with the development of a hectometer scale F2 isoclinal fold with a nearly horizontal axial plane and north trending fold axis by analogy with microstructural F2 axis. Early D2 isoclinal folding is responsible for the inverted polarity. Subsequently, F2 isoclinal fold was deformed by F3 open folds with ENE-WSW steeply dipping axial planes and axes gently to moderately plunging to the ENE. F3 folding resulted in the formation of the map-scale Rasiguères anticline and La Peyrière syncline (Fig. 15). D3 deformation resulted in the development of a vertical S3 axial plane cleavage best observed in the southern limb of the F3 "Rasigueres anticline" where the F2 hectometer fold hinges is observed and the tight "La Peyrière" syncline (Fig. 15). The Roque Courbe folded structure has been interpreted as due to Alpine tectonism (Delay, 1989) or as Variscan nappe stacking event (Berger *et al.*, 1993; Fonteilles *et al.*, 1993). We interpreted it as a kilometer scale D2/D3 fold interference pattern (Fig. 15).

4 Deformation pattern in the late-Variscan magmatic intrusions

4.1 Ansignan charnockite and Cassagnes granites

The Ansignan charnockite is emplaced in the deepest part of the Agly Massif at ca. 5 ± 0.5 kbar and 700–900 °C (Vielzeuf, 1984; Delay, 1989; Siron *et al.*, 2012, 2020; Fig. 5). A magmatic foliation is defined by the preferential orientation of K-feldspar and a compositional banding corresponding to the alternation of charnockitic and leucogranitic magmas. This fabric parallels S2 foliation in the migmatitic paragneiss, arguing for syn-D2 emplacement, as already suggested in previous studies (Bouhallier *et al.*, 1991; Berger *et al.*, 1993; Althoff *et al.*, 1994). Preferential alignment of K-feldspar porphyroblasts also defines a N-S trending lineation, consistent with the regional L2 stretching direction. The gabbro-norites enclaves contained in the Ansignan charnockite are mostly concordant with the S2 magmatic foliation (see Delay, 1989; Berger *et al.*, 1993; Althoff *et al.*, 1994) and stretched in some places toward a NE-SW

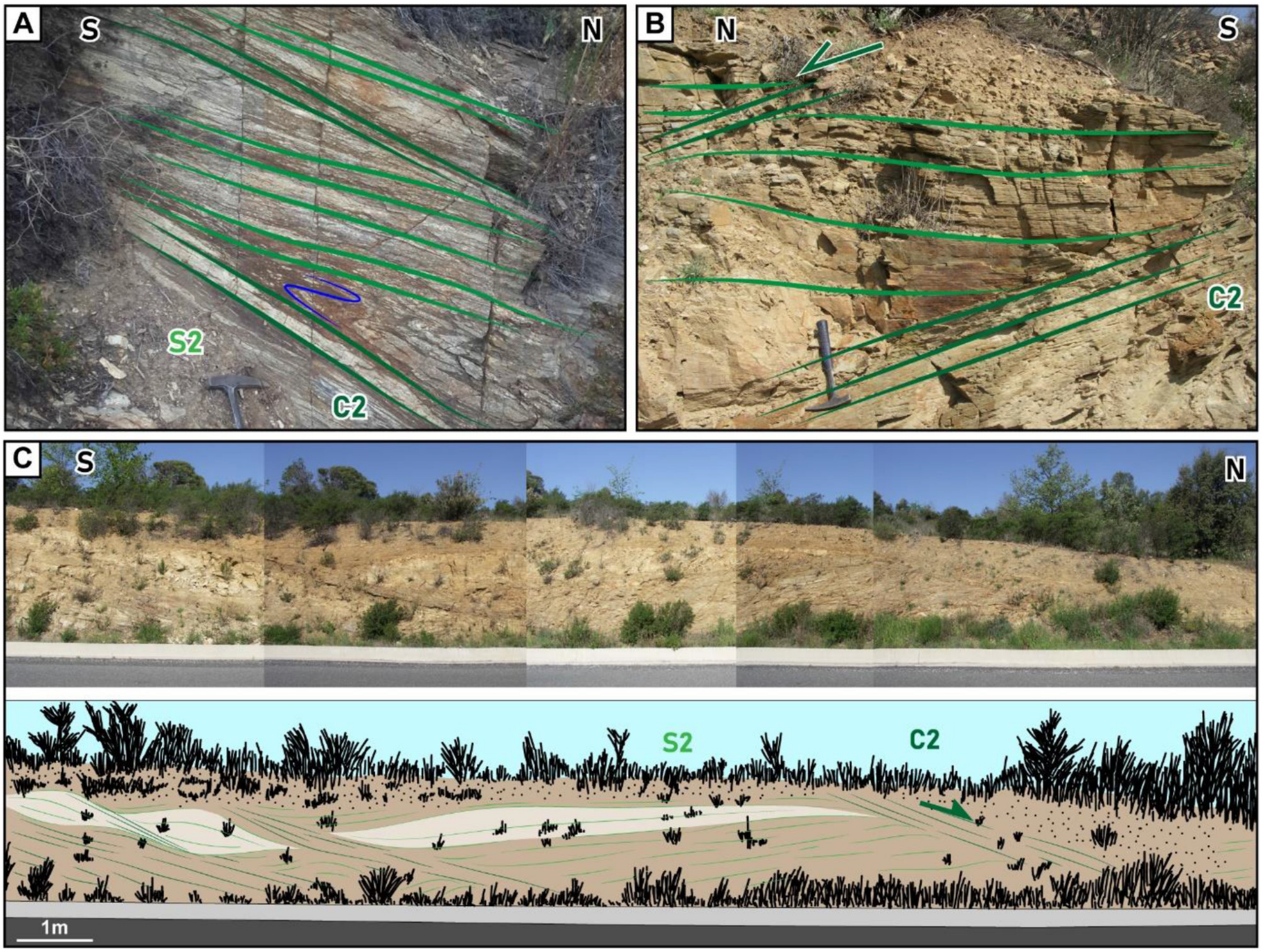

Fig. 9. C/CS relationships during D2 deformation with a top-to-the-north kinematics in paragneisses (A and C) and in micaschists (B).

direction. Deformation in the pluton was active from magmatic stage to sub-solidus conditions as attested by the injection of magma in small C2 shear bands, and by the solid state deformation of magmatic crystals like the development of quartz ribbons and the fracturation of K-feldspars. The Cassagnes granites show the same strain pattern as the Ansignan Charnockite, with a gently dipping S2 foliation and a N10-N20 trending L2 mineral and stretching lineation. Like in the Ansignan laccolith, magmatic fabric is outlined by large K-feldspar preferential orientation. However, D2 sub-solidus deformation is more intense in Cassagnes sills, resulting in the formation of elongated recrystallized K-feldspar and the recrystallisation of the matrix.

4.2 The Tournefort / Saint-Arnac intrusion

The Tournefort dioritic and Saint-Arnac granite intrusions belong to a same large plutonic complex that has been extensively studied from a chemical, structural and geochronological point of view by Olivier *et al.* (2004, 2008). The Hbl + Bt + Pl ± Cpx bearing Tournefort diorite is intrusive into the micaschists and anatectic gneisses (Delay, 1989; Figs. 3C, 11C and 13A). It is located in the TDZ and contains a weak but penetrative E-W to NE-SW vertical magmatic foliation with a near vertical lineation (Olivier *et al.*, 2008 and Figs. 3C, 11C and 13A). The magmatic foliation is defined by the preferred alignment of biotite and hornblende and the compositional layering. Locally, the magmatic foliation is affected by localized, a few meters-wide vertical high strain zones developed under solid-state conditions (Fig. 13A). The magmatic and solid state deformation pattern is consistent with the D3 deformation.

As previously documented by Delay (1989) and Olivier *et al.* (2008), the Tournefort diorite intrusion induced a local partial melting of the surrounding micaschists that show F3 tight folds and an E-W S3 crenulation cleavage. Few tens of meters away from the diorite, contact metamorphism in the micaschists was also responsible for crystallization of andalusite preferentially oriented parallel to the S3 steep foliation. This suggest that diorite emplacement and associated contact metamorphism are contemporaneous with D3 deformation during development of the TDZ (Figs. 4, 13A and 13B). Nonetheless, the anatectic micaschists at the vicinity of the diorite do not have magmatic injections in their F3 axial planes, all the leucosomes are folded by the D3, which indicate that the D3 affecting the micaschists has occurred in sub-solidus conditions. So, D3 may has been active at several stages from supra- to sub-solidus conditions.

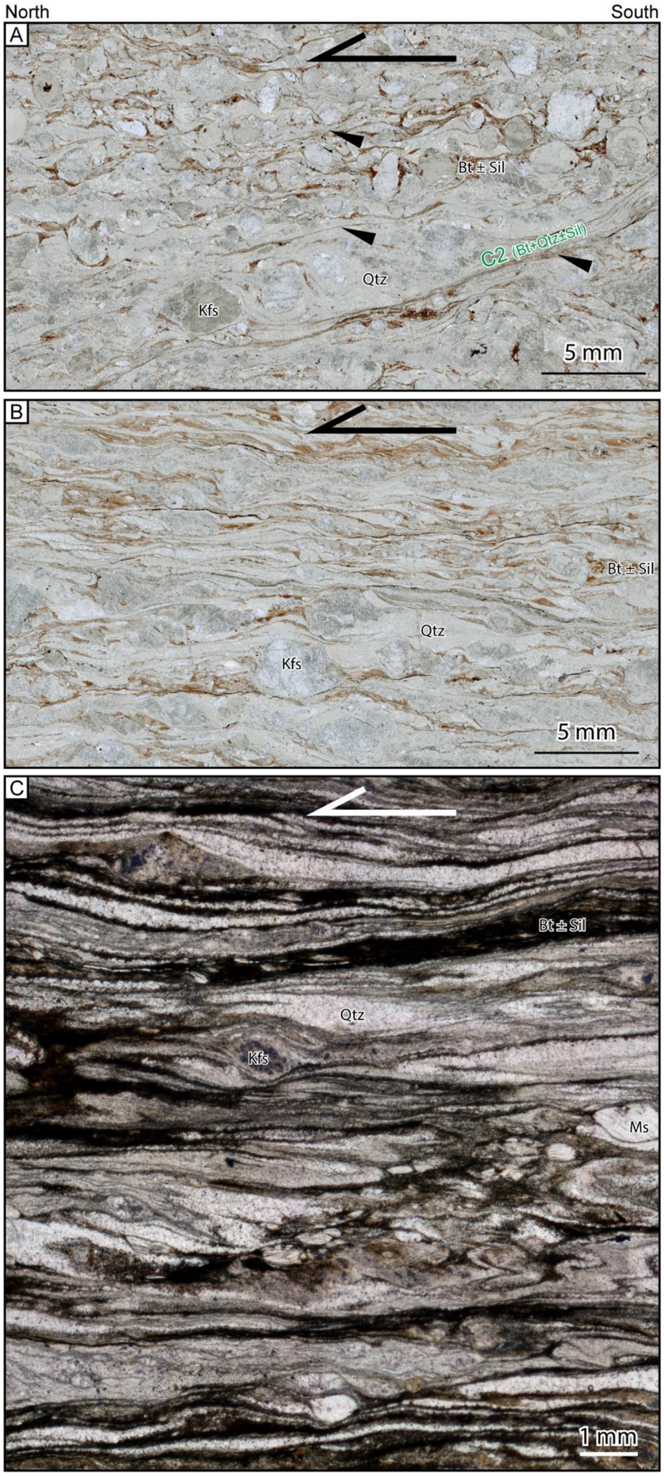

Fig. 10. Thin sections of a D2 strain gradient in paragneisses from the eastern part of the massif, close to Caladroy with a top-to-the-north kinematic. (A) low-strain deformation with local mylonites indicated by black arrows; (B) mylonitization generalized to the entire rock; (C) ultramylonitic texture with Qtz – Kfs – Bt – Sil assemblages (polarized normal light).

The Saint-Arnac granite has a weak magmatic foliation marked by the preferred orientation of biotite and K-feldspar (Olivier *et al.*, 2008). The pluton contains numerous meter-scale xenoliths of micaschists and mafic enclaves oriented parallel to the foliation. In the western and southeastern parts of the pluton, xenoliths and mafic enclaves define an E-W trending and vertical foliation. The Saint-Arnac granite intrusion deforms and cross-cuts the M2 isograds (Fig. 2). It is also responsible for a weak contact metamorphism of the surrounding schists and micaschists with the crystallization of large muscovite flakes that are post-kinematic and secant on the S2 foliation (Delay, 1989; Berger *et al.*, 1993). These observations indicate that the Saint-Arnac pluton is posterior to the M2 peak. In the northern part of the Agly massif, the huge amount of magma intruding the suprastructure is responsible for the deformation and the reorientation of S2 from a subhorizontal orientation to a NW-SE direction steeply dipping to the NE for several hundreds of meters (Figs. 13A and 13B; Delay, 1989). The schists and micaschists, located in the vicinity of the eastern margin of the pluton, are affected by a deformation D4, characterized by centimeter-scale folds (F4) of S2 with NNE-SSW trending and steeply dipping axial planes. Fold hinges are vertical or steeply plunging toward the East. Locally, F4 folding is associated with the development of non-pervasive axial planar fabric S4 that is sub-vertical with a N20 azimuth, with no visible mineral or stretching lineation. The contact between the D4 and the D3 TDZ forms a triple point (Fig. 13A). Such deformations and reorientations of foliations have been described for several emplacements of Pyrenean plutons with dextral transcurrent settings (*e.g.* Gleizes *et al.*, 1998b, 2001, 2006; Auréjac *et al.*, 2004).

Based on Anisotropy of Magnetic Susceptibility (AMS) on the Saint-Arnac, Olivier *et al.* (2008) proposed that the pluton emplaced during a transpressive regime. This dextral transpression is documented in most of the pluton emplacements of the Axial Zone (Leblanc *et al.*, 1993; Gleizes *et al.*, 1998b, 2006; Olivier *et al.*, 1999, 2016; Auréjac *et al.*, 2004; Hilario Orús, 2004; Román-Berdiel *et al.*, 2004, 2006; Antolín-Tomás *et al.*, 2009; Izquierdo-Llavall *et al.*, 2012), and also in two plutons of the NPZ (Lacourt: Gleizes *et al.*, 1992; Pic des Trois-Seigneurs: Leblanc *et al.*, 1996). Based on these observations and studies, some intrusions of the Saint-Arnac pluton may have took place during a dextral transcurrent setting, which may correspond to the D3. Nonetheless, the AMS lineations in the northern part of the pluton are N20, which may indicate an emplacement synchronous with the D2.

4.3 The garnet-bearing leucogranites

A third type of magmatic intrusion is represented by garnet-bearing leucogranites that form sills and dykes a few centimeters to tens meters in width. Of particular interest are the leucogranite dyke that crops out east of the Saint-Arnac intrusion (Fig. 13A) and the leucogranite pluton south of Latour-de France village (Fig. 14A). In both localities, the leucogranites are composed of quartz, alkali feldspar,

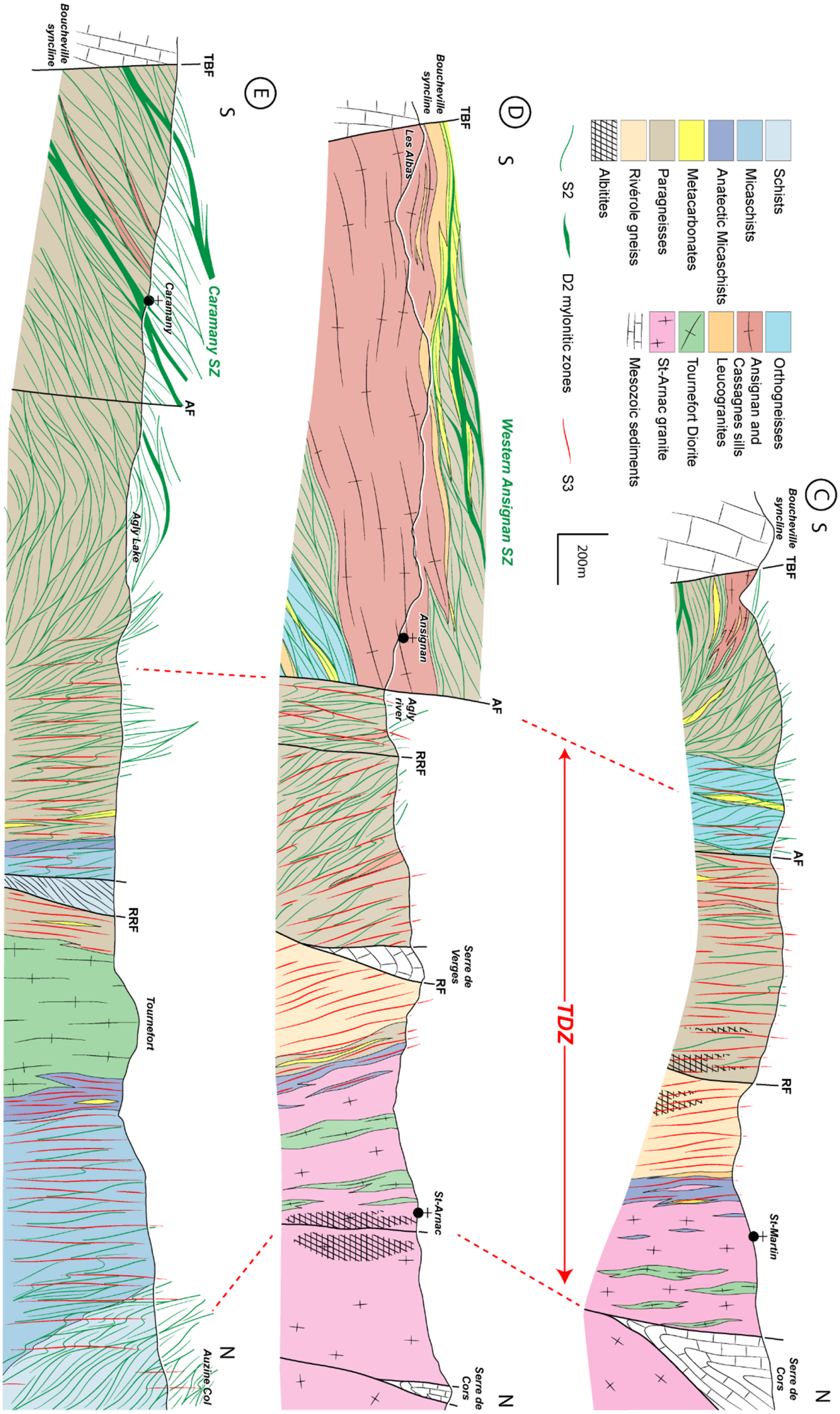

Fig. 11. N-S cross-sections through the Agly Massif. (C) Western part of the massif. (D) Cross-section through Ansignan charnockite and Serre de Vergès with pinched Mesozoic rocks. (E) Cross-section through the Tournefort Diorite. TDZ: Tournefort Deformation Zone.

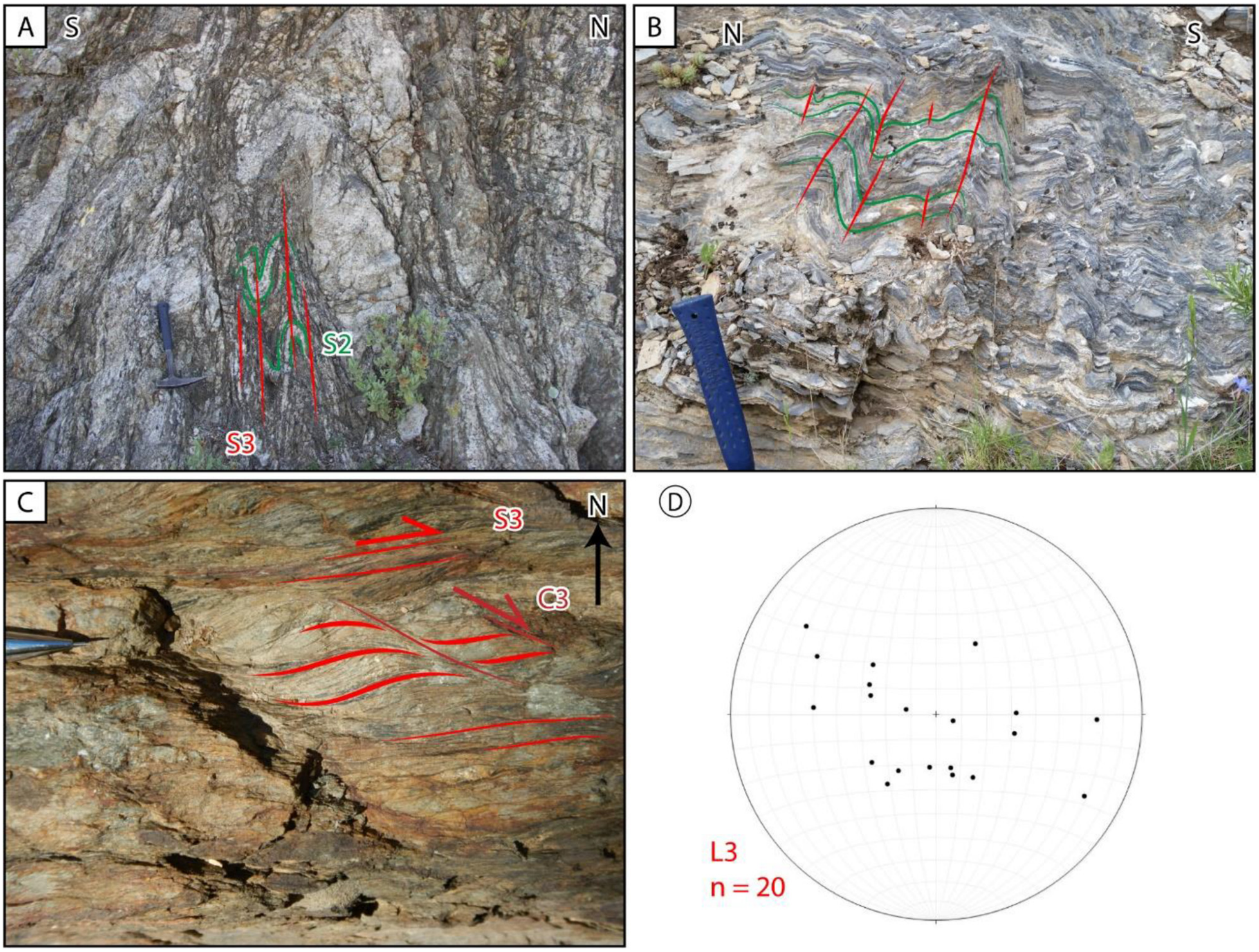

Fig. 12. D3 deformation structures. F3 folds in (A) paragneisses and (B) Devonian "calc-schist" marbles. (C) Dextral Kinematics in micaschists with C/S structures relationships. (D) L3 lineations plotted in lower hemisphere Wulf stereogram.

plagioclase, biotite, muscovite and garnet. The east Saint-Arnac dyke cuts accross the S2-S3 foliations and post-date early D3 deformation (Fig. 13A). The Latour-de-France leucogranite is located in a D3 fold hinge (Fig. 14A) and does not show visible solid-state deformation. But, microstructures like microfractures in feldspar megacrysts infilled by quartz, replacement of K-feldspar margins by myrmekites, and plastic deformation of quartz with chessboard extinction suggest that the leucogranite was deformed under high temperature sub-magmatic conditions (Marmo, 1971; Hibbard, 1987; Vernon, 1991, 2000; Bouchez *et al.*, 1992, 2006; Pawley and Collins, 2002). We suggest that the Latour-de-France garnet-bearing leucogranite emplaced after D2 deformation, probably during the final stage of the D3 deformation.

4.4 Pegmatites

Abundant pegmatites are observed from the top of the migmatitic gneisses to the cordierite-bearing Ordovician micaschists. Pegmatites form both concordant and discordant dykes and lense-shaped bodies ranging in size from a few decimeters up to several 10 meters. These bodies are interpreted to be the result of the ascent of residual hydrous silicate melt coming from the crystallization of the anatectic melt of the migmatitic infrastructure. The pegmatite mineralogical assemblage is made of Qtz + Kfs + Pl + Ms ± Bt ± Tur. Some pegmatites cross-cut the S2 foliation and are undeformed whereas others are boudinaged in D2 mylonitic fabrics. Mutually cross-cutting relationships between pegmatites and S2, and N20 stretching lineations in the D2 mylonites suggest a syn- to late-D2 age for the pegmatite emplacement.

5 Discussion

5.1 Impact of the Cretaceous thinning and Alpine tectonic on the Agly massif gneissic basement.

The Agly massif belongs to the North Pyrenean Zone (NPZ) that has been recently interpreted as an analogue of modern passive margin (Lagabrielle and Bodinier, 2008; Jammes *et al.*, 2009; Debroas *et al.*, 2010; Lagabrielle *et al.*, 2010; Clerc, 2012; Clerc *et al.*, 2012, 2013; Masini *et al.*, 2014). This tectono-metamorphic model is supported by a HT/LP metamorphism recorded in the Mesozoic sediments reaching up to 550 °C in the eastern Pyrenees within inverted E-W trending basins (Boucheville and Bas-Agly synclines, Fig. 1). This high-grade metamorphism is proposed to be

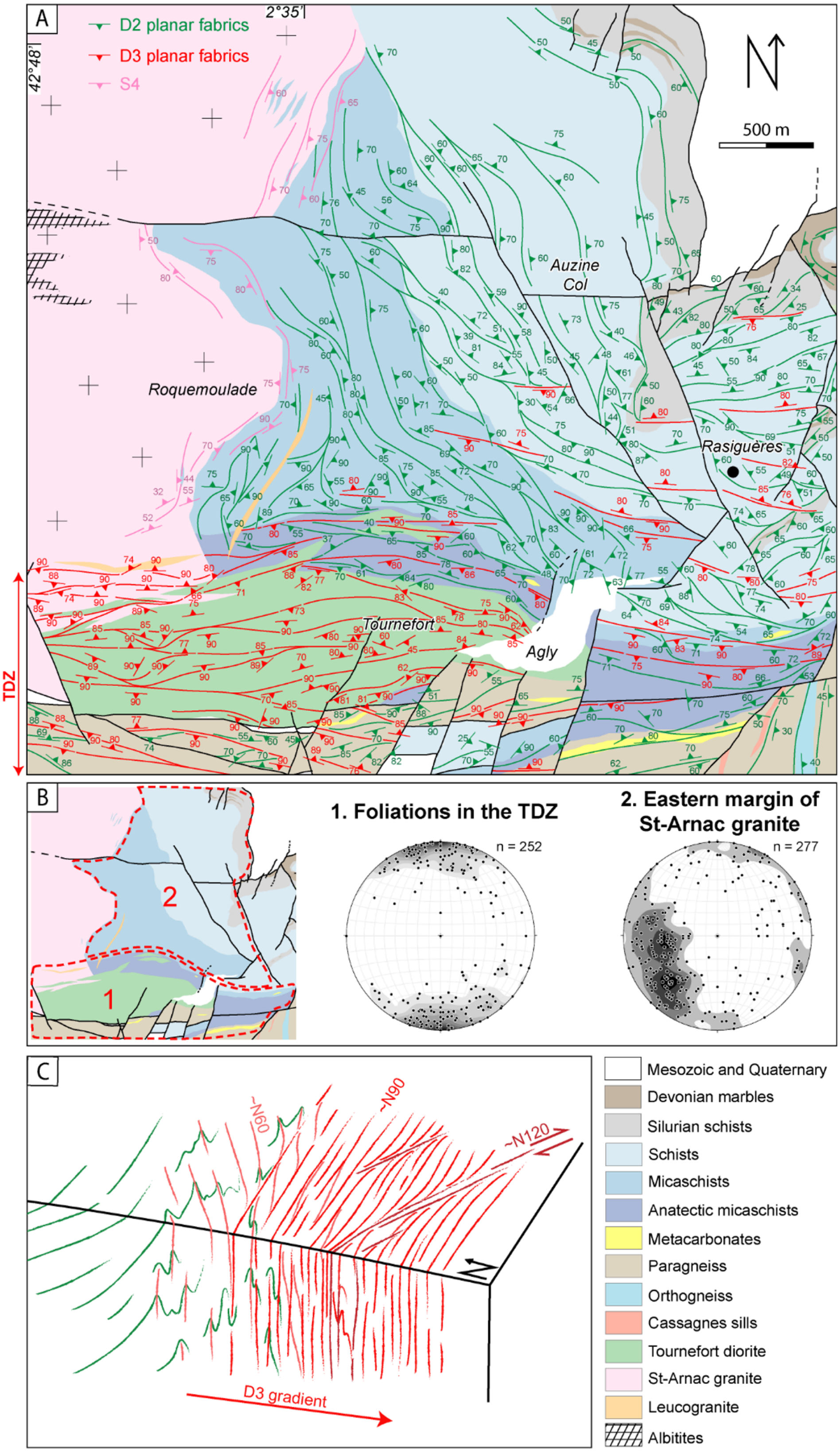

Fig. 13. Detailed structure of the eastern margin of Saint-Arnac granite with: (A) map of the foliations and their trajectories. (B) Poles of undifferentiated planar fabrics (lower hemisphere Wulf net) of the TDZ and of the eastern margin of Saint-Arnac granite. (F) Sketch of the deformation gradient of the TDZ.

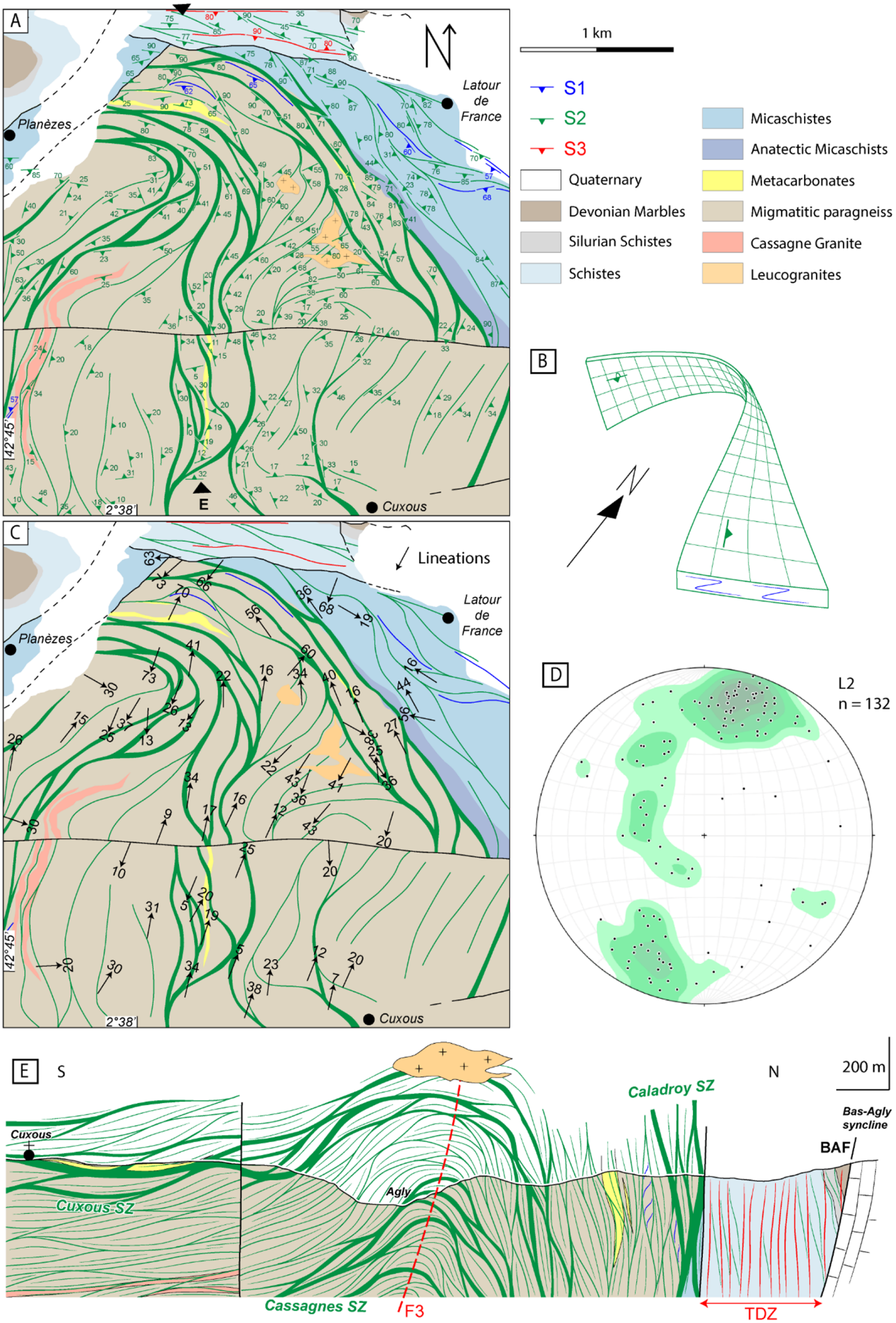

Fig. 14. Detailed structure of the northeastern part of the massif in Latour-de-France area. (A) Map of the foliations and their trajectories. (B) 3D sketch of the general S2 foliation shape. (C) Map of the L2 lineations and (D) L2 stereogram of the area. (E) N-S cross-section through the Latour-de-France structure showing S2/S3 relationships. They line up on a stereogram and indicate an E-W trending axis fold plunging towards the East.

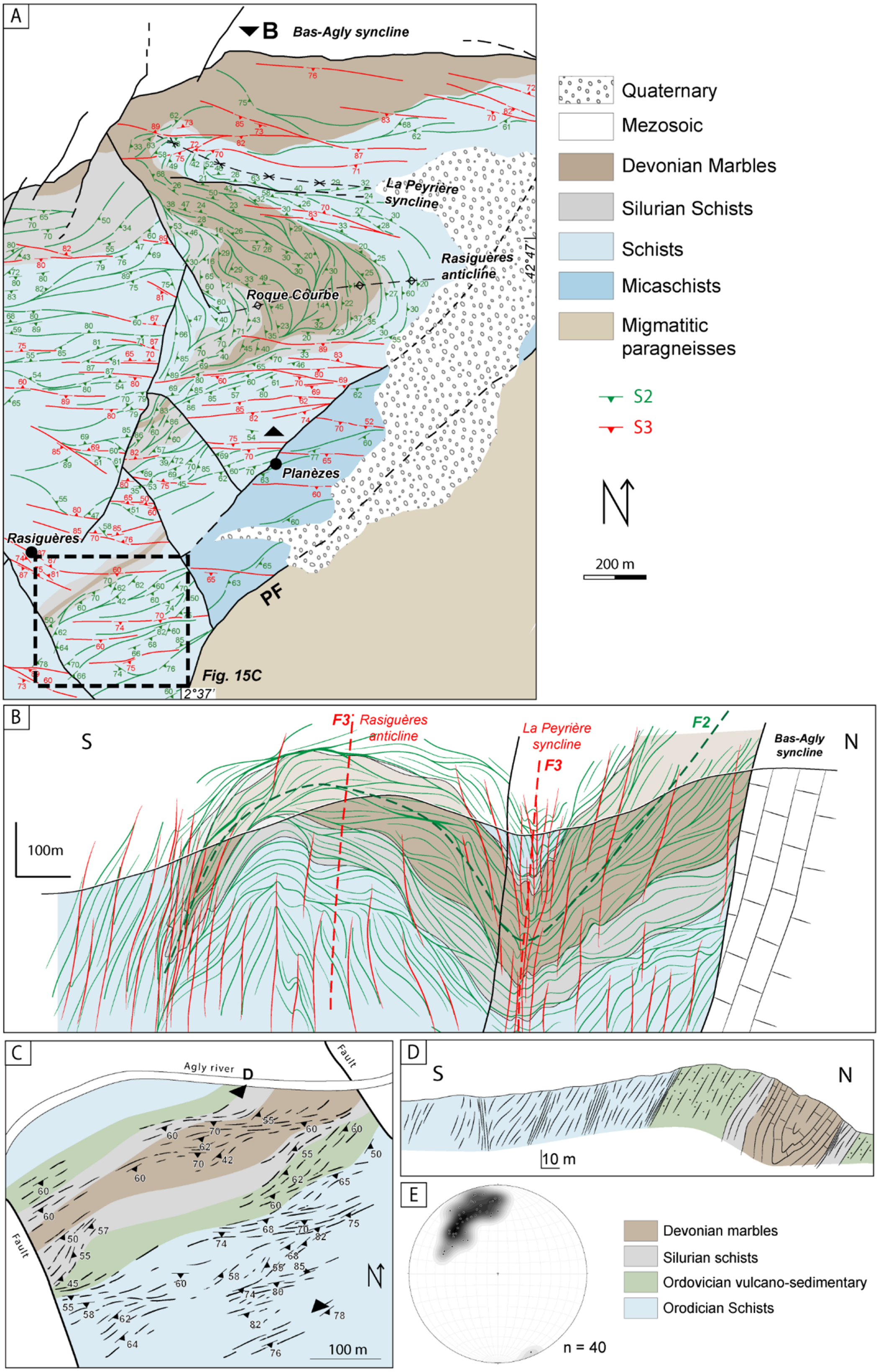

Fig. 15. (A) Map of S2 and S3 foliations in the Roque Courbe area. (B) N-S cross-section through the Roque Courbe showing S2/S3 relationships. (C) Detailed area located on map (A), illustrating the different directions of planar fabrics in the TDZ. (D) Cross-section through map (C) showing the isoclinal F2 fold in the Devonian marbles. (E) Poles of undifferentiated planar fabrics plotted in lower hemisphere Wulf stereograms of map (C).

associated with significant Cretaceous crustal thinning, locally reaching to unroofing of subcontinental mantle (Clerc *et al.*, 2015). South of the AM, this HT/LP Pyrenean event related to crustal thinning was strong enough to imply partial melting of the crustal rocks below the Boucheville basin (Chelalou *et al.*, 2016). A reasonable question arises about the thermo-mechanical impact of Cretaceous extensional tectonic and metamorphism on the Variscan basement within the Agly massif. Some localized mylonites within the gneissic basement were considered as Cretaceous (Paquet and Mansy, 1991; Vauchez *et al.*, 2013). Apatite U-Pb results yield Odlum and Stockli (2019) to propose the existence of a high temperature shear zone located below the Saint-Arnac pluton that was responsible for (1) the Cretaceous thinning during crustal scale boudinage and necking of the continental crust, and (2) the present-day apparent high temperature gradient within the AM. In agreement with Bouhallier *et al.* (1991) our field observations demonstrate that extensional deformation occurred together with Variscan migmatization and granitoid intrusions that gave ages at ca. 307 Ma (Tournaire Guille *et al.*, 2018). The emplacement of the Saint-Arnac pluton at 304 ± 5 Ma (Olivier *et al.*, 2008) led to the local re-orientation of S2 in the micaschists and induced a contact metamorphism cutting the M2 isograds (Fonteilles *et al.*, 1993; Olivier *et al.*, 2008).

Following Corre *et al.* (2018), we suggest that the Cretaceous rifting leading to the strong thinning of the continental crust and unroofing of subcontinental mantle is restricted to the bottom of the Cretaceous basins and did not affect the Variscan basement that crop out in the Agly massif. Recent thermochronological and RSCM studies reported that the Cretaceous temperatures measured in the Agly Paleozoic rocks did not exceed 450 °C and could not account for the HT-LP mineralogical assemblages induced by the M2 metamorphism in the Agly gneisses (Boulvais, 2016; Ducoux, 2017; Ternois *et al.*, 2019). Hydrothermal fluid circulations in the basement, without clear evidence of metasomatic alteration, is also expected and may have been at the origin of the complete or partial resetting of the isotopic U-Th-Pb systems of monazite and apatite observed in the gneiss from the southern part of the Agly massif, close to the Boucheville bassin (Odlum and Stockli, 2019).

5.2 Reappraisal of the Variscan structure of the Agly massif

The Variscan basement of the Agly Massif is commonly described by a single foliation envelope that draws a half-dome structure (*e.g.* Delay, 1989; Olivier *et al.*, 2004; Tournaire Guille *et al.*, 2018). Conversely, we propose that the AM resulted from the superimposition of three deformations D1, D2 and D3 that corresponded to crustal thickening, extensional orogenic collapse and late-transpression, respectively.

In the Variscan massifs of the Pyrenees, relics of early barrovian metamorphic conditions have been documented (Fonteilles *et al.*, 1964; Besson, 1974; Roux, 1977; Azambre and Ravier, 1978; Vielzeuf, 1980; Vielzeuf, 1984; Ayora *et al.*, 1993; Azambre and Guitard, 2001; de Hoÿm de Marien *et al.*, 2018) that might be related to crustal thickening (Bouhallier *et al.*, 1991; Carreras and Capella, 1994; Matte, 2002; Vilà *et al.*, 2007; Denèle *et al.*, 2009, 2014; Laumonier *et al.*, 2010; Aguilar *et al.*, 2015). In the Agly massif, we document a D1 deformation event characterized by a ∼ N-S striking and moderately dipping S1 foliation. The steeply dipping S1 may account for an early period of crustal contraction. Mineral assemblages observed within D1 fabrics do not allow us to distinguish the M1 metamorphism from the M2 high-grade metamorphism. The description of relics of kyanite in the Agly massif by Fonteilles (1970) and Fonteilles and Guitard (1971) led us to speculate that the Agly might have been affected by a slight crustal thickening during D1 crustal contraction. An early planar fabric with the same orientation as the S1 is documented in the Cap de Creus and is also attributed to a crustal thickening stage (Druguet, 1997, 2001).

Ages reported for the D1 crustal thickening range between 340–320 Ma. Mezger and Gerdes (2016) obtained ages of ca. 339–337 Ma from the Soulcem and Bossost plutons interpreted to date the thickening stage. Denèle *et al.* (2014) proposed an age for D1 thickening between 323 and 308 Ma based on a synthesis of the previous works on the Axial Zone. Lemirre (2016) obtained several dates around 320 Ma from the NPZ (Castillon and Bessède massifs) and proposed to link them to the early crustal thickening.

The main deformation in the Agly massif is recorded by the development of a shallowly dipping S2 foliation with a conspicuous N20°E directed stretching lineation and dominant top-to-the-north normal shearing. The D2 deformation reworked an early S1 foliation preserved in D2 low strain zones. This results in the N-S trending kilometer-scale undulation observed along an E-W profile, in response of the superimposition of D1 and D2 rather than folding of a single low-dipping (S2) foliation as previously documented (Delay, 1989; Berger *et al.*, 1993; Tournaire Guille *et al.*, 2018).

In the infrastructure, the high temperature conditions (T>550 °C) of the D2 deformation is attested by the synkinematic mineralogical assemblage quartz-biotite-sillimanite observed in D2 mylonitic to ultramylonitic normal shear zones in gneisses (Paquet and Delay, 1989; Siron *et al.*, 2012, 2020) and by the magmatic state to solid state of D2 in the Ansignan charnockite (Althoff *et al.*, 1994). The S2 foliations are parallel to the HT-LP metamorphic isograds and to the migmatitic layering, and the L2 is outlined by preferential alignment of minerals of this HT-LP metamorphism (Fig. 7). These observations indicate that D2 shearing developed from peak metamorphism (under suprasolidus conditions) toward subsolidus amphibolite facies conditions along a retrograde P-T evolution as previously observed in the Saint Barthélémy massif (de Saint Blanquat *et al.*, 1990).

These D2 high strain zones are responsible for the significant thinning of the massif and the juxtaposition of different structural levels along main high-strain zones, like the Caladroy SZ at the interface between the infra- and suprastructure (This study, Delay, 1989; Bouhallier *et al.*, 1991; Siron *et al.*, 2012, 2020) and the Cuxous, Cassagnes, East and West Ansignan shear zones in the partially molten infrastructure (This study, Delay, 1989; Paquet and Mansy, 1991; Siron *et al.*, 2012, 2020). We did not observe the bottom boundary of the S2 domain and it is likely that D2 thinning continues downward in the lower structural level. The D2 deformation represents a wide zone of ductile thinning that spreads out over the whole tectonic pile. A significant part of the thinning is likely to have been accommodated during retrograde cooling along numerous smaller C2 shear zones.

Timing of D2 is constrained by geochronological data obtained on syn-D2 migmatites and granitoids. Siron *et al.* (2012, 2020) reported LA-ICP-MS U-Pb monazite ages at 305 ± 4 Ma and 306 ± 2 Ma attributed to peak-metamorphic conditions. Tournaire Guille *et al.* (2018) give an age at 299 ± 4 Ma that may represent the crystallization of migmatitic melt. The Ansignan charnockite gave LA-ICP-MS U-Pb ages and ID-TIMS ages that range in between ca. 315 and 300 (Postaire, 1982; Respaut and Lancelot, 1983; Tournaire Guille *et al.*, 2018). The syn-D2 Cassagnes granite is dated at 308 ± 3 Ma (Tournaire Guille *et al.*, 2018). All these geochronological data are consistent and argue for D2 deformation at suprasolidus conditions in the range 315–300 Ma. Siron *et al.* (2012, 2020) constrain the cooling history between 300 and 296 Ma.

In the northern part of the Agly Massif and along the southern boundary of the St-Arnac-Tournefort plutonic body the foliation is steeply dipping. Paquet and Mansy (1992) attributed this northern steepening to Alpine collision whereas Olivier *et al.* (2004, 2008) argued for a 45° tilt toward north of the northern part of the Agly massif in response of the Cretaceous rifting and formation of tilted blocks during extension tectonics. The hypothesis of Alpine or Cretaceous tectonics as partially or totally responsible for the steepening of the foliations in the northern Agly (Paquet and Mansy, 1992; Olivier *et al.*, 2004, 2008) is inconsistent with our structural results. The vertical domain corresponds to an E-W trending transpressional strike-slip shear zone (TDZ) responsible for the folding and steepening of the previous D1/D2 structures. At the western part of the AM, *i.e.* the deepest structural level, the D3 is several kilometers wide. At the eastern part, *i.e.* upper structural levels of the suprastrucutre, D3 localizes as a pinched synform. In the Agly massif, the TDZ shows both shallowly- and steeply-plunging lineations that are a common feature of transpressional shear zones (Fossen and Tikoff, 1993; Tikoff and Teyssier, 1994; Greene and Schweickert, 1995; Tikoff and Greene, 1997). Emplacement of Saint-Arnac and Tournefort plutons may have occasioned a N-S directed shortening inducing a pure-shear component of transpression into the TDZ during D3 dextral shearing with both subhorizontal and subvertical stretching L3 lineations. The TDZ is intruded by the syn-D3 Tournefort diorite dated at 307 ± 1 Ma and 308 ± 1 Ma (Olivier *et al.*, 2004, 2008). This age may constitute a lower boundary for the timing D3 ductile shearing. Since it reworked the D2 mylonites, the D3 transpression was still active after 295 Ma.

5.3 Comparison with the surrounding Variscan massifs

The relative position of the Agly massif in relation to the Pyrenean Axial Zone and the French massif central mainly depends on the movements attributed to the NPF that are debated (*e.g.* Olivet, 1996; Sibuet *et al.*, 2004; Jammes *et al.*, 2009; Carreras and Druguet, 2014; Tugend *et al.*, 2015). Regardless of the amount of displacement of Iberia, the AM is located north of the NPF and should share more features with the NPZ and Montagne Noire massifs (Burg *et al.*, 1994) than with the Axial Zone. In the Western European Variscides, late-Carboniferous to early-Permian extension is mainly N-S directed north of the NPF whereas it is E-W trending, *i.e.* nearly parallel to the belt in the Pyrenean Axial Zone (Burg *et al.*, 1994; Cochelin *et al.*, 2017). Also, at this time, dextral strike-slip tectonic, widely documented in the internal and external zones of the Variscan orogen (*e.g.* Edel *et al.*, 2018), has largely contributed to the flow of the thickened Variscan crust and was still active during extensional collapse (Burg *et al.*, 1994, Gébelin *et al.*, 2007, 2009). As proposed by Cochelin (2016), the NPMs are comparable to the southern part of the Central Massif and to the Montagne Noire, where an extensional setting is described with a main N-S kinematics (Van Den Driessche and Brun, 1992; Burg and Vanderhaeghe, 1993; Faure, 1995; Faure *et al.*, 2009; Pitra *et al.*, 2012; Barbey *et al.*, 2015), coeval with HT-LP metamorphism and magmatism between 305 and 295 Ma (Pitra *et al.*, 2012; Couzinié *et al.*, 2016; Barbey *et al.*, 2015). Transtensional and extensional settings are dominant in the NPZ (Thiébaut, 1964; Roux, 1977; de Saint Blanquat, 1989, 1993; de Saint Blanquat *et al.*, 1990; this study). In the St-Barthélémy massif (NPZ), Variscan mylonitization evolved from HT to LT conditions and is responsible for several kilometers of crustal thinning (de Saint Blanquat, 1989, 1993; de Saint Blanquat *et al.*, 1990; Delaperrière *et al.*, 1994).

In the Montagne Noire (southern French massif central), the finite strain pattern is the result of a D2 dextral strike-slip shearing in the infrastructure, coeval with D3 extensional collapse localized along the anatectic front between 315 and 295 Ma (Pitra *et al.*, 2012; Rabin *et al.*, 2015; Roger *et al.*, 2015; Trap *et al.*, 2017). The HT-LP metamorphism reaches 700 °C at 0.35 GPa (Rabin *et al.*, 2015; Fréville *et al.*, 2016) and is contemporaneous with a main partial melting and magmatic event dated at ca. 310–300 Ma (Roger *et al.*, 2015; Trap *et al.*, 2017). Poujol *et al.* (2017) have also found ages at 320 Ma and attributed it to another partial melting event. This ancient partial melting event could be linked and compared to the ages of Lemirre (2016) at 320 Ma in the NPMs.

Looking at the Agly massif and the Pyrenean Axial Zone, the metamorphism is very similar in both domains, with HT-LP metamorphic gradients between 60 and 80 °C/km in the suprastructure, and near isothermal gradients in the infrastructure (Siron *et al.*, 2012, 2020; Lemirre, 2016). Temperatures are slightly higher in the Agly massif and the NPZ than in the Axial Zone, 800–850 °C and 700–750 °C respectively (Lemirre, 2016). The metamorphism and the magmatism ages are similar with estimations that range between ca. 305 and 275 Ma in the NPZ (Hart *et al.*, 2016; Lemirre, 2016) and at ca. 315–295 Ma in the Axial Zone (Denèle *et al.*, 2014; Druguet *et al.*, 2014). In the Variscan Eastern Pyrenees, the peak of magmatic activity is well constrained around 306 Ma (Denèle *et al.*, 2014).

The main difference between the NPZ and the Axial Zone lays on geometrical and kinematics aspects. In the Axial Zone, the lineations are predominantly parallel to the belt elongation and the regional finite strain pattern defines a dextral transpression (*e.g.* Soliva, 1992; Gleizes *et al.*, 1997, 1998a, 2001; Olivier *et al.*, 1999, 2016; Román-Berdiel et al., 2004, 2006; Denèle *et al.*, 2009, 2014; Carreras and Druguet, 2014; Cochelin *et al.*, 2017). Dextral transpression in the Axial Zone is interpreted as the result of lateral escape of the partially molten crust during closure of the Iberian-Armorican syntax between ca. 305 and 295 Ma (Denèle *et al.*, 2009; Cochelin *et al.*, 2017). Although transpressive tectonics is preponderant in the Axial Zone, some studies reported late-Carboniferous thinning with a N-S to NE-SW direction synchronous with late Carboniferous granodiorite pluton emplaced at 305–310 Ma (Bouchez and Gleizes, 1995, Casas *et al.*, 2007),

In the NPZ stretching lineations are mostly transversal and strain pattern is related to an extensional setting (Bouhallier *et al.*, 1991; de Saint Blanquat, 1993; Cochelin, 2016; this study). However, some studies proposed that the eastern NPM and Axial Zone shared the same transpressional tectonic event at the end of the Variscan orogeny with partitioning into domains of localized dextral strike-slip shear zones (Carreras and Druguet, 2014). In the Trois-Seigneurs and St-Barthelemy massifs of the NPZ, few localized strike-slip shear zones are attributed to a late wrench-dominated transpression developed under retrograde metamorphic conditions (Carreras and Druguet, 2014).

The Agly massif and the eastern Axial Zone share the same strain pattern with pinched synforms surrounding wide domes, sheet-shaped plutons along the infrastructure/suprastructure interface that are lately affected by transpression. Carreras and Druguet (2014) proposed that the Agly, Mouthoumet and Montagne Noire massifs shared the same compression-dominated transpression as documented in the Axial Zone.

5.4 Late-Variscan tectonic evolution of the Agly massif

In the following, we propose a tectonic model for the middle-Carboniferous to early-Permian evolution of the Agly massif late-Varsican crust that describes the progressive switch from gravitational collapse to dextral transpression in a syn-plate convergence context.

The initial stage of our conceptual model is a thickened orogenic crust corresponding to a portion of the external part of an orogenic plateau that has reached a critical thickness. Regardless of the ante-D2 attitude of S1 that remains unknown, D1 upright folding and a steeply dipping S1 foliation featured the crust before ca. 315 Ma and set up the initial conditions for the development of the Agly massif (Fig. 16A). Subsequently to thermal relaxation of the thickened crust, the middle crust reached partial melting conditions and started to flow in response to gravitational gradients. Vertical shortening and S2 foliation may have been initiated in the partially molten and weak middle crust at a depth where gravitational instabilities overcome the horizontal compressional forces (Fig. 16B). With ongoing D2 thinning, the S2 penetrative foliation may have formed a large-scale and flat-lying mechanical anisotropy in the middle crust that controlled the emplacement of sheet-shaped granitoid plutons fed through melt ascension along proto-D3 strike-slip shear zones (Fig. 16C). At that stage, the upper-middle crust is preponderantly subjected to gravitational instabilities while the middle-lower crust is subjected to compressional tectonic forces. We consider that the TDZ first onset as a proto-D3 TDZ in the partially molten infrastructure and acted as a preferential magma pathway leading to the ascent of early magmatic pulses of the Tournefort diorite and Saint Arnac granite, emplaced between 308 and 304 Ma at the bottom of the flat lying D2 domain (Fig. 16C). In the upper crust, the syn-orogenic extension is achieved by kilometer scale low-angle brittle normal faults.

In response to ongoing crustal thinning and granitoid emplacements, the anatectic front advanced upward, driving broadening of the flat-lying S2 domain while more evolved magmas intruded into the upper low-grade crust. Thinning is shifted to the upper crust with the likely growth of pull-apart basins.

After thermal and magmatic peak activity and during subsequent cooling, D2 thinning localized along more discrete shear zones forming a lens-shaped anastomosed network (Fig. 16D). Some late pegmatites intruding the low-grade schists are strongly mylonitized whereas others escaped the heterogeneous late-D2 deformation. D2 is now restricted to the upper crust where dextral pull-apart basins developed in which late-Carboniferous to early Permian sediments deposited. In the same time, strike-slip shear zones under transpression are growing further in the lower-middle crust dominated by ongoing convergence.

The final stage corresponds to the D3 subhorizontal shortening that overcomes extensional shearing. D3 developed open to tight folds and S3 foliation. In the infrastructure, TDZ widened and migrated upward due to ongoing strike-slip shearing under transpression (Fig. 16E). A pinched synform of the suprastructural schist and micaschists develops along the TDZ.

The progressive switch from thinning to transpression is attributed to the lessening of gravitational forces at an advanced stage of extensional collapse that became overcome by ongoing compressional tectonic forces. In that case, a change in the far field stress is not necessary since the driving mechanism is the fall of gravity forces. However, extension in the core of the orogenic plateau is a potential driving mechanism responsible for shortening of the foreland domain (Teyssier *et al.*, 2008). N-S extension and lateral flow of the partially molten crust recorded in the collapsing French Massif Central may have provoked compression in the Agly massif. Following Cochelin *et al.* (2017), it is likely that a rise of compressional forces may has occurred in response to the closure of the Ibero-Armorcian Arc and has been responsible for dextral transpression during early Permian.

6 Conclusion

Structural analysis of the Paleozoic Variscan basement of the Agy massif shows that the apparent dome shape of the massif is the result of the superimposition of three major ductile deformations D1, D2, and D3. D1 deformation is preserved as relictual foliation in low strain zones and we speculate that it could be related to middle Carboniferous thickening and building of the orogenic plateau. D2 deformation is a heterogeneous non-coaxial deformation, affecting the whole massif, that produced a shallowly dipping S2 foliation, and an anastomosed network of C2 shear zones that accommodated vertical thinning and N20 directed extension. D2 is coeval with LP-HT metamorphism and plutonism at ca 315–295 Ma. D2 corresponds to the

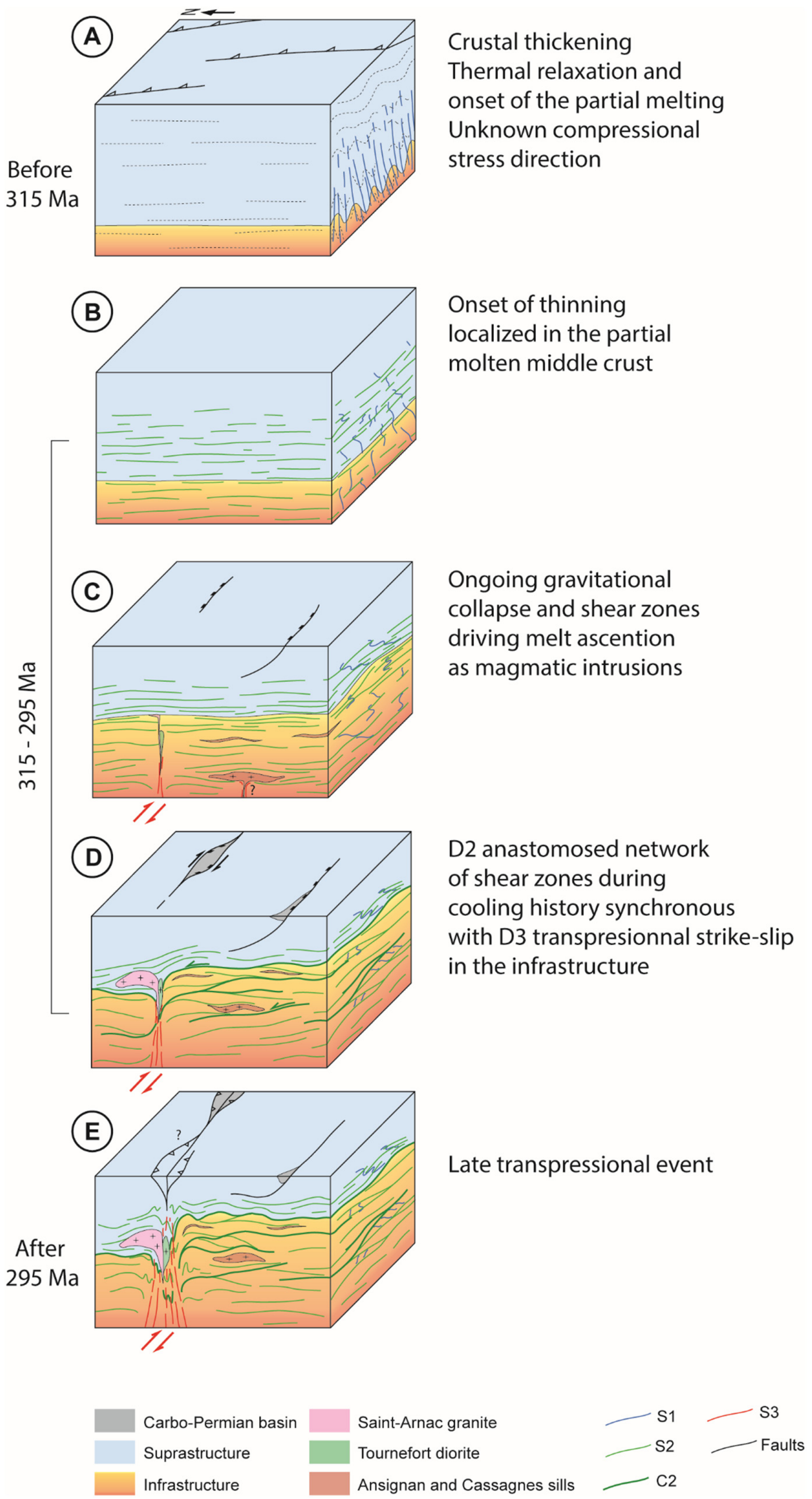

Fig. 16. Tectonic model showing the deformation history of the late-Variscan orogenic crust in the Agly massif.

extensional collapse of the partially molten orogenic crust in a global dextral strike-slip at the scale of the whole Variscan belt. D3 deformation is a record of E-W striking dextral shearing that facilitated and localized the ascent and emplacement of the Tournefort diorite and the Saint-Arnac granite. D3 outlasted D2 and turned compressional in response to the closure of the Ibero-Armorican Arc.

The ductile deformation and HT metamorphism observed in the Paleozoic basement of the Agly massif are related to the late Carboniferous to early Permian tectonic. Cretaceous extension did not impact the Variscan tectono-thermal record but was only expressed as the hydrothermal alteration localized along ~ N100 faults. Tertiary Pyrenean collision is responsible for the final thrusting of the Agly massif upon the Saint-Paul-de-Fenouillet basin as well as the local pinching and incorporation of weakly metamorphosed Mesozoic limestones into the gneissic basement.

Acknowledgement. This work was supported by the BRGM through the Référentiel Géologique de la France program (RGF). Philippe Olivier and Sebastien Ternois are gratefully acknowledged for stimulating discussions. Didier Convert provided generous support with thin section preparation. The newly acquired and compiled structural data will be available on the RGF website (http://rgf.brgm.fr).

References

Aguilar C, Liesa M, Castiñeiras P, Navidad M. 2013. Late Variscan metamorphic and magmatic evolution in the eastern Pyrenees revealed by U–Pb age zircon dating. *J Geol Soc London* 171: 181–192.

Aguilar C, Liesa M, Štípská P, Schulmann K, Muñoz JA, Casas JM. 2015. P–T–t–d evolution of orogenic middle crust of the Roc de Frausa Massif (Eastern Pyrenees): A result of horizontal crustal flow and Carboniferous doming? *J Metamorph Geol* 33: 273–294.

Althoff F, Barbey P, Pons J. 1994. La charnockite d'Ansignan et le granite de Saint-Arnac, témoins d'une extension crustale d'âge hercynien dans le massif de l'Agly (Pyrénées Orientales, France). *C R Acad Sci Paris* 319: 239–246.

Andrieux P. 1982a. Conditions de cristallisation et évolution paragénétique d'une charnockite hercynienne : le complexe granulitique d'Ansignan (massif de l'Agly, Pyrénées-Orientales). *B Minéral* 105: 253–266.

Andrieux P. 1982b. La charnockite d'Ansignan (Massif d'Agly, Pyrénées Orientales). Mise en place et évolution paragénétique. Introduction à l'étude des équilibres grenat-orthopyroxène. 3rd Cycle Thesis, Clermont-Ferrand (France), Univ. Blaise Pascal.

Antolín-Tomás B, Román-Berdiel T, Casas-Sainz A, Gil-Peña I, Oliva B, Soto R. 2009. Structural and magnetic fabric study of the Marimanha granite (Axial Zone of the Pyrenees). *Int J Earth Sci* 98: 427–441.

Auréjac JB, Gleizes G, Diot H, Bouchez JL. 2004. Le complexe granitique de Quérigut (Pyrénées, France) ré-examiné par la technique de l'ASM : un pluton syntectonique de la transpression dextre hercynienne. *Bull Soc geol Fr* 175: 157–174.

Ayora C, Liesa M, Delgado J. 1993. Low-thermal-gradient Hercynian metamorphism in the eastern Pyrenees. *J Metamorph Geol* 11:49–58.

Azambre B, Guitard G. 2001. Disthène et staurotide reliques dans les métapélites du Canigou (Pyrénées orientales). Relations avec les épisodes hercyniens de basses et moyennes pressions. *C R Acad Sci Paris* 333: 601–609.

Azambre B, Ravier J. 1978. Les écailles de gneiss du faciès granulite du Port de Saleix et de la région de Lherz (Ariège), nouveaux témoins du socle profond des Pyrénées. *Bull Soc geol Fr* 7: 221–228.

Barbey P, Villaros A, Marignac C, Montel JM. 2015. Multiphase melting, magma emplacement and P-T-time path in late-collisional context: The Velay example (Massif Central, France). *Bull Soc geol Fr* 186: 93–116.

Berger GM, Fonteilles M, Leblanc D, Clauzon G, Marchal JP, Vautrelle C. 1993. Notice de la carte géologique de la France, feuille Rivesaltes (1090), scale 1:50 000. Orléans : BRGM.

Besson M. 1974. Présence de disthène dans les gneiss du massif de l'Aston. *Bull Soc Fr Minéral Cristallogr* 97: 487–490.

Bouchez JL, Gleizes G. 1995. Two stage deformation of the Mont-Louis-Andorra granite pluton (Variscan Pyrenees) inferred from magnetic susceptibility anisotropy. *J Geol Soc* 152: 669–679.

Bouchez JL, Delas D, Gleizes G, Nedelec A, Cuney M. 1992. Submagmatic microfractures in granites. *Geology* 20:35–38.

Bouchez JL, Nguema TMM, Esteban L, Siqueira R, Scrivener R. 2006. The tourmaline-bearing granite pluton of Bodmin (Cornwall, UK): Magnetic fabric study and regional inference. *J Geol Soc* 163: 607–616.

Bouhallier H, Choukroune P, Ballevre M. 1991. Evolution structurale de la croûte profonde hercynienne : exemple du massif de l'agly (pyrenees-orientales, france). *C R Acad Sci Paris* 312: 647–654.

Boulvais P. 2016. Fluid generation in the Boucheville Basin as a consequence of the North Pyrenean Metamorphism. *C R Geosci* 348: 301–311.

Burg JP, Vanderhaeghe O. 1993. Structures and way-up criteria in migmatites, with application to the Velay dome (French Massif Central). *J Struct Geol* 15: 1293–1301.

Burg JP, Van Den Driessche J, Brun JP. 1994. Syn- to post-thickening extension in the Variscan Belt of Western Europe: Modes and structural consequences. *Géologie de la France* 3: 33–51.

Carreras J, Capella I. 1994. Tectonic levels in the Palaeozoic basement of the Pyrenees: A review and a new interpretation. *J Struct Geol* 16: 1509–1524.

Carreras J, Druguet E. 2014. Framing the tectonic regime of the NE Iberian Variscan segment. *Geol Soc Spec Publ London* 405. https://doi.org/10.1144/SP405.7.

Casas JM, Palacios T. 2012. First biostratigraphical constraints on the pre-Upper Ordovician sequences of the Pyrenees based on organic-walled microfossils. *C R Geosci* 344: 50–56.

Casas JM, Fernández O, Domingo F. 2007. Carboniferous normal faults in the Eastern Pyrenees: Evidences and age constrains of syn-orogenic Variscan extension. *Geodin Acta* 20: 385–392.

Chelalou R. 2015. Formation et évolution du bassin de Boucheville, implication sur l'évolution tectonique, métamorphique et sédimentaires des bassins sédimentaires mésozoïques du Nord-Est des Pyrénées. PhD thesis, Rennes (France), Univ. Rennes 1.

Chelalou R, Nalpas T, Bousquet R, Prevost M, Lahfid A, Poujol M, *et al.* 2016. New Sedimentological, Structural and Paleo-Thermicity Data in the Boucheville Basin (Eastern North Pyrenean Zone, France). *C R Geosci* 348: 312–321.

Clerc C. 2012. Évolution du domaine nord-pyrénéen au Crétacé. Amincissement crustal extrême et thermicité élevée : un analogue pour les marges passives. PhD thesis, Paris (France), Univ. Pierre et Marie Curie – Paris VI.

Clerc C, Lagabrielle Y. 2014. Thermal control on the modes of crustal thinning leading to mantle exhumation: Insights from the Cretaceous Pyrenean hot paleomargins. *Tectonics* 33: 1340–1359.

Clerc C, Lagabrielle Y, Neumaier M, Reynaud JY, St Blanquat M. 2012. Exhumation of subcontinental mantle rocks: Evidence from ultramafic-bearing clastic deposits nearby the Lherz peridotite body, French Pyrenees. *Bull Soc geol Fr* 183: 443–459.

Clerc C, Boulvais P, Lagabrielle Y, Blanquat M. 2013. Ophicalcites from the northern Pyrenean belt: A field, petrographic and stable isotope study. *Int J Earth Sci* 103: 141–163.

Clerc C, Lahfid A, Monié P, Lagabrielle Y, Chopin C. 2015. High-temperature metamorphism during extreme thinning of the continental crust: A reappraisal of the North Pyrenean passive paleomargin. *Solid Earth* 6: 643–668.

Clerc C, Lagabrielle Y, Labaume P, Ringenbach JC, Vauchez A, Nalpas T, *et al*. 2016. Basement – Cover decoupling and progressive exhumation of metamorphic sediments at hot rifted margin. Insights from the Northeastern Pyrenean analog. *Tectonophysics* 686: 82–97.

Cochelin B. 2016. Champ de déformation du socle paléozoïque des Pyrénées. PhD thesis, Toulouse (France), Univ. Paul Sabatier.

Cochelin B, Chardon D, Denèle Y, Gumiaux C, Le Bayon B. 2017. Vertical strain partitioning in hot Variscan crust: Syn-convergence escape of the Pyrenees in the Iberian-Armorican syntax. *Bull Soc geol Fr* 188. https://doi.org/10.1051/bsgf/2017206.

Corre B, Boulvais P, Boiron MC, Lagabrielle Y, Marasi L, Clerc C. 2018. Fluid circulations in response to mantle exhumation at the passive margin setting in the north Pyrenean zone, France. *Mineral Petrol* 112: 1–24.

Couzinié S, Laurent O, Moyen JF, Zeh A, Bouilhol P, Villaros A. 2016. Post-collisional magmatism: Crustal growth not identified by zircon Hf–O isotopes. *Earth Planet Sci Lett* 456: 182–195.

de Hoÿm de Marien L, Le Bayon B, Pitra P, Van Den Driessche J, Poujol M, Cagnard F. 2018. Two-stage Variscan metamorphism in the Canigou massif: Evidence for crustal thickening in the Pyrenees. *J Metamorph Geol* 37: 863–888.

de Saint Blanquat M. 1989. La faille normale ductile du massif du Saint Barthélémy. Age et signification de l'extension crustale dans le zone Nord-pyrénéenne. PhD thesis, Montpellier (France), Univ. Montpellier 2.

de Saint Blanquat M. 1993. La faille normale ductile du massif de Saint-Barthélémy. Évolution hercynienne des massifs nord-pyrénéens catazonaux considérée du point de vue de leur histoire thermique. *Geodin Acta* 6: 59–77.

de Saint Blanquat M., Lardeaux JM, Brunel M. 1990. Petrological arguments for high-temperature extensional deformation in the Pyrenean Variscan crust (Saint Barthélémy Massif, Ariège, France). *Tectonophysics* 177: 245–262.

Debroas EJ, Canérot J, Bilotte M. 2010. Les Brèches d'Urdach, témoins de l'exhumation du manteau pyrénéen dans un escarpement de faille vraconnien-cénomanien inférieur (zone nord-pyrénéenne, Pyrénées-Atlantiques, France). *Geol Fr* 2: 53–64.

Delaperrière E, de Saint-Blanquat M, Brunel M, Lancelot JR. 1994. Geochronologie U-Pb sur zircons et monazites dans le massif du Saint Barthelemy (Pyrenees, France) ; discussion des âges des évènements varisques et pré-varisques. *Bull Soc geol Fr* 165: 101–112.

Delay F. 1989. Le massif nord-pyrénéen de l'Agly (Pyrénées orientales) : Évolution tectono-métamorphique et exemple d'un amincissement crustal polyphasé. PhD thesis, Lille (France), Univ. Lille 1.

Denèle Y, Olivier P, Gleizes G, Barbey P. 2009. Decoupling between the Middle and Upper Crust during Transpression-Related Lateral Flow: Variscan Evolution of the Aston Gneiss Dome (Pyrenees, France). *Tectonophysics* 477: 244–261.

Denèle Y, Laumonier L, Paquette JL, Olivier P, Gleizes G, Barbey P. 2014. Timing of granite emplacement, crustal flow and gneiss dome formation in the Variscan segment of the Pyrenees. *Geol Soc London Spec Publ* 405: 265–287.

Dewey JF. 1988. Extensional collapse of orogens. *Tectonics* 7: 1123–1139.

Dörr W, Zulauf G. 2010. Elevator tectonics and orogenic collapse of a Tibetan-style plateau in the European Variscides: The role of the Bohemian shear zone. *Int J Earth Sci* 99: 299–325.

Druguet E. 1997. The structure of the NE Cap de Creus NE peninsula. Relationships with metamorphism and magmatism. PhD thesis, Barcelona (Spain), Univ. Autónoma de Barcelona.

Druguet E. 2001. Development of High Thermal Gradients by Coeval Transpression and Magmatism during the Variscan Orogeny: Insights from the Cap de Creus (Eastern Pyrenees). *Tectonophysics* 332: 275–293.

Druguet E, Castro A, Chichorro M, Pereira MF, Fernández C. 2014. Zircon geochronology of intrusive rocks from Cap de Creus, Eastern Pyrenees. *Geol Mag* 151: 1095–1114.

Ducoux M. 2017. Structure, thermicité et évolution géodynamique de la Zone Interne Métamorphique des Pyrénées. PhD thesis, Orléans (France), Univ. d'Orléans.

Edel JB, Schulmann K, Lexa O, Lardeaux JM. 2018. Late Palaeozoic palaeomagnetic and tectonic constraints for amalgamation of Pangea supercontinent in the European Variscan belt. *Earth Sci Rev* 177: 589–612.

Fallourd S, Poujol M, Boulvais P, Paquette JL, de Saint Blanquat M, Rémy P. 2014. *In Situ* LA-ICP-MS U–Pb titanite dating of Na–Ca metasomatism in orogenic belts: The North Pyrenean example. *Int J Earth Sci* 103: 667–682.

Faure M. 1995. Late orogenic carboniferous extensions in the Variscan French Massif Central. *Tectonics* 14: 132–153.

Faure M, Lardeaux JM, Ledru P. 2009. A review of the pre-Permian geology of the Variscan French Massif Central. *C R Geosci* 341: 202–213.

Fonteilles M. 1970. Géologie des terrains métamorphiques et granitiques du massif hercynien de l'Agly (Pyrénées orientales). *Bull BRGM* 3: 1–54.

Fonteilles M. 1976. Essai d'interprétation des compositions chimiques des roches d'origine métamorphique et magmatique du massif hercynien de l'Agly (Pyrénées Orientales). State thesis, Paris (France), Univ. Paris VI.

Fonteilles M, Guitard G. 1971. Disthène relique et disthène hystérogène dans les terrains métamorphiques hercyniens des Pyrénées orientales franco-espagnoles. *C R Acad Sci Paris* 272: 361–363.

Fonteilles M, Guitard G, Raguin E. 1964. Sur la présence de gneiss à disthène et cordiérite dans le massif du Saint-Barthélémy (Pyrénées de l'Ariège). *C R Acad Sci Paris* 258: 3524–3525.

Fonteilles M, Leblanc D, Clauzon G, Vaudin JL, Berger GM. 1993. Carte géologique de la France, feuille Rivesaltes (1090), scale 1:50 000. Orléans : BRGM.

Fossen H, Tikoff B. 1993. The deformation matrix for simultaneous simple shearing, pure shearing and volume change, and its application to transpression-transtension tectonics. *J Struct Geol* 15: 413–422.

Franke W, Doublier MP, Klama K, Potel S, Wemmer K. 2011. Hot metamorphic core complex in a cold foreland. *Int J Earth Sci* 100: 753–785.

Fréville K, Cenki-Tok B, Trap P, Rabin M, Leyreloup A, Régnier JL, *et al*. 2016. Thermal interaction of middle and upper crust during gneiss dome formation: Example from the Montagne Noire (French Massif Central). *J Metamorph Geol* 34: 447–462.

Gébelin A, Brunel M, Monié P, Faure M, Arnaud N. 2007. Transpressional tectonics and Carboniferous magmatism in the Limousin, Massif Central, France: Structural and $^{40}Ar/^{39}Ar$ investigations. *Tectonics* 26. https://doi.org/10.1029/2005TC001822.

Gébelin A, Roger F, Brunel M. 2009. Syntectonic crustal melting and high-grade metamorphism in a transpressional regime, Variscan Massif Central, France. *Tectonophysics* 477: 229–243.

Gibson R. 1991. Hercynian low-pressure-high-temperature regional metamorphism and subhorizontal foliation development in the Canigou massif, Pyrenees, France – Evidence for crustal extension. *Geology* 19: 380–383.

Gleizes G, Bouchez JL, Lespinasse P, Roux L. 1992. Structure du granite de Lacourt (Arize occidentale) : une signature syntectonique de phase 2 dans l'Hercynien des Pyrénées. *Bull Soc Hist Nat Toulouse* 128: 53–57.

Gleizes G, Leblanc D, Bouchez JL. 1997. Variscan Granites of the Pyrenees Revisited: Their Role as Syntectonic Markers of the Orogen. *Terra Nova* 9: 38–41.

Gleizes G, Leblanc D, Bouchez JL. 1998a. The main phase of the Hercynian orogeny in the Pyrenees is a dextral transpression. *Geol Soc London Spec Publ* 135: 267–273.

Gleizes G, Leblanc D, Santana V, Olivier O, Bouchez JL. 1998b. Sigmoidal structures featuring dextral shear during emplacement of the Hercynian granite complex of Cauterets–Panticosa (Pyrenees). *J Struct Geol* 20: 1229–1245.

Gleizes G, Leblanc D, Olivier P, Bouchez JL. 2001. Strain partitioning in a pluton during emplacement in transpressional regime: The Example of the Néouvielle Granite (Pyrenees). *Int J Earth Sci* 90: 325–340.

Gleizes G, Crevon G, Asrat A, Barbey P. 2006. Structure, age and mode of emplacement of the Hercynian Bordères-Louron pluton (Central Pyrenees, France). *Int J Earth Sci* 95: 1039–1052.

Golberg JM, Leyreloup AF. 1990. High temperature-low pressure Cretaceous metamorphism related to crustal thinning (Eastern North Pyrenean Zone, France). *Contrib Mineral Petrol* 104: 194–207.

Greene D, Schweickert R. 1995. The Gem Lake shear zone: Cretaceous dextral transpression in the Northern Ritter Range pendant, eastern Sierra Nevada, California. *Tectonics* 14: 945–961.

Guitard G, Vielzeuf D, Martinez F. 1996. Le métamorphisme hercynien. In: Chiron JC, Barnolas A, eds. *Synthèse géologique et géophysique des Pyrénées*. Orléans (France): Bureau de Recherches Géologiques et Minières, vol. 1, pp. 501–584.

Hart NR, Stockl, DF, Hayman NW. 2016. Provenance evolution during progressive rifting and hyperextension using bedrock and detrital zircon U-Pb geochronology, Mauléon Basin, western Pyrenees. *Geosphere* 12: 1166–1186.

Hibbard MJ. 1987. Deformation of incompletely crystallized magma systems: Granitic gneisses and their implications. *J Geol* 95: 543–561.

Hilario Orús A. 2004. Relación entre magmatismo y deformación en la transversal de Benasque a Luchon (Zona Axial del Pirineo). Tesis Doctoral, Leioa (Spain), Univ. del País Vasco.

Izquierdo-Llavall E, Román-Berdiel T, Casas AM, Oliva-Urcia B, Gil-Peña I, Soto R, *et al*. 2012. Magnetic and structural study of the Eaux-Chaudes intrusion: Understanding the Variscan deformation in the Western Axial Zone (Pyrenees). *Int J Earth Sci* 101: 1817–1834.

Jammes S, Manatschal G, Lavier LL, Masini E. 2009. Tectonosedimentary evolution related to extreme crustal thinning ahead of a propagating ocean: Example of the western Pyrenees. *Tectonics* 28. https://doi.org/10.1029/2008TC002406.

Lagabrielle Y, Bodinier JL. 2008. Submarine reworking of exhumed subcontinental mantle rocks: Field evidence from the Lherz peridotites, French Pyrenees. *Terra Nova* 20: 11–21.

Lagabrielle Y, Labaume P, St Blanquat M. 2010. Mantle exhumation, crustal denudation, and gravity tectonics during Cretaceous rifting in the Pyrenean realm (SW Europe): Insights from the geological setting of the lherzolite bodies. *Tectonics* 29. https://doi.org/10.1029/2009TC002588.

Lagabrielle Y, Clerc C, Vauchez A, Lahfid A, Labaume P, Azambre B, *et al*. 2016. Very High Geothermal Gradient during Mantle Exhumation Recorded in Mylonitic Marbles and Carbonate Breccias from a Mesozoic Pyrenean Palaeomargin (Lherz Area, North Pyrenean Zone, France). *C R Geosci* 348: 290–300.

Laumonier B. 1998. Les Pyrénées centrales et orientales au début du Paléozoique (Cambrien s.l.) : évolution paléogéographique et géodynamique. *Geodin Acta* 11: 1–11.

Laumonier B, Marignac C, Kister P. 2010. Polymétamorphisme et évolution crustale dans les Pyrenees Orientales pendant l'orogénèse Varisque au Carbonifère supérieur. *Bull Soc geol Fr* 181: 411–428.

Leblanc D, Gleizes G, Lespinasse P, Olivier P, Bouchez JL. 1993. The Maladeta granite polydiapir, Spanish Pyrenees: A detailed magnetostructural study. *J Struct Geol* 16: 223–235.

Leblanc D, Gleizes G, Roux L, Bouchez JL. 1996. Variscan dextral transpression in the French Pyrenees: New data from the Pit des Trois-Seigneurs granodiorite and its country rocks. *Tectonophysics* 261: 331–345.

Ledru P, Courrioux G, Dallain C, Lardeaux JM, Montel JM, Vanderhaeghe O, *et al*. 2001. The Velay dome (French Massif Central): Melt generation and granite emplacement during orogenic evolution. *Tectonophysics* 342: 207–237.

Lemirre B. 2016. Origine et développement de la thermicité dans les Pyrénées varisques. PhD thesis, Toulouse (France), Univ. Toulouse.

Maierová P, Schulmann K, Lexa O, Guillot S, Štípská P, Janoušek V, *et al.* 2016. European Variscan orogenic evolution as an analogueof Tibetan-Himalayan orogen: Insights frompetrology and numerical modeling. *Tectonics* 35: 1760–1780.

Malavieille J, Guihot P, Costa S, Lardeaux JM, Gardien V. 1990. Collapse of a thickened Variscan crust in the French Massif Central: Mont-Pilat extensional shear zone and Saint-Etienne Upper Carboniferous basin. *Tectonophysics* 177: 139–149.

Marmo V. 1971. Granite petrology and the granite problem: Amsterdam: Elsevier, 244 p.

Masini E, Manatschal G, Tugend J, Mohn G. 2014. The tectono-sedimentary evolution of a hyper-extended rift basin: The example of the Arzacq-Mauléon rift system (Western Pyrenees, SW France). *Int J Earth Sci* 103: 1565–1596.

Matte P. 2002. Les plis hercyniens kilométriques couchés vers l'ouest-sud-ouest dans la région du pic du Midi d'Ossau–col du Somport (zone axiale des Pyrénées occidentales). *C R Geosci* 334: 773–779.

Mezger J, Gerdes A. 2016. Early Variscan (Visean) granites in the core of central Pyrenean gneiss domes: Implications from laser ablation U-Pb and Th-Pb studies. *Gondwana Res* 29: 181–198.

Mezger J, Passchier C. 2003. Polymetamorphism and ductile deformation of staurolite–cordierite schist of the Boss'ost dome: Indication for Variscan extension in the Axial Zone of the central Pyrenees. *Geol Mag* 140: 595–612.

Odlum ML, Stockli DF. 2019. Thermotectonic evolution of the North Pyrenean Agly Massif during Early Cretaceous hyperextension using multi-mineral U-Pb thermochronometry. *Tectonics* 38. https://doi.org/10.1029/2018TC005298.

Olivet JL. 1996. La cinématique de la plaque Ibérique. *Bull Cent Rech Explor Prod Elf Aquitaine* 20: 131–195.

Olivier P, Améglio L, Richen H, Vadeboin F. 1999. Emplacement of the Aya Variscan granitic pluton (Basque Pyrenees) in a dextral transcurrent regime inferred from a combined magneto-structural and gravimetric study. *J Geol Soc London* 156: 991–1002.

Olivier P, Gleizes G, Paquette JL. 2004. Gneiss domes and granite emplacement in an obliquely convergent regime: New interpretation of the Variscan agly massif (eastern pyrenees, france). *Geol Soc Am* sp pap 380: 229–240.

Olivier P, Gleizes G, Paquette JL, Muñoz Sáez C. 2008. Structure and U–Pb dating of the Saint-Arnac pluton and the Ansignan Charnockite (Agly Massif): A cross-section from the upper to the middle crust of the Variscan Eastern Pyrenees. *J Geol Soc* 165: 141–52.

Olivier P, Druguet E, Castaño L M, Gleizes G. 2016. Granitoid emplacement by multiple sheeting during Variscan dextral transpression: The Saint-Laurent– La Jonquera pluton (Eastern Pyrenees). *J Struct Geol* 82: 80–92.

Paquet J, Delay F. 1989. Analyse en microscopie électronique des textures et des phases des mylonites nord-pyrénéennes des massifs de St-Barthélémy et de l'Agly et discussion des âges. *Bull Soc geol Fr* 8: 1111–1122.

Paquet J, Mansy JL. 1991. The structure of the Eastern Pyrenees (transect of the Agly massif): An example of crustal thinning. *C R Acad Sci Paris* 312: 913–919.

Paquet J, Mansy JL. 1992. Evolution alpine du massif nord-pyrénéen de l'Agly (Pyrénées-Orientales). *C R Acad Sci Paris* 315: 487–494.

Pascal ML, Fonteilles M, Guitard G. 1976. Contribution à l'étude géométrique des plissements superposés hercyniens des Pyrénées orientales : Paléozoïque épizonal du massif de l'Agly. *Bull Soc geol Fr* 18:1471–1487.

Pawley MJ, Collins WJ. 2002. The development of contrasting structures during the cooling and crystallisation of a syn-kinematic pluton. *J Struct Geol* 24: 469–483.

Pitra P, Poujol M, Van Den Driessche J, Poilvet JC, Paquette JL. 2012. Early Permian extensional shearing of an Ordovician granite: The Saint-Eutrope "C/S-like" orthogneiss (Montagne Noire, French Massif Central). *C R Geosci* 344: 377–384.

Postaire B. 1982. Systématique Pb commun et U-Pb sur zircons : applications aux roches de haut grade métamorphique impliquées dans la chaîne hercynienne (Europe de l'ouest) et aux granulites de Laponie (Finlande). *Mémoires de la société géologique et minéralogique de Bretagne* 15: 29–72.

Poujol M, Boulvais P, Kosler J. 2010. Regional-Scale Cretaceous Albitization in the Pyrenees: Evidence from *in situ* U-Th-Pb Dating of Monazite, Titanite and Zircon. J Geol Soc 167: 751–767.

Poujol M, Pitra P, Van Den Driessche J, Tartèse R, Ruffet G, Paquette JL, *et al*. 2017. Two-stage partial melting during the Variscan extensional tectonics (Montagne Noire, France). *Int J Earth Sci* 106: 477–500.

Rabin M, Trap P, Carry N, Fréville K, Cenki-Tok B, Lobjoie C, *et al.* 2015. Strain partitioning along the anatectic front in the Variscan Montagne Noire massif (Southern French Massif Central). *Tectonics* 34: 1709–1735.

Respaut JP, Lancelot JR. 1983. Datation de la mise en place synmétamorphe de la charnockite d'Ansignan (massif de l'Agly) par la méthode U/Pb sur zircons et monazites. *Neues Jahrb Mineral Abh* 147: 21–34.

Rey, P.F., Teyssier, C., Whitney, D.L., 2010. The limit of channel flow in orogenic plateaux. *Lithosphere* 2: 328–332.

Roger F, Teyssier C, Respaut JP, Rey PF, Jolivet M, Whitney DL, *et al*. 2015. Timing of formation and exhumation of the Montagne Noire double dome, French Massif Central. *Tectonophysics* 640–641: 53–69.

Román-Berdiel T, Casas AM, Oliva-Urcia B, Pueyo EL, Rillo C. 2004. The main Variscan deformation event in the Pyrenees: New data from the structural study of the Bielsa granite. *J Struct Geol* 26: 659–677.

Román-Berdiel T, Casas AM, Oliva-Urcia B, Pueyo EL, Liesa C, Soto R. 2006. The Variscan Millares granite (central Pyrenees): Pluton emplacement in a T fracture of a dextral shear zone. *Geodin Acta* 19: 197–211.

Roux L. 1977. L'évolution des roches du faciès granulite et le problème des ultramafites dans le massif de Castillon (Ariège). State thesis, Toulouse (France), Univ. Toulouse.

Sibuet JC, Srivastava SP, Spakman W. 2004. Pyrenean orogeny and plate kinematics. J *Geophys Res Solid Earth* 109. https://doi.org/10.1029/2003JB002514.

Siron G, Goncalves P, Marquer D. 2012. The origin of high geothermal gradient: Post-orogenic extension or large intrusion in the middle crust? A case study from the Agly Massif, French Pyrenees. Abstract, Variscan 2012 meeting, Sassari, Italy.

Siron G, Goncalves P, Marquer D, Pierre T, Paquette JL, Vanardois J. 2020. Contribution of magmatism, partial melting buffering and localized crustal thinning on the late-Variscan thermal structure of the Agly massif (French Pyrenees). *J Metamorph Geol* (in press). https://doi.org/10.1111/jmg.12549.

Soliva J. 1992. Les déformations ductiles dans la zone axiale des Pyrénées-Orientales : la convergence varisque, la mise en place des granites tardi-hercyniens, la convergence pyrénéenne. PhD thesis, Montpellier (France), Univ. Montpellier 2.

Teyssier C, Whitney DL, Rey P. 2008. Dynamic coupling and coeval contraction/extension in and around orogenic plateaux. American Geophysical Union, Fall Meeting 2008, Abstract #T23C–2040.

Ternois S, Odlum M, Ford M, Pik R, Stockli D, Tibari B, *et al.* 2019. Thermochronological evidence of early orogenesis, eastern Pyrenees, France. *Tectonics* 38: 1308–1336.

Thiébaut J. 1964. Étude géologique du Massif de la forêt de Castillon. *Bull Soc Hist Nat Toulouse* 99: 363–389.

Tikoff B, Greene D. 1997. Stretching lineations in transpressional shear zones: An example from the Sierra Nevada Batholith, California. *J Struct Geol* 19: 29–39.

Tikoff B, Teyssier C. 1994. Strain modeling of displacement-field partitioning in transpressional orogens. *J Struct Geol* 16: 1575–1588.

Tournaire Guille B, Olivier P, Paquette JL, Bosse V, Guillaume D. 2018. Evolution of the middle crust of the Pyrenees during the Paleozoic: New data on the plutonic rocks from the North Pyrenean Agly Massif. *Int J Earth Sci* 108: 245–265.

Trap P, Roger F, Cenki-Tok B, Paquette JL. 2017. Timing and duration of partial melting and magmatism in the Variscan Montagne Noire gneiss dome (French Massif Central). *Int J Earth Sci* 106: 453–476.

Tugend J, Manatschal G, Kusznir NJ. 2015. Spatial and temporal evolution of hyperextended rift systems: Implication for the nature, kinematics, and timing of the Iberian-European plate boundary. *Geology* 43: 15–18.

Van Den Driessche J, Brun JP. 1992. Tectonic evolution of the Montagne Noire (French Massif Central): A model of extensional gneiss dome. *Geodin Acta* 5: 85–97.

Vanderhaeghe O, Burg JP, Teyssier C. 1999. Exhumation of migmatites in two collapsed orogens: Canadian Cordillera and French Variscides. *Geological Society Special Publication* 154: 181–204.

Vauchez A, Clerc C, Bestani L, Lagabrielle Y, Chauvet A, Lahfid A, *et al*. 2013. Preorogenic exhumation of the North Pyrenean Agly massif (Eastern Pyrenees, France). *Tectonics* 32: 95–106.

Vernon RH. 1991. Interpretation of microstructures of microgranitoid enclaves. In: Didier J, Barbarin B, eds. *Enclaves and granite petrology. Developments in petrology 13*. Amsterdam: Elsevier, pp. 277–291.

Vernon RH. 2000. Review of microstructural evidence of magmatic and solid-state flow. *Electron Geosci* 5: 1–23.

Vielzeuf D. 1980. Orthopyroxene and cordierite secondary assemblages in the granulitic paragneisses from Lherz and Saleix (French Pyrenees). *Bull Mineral* 103: 66–78.

Vielzeuf D. 1984. Relations de phases dans le faciès granulite et implications géodynamiques. L'exemple des granulites des Pyrénées. State thesis, Clermont-Ferrand (France), Univ. Blaise Pascal.

Vilà M, Pin C, Liesa M, Enrique P. 2007. LPHT metamorphism in a late orogenic transpressional setting, Albera Massif, NE Iberia: Implications for the geodynamic evolution of the Variscan Pyrenees. *J metamorph Geol* 25: 321–347.

Vissers R. 1992. Variscan extension in the Pyrenees. *Tectonics* 11: 1369–1384.

Whitney DL, Roger F, Teyssier C, Rey PF, Respaut JP. 2015. Syn-collapse eclogite metamorphism and exhumation of deep crust in a migmatite dome: The P–T–t record of the youngest Variscan eclogite (Montagne Noire, French Massif Central). *Earth Planet Sci Lett* 430: 224–234.

Cite this article as: Vanardois J, Trap P, Goncalves P, Marquer D, Gremmel J, Siron G, Baudin T. 2020. Kinematics, deformation partitioning and late Variscan magmatism in the Agly massif, Eastern Pyrenees, France, *BSGF - Earth Sciences Bulletin* 191: 15.

Gravity-driven channel flow in the Variscan foreland revealed by U-Th-Pb dating of metamorphism, magmatism and deformation (Agly Massif, eastern Pyrenees).

Vanardois[1*] J., Trap[1] P., Roger[2] F., Goncalves[1] P., Marquer[1] D., Paquette[3] JL., Siron[4] G., Baudin[5] T.

jonas.vanardois@univ-fcomte.fr; pierre.trap@univ-fcomte.fr; francoise.roger@umontpellier.fr; philippe.goncalves@univ-fcomte.fr; didier.marquer@univ-fcomte.fr; j.l.paquette@opgc.univ-bpclermont.fr; siron@wisc.edu ; t.baudin@brgm.fr

[1]UMR 6249 Chrono-environnement, Université de Bourgogne-Franche-Comté, 25030 Besançon, France.

[2]Géosciences Montpellier, Campus Triolet, Université Montpellier, CNRS, 34095 Montpellier Cedex 5, France.

[3]Laboratoire Magmas et Volcans (CNRS-UMR 6524), Campus Universitaire des Cézeaux, 63178 Aubière Cedex, France.

[4]WiscSIMS Laboratory, University of Wisconsin-Madison, Madison, Wisconsin 53706, United States of America.

[5]BRGM-French Geological Survey, 3 Avenue Claude Guillemin, 45100, Orléans, France.

*Corresponding author: jonas.vanardois@univ-fcomte.fr +33(0)381666242 Present address: 16 route de Gray, 25030 Besançon.

Keywords: HT-LP metamorphism, Pegmatites, Variscan orogen, Agly Massif, LA-ICPMS U-Th-Pb dating

1. Introduction

The Variscan belt is considered as an ancient analogue of large and hot orogen (e.g. Maierova et al., 2016) and constitutes a natural laboratory to observe deep crustal flow mechanisms (e.g. Schulmann et al., 2008) as those operating beneath Andean or Tibetan orogenic plateaus (e.g. Hodges, 2006). In the French part of the Variscan belt, the lower-middle crust is thought to have flown horizontally during Carboniferous times, between ca. 345 to 310 Ma, from the hinterland to the foreland in response to pressure gradient (Fig. 1, Whitney et al., 2015, Vanderhaeghe et al., 2020). The occurrence of eclogite boudins hosted in migmatites in the foreland has been interpreted as a rock record of southern lower crustal southern flow of partially molten crust (Whitney et al., 2015, Pitra et al., 2021). In the Eastern French Massif Central, southward lower-crustal flow is also highlighted through the southward decrease in age of partial melting and the progressive evolution of crustal-derived plutonic rocks from c. 345 Ma to c. 310 Ma (Vanderhaeghe et al., 2020, Laurent et al., 2017). However, unequivocal documentation of lower-crustal flow related structures is still uncertain since most of the strain patterns identified on the field are mostly related to the development of low-angle detachment, gravitational instabilities, and exhumation of migmatitic domes in a dextral strike-slip dominated far field stress interpreted as a late-orogenic gravitational collapse recorded between 305 and 290 Ma (Vanderhaeghe et al., 2020 and references therein).

In addition to melt-assisted lateral flow, the Carboniferous building of the Variscan belt was also associated with the development of crustal-scale strike-slip shear zones (e.g. Carreras and Druguet, 2014; Franke et al., 2017; Chardon et al., 2020; Edel et al., 2018 and references therein). It is far from being clear to which extent the gravity-driven lateral flow and the strike-slip-controlled longitudinal or extrusional flow interact in the partially molten orogenic root. Accurate dating of the timing of melt-present and solid-state deformation, and characterizing the feedback relationships between plutonism and crustal-scale shear zones are still needed for the understanding of the evolutionary processes and dynamics of the flow of the partially molten crust.

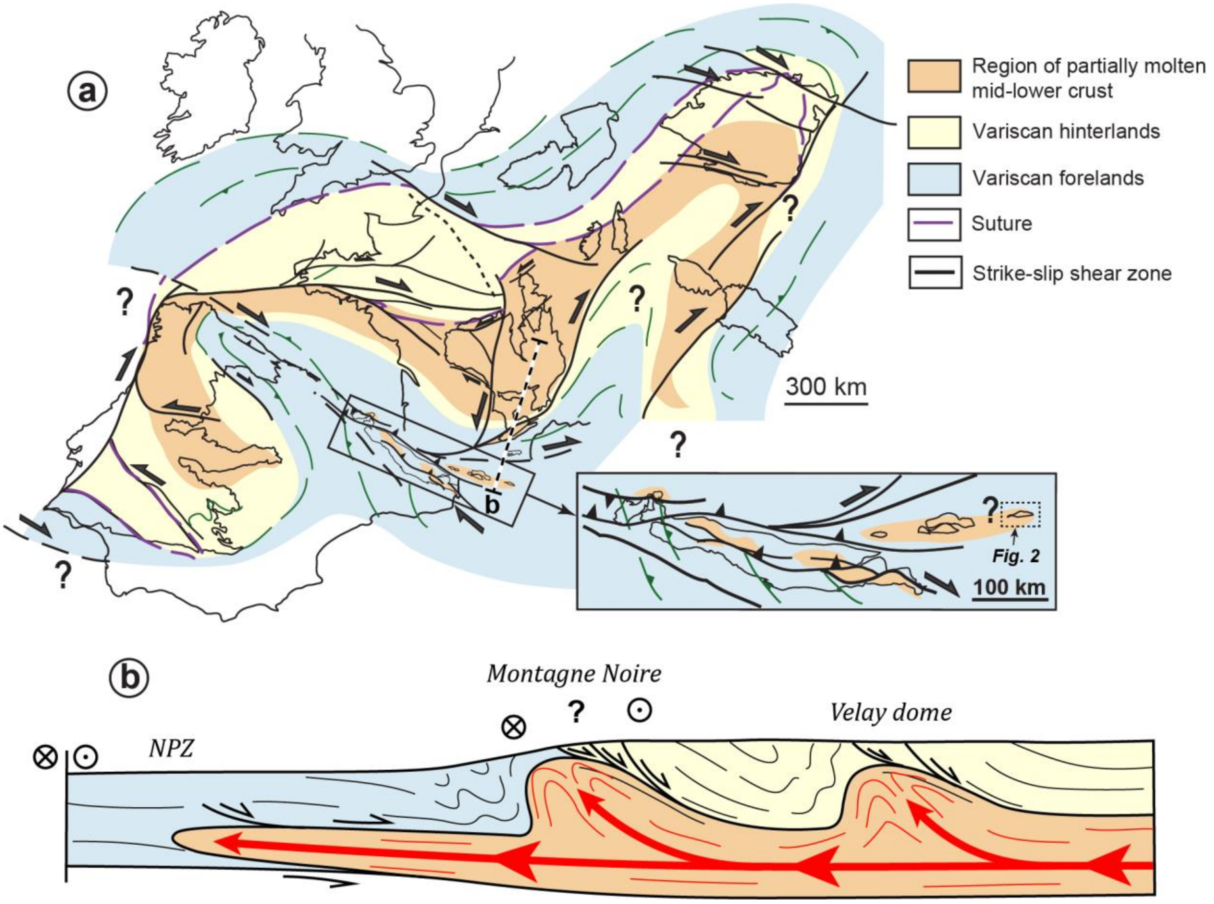

Figure 1 : (A) Paleogeographic reconstruction of the Variscan Belt during Late-Carboniferous modified from Cochelin et al. (2021). (B) Simplified cross-section from the southern edge of the French Central Massif showing the lateral flow of the partially molten crust, modified from Vanderhaeghe et al. (2020).

The North-Pyrenean-Zone (NPZ, Fig. 1) represents the southern foreland of the Variscan belt where the partially molten orogenic root might have flown towards the south (Vanderhaeghe et al., 2020). In comparison with the hinterland portions, the NPZ still lacks precise geochronological data that are required, in addition to structural analysis, to fully understand the flow pattern of the partially molten crust in the external portion of the variscan orogenic plateau. In the eastern edge of the NPZ, the Agly Massif (AM) shows a finite strain pattern that results from the superposition of flat-lying and vertical foliations related to a bulk thinning and a dextral wrenching, respectively. Based on U-Th-Pb dating of plutons (Olivier et al., 2004, 2008; Tournaire Guille et al., 2019) and their relationships with these deformation phases, Vanardois et al. (2020) suggested that the flat-lying structure (D2) and wrench-related vertical structures (D3) may have been partially coeval. In this contribution, LA-ICPMS U-Th-Pb dating of zircon and monazite from pegmatites, leucogranites and metamorphic rocks (i.e. orthogneiss and paragneiss), that record both D2 thinning and D3 wrenching, has been conducted to better constrain the timing of both deformation phases and associated metamorphism and magmatism. Combining structural, metamorphic and geochronological data, we discuss strain partitioning in space and time during mid-lower crustal flow of the Variscan belt foreland.

2. Geological Setting

The Variscan Pyrenees are located in the external domain of the Variscan belt and represent its southern orogenic foreland (Edel et al., 2018; Laurent et al., 2017; Aguilar et al., 2013) (Fig. 1A). The Pyrenean Axial Zone (PAZ) and the North Pyrenean Zone (NPZ) are separated by the EW-striking North Pyrenean Fault (NPF). These two zones consist of Proterozoic to Paleozoic sedimentary rocks deformed and metamorphosed between the middle Carboniferous and the early Permian (Mezger and Gerdes, 2016; Denèle et al., 2014; Aguilar et al., 2013; Schnapperelle et al., 2020; Vacherat et al., 2017; Cochelin et al., 2021; Cugerone et al., 2021).

In the NPZ, few relics of kyanite have been described (Fonteilles et al., 1964; Fonteilles, 1970; Fonteilles and Guitard, 1971) that led some authors to propose an early thickening event (D1) related to a nappe stacking (e.g. Bouhallier et al., 1991; Olivier et al., 2004). U-Th-Pb LA-ICPMS ages at ca. 325-320 Ma obtained in the NPZ are interpreted as the onset of partial melting during D1 prior to the widespread M2 high temperature and low-pressure event widely recorded in the Pyrenees (Lemirre, 2016). This high temperature event is coeval with the widespread development of a sub-horizontal foliations interpreted as the result of a D2 extensional collapse during Late-Carboniferous (Bouhallier et al., 1991; de Saint-Blanquat., 1993; Vanardois et al., 2020).

At the eastern edge of the NPZ, the Agly Massif (AM) forms a WNW-ESE trending, 30 km long and 10 km wide Variscan massif that was exhumed during Cretaceous extension and subsequent Tertiary Pyrenean continental collision. The AM is composed of a Proterozoic to Devonian metasedimentary sequence (Fonteilles, 1970; Berger et al., 1993) that contains sills of orthogneisses whose magmatic protoliths emplaced during Cambrian (ca. 540 Ma) and Ordovician times (ca. 450 Ma) (Tournaire Guille et al., 2019; Paquette et al., 2021). Both sedimentary and igneous rocks have been deformed and metamorphosed during the Variscan orogeny.

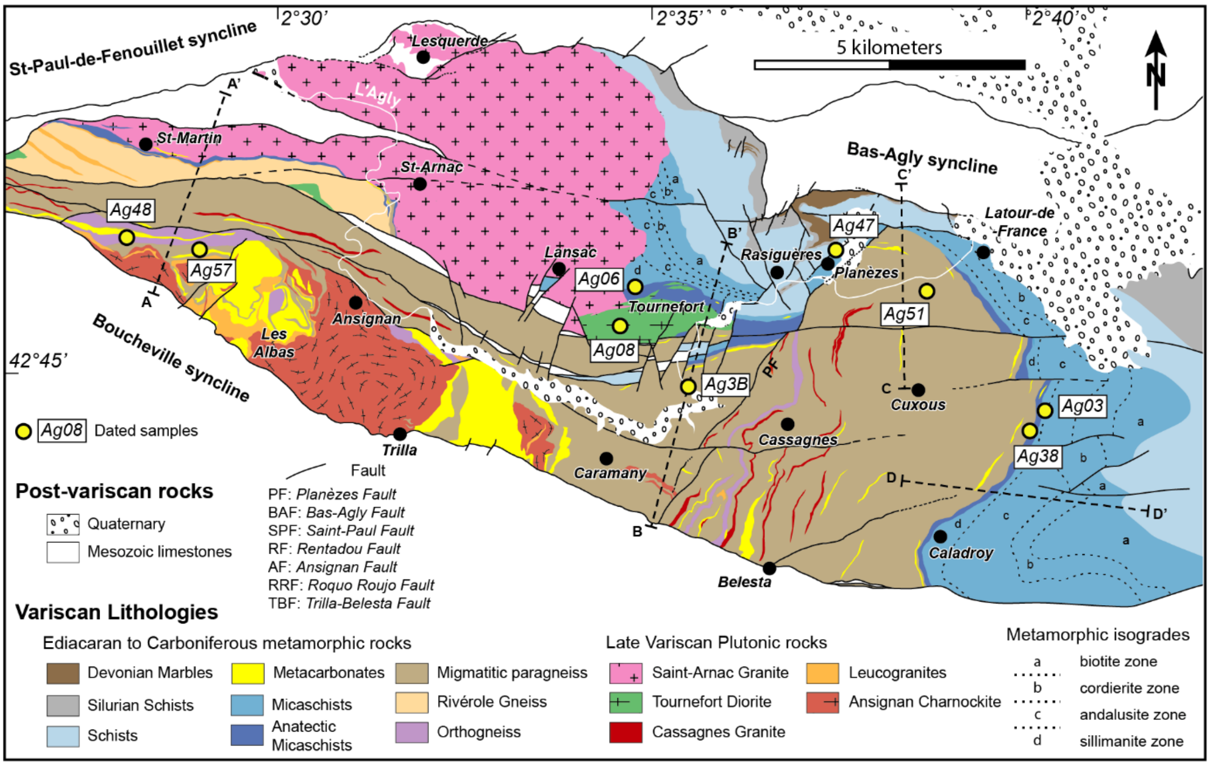

Figure 2 : Geological map of the Agly massif with localisation of the dated samples. NPF: North Pyrenean Fault; SH: Sillon Houiller; NPZ: North Pyrenean Zone; AZ: Axial Zone; CCR: Catalan Coastal Ranges; MN: Montagne Noire; VD: Velay Dome.

The metasedimentary sequence is classically subdivided into an infrastructure and a suprastructure (Fonteilles, 1970). The suprastructure consists of non-migmatitic metasediments represented by Cambrian to Ordovician micaschists and schists, Silurian black-schists and Devonian marble (Fig. 2). The suprasutructure is characterized by a HT-LP metamorphic gradient of ~55°C/km (Vielzeuf, 1984; Andrieux, 1982a, 1982b; Delay, 1989; Bouhallier et al., 1991; Siron et al., 2020) with a maximum temperature of 680°C at the base of the suprastructure (Siron et al., 2020; Bouhallier et al., 1991; Delay, 1989). The infrastructure is composed of partially molten metapelites, metagrauwackes, metacarbonates and meta-igneous rocks mainly orthogneissified (Fig. 2). Siron et al. (2020) have shown that the infrastructure is characterized by a near isothermal gradient buffered at around 740-790°C between 0.5 and 0.66 GPa. The LA-ICPMS U-Th-Pb monazite dating of two kinzigites allowed to date the peak of the HT-LP metamorphism at ca. 305 Ma (Siron et al, 2020). Several hectometric flat-lying mylonitic shear zone are documented in the infrastructure with the main one, i.e. the Caladroy shear zone (CSZ) located near the anatectic front (Delay et al., 1989; Bouhallier et al., 1991; Siron et al., 2020; Vanardois et al., 2020). This CSZ separates the infra- and suprastructure

(Fig. 3) (Vanardois et al., 2020) and subtracted about 5 km of crustal material (Delay, 1989; Bouhallier et al., 1991; Siron et al., 2020).

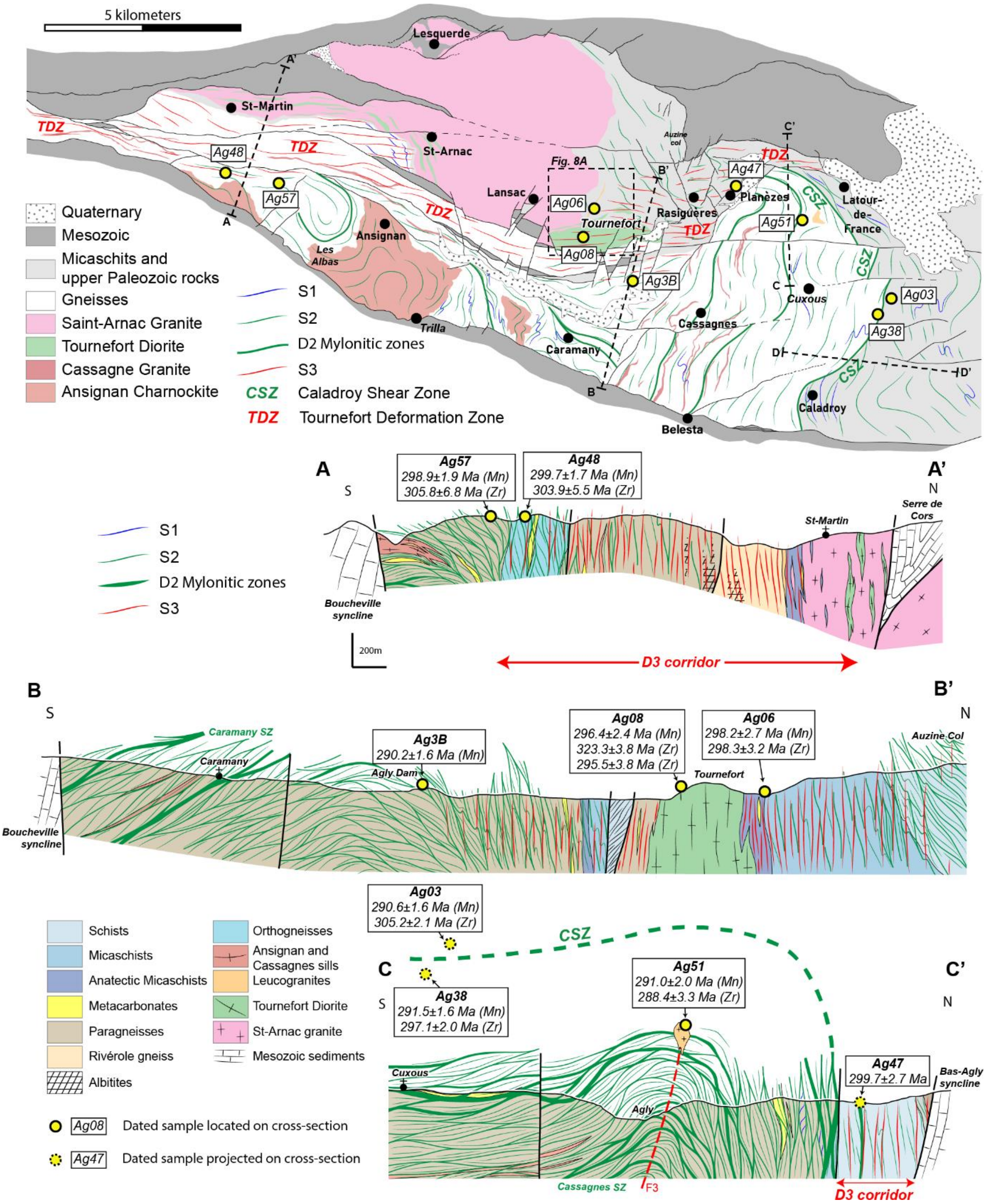

Figure 3 : Structural map and cross-sections of the Agly massif modified from Vanardois et al. (2020). Dated samples are located on the map and cross-sections.

Several Carboniferous magmatic rocks are intrusive at different levels into the infra- and supra-structures. The Ansignan charnockitic pluton is a 500 meters-thick sheet-like laccolith emplaced in the deepest part of the infrastructure, with smaller satellite sills observed in the southern part of the massif (Fig. 2) (Delay et al., 1989; Vanardois et al., 2020; Fonteilles et al., 1993). It is made of three facies: (i) a melanocratic K-feldspar porphyric, garnet and orthopyroxene-bearing granodiorite, (ii) a garnet-bearing leucogranite and (iii) mafic enclaves (Berger et al., 1993; Delay, 1989; Althoff et al., 1994; Olivier et al., 2008). These three facies have been dated by U-Th-Pb method by ID-TIMS on zircon and monazite and yielded ages between 315 and 290 Ma (Postaire, 1982; Respaut and Lancelot, 1983). Recent age at 307 ± 3 Ma (U-Pb LA-ICPMS on zircon) is considered by Tournaire Guille et al. (2019) as the emplacement age of the Ansignan charnockite. However, these authors also obtained on a mylonitized charnockitic sill two distinct concordia ages, one at 313.9 ± 2.9 Ma on zircon cores and the other at 298.6 ± 2.7 Ma on the zircon rims. The Cassagnes granite occurs as a set of meters-thick sills in the infrastructure localized near the Cassagnes village (Fig. 2). It is a melanocratic K-feldspar porphyric, garnet-bearing granodiorite, very similar to the Ansignan charnockite except that orthopyroxene is rare, and it was emplaced at 308 ± 3 Ma (U-Pb LA-ICPMS on zircon; Tournaire et al., 2019). The emplacement of a monzogranitic sill into the infrastructure has been dated by upper intercept at 317 ± 3 Ma (ID-TIMS on zircon; Olivier et al., 2004), but this age is considered by Olivier et al. (2008) as a mixing date between inherited cores and Variscan rims.

The suprastructure is intruded by the Tournefort diorite and the Saint-Arnac pluton (Fig. 2). The Tournefort diorite has been dated by upper intercept at 308 ± 1 Ma and by concordia age at 307 ± 1 Ma (ID-TIMS on zircon; Olivier et al., 2004, 2008). The southern part of the Saint-Arnac pluton is composed of several granitic facies partly mingled with dioritic facies and may be cogenetic with the Tournefort diorite (Olivier et al., 2008). On the southern edge of the Saint-Arnac pluton, the age of the granodiorite has been dated by upper intercept at 304 ± 5 Ma (ID-TIMS on zircon; Olivier et al., 2008) and by weighted mean ^{206}Pb/^{238}U ages at 308 +4/-2 Ma (LA-ICPMS on zircon; Odlum and Stockli, 2019), whereas the zircons of the northern edge yield a mean ^{206}Pb/^{238}U ages of 301 +3/-2 Ma (LA-ICPMS; Odlum and Stockli, 2019). Numerous meter-sized pegmatitic and leucogranitic dykes and sills intruded both the infra- and supra-structures.

The main penetrative strain pattern is related to the D2 deformation event defined by a pervasive flat-lying foliation S2 (Vanardois et al., 2020). D2 reworked an early vertical N-S trending foliation attributed to the D1 thickening event (Fig. 3 and 4A-B, Vanardois et al., 2020). The D2 deformation was coeval with the HT/LP M2 metamorphism, migmatization, and the Ansignan and Cassagnes intrusions (Delay, 1989; Paquet and Mansy, 1991; Bouhallier et al., 1991; Althoff et al., 1994, Vanardois et al., 2020). D2 deformation continued during retrogressed conditions and formed C2 extensional shear zones (Fig. 3 D2 Mylonitic zones and 4C-D) responsible for the bulk thinning of the Agly massif. The Caladroy shear zone (CSZ), separating the infra- and suprastructure, is one of these C2 shear zones (Fig. 3). The evolution of the D2 from suprasolidus S2 foliations to subsolidus C2 strain localization is defined in the following sections as S2 and C2 phases, respectively. Siron et al. (2020) documented LA-ICP-MS U-Th-Pb ages at ca. 296-300 Ma from monazite overgrowths of a C2 mylonite, interpreted as the timing of late D2 crustal thinning.

In the northern part of the studied area, a third deformation phase D3 has been described by Vanardois et al. (2020) (Fig. 3 TDZ). It corresponds to a dextral transpression localized along an E-W 2 km-wide corridor. This D3 corridor shows a prominent vertical foliation S3 that reworked former D2 (S2 and C2) planar fabrics (Fig. 3 and 4E-F). The D3 event is subdivided into an early transtensional deformation, named proto-D3 and a late transpressional regime D3 sensu stricto, named Late-D3 (Vanardois et al., 2020). The D3 corridor acted as preferential pathways for upward migration of the Tournefort diorite and Saint-Arnac granite magmas (Vanardois et al. 2020).

The Tertiary Pyrenean tectonics is characterized in the Agly Variscan basement by brittle deformation with steep reversed faults affecting the Paleozoic and Mesozoic rocks. This last stage is characterized by N20 and N150 striking conjugate strike-slip faults accommodating the N-S Pyrenean compression.

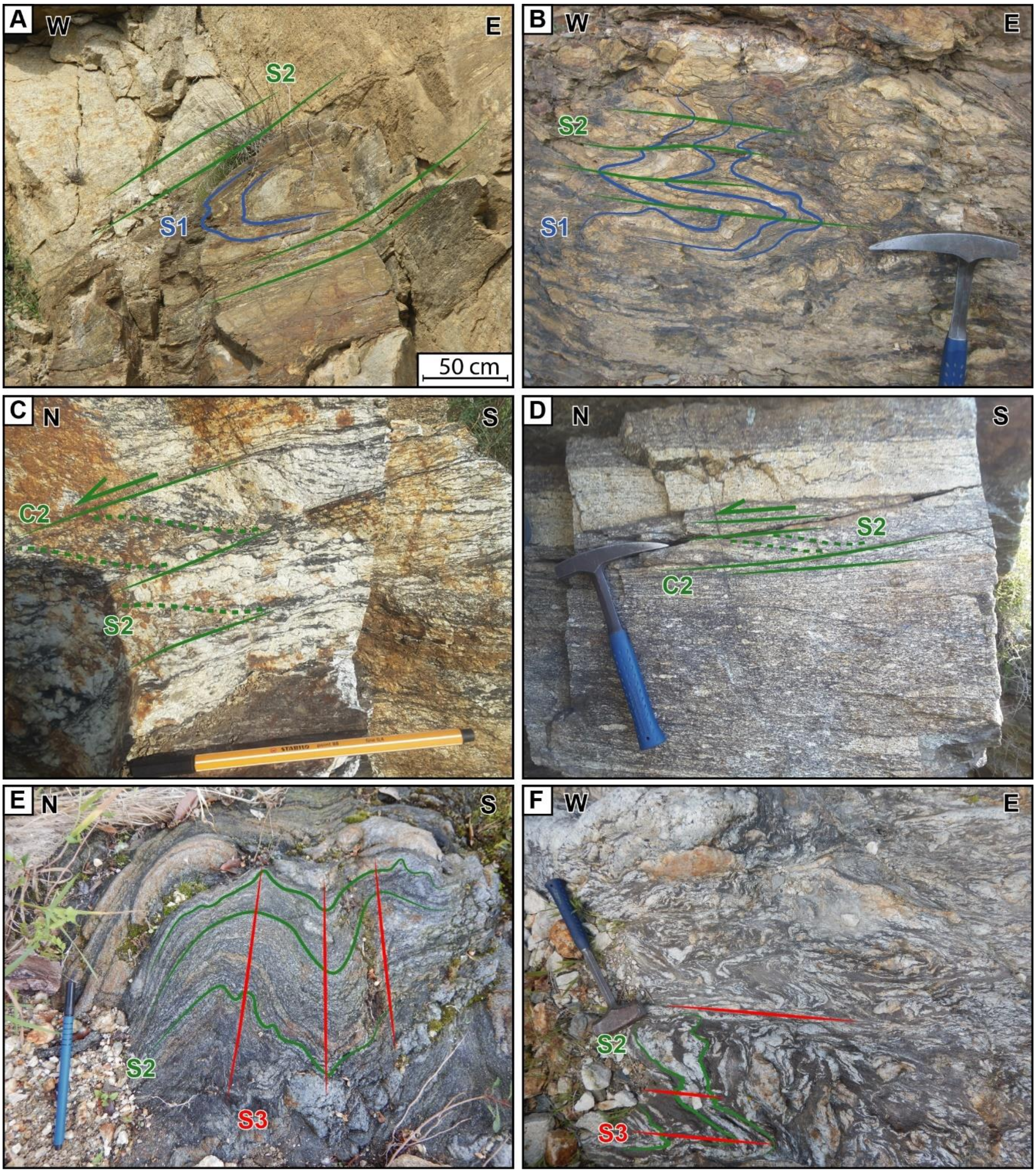

Figure 4 : Structural evidence of D1, D2 and D3 planar fabrics in the Agly massif. S1 foliations affected by F2 folds in the migmatitic basement (A) and in the schists (B). (C and D) C-S structures showing top-to-the-north kinematics in high-D2 strain domains from the migmatitic basement. S2 foliations affected by F3 folds with S3 vertical axial planes in gneiss (E) and in anatectic micaschists (F).

3. U-Th-Pb LA-ICPMS dating

Nine rock samples corresponding to syn-tectonic granitoids or mylonitic rocks have been collected with respect to the main deformation events (Fig. 2 and 3 and Table 1 for location):

(i) samples Ag57 and Ag3B are located in S2 strain domains, (ii) samples Ag38, Ag03 and Ag47 are located within the C2 shear zones, (iii) samples Ag08 and Ag06 are associated and post-dated the Proto-D3 transtensional deformation from the Tournefort area and (iv) samples Ag48 is located in the Late-D3 transpression of the D3 corridor and Ag51 is located within the axial plane of a late-D3 fold.

Table 1: Summary of geographic location, rock types, and U-Th-Pb geochronological results for samples analysed in this study. (Zr): zircon age; (Mn): monazite age; T.S.: monazite age obtained on thin section.

Sample	**Rock type**	**Structure**	**GPS location**	**U-Th-Pb age (±2σ)**	
				Monazite	**Zircon**
Samples from S2 strain domains					
Ag57	Vivier deformed leucogranite	Infrastructure	N42°46'07'' E02°29'12''	298.9 ± 1.9 Ma	305.8 ± 6.8 Ma 339.5 ± 13 Ma ~ 535 - 620 Ma ~ 620 - 730 Ma
Ag3B (T.S.)	Dam migmatitic paragneiss	Infrastructure	N42°44'51'' E02°35'26''	290.2 ± 1.6 Ma	
Samples from the C2 Shear Zones					
Ag03	Undeformed pegmatite	Suprastructure	N42°44'47'' E02°39'44''	290.7 ± 1.5 Ma	304.6 ± 2.7 Ma
Ag38	Deformed pegmatite	Infrastructure	N42°44'47'' E02°40'06''	291.5 ± 1.6 Ma	297.6 ± 2.3 Ma
Ag47	Planèze mylonitic pegmatite	Suprastructure	N42°46'07'' E02°37'16''		299.7 ± 2.7 Ma 527.1 ± 9.4 Ma 326.6 ± 6.2 Ma
Samples from the Proto-D3 Tournefort area					
Ag08	Tournefort undeformed pegmatite	Suprastructure	N42°45'27'' E02°34'12''	296.4 ± 2.4 Ma	295.5 ± 3.8 Ma 323.3 ± 3.8 Ma
Ag06	Tournefort undeformed Leucogranite	Suprastructure	N42°45'54'' E02°34'32''	298.2 ± 2.7 Ma	298.3 ± 3.2
Samples from the Late-D3 Tournefort Deformation Zone					
Ag48	Vivier Orthogneiss	Infrastructure	N42°46'16'' E02°28'42''	299.7 ± 1.7 Ma	303.9 ± 5.5 Ma ~ 440 - 480 Ma

					551.8 ± 4.8 Ma 597.2 ± 7.7 Ma
Ag51	Latour de France leucogranite	Infrastructure	N42°45'38'' E02°38'50''	291 ± 2 Ma	289.4 ± 4.2 Ma

3.1. Analytical method

Monazite and zircon were obtained by standard crushing and heavy liquid and magnetic separation using Frantz isodynamic techniques. The crystals were handpicked under a binocular microscope, then mounted in epoxy resin discs and polished to expose mid-grain sections. Except for the monazite from the sample Ag3B, which has been analysed in thin section in order to preserve textural relationships, the rock-forming mineralogical assemblage and the fabrics. Cathodoluminescence (CL) and backscattered electrons (BSE) images were used to select points for analysis. U-Th-Pb geochronology of zircon and monazite was obtained by laser ablation inductively coupled plasma spectrometry (LA-ICPMS) at the Laboratoire Magmas et Volcans (Clermont-Ferrand, France). The analysis involved the ablation of minerals with a Resonetics Resolution M-50 powered by an ultra-short pulse ATL Atlex Excimer laser system operating at a wavelength of 193 nm. For zircon and monazite, spot diameters of 27 µm or 33 µm and 12 µm were used, associated with repetition rates of 3 Hz and 1 Hz, and laser fluences of 4J/cm2 and 9J/cm2 respectively. The ablated material was carried by helium and then mixed with nitrogen and argon before injection into the plasma source of an Agilent 7500 cs ICP-MS equipped with a dual pumping system to enhance sensitivity (Paquette et al., 2014). The detailed analytical procedures are described in Paquette et al. (2014) and detailed in Paquette and Tiepolo 2007; Hurai et al. 2010 and in the supplementary material (Table S1). Data reduction was carried out with the GLITTER® software package from Macquarie Research Ltd (Van Achterbergh et al., 2001). Calculated ratios were exported and ages and diagrams were generated using Isoplot/Ex v. 2.49 software package of Ludwig (2001). In the text and figures, all uncertainties in ages are given at the ± 2σ level. The decay constants used for the U-Th-Pb system are those determined by Jaffey et al. (1971) and recommended by IUGS (Steiger and Jäger, 1977). Analytical results are given in Tables S2 and S3. Monazite data by LA-ICPMS were plotted in a U-Th-Pb modified concordia diagram (^{206}Pb/^{238}U vs ^{208}Pb/^{232}Th) because ^{232}Th measurement is more accurate than ^{235}U.

3.2. Results of the U-Th-Pb dating

3.2.1. Samples from S2 strain domains

3.2.1.1. The Vivier deformed leucogranite (Ag57)

The Vivier leucogranite (Ag57) is a two-meter-thick magmatic sill composed of Qtz + Kfs + Pl ± Grt ± Bt. The sill is sub-horizontal, undeformed and parallel with the surrounding S2 foliation. Most of the analysed monazite crystals in sample *Ag57* are round-shaped, translucent to slightly opaque and yellow. BSE images of some monazite grains show a simple growth zoning (Fig. S1). Twenty-nine analyses were performed on nineteen monazite crystals (Fig. 5A; Table S2). Unlike Pb concentrations (1356-2152 ppm), Th and U contents vary significantly to crystals or different domains of a crystal. Th and U contents range from 18394 to 75616 ppm and 1847 to 11425 ppm, respectively. Th/U ratios are between 1.6 and 33.5 (Table S2). All these data are concordant between 280 and 320 Ma and, excluding two analyses (dotted ellipses), yield a concordia age of 298.9 ± 1.9 Ma ($\text{MSWD}_{(\text{C+E})}$ = 1.7; n = 26) (Fig. 5A).

The analysed zircon crystals are transparent, colourless and slightly rounded. CL imaging shows complex internal textures with the systematic occurrence of inherited core displaying either a typical magmatic concentric oscillatory zoning or patchy zoning textures surrounded by rims (Fig. S2). Forty-five analyses were performed on thirty zircon grains (Table S3). Among these data, thirty-seven are concordant but scattered along the concordia curve between around 700 to 300 Ma and form two distinct clusters: a scattered population between 700 and 450 Ma (group 1) and a range of ages between 350 and 300 Ma (group 2) (Fig. 5B; Table S3). The concordia ages histogram suggests that the group 1 data are distributed to at least two main populations, one at 630-710 Ma and the other at 550-610 Ma, with perhaps a third minor around ca. 450 Ma (Table S3; Fig. 5B). The oldest peak is constituted by 13 data (9 cores and 4 rims, S2), characterized by Th contents ranging from 13 to 254 ppm, with Th/U from 0.11 to 1.77 (most >0.3), values typical of magmatic zircon (Tiepel et al., 2004; Linnemann et al., 2011) (Table S3). The dates range from 637 ± 19 Ma to 709 ± 20 Ma with a weighted average of concordia ages of 671 ± 15 (MSWD = 6.3; n =13). The next peak is also composed of 13 data (9 rims and 4 cores, S3) that have Th concentrations between 19-347 ppm with the Th/U ratios ranging from 0.14-1.22 except for three rims (Th/U = 0.02-0.04) (Table S3). These dates are between 550 ± 16 Ma and 608 ± 18 Ma with a weighted average of concordia ages of 578 ± 13 Ma (MSWD = 6.1; n =13) (Fig. 5B).

The youngest cluster (group2) is constituted by 8 rim data including 5 concordant ones showing Th contents between 3 and 17 ppm (except for one at 196 ppm) and low Th/U ratios of 0.01-0.08 (except for one at 0.38) (Table S3; Fig. 5B; S2). Among the five concordant dates, three (Zr27b, Zr43b, Zr41b) yield a concordia age of 339.5 ± 13 Ma ($MSWD_{(C+E)}$ = 2.8) and the two youngest data (Zr57b, Zr44b) give a concordia age of 305.8 ± 6.8 Ma ($MSWD_{(C+E)}$ = 0.23). This date is consistent with the lower intercept date obtained by the linear regression on the 4 youngest data (2 concordant and 2 discordant data (Zr20b, Zr42b)) of 305.1 ± 7.8 Ma (MSWD = 0.16). Other data (dotted ellipses) are not taken into account because they are discordant probably due to radiogenic Pb losses and common Pb contamination (Fig. 5B).

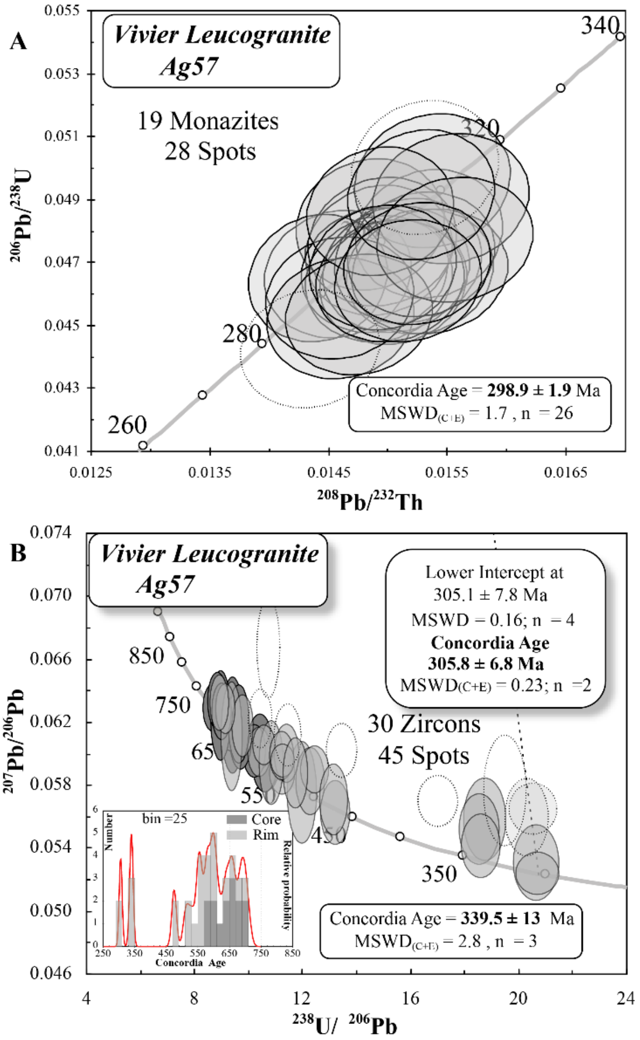

Figure 5 : Monazite U-Th-Pb concordia diagram (A) and zircon U-Pb Tera Wasserburg diagram (B) obtained by LA-ICPMS on the Vivier leucogranite (Ag57). Error ellipses and uncertainties in ages are ± 2σ. Dotted ellipses are not taken into account for the age calculation.

3.2.1.2. The migmatitic paragneiss from the Agly dam (Ag3B)

Ag3B is a migmatitic paragneiss sampled near the Agly dam composed of Kfs + Qtz leucosomes and Bt + Sill melanosomes, both containing garnets (Fig. 6A). It is located in the upper structural levels of the infrastructure, close to the southern boundary of the D3 corridor (Fig. 3). Small C2 shear zones are located in the melanosomes whereas the leucosomes are weakly deformed. Garnets are elongated and fractured parallel to the S2 foliation. Thus, we suggest that melting and subsequent leucosome crystallization are earlier than the C2 event.

Monazite crystals from this sample (*Ag3B*) have been analysed in a thin section in order to preserve textural relationships. Monazite occurs both in the Qtz-Kfs matrix (e.g. Mn7; Mn19, Fig. 6B), as inclusions in the elongated and fractured garnet (e.g. Mn5; Mn10, Fig. 6C and D) and in Bt-Sill shear band (e.g. Mn9; Mn16, Fig. 6E and F). In relation to their textural position, thirty-seven analyses on thirty monazite grains have been performed (Table S2). High to very high Pb, Th and U contents of matrix-monazite or inclusion-monazite inclusion are similar with very wide ranges between 1084-3782 ppm (most 1084-2879 ppm), 35693-118463 ppm (most 35693–80990 ppm) and 1587–13134 ppm, respectively. The Th/U ratios are between 3.8 and 29.9. The highest ratios are found in some monazite grains included in the garnet (Table S2).

The three matrix-monazite grains analysed (Mn 7, 18 and 19) are anhedral small grains (30 to 60 µm) without clear zonation (Fig. 6B). These analyses yield a concordia age of 292 ± 4 Ma ($\text{MSWD}_{(\text{C+E})}$ = 1.8; n = 3; Fig. 7A).

Ten monazite inclusions within garnet (Mn 10, 41, 39, 28, 5, 27, 2, 1, 24 and 26) are anhedral and 50-150 µm in size with sometimes slight patchy zoning in BSE (Fig. 6C and D). They are present in garnet from core to rim and thus grow before or synchronously with garnet crystallization. However, the well-known armouring effect of garnet (e.g. Goncalves et al., 2004; Dumond et al., 2015) is limited by the presence of numerous fractures that may have favored fluid-assisted dissolution-precipitation of monazite after garnet crystallization. The thirteen analyses yield an upper intercept date of 295 ± 8 Ma (MSWD = 1.3; n = 13; Fig. 7B). Among these data, nine yield a concordia age of 290.6 ± 3.4 Ma ($\text{MSWD}_{(\text{C+E})}$ = 1.3; n = 9). Both dates are similar, the best date estimate probably is the concordia age.

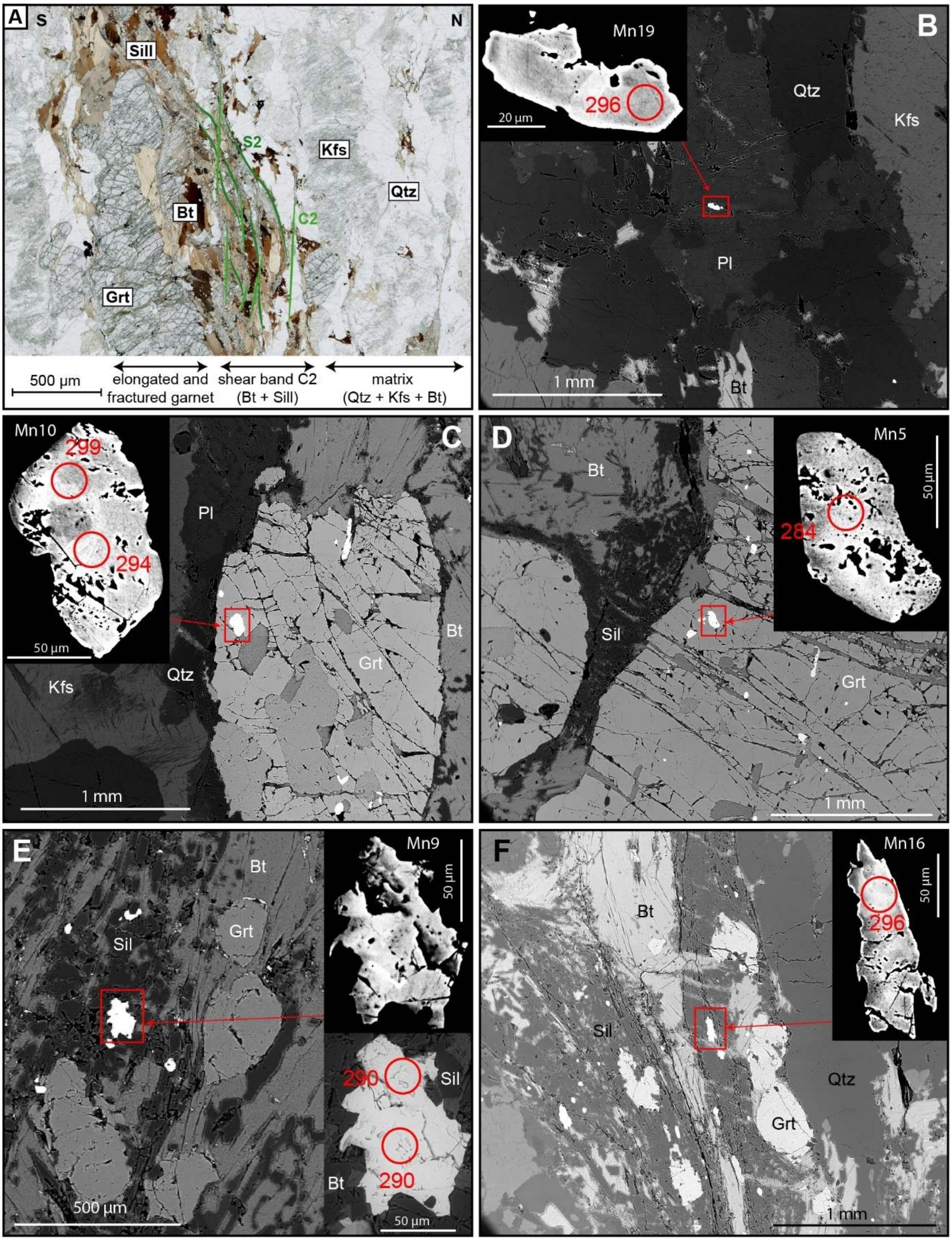

Figure 6 : Locations and morphologies in BSE images of monazite from the Dam migmatitic paragneiss (Ag3B). (A) Thin section of the dam migmatitic paragneiss (Ag3B) with the three textural domains where monazite grains are located. (B) is located in the matrix, (C) and (D) are within the garnet, (E) and (F) are in the deformed zone. Red circles indicate laser spot analyses with a diameter of 12 µm and red numbers correspond to concordia age obtained to the monazite grain numbers reported in Table S3.

Among the sixteen monazite crystals analysed in the deformed zone, nine are included in sillimanite aggregates and are anhedral, elongated and marking the foliation with patchy zonings (Fig. 6F). Two crystals (Mn 3 and 8) are included in biotite and show sub-euhedral shapes. Five monazite grains (Mn 9, 15, 32, 34 and 35) are in contact with both biotite and sillimanite. They are anhedral, stubbier with irregular borders and do not show a preferential orientation (Fig. 6E; Table S2). The spot analyses carried on the monazite crystals included in sillimanite and in biotite yield two similar concordia ages within error of 289 ± 2 Ma ($MSWD_{(C+E)}$ = 1.17; n = 13) and 297 ± 9 Ma ($MSWD_{(C+E)}$ = 2.6; n = 3), respectively (Fig. 7C). Combining all the analyses (except two) performed on the sixteen monazite grains in the deformed zone yields a concordia age of 289.7 ± 2.0 Ma ($MSWD_{(C+E)}$ = 1.5; n = 14).

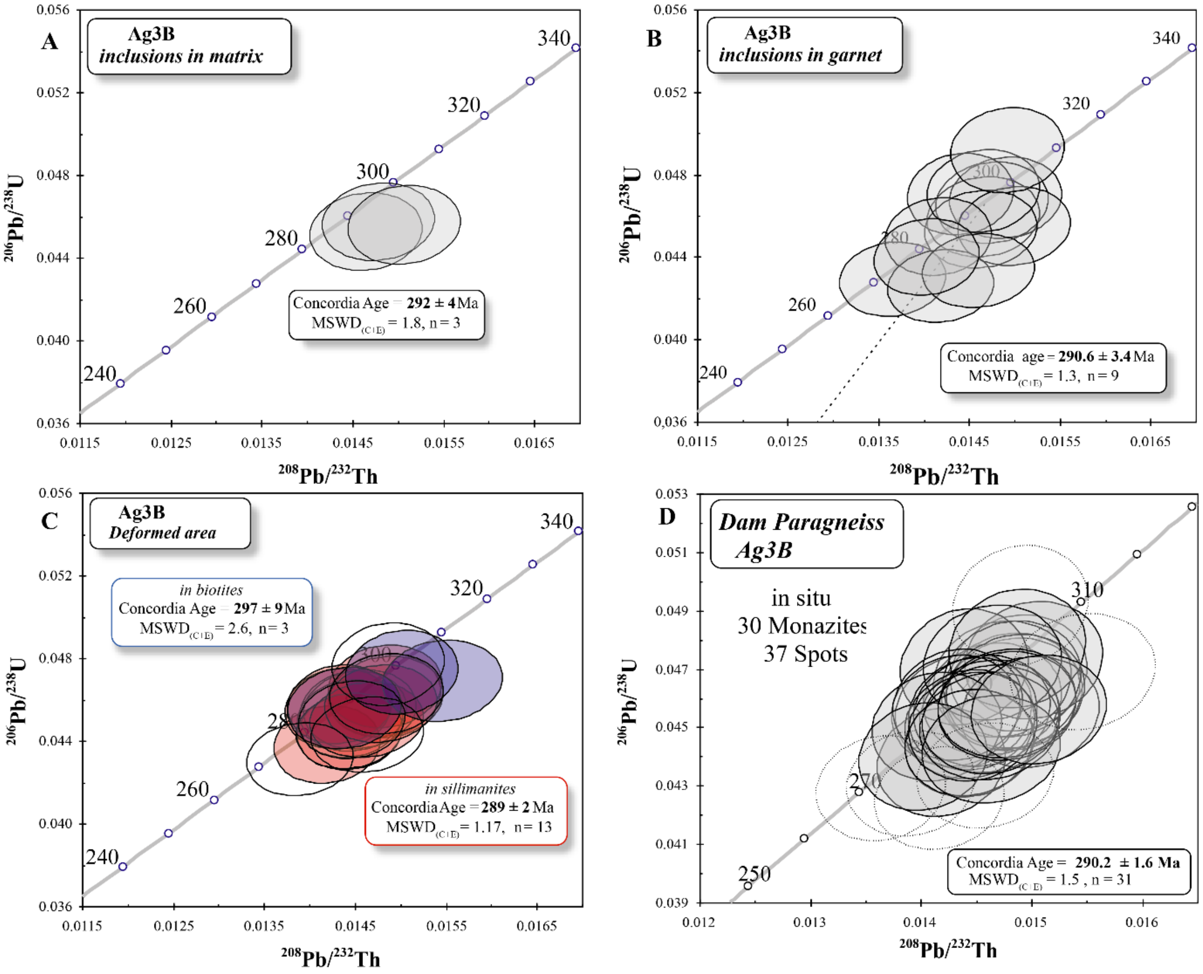

Figure 7 : Monazite U-Th-Pb concordia diagrams of the Dam migmatitic paragneiss Ag3B. Error ellipses and uncertainties on ages are ± 2σ. Dotted ellipses are not taken into account only for the age calculation. Monazite grains within the (A) matrix, (B) the garnet, (C) the deformed zone and (D) all data.

No correlation is observed within the errors between the textural position of the various populations (e.g. inclusion vs. matrix), U-Th-Pb contents and dates. Moreover, whatever the textural position of monazite, all dates are similar within uncertainties. Therefore, crystallization of monazite is unrelated to structural location and a single age can be calculated for the whole population. Thirty-one analyses on thirty monazite grains (inclusion and matrix) form a cluster, which yields a concordia age of 290.2 ± 1.6 Ma ($MSWD_{(C+E)}$ = 1.5; n = 31) (Fig. 7D).

3.2.2. Samples from the C2 Shear Zones

The Caladroy Shear Zone (CSZ) is the main C2 high strain zone that separates the supra and infrastructure (Fig. 8), and largely accommodated late-D2 thinning (Bouhallier, 1991; Vanardois et al., 2020; Siron et al., 2020). It appears as a 1-kilometre thick anastomosed network of mylonitic shear zones (C2) separating lense-shaped lower D2 strain domains where S2 predominates (Fig. 8A, Vanardois et al., 2020). Two meter-thick pegmatitic dykes were sampled in the core of the CSZ, located in the Brosse ravine (Fig. 8B). The pegmatite sample Ag03 is weakly deformed and lies within a low D2 strain domain while sample Ag38 is strongly deformed and located in the core of a C2 shear zone.

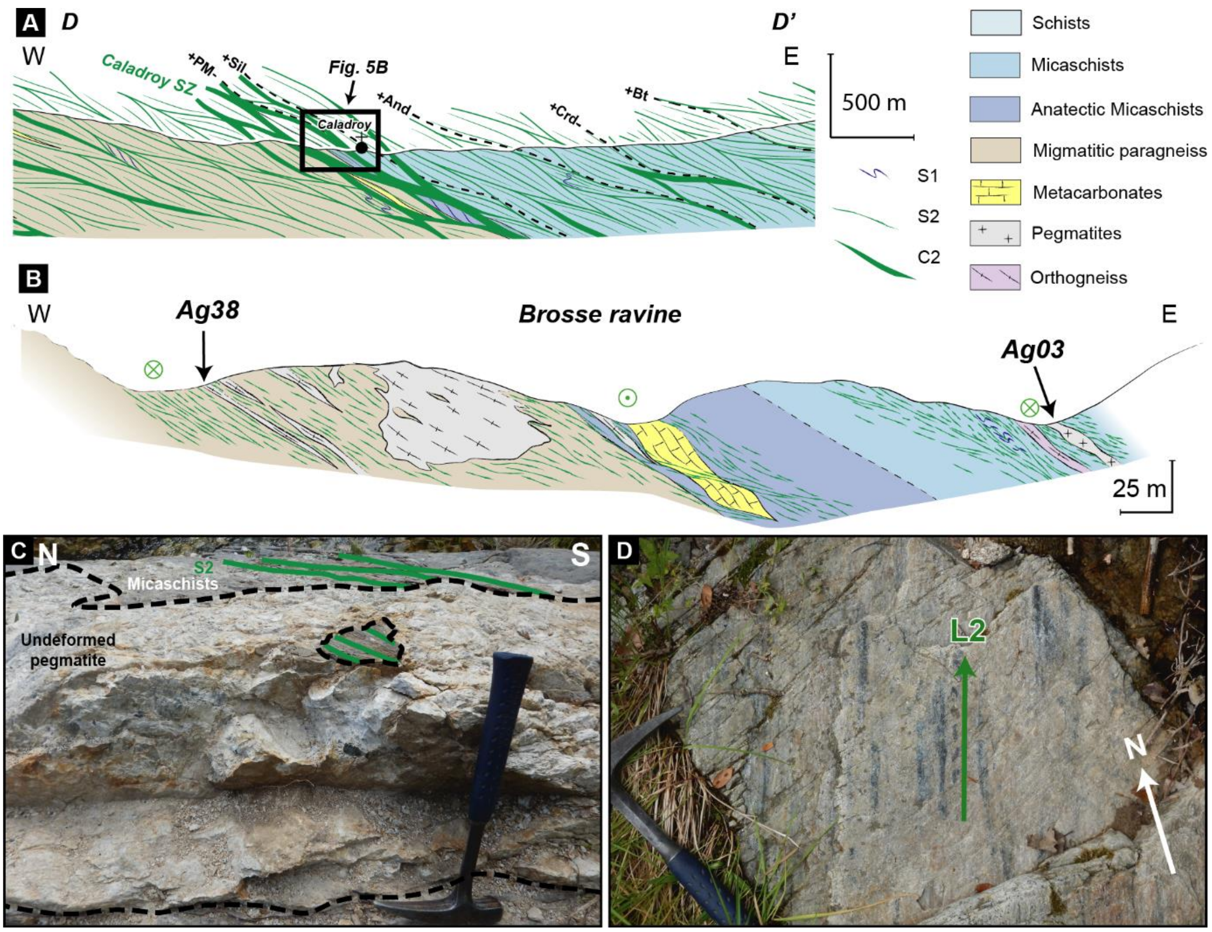

Figure 8 : Field relations of the Brosse Ravine pegmatites (Ag03 and Ag38). (A) Cross-section passing by the boundary of the infra- and suprastructure marked by the Caladroy Shear Zone (CSZ), location on Fig. 2 and 3A. (B) Cross-section of the Brosse Ravine. Outcrop photographs of the Brosse ravine pegmatites (C) Ag03 cross-cutting S2 foliations and bearing a xenolith of micaschist and (D) Ag38 with L2 stretching lineation marked by tourmalines (RHR orientation).

3.2.2.1. The Brosse ravine weakly deformed pegmatite (Ag03)

Sample Ag03 corresponds to a one-meter thick pegmatitic dyke that is subconcordant to the S2 foliation within the sillimanite-bearing micaschists (Fig. 8C). The pegmatite contains xenoliths of the surrounding micaschist. The pegmatite is made of a coarse-grained Qtz + Kfs + Pl + Ms + Bt + Tur pegmatitic assemblage, with no clear preferential orientation of minerals but slightly solid-state deformed, attested by the recrystallization of quartz grains. Biotite is not chloritized and feldspar is slightly sericitized, indicating limited fluid-rock interaction.

Monazite crystals are anhedral, sometimes rounded or in a fragmented form, green and transparent to slightly opaque. BSE imaging shows some grains to have a weakly patching zonation (Fig. S1). Twenty-six analyses on twenty-three crystals were analysed (Table S2).

These data have a wide high to very high range of Pb (5443-13712 ppm), Th (46617-269584 ppm) and U (29933-105937 ppm) contents and moderate Th/U ratios (0.58-9.01; most 0.58-4.13). In the concordia diagram, all these data are concordant between 310 and 270 Ma (Fig. 9A). Two data are younger (dotted ellipses) than the rest, presumably because of minor radiogenic Pb loss. Omitting those two data and an older one yields a concordia age of 290.6 ± 1.6 Ma ($MSWD_{(C+E)}$ = 1.5; n = 23; Fig. 9A).

Zircon is euhedral, prismatic with a shape ratio up to 3:1 and usually metamict and brownish except two crystals, which are transparent and colourless. CL imaging shows that the two colourless zircons have concentric zoning, but for others no zonation could be observed due to the metamictization (Fig. S2). Twenty-five analyses were carried out on twenty zircons (Table S3; Fig. 9B). Nineteen yield a lower intercept date of 305.2 ± 2.1 Ma (MSWD = 0.38) and among these data, eleven give a concordia age of 304.4 ± 2.6 Ma ($MSWD_{(C+E)}$ = 1.03). Except for datum Z9c, the concordant data are characterized by high Pb (102-330 ppm) and U (2425-7356 ppm, most 2425-3568 ppm) contents and low Th (4-13 ppm) concentrations (Table S3). The four discordant data slightly above the concordia curve have a similar range in Pb (113-174 ppm) and U (2532-3838 ppm) contents and higher Th contents (10-132 ppm) than those from the concordant data. All these data have very low Th/U (0.001-0.019; most of them are between 0.001-0.004). Moreover, the core analyses of Zr2, Zr4 and Zr15 are concordant at 1762 ±22 Ma, 501 ± 15 Ma and 359 ± 10 Ma, respectively (Table S3; Fig. 9B).

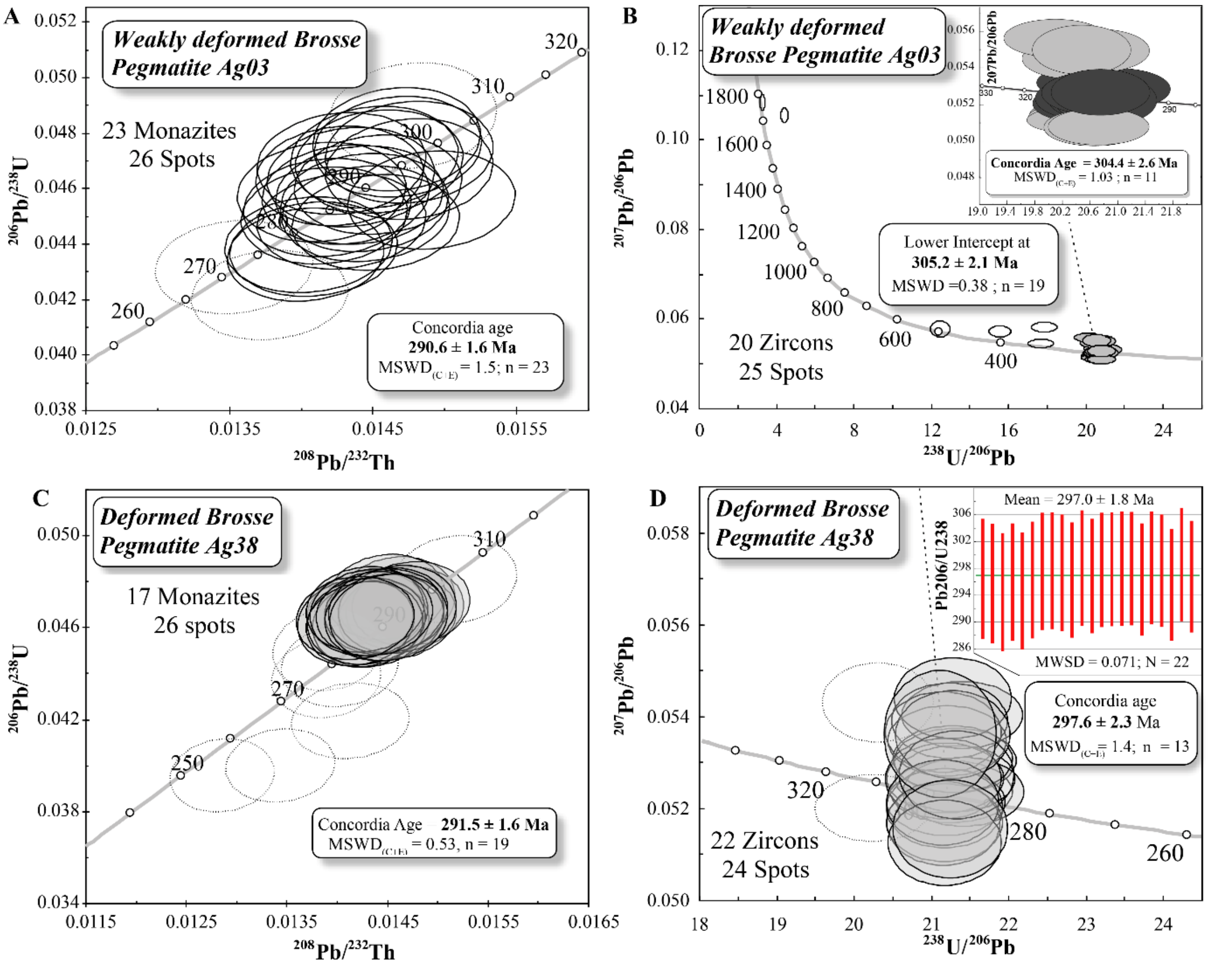

Figure 9 : Monazite U-Th-Pb concordia diagrams (A and C) and zircon Tera Wasserburg diagrams (B and D) of the Brosse ravine pegmatites Ag03 and Ag38. Error ellipses and uncertainties in ages are ± 2σ. In the (A), (C) and (D) diagrams, the dotted ellipses are taken into account for the concordia age calculation while in diagram (B) these are the white ellipses.

3.2.2.2. The Brosse ravine mylonitic pegmatite (Ag38)

The mylonitic pegmatite (Ag38) underwent high-strain D2 along a decametre-thick C2 shear zone (Fig. 8B). It shows the same mineralogical assemblage as Ag03 with Qtz + Kfs + Pl + Ms + Tur ± Grt. Feldspar is slightly sericitized. The pegmatite is strongly deformed and totally transposed along the C2 shearing plane. Quartz, feldspar, and tourmaline are strongly elongated and stretched along the N20 L2 stretching lineation trend (Fig. 8D).

Two types of monazite crystals can be distinguished macroscopically, according to their colour, either green and transparent (Mn 1 to 7) or yellow to greenish and slightly opaque (Mn 8 to 17). In both cases, they are anhedral, and have no zonation in BSE. Moreover, they have similar concentrations (U = 22009 – 101992 ppm (most > 50000 ppm); Th = 42249 – 92063 ppm; U/Th = 0,45 – 2,97) (Table S2). In the concordia diagram, the two populations of monazite cannot be distinguished (Fig. 9C). Twenty-six analyses on seventeen monazites were performed (S2 and Table S2). Except two data (Mn12 and Mn 8-1, dotted ellipses), all ellipses are concordant between 250 and 310 Ma and, excluding 5 analyses (dotted ellipse), yield a concordia age of 291.5 ± 1.6 Ma ($MSWD_{(C+E)}$ = 0.53; n = 19) (Fig. 9C).

Zircon crystals are euhedral, brown, usually metamict. In CL, they are uniform enough without real internal structures (Fig. S2). Twenty-four analyses were performed on twenty-two zircons (S2 and Table S3). Except data Z4 and Z34, all data have very low Th/U ratios (<< 0.1, most <0.001) with low Th contents (< 10 ppm). In the Tera-Wasserburg diagram, except two data (Zr6c and Zr29C around 310 Ma), all ellipses have a concordant to sub concordant position at ca. 300 Ma and are aligned along a common-Pb discordia (Fig. 9D). Amongst these twenty-two data, thirteen give a concordia age of 297.6 ± 2.3 Ma ($MSWD_{(C+E)}$ = 1.4; Fig. 9D).

3.2.2.3. The Planèzes mylonitic pegmatite (Ag47)

Sample Ag47 is a mylonitized 10-meter thick pegmatite (Ag47) in the micaschists of the suprastructure, north of the Planèzes village (Fig. 2**).** This pegmatite is mineralogically similar to the Brosse Ravine pegmatites and consists of Kfs + Qtz + Pl + Ms + Tur assemblage, with slightly sericitized feldspars. The pegmatite shows a strong D2 mylonitization and is transposed along a C2 shear zone. The C2 high-strain planar fabric and L2 lineation marked by elongated quartz and tourmaline crystals are steepened due to Late-D3 deformation (Fig. 3).

Only a few zircons could be analysed that are usually anhedral, metamict and brownish-pink coloured. Most crystals preserve at least some crystal faces, although on some others those faces are almost entirely erased. One crystal (Z1) is subhedral, transparent and colourless. Fifteen analyses on seven zircons were performed (S2; Table S3). In the Tera-Wasserburg diagram, all data are concordant or sub-concordant and form two clusters at ~ 490-530 Ma (group 1) and ~ 300-330 Ma (group 2) (Table S3; Fig. 10). The three analyses of group 1 were acquired on a single atypical and colourless crystal (Zr1). The Pb, Th and U contents are between 34-95 ppm, 39-69 ppm and 431-1212 ppm, respectively and with low Th/U ratios < 0.1 (i.e 0.045-0.091). Two analyses (Zr1-1 and Zr1-2) yield a concordia age of 527.1± 9.4 Ma ($MSWD_{(C+E)}$ = 1.5; n = 2) and the third datum (Zr1-3) gives a younger date at 490 ± 12 Ma. The group 2 data were obtained from 12 analyses on 6 zircon crystals showing a very low Th content (<3 ppm), a high to very high U content (1453-3900 ppm) with a very low Th/U (<<0.01) (S2; Table S3; Fig. 10). Ten ellipses give a lower intercept date at 299.5 ± 2.6 Ma (MSWD = 0.32) and among these data, nine yield a concordia age of 299.7 ± 2.7 ($MSWD_{(C+E)}$

= 0.56). Two concordant ellipses (Zr5-2 and Zr7-2) yield an older concordia age of 326.6 ± 6.2 Ma (MSWD$_{(C+E)}$ = 2.6; n = 2) (Table S3; Fig. 10).

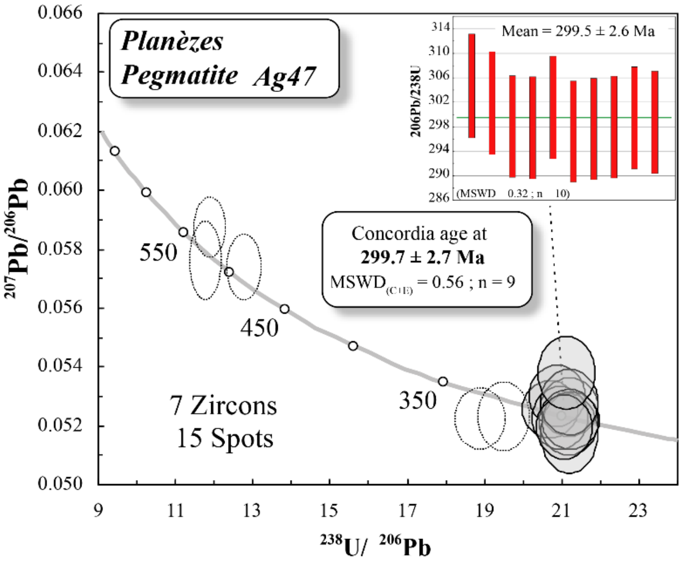

Figure 10 : Zircon U-Pb Tera Wasserburg diagram obtained by LA-ICPMS on the Planèzes pegmatite (Ag47). Error ellipses and uncertainties in ages are ± 2σ. Dotted ellipses are not considered for the age calculation.

3.2.3. Samples from the Proto-D3 Tournefort area

3.2.3.1. The Tournefort pegmatitic dyke (Ag08)

Sample Ag08 is a 30-centimeter thick pegmatitic dyke that intrudes the Tournefort diorite (Fig. 11A and B). It cross-cuts the magmatic S3 foliation of the Tournefort diorite in a place where S3 is NE-SW trending and interpreted by Vanardois et al. (2020) as Proto-D3 planar fabrics (Fig. 11B). The pegmatite consists of a Qtz + Kfs + Pl ± Ms assemblage and shows brittle fractures, and localized ductile deformation of quartz (Fig. 11C). The feldspars are unaltered.

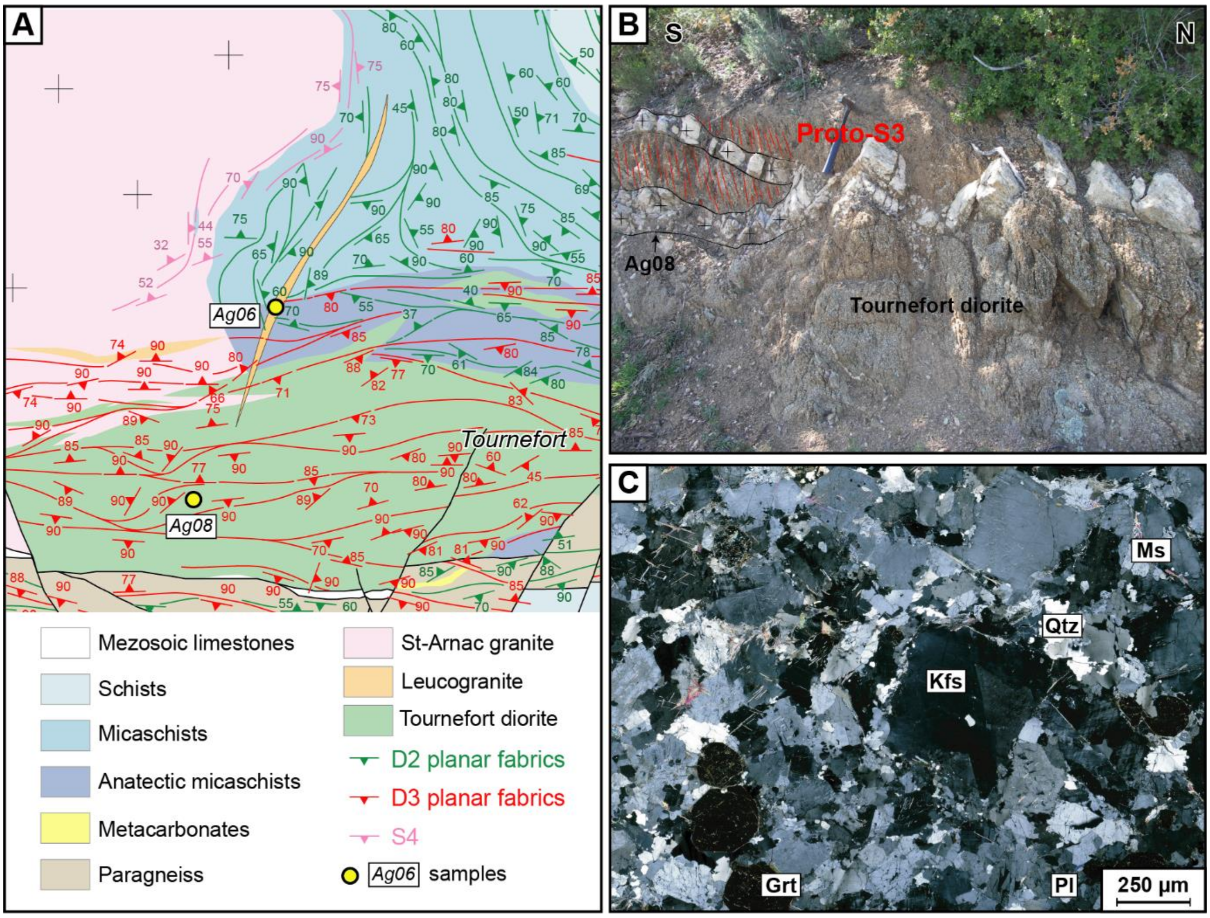

Figure 11 : Microphotographs and field relations from samples within the D3 corridor and from the two Tournefort dykes. (A) Foliations map of the Tournefort area modified from Vanardois et al. (2020). S4 is a local planar fabric induced by the emplacement of the Saint-Arnac pluton. (B) Outcrop photograph from the Tournefort pegmatite (Ag08) and its relation with de Proto-S3 magmatic foliation of the Tournefort diorite. (C) Leucogranite dyke (Ag06) thin section showing no marked deformation. Kfs: K-feldspar – Qtz: quartz – Grt: garnet – Bt: biotite – Ms: muscovite – Pl: plagioclase – Myr: myrmekite – Sill: sillimanite.

Monazite is anhedral, rounded with few preserved faces, clear and light-yellow coloured. BSE images show that in some crystals, margins are irregular and that there are cavities in rims where monazite might have been partly dissolved out. Moreover, some crystals contain mineral inclusions, are fractured and have a weak intergrowth zoning (Fig. S1). Fifteen analyses were carried out on ten monazite crystals characterized by a wide range of Pb (most 1603-5982 ppm), Th (most 81772-190088 ppm) and U (most 2084-15431 ppm) contents and Th/U ratios (most 7.1-26.7) (S1; Table S2; Fig. 12A). Except for three analyses (2 discordant and 1 concordant), all these data yield a concordia age of 296.4 ± 2.4 Ma (MSWD$_{(C+E)}$ = 1.3; n = 13). The difference in date of ~45 Ma between the younger concordant date (Mn 13) (not plotted because partially outside the range) at 249 ± 9 Ma and the average date of the cluster may be the result of radiogenic Pb loss (Table S2; Fig. 12A).

Two zircon types were found in this sample. The first type consists of euhedral, clear, colourless zircon crystals with CL images showing concentric zoning and few inherited cores. The second euhedral, metamict, opaque and red crystal with CL images exhibiting mainly grains with cores containing many inclusions and cavities and which are sometimes enveloped by thin and homogenous rims (Fig. S2). Twenty-seven analyses on both cores and rims of eighteen zircon grains were analysed (Table S3). In the Tera-Wasserburg diagram, three inherited cores are concordant at 621 ± 22 Ma, 432 ± 16 Ma and 390 ± 15 Ma (Fig. 12B). They have enough similar Pb, Th and U concentrations, of about 23-32 ppm, 83-112 ppm and 207-538 ppm respectively. Their Th/U ratios are 0.16, 0.22 and 0.54 (Table S3). However, the majority of the data are clustered between ca. 350 Ma and 290 Ma (Fig. 12B). In the concordia ages histogram, the data are distributed into 2 main populations at ~295 Ma and at 320-330 Ma, with an additional data at 353 ±13 Ma (Fig. 12B; S2). The youngest population at 295 Ma is performed on eleven zircon rims from 6 colourless and 5 metamict zircon grains. The six colourless zircons yield concordant data and characterized by moderate Pb (59-110 ppm) and Th (85-352 ppm) contents and high to very high U (1350-2455 ppm) and with low Th/U ratios (0.06-0.25; most 0.06-0.12). While the rims of five metamict zircon give four discordant data which are characterized by higher Pb (123-225 ppm) and U (2901-5254 ppm) contents and lower Th concentrations (31-82 ppm) and with Th/U at 0.01-0.02 (Table S2). The linear regression on all these data yields a date of 293.8 ± 3.4 Ma by lower intercept (MSWD = 0.16; n = 11). Among these data, nine give a concordia age of 295.5 ± 3.8 Ma ($MSWD_{(C+E)}$ = 1.9) (Fig. 12B). The best date estimate is probably the concordia age. The second population at 320-330 Ma is only constituted by twelve concordant data performed on 10 colourless crystals (8 cores and 4 rims). These data have low to moderate in Pb (10-81 ppm) and in Th (36-168 ppm) and moderate to high U (199-1695 ppm most 199-465 ppm) contents and moderate Th/U ratios (0.1-0.42 most 0.14-0.42) (Table S3). The highest U contents (1131 and 1695 ppm) associated with the lowest Th/U ratios (0.01) are obtained on the rims of two zircon grains (Z15 and Z23). These twelve data yield a concordia age of 323.3 ± 3.8 Ma ($MSWD_{(C+E)}$ = 0.7; n = 12) (Fig. 12B).

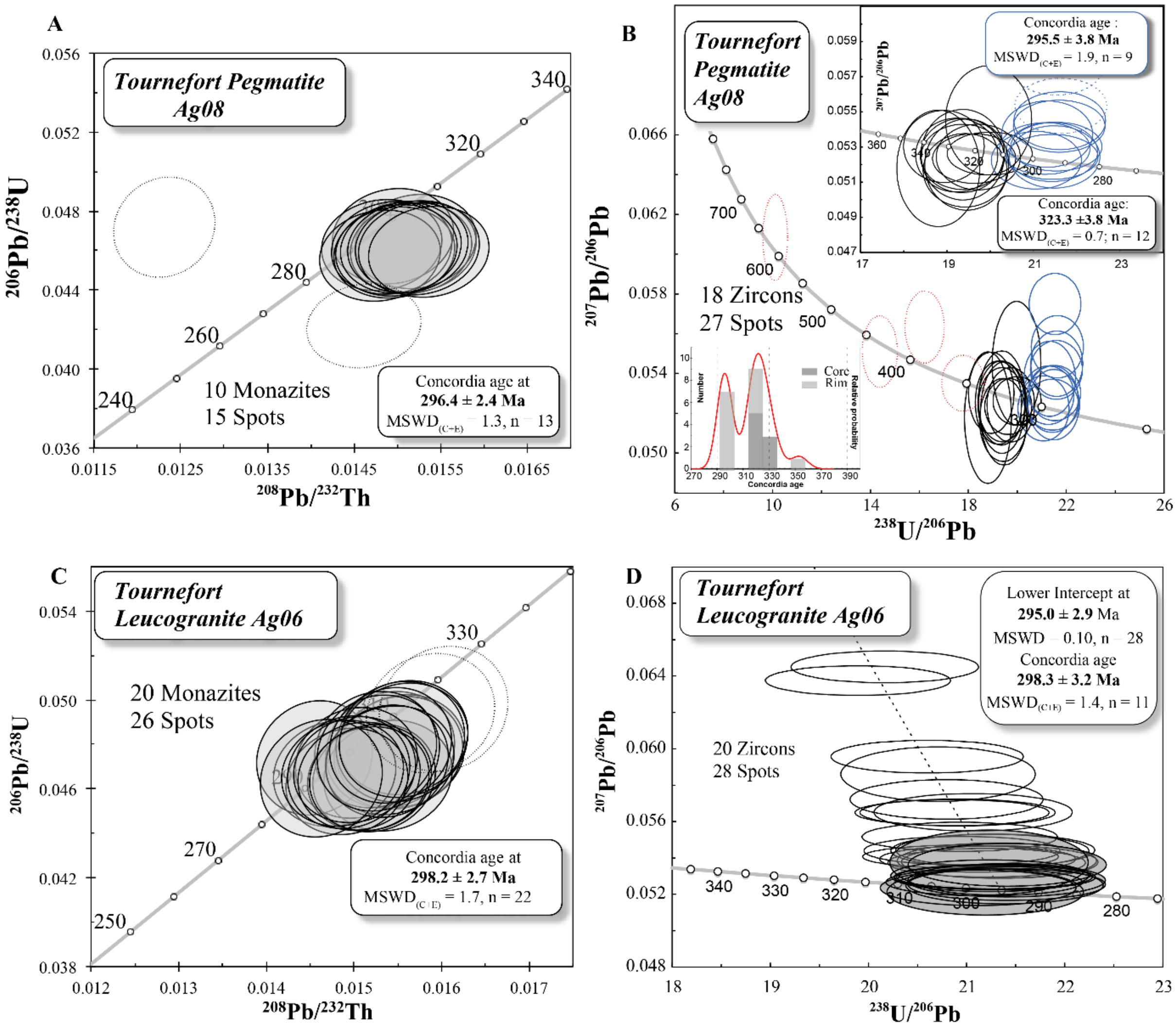

Figure 12 : Monazite U-Th-Pb concordia diagrams (A and C) and zircon Tera Wasserburg diagrams (B and D) of the Tournefort pegmatite (Ag08) and of the Tournefort leucogranite (Ag06). Error ellipses and uncertainties on ages are ± 2σ. Dotted ellipses are not considered for the age calculation. In A and C, Mn 13 and Mn10 are not plotted because they are outside the ranges, respectively.

3.2.3.2. The garnet-bearing leucogranite dyke (Ag06)

Sample Ag06 has been collected north of the Tournefort diorite and east of the Saint-Arnac granite (Fig. 11A). Interference between far field deformation and local deformation induced by pluton emplacement makes a complex strain pattern where D2, Proto-D3 and D4 planar fabrics are observed (Fig. 11A) (Vanardois et al., 2020). The sample Ag06 consists of a 2-meters thick peraluminous leucogranite dyke. This dyke cross-cuts the Tournefort diorite magmatic foliation, the S2 foliation observed in surrounding partially melted micaschists and M2 isograd (Fig. 11A). Field relationships suggest that the emplacement of the leucogranite

(Ag06) post-dates M2 peak metamorphism, the emplacement of the Tournefort diorite and the Proto-D3 deformation. This interpretation is consistent with the lack of solid-state deformation of the magmatic assemblages that consist of Kfs + Pl + Qtz + Grt + Ms (Fig. 11C; Vanardois et al., 2020).

Monazite crystals are subhedral to sometimes slightly rounded, clear, pale yellow. BSE imaging shows most grains to present a weak concentric or intergrowth zoning (Fig. S1). Twenty-six analyses on twenty monazite grains were performed (Table S2; Fig. 12C). They are characterized by high Pb (1578-4029 ppm) and U (506-9127 ppm) and very high Th (37498- 140262 ppm) concentrations giving a range of relatively high to very high Th/U ratios (6.2-138; most 26.2-138) (Table S2). Except for two analyses (Mn7, Mn19r, dotted ellipses)), all data are concordant to subconcordants around 290-310 Ma (Fig. 12C). Twenty-two data give a concordia age of 298.2 ± 2.7 Ma ($MSWD_{(C+E)}$ = 1.7; n = 22) (Fig. 12C).

Zircon crystals are relatively small (~100 µm), transparent, slightly pink to opaque pink-brown and mostly are euhedral prismatic crystal fragments. CL imaging shows strong evidence of concentric or oscillatory igneous growth zoning with no obvious cores (Fig. S2). Twenty-eight analyses were carried on twenty-one zircon grains (Fig. S2; Table S3). These data are characterized by a wide range of Pb (37-195 ppm), Th (94-1134 ppm) and U (807-4076 ppm) concentrations and Th/U ratios (0.08-0.67, most 0.11-0.67) (Table S3). The distribution of all ellipses near 300 Ma in the Tera-Wasserburg diagram suggests that discordant analyses are probably affected by a common Pb contamination (Fig. 12D). The linear regression on the data set gives a date of 295.0 ± 2.9 Ma by lower intercept (MSWD = 0.10; n = 28) and the eleven data yield a concordia age of 298.3 ± 3.2 Ma ($MSWD_{(C+E)}$ = 1.4; n = 11) (Fig. 12D). Both dates are equal within the uncertainties and the best date estimation is the concordia age.

3.2.4. Samples from the Late-D3 Tournefort Deformation Zone

3.2.4.1. The Vivier orthogneiss (Ag48)

The Vivier orthogneiss is a 200-meter thick vertical sill that contains paragneiss and marble elongated xenoliths and is only found structured by S3 foliations in the D3 corridor (Fig. 3). It is composed of Qtz + Kfs + Grt + Bt ± Pl assemblage. It is partially molten and deformed at high temperatures with formation of myrmekite replacing Kfs margins, and recrystallization of quartz and K-feldspars. The main fabric observed, which is vertical, is interpreted as a late-D3 foliation. The partial melting affecting the Vivier orthogneiss sample (Ag48) is ante-D3.

Monazite crystals are subhedral to anhedral, light yellow and transparent. BSE images show that most crystals present a patchy zoning with sometimes a rim (Fig. S1). The analysed crystals have Pb (2076-5805 ppm), Th (63234-195033 ppm) and U (3391-8618 ppm) contents and Th/U ratios (9.18-31.17), which vary from crystal to crystal and within the same monazite (Table S2). Twenty-eight spots on eighteen monazite crystals were performed (Table S2; Fig. 13A). In the concordia diagram, all ellipses yield a concordia age of 299.7 ± 1.7 Ma ($MSWD_{(C+E)}$ = 1.4; n = 28) without apparent difference between the rims and cores of the various crystals.

Zircon crystals are euhedral, transparent and colourless to slightly pinkish. CL images also show complex internal textures such as the presence of inherited cores and concentric oscillatory zoning and patchy zoning textures (Fig. S2). Thirty-six analyses were carried out on twenty zircon grains (Table S3; Fig. 13B). Among these data, thirty-three are concordant between ca. 630 Ma and 290 Ma. In the ages histogram, the data are distributed into 4 variable-sized populations: two minor ones at 430-490 Ma (group 1) and 570-630 Ma (group 2) and two major groups at 510-570 Ma (group 3) and 300-350 Ma (group 4) and (Fig. 13B).

Group 1 dates are determined from 4 rims and 1 core that have moderate Pb (23-103 ppm) and Th (21-58 ppm) contents and low Th/U ratios (0.03-0.18). These five data are ranging from 446 ± 12 Ma to 479 ± 12 Ma and yield a weighted average of 462 ± 17 Ma (MSWD = 5.2) (S2; Fig. 13B; Table S3).

Group 2 dates are acquired on four zircon cores, which are characterized by moderate Pb contents (11-74 ppm) and variable Th (26-300 ppm) and U (113-713 ppm) concentrations, with Th/U ratios ranging from 0.08-0.42. They yield a concordia age of 597.2 ± 7.7 Ma ($MSWD_{(C+E)}$ = 0.68) (S2; Fig. 13B; Table S3).

Group 3 dates are obtained from 10 cores and 3 rims. Pb and Th contents ranging from 11-158 ppm and 20-148 ppm, respectively, characterize these data. The U contents of the rims (758-2088 ppm) are higher than those of the cores (131-645 ppm). Th/U ratios of the cores (0.06-0.6; most 0.06-0.25) are thus higher than those of the rims (0.05-0.03). These data give a weighted average of 541 ± 11 Ma (MSWD = 6.6; n = 13). Among these 13 dates, nine yield a concordia age of 551.8 ± 4.8 Ma ($MSWD_{(C+E)}$ = 1.1; n = 9) (Fig. 13B, S2; Table S3).

Group 4 dates were determined from rims of ten zircon crystals characterized by moderate Th and Pb contents ranging from 5 to 18 ppm and 20 to 31 ppm, respectively and by very low Th/U ratios from 0.01 to 0.03 (Table S2). Seven among these zircon rims yield a concordia age of 303.9 ± 5.5 Ma ($MSWD_{(C+E)} = 2.5$). The rims of three zircon grains Zr31, Zr18 and Zr27 have older dates at 344 ± 9 Ma, 323 ± 9 Ma and 391 ± 11 Ma, respectively. These dates are probably meaningless because they correspond to a mixture between an old core (~ 550 Ma) and a younger rim (probably ~ 300 Ma) (S2; Fig. 13B, Table S3).

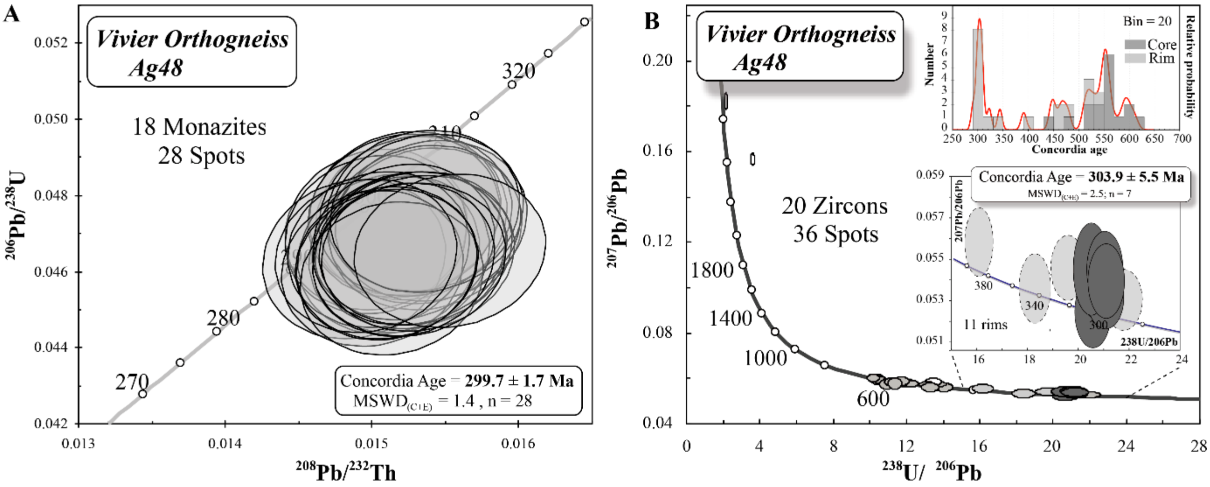

Figure 13 : Monazite U-Th-Pb concordia diagram (A) and zircon U-Pb Tera Wasserburg a diagram (B) obtained by LA-ICPMS on the Vivier orthogneiss (Ag48). Error ellipses and uncertainties in ages are ± 2σ. White ellipses are discordant data and are not considered in the histogram diagram and for the age calculation and dotted ellipses are not taken into account only for the age calculation.

3.2.4.2. Latour de France leucogranite (Ag51)

The Latour-de-France leucogranite (Ag51) located to the southwest of Latour de France village in the infrastructure (Fig. 3) is a 50-meter thick pluton and is composed of Qtz + Kfs + Pl + Bt + Grt + Ms. It does not show visible solid-state deformation but microstructures such as myrmekites replacing Kfs margins, plastic deformation of quartz indicated by chessboard extinction and microfractures in Kfs infilled by quartz indicate that the leucogranite was deformed under sub-magmatic conditions (Fig. 14A). The pluton cross-cuts S2 foliations and C2 shear zones and was emplaced in a kilometre-scale D3 fold hinge (Fig. 3; Vanardois et al., 2020). These observations suggest that the Latour de France leucogranite sample (Ag51) is syn-late-D3.

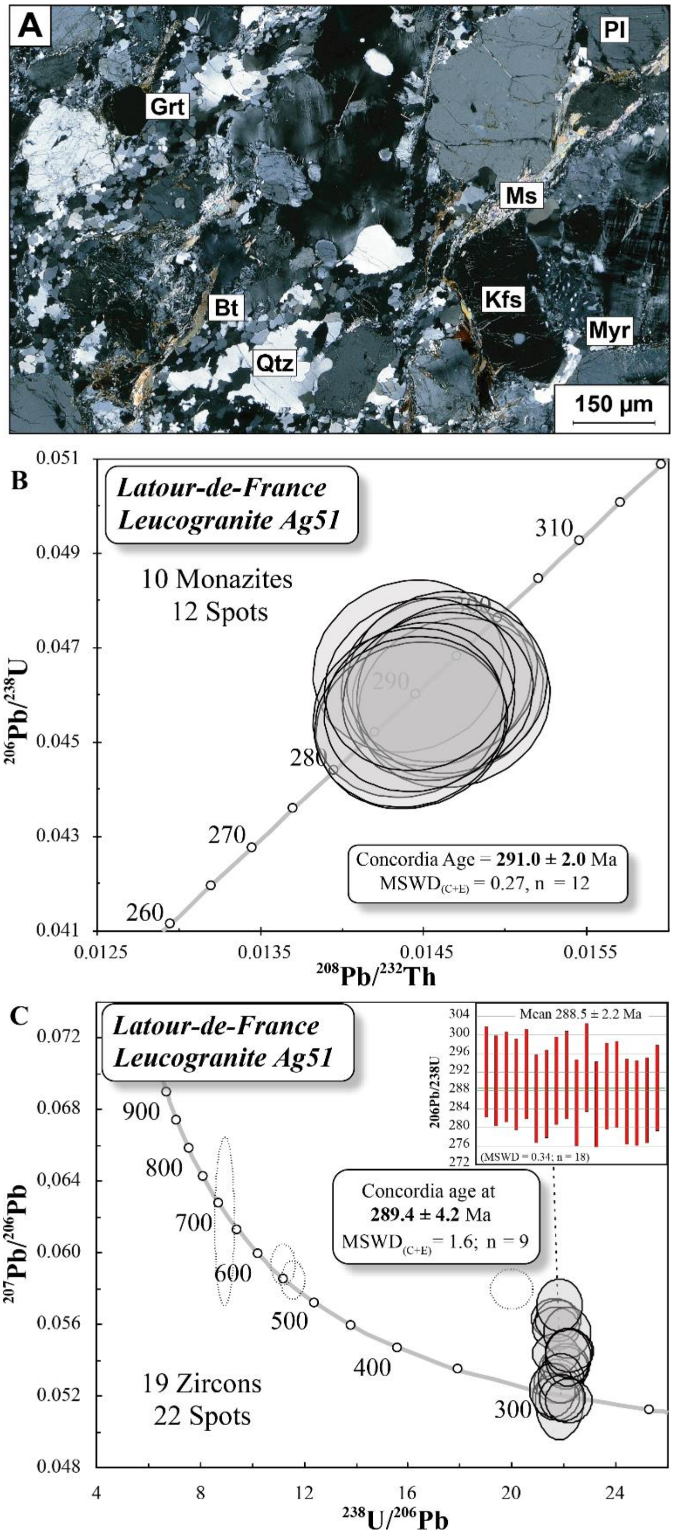

Figure 14 : (A) Ag51 Latour-de-France Leucogranite thin section presenting myrmekites, plastic quartz deformation and recrystallization. Monazite U-Th-Pb concordia diagram (B) and zircon Tera Wasserburg diagram (C) of the Latour-de-France leucogranite (Ag51). Error ellipses and uncertainties on ages are ± 2σ. Dotted ellipses are not considered for the age calculation.

Monazite is sub-euhedral prismatic with a shape ratio up to 2:1, clear and light-yellow coloured. BSE images show that the zoning in the centre of most crystals is patchy and that the rim is characterized by a darker slight concentric zoning (Fig. S1). The analysed spots have high Pb (2611-4672 ppm), high to very high U (5958 – 14794 ppm) and very high Th (75731 – 147318 ppm) concentrations with a range of relatively moderate Th/U (6.3 - 16.6) (Table S2). Twelve analyses were performed on 10 crystals (Fig. 14B; Table S2). These twelve data yield a concordia age of 291.0 ± 2.0 Ma ($MSWD_{(C+E)}$ = 0.27; n = 12) (Fig. 14B).

Most of the zircon crystals analysed are euhedral, either prismatic with a shape ratio up to 3:1 or stubbier with a shape ratio of 1:1. They are transparent, slightly pink to opaque pink-brown. CL imaging shows strong evidence of concentric or oscillatory igneous growth zoning and the presence of some inherited cores (Fig. S2). Twenty-two analyses were carried out on nineteen zircon grains (Fig. 14C; Table S3). Among these analyses, eighteen have a concordant to discordant position around 290 Ma suggesting a common Pb contamination. The linear regression calculated with these 18 data yields a date of 288.4 ± 3.3 Ma by lower intercept (MSWD = 0.36; n = 18) and amongst nine data give a similar concordia age of 289.4 ± 4.2 Ma ($MSWD_{(C+E)}$ = 1.6; n = 9) (Fig. 14C). These data are obtained on rims and cores of crystal and present Th/U ratios ranging between 0.004 and 0.26 (most 0.004-0.06) (Table S3). Moreover, the analyses of two zircon cores (Zr12c, Zr24c) yield a concordia age of 549 ± 11 Ma ($MSWD_{(C+E)}$ = 1.7). Furthermore, a third analytical point (Zr36c) is concordant at 684 ± 23 Ma (Table S3; Fig. 14C). The Th/U ratios of these three data are between 0.43 and 0.17.

4. Interpretation and discussion

4. 1. Pre-Variscan history: Cadomian and Ordovician magmatism

Two samples collected near Le Vivier (Ag48, Ag57), in the infrastructure, show an early and complex history with inherited Precambrian and Ordovician zircon population ages (Table 1; Fig. 5B and 13B). The concordia ages histogram of the Vivier deformed leucogranite (Ag57) highlights the presence of two major date populations at 630-710 Ma and at 550-610 Ma which could be correlated with Pan-African (750-600 Ma) and Cadomian (590-540 Ma) orogeneses (Linneman et al., 2014) (Fig. 5B). Similarly, the oldest dates from the Vivier orthogneiss (Ag48) are divided into three variable-sized populations: one main at 510-570 Ma and two minor ones at 430-490 Ma and 570-630 Ma (Fig. 12B). The two middle Ediacaran - middle Cambrian populations formed mainly by zircon cores yield concordia ages of 551.8 ± 4.8 Ma and 597.2 ± 7.7 Ma. The youngest age population of the sample Ag48, composed essentially by zircon rims, gives a poor-quality weighted average at 462 ± 17 Ma with a MSWD of 5.2 (Fig. 13B). This result might suggest the presence of the Ordovician inherited zircon grains in this sample, possibly related to the emplacement of the protolith of the Rivérole orthogneiss at 461 ± 3 Ma in the infrastructure of the AM (Paquette et al., 2021). The date obtained on the Vivier orthogneiss (Ag48) of 551.8 ± 4.8 Ma is interpreted as the emplacement age of the magmatic protolith, and indeed is consistent with the ages at ca. 540-530 Ma obtained on five igneous rocks from the Agly massif infrastructure by Tournaire Guille et al. (2019). These Pan-African and Cadomian inherited zircon ages are common in the South-Western Variscan belt (e.g. Schnapperelle et al., 2020; Melleton et al. 2010; Roger et al., 2004) with a possible source region linked to the north-eastern Gondwana margin (von Raumer et al., 2015; Linnemann et al., 2014; Couzinié et al., 2014; Chelle-Michou et al., 2017).

4.2. Middle Carboniferous crustal partial melting and magmatism (~340-320 Ma) event

Three zircon rims from the Vivier leucogranite (Ag57) yielded a concordia age of 339.5 ± 13 Ma. In the suprastructure, two inherited cores of slightly metamict zircon from the Planèzes mylonitic pegmatite (Ag47) yielded a concordia age of 326.6 ± 6.2 Ma. The Tournefort undeformed pegmatite (Ag08) has a zircon population consisting of colourless crystals (cores and rims) that yielded a concordia age of 323.3 ± 3.8 Ma. These ages are similar within error and define a 340-320 Ma interpreted as the thermal peak activity. Similarly, monazite and zircon ages of 340-320 Ma have been reported in migmatites from the southern French Central Massif (Faure et al., 2014b), from granites of the PAZ (Mezger and Gerdes, 2016; Schnapperelle et al., 2020) and migmatites of the NPZ (Lemirre, 2016). The origin of this Visean/Serpukhovian magmatic and metamorphic event in the foreland is still elusive (Schnapperelle et al., 2020). Thermobarometric estimates on the Montagne Noire (MN) gneiss dome suggest that, between 330 and 320 Ma, the continental crust was slightly overthickened with a partially molten lower-middle crust, between 30 and 40 km depth (Trap et al., 2017). The strain fabrics that could be attributed to this 340-320 Ma event were not directly dated on the field and could be attributed to the D1 or proto-D2 deformations.

4.3. Peak of magmatism at ca. 305 Ma

Our results, as data from the literature, show that most of the AM magmatic bodies range in crystallization age between 308 and 304 Ma (Olivier et al., 2004, 2008; Tournaire Guille et al., 2019) (Fig. 15a). The two Brosse Ravine pegmatites (Ag38, Ag03) show zircon grains with a high U and Th contents and low Th/U ratios (Table S3). Although the low Th/U ratios (<<0.01) is commonly interpreted as the fingerprint of metamorphic crystallization, magmatic zircons with low Th/U ratios (<0.1) have also been reported in high-SiO_2 and/or peraluminous granitoids (Lopez-Sanchez et al., 2016). Thus, we interpret the zircon concordia age at 304.4 ± 2.6 Ma from the weakly deformed Ag03 pegmatite (Fig. 9B) as the emplacement age. A similar zircon concordia age at 305.8 ± 6.8 Ma (Fig. 5B) is given by the undeformed Vivier leucogranite (Ag57), emplaced as a sill into the flat-lying S2 foliation. The sills of Ansignan charnockite and Cassagnes granite have been dated 307 ± 3 Ma and 308 ± 3 Ma (Tournaire Guille et al., 2019). They are intrusive into the migmatitic S2 foliation with concordant to slightly discordant cross-cutting relationship (Vanardois et al., 2020). This argues for the development of suprasolidus S2 foliation before 308 Ma. Several ID-TIMS analyses and one LA-ICPMS analysis on syn-S2 charnockitic sills yield emplacement ages at ca. 315 Ma (Fig. 15a; Postaire, 1982; Respaut and Lancelot, 1983; Olivier et al., 2004; Tournaire Guille et al., 2019) that might suggest an older development of D2 deformation. The undeformed Vivier leucogranite (Ag57) also intrudes into the S2 and gives a zircon concordia age at 305.8 ± 6.8 Ma and a monazite concordia age at 299.7 ± 1.7 Ma (Fig. 5A). Both zircon and monazite dates are similar within uncertainties but it is more likely that the emplacement of the Vivier leucogranite is best constrained by the zircon concordia age at 305.8 ± 6.8 Ma. The 299.7 ± 1.7 Ma monazite age might represent a partial reset during D2 fluid-rock interactions. These results are consistent with Siron et al. (2020) that dated M2 partial melting and S2 planar fabric at ca. 305 Ma within kinzigites from different structural levels of the infrastructure.

The U-Th-Pb ages of the syn-D3 Tournefort diorite and Saint-Arnac granite in the Tournefort Deformation zone (TDZ) between 308 and 304 Ma (Olivier et al., 2004, 2008) also constrain the timing of Proto-D3 dextral strike-slip shearing (Fig. 15a). We propose that the D3 deformation started with the development of a vertical S3 within the dextral Proto-D3 shear zone at ca. 308 Ma. Vertical planar fabrics are pathways for the ascent of melts from the lower crust towards the middle and upper crusts (e.g. de Saint-Blanquat et al., 1998; Handy et al., 2001). The southern part of the St-Arnac pluton and Tournefort diorite bear magmatic foliations parallel with the D3 foliation and vertical migmatitic lineation suggest a vertical ascent of the magmas (Olivier et al., 2008; Vanardois et al., 2020). The northern part of the St-Arnac pluton is structured by gently dipping magmatic foliations indicating a horizontal expansion with a lineation trending toward N50 that fits with the D3 dextral bulk kinematics during syn-tetonic pluton emplacement (Olivier et al., 2008).

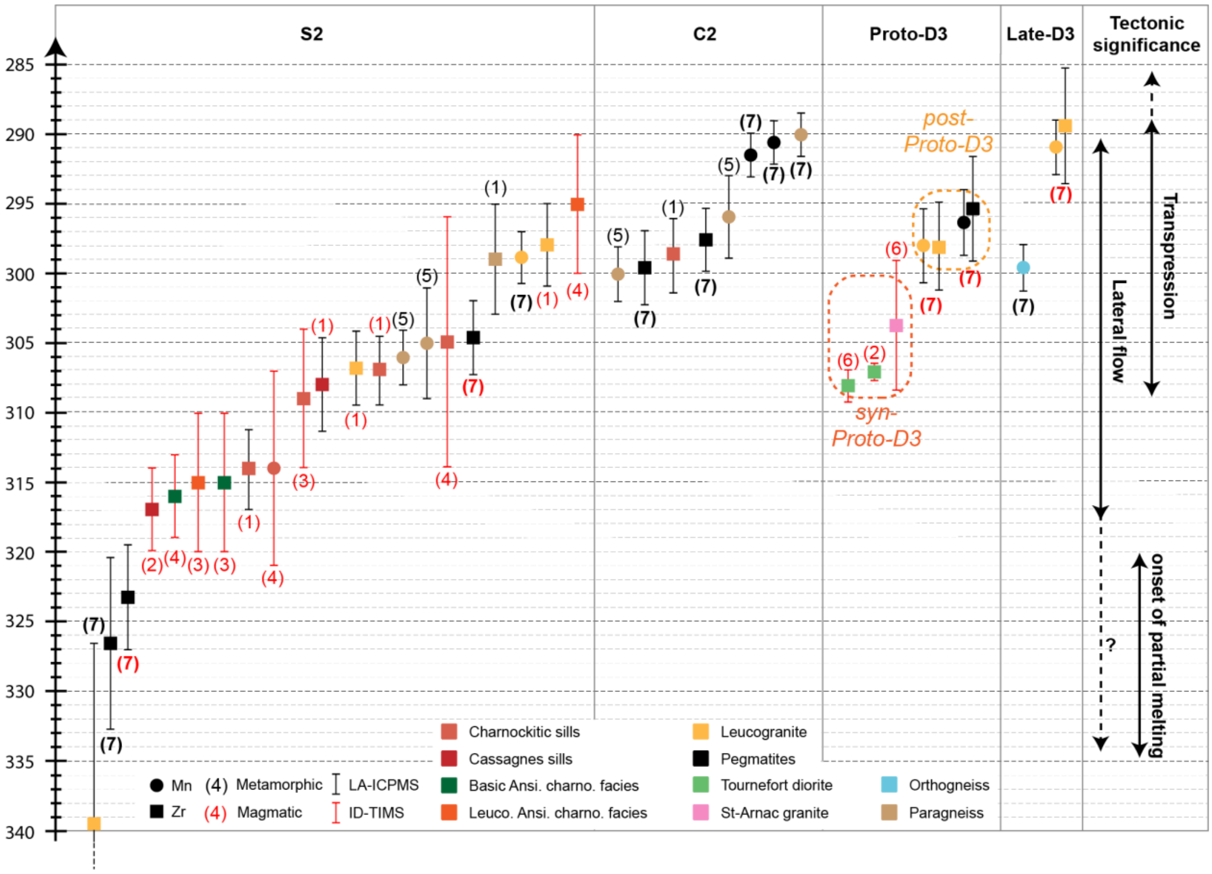

Figure 15 : Compilation of ages from the Agly massif constraining deformations and/or metamorphism and tectonic evolution. References: (1) Tournaire Guille et al., (2019); (2) Olivier et al. (2004); (3) Postaire, 1982; (4) Respaut and Lancelot; (5) Siron et al. (2020); (6) Olivier et al., 2008; (7) This study. Geochronological data from Odlum and Stockli (2019) were not processed to decipher Variscan tectonics and are not included in this compilation. Basic Ansi. charno. facies: Basic Ansignan charnockite facies – Leuco. Ansi. charno. facies: Leucocrate Ansignan charnockite facies.

4.4. Late Carboniferous-early Permian 300-295 Ma metamorphism and deformation.

Our U-Pb datings report a group of ages in the range 300-295 Ma. The age of 297.6 ± 2.3 Ma obtained on zircon of the mylonitic pegmatite (Ag38) is interpreted as the synkinematic emplacement of the pegmatite during D2 strain localization along C2 shear zones (Fig. 9D). The zircon rims and cores from the syn-C2 Planèzes mylonitic pegmatite (Ag47) located in the micaschists of the suprastructure yield a concordia age at 299.7 ± 2.7 Ma (Fig. 3 and 9). This date is consistent with the emplacement age of the Brosse Ravine pegmatite (Ag38) and can be interpreted as the syn-C2 emplacement age of the Planèzes pegmatite. Tournaire Guille et al. (2019) dated partial melting of a paragneiss at 299 ± 4 Ma and the crystallization of leucogranites in the infrastructure at 307 ± 3 and 298 ± 3 Ma (Fig. 15a). The range of ages around 300 Ma are very consistent with the ages of ~296 to 300 Ma ages recently obtained on monazite overgrowths with highly variable Th/U ratio from mylonitized kinzigites (Siron et al., 2020) and might constrain the onset of sub-solidus solid-state deformation on the cooling crust.

The undeformed garnet-bearing leucogranite dyke (Ag06) that crosscuts both the magmatic Proto-D3 foliation and the S2 foliation (Fig. 11A) yields zircon and monazite concordia ages at 298.3 ± 3.2 and 298.2 ± 2.7 Ma (Fig. 12C and D). Zircon rims and monazite from the undeformed Tournefort pegmatitic dyke (Ag08) yield similar concordia ages at 295.5 ± 3.8 Ma and 296.4 ± 2.4 Ma (Fig. 12A-B). These ages record the intrusion of the Ag06 and Ag08 dykes that cross-cuts the Proto-D3 foliation at ca 300-295 Ma. Finally, the Vivier orthogneiss sample (Ag48) is deformed by D3 and yields concordia age on zircon and monazite at 303.9 ± 5.5 Ma and 299.7 ± 1.7 Ma, respectively (Table 1, Fig. 13). Both dates are similar within error bars but we interpret the monazite concordia age at ca. 300 Ma as the best estimate of the D3 deformation age paroxysm.

4.5. The 290 Ma event

Monazite grains from pegmatites (Ag 03 and Ag38) give concordia ages at 290.6 ± 1.6 Ma and 291.5 ± 1.6 Ma, respectively (Fig. 9A and C). Both AG03 and AG38 pegmatites are located along a D2 high-strain zone (i.e. Caladroy Shear Zone). There is no evidence of garnet- or biotite-breakdown reactions in these samples that could have induced monazite crystallization. Thus, we interpret these ages as the final stage of C2 strain localization in the Caladroy shear zone that corresponds to the timing of deformation-recrystallization leading to a reset of the U-Th-Pb isotopic system via fluid-assisted syn-kinematic dissolution/precipitation of monazite processes. The migmatitic paragneiss (Ag3B), from the upper structural levels of the infrastructure, shows a well-developed syn-partial melting S2 foliation that is also affected by localized small C2 shear zones. Irrespective of their textural position (e.g. included in garnet or in C2 high strain zones), all monazite dates give a concordia age at 290.2 ± 1.6 Ma (Fig. 7D). The lack of preservation of older ages in monazite included in peritectic phases like garnet, the numerous fractures in garnet, and the absence of garnet-consumption (Fig. 6) suggest that monazite were reset or crystallized during a penetrative fluid-rock interaction during C2 shearing. In comparison with aforementioned ages, the C2 subsolidus shearing started at ca. 300 Ma and lasted until at least 290 Ma.

The 290 Ma event is also recorded in Late-D3 structures. The Latour-de-France leucogranite (Ag51) emplaced in a F3 fold hinge along the southern edge of the D3 corridor (Fig. 3C), has been dated by similar concordia ages obtained on zircon and monazite at 289.4 ± 4.2 Ma and 291 ± 2 Ma, respectively (Fig. 14). This age at ca. 290-291 Ma is interpreted as the emplacement age of the Latour-de-France leucogranite in the upper part of the infrastructure contemporaneously with the D3 folding (Fig. 3C). The crystallization of these magmatic bodies may have provided hydromagmatic fluids that may be partly responsible for the reset of monazite at ca. 290 Ma. Similarly, Van Lichterveld et al. (2017) documented a 290 Ma old late post-solidus hydrothermal remobilization and coeval magmatism in a wrench tectonic regime (Carreras and Druguet, 2014).

4.6. Tectonic implications

In the PAZ, flat-lying foliations with top-to-the-south kinematics have been described and interpreted as evidence of an early nappe stacking event (Denèle et al., 2009, 2014) before being mostly transposed by the pervasive dextral transpression (Gleizes et al., 1998a; Carreras and Druguet, 2014) associated with a longitudinal extrusional crustal flow (Cochelin et al., 2017, 2021). A similar evolution is described in the MN where a nappe stacking event is described (Charles et al., 2009; Faure et al., 2014b) and followed by a pervasive dextral wrenching in a transtension regime inducing a longitudinal flow of the partially molten crust between 315 and 300 Ma (Rabin et al., 2015; Trap et al., 2017; Roger et al., 2015). Some authors recently proposed that, previously to the longitudinal flow, a gravity-driven flow of the partially molten crust from the orogenic plateau toward its southern foreland occurred at ca. 320 Ma (Whitney et al., 2015; Vanderhaeghe et al., 2020; Roger et al., 2020). However, the pervasive deformation induced by the dextral wrenching in the PAZ and in the MN avoid to investigate properly this hypothesis.

On the other hand, the Agly massif is only affected by local transcurrent tectonics which allows us to discuss the origin of the flat-lying foliation. Initially, this sub-horizontal foliation (S2) in the Agly massif has also been interpreted as a nappe stacking event toward the South (Bouhallier et al., 1991; Olivier et al., 2004). Nevertheless, Vanardois et al. (2020) have recently emphasized the existence of a high-grade early planar fabric (S1) that may represent relics of crustal thickening and that the flat-lying S2 foliation is not related to a nappe stacking event. Olivier et al. (2004) emphasized top-to-the-South kinematics of the supra-solidus S2 foliations whereas the CSZ located at the anatectic front displays top-to-the-North kinematics (Bouhallier et al., 1991; Vanardois et al., 2020). These structural features fit well with the geometry of horizontal channel flow models describing a normal shear zone located at the top of the channel flow (e.g. Godin et al., 2006; Raimondo et al., 2009) (Fig. 1B). Therefore, we propose that the supra-solidus S2 foliation developed during a gravity-driven flow toward the South (Fig. 16A). Similar gravity-driven flow has also been proposed in other Variscan massifs (Schulmann et al., 2008, 2014; Bento dos Santos et al., 2021). Our U-Th-Pb results and compilation on the Agly massif highlight that the S2 foliation developed at least at ca. 315 Ma and very likely at ca. 325 Ma during the onset of partial melting (Fig. 15a). HT metamorphism and migmatization between ca. 340–320 Ma has been already documented in the NPZ and PAZ (Lemirre, 2016; Mezger and Gerdes, 2016; Schnapperelle et al., 2020), which might indicate that the whole NPZ and the PAZ have also been affected by this gravity-driven flow toward the South. Considering the Visean – Serpukhovian magmatism in the PAZ (Mezger and Gerdes, 2016; Schnapperelle et al., 2020; Cugerone et al., 2021), it seems more likely that the whole lower crust of the PAZ, NPZ and MN melted at ca. 325 Ma and flow, rather than the hypothesis of a channel flow from the French Central Massif to the Pyrenees (Fig. 16A).

The syn-tectonic emplacements of the Tournefort diorite and St-Arnac granite in the TDZ (Vanardois et al., 2020) indicate that the dextral wrenching started at ca. 308 Ma in the A gly massif and favoured the emplacement of plutons in the upper crust. Similar emplacements of plutons driven by vertical dextral shear zones at 310-300 Ma are widely described in the PAZ (e.g. Gleizes et al., 1998b, 2001, 2006; Aujérac et al., 2004; Román-Berdiel et al., 2006; Antolín-Tomás et al., 2009) or in the MN (Trap et al., 2017; Roger et al., 2020), synchronously with the longitudinal flow of the lower crust (Cochelin et al., 2017, 2021; Trap et al., 2017; Roger et al., 2020). The limited dextral deformation in the Agly massif and in the rest of the NPZ compared to the PAZ and the MN is interpreted as a gradient of deformation across a lithospheric-scale high-strain wrench zone represented by the PAZ (Fig. 16B). IN the PAZ, during ongoing transpression, the high-strain dextral shearing reworked the flat-lying foliations related to gravity-driven flow into a longitudinal flow, while in the Agly massif, the dextral wrenching remains limited with the partially molten crust recording southward flow until ca. 300 Ma (Fig. 16B).

After the crystallisation of most of the anatectic melts in the infrastructure of the Agly massif, the dextral wrenching lasted until 290 Ma in the TDZ (Fig. 15a). Our results also highlight that C2 subsolidus flat-lying shear zones are still active at ca. 290 Ma (Fig. 15a) with top-to-the-North kinematics (Vanardois et al., 2020). We propose that these shear zones accommodated a local extensional regime in the D3 low-strain domain induced by the dextral movements, mainly accommodated by the NPF (e.g. Denèle et al., 2014), while the transpression was still active in the PAZ and in the MN (Cochelin et al., 2017; Roger et al., 2020) (Fig. 16C).

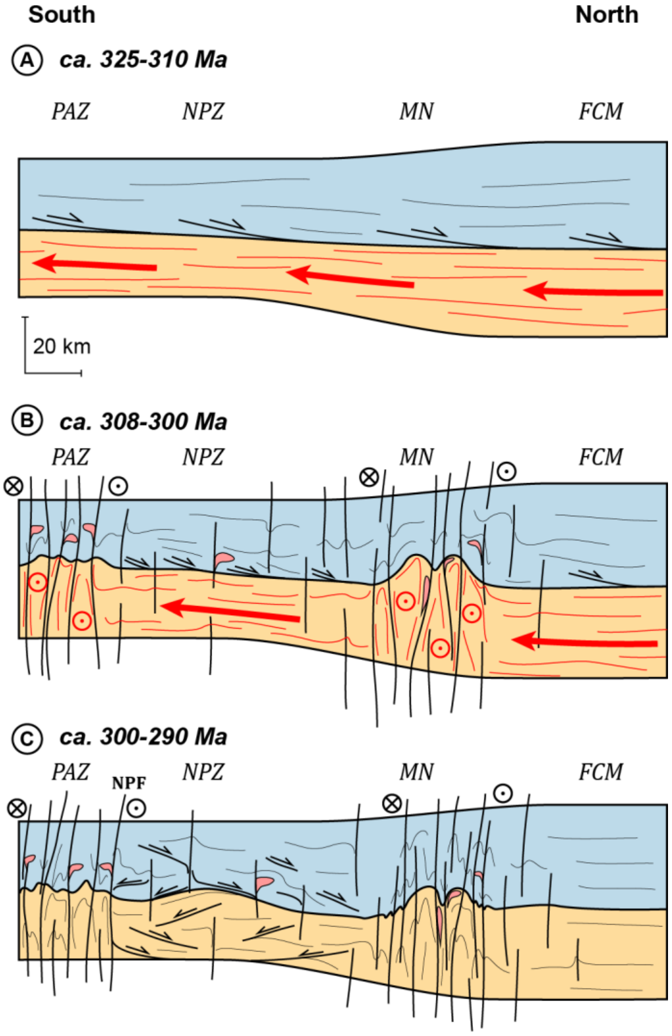

Figure 16 : Tectonic evolution of the southern edge of the Variscan orogenic plateau. See text for details.

5. Conclusion

The new geochronological results and the compilation of available age data from the Agly massif indicate that the Variscan lower-middle crust was partially molten from ca. 325 to 300

Ma. These new results emphasize the first evidence of a middle Carboniferous event at ca. 325 Ma in the Agly massif and highlight a partitioning of the deformation between a flat-lying foliations S2 and a dextral shear zone D3 from ca. 308 Ma to 290 Ma. Compilation of geochronological data on the Agly massif and comparison with tectonic evolutions of the Montagne Noire and of the Pyrenean Axial Zone allow us to propose a new tectonic evolution for the southern edge of the French Central Massif: (i) the maturation of the orogenic crust induced the partial melting of the lower crust that evolved into a gravity-driven flow from the French Central Massif to the PAZ toward the South at ca. 325 Ma. (ii) The dextral wrenching affecting the whole Variscan belt became pervasive in the Montagne Noire and in the PAZ and reoriented the gravity-driven flow into a longitudinal flow, while the NPZ is only locally affected by this dextral wrenching. (iii) The crystallisation of most of the anatectic melts stopped the flow of the lower crust at ca. 300 Ma. The dextral wrenching stayed active until 290 Ma in the Agly massif, the PAZ and the MN. Synchronously with the local wrenching in the TDZ of the Agly massif, subsolidus C2 shear zones accommodated a local extensional regime in the NPZ until ca. 290 Ma.

Acknowledgments

This research was supported by the BRGM through the Référentiel Géologique de la France program (RGF program). We thank Cyprien Astoury for mineral separation. Didier Convert provided generous support with thin section preparation.

Supplementary material

Tables S1, S2 and S3 are presented in Annexe 1.

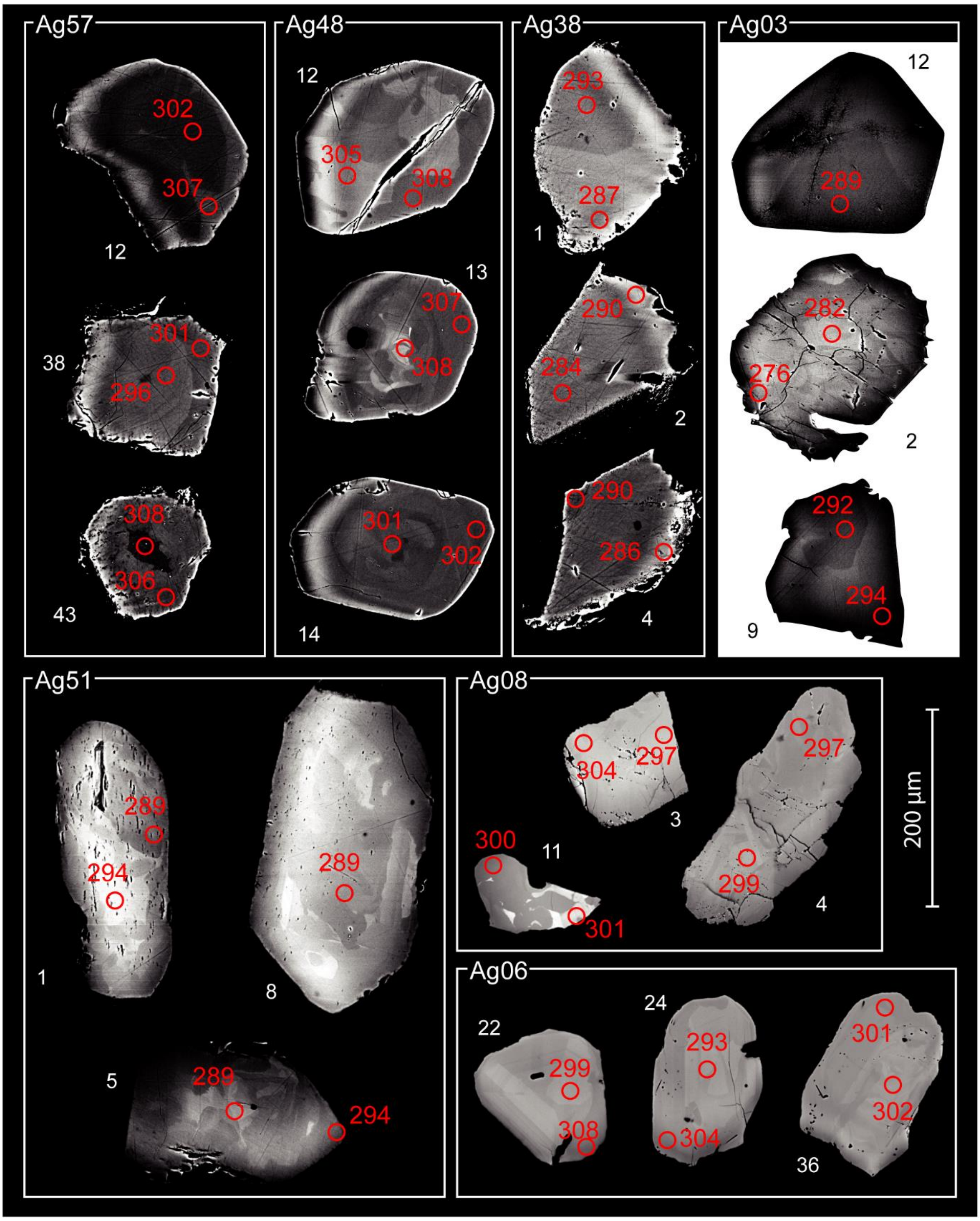

Figure S1 : Monazite morphologies in BSE images. Red circles indicate laser spot locations and 208Pb/232Th age without error associated.

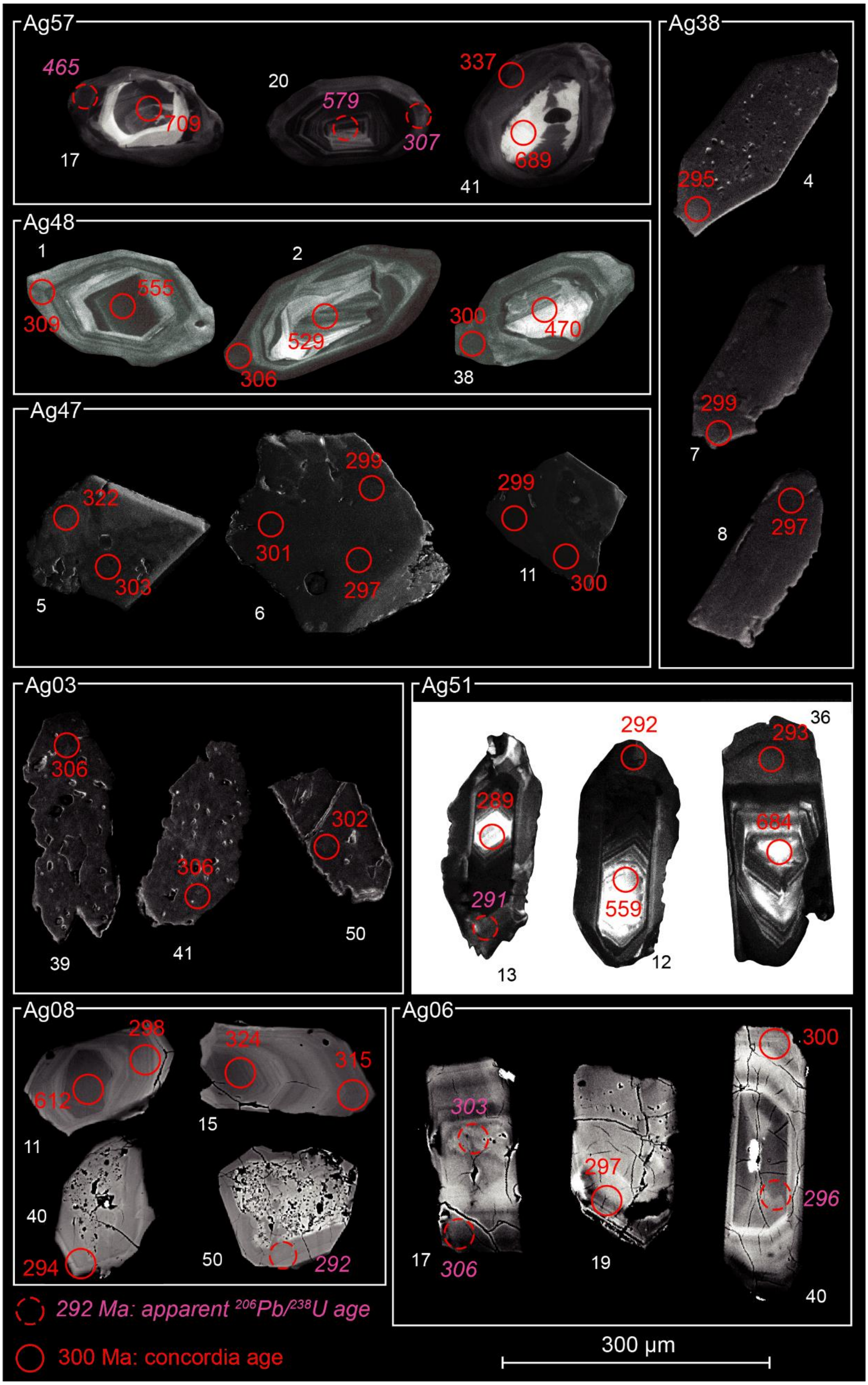
Ag57
465
709
17
20
579
307
337
689
41
Ag38
295
4
299
7
8
297
Ag48
1
309
555
2
529
306
300
470
38
Ag47
322
303
5
299
301
297
6
299
300
11
Ag03
306
39
306
41
302
50
Ag51
289
291
13
292
559
12
293
36
684
Ag08
298
612
11
324
315
15
40
294
50
292
Ag06
303
306
17
297
19
300
296
40
292 Ma: apparent ^{206}Pb/^{238}U age
300 Ma: concordia age
300 µm

Figure S2 : Zircon morphologies in CL images for Ag57, Ag48, Ag47, Ag51, Ag38 and Ag03, and in BSE images for Ag06 and Ag08. Red circles indicate laser spot locations and age without errors associated.

Chapitre 4. Exhumation de la croûte profonde continentale en régime transpressif : les éclogites du Lac Cornu.

Chapitre 4. Exhumation de la croûte profonde continentale en régime transpressif : les éclogites du Lac Cornu.

Ce chapitre 4 s'intéresse aux éclogites du Lac Cornu du massif des Aiguilles-Rouges. Le but de cette étude est de contraindre le trajet Pression – Température – temps – Défomation enregistré par ces éclogites pour pouvoir discuter (i) de l'origine des reliques de conditions de haute pression dans les Aiguilles-Rouges mais aussi dans les autres Massifs Cristallins Externes et les massifs Varisques proches ; (ii) de l'exhumation de ces roches initiallement enfouies à de grandes profondeurs. Pour ce faire, nous présentons une étude dans laquelle nous complons des analyses microstructurales (EBSD), des observations pétrologiques, des modélisations thermodynamiques et thermobarométriques empiriques, de la géochronologie U-Pb sur zircons, rutiles et titanites, ainsi que des analyses d'éléments traces dans les zircons datés. Ce chapitre est présenté sous la forme d'un article actuellement en révision à *Journal of Metamorphic Geology*.

Exhumation of deep continental crust in a transpressive regime: the example of Variscan eclogites from the Aiguilles-Rouges Massif (Western Alps).

Jonas Vanardois[1]*, Françoise Roger[2], Pierre Trap[1], Philippe Goncalves[1], Pierre Lanari[3], Jean-Louis Paquette[4], Didier Marquer[1], Florence Cagnard[5], Benjamin Le Bayon[5], Jérémie Melleton[5] and Fabrice Barou[2].

jonas.vanardois@univ-fcomte.fr; pierre.trap@univ-fcomte.fr; francoise.roger@umontpellier.fr; didier.marquer@univ-fcomte.fr; j.l.paquette@opgc.univ-bpclermont.fr; f.cagnard@brgm.fr; b.lebayon@brgm.fr; j.melleton@brgm.fr

[1]UMR 6249 Chrono-environnement, Université de Bourgogne-Franche-Comté, 25030 Besançon, France.

[2]Géosciences Montpellier, Campus Triolet, Université Montpellier, CNRS, 34095 Montpellier Cedex 5, France.

[3]Institute of Geological Sciences, University of Bern, Baltzerstrasse 3, Bern, CH-3012 Switzerland

[4]Laboratoire Magmas et Volcans (CNRS-UMR 6524), Campus Universitaire des Cézeaux, 63178 Aubière Cedex, France.

[5]BRGM-French Geological Survey, 3 Avenue Claude Guillemin, 45100, Orléans, France.

*Corresponding author: jonas.vanardois@univ-fcomte.fr +33(0)381666242 Present address: 16 route de Gray, 25030 Besançon.

Abstract

Mafic eclogites are found in many orogens as lenses embedded in quartzo-feldspathic migmatites. These high-pressure relics are interpreted either as remnants of ancient sutures and thus formed during oceanic subduction, or as fragments of lower crust exhumed from the root of orogenic thickened crust. It is critical to distinguish between these two end-member scenarios as the resulting paleogeographic and geodynamic reconstructions may significantly differ. In this contribution, we investigated eclogite relics from Lac Cornu in the Aiguilles-Rouges massif, one of the External Crystalline Massifs of the Western Alps. Phase equilibrium modelling suggests that these mafic rocks were buried along a prograde path (M1) from ~600 °C/1.2–1.6 GPa to peak conditions of ~630–775 °C and >1.6 GPa. Zircon rims, with a rare earth element signature typical of eclogite facies zircon (no Eu anomalies, flat HREE spectrum), and rutile were dated by U-Th-Pb laser ablation-inductively coupled plasma-mass spectrometry (LA-ICPMS) at c. 335-330 Ma. Prograde deformation has not been identified in the field and is only recognized thanks to the crystallographic preferred orientation (CPO) of inclusions of omphacite and rutile in garnet. Peak pressure conditions were followed by a decompression stage (M2) from ~760 °C/1.4 GPa to ~600-650°C/0.9 GPa supported by the breakdown of omphacite into plagioclase-clinopyroxene symplectite and the crystallization of plagioclase-amphibole corona around garnet. The M2 retrogression stage is associated with the development of a main sub-horizontal planar fabric and the crystallographic preferred orientations of minerals composing symplectite. This deformation stage is interpreted as the result of horizontal lower-crustal flow. The final stage of exhumation (M3) is characterized by the replacement of symplectite and garnet by plagioclase and large euhedral amphibole and by the breakdown of rutile and ilmenite into titanite dated at c. 300 Ma. The crystallographic preferred orientations of titanite and amphibole are consistent with the development of vertical dextral shear zone in a transpressive regime. The combination of field observations, petrological, microtextural and geochemical analyses, suggests that the mafic eclogites preserved in migmatitic rocks of the Aiguilles-Rouges massif are remnants of a continental lower-crust exhumed and juxtaposed with lower-grade migmatites in crustal-scale vertical transpressive shear zones.

Keywords: External Crystalline Massif; Eclogite; Petrochronology; LA-ICPMS U-Th-Pb dating of zircon, rutile and titanite, EBSD

1. Introduction

Eclogites are fundamental rocks as they record processes related to high-pressure (HP) metamorphism associated with the burial and exhumation of crustal material. More generally eclogites give insight into the way crustal material flows during an orogenic event (e.g. Chopin, 1984; Spalla et al., 1996; Duchene et al., 1997; Lardeaux et al., 2001; O'Brien et al., 2001; Lanari et al., 2013). Eclogitic rocks have been identified in most of the massifs forming the hinterland of the Paleozoic Variscan belt (Fig. 1A), which is often considered as an analogue to the Tibetan-Himalayan orogenic plateau (e.g. Maierová et al., 2016). In these massifs, eclogites commonly occur as meter-scale lenses and are embedded in felsic migmatites preserving mineral assemblages equilibrated at lower pressure conditions (e.g. Štípská et al., 2006; Whitney et al., 2015, 2020; Ferrando et al., 2008; Jacob et al., 2021). In the Variscan belt, the eclogite relicts were often interpreted as remnants of suture zones (e.g. Lardeaux et al., 2001; Guillot & Ménot, 2009; Rubatto et al., 2010; Jouffray et al., 2020; Pitra et al., 2021). However, some of these eclogitic occurrences were also interpreted as the witnesses of thickened orogenic crust (e.g. Whitney et al., 2015, 2020; Benmammar et al., 2020; Roger et al., 2020; Jacob et al., 2021). Although most recent studies on eclogites integrate a wide variety of data (structural, petrological, geochemical, geochronological, numerical modelling), the interpretation regarding the significance and origin of high-pressure (HP) metamorphism remains in some case controversial (i.e. Pitra et al., 2021; Whitney et al., 2015, 2020). This uncertainty regarding the tectonic setting associated with HP metamorphism leads to a debate about the number and location of suture zones within the Variscan belt (Kroner & Romer, 2013; Franke et al., 2017; Regorda et al., 2020).

Besides constraining the timing and metamorphic conditions of formation of these eclogite, the next challenge is to decipher from the rock record (mineralogy, structure and microtexture) the processes responsible for the exhumation and the exposure of these HP mafic rocks, which have a higher density than the surrounding crustal rocks (e.g. Schulmann et al., 2008; Whitney et al., 2015, 2020). In the south-western branch of the Variscan belt formed by the Montagne Noire, Corsica-Sardinia and Maures-Tanneron massifs and the Variscan alpine basement (Fig.

1A), eclogites are commonly associated with vertical strike slip shear zones (e.g. Giacomini et al., 2008; Cruciani et al., 2011, 2012, 2015a; Whitney et al., 2015, 2020; Trap et al., 2017; Roger et al., 2020; Jouffray et al., 2020; Schneider et al., 2014) and were exhumed throughout various mechanisms such as vertical channel flow in a double gneiss dome (Rey et al., 2011, 2017; Whitney et al., 2015, 2020) or diapirism (Faure & Cottereau, 1988; Soula et al., 2001; Charles et al., 2009). The significance of such eclogite relics within steeply dipping high strain zones remains unclear.

The aim of this study is to decipher the origin of the HP–high temperature (HT) eclogites in the Variscan belt and to constrain their exhumation mechanisms. To this end, we investigated eclogite lenses embedded in migmatitic orthogneisses and affected by a kilometre-scale high-strain dextral shear zone from the Lac Cornu area of the Aiguilles-Rouges Massif (ARM) in the Western Alps (Fig. 1; von Raumer & Bussy, 2004). The tectono-metamorphic evolution is reconstructed by combining forward and inverse thermodynamic modelling (phase diagrams, exchange thermobarometry and Zr-in-rutile thermometry), with geochronology (LA-ICPMS U-Th-Pb dating of zircon, rutile and titanite), geochemistry (whole-rock and zircon trace element composition), and deformation analyses (field-based observations and Electron Backscatter Diffraction (EBSD)). These results give insight into the origin and geodynamic setting of these Variscan HP–HT metamorphic rocks from the ARM and to propose a tectonic model for their exhumation.

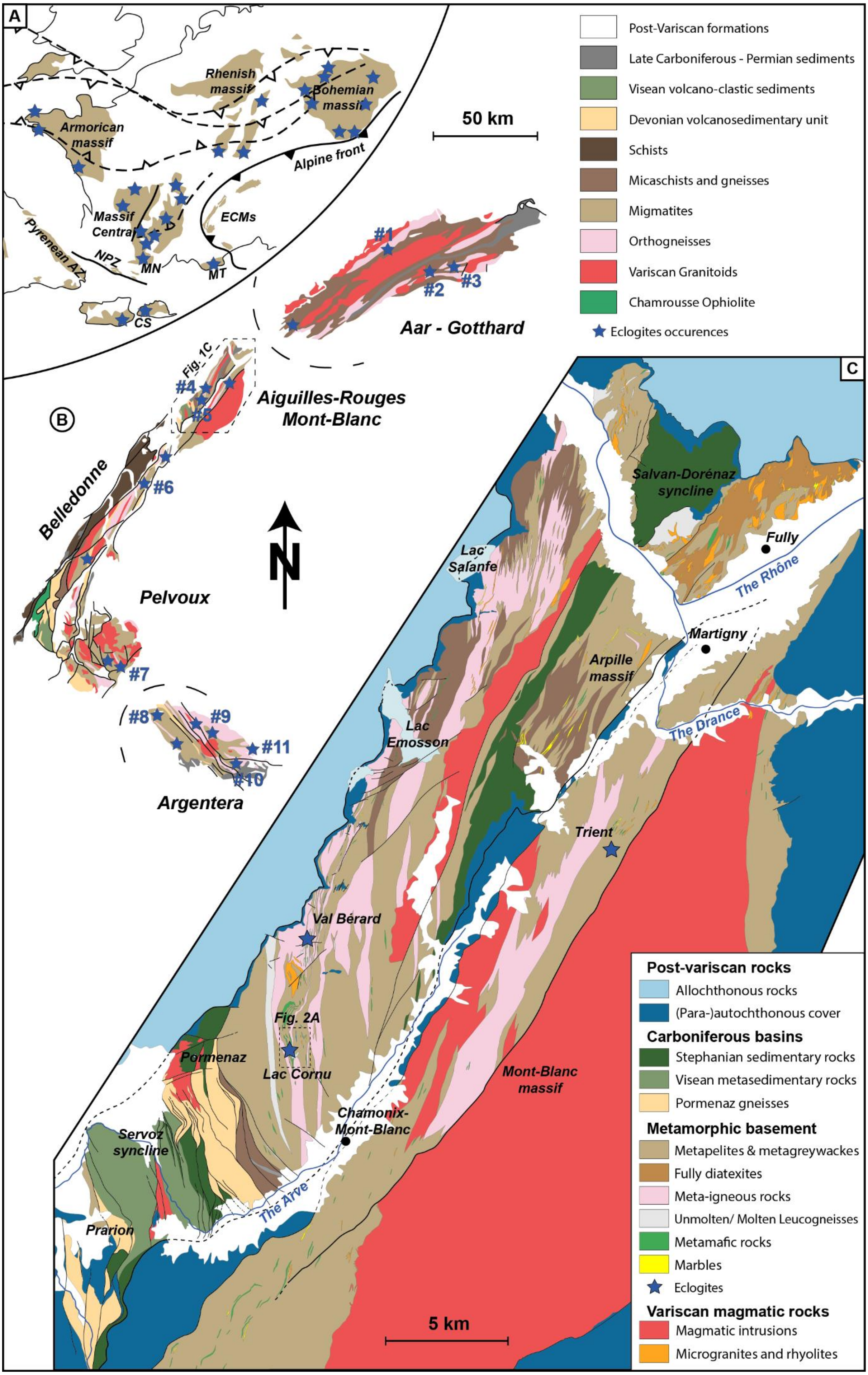
A
Rhenish massif
Bohemian massif
Armorican massif
Alpine front
ECMs
Massif Central
Pyrenean AZ
NPZ
MN
MT
CS
50 km
#1
#2
#3
Aar - Gotthard
Post-Variscan formations
Late Carboniferous - Permian sediments
Visean volcano-clastic sediments
Devonian volcanosedimentary unit
Schists
Micaschists and gneisses
Migmatites
Orthogneisses
Variscan Granitoids
Chamrousse Ophiolite
Eclogites occurences
B
Fig. 1C
#4
#5
Aiguilles-Rouges Mont-Blanc
Belledonne
#6
N
Pelvoux
#7
#8
#9
#11
#10
Argentera
C
Salvan-Dorénaz syncline
Fully
The Rhône
Lac Salanfe
Martigny
Arpille massif
Lac Emosson
The Drance
Trient
Val Bérard
Fig. 2A
Pormenaz
Lac Cornu
Mont-Blanc massif
Chamonix-Mont-Blanc
Servoz syncline
The Arve
Prarion
5 km
Post-variscan rocks
Allochthonous rocks
(Para-)autochthonous cover
Carboniferous basins
Stephanian sedimentary rocks
Visean metasedimentary rocks
Pormenaz gneisses
Metamorphic basement
Metapelites & metagreywackes
Fully diatexites
Meta-igneous rocks
Unmolten/ Molten Leucogneisses
Metamafic rocks
Marbles
Eclogites
Variscan magmatic rocks
Magmatic intrusions
Microgranites and rhyolites

Figure 1 : (A) Paleogeographic reconstruction of the Variscan Belt during Permian time modified from Carreras & Druguet (2014) and Laurent et al. (2017), with eclogitic occurrences reported from Lotout et al., (2018). The location of the ECMs and the External Variscan Shear Zone (EVSZ) from Bellahsen et al. (2014), Ballèvre et al., (2018) and Simonetti et al. (2020a). AZ: Axial Zone; CS: Corsica-Sardinia block; MND: Montagne Noire Dome; MT: Maures-Tanneron; NPZ: North Pyrenean Zone. (B) Geological map of the Variscan basement of the External Crystalline Massifs in the French and Swiss Alps with the eclogitic occurrences, the number corresponds to those reported in Table 1. (C) Geological map of the ARM and Mont-Blanc Massifs. Location of figure 2A is shown.

2. Geological setting

The Variscan belt resulted from late Paleozoic continental collision between Laurussia and Gondwana continents, preceded by oceanic and continental subduction and possibly by collage of islands arcs and/or continental fragments throughout the late Paleozoic time (e.g. Matte, 1991; Stampfli et al., 2002, 2013; von Raumer et al., 2015; Franke et al., 2017). From North to South, the External Crystalline Massifs (ECMs), comprise the Aar-Gothard, ARM, Mont-Blanc, Belledonne, Pelvoux and Argentera massifs and represent remnants of the Variscan belt. They belong to the para-autochthonous Helvetic domain of the Alps. Alpine deformation and metamorphism are restricted along narrow shear zones with recorded peak metamorphic conditions not overpassing greenschist facies (e.g. Rolland et al., 2003; Rossi et al., 2005; Bellanger et al., 2014; Boutoux et al., 2016).

2.1. Eclogitic occurrences within the ECMs

Several occurrences of mafic lenses or boudins with relictual eclogitic assemblages are documented in the ECMs (Fig. 1B; Table 1; e.g. Paquette et al., 1989; Ménot & Paquette, 1993). In the ARM, Belledonne, Pelvoux and Argentera massifs (Fig. 1B; Table 1), these metabasites have mostly a MORB-type geochemical signature. Their protoliths are interpreted as tholeiitic intrusions emplaced within a thin continental crust during continental rifting that may have reached the opening of a narrow oceanic basin (Paquette et al., 1989; von Raumer et al., 1990; Ménot & Paquette, 1993; Rubatto et al., 2010; Liégeois & Duchesne, 1981). Alternatively, Jouffray et al. (2020) interpreted the geochemical signature of Argentera eclogites as MORBs contaminated by continental crust components, i.e. either basalts from a supra-subduction zone (back-arc basalts) or MORB-type magmas contaminated by crust-derived fluids. In the Aar-Gothard massifs, mafic protoliths have been interpreted as metabasalts with ophiolitic affinity while metagabbros show an island arc affinity (Biino &

Meisel, 1993). The protolith ages for the HP mafic rocks of ECMs have been determined by U-Pb on zircon dating (ID-TIMS and LA-ICPMS) between c. 483 Ma and 453 Ma (Table 1; e.g. Paquette et al., 1989; Oberli et al., 1994; Rubatto et al., 2001, 2010; Schaltegger et al., 2003; Bussy et al., 2011; Fréville, 2016).

The HP metamorphism occurred at 340.7 ± 4.2 Ma and 336.3 ± 4.1 Ma in the Argentera massif (SHRIMP and ID-TIMS U-Pb on zircon; Rubatto et al., 2010) and ~345 Ma in the ARM (LA-ICPMS on zircon; Bussy et al., 2011). Alternatively, Paquette et al. (1989) suggested the existence of two distinct stages within a 30 Ma gap: the earliest is recorded in the Argentera Massif at ~424 Ma and the second episode in the Belledonne massif at ~395 Ma (eclogite boudins; ID-TIMS U-Pb on zircon). Nonetheless, similar Silurian – early Devonian HP ages and interpretations proposed for the French Central massif are nowadays re-evaluated (Paquette et al., 2017). The range of ages proposed for the HP stage between Ordovician and Visean (Paquette et al., 1989; Abrecht et al., 1991; Rubatto et al., 2010; Bussy et al., 2011; Jouffray et al., 2020) is a source of confusion and constitutes a barrier for the interpretation of the tectonic and geodynamic significance of these eclogites at the scale of the Variscan belt. The pressure–temperature (P–T) conditions of the HP metamorphism are estimated in the Argentera massif at ~700 °C and 1.4–1.5 GPa (Latouche & Bogdanoff, 1987; Ferrando et al., 2008; Jouffray et al., 2020), in the Belledonne massif at 690–740 °C and 1.4 GPa (Jacob et al., 2021), in the ARM at 650–780 °C and 1.1–1.5 GPa (Liégeois & Duchesne, 1981; Schulz & von Raumer, 1993, 2011), and in the Aar-Gothard massif at ~700–750 °C and 1.8 GPa (Abrecht et al., 1991; Biino, 1994).

In the ECMs, the eclogitic occurrences are mainly interpreted as resulting from a continental subduction (Ferrando et al., 2008; Rubatto et al., 2010; Bussy et al., 2011) and are regarded as remnants of dismembered fragments of a suture zone (Abrecht et al., 1991; Jouffray et al., 2020). Recently, Jacob et al. (2021) suggested that HP metamorphism in the Belledonne massif might be induced by crustal thickening of the orogenic crust rather than by oceanic subduction.

Table 1 : Eclogitic metabasites characteristics in the ECMs. The ages are ± 2σ. ID-TIMS: Isotopic Dilution Thermal Ionization; LA-ICPMS: Laser Ablation-Inductively Coupled Mass Spectrometry EMPA: Electron Probe MicroAnalysis; SHRIMP: Sensitive High Resolution Ion Microprobe; LI: Lower Intercept; Zr: zircon; Mz: monazite; Rt: rutile; Amph: amphibole. Previous works: (a) Schaltegger et al., 2003; (b) Abrecht & Biino, 1994; (c) Oberli et al., 1994; (d) Mercolli et al., 1994; (e) Abrecht et al., 1991; (f) Biino, 1994; (g) Gebauert et al. 1988; (h) Schulz & von Raumer, 1993; (i) Schulz & von Raumer, 2011; (j) Paquette et al., 1989; (k) Liégeois &

Duchesne, 1981; (l) Bussy et al., 2011; (m) Jacob et al., 2021; (n) Fréville et al, 2016; (o) Latouche & Bogdanoff, 1987; (p) Rubatto et al., 2001; (q) Jouffray et al., 2020; (r) Ferrando et al., 2008 and (s) Rubatto et al., 2010.

Massif (refences)	n°	Locality	Protolith geochemistry	Protolith age (± 2σ)	Method	HP conditions	HP metamorphism age (± 2σ)	Method
Aar $^{(a)}$	1	Sustenhorn	Gabbros	478 ± 5 Ma	ID-TIMS (Zr)			
Gothard $^{(b-g)}$	2	Kastelhorn	Gabbros with island arc affinity	467-475 Ma	ID-TIMS (Zr)			
	3	Val Naps	N-MORB tholeiite and gabbros with island arc affinity	467-475 Ma	ID-TIMS (Zr)	700-750°C	468-461 Ma	ID-TIMS (Zr)
				or c. 870 Ma		1.8 GPa		
Aiguilles-Rouges $^{(h-l)}$	4	Val Bérard				700 ± 50°C		
						1.4 ± 0.1 GPa		
	5	Lac Cornu	N-MORB tholeiite in thin continental crust	453 +3/-2 Ma	ID-TIMS (Zr)	c. 780°C		
				463 +3/-2 Ma	LA-ICPMS (Zr)	≥1.1 GPa	345 ± 14 Ma	LA-ICPMS (Zr)
				458 ± 5 Ma	LA-ICPMS (Zr)			
Belledonne $^{(j-m)}$	6	Lac des Tempètes	N-MORB tholeiite in thin continental crust	456 ± 4 Ma	LA-ICPMS (Zr)	690-740°C	~ 395 Ma	ID-TIMS (Zr) – LI
				448 ± 6 Ma	LA-ICPMS (Zr)	≥1.4 GPa	340 ± 11 Ma	LA-ICPMS (Rt)
Pelvoux $^{(n)}$	7	Peyre-Arguet		471 ± 5 Ma	LA-ICPMS (Zr)			
Argentera $^{(o-s\,;\,j)}$	8	Rabuons				c. 660-800°C		
						1.4 GPa		
	9	Val Meris	Basalt	457 ± 6 Ma	SHRIMP (Zr)			
				462 + 6 Ma	ID-TIMS (Zr)			
	10	Madone de Fenestre	N-MORB, E-MORB and cumulates with crustal contamination	471 +40/-29 Ma	ID-TIMS (Zr)	640–740 °C	~ 424 Ma	ID-TIMS (Zr) – LI
						1.5 ± 0.25 GPa	> 339.7 ± 12 Ma	$^{40}Ar/^{39}Ar$ (Amph)
	11	Frisson lakes		486 ± 7 Ma	SHRIMP (Zr)	735 ± 15°C	340.7 ± 4.2	SHRIMP (Zr)
						1.38 ± 0.05 GPa	336.3 ± 4.1 Ma	

2.2. The Aiguilles-Rouges massif

The ARM is an elongated massif striking NNE, composed of a gneissic complex and two Carboniferous synclines (Fig. 1C). The gneissic complex consists of paragneisses and orthogneisses, derived from Ordovician granitoids (von Raumer & Bussy, 2004) that were affected by partial melting. Marble, metabasite and ultramafic rocks occur as lenses in the gneissic complex (von Raumer & Bussy, 2004). The whole sequence is intruded by Carboniferous granites (Bussy et al., 2000). In the ARM, the main Variscan deformation is characterized by dextral transpression forming vertical foliations and large-scale S-C-C' structures (Simonetti et al., 2020a) striking from N150 to N40 (Bellière, 1958). Remnants of ancient planar fabrics are also mentioned, but their tectonic and geodynamic significances are neither discussed nor interpreted (e.g. von Raumer & Bussy, 2004; Joye, 1989). The onset of transpressive deformation was dated at c. 320 Ma (U/Pb on monazite, Simonetti et al, 2020a). Zircon and monazite U-Th-Pb ages at c. 305 Ma dating the emplacement of on the Vallorcine, Montenvers and Mont-Blanc syntectonic granites are interpreted as the timing of the end of the transcurrent continental deformation (Bussy et al., 2000; Bussy & von Raumer, 1993, 1994).

At least two main metamorphic stages can be distinguished in the ARM: a high pressure and high temperature (HP and HT) stage preserved in eclogites of the Lac Cornu and Val Bérard areas (Fig. 1C; von Raumer & Bussy, 2004). The minimum P–T conditions of this HP stage are 780 °C and 1.1 GPa (Liégeois & Duchesne, 1981) and 650–750 °C and 1.25–1.5 GPa (Schulz & von Raumer, 1993, 2011). These eclogitic lenses are surrounded by migmatitic gneisses recording a HT and medium pressure (MP) metamorphism affecting the whole gneissic basement with P–T conditions varying from 600–700 °C and 0.4–0.7 GPa (Schulz & von Raumer, 1993, 2011; Joye, 1989; Chiaradia, 2003; Genier et al., 2008; Dobmeier, 1998). Two samples (AR483 and AR481) were collected in a mafic layer near the Lac Cornu (Fig. 2).

3. Methods

3.1. Whole rock and mineral major and trace elements

Major and trace elements data for whole rocks (AR481 and AR483) (Table S1) were obtained using a PANalytical AxiosmAX X-Ray Fluorescence (XRF) Spectrometer at the University of Lausanne (Switzerland). Quality control was performed on BHVO2 reference material for trace elements and on BHVO2 and JA-3 references material for major elements.

X-ray maps were acquired using an electron probe microanalyser (EPMA) at the University of Bern (Switzerland) and standardized into maps of oxide weight percentage using an internal standard technique and the program XMapTools 3.4.1 (Lanari et al., 2014; Lanari et al., 2019). Compositional maps of structural formula expressed in atom per formula unit (apfu) were calculated and used to investigate the compositional variability of each mineral phase at the thin section scale. Representative mineral compositions are given in Table S2.

Zr-in-rutile thermometry (Table S3) was also performed using EPMA at the University of Bern following the protocol described in Pape et al. (2016). A knowledge of the pressure of rutile crystallization is required for estimating temperatures at HP conditions (Zhang et al., 2010), therefore we used the thermometer calibration of Tomkins et al., (2007). In order to simplify the description of Zr-in-Rutile thermometer results, we compared temperatures calculated for a fixed pressure of 1.5 GPa; results using other pressure conditions lead to similar results within a temperature range of 650–700 °C. All uncertainties are given at 2σ level. To highlight the possible effects of diffusion on the Zr content of the rutile, we analysed, in both samples, rutile armored by garnet and rutile grains in the mineral matrix that are more likely to re-equilibrate (Zhang et al., 2010). We also avoided rutile partially replaced by ilmenite as it can affect the Zr content in rutile (e.g. Whitney et al., 2015).

Rare Earth Elements (REE) analyses on zircon were carried out at the Laboratoire Magmas et Volcans (Clermont-Ferrand, France) with a Thermo Element XR ICP-MS coupled to a Resonetics M-50 laser system operating at a wavelength of 193 nm. Zircon analyses were performed with a spot size of 27 µm, a repetition rate of 3 Hz and a fluency of 2.7 J/cm2. External calibration was determined relative to NIST 612 glass and internal standard was 28Si. The glass BRC-2G served as secondary standards for data quality control. Data reduction was carried out with the GLITTER® software package (Macquarie Research Ltd 2001; van Achterberg et al., 2001). The REE contents were normalized to the chondritic values of Sun & MacDonough (1989). REE analyses were acquired on the same zone of the dated zircon crystals to infer the geochemical context of zircon crystallization.

3.2. Thermodynamic modelling

Pressure–Temperature phase diagrams were computed in the Na_2O–CaO–FeO–MgO–Al_2O_3–SiO_2–H_2O–TiO_2–Fe_2O_3 (NCFMASHTiO) chemical system using Perple_X 6.9.1. software (Connolly, 2005) and the hpver62 thermodynamic database from Holland & Powell

(2011). The solution models used in the calculations were garnet (White et al., 2014); clinopyroxene (Green et al., 2007); amphibole and melt (Green et al., 2016), plagioclase (Fuhrman & Lindsley, 1988), orthopyroxene and chlorite (White et al., 2014), ilmenite (White et al., 2000) and epidote (Holland & Powell, 2011).

For sample AR483, due to relictual mineral assemblages, the phase diagrams were calculated using a local bulk composition extracted from the compositional maps using XMapTools (Table S4) (e.g. Duesterhoeft & Lanari 2020). For sample AR481, the bulk rock composition obtained by XRF was used. The H_2O content was refined using a P–MH_2O diagram for sample AR483 and by T–MH_2O diagram for sample AR481 to reproduce the observed mineral assemblages. In addition, in sample AR483, the Fe^{3+} content was approximated using mineral structural formula of each mineral calculated in XMapTools and their molar concentration in the area analysed. For sample AR481, a T–XFe^{3+} (XFe^{3+} = Fe^{3+}/Fetotal) diagram emphasizes the growth of epidote in equilibrium with titanite for XFe^{3+} > 0.2 and was therefore fixed at 0.1. In this sample, the amount of CaO associated with apatite was removed from the measured bulk composition assuming apatite as the only P-bearing phase.

For sample AR483 we used the mineral compositions extracted from the compositional maps as reference compositions. The P–T conditions of mineral equilibrium were estimated using isopleths and also the third model quality factor Qcmp described in Duesterhoeft & Lanari (2020) in order to have a quantitative approach considering more compositional variables. This factor calculates the fitting between the observed and modelled mineral compositions including the relative analytical uncertainty of the measured compositions. The comparison of mineral composition was restricted to CaO, MgO and FeO contents for garnet, of Na_2O, CaO, Al_2O_3, and SiO_2 contents for plagioclase, and of CaO, FeO, MgO, Na_2O, TiO_2, SiO_2, Al_2O_3 contents for amphibole.

The P–T conditions from local equilibria in sample AR483 were estimated using empirical and semi-empirical thermobarometers implemented in the XMapTools program following the protocol described in Lanari et al. (2013). The P–T conditions of symplectite were calculated using equilibria involving clinopyroxene, plagioclase, and amphibole (in absence of quartz). The temperature was first estimated from the distribution of Na and Ca between plagioclase and hornblende using the edenite-richterite calibration of Holland and Blundy (1994). Pressure was estimated with fixed composition of amphibole and plagioclase (Table S2) for the defined temperature ranges using the calibration of Waters (2003) based on the reaction jadeite + tremolite = albite + edenite. Temperature conditions of crystallization of amphibolite-plagioclase corona were also estimated using the edenite-richterite calibration of Holland & Blundy (1994).

3.3. U-Pb analyses

Zircon and rutile crystals were obtained by conventional mineral separation. The selected grains (size ~100–200 µm) were mounted in epoxy resin and polished down to expose their near equatorial sections. Rutile and titanite were also analysed in-situ on thin section to preserve the textural relationships between accessory minerals, mineralogical assemblage and the fabric. Before analysis, backscatter electron (BSE) and cathodoluminescence (CL) images were acquired for each grain using a scanning electron microscope (SEM), the locations of LA-ICPMS spot were selected based on the internal microstructures and to avoid inclusions, fractures and other physical defects.

U-Th-Pb isotope data of zircon, rutile and titanite were obtained at the Laboratoire Magmas & Volcans (LMV), Clermont-Ferrand, France by Laser-Ablation Inductively-Coupled Plasma Mass-Spectrometry (LA-ICPMS). The analytical method for isotope dating with LA-ICPMS is similar to that reported in Paquette & Tiepolo (2007), Hurai et al. (2010), and Paquette et al. (2014).

The analyses involved the ablation of minerals with a Resonetics M-50 laser system operating at a wavelength of 193 nm (Müller et al., 2009). The ablated material was carried in helium and then mixed with nitrogen and argon before injection into the plasma source of a Thermo Element XR Sector Field high-resolution ICP-MS. The alignment of the instrument and mass calibration were performed before each analytical session using the NIST SRM612 reference glass, by inspecting the signal of 238U and by minimising the ThO^+/Th^+ ratio (< 1%). Raw data were corrected for U and Pb fractionation during laser sampling and for instrumental mass bias by standard bracketing with repeated measurements of the GJ-1 zircon or Sugluk-4 rutile standards (Jackson et al., 2004; Bracciali et al., 2013). The reproducibility and accuracy of the corrections were controlled by repeated analyses of the 91500 zircon or PCA-S207 rutile standards (Wiedenbeck et al., 1995; Bracciali et al., 2013) treated as unknown (Table S5). For the titanite analyses, owing to a lack of high quality titanite natural standards (i.e. negligible common Pb), zircon standards were used (Table S5). For zircon, rutile and titanite, because of the non-negligible mercury content of the Ar gas creating an isobaric interference between ^{204}Pb and ^{204}Hg, no common Pb correction was applied prior to data reduction using the GLITTER® software package (van Achterbergh et al., 2001). The detailed analytical procedures are presented in the supplementary material (Table S5). The calculated ratios were exported and ages and diagrams generated using Isoplot/Ex v. 2.49 software package (Ludwig, 2001). The decay constants used for the U-Pb system are those determined by Jaffey et al. (1971) and recommended by the IUGS (Steiger & Jäger, 1977). In the text, tables and figures, all uncertainties are given at 2σ level.

3.4. Microstructures and EBSD analysis

EBSD analyses were performed at Geosciences Montpellier laboratory (University of Montpellier, France) using electron microscopes dedicated to high-resolution crystallographic mapping (JEOL 5600 SEM and CamScan CrystalProbe X500FE), an accelerating voltage of 20 kV and a working distance of 25 mm in “low vacuum” mode. Grid spacing was between 2 and 11 µm in function of the size of the map. All data points that presented misorientation >5° with respect to their eight neighbouring measurements were removed. The EBSD data were reduced using the program Channel 5 from HKL software. “GROD” (Grain Reference Orientation Deviation) filter has been used to illustrate the internal deformation of each mineral. This method provides the average orientation for each grain and the deviation angle from this mean orientation is then plotted for each pixel (program Channel 5 from HKL software). However, it is dependent on the grain’s detection and division, and thus can be inefficient on small grains. Therefore, local internal deformation was illustrated on small grains by local misorientation map based on a referential orientation.

4. Results

4.1. Field occurrences of the Lac Cornu eclogites

In the Lac Cornu area, mafic rocks form either kilometric-length layers consisting of amphibolite-rich layers or metric to decametric lenses (Fig. 2 and 3A). A mineralogical layering is mainly defined by the different proportion of amphibole, plagioclase and garnet (Fig. 3B). These mafic lenses are surrounded by anatectic orthogneiss and paragneiss. The study area lies within a N-S trending vertical dextral transpressional high-strain shear zone responsible for stretching and boudinage of mafic layers. A vertical pervasive and sometimes mylonitic foliation (S_V, with “v” standing for vertical) dominates in mafic lenses and in the surrounding gneissic rocks (Fig. 2 and 3). Dextral kinematics are inferred from S-C-C’ structures displaying sub-horizontal stretching lineations. Sv is defined by amphibole-plagioclase mineralogical banding and migmatitic layering (Fig. 3C, D and E). Part of the melt was collected within dilatant structural sites during the stretching and boudinage of the mafic layers (Fig. 3A). Deformed leucosomes within the local shear zones also indicate that deformation occurred at subsolidus conditions. In the anatectic gneiss, numerous folds suggest the existence of a previous planar fabric. Based on these observations, this pervasive dextral transpression is interpreted as the main deformation named “D_V” forming a “S_V” foliation and dextral S_V-C_V-C_V’ structures.

Locally, D_V low-strain domains preserve relics of a previous planar fabric. This fabric forms a sub-horizontal foliation (S_H, with “$_H$” for horizontal) that is folded by S_V (Fig. 2, 3C to 3E). High-strain associated with S_V does not allow us to investigate in greater detail the original orientation and the kinematics of D_H deformation. In gneisses, the S_H foliation is defined by a migmatitic layering also indicating a suprasolidus origin. In mafic boudins, S_H is recognized by the mineralogical banding (Fig. 3B) where clinopyroxene is still visible, indicating pressure conditions higher than the clinopyroxene amphibole-free assemblage of the S_V foliation.

Within the D_V shear zones, eclogites are extensively retrogressed into amphibolites (Fig. 3; e.g. von Raumer & Bussy, 2004; Liégeois & Duchesne, 1981). Eclogite facies paragenesis and more particularly clinopyroxene-bearing assemblages are best preserved within the S_H foliation in low- D_V strain domains (Fig. 3). Both samples (AR483 and AR481) were collected in a 50 meter-thick mafic layer (Fig. 2). Sample AR483 (N45°57’36’’; E06°50’42’’) is a well-preserved eclogite collected as a boulder in the eclogitic area. The S_H foliation is defined by the mineralogical layering with clinopyroxene-bearing assemblages. Sample AR481 (N45°57’33’’; E06°50’47’’) is a more retrogressed eclogite than the sample AR483 and is collected in an amphibolite facies D_V shear zone with a vertical S_V foliation mainly composed of amphibole and plagioclase (Fig. 3C).

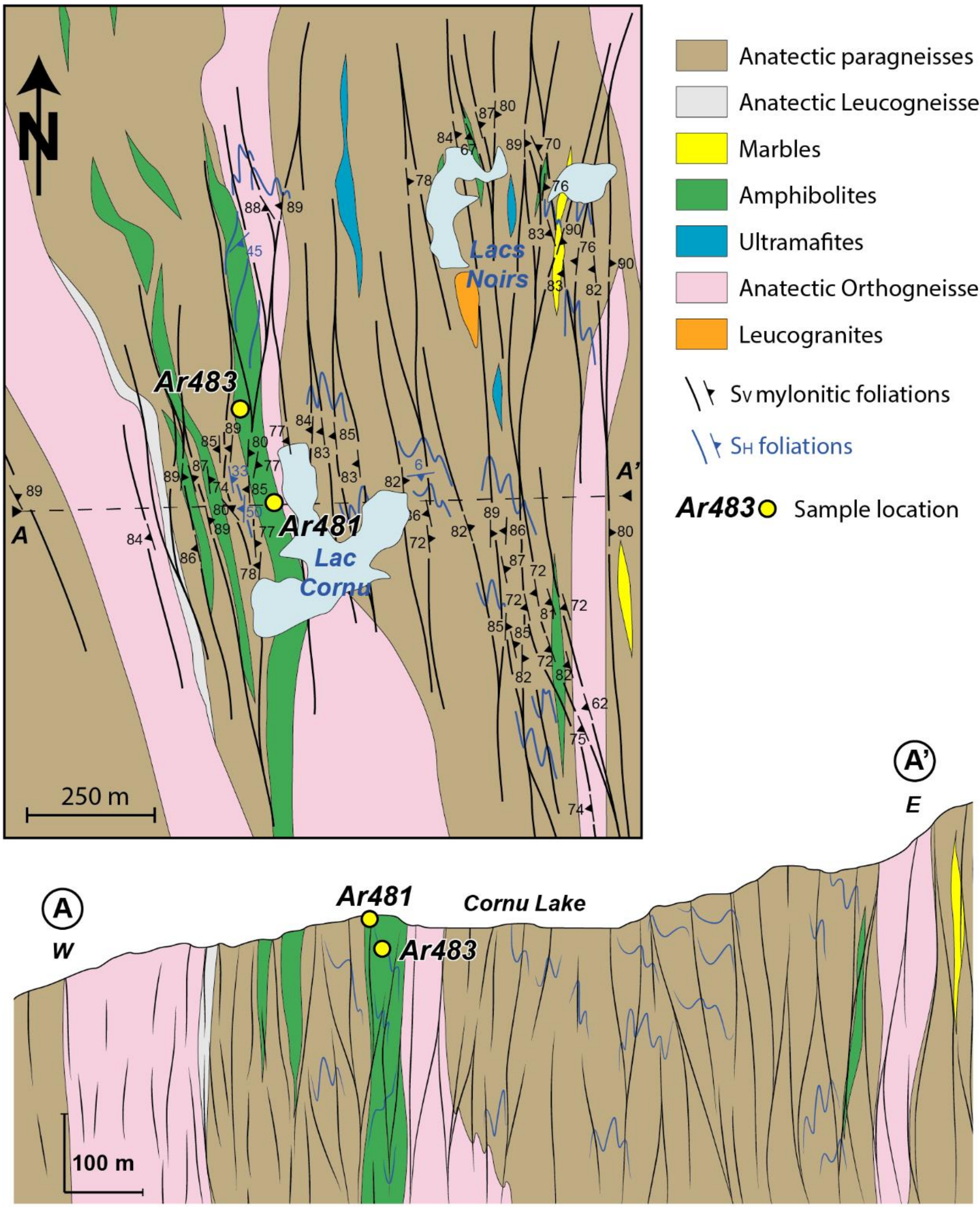

Figure 2 : (A) Detailed geological map modified from von Raumer & Bussy (2004) with foliation measurements of D_H and D_V and foliation trajectories in the Lac Cornu area. (B) E-W cross section of the Lac Cornu area. Samples AR483 and AR481 are localized in both figures.

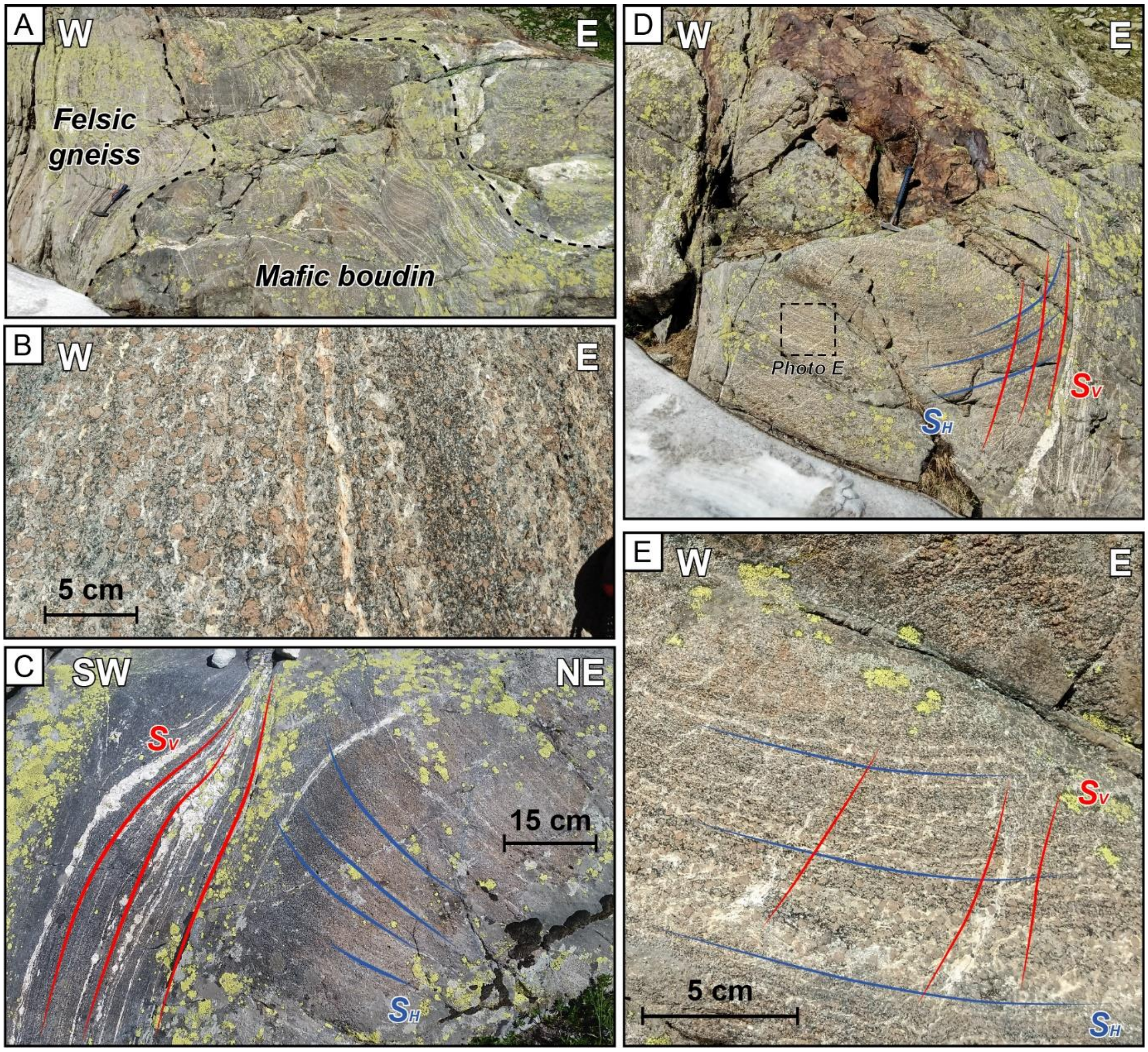

Figure 3 : Field observations: (A) Mafic boudin from the Lac Cornu area. (B) S_H foliation with preservation of eclogitic facies. (C) and (D) relationships between the S_H – S_V foliations and the metamorphic facies of the mafic boudins. (E) Details from photo D with S_H layering and weak S_V in a preserved eclogitic boudin.

4.2 Bulk composition of eclogites

Major and trace element contents from samples AR483 and AR481 are similar (Table S1). In the total Alkali versus Silica diagram (Le Bas et al., 1986) (Fig. S1A), the two samples plot in the basalt field (2.85 and 2.63 wt% Na_2O+K_2O, and 50.05 and 51.71 wt% SiO_2), with the sample AR481 near the basaltic andesite field. In the AFM diagram (Irvine & Baragar, 1971), they belong to the tholeiitic series (Fig. S1B). Samples AR483 and AR481 have typical N-MORB compositions (Fig. S1C) with a tholeiitic to andesitic basalt affinity (Fig. S1C and D; Meschede, 1986; Pearce, 1996). In the Al_2O_3 vs TiO_2 diagram (Konzett et al., 2012), both samples plot in the basalt field (Fig. S1E). These compositions are similar with published data from the ARM (see white circle, black and grey dots on Fig. S1; Paquette et al., 1989; von Raumer et al., 1990; Liégeois & Duchesne, 1981).

4.3. Petrology and mineral compositions

4.3.1. Weakly retrogressed eclogite AR483

Sample AR483 is a weakly retrogressed eclogite composed of amphibole, garnet, clinopyroxene, plagioclase, quartz, with minor epidote, rutile, ilmenite, apatite, zircon and epidote (Fig. 4A). Two mineralogical layers are recognized based on the amount of quartz (Fig. 4A): quartz-rich layers are associated with symplectites whereas quartz-poor layers are composed of large clinopyroxene and amphibole grains. Mineralogical layering and preferential orientation of amphibole and clinopyroxene define the S_H foliation. Clinopyroxene occurred as coarse grains often partially retrogressed into clinopyroxene-plagioclase-bearing symplectites (Fig. 4A).

Clinopyroxene shows a variable composition with the jadeite content ranging from 35 mol% to 11% depending on the textural location (Fig. 5B; Table S2). Clinopyroxene included in garnet is an omphacite with jadeite content of 31–35% (Cpx_1). Omphacite is also present in the matrix as relict compositionally zoned and partially recrystallized in amphibole (Fig. 5B). The breakdown of Cpx_1 involves the formation of sodic-poor clinopyroxene (Cpx_2) in symplectite. Clinopyroxene compositions from the symplectites (Cpx_2) vary between 25 and 11 mol% of jadeite (Fig. 5B).

Garnet is sub-euhedral and grain size ranges from 2 to 15 mm in diameter. It contains abundant inclusions of quartz, rutile, zircon, apatite and omphacite (Cpx_1) and scarce inclusions of epidote and small amphibole. Garnet exhibits compositional zoning with a large Ca-rich core (Grt_1) ($Alm_{52}Prp_{21}Grs_{24}Sps_1$), and a thin Ca-poor, Fe- and Mg-rich overgrowth (Grt_2) ($Alm_{55}Prp_{24}Grs_{17}Sps_1$) (Fig. 5C and D). Garnet core (Grt_1) shows an euhedral shape without significant variation in chemical composition or zoning (Fig. 5D). The transition between core Grt_1 and overgrowth Grt_2 is sharp (Fig. 5C and D). Garnet overgrowths (Grt_2) are better developed when in contact with the symplectite (Fig. 5C), which suggests that Grt_2 and Cpx_2-symplectite formed at the same time.

Amphibole occurs in two distinct textural positions: amphibole associated with clinopyroxene (Cpx_2)–plagioclase-bearing symplectites and amphibole associated with plagioclase in coronas surrounding garnet overgrowths (Grt_2) (Fig. 5A). Although both types of amphibole have different compositions they are referred to $Amph_2$. Amphibole in the Cpx_2-symplectites is homogeneous in composition and corresponds to magnesio-hornblende (Leake et al., 1997). Amphibole in corona shows a zoning with XMg and Si apfu varying from 0.60 and 6.48 to 0.63 and 5.75, respectively (Fig. 5E) (Table S2). It evolves from a ferroan-pargasite in contact with garnet to tschermakitic-hornblende (Leake et al., 1997). Plagioclase (Pl_2) from the matrix, symplectite and corona is homogeneous in composition with an albite content varying from 87 to 89 mol% (Fig. 5F; Table S2). Rutile and zircon are present in the matrix and rutile is partly replaced by ilmenite.

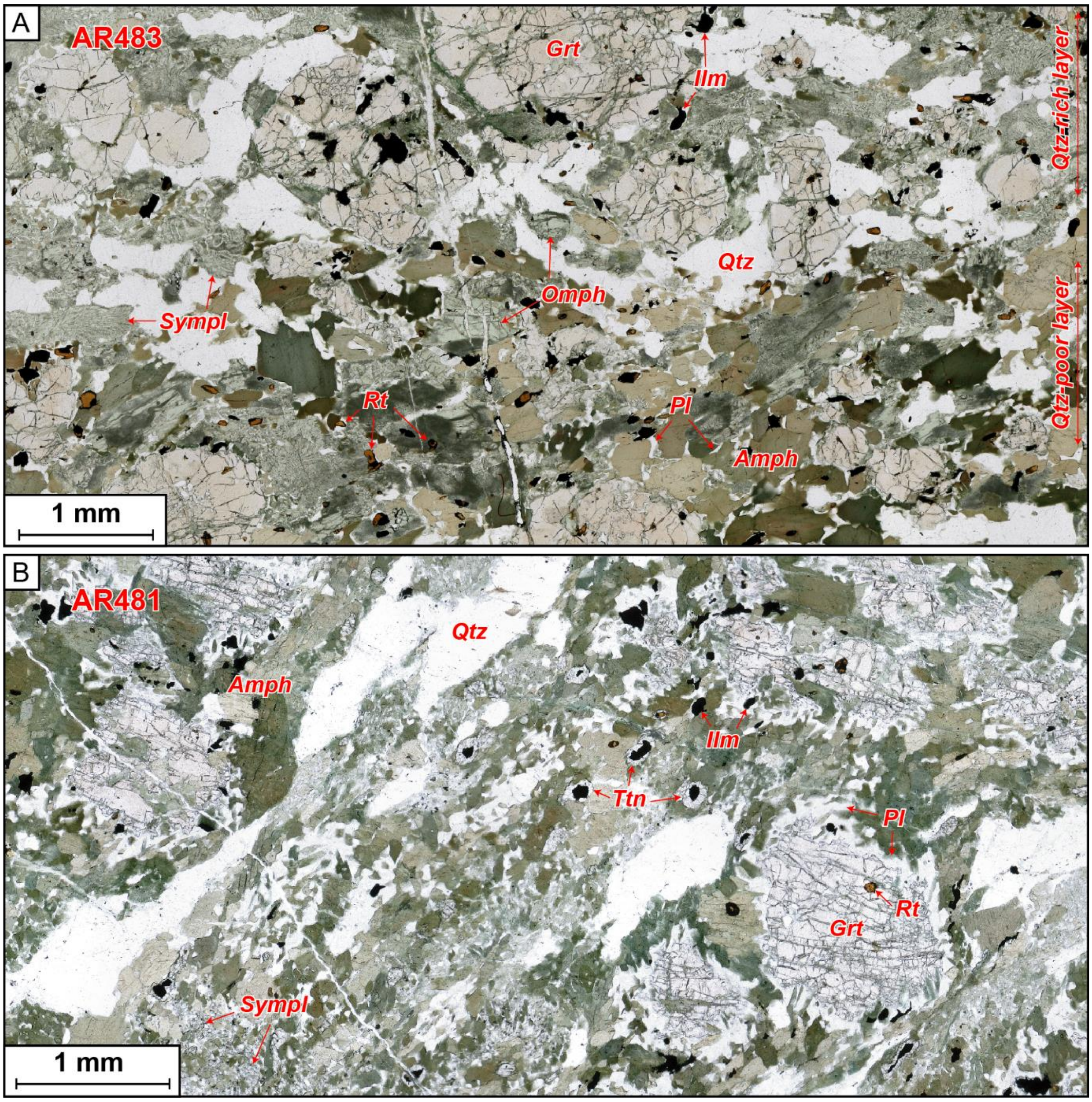

Figure 4: Thin sections images of (A) AR483 and (B) AR481 samples, collected within a mafic boudin of the Lac Cornu area, localization in Figure 3. Amph: amphibolite; Grt: garnet; Ilm: ilmenite; Omph: omphacite; Pl: plagioclase; Qtz: quartz; Rt: rutile; Ttn: titanite; Sympl: symplectite.

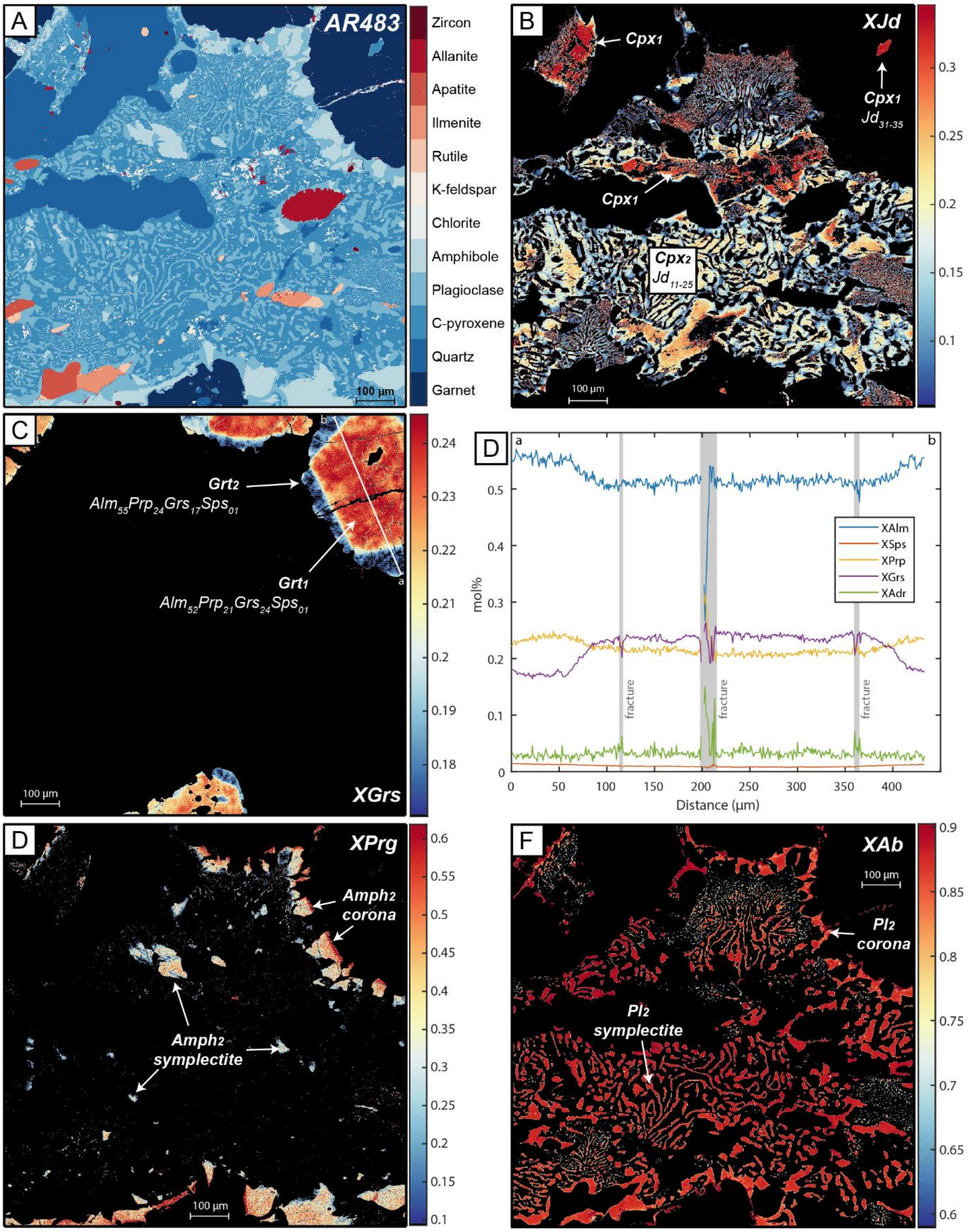

Figure 5 : Compositional maps acquired by electron probe microanalyser (EPMA) from sample AR483. (A) Map of the minerals. Compositional maps of (B) clinopyroxene in function of their jadeite content (XJd), (C) garnet in function of the grossular content (XGrs), (E) amphiboles in function of the pargasite content (XPrg) and (F) Plagioclase in function of their albite content (XAb). (D) The chemical profile of garnet located on the map C.

Alm: almandine; Adr: andradite; Grs: grossular; Jd: jadeite; Prg: Pargasite; Prp: pyrope; Sps: spessartine. Mineral compositions are detailed in Table S2.

4.3.2. Strongly retrogressed eclogite AR481

The sample AR481 is a retrogressed eclogite composed of amphibole, plagioclase, quartz, garnet, it also contains minor clinopyroxene, titanite, ilmenite, rutile, zircon, apatite and magnetite as relics or accessory minerals (Fig. 4B). Omphacite is absent. Clinopyroxene-plagioclase symplectites are replaced by large euhedral magnesio-hornblende ($Amph_3$) and plagioclase (Pl_3) with lower albite content (62 mol%; Table S2). Garnet compositions and chemical zoning (Table S2) are similar to those observed in sample AR483. Garnet shows resorption textures at the expense of the plagioclase-hornblende corona and is sometimes totally replaced by plagioclase and amphibole (Pl_3 + $Amph_3$). Euhedral amphibole in the matrix has XMg and Si apfu of 0.60 and 6.56 (Table S2). Rutile is partially replaced by lamellae and patches of ilmenite, and both phases breakdown into titanite forming coronas (Fig. 4B). Magnetite is present in fractures of the sample and does not show clear relationships with other minerals.

4.3.3. Petrological interpretations

Three main mineral assemblages corresponding to three metamorphic stages M1, M2 and M3 are inferred from the petrological observations.

(1) The earliest stage M1 corresponds to the garnet core (Grt_1) and its inclusions (Cpx_1 + Qtz + Rt + Ap ± Ep ± Amph).

(2) The M2 stage can be subdivided into the formation of two assemblages M2a and M2b. The M2a assemblage is associated with the development of garnet (Grt_2) overgrowths at equilibrium with formation of Cpx_2-Pl_2-$Amph_2$-symplectites replacing omphacite (Cpx_1). The M2b stage is characterized by the development of $Amph_2$-Pl_2 corona around garnet and by the breakdown of rutile into ilmenite. The progressive decrease of jadeite content within Cpx_2 suggests that symplectites developed progressively from M2a to M2b.

(3) The third stage M3 is marked by large amphibole crystals and plagioclase replacing garnet and clinopyroxene-plagioclase symplectites ($Amph_3$ + Pl_3). Ilmenite and rutile breakdown into titanite.

4.4. Crystallographic preferred orientations (CPO)

To establish the relationships between the three metamorphic stages M1, M2, M3 and deformation (i.e. DH and DV), the CPO of each mineral assemblages were investigated. The CPO are plotted in the structural reference frame of the sample, where X-, Y- and Z- axes correspond to the three principal directions of the strain ellipsoid of either S_H or S_V planar fabrics. The main planar fabric in sample AR483 is the S_H foliation defined by compositional layering and preferential alignment of matrix minerals (Fig. 6). Clinopyroxene in the matrix (i.e. Cpx_1 and Cpx_2) is characterized by the alignment of {010} planes parallel to the S_H foliation. The C-axis <001> defines a girdle with a maximum close to the stretching lineation (Fig. 6E). The D_H stretching direction is also defined by the orientation of rutile C-axis <100> (Fig. 6E). Omphacite and rutile included in garnet do not display the same CPO as in the matrix. Omphacite (Cpx_1) armoured in garnet CPO shows a single point maximum of {100} poles and a poorly defined girdle C-axis <100> CPO. Quartz included in garnet or located in the matrix does not show a preferential orientation (Fig. 6E). The GROD map of clinopyroxene (Fig. 6B) indicates that clinopyroxene in symplectite has only internal misorientations inferior to 1° suggesting an absent or weak plastic deformation (Fig. 6C). Local misorientation map on clinopyroxene in late fine-grained symplectites highlights a weak plastic deformation (Fig. 6D).

Sample AR481 shows a mylonitic foliation S_V and is nearly totally retrogressed into amphibolite (Fig. 7A). A large EBSD map from this sample indicates that amphiboles have low internal misorientation, mostly inferior to 1° (Fig. 7A and B). The CPO of amphibole indicates that {100} planes are parallel to the main S_V mylonitic foliation and C-axis <001> defines a girdle parallel to the S_V foliation (Fig. 7C). Titanite has very weak CPO (Fig. 7C), nonetheless, its C-axis <001> presents a broad orientation perpendicular to the S_V foliation.

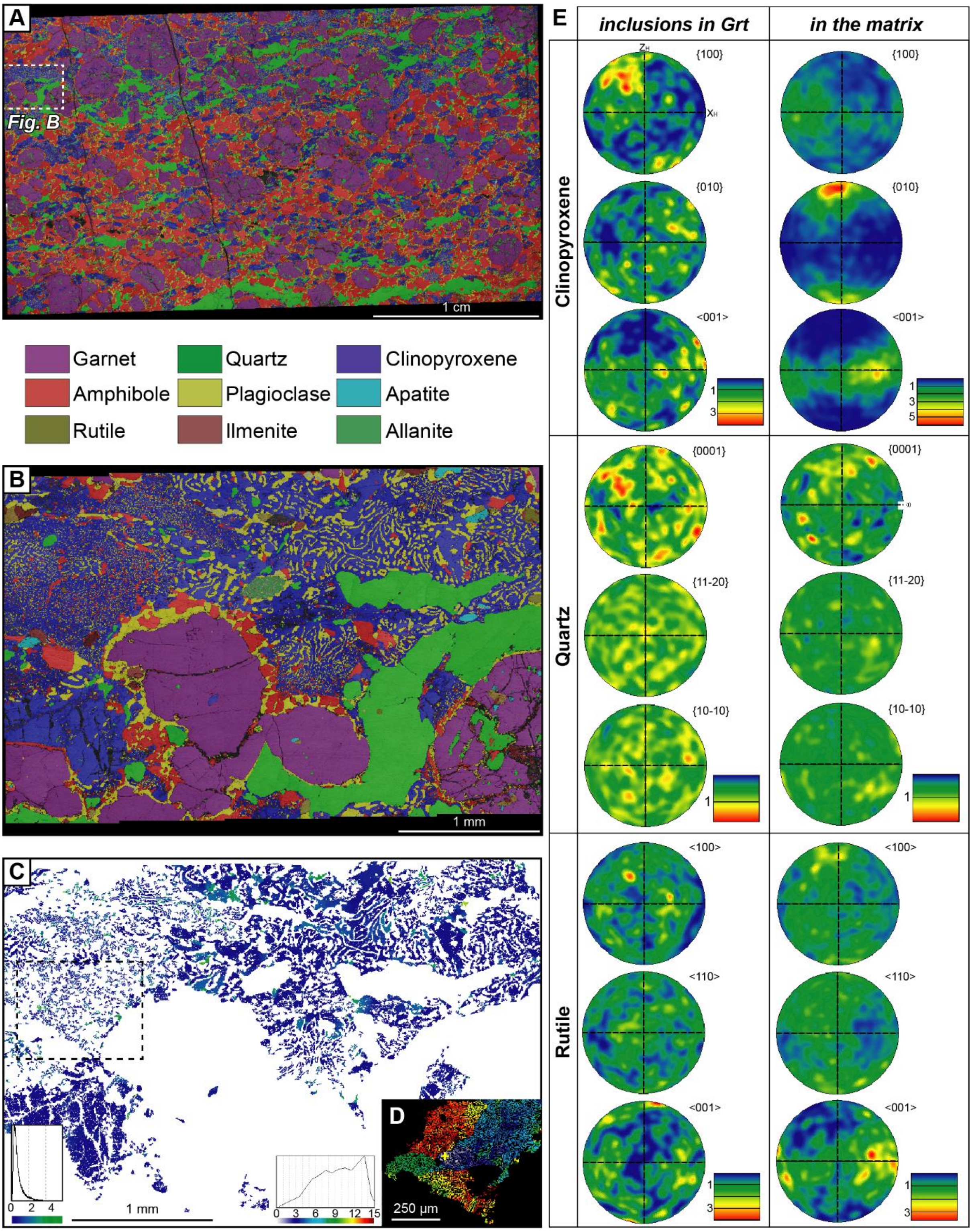

Figure 6: EBSD results from weakly retrogressed eclogite (AR483). (A) Phases map from the whole thin section, resolution of 11 µm. (B) Phases map from a zoom on symplectites with associated GROD Angle map of clinopyroxene grains (C), resolution of 4 µm is inadequate with the grain sizes of the late symplectites and creates artefacts on the GROS Angle map. Dashed square indicates the localization of Figure D. (D) Local misorientation map of clinopyroxene in fine-grained symplectites. Referential orientation is localized by the yellow cross. Sharp

changes of colour indicate grain boundaries and shades highlight internal deformation. (E) Orientations of clinopyroxene, quartz and rutile within garnet grains or in the matrix in Wulf lower hemisphere stereogram from the whole thin section. X_H and Z_H orientations of the stereograms are parallel to the borders of the maps A, B and C.

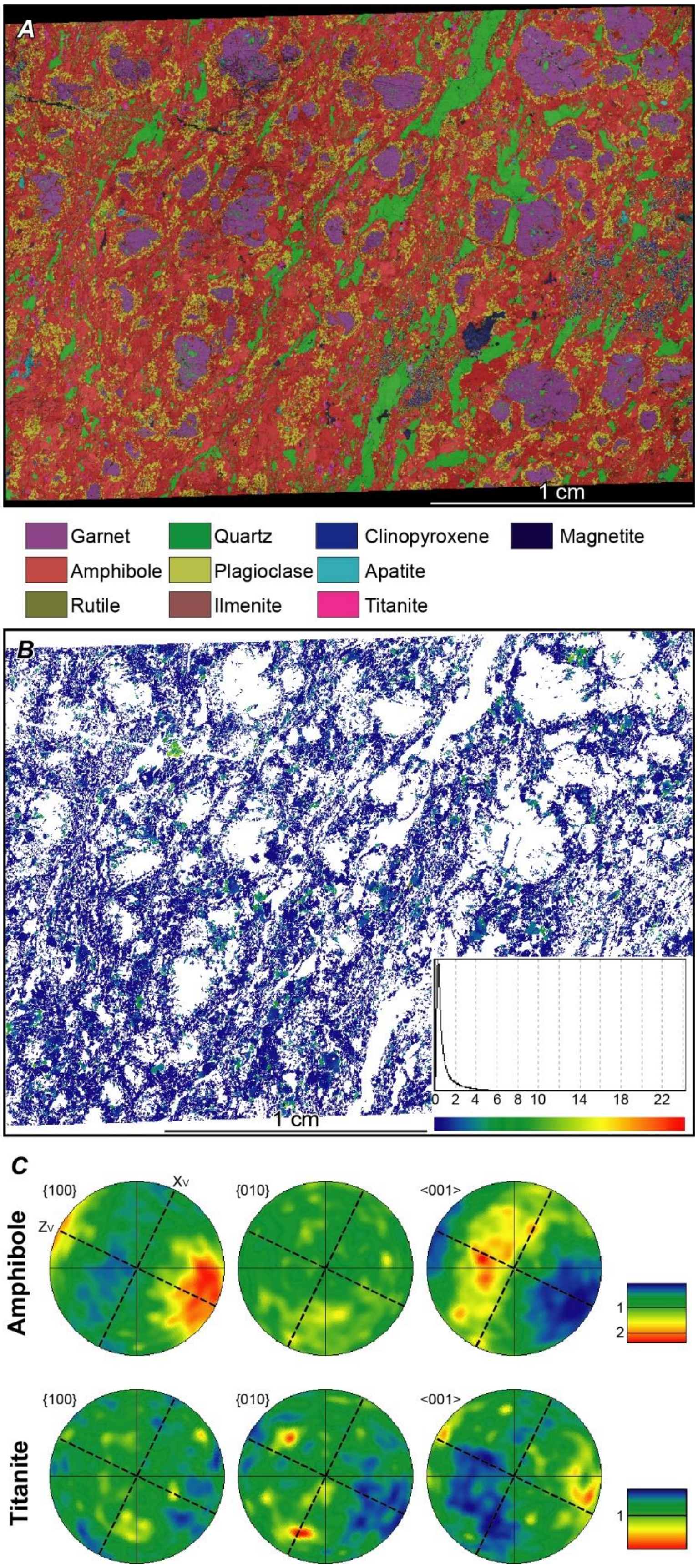
A
1 cm
Garnet
Quartz
Clinopyroxene
Magnetite
Amphibole
Plagioclase
Apatite
Rutile
Ilmenite
Titanite
B
1 cm
0 2 4 6 8 10 14 18 22
C
{100}
Xv
Zv
{010}
<001>
Amphibole
1
2
{100}
{010}
<001>
Titanite
1

Figure 7: EBSD results from strongly retrogressed eclogite (AR481). (A) Phases map from the whole thin section and associated GROD Angle map of amphibole grains (B), resolution of 9 µm. (C) Orientations of amphibole and titanite in the Wulf lower hemisphere stereogram. X_V and Z_V orientations of the stereograms are not parallel to the borders of the maps A and B.

4.5. Thermodynamic modelling

4.5.1. Peak pressure record (eclogite AR483)

In this sample (AR483), the M1 stage is defined by garnet core composition and its inclusions (Cpx_1 + quartz + rutile) and omphacite (Cpx_1) within the matrix. Scarce epidote and amphibole inclusions in garnet cores (Grt_1) indicates that the rock was not fully dehydrated during the crystallization of the garnet cores. The amount of H_2O was investigated through P–MH_2O and T–MH_2O phase diagrams (Fig. S2A and B). These diagrams indicate that an amount of c. 0.4 wt% of H_2O is necessary to crystallize epidote during the prograde metamorphism. At higher H_2O content, rutile is replaced by titanite. The absence of titanite inclusions in garnet cores and the presence of numerous inclusions of rutile suggest H_2O undersaturated conditions for the M1 stage.

The Grt + Cpx + Rt + Qtz mineral assemblage is observed above the stability field of plagioclase with additional phases (Ttn, Ep, Amph, H_2O or melt) (Fig. 8A). Measured grossular, almandine and pyrope isopleths of Grt1 and jadeite isopleth of Cpx1 intersect at ~ 710 °C and 1.75 GPa (Fig. 8A) in the stability field of Cpx + Grt + Amph + Rt + H_2O, which is consistent with the observed garnet inclusions (compositions used for minerals isopleths are summarized in Table S2). Considering analytical uncertainties from Grt_1 composition, the Qcmp factor reaches 100% between ~ 650–750 °C and 1.70–1.95 GPa and at ~ 780 °C and 1.53 GPa (Fig. 8B). The first P–T conditions at 650–750 °C and 1.70–1.95 GPa are also consistent with the observed jadeite content of Cpx1. Therefore, P–T conditions defined by the Grt_1 and Cpx_1 isopleths at ~ 710 °C and 1.75 GPa are interpreted as the conditions of the M1 stage.

The P–T phase diagram shown in Figure 8A indicates that epidote was not stable at the M1 conditions whereas it is predicted to be stable at lower P–T conditions. This suggests that epidote could be the only relict of the prograde stage. However, because the epidote stability is strongly dependent on Fe_2O_3 and H_2O content, that are difficult to quantify with confidence, the prograde P–T path is not constrained.

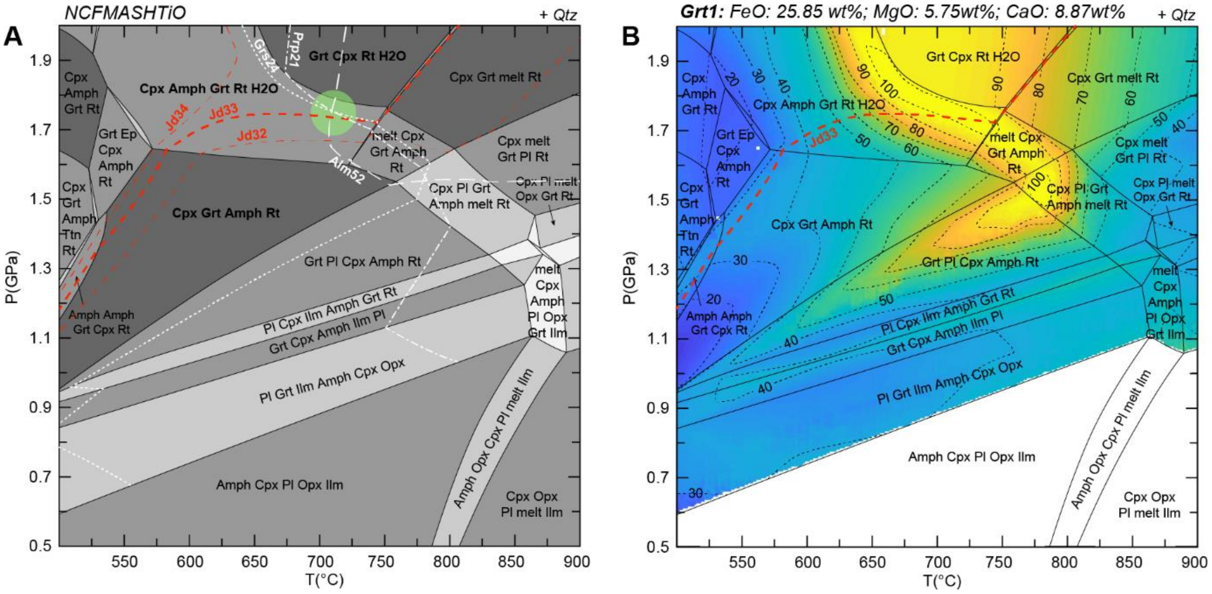

Figure 8 : Phase diagram obtained from sample AR483: (A) Mineral assemblage diagram of sample AR483 with isopleths of jadeite content in Cpx_1 (in red) and of almandine, grossular and pyrope contents in Grt_1 (in white). The green ellipse indicates the region most consistent with Cpx_1 and Grt_1 compositions defining the M1 conditions. (B) Modelling of the Qcmp factor of the mineral composition of garnet core (Grt_1) based on CaO, MgO and FeO contents (Table S2). Amph: amphibole; Cpx: clinopyroxene; Ep: epidote; Grt: garnet; Ilm: ilmenite; Opx: orthopyroxene; Pl: plagioclase; Qtz: quartz; Rt: rutile; Ttn: titanite.

4.5.2. Retrograde path of weakly retrogressed eclogite AR483

The M2 stage consists of Grt_2 + Cpx_2 + $Amph_2$ + Pl_2 + Qtz + Rt/Ilm. The amount of H_2O required to stabilize amphibole was investigated through a P–MH_2O diagram (Fig. S2C). The best estimate of H_2O content is again constrained at c. 0.4 wt% to avoid the stability of orthopyroxene at low-water content and titanite at higher-water content.

The computed phase diagram is shown in Figure 9A. The M2a mineral assemblage (Grt + Cpx + Amph + Pl + Qtz + Rt) is predicted to be stable at temperatures below 850 °C for a pressure of 1.6 GPa. Between 750 °C and 850 °C, melt is expected. Considering the mineral assemblage and the grossular, almandine and pyrope isopleths of the Grt_2 (compositions in Table S2), the best P–T estimate (Qcmp factor = 100%) for M2a are ~ 800 °C and 1.50 GPa (Fig. 9A and B). The highest jadeite content isopleth of Cpx_2 (XJd = 25 mol%; Table S2) is also consistent with these P–T conditions (Fig. 9A). Considering the Cpx_2-symplectite and Grt_2 equilibrium observed in this sample, we propose the conditions 800 °C and 1.50 GPa for of the stage M2a.

The M2b stage is characterized by the replacement of rutile by ilmenite, and the formation of Pl_2-$Amph_2$-corona around garnet. The crystallization of ilmenite at the expense of rutile and the decrease of jadeite content in the Cpx_2 are consistent with a decompression down to ~ 0.80–0.90 GPa (Fig. 9A). The lack of orthopyroxene constrains the maximum temperature of the M2b stage at 775 °C. The highest values of Qcmp factor for $Amph_2$ in the symplectite and in the corona (80% and 70% respectively) indicate pressure conditions between 0.9 and 1.1 GPa (Fig. 9C and D). These pressure conditions are also consistent with the Cpx_2 jadeite content (11% to 25%) (Fig. 9C and D). These relatively poor Qcmp values (80% and 70%) may be related to uncertainties in the thermodynamic models (Duesterhoeft & Lanari, 2020) or local equilibrium for which the selected reactive bulk composition becomes inappropriate (Lanari & Engi, 2017).

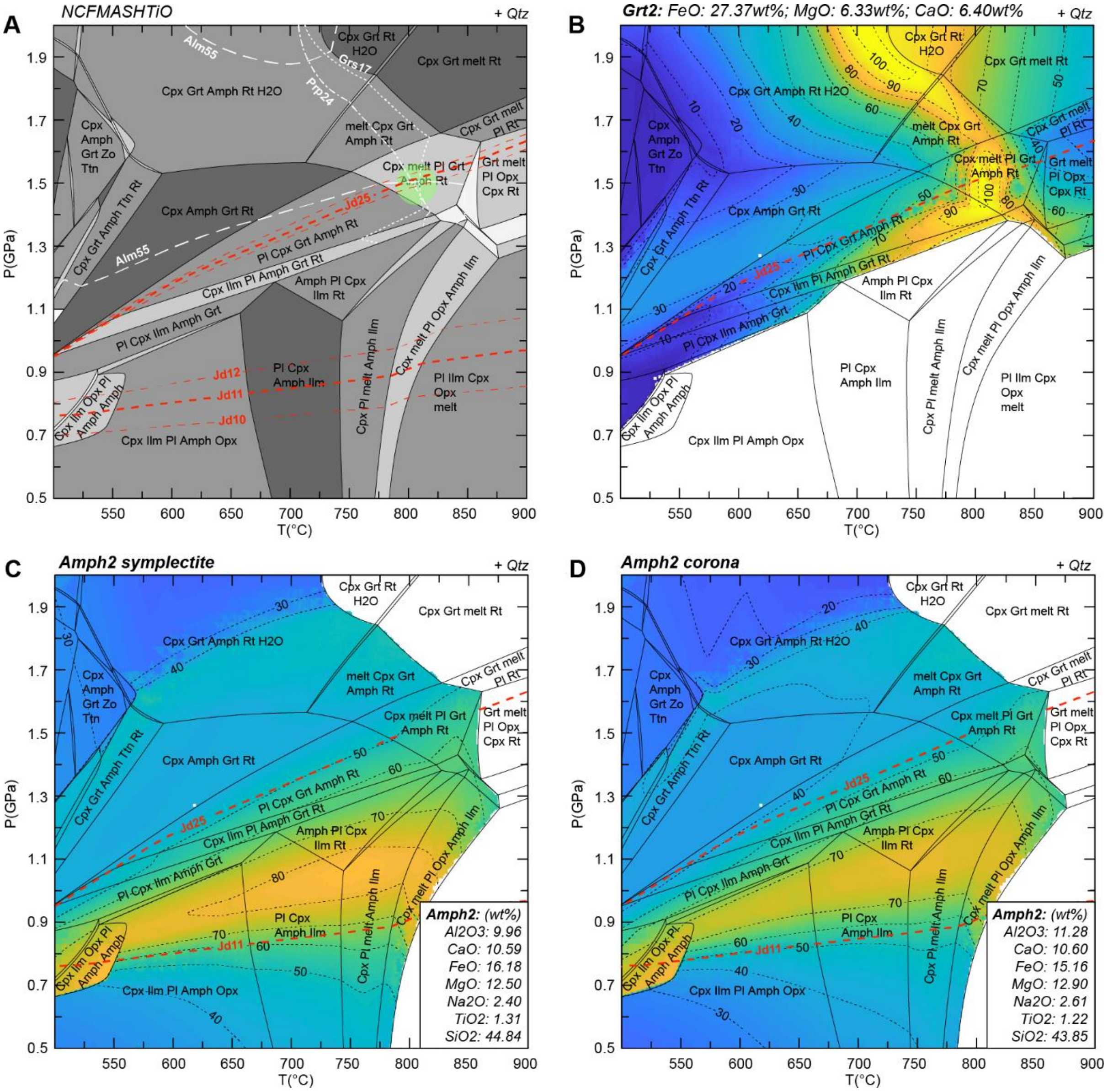

Figure 9 : Phases diagrams obtained from sample AR483 bulk composition without garnet core and its inclusions. (A) Mineral assemblage diagram with isopleths of highest and lowest jadeite contents in Cpx$_2$ (in red) and of almandine, grossular and pyrope contents in Grt$_2$ (in white). The green ellipse indicates the region most consistent with jadeite rich Cpx$_2$ and Grt$_2$ compositions defining the M2a conditions. (B) Modelling of the Qcmp factor of the garnet overgrowth (Grt$_2$) based on CaO, MgO and FeO contents (Table S2). (C and D) Modelling of the Qcmp factor of the symplectite and corona amphiboles (Amph$_2$) based on CaO, FeO, MgO, Na$_2$O, TiO$_2$, SiO$_2$ and Al$_2$O$_3$ contents (Table S2). Amph: amphibole; Cpx: clinopyroxene; Grt: garnet; Ilm: ilmenite; Opx: orthopyroxene; Pl: plagioclase; Qtz: quartz; Rt: rutile; Ttn: titanite.

4.5.3. Strongly retrogressed eclogite AR481

Sample AR481 is characterized by the replacement of clinopyroxene and garnet by amphibole ($Amph_3$) and plagioclase (Pl_3) and rutile by ilmenite. The increase of amphibole mode requires the addition of H_2O prior or during the M3 stage. The P–MH_2O diagram, shown in Figure 10A, suggests that the mineralogical evolution observed requires an increase of the water content from at 0.4 wt% to at least 1.6 wt%. In the sample AR481, during the final retrograde stage, ilmenite and remnants of rutile are replaced by titanite and minor chlorite crystallized in garnet fractures. The amount of H_2O required to stabilize this final paragenesis, without the crystallization of epidote, was constrained between 1.6 and 2.5 wt% at LT–LP conditions (Fig. S2D). To conclude, the retrogression of eclogite into amphibolite is characterized by an increase of H2O content all along the retrograde path from ~0.4 to 2.5 wt%.

The phase diagram shown in Figure 10B, has been computed with a H_2O content of 2.4 wt%. The mineral assemblage Amph + Pl + Qtz + Ilm forms a large stability field ranging between ~525–775 °C and 0.35–0.90 GPa (less than 0.20 GPa if we include the stability field with a second amphibole). If we consider the $Amph_3$ composition, the highest Qcmp factor (70%) is obtained between ~630–715 °C and 0.22–0.34 GPa (Fig. 10C; Table S2). These conditions are consistent with the stability of Ca-Amph + Fe-Amph + Grt + Pl + Qtz + Ilm. Qcmp factor of the Pl_3 composition reaches 100% in the stability field of Amph + Grt + Pl + Ilm + Qtz from ~ 700 °C and 0.85 GPa to 580 °C and 0.40 GPa (Fig. 10D; Table S2). The combination of Pl_3 and $Amph_3$ best P–T estimates roughly define HT-LP conditions at ~650–700 °C and 0.20-0.60 GPa. The last stage of M3 metamorphism corresponds to the appearance of titanite at P–T conditions below 500 °C and 0.5 GPa.

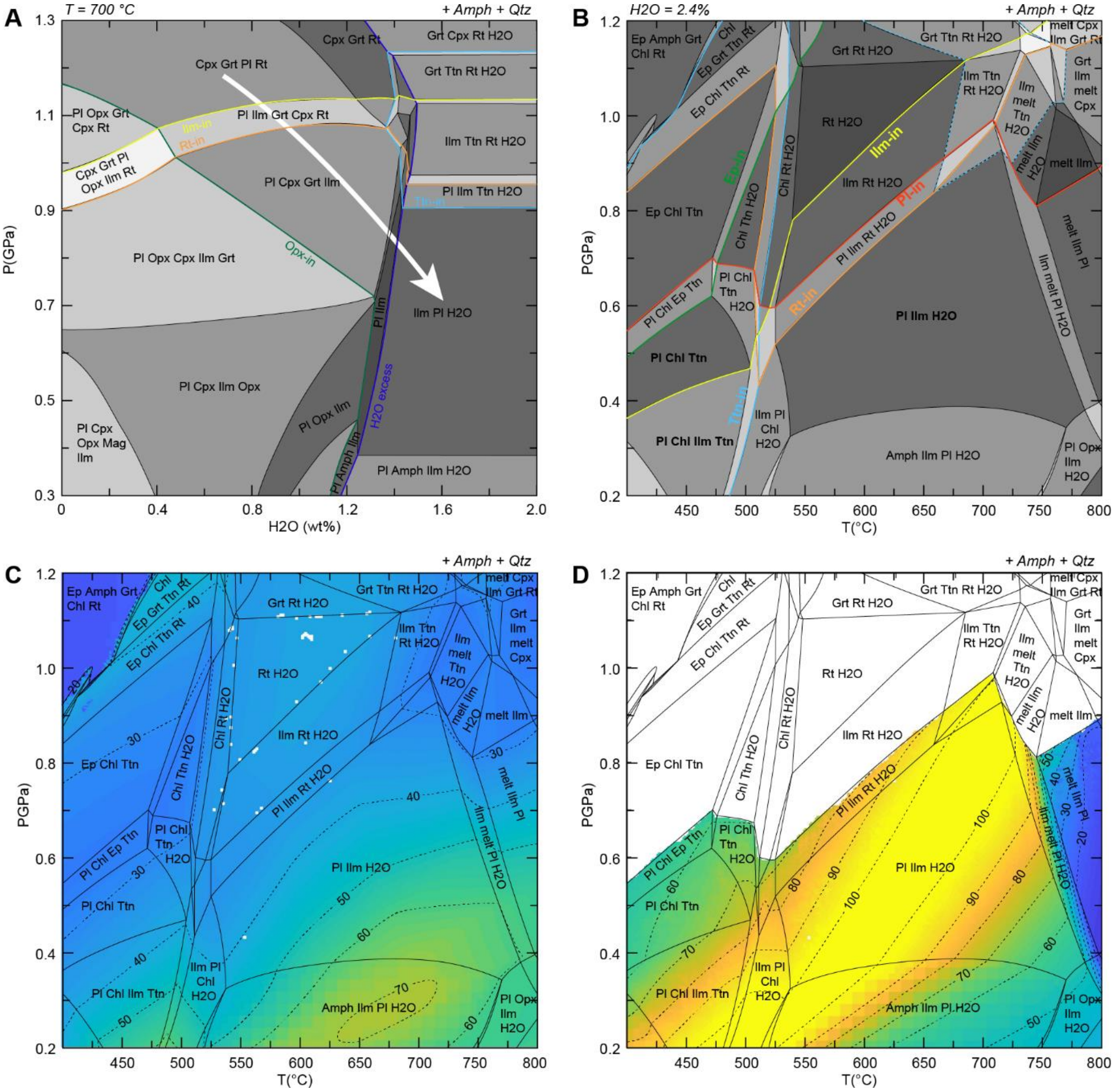

Figure 10: Phases diagrams obtained from sample AR481: (A) P–MH_2O diagram highlighting the increase of water content during the decompression of the eclogite constrained by the appearance of titanite at high-pressure and high-water content conditions and orthopyroxene at low-pressure and low-water content conditions. (B) Mineral assemblage diagram obtained from sample AR481 bulk composition with high-water content (H_2O = 2.4 wt%). (C) Modelling of the Q_{cmp} factor of large euhedral amphibole ($Amph_3$) based on CaO, FeO, MgO, Na_2O, TiO_2, SiO_2 and Al_2O_3 contents (Table S2). (D) Modelling of the Q_{cmp} factor of the plagioclase (Pl_3) based on CaO, Na_2O, SiO_2 and Al_2O_3 contents (Table S2). Amph: amphibole; Chl: chlorite; Cpx: clinopyroxene; Ep: epidote; Grt: garnet; Ilm: ilmenite; Opx: orthopyroxene; Pl: plagioclase; Qtz: quartz; Rt: rutile; Ttn: titanite.

4.5.4. Empirical thermobarometry of local equilibria

Temperatures of the Cpx_2–$Amph_2$–Pl_2 symplectite in sample AR483, were estimated with the amphibole–plagioclase thermometer of Holland & Blundy (1994) and range from 550 °C to 770 °C (Fig. 11A). The clinopyroxene–hornblende–plagioclase thermo-barometer of Waters (2003) was used with two distinct compositions of amphibole located in the symplectite (Amph$_2$ symplectite in Table S2) and a fixed composition of plagioclase (Pl$_2$, Table S2). Our results show that the symplectite crystallized at P–T conditions ranging from ~1.65 GPa and 765 °C to ~1.0 GPa and 625 °C for both amphibole compositions (n = 302313; Fig. 11A). These P–T conditions are consistent with plagioclase stability modelled with the bulk composition of sample AR483 with garnet cores excluded (Fig. 9). Both P-T conditions carried out via forward and inverse modeling are consistent (Fig. 9 and 11).

4.5.5. Zr-in-rutile trace element thermometry

One hundred and twenty analyses were performed on 80 rutile crystals from samples AR483 and 40 rutiles from AR481 (Table S3). In the weakly retrogressed eclogite (AR483), Zr contents of rutile inclusions in garnet vary between 245 and 566 ppm with a mean value of 421 ppm and a standard deviation of 162 ppm (2σ, n = 27). Zr contents of matrix rutile range from 309 to 644 ppm with a mean value of 435 ppm and a standard deviation of 126 ppm (2σ, n = 53). The estimated temperature values for rutile inclusions in garnets (n= 27) and matrix rutile (n= 53) range between 655 °C to 726 °C and between 673 °C to 739 °C, respectively (Fig. 11C, Table S3) with mean temperatures of 698 ± 36 °C (n = 27) and of 702 ± 26 °C (n = 53) for rutile inclusions and matrix rutile, respectively. The histogram of Zr-in-rutile temperature shows modal and similar distributions for the two populations (i.e. rutile inclusions and matrix-rutile grains) centred around ~700–710 °C (Fig. 11C). All of these data yield a mean temperature of 701 ± 30 °C (n= 80).

For the strongly retrogressed eclogite (AR481), the Zr contents of rutile inclusions range between 280 and 582 ppm with a mean value of 376 ppm and a standard deviation of 170 ppm (n = 16). Zr contents of matrix rutile vary between 356 ppm and 729 ppm with a mean value of 503 ppm and a standard deviation of 156 ppm (n = 24). Estimated temperatures for the inclusion rutile (n=16) range between 665 °C and 729 °C (Fig. 11D). Histogram of Zr-in-rutile temperature for inclusion rutile shows a bimodal distribution with a high temperature peak at ~695 °C and a low temperature peak at ~670 °C (Fig. 11D). The low temperature group composed by six analyses has a mean temperature of 670 ± 6 °C while the group at higher temperature (except one analysis at 729 °C), yields an average temperature of 696 ± 20 °C (n=9). The twenty-four analyses obtained on matrix rutile yield temperatures ranging from 685 °C to 750 °C with a mean temperature of 715 ± 28°C.

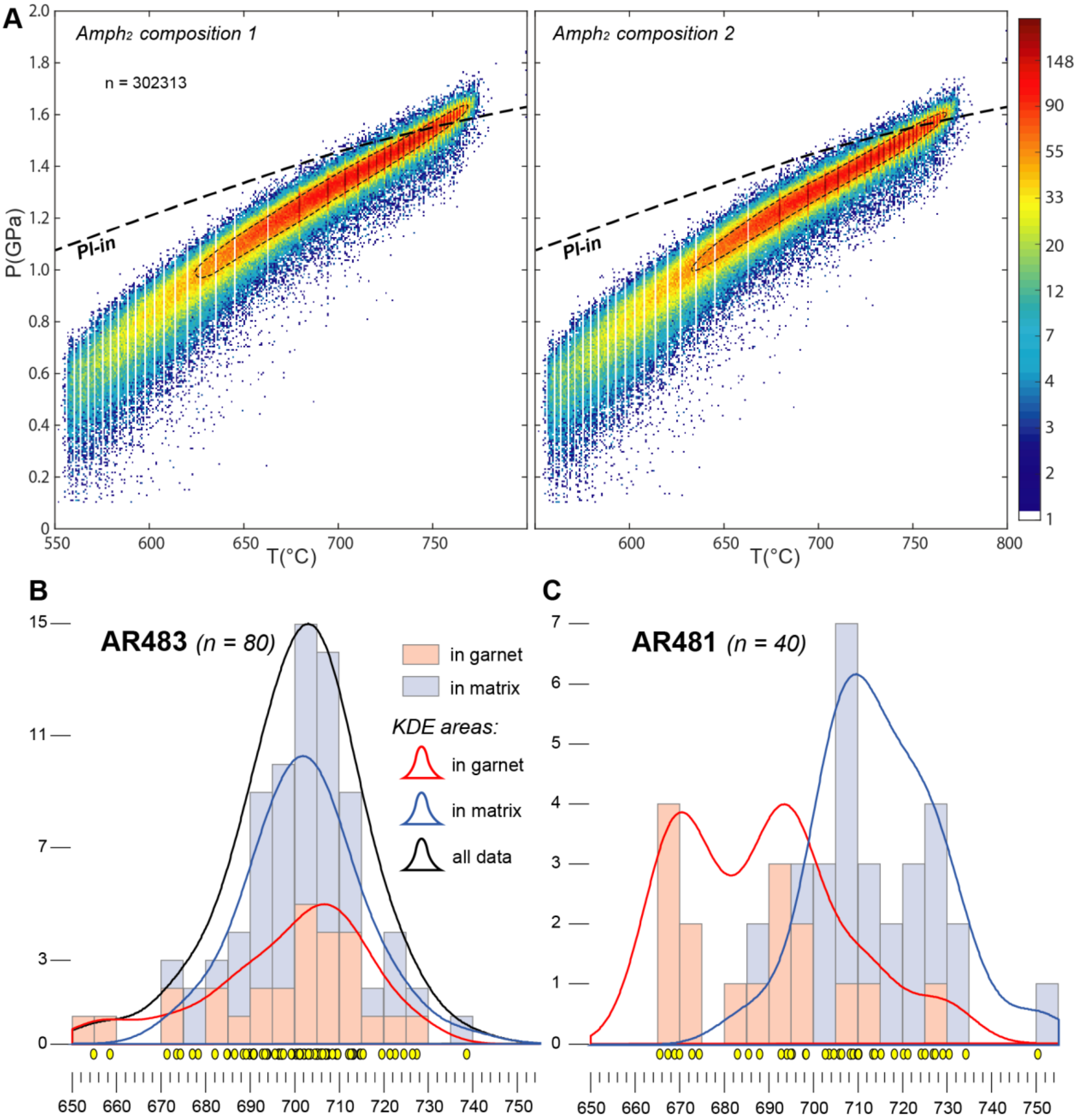

Figure 11 : Empirical and semiempirical thermobarometers and thermometers. (A) Range of P–T conditions of clinopyroxene within symplectite using calibration of Waters (2003) based on fixed composition of plagioclase and two compositions of amphibole within symplectite (Table S2). Temperatures are estimated from the edenite-richterite calibration of Holland & Blundy (1994). Plagioclase-in curve is from the mineral assemblage diagram of Figure 9. Zr-in-rutile thermometer results from sample (B) AR483 and (C) AR481. Diagrams and KDEs obtained from Density Plotter software (Vermeesch, 2012). Bandwidth = 5; Bin width = 5.

4.6. U-Th-Pb geochronology

4.6.1. Zircon dating

The zircon crystals from both samples are transparent and colourless. Zircon ranges in shape from rounded to sub-euhedral, equant to elongate and some grains are multi-faceted typical of HP rocks. CL images show prismatic crystals characterized by oscillatory zoning and rounded edges reflecting probably the magmatic growth of the crystals and rounded crystals with an irregular, chaotic and patchy zoning often described in HP zircons (Corfu et al., 2003). A few grains show cores, which are CL-dark with patchy or sector-like zoning or oscillatory zoning and rims, which are bright and featureless in CL (Fig. 12A and B).

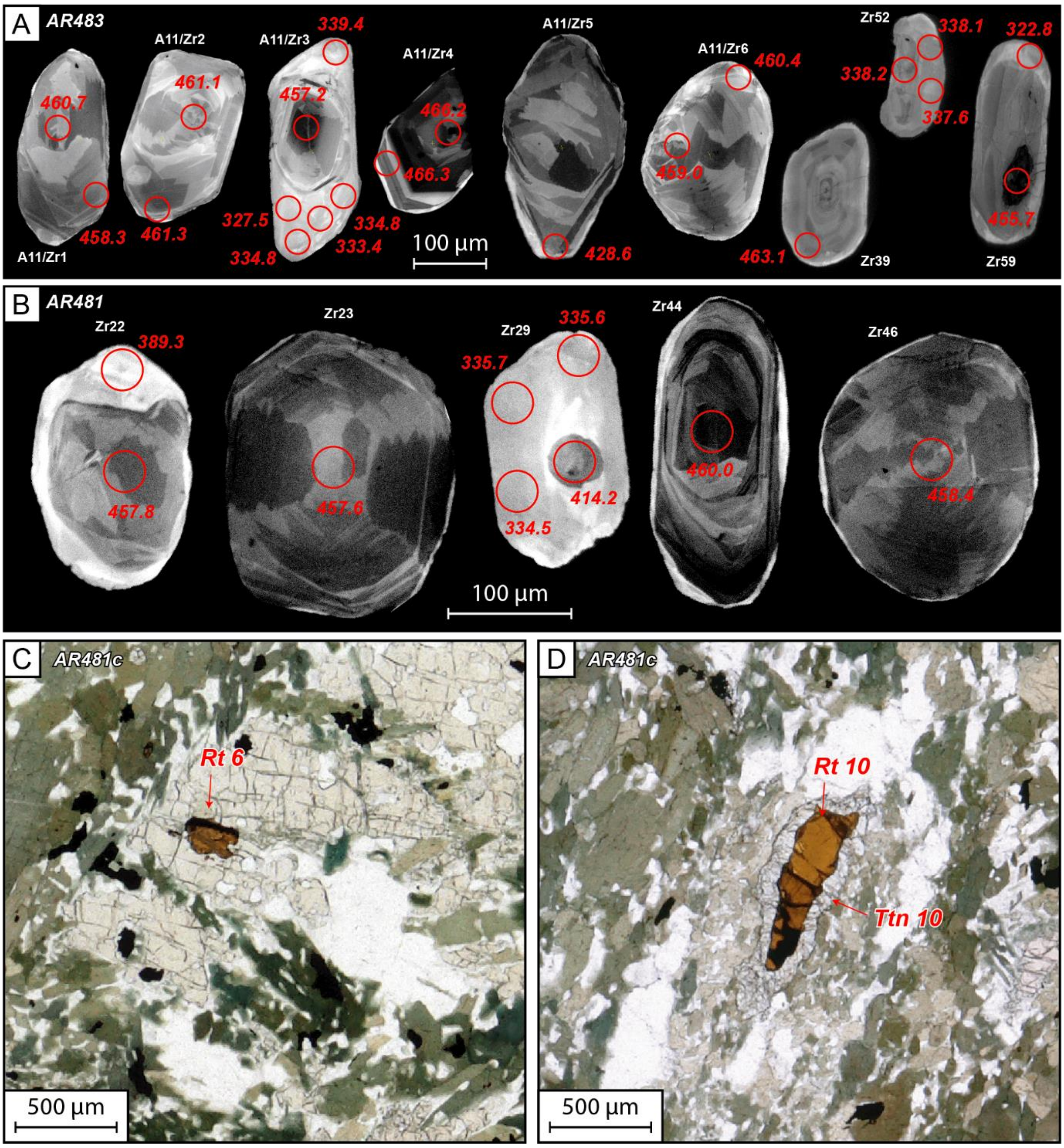

Figure 12: Cathodoluminescence photos of zircons from (A) Sample AR483 and (B) Sample AR481. Rutile from thin section AR481C (C) in garnet inclusion and (D) in the matrix with titanite-coronas also dated.

4.6.1.1. Weakly retrogressed eclogite AR483

Seventy-five analyses were performed on fifty-nine zircons (Table S6). In a concordia diagram, the two distinct populations of zircon can be distinguished around c. 460 Ma and c. 330–340 Ma (Fig. 13A). The major and oldest population is characterized by low to medium Pb (3.2–20 ppm), U (44–247 ppm) and Th (most 7.6–55 ppm) contents with Th/U ratios in the range 0.14 to 0.46. It consists essentially of cores with oscillatory zoning and a few CL-dark rims (Table S6; Fig. 12A). Fifty-five data yield a concordia age of 461.6 ± 1.2 (MSWD(C+E) = 1.02) (Fig. 13A). The youngest population (ca. 330 Ma) is constituted by eleven data performed on two zircon rims (Zr59 and A11/Zr3), bright and featureless in CL and on three grains likely neoformed (Zr23, Zr63 and Zr52) (Fig. 12A). Except for one (Zr63), these analyses have very low to low Pb (0.9– 2.4 ppm), U (18–49 ppm) and Th (most 0.1–1.8 ppm) contents and low Th/U ratios (< 0.01) (Table S6). Among these, ten analyses yield a concordia age of 337.3 ± 4.7 Ma (MSWD(C+E) = 2.2). The discordant position of the analysis obtained for the CL-bright rim of zircon Zr59 (dashed line) is probably due to common-Pb contamination. The three concordant ellipses around c. 440 Ma (Zr27), 390 Ma (Zr19) and 365 Ma (Zr15) may correspond to a mixture between the Ordovician component (460 Ma) and the Variscan component (330–340 Ma).

4.6.1.2. Strongly retrogressed eclogite AR481:

Sixty-eight analyses were carried out on fifty-three zircons (Table S6; Fig. 13B). The results are very similar to those obtained on zircon of the sample AR483. The data form a cluster around 460 Ma. These analyses of cores and rims are characterized by low to medium Pb (most 2.7–22 ppm), U (most 37–287 ppm) and Th (most 6.2–52 ppm) contents with Th/U ratios in the range 0.12 to 0.27. Sixty-one analyses yield a concordia age of 461.7 ± 1.6 Ma (MSWD(C+E) = 1.09, n = 61) (Fig. 13B). Only analyses obtained on the CL-bright rim of zircon Zr29 yielded young date at 334 ± 12 Ma (n = 3) using a lower intercept (Fig. 11B and 12B). This rim has very low to low Pb (1.3–1.4 ppm), U (27–30 ppm) and Th (0.1–0.3 ppm) contents and low Th/U ratios (< 0.01).

4.6.2. Rutile dating

Rutile of both dated samples shows euhedral to anhedral forms with a reddish color. Each grain is generally unzoned in BSE images, with no indication of preservation of more than one generation. Rutile of the sample AR481 analysed in situ on a thin section (AR481c) forms mainly crystals in the matrix composed of amphibole, plagioclase and quartz, but also occurs as inclusion in garnet (Fig. 12C and D). Matrix rutile has titanite-coronas. The eclogitic samples have rutile with low U contents between 0.5 and 20 ppm and very low Pb contents of 0.02–0.5 ppm (Table S6).

4.6.2.1. Weakly retrogressed Eclogite AR483:

Fifty-one separate rutile crystals (100–200 µm size) were analysed. In a Tera-Wasserburg diagram, the ellipses plot in concordant to discordant position according to the various proportions of common Pb compared to the radiogenic Pb. The linear regression using all data yields a lower intercept date of 330.1 ± 1.7 Ma (MSWD = 0.55, n = 51) and forty-four of these data give an equivalent concordia age of 330.6 ± 1.8 Ma (MSWD(C+E) = 1.02; n = 44) (Table S6; Fig. 13C).

4.6.2.2. Strongly retrogressed eclogite AR481 and AR481c

Nineteen separate crystals were dated (Table S6). Most of the data are close to the concordia curve, in the Tera-Wasserburg diagram (Fig. 13D). The linear regression using entire dataset gives a lower intercept date of 326.6 ± 3.3 Ma (MSWD = 0.41; n = 19). Twelve among these data yield a concordia age of 328.3 ± 3.7 Ma (MSWD(C+E) = 1.14).

Twenty spots on thirteen rutile grains were also analysed in situ on a thin section (AR481c). Among these analyses, eight were performed on eight crystals included in the garnet and yield a lower intercept date of 340.0 ± 8.6 Ma (MSWD = 0.34; n=8) (Fig. 13E; pink ellipse). Twelve spots were carried on five rutile crystals located in the mineral matrix. In the Tera-Wasserburg diagram, these ellipses are generally less discordant than those obtained on rutile included in garnet (Fig. 13E). The linear regression yields a lower intercept date of 339.9 ± 4.2 Ma (MSWD = 0.43; n=12) and five give a concordia age of 342.5 ± 8.0 Ma (MSWD(C+E) = 1.8). All these dates obtained on rutile included in garnet or in the matrix are similar within the uncertainties. The dataset obtained on 32 rutile grains (separate, inclusion and matrix) yield a lower intercept date of 331.7 ± 2.3 Ma (MSWD = 1.2; n = 39) and among these data, seventeen give a concordia age of 332.6 ± 4.0 Ma (MSWD(C+E) = 1.9) which is identical within uncertainty to the concordia age of 330.6 ± 1.8 Ma (MSWD(C+E) = 1.02; n = 44) obtained on the rutiles of the sample AR483.

4.6.3. Titanite dating

Nineteen analyses on seventeen titanite crystals were also analysed in situ on a thin section (AR481c). Part of the analysed titanite takes the form of a corona texture around rutile (Fig. 12C; Table S6).

Titanite has very low contents of U (1–4.6 ppm) and Pb (< 2 ppm) with low Th/U ratios (<1) (Table S6). The uncorrected data are plotted in the Tera–Wasserburg diagram (Fig. 13F), and a linear regression through all these analyses forms a lower intercept that yields a date of 297.6 ± 9.8 Ma (MSWD = 0.71; n = 19). The y-intercept of 0.872 ± 0.009 represents the initial 207Pb/206Pb (Aleinikoff et al., 2002), which can be used for common Pb correction (Stern, 1997; Frost et al., 2000). This value is in a relatively good agreement with the Stacey & Kramers (1975) terrestrial Pb evolution model (0.86 at 300 Ma). Subsequently, the individual 207Pb-corrected 206Pb/238U dates can be calculated and yield the weighted average of 297 ± 1 Ma (MSWD = 2.1; n = 19), consistent with the lower intercept date within the error range.

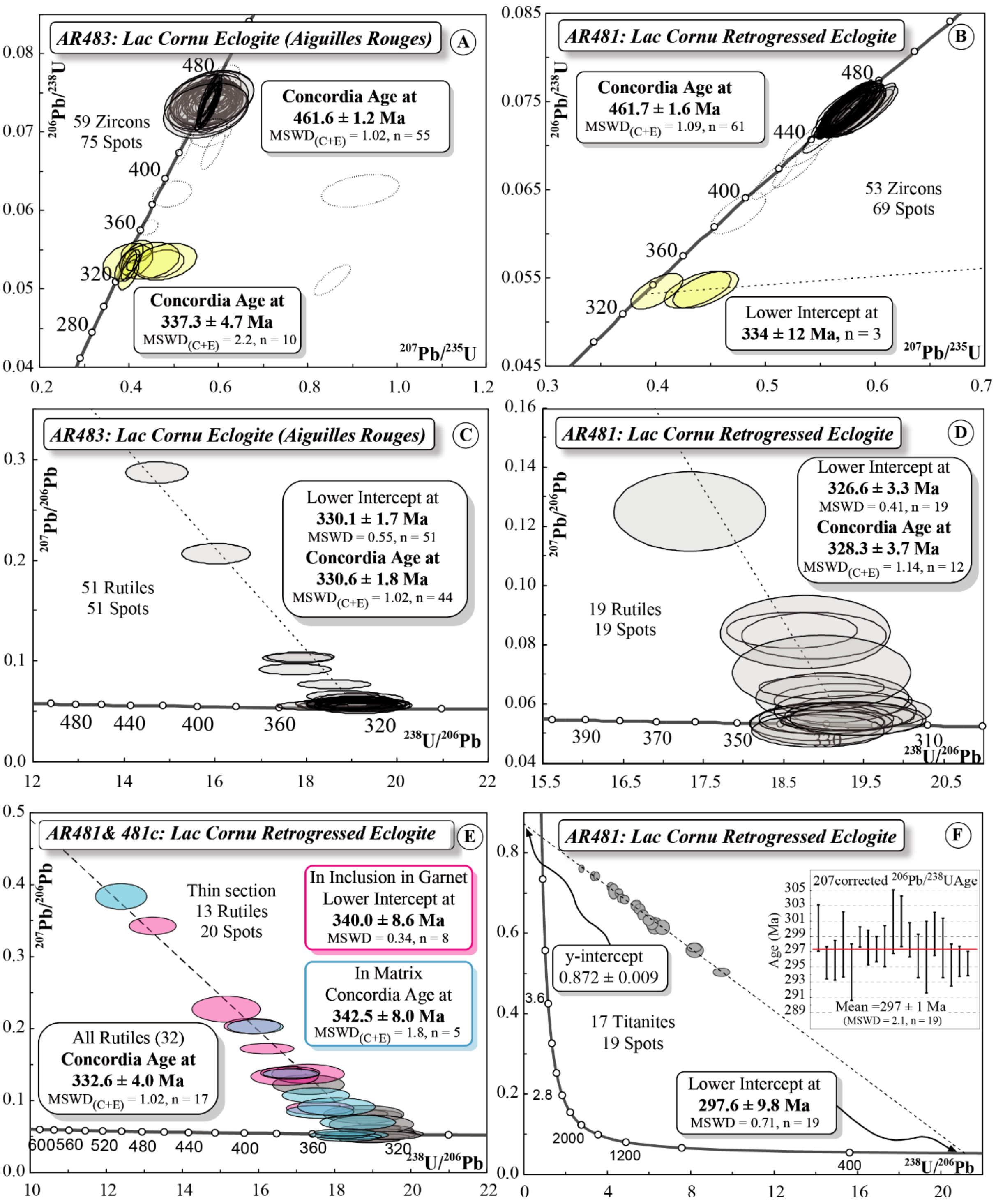

Figure 13 : U-Pb results of zircon, rutile and titanite datings from weakly retrogressed eclogite (AR483) and strongly retrogressed eclogite (AR481). Zircon separated grains U-Pb concordia diagrams (A and B). Rutile separated grains U-Pb Tera Wasserburg diagrams (C and D). Rutile separated and in situ grains from AR481 sample and AR481c thin section U-Pb Tera Wasserburg diagram (E). In situ titanite from AR481c thin section U-Pb Tera Wasserburg diagram (F). Error ellipses and uncertainties in ages are ± 2σ. Dotted ellipses are not

considered for the age calculation. MSWD (C+E): Mean Square of Weighted Deviates for Concordance and Equivalence.

4.7. Zircon trace element analyses

Fourteen trace element analyses were carried out on nine and two zircons for samples AR483 and AR481, respectively (Fig. 14; Table S7). The chondrite-normalised REE patterns of the zircon from these two eclogites are similar and exhibit two distinct populations of spectra according to the obtained ages. The first population is constituted by seven Ordovician cores (~455–460 Ma) and one core dated at c. 364 Ma. It is characterised by a steeply-rising slope from the Light REE (LREE) to heavy REE (HREE), in particular with a strong variable enrichment in heavy REE (HREE) with respect to middle REE (MREE) (LuN/SmN = 219–1038), and with a positive Ce anomaly (25.3–79.9) and a moderate negative Eu anomaly (0.64–0.78) (Fig. 14A). The total REE abundances are ranging between 184 ppm and 340 ppm with low LREE contents around 2 ppm (Table S7). The Variscan population consists mainly of zircon rims dated at c. 330 Ma as well as two analyses dated to c. 390 Ma. It shows lower total REE contents (27–159 ppm). It displays a weaker enrichment in HREE with respect to MREE (most LuN/SmN= 10.7– 59) but with a flat HREE pattern (most LuN/DyN = 1.64–4.35) at 30–110 times chondrite, with a positive anomaly in Ce (3.9–36.4) and no Eu anomaly (0.92–1.08) (Table S7; Fig. 14B).

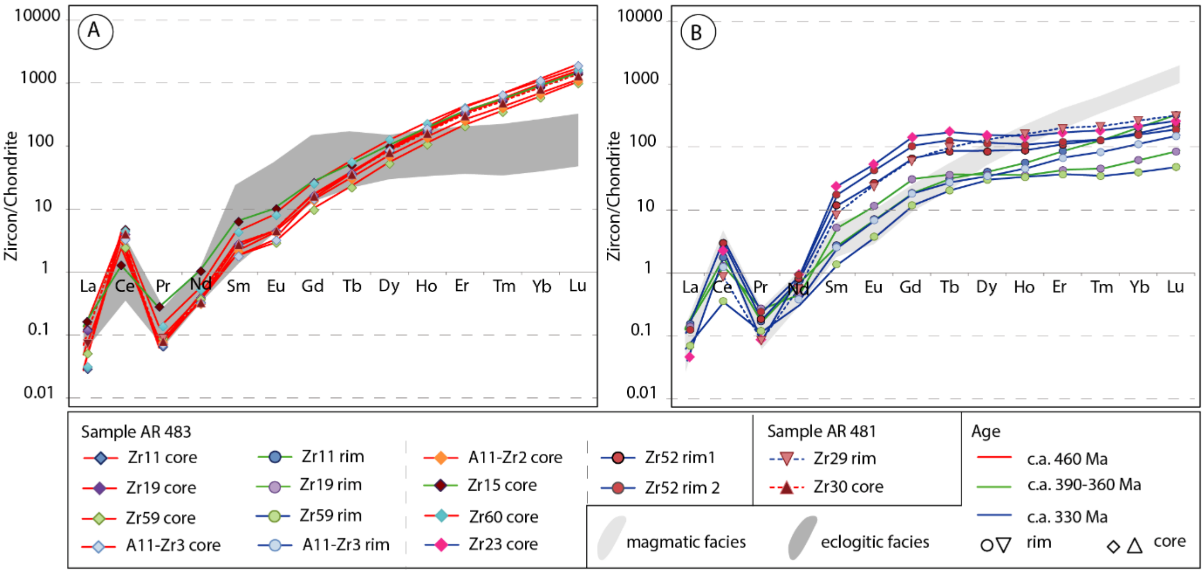

Figure 14 : Chondrite normalised REE patterns of zircon cores and metamorphic overgrowths from samples AR483 and AR481. (A) Zircon cores displaying Ordovician dates and characterized by a strong HREE enrichment

and a moderate negative Eu anomaly and (B) Zircon rims displaying Variscan dates and characterized by a flat HREE pattern and no Eu anomaly. Normalization values from Sun & McDonough (1989).

5. Discussion

5.1. P–T–D–t path of the ARM eclogites

Mineralogical and structural analyses coupled with thermodynamic modelling, geochronology and microstructural analyses allows the retrograde P–T–D–t evolution of the Lac Cornu eclogites to be reconstructed (Fig. 15A).

5.1.1. The high-pressure stage (M1)

Eclogitic facies M1 stage is defined by the Grt_1 + Cpx_1 + Qtz + Rt mineral assemblage. The Grt_1 and Cpx_1 compositions yield P-T conditions at 710 °C and 1.75 GPa (Fig. 8). The presence of a few epidote inclusions in garnet core indicates that garnet could have started to grow during the prograde path. However, garnet composition and zoning do not preserve chemical evidences of this prograde path, which were very likely overprinted by chemical diffusion at high-grade conditions (e.g. Yardley, 1977; Tedeschi et al., 2017).

Rutile crystallized at high-pressure conditions (Fig. 8). Rutile included and armoured Grt_1 cores yield slightly lower temperatures, between 650 to 730 °C, interpreted as the temperature of crystallization of rutile during the prograde M1 metamorphic evolution (Fig. 11B and C). In the most retrogressed sample (AR481), Zr-in-rutile thermometry of rutile in the matrix yields consistent temperatures though slightly higher from 680 °C and up to 750 °C (Fig. 11C). Considering a M1 peak pressure of 1.8 GPa with all the Zr-in-rutile temperatures, we obtain an average temperature for pressure peak of 701 ± 30 °C similar within uncertainties to those obtained by forward phase relation modelling (Fig. 15).

Geochronology on separated rutile grains, from samples AR483 and AR481, yield concordia ages of 330.6 ± 1.8 Ma and 328.3 ± 3.7 Ma respectively (Fig. 13C and 13D). In the strongly retrogressed eclogite AR481, in-situ dating of rutile included in garnet yields a similar age of 332.6 ± 4.0 Ma (Fig. 13E). We interpret these dates as the peak pressure age. Both eclogite samples contain zircon rims and neoformed crystals with very low Th/U ratios (<0.01), a lack of Eu anomalies, and only weakly enriched in HREE with respect to MREE with a flat HREE spectrum. These characteristics suggest zircon grew in equilibrium with a garnet-bearing and plagioclase-free assemblage under eclogite facies conditions (Rubatto, 2017). Metamorphic zircon from eclogite samples AR483 and AR481 yield a concordia age of 337.3 ± 4.7 Ma and a lower intercept date of 334 ± 12 Ma, respectively (Fig. 13A and B), both interpreted as the age of the peak pressure. In summary, U-Pb dating of zircon and rutile provides a reliable timing of HP metamorphism in the ARM between 330–340 Ma.

EBSD results obtained on the weakly retrogressed eclogite (AR483) highlight different CPO between matrix minerals and inclusions in garnet. We interpret this result as evidence of deformation prior to D_H recorded by the Cpx_1 and rutile armoured in the garnet cores, and unrecognized at the macro-scale on the field. We speculate that this deformation is related to crustal thickening, and possible nappe stacking, that took place contemporaneously with prograde metamorphism and before the pressure peak at 330–340 Ma (Fig. 15A).

5.1.2. Onset of the decompression (M2)

The onset of the decompression path (stage M2) is highlighted by the crystallization of Grt_2 rims, Cpx_2–Pl_2–$Amph_2$ symplectites and rutile breakdown into ilmenite (Fig. 9 and 15). This decompression is also emphasized by the progressive decrease of jadeite content in Cpx_2 (Fig. 5B). Grt_2 and Cpx_2 compositions indicates P–T conditions of ~800 °C and 1.5 GPa (Fig. 9) interpreted as conditions of the early stage of decompression temperature in suprasolidus conditions. Thermobarometry applied on Cpx_2 and $Amph_2$ indicates a progressive pressure decrease from ~1.6 to 0.9 GPa. Combining all these data, we propose that the decompression from 1.6 to 0.8 GPa occurred at temperatures between 650 and 775 °C (Fig. 9 and 11A). The preservation of garnet zoning may suggest that the rocks were not exposed to the high-temperature conditions for a long time (e.g. O'Brien, 1997).

EBSD results on sample AR483 indicate that clinopyroxene in symplectite (Cpx_2) is weakly plastically deformed. We suggest that symplectite growth was contemporaneous with DH deformation active during the onset of decompression. Therefore, we suggest that the development of the sub-horizontal S_H along the decompression path occurred during unroofing of lower crustal material. In the gneissic basement, the sub-horizontal S_H foliation is associated with widespread anatexis, suggesting that D_H could be associated with horizontal flow of the lower anatectic crust (e.g. Beaumont et al., 2001; Vanderhaeghe, 2009; Rosenberg et al., 2007) that began after the peak of pressure at c. 330–340 Ma.

5.1.3. Late exhumation stage (M3)

The most retrogressed mafic boudins (AR481) consist of plagioclase (Pl_3) + amphibole ($Amph_3$) + quartz + ilmenite + titanite ± chlorite (Fig. 4B) predicted to be stable below 500 °C and 0.5 GPa, suggesting that the ARM was affected by a late HT-LP metamorphism (Fig. 10B). Although the Qcmp factor of Amph3 is low (i.e. 0.70%), we consider this result as meaningful because similar P–T conditions have already been obtained on metasedimentary rocks of the ARM (Genier et al., 2008; Chiarada, 2003). Furthermore, HT-LP metamorphism has also been identified in the north-eastern ARM (Fully area, Fig. 1C) with cordierite-bearing migmatites (Krummenacher, 1959; Bussy et al., 2000).

The CPO of amphibole (Amph3) in sample AR481 is consistent with high-temperature (>600 °C) and low-stress conditions (Ko & Jung, 2015) during an active shearing (e.g. Ko & Jung, 2015; Kim & Jung, 2019; Getsinger & Hirth, 2014). Furthermore, CPO of titanite also indicates crystallization during active shearing (Papapavlou et al., 2017). Therefore, crystallization of $Amph_3$ and titanite are coeval with D_V shearing. Titanite exhibits low U and Pb contents with high proportion of common Pb, resulting in a large uncertainty on the calculated age. Moreover, Sun et al. (2012) demonstrated that titanite can be up to ~12 % younger than their known ages using either spot or raster analyses when a zircon standard is used, so we cannot completely rule out that this lower intercept age could be younger than the titanite crystallization age. Thus, the lower intercept date (297.6 ± 9.8 Ma) is interpreted as a minimum age of the crystallization age of titanite. Nonetheless, this age at c. 300 Ma is consistent with Ar/Ar radiogenic ages at c. 300 Ma obtained on muscovite from gneissic boulders in the Salvan-Dorenaz syncline (Capuzzo et al., 2003). Therefore, titanite crystallization at conditions below 500 °C and 0.5 GPa (Fig. 10) was synchronous with the D_V deformation and the latest stage of exhumation of the ARM at ~300 Ma (Fig. 13F). This timing also corresponds to the emplacement of the Vallorcine and Mont-Blanc granites during the dextral (D_V) shearing deformation at c. 305 Ma (Bussy & von Raumer, 1993, 1994; Bussy et al., 2000). Since the dextral shearing began at suprasolidus conditions (Genier et al., 2008; von Raumer & Bussy, 2004) with the crystallization of anatectic melt starting to occur at 320 ± 1 Ma (Bussy et al., 2000), a minimum duration of dextral transpressional shearing stage of 20 Ma is proposed for the ARM (Fig. 15A). It is very likely that the transition between D_H lateral flow and D_V dextral shearing was progressive and that they were spatially partitioned during a single transpressive regime. This M3 HT-LP metamorphism is also dated at c. 305 Ma by the synchronous emplacement of the Crd-bearing Vallorcine pluton and Fully Crd-bearing migmatites (Bussy et al., 2000).

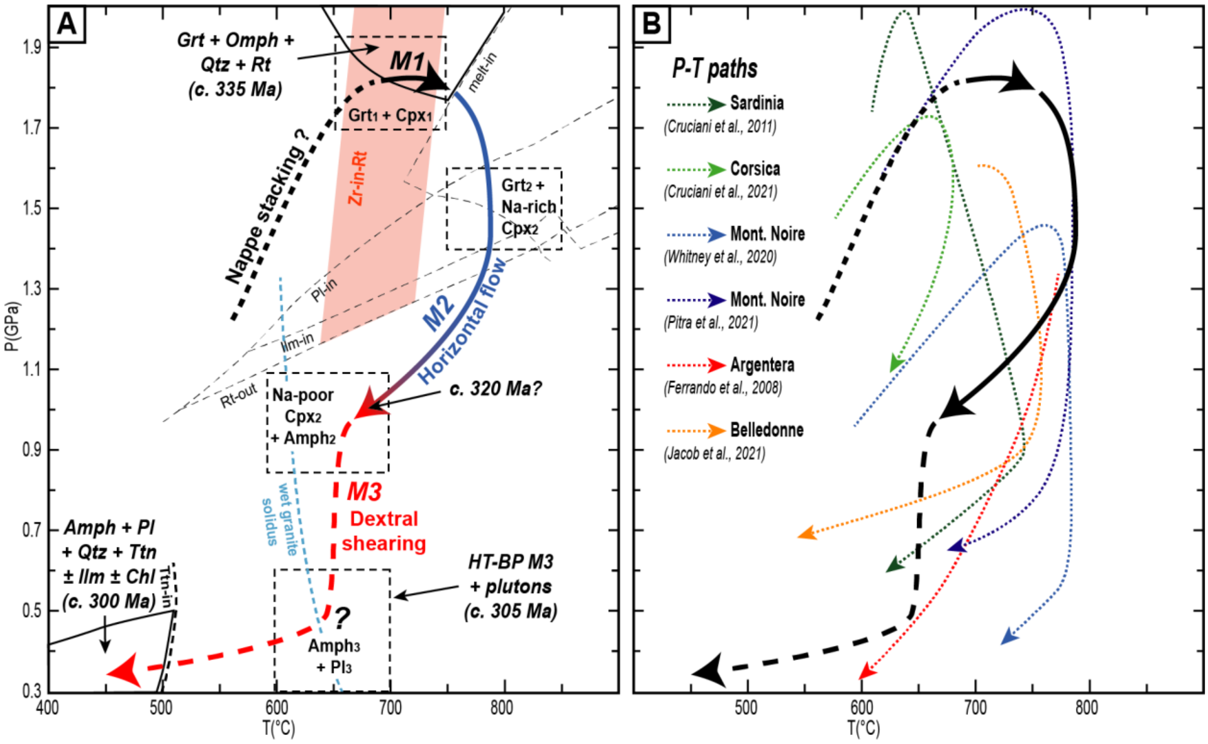

Figure 15 : (A) P–T–t–D path of the Lac Cornu eclogite inferred from thermobarometrical, geochronological and EBSD structural results. (B) Comparison with P–T paths from Corsica, Sardinia, Montagne Noire, Argentera and Belledonne massifs.

5.2. Significance of HT eclogites—are the eclogites of the ARM part of a suture zone?

Two main geodynamic mechanisms are proposed to explain the HP conditions reached by mafic rocks in the Variscan belt: (i) subduction-related eclogite, associated to either oceanic subduction (e.g. Jouffray et al., 2020; Bellot et al., 2010; Schneider et al., 2014; Lardeaux et al., 2001; Berger et al., 2010) or continental subduction (e.g. Giacomini, Braga, Tiepolo, Tribuzio, 2007; Miller & Thöni, 1995; Lotout et al., 2020) and (ii) continental crust thickening allowing material located at the roof of the crust to reach eclogitic conditions through horizontal compression and lateral flow (e.g. Whitney et al., 2015, 2020; Roger et al., 2020; Benmammar et al., 2020; Štípská & Powell, 2005).

Bulk rock compositions indicate that the protolith of Lac Cornu eclogite has a geochemical signature of tholeiitic basalt, probably N-type MORB (Fig. S1; this study; Paquette et al., 1989; Liégeois & Duchesne, 1981), as also reported for amphibolites near the Emosson Lake (von

Raumer et al., 1990). The U/Pb zircon ages at 461.6 ± 1.2 Ma and 461.7 ± 1.6 Ma (Fig. 13) were obtained on euhedral zircons or inherited cores that show oscillatory zoning (Fig. 12) and high Th/U ratios (>0.1) typical of magmatic zircon (Teipel et al., 2004; Linnemann et al., 2011). Thus, these ages are interpreted as the emplacement age of the tholeiitic protolith, in agreement with previous studies in the ARM (Paquette et al., 1989; Bussy et al., 2011), in the Argentera, Belledonne and Pelvoux massifs (Paquette et al., 1989; Rubatto et al., 2001, 2010; Fréville, 2016) (Table 1). Moreover, these zircons are enriched in HREEs over MREEs and have a positive Ce anomaly and negative Eu anomaly (Fig. 14), indicating a crystallization in the presence of plagioclase (Rubatto, 2002; Hoskin & Schaltergger; 2003). Thus, trace and REE patterns suggest that the eclogite protoliths from the ARM, Belledonne and Argentera massifs were tholeiitic sills or dykes intruding a thinned continental crust (Paquette et al., 1989; Ménot & Paquette, 1993; Rubatto et al., 2010). This interpretation is consistent with Ordovician magmatism observed in the whole northern Gondwana margin (e.g. Melleton et al., 2010 and references therein). Recently, Jouffray et al. (2020) identified a crustal-contamination in the geochemical signature of the basaltic protolith of the Argentera massif eclogite that could indicate high-temperature hydrothermalism or formation in a supra-subduction zone context. Unlike the late Devonian eclogites of the internal zone of the Variscan belt (e.g. Paquette et al., 2017), the ARM eclogites are not associated with blueschist facies metamorphic units as expected in a subduction process and do not record the typical low-temperature gradient of subduction zone (e.g. Ernst, 1971). Moreover, our thermodynamic models indicate that the mafic rocks were not H2O-saturated (Fig. S2A and B) as expected for subducted oceanic crust (e.g. Katayama et al., 2003; Faccenda et al., 2009; Angiboust and Agard, 2010; van Keken et al., 2011; Freundt et al., 2014). Therefore, we suggest that burial and eclogite metamorphism of basaltic protolith are the result of continental crust thickening as proposed in some recent studies in the ECMs and the Montagne Noire (Jacob et al., 2021; Whitney et al., 2015, 2020; Roger et al., 2020).

5.3. Comparison with other eclogites from the South-Western branch of the Variscan belt

Our P–T results of 1.75 GPa at 710 °C are slightly higher in pressure than those documented in previous studies in the ARM (Fig. 15; Table 1). Compared to other ECMs, the peak pressure conditions of HP metamorphism in the ARM are similar to the ~1.8 GPa recorded in the Gothard massif (Abrecht et al., 1991; Biino, 1994), but slightly higher than the ~1.5 GPa estimated in the Argentera massif (Ferrando et al., 2008; Jouffray et al., 2020) or the 1.4 GPa estimated in the NE Belledonne massif (Jacob et al., 2021) (Fig. 15B). Our P–T path of the ARM is similar to those calculated for the eclogites from the Montagne Noire gneiss dome (Whitney et al., 2015, 2020; Pitra et al., 2021) and the Sardinia-Corsica massifs (Giacomini et al., 2005; Libourel & Vielzeuf, 1988; Cortesogno et al., 2004; Cruciani et al., 2011, 2012, 2015a, 2021) (Fig. 15B), and also for pre-alpine eclogites occurrences in the internal Alps in the Adula, Tambo and Suretta nappes (see Biino et al., 1997).

Regarding our U-Pb age of the HP metamorphic stage (c. 330-340 Ma), similar ages were also determined on zircon and rutile formed under HP conditions in the Argentera massif (Rubatto et al., 2001, 2010) and in the Belledonne massif (Jacob et al., 2021) (Table 1). These results are also consistent with the timing of HP prograde metamorphism in the Maures-Tanneron massif that ended at c. 331 Ma (monazite EPMA, Oliot et al., 2015). The timing of the HP in the Montagne Noire massif is still debated: c. 315 Ma estimated by U-Pb on zircon (Whitney et al., 2015, 2020) or c. 360 Ma estimated by Sm-Nd on garnet and U-Pb on zircon (Pitra et al., 2021; Faure et al., 2014b).

Given the P–T conditions, the shape of the P–T path and the geochronological record, the eclogites of the ARM can be compared with those of the Belledonne, Argentera and Sardinia-Corsica massifs that share a similar timing and P–T evolution (Fig. 15) with peak pressure conditions between 1.5–2 GPa at 600–750 °C (Fig.14; Table 1) (Cruciani et al., 2011, 2012, 2015a, 2021; Giacomini et al., 2005; Franceschelli et al., 2007; Ferrando et al., 2008; Jouffray et al., 2020; Jacob et al., 2021). The P–T–t similarities between eclogites of the ARM and others massifs of the south-western branch of the Variscan belt suggest that all these mafic rocks might be the HP relics of the root of an orogenic plateau that could correspond to the French Central massif (Vanderhaeghe et al., 2020).

Interestingly, in all the aforementioned massifs, the eclogitic rocks crop out in or near kilometre-wide wrenching continental shear zone corridors. In the Montagne Noire massif, an intracontinental thickening along a kilometre-wide transpressional shear zone is proposed for explaining the burial and eclogitization (Whitney et al., 2020). A similar system can be invoked for the burial of the deep crust, in addition to the nappe stacking that was previously documented in the in the ARM (Dobmeier, 1998; von Raumer & Bussy, 2004) and dated at c. 340 Ma in the adjacent Belledonne massif (e.g. Fréville et al., 2018).

5.4. Exhumation of the eclogites

In the south-western branch of the Variscan belt, the presence of HP rocks is often associated with vertical transcurrent shear zones (Sardinia-Corsica: Giacomini et al., 2008; Cruciani et al., 2011, 2012, 2015a; Montagne Noire: Whitney et al., 2015, 2020; Trap et al., 2017; Roger et al., 2020; External Crystalline massifs: Jouffray et al., 2020; this study; Maures-Tanneron: Schneider et al., 2014) (Fig. 1). In these different domains, the exhumation of eclogite-bearing deep crust is mainly explained by vertical-upwelling dominated processes, assisted by vertical channel flow (Rey et al., 2011, 2017; Whitney et al., 2015, 2020), diapirism (Faure et al., 2014b; Soula et al., 2001; Charles et al., 2009) and /or vertical extrusion during transpression (Schneider et al., 2014; Gerbault et al., 2018; Simonetti et al., 2020b). Nonetheless, mineral and stretching lineations in the vertical planar foliations in the ARM are mainly gently dipping, in agreement with dominant strike-slip motion but in apparent disagreement with a direct vertical motion (e.g. von Raumer & Bussy, 2004; Simonetti et al., 2020a).

In the Montagne Noire Massif, occurrences of HP mafic are described within and at the periphery of a dextral continental scale transcurrent shear zone associated with a double migmatitic dome structure (e.g. Rabin et al., 2015; Whitney et al, 2015, 2020; Roger et al., 2020). Several authors proposed that these eclogites were rapidly exhumed through a vertical channel flow from 1.5 GPa to 0.5 GPa within a few million years from the deep orogenic crust setting (Rey et al., 2011, 2017; Whitney et al., 2015, 2020). This model is supported by a short time gap of less than 5 Ma between the age of HP metamorphism and widespread partial melting occurring at lower pressure in the Montagne Noire Massif (Whitney et al., 2015, 2020; Roger et al., 2015, 2020; Trap et al., 2017). Recorded exhumation was much slower in the ARM and lasted c. 35 Ma from c. 335 Ma to 300 Ma, suggesting a different integrated-time exhumation mechanism.

The decompression history, from 1.75 to 1.0 GPa (Fig. 15) is recorded in symplectites of the core of eclogitic lenses where the flat-lying S_H is observed. These results support the idea that the first stage of exhumation was accommodated by horizontal flow that is widely documented in mature orogenic plateau (e.g. Beaumont et al., 2001; Vanderhaeghe, 2009; Rosenberg et al., 2007) and may induce significant unroofing if the flow is not strictly horizontal (e.g. Trap et al., 2011). Such horizontal flow is described in the French Central massif (Vanderhaeghe et al., 2020; Roger et al., 2020) and in the Bohemian massif (e.g. Schulmann et al., 2005, 2008).

The second stage of the exhumation path is recorded within amphibolitic facies of metabasites and corresponds to the vertical dextral transpression and related planar surface S_V (Fig. 15). Dextral shear zones show a stretching lineation that plunges at c. 35° toward the north mainly and sometimes more (von Raumer & Bussy, 2004). Consequently, a horizontal displacement of 50-60 km is sufficient to account for a vertical exhumation of about 30 km. Such horizontal displacement is far below the 300 km offset considered for the External Variscan Shear Zone ("ECM SZ" in Guillot et al., 2009). Furthermore, our thermodynamic models indicate an increase in the water content during the exhumation. This is consistent with the aqueous fluid drainage reported in the dextral shear zones of the ARM (Genier et al., 2008), and further argues for the role of transpressional shearing during the exhumation of eclogites. Exhumation of partially molten crust along crustal scale transpressive shear zone is well documented in the Variscan belt (Pereira et al., 2017). One may consider that the buoyancy vertical flow might have also partly contributed to the exhumation of the eclogite bearing partially-molten crust. These results suggest that exhumation of the HP–HT eclogites in the SE branch of the Variscan belt was mostly accommodated by horizontal flow along transpressional shear zones, as proposed in the Sardinia massif (Giacomini et al., 2008; Cruciani et al., 2011; Carosi et al., 2009), in the Maures-Tanneron massif (Corsini & Rolland, 2009) or in the Central Iberian Zone (Pereira et al., 2017).

6. Conclusion

Geochemical, petrological and thermodynamic modelling associated to U-Th-Pb geochronology, structural and microstructural analyses permitted to reconstruct the P–T–t–D path of the Lac Cornu eclogites in the ARM. Our results obtained on weakly and strongly retrogressed eclogites highlight the following tectono-metamorphic evolution: (i) emplacement of a tholeiitic protolith at c. 461 Ma; (ii) a high-pressure stage (M1) at 710°C and 1.75 GPa dated at c. 340–330 Ma; (iii) a first decompression stage (M2) down to pressures around 1.0 GPa at temperatures between 650 °C and 775 °C during a horizontal flow of the partially-molten lower crust followed by (iv) final unroofing below 0.5 GPa and 500 °C (M3) mainly accommodated by dextral transpressive deformation. Cooling at low pressure conditions ended at c. 300 Ma. Based on these results and a comparison with the others surrounding Variscan massifs, we propose that the eclogites of the ECMs correspond to exhumed portions of root of orogenic thickened crust of the Variscan belt after the collision of the Galatian-Armorica terranes.

Acknowledgements

This work was supported by the BRGM through the Référentiel Géologique de la France program (RGF program). We thank two anonymous reviewers and Simon Harley for his constructive and helpful comments as well as the editorial handling of this manuscript. We thank Cyprien Astoury for mineral separation, Didier Convert-Gaubier for his generous support with thin section preparation and Jean-Luc Devidal for his help during REE analyses acquisition. The newly acquired and compiled structural data will be available on the RGF website (http://rgf.brgm.fr).

Supplementary material

Tables S1, S2, S3, S4, S5, S6 and S7 are presented in Annexe 2.

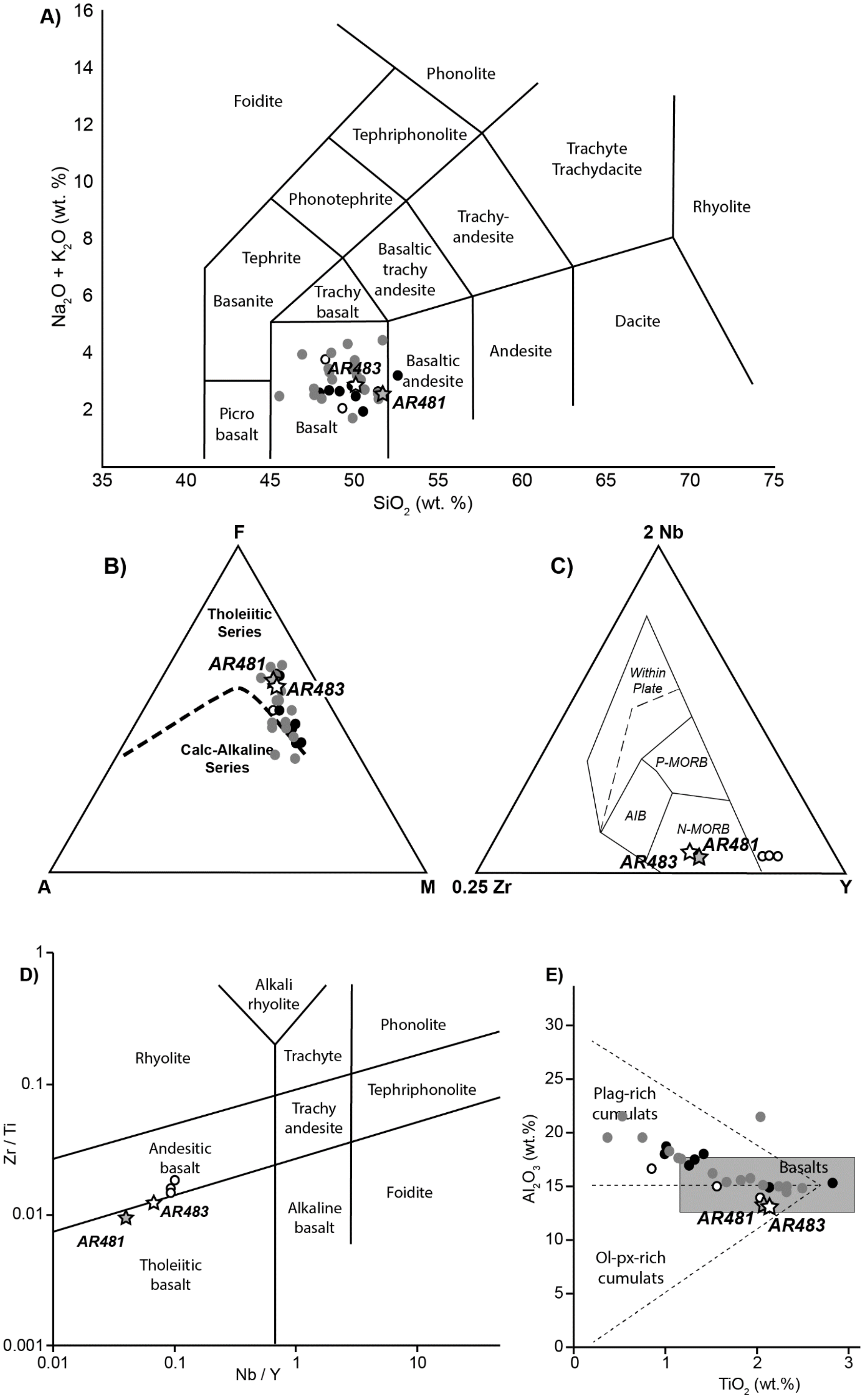
A)
Foidite
Phonolite
Tephriphonolite
Trachyte
Trachydacite
Rhyolite
Phonotephrite
Trachy-
andesite
Tephrite
Basaltic
trachy
andesite
Basanite
Trachy
basalt
Dacite
Basaltic
andesite
Andesite
Picro
basalt
Basalt
AR483
AR481
Na2O + K2O (wt. %)
SiO2 (wt. %)
16
14
12
10
8
6
4
2
35
40
45
50
55
60
65
70
75
B)
F
Tholeiitic
Series
AR481
AR483
Calc-Alkaline
Series
A
M
C)
2 Nb
Within
Plate
P-MORB
AIB
N-MORB
AR481
AR483
0.25 Zr
Y
D)
Zr / Ti
1
0.1
0.01
0.001
Alkali
rhyolite
Rhyolite
Trachyte
Phonolite
Tephriphonolite
Trachy
andesite
Andesitic
basalt
AR483
AR481
Alkaline
basalt
Foidite
Tholeiitic
basalt
0.01
0.1
1
10
Nb / Y
E)
Al2O3 (wt.%)
30
25
20
15
10
5
0
Plag-rich
cumulats
Basalts
AR481
AR483
Ol-px-rich
cumulats
0
1
2
3
TiO2 (wt.%)

Figure S1 : Geochemical results. A: Total Alkali versus Silica diagram; B: AFM diagram; C: Y-Nb-Zr diagram from Meschede (1986); D: Zr-Ti-Nb-Y diagram from (Pearce) 1996. E: Al2O3 vs TiO2 diagram from Konzett et al. (2012). Published data on metabasites from the ARM are also plotted. White circles = Paquette et al. (1989); black dots: von Raumer et al. (1990); grey dots: Liégeois & Duchesne (1981).

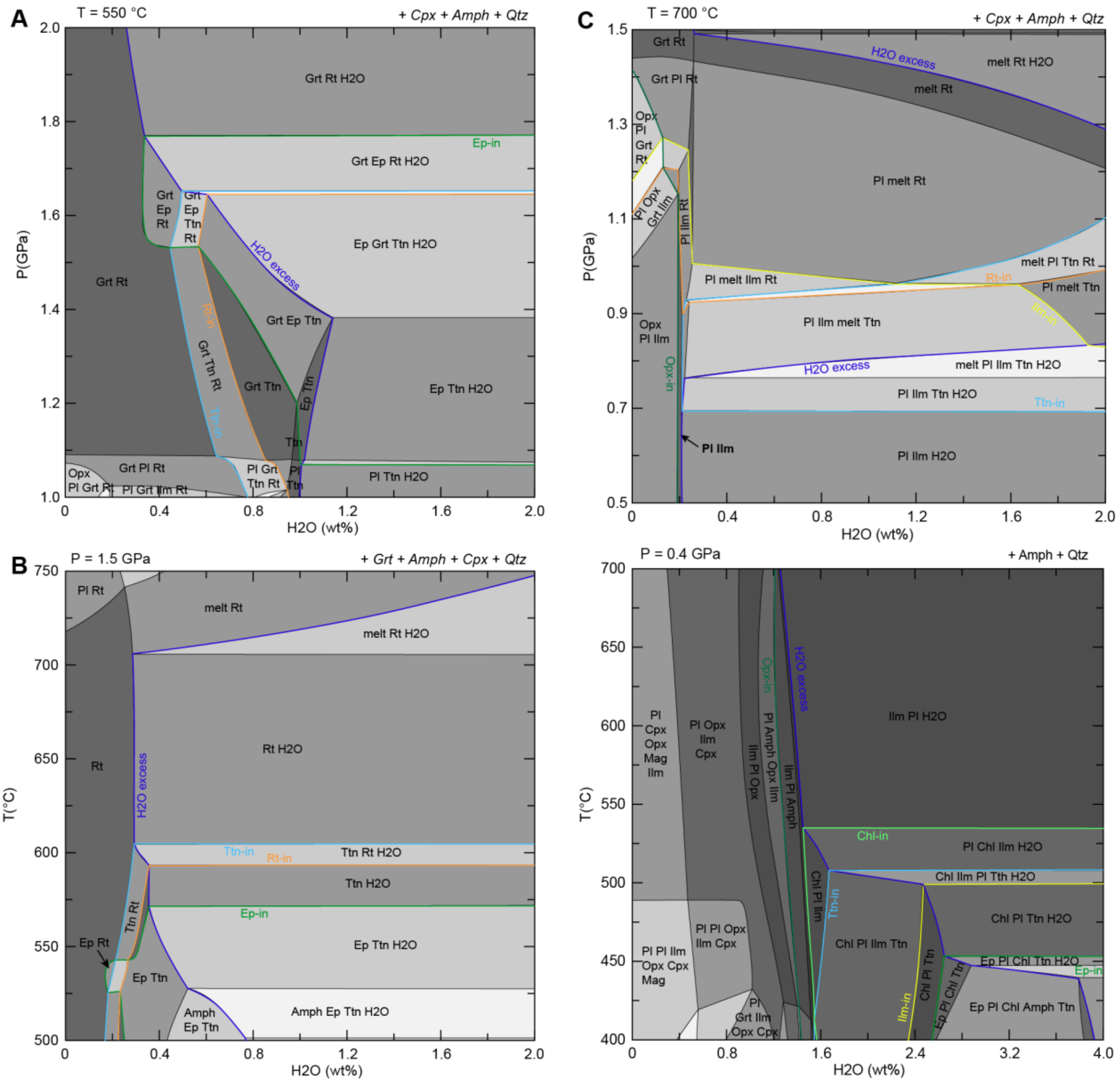

Figure S2 : T–MH_2O (A) and P–MH_2O (B) diagrams constraining the H_2O content during the prograde metamorphism in sample AR483: water is required to produce epidote but the amount of H_2O must remain low in order to crystallize rutile instead of titanites. (C) T–MH_2O diagram constraining the amount of H_2O volume during the retrogression of sample AR483: the amount of water is constrained by the stability fields of orthopyroxene and titanite. (D) T–MH_2O diagram constraining the final water content in sample AR481: H_2O content must be higher than 1.6 wt% to allow the crystallization of titanite and lower than 2.5 wt% to avoid the crystallization of epidote.

Chapitre 5. Subduction ou épaississement crustal ? Reconstruction du trajet prograde du socle gneissique.

Ce chapitre a pour but de reconstituer le trajet prograde des métasédiments du socle gneissique des Aiguilles-Rouges durant leur enfouissement. L'objectif de cette étude est de savoir si les roches du socle gneissique enregistrent un trajet prograde avec un gradient de haute-pression et de basse-température typique des zones de subduction, ou plutôt un gradient de moyenne-pression et de moyenne température généralement associée aux collisions continentales. Pour ce faire, nous avons conduit une étude pétrologique sur deux échantillons de métapélites n'ayant pas été affectées par de la fusion partielle. Nous avons aussi produit des cartes de composition de grenat et des modélisations thermodynamiques à l'aide de Perplex. Enfin, de la géochronologie U-Pb LA-ICPMS in-situ sur des monazites nous permet de contraindre le timing de ce trajet métamorphique. Nos résultats nous permettent de discuter des événements antérieurs au pic de pression mais aussi de comparer les évolutions de la croûte profondes (i.e. les éclogites du Lac Cornu, Chapitre 4) et de la croûte supérieure. Ce chapitre est présenté sous la forme d'un article en préparation pour une soumission à *Lithos*.

Subduction vs crustal thickening? Insights on early-Variscan tectonics from metapelites of the Aiguilles-Rouges massif (External Crystalline Massifs, Western Alps)

Jonas Vanardois[1*], Pierre Trap[1], Philippe Goncalves[1], Françoise Roger[2], Didier Marquer[1], Jean-Louis Paquette[3], Pierre Lanari[4], Jérémie Melleton[5]

jonas.vanardois@univ-fcomte.fr; pierre.trap@univ-fcomte.fr; philippe.goncalves@univ-fcomte.fr; francoise.roger@umontpellier.fr; didier.marquer@univ-fcomte.fr; j.l.paquette@opgc.univ-bpclermont.fr; j.melleton@brgm.fr; blacroix@ksu.edu

[1]UMR 6249 Chrono-environnement, Université de Bourgogne-Franche-Comté, 25030 Besançon, France.

[2]Géosciences Montpellier, Campus Triolet, Université Montpellier, CNRS, 34095 Montpellier Cedex 5, France.

[3]Laboratoire Magmas et Volcans (CNRS-UMR 6524), Campus Universitaire des Cézeaux, 63178 Aubière Cedex, France.

[4]Institute of Geological Sciences, University of Bern, Baltzerstrasse 3, Bern, CH-3012 Switzerland

[5]BRGM-French Geological Survey, 3 Avenue Claude Guillemin, 45100, Orléans, France.

*Corresponding author: jonas.vanardois@univ-fcomte.fr +33(0)381666242 Present address: 16 route de Gray, 25030 Besançon.

Keywords: Garnet, Compositional mapping, Prograde metamorphism, Monazite dating

Abstract

Deciphering the early stages of metamorphism associated either with subduction or crustal thickening is a fundamental task to fully understand the geodynamic evolution of an orogenic system. The effects of retrograde transformations during cooling and exhumation are problematic as they affect the preservation of the mineral record which is essential for obtaining prograde Pressure–Temperature-time (*P–T–t*) paths. In this study, we investigated garnet from two metapelitic samples from the Variscan Alps using quantitative compositional mapping and phase equilibrium modelling. The compositions of garnet cores and inclusions permitted to constrain a fragment of the prograde *P–T* path from ca. 550 °C and 0.48 GPa to ca. 630-680 °C and 0.82-0.97 GPa in these two samples. A retrograde *P–T* stage defined by thin garnet rims occurred at 545 °C and 0.45 GPa. Furthermore, petrological observations highlight a link between garnet breakdown during retrograde metamorphism and the crystallization of monazite dated by LA-ICPMS (U-Pb) at 330–310 Ma. Comparison with *P–T* paths obtained from eclogitic lenses highlights a juxtaposition of the upper and lower crustal domains at ca. 335-330 Ma followed by a final exhumation during dextral transpression at ca. 310-305 Ma. The reconstitution of this prograde path for the two metapelites indicates a mid-pressure – mid-temperature geothermal gradient rather associated to continental collision than to subduction.

We propose that there is no Variscan oceanic suture preserved in the External Crystalline Massifs of the Alps.

1. Introduction

Pressure– temperature (*P–T*) paths obtained from the investigation of metamorphic rocks are indicative of tectonic and thermal processes (e.g. England and Thompson, 1984; Davy and Gillet, 1986; Gerbi et al., 2006). Clockwise *P–T* paths at middle pressure conditions are usually interpreted as markers of crustal thickening followed by exhumation (Ellis, 1987; Harley, 1989; Harley and Hensen, 1990; Jones and Brown, 1990), whereas anticlockwise *P–T* paths are thought to be related to advection of hot material and/or melts during crustal thickening (Bohlen, 1987; Bohlen and Mezger, 1989; Collins and Vernon, 1991; Xiang et al., 2012). Geothermal gradients depicted from *P–T* path reconstructions are fundamental to distinguish between cold *vs* hot orogens (e.g. Chardon et al., 2009) and to unravel the conditions of paleo-subduction zones (e.g. Benmammar et al., 2020). In addition, disparity in *P–T* paths with contrasting shapes may be related to variations in vertical displacement rates of crustal material and/or interactions with magmas leading to conductive/advective exchanges. Such conditions can occur in crustal-scale shear zones. However, the reconstruction of detailed *P–T* path, from early prograde to late retrograde stages is not straightforward as mineral relics formed during prograde metamorphism are commonly re-equilibrated by diffusion or replacement during retrogression.

The External Crystalline Massifs (ECMs; Fig. 1A) located in the Western Alps are relics of Variscan domains showing exposure of mid-lower crustal rocks along a crustal-scale shear zone known as the East Variscan Shear Zone (Guillot et al., 2009). This shear zone is exposed from the Aiguilles-Rouges massif (ARM) to the Argentera Massif (Simonetti et al., 2018). Recently, a petrochronological effort has been made to constrain precise *P–T–t* paths on mafic eclogites. In the case of the Variscan massifs of the ECMs, the obtained *P–T–t* conditions are either interpreted as subduction-related, reflecting the presence of a suture zone (Rubatto et al., 2010; Jouffray et al., 2020) or as portions of the root of an overthickened crust exhumed within transpressional high-strain zones (Jacob et al., 2020; Vanardois et al., in press). The *P–T–t* data are critical to distinguish between these two models and therefore to better understand the Variscan orogenic system

This study is focussed on the Aiguilles-Rouges massif (Fig. 1) for which a large variety of *P–T* paths is documented, including anticlockwise *P–T* paths in the south-western part of the massif (Fig. 2A) (Dobmeier, 1996, 1998) and clockwise *P–T* path in the central part (Fig. 2B) (Schulz and von Raumer, 1993, 2011; Joye, 1989). Eclogite relics embedded in migmatitic orthogneisses indicate that some parts of the massif where buried down to high-pressure and high-temperature (HP-HT) conditions (Fig. 2C) (Schulz and von Raumer, 1993, 2011; Liégeois and Duchesne, 1981; von Raumer et al., 1996; Vanardois et al., in review), whereas others localities reached lower metamorphic conditions indicated by an absence of evidence for partial melting and high-pressure relicts (Schulz and von Raumer, 1993, 2011; Joye, 1989; von Raumer and Bussy, 2004).

The *P–T–t* paths of two metapelitic samples were reconstructed using petrological observations, phase equilibrium modelling and in-situ LA-ICPMS dating of monazite (U-Pb). We chose to study metapelites that do not show evidence of partial melting to compare with those of higher grades. As the main goal was to reconstruct the prograde evolution, the absence of partial melting and intragranular diffusion associated to high-temperature metamorphism was important to avoid additional uncertainties.

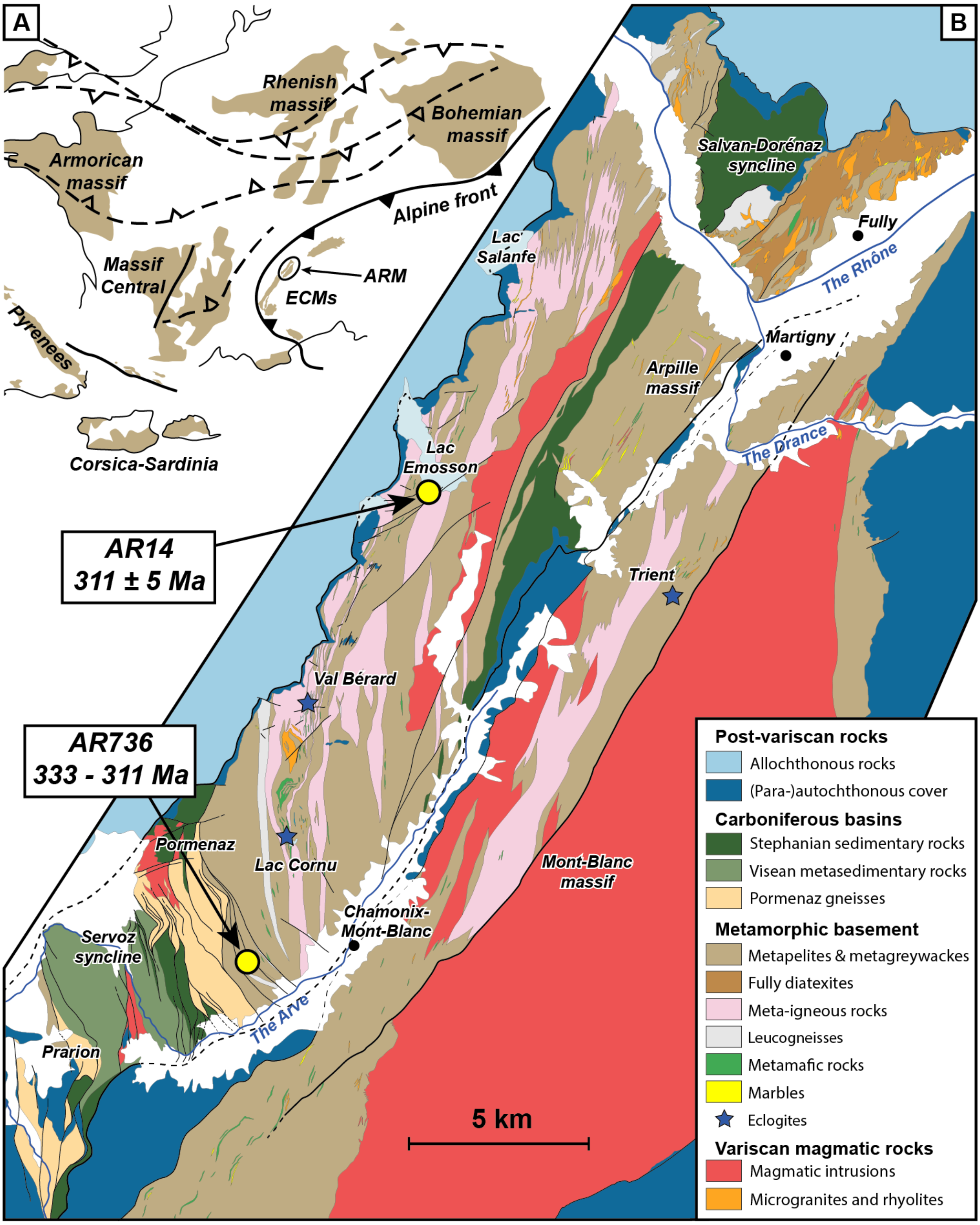

Figure 1 : (A) Paleogeographic reconstitution of the European Variscan Belt at the end of the Variscan orogeny modified from Franke et al. (2017). (B) Geological map of the Aiguilles-Rouges and the Mont-Blanc Massifs with localization of the two samples used in this study and the monazite ages obtained.

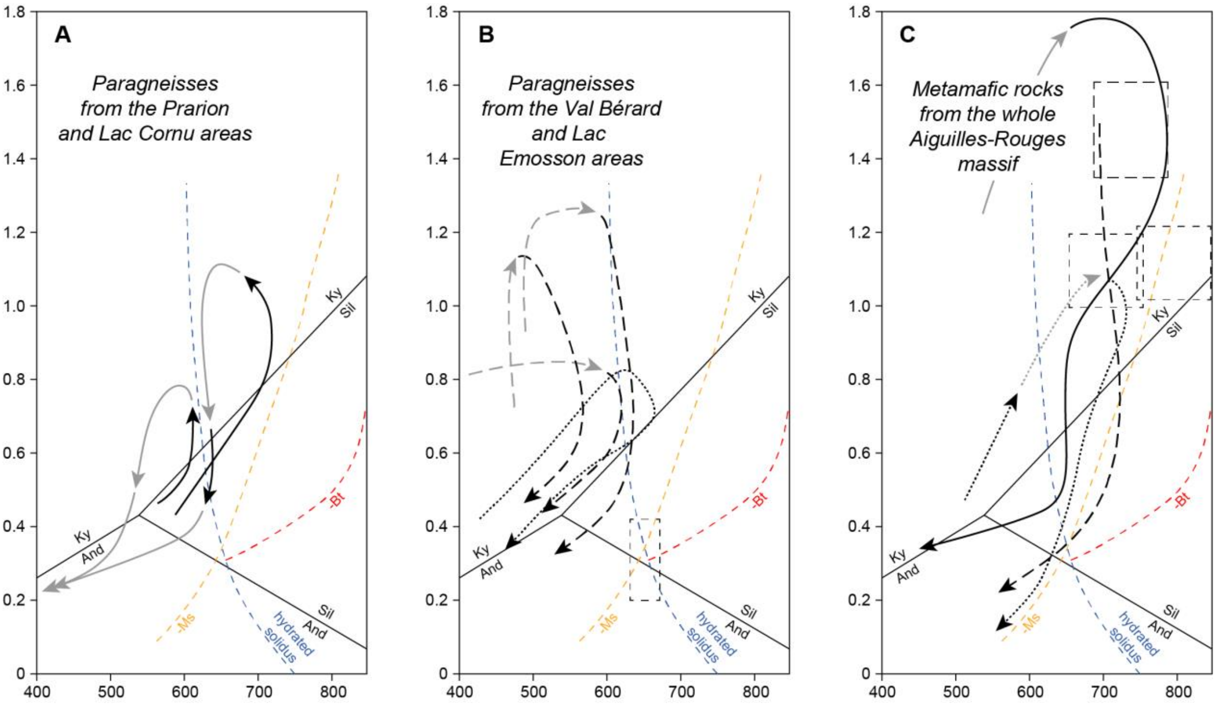

Figure 2 : Various P–T paths proposed for the Aiguilles-Rouges massif. (A) Anticlockwise P–T paths of paragneiss in the Prarion and Lac Cornu areas from Dobmeier (1998). (B) Clockwise P–T paths of paragneiss from the Val Bérard and Lac Emosson areas from Schulz and von Raumer (1993, 2011; dashed arrows) and Joye (1989; dotted arrow). Dashed squares are P–T conditions determined by Genier et al. (2008). (C) P–T paths from metamafic rocks of the whole massif from Vanardois et al. (in review; thick arrow), Schulz and von Raumer (1993, 2011; dashed arrow) and Joye (1989; dotted arrow). Dashed squares are from Liégeois and Duchesne (1981), von Raumer et al. (1996) and Schulz and von Raumer (1993). Black arrows represent sections of P–T paths constrained by thermobarometric results and grey arrows interpreted sections.

2. Geological setting

The Aiguilles-Rouges massif (ARM), part of the External Crystalline Massifs (ECMs) of the western Alps (Fig. 1A), is a 45-km-long, NE-trending Variscan massif bounded by para-autochthonous and allochthonous Mesozoic and Cenozoic sedimentary rocks (Fig. 1B). The ARM is formed of two Carboniferous basins (von Raumer and Bussy, 2004) as well as a gneissic basement consisting of micaschists, paragneiss and Ordovician orthogneisses (Bussy et al., 2000) (Fig. 1B). Alpine deformation is localized into low-grade shear zones (e.g. von Raumer and Bussy, 2004). The associated metamorphism was described in similar shear zones observed in the adjacent Mont-Blanc massif and just reached the greenschist facies conditions (~0.5 GPa-400°C) (e.g. Marshall et al., 1998; Rolland et al., 2003; Rossi et al., 2005). In the AMR, traces of Alpine metamorphism are scarce and very localized with peak temperature conditions below ~350 °C (Boutoux et al., 2016) allowing the preservation of Variscan metamorphism (Schulz and von Raumer, 1993, 2011) and deformations (Simonetti et al., 2020a).

The ARM, or a part of it, underwent firstly a high-pressure metamorphic stage preserved in eclogites (Liégeois and Duchesne, 1981; Schulz and von Raumer, 1993, 2011) and kyanite-bearing metapelites (von Raumer, 1983). Pressure peak conditions of ca. 650 °C/1.25-1.5 GPa were reached in the Val Bérard area (Schulz and von Raumer, 1993, 2011) and ca. 710 °C/1.75 GPa in the Lac Cornu area dated at 340–330 Ma by U-Pb LA-ICPMS on zircon and rutile (Vanardois et al., in review). This high-pressure stage was followed by a decompression and a high-temperature – low-pressure (HT-LP) stage at 600–700 °C/0.2–0.6 GPa (Schulz and von Raumer, 1993, 2011; Chiaradia, 2003; Genier et al., 2008; Vanardois et al., in review). These *P–T* conditions were estimated using phase equilibrium modelling (Genier et al., 2008; Vanardois et al., in review) or empirical thermobarometry (Joye, 1989; Schulz and von Raumer, 1993, 2011; von Raumer et al., 1996; Chiaradia et al., 2003).

In the ECMs, crystallization of anatectic melts occurring during decompression was dated by ID-TIMS using monazite at 320 ± 1 Ma near the Lac Emosson (Bussy et al., 2000) and at 317 ± 2 Ma in the Mont-Blanc massif (Bussy and von Raumer, 1994). A second stage of partial melting is locally recorded in the NE part of the ARM (i.e. Fully area) with the formation cordierite-bearing migmatites and diatexites (Krummenacher, 1959); this stage was dated at 307 ± 2 Ma (ID-TIMS on zircon and monazite; Bussy et al., 2000).

The conditions of HP-HT metamorphism are attributed to crustal thickening through nappe-stacking before ca. 340 Ma (Ar-Ar on muscovite and U-Pb LA-ICPMS on zircon and rutile; Dobmeier, 1998; Vanardois et al., in review). The exhumation of lower crust is firstly accommodated by a horizontal extrusional flow forming shallow dip foliations S1 (Vanardois et al., in review). This deformation stage is followed by a dextral transpressive regime forming N-S vertical S2 foliations and C2 shear zones (e.g. Bellière, 1958; von Raumer and Bussy, 2004; Simonetti et al., 2020a; Vanardois et al., in review). The transpressional shear zones were active at least between 320 and 300 Ma (EPMA on monazite; Simonetti et al., 2020a) and could have been already active at 335–330 Ma (Bussy et al., 2000). The tectono-metamorphic evolution of the ARM is also characterised by two well constrained magmatic pulses, a first Visean magmatic event at 335–330 Ma with the emplacement of high-K calc-alkaline to shoshonitic plutons such as the Montées-Pélissier and Pormenaz granites (Bussy et al., 2000) and a second Late-Carboniferous event at ca. 305 Ma with the syn-transpressional growth of peraluminous granites such as the Morcles and Vallorcine granites in the ARM and the Mont-Blanc and Montenvers granites in the Mont-Blanc massif (Bussy and von Raumer, 1993, 1994; Bussy et al., 2000; Bussien Grosjean et al., 2017).

3. Petrology and garnet compositions

3.1.Quantitative compositional mapping

X-ray maps were acquired using an electron probe micro-analyser (EPMA) instrument (JEOL JXA-8530F HyperProbe) at the University of Lausanne with dwell times of 40 ms, current of 3x10-7 A and voltage of 15.0 kV. X-ray maps were standardized into maps of oxide weight percentage using an internal standard approach and the program XMapTools 3.4.1 (Lanari et al., 2014, 2019). Compositional maps of structural formulas expressed in atom per formula unit (apfu) were calculated and used to investigate the compositional variability of garnet at the thin section scale. Representative garnet compositions are given in Table 1.

Table 1: Representative compositions of garnet.

	AR14				**AR736**							
wt%	Grt$_{I}$	±1σ	Grt$_{II}$	±1σ	Grt$_{1}$	±1σ	Grt$_{2}$	±1σ	Grt$_{3}$	±1σ	Ms	±1σ
SiO2	35.81	1.24	34.94	1.54	38.69	3.24	38.24	2.34	37.23	1.96	46.25	0.58
Al2O3	21.19	0.87	20.62	1.07	22.03	2.62	21.30	1.82	20.44	1.14	36.69	0.44
FeO	34.74	2.26	32.80	2.07	29.96	5.54	31.80	4.34	34.99	3.42	1.18	0.10
MgO	3.56	0.13	2.08	0.20	1.57	0.33	2.68	0.30	1.70	0.19	0.49	0.10
MnO	2.31	0.23	8.25	0.48	3.40	0.70	2.20	0.44	4.08	0.55	-	-
CaO	2.97	0.23	1.99	0.19	2.61	0.53	3.06	0.55	2.27	0.39	-	-
TiO2	0.11	0.08	0.12	0.08	0.06	0.04	0.05	0.03	0.05	0.03	-	-
Na2O	-	-	-	-	-	-	-	-	-	-	0.23	0.01
K2O	-	-	-	-	-	-	-	-	-	-	9.91	0.10
%alm	73.18	4.80	69.17	4.37	75.76	14.00	74.45	10.17	77.65	7.58	-	-
%prp	15.42	0.47	7.82	0.74	7.09	1.50	11.17	1.24	6.71	0.73	-	-
%sps	4.29	0.37	17.63	1.02	8.71	1.80	5.21	1.04	9.18	1.24	-	-
%grs	7.11	0.53	5.38	2.08	8.44	1.71	9.16	1.66	6.47	1.10	-	-

3.2.Bellachat micaschist (AR736)

Sample AR736 is a micaschist from the south-western part of the ARM gneissic basement (Fig. 1B). It is structured by a highly dipping foliation striking N150 and few shear bands forming dextral C-S structures (Fig. 3A). The sample consists of quartz, biotite, muscovite, ilmenite and staurolite with minor amounts of plagioclase, garnet, apatite, pyrite and rutile (Fig. 3A). Garnet porphyroblasts are rounded or elongated parallel to the main foliation with maximum radius diameter around 2 mm. They contain numerous quartz inclusions forming trails indicating dextral rotation of garnet. Plagioclase and staurolite contain numerous rutile inclusions while ilmenite is absent (Fig. 3C-D). The rims contain inclusions of biotite, plagioclase, apatite and rutile (Fig. 4E-F). Garnet cores and rims also show widespread small inclusions of muscovite without any apparent preferential orientation. Garnet is often surrounded by biotite (Fig. 3B). The whole sample is affected by a retrograde stage involving the replacement of biotite by chlorite (Fig. 3C) and the replacement of staurolite and plagioclase by white mica (Fig. 3D). The staurolite crystals also show numerous fractures filled by muscovite and biotite or by chlorite and white mica.

Compositional maps of garnet highlight a moderate compositional zoning with three distinct zones (Fig. 4 and S1). The first generation Grt_1 is very narrow and is located on the edge of the grain (Grt_1: $Alm_{76}Prp_7Sps_9Grs_8$). It is partially surrounded by Grt_2 representing most of the garnet grain. The composition of Grt_2 evolves from $Alm_{74}Prp_{11}Sps_5Grs_9$ to $Alm_{81}Prp_{13}Sps_2Grs_3$ toward the rim. Finally, the outer part of the grain displays a narrow zone (about 20 µm wide) with high Mn and low Mg contents (Grt_3: $Alm_{78}Prp_7Sps_9Grs_6$). This latest generation is not visible on the Ca map (Xgrs in Fig. 4D). The yttrium content decreases from Grt_1 to the edge of Grt_2 (Fig. S1c). This garnet is surrounded by a biotite-corona (Fig. 4A).

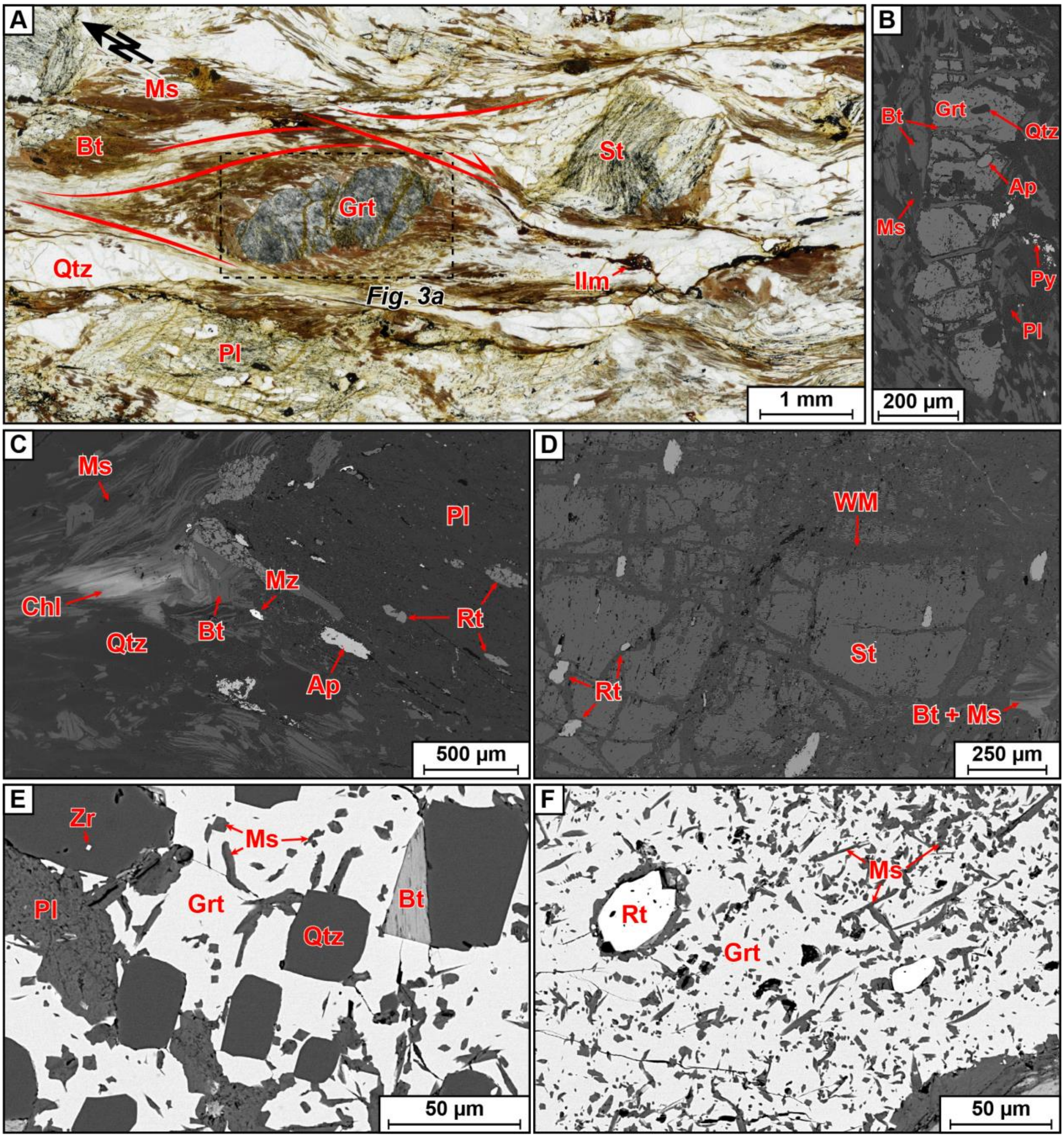

Figure 3 : Thin section and back-scattered electron images showing petrological characteristic of the Bellachat micaschist (AR736). (A) Main paragenesis of the sample with dextral C-S structures corresponding to the S2 and C2 planar fabrics. (B) Garnet grain showing consumption features. (C) Partial replacement of biotite by chlorite and rutile inclusions in a plagioclase. (D) Rutile inclusions in staurolite and partial breakdown of staurolite into white mica. (E and F) Inclusions in the external part of garnet grains. Ap: apatite; Bt: biotite; Chl: chlorite; Grt: garnet; Ilm: ilmenite; Ms: muscovite; Mz: monazite; Pl: plagioclase; Py: pyrite; Qtz: quartz; Rt: rutile; St: staurolite; WM: white mica; Zr: zircon.

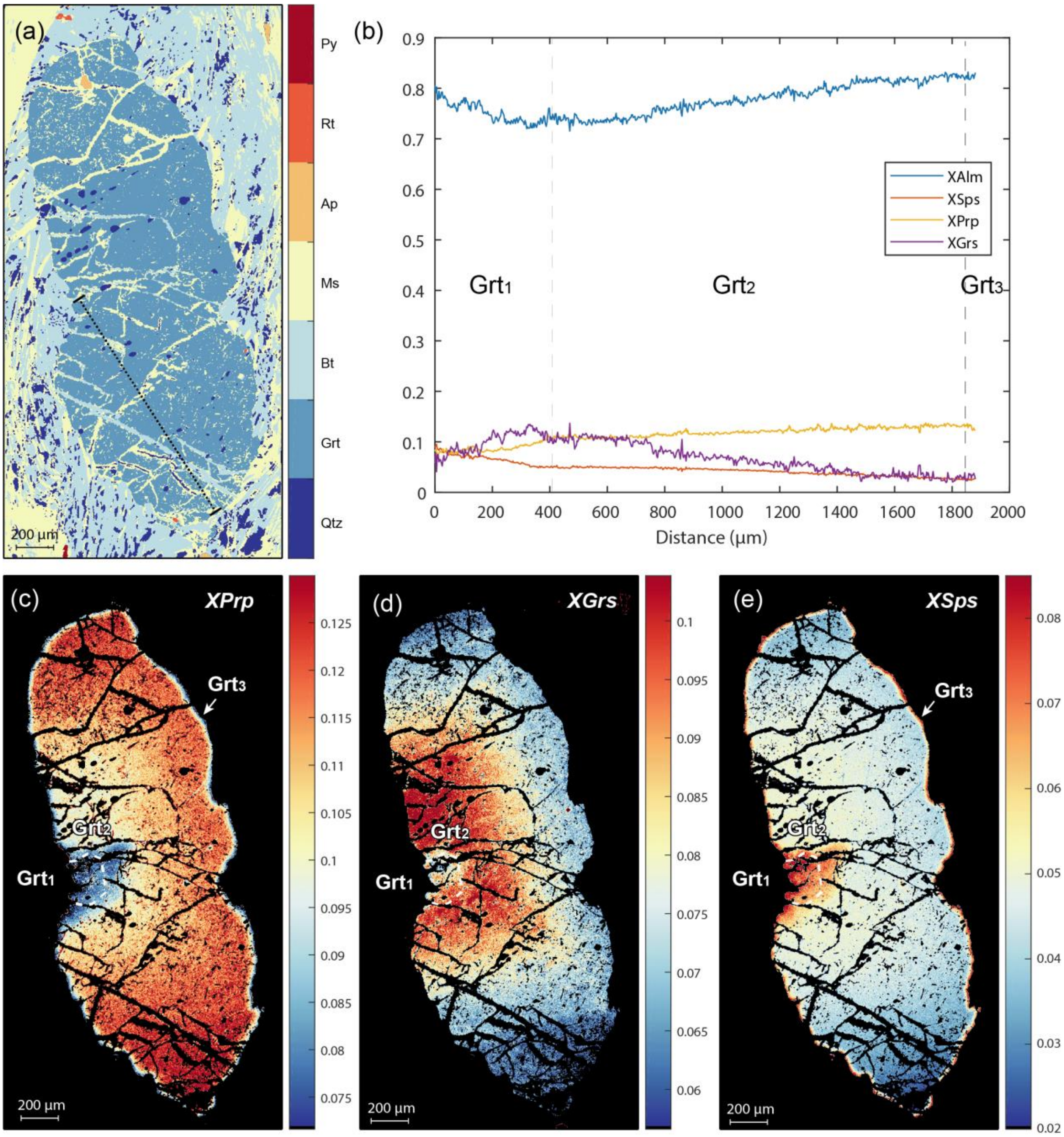

Figure 4 : Compositional maps acquired by electron probe microanalyser (EPMA) from sample AR736. (A) Mask image showing the mineral distribution. (B) Chemical profile of the garnet located in map A. Compositional maps of garnet in function of (C) pyrope, (D) grossular and (E) spessartine contents. Alm: almandine; Grs: grossular; Prp: pyrope; Sps: spessartine. Representative mineral compositions are provided in Table 1.

3.3.Lac Emosson micaschist (AR14)

The sample AR14 is a micaschist located near Lac Emosson (Fig. 1B) and is structured by a vertical planar fabric oriented N40 with a sub-horizontal stretching lineation and asymmetric sigmoids indicating a dextral kinematics (Fig. 5A). Sample AR14 stands within the high-strain EBSZ. The rock is composed of quartz, biotite, muscovite, garnet, plagioclase, ilmenite and apatite (Fig. 5A). Garnet grains are small (ca. 1 mm large) and are often elongated parallel to the foliation (Fig. 5A-B). They contain numerous inclusions of biotite, muscovite, quartz, apatite and plagioclase (Fig. 5B) and also small rutile crystals (10-20 µm), which are absent in the matrix where ilmenite is observed. Few small xenotime grains are located in the vicinity or as inclusion of garnet (Fig. 5B). Biotite is locally replaced by chlorite.

Garnet exhibits a moderate compositional zoning with a core Grt_I and a thin rim Grt_{II} (Fig. 5C-F and S1). The garnet core is rather homogeneous in composition (Grt_I: $Alm_{74}Prp_{13}Sps_5Grs_8$) except for Ca which shows a patchy pattern (Fig. 5F). The absence of typical growth zoning suggests post-growth diffusion, maybe less pronounced for Ca. The yttrium content is low and slightly decreases from core to rim (Fig. S1D). The transition between the garnet core and the overgrowth is well marked for Fe, Mg and Mn elements (Fig. 5C-E) (Grt_{II}: $Alm_{69}Prp_8Sps_{18}Grs_5$) with a slight diffusion of elements, which suggests different *P–T* conditions of crystallization and mineral assemblage. The irregular shape of the garnet core suggests a slight resorption of the garnet before the overgrowth crystallization.

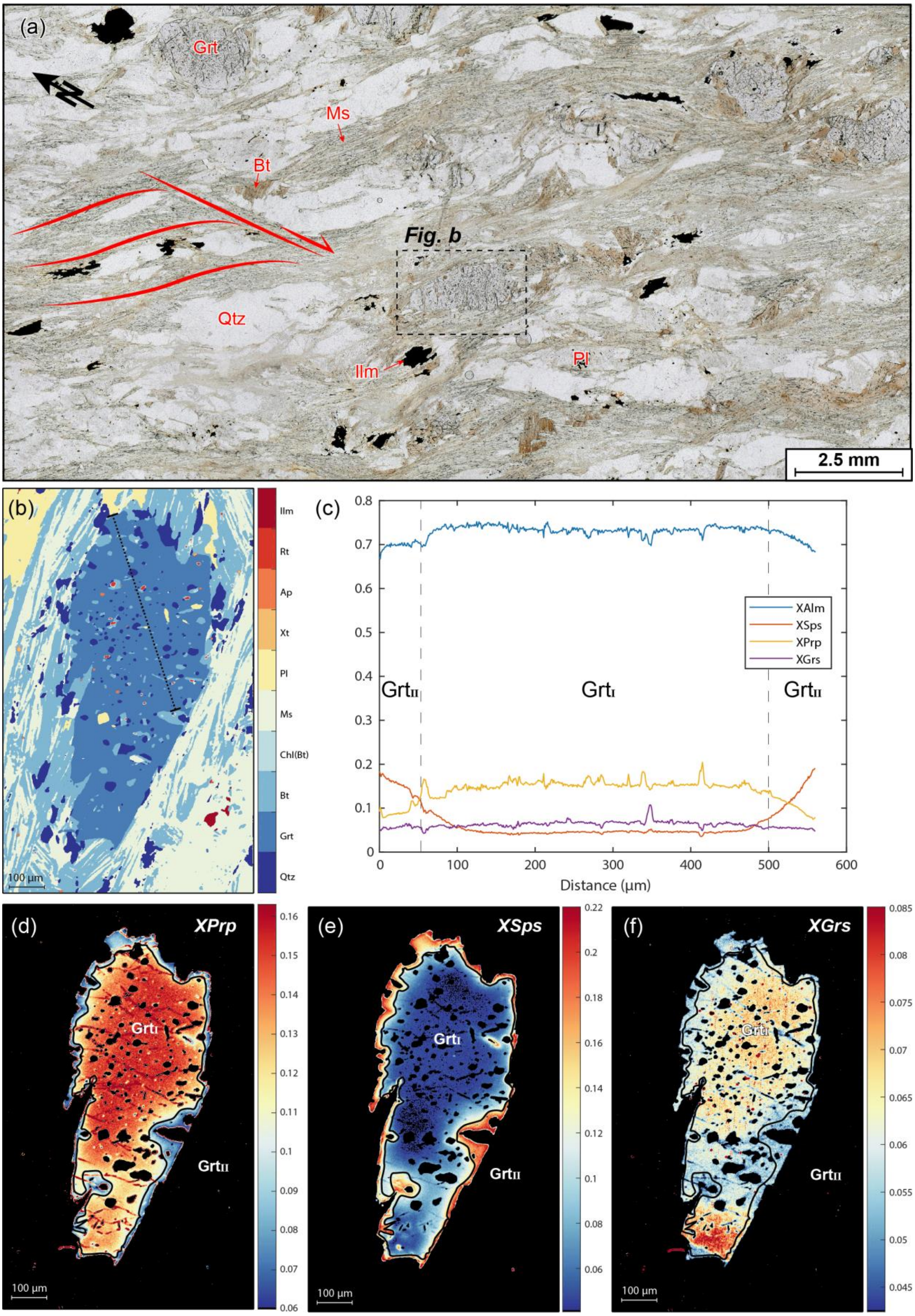
(a)
Grt
Ms
Bt
Fig. b
Qtz
Ilm
Pl
2.5 mm
(b)
Ilm
Rt
Ap
Xt
Pl
Ms
Chl(Bt)
Bt
Grt
Qtz
100 µm
(c)
0.8
0.7
0.6
0.5
0.4
0.3
0.2
0.1
0
XAlm
XSps
XPrp
XGrs
Grt$_{II}$
Grt$_{I}$
Grt$_{II}$
0
100
200
300
400
500
600
Distance (µm)
(d)
XPrp
Grt$_{I}$
Grt$_{II}$
100 µm
0.16
0.15
0.14
0.13
0.12
0.11
0.1
0.09
0.08
0.07
0.06
(e)
XSps
Grt$_{I}$
Grt$_{II}$
100 µm
0.22
0.2
0.18
0.16
0.14
0.12
0.1
0.08
0.06
(f)
XGrs
Grt$_{I}$
Grt$_{II}$
100 µm
0.085
0.08
0.075
0.07
0.065
0.06
0.055
0.05
0.045

Figure 5 : (A) Representative thin section image of the paragenesis of the sample AR14 with dextral C-S structures and compositional maps acquired by electron probe microanalyser (EPMA) from sample AR14. (B) Mask image showing the mineral distribution. (C) Chemical profile of the garnet located in map B. Compositional maps of garnet shown as fractions of (D) pyrope, (E) spessartine and (F) grossular. Ap: apatite; Bt: biotite; Chl(Bt): chlorite replacing biotite; Grt: garnet; Ilm: ilmenite; Ms: muscovite; Pl: plagioclase; Qtz: quartz; Rt: rutile; Xt: xenotime. Alm: almandine; Grs: grossular; Prp: pyrope; Sps: spessartine. Representative mineral compositions are given in Table 1.

4. Thermobarometric modelling

4.1.Methods

Major elements of whole rock samples (Table 2) were obtained using a PANalytical AxiosmAX X-Ray Fluorescence (XRF) spectrometer at the University of Lausanne, Switzerland. Quality control was performed on the reference materials BHVO2 and JA-3. Pressure–Temperature mineral assemblage diagrams were calculated in the compositional system $MnO–Na_2O–CaO–FeO–MgO–Al_2O_3–SiO_2–H_2O–TiO_2–Fe_2O_3$ (MnNCFMASHTO) using Perple_X 6.9.1. software (Connolly, 2005) and the hpver62 thermodynamic database from Holland & Powell (2011). Solution models used in the calculations were garnet, biotite, white mica, staurolite, cordierite, chlorite, chloritoid and melt (White et al., 2014) as well as plagioclase (Fuhrman & Lindsley, 1988), ilmenite (White et al., 2000) and an ideal stilpnomelane model.

Peak mineral assemblages in samples AR736 and AR14 are interpreted to have formed under subsolidus conditions and therefore, H_2O was considered as in excess. The amount of Fe_2O_3 was investigated through P–$X$$Fe_2O_3$ diagrams (Fig. S2). Above 5 wt% of Fe_2O_3, rutile-bearing and ilmenite-free assemblages—as observed in garnet inclusions—are no longer predicted to be stable for pressure conditions at least lower than 1.4 GPa (Fig. S2). Furthermore, the presence of small pyrite in sample AR736 (Fig. 3B) also supports a reduced environment. Therefore, all Fe was considered as FeO in the models.

Isopleths of spessartine, grossular and pyrope fractions were used to constrain the P–T paths of samples AR14 and AR736. The almandine isopleth is not considered due to its large uncertainties (Table 1). Considering the small amount of garnet in these two samples (<5 vol%), garnet fractionation of the reactive bulk composition during growth was not considered (Lanari & Engi, 2017).

Table 2: Bulk compositions of samples AR736 and AR14.

wt%	AR14	AR736
SiO_2	56.38	52.00
TiO_2	0.81	1.13
Al_2O_3	19.46	26.11
FeO	8.54	6.58
MnO	0.19	0.06
MgO	3.04	1.57
CaO	0.35	0.19
Na_2O	1.05	1.12
K_2O	4.84	5.00
P_2O_5	0.11	0.17
Cr_2O_3	0.01	0.02
NiO	0.01	0.00
LOI	3.89	5.44
Total	99.63	100.11

4.2.Results

4.2.1. Bellachat micaschist (AR736)

The mineral assemblage defined by the garnet inclusions (i.e. Qtz + Bt + Ms + Pl + Rt + Ap) is predicted to be stable at pressure conditions between 0.82 and 0.97 GPa and at temperatures between ca. 630-680 °C in presence of staurolite (Fig. 6A). This stability field is bounded by the solidus reaction at higher temperatures as well as the replacement of rutile by ilmenite at lower pressures and by the stability field of plagioclase at higher pressures. This field is also consistent with the presence of rutile inclusions in plagioclase and staurolite.

The isopleths of Grt_1 intersect 10-15 °C above the garnet-in curve at 550 °C and 0.48 GPa with a modelled assemblage of Ilm + Chl + St + Ms + Pl (Fig. 6A). Under these conditions, the calculated garnet and staurolite modes are less than 1 vol% (Fig. 6B-C). The composition of Grt_2 plots at higher *P–T* conditions (575 °C and 0.62 GPa; Fig. 6A) in a mineral stability field of Pl + Bt + Ms + Ilm + St. Under the *P–T* conditions defined by Grt_2, the garnet volume is still low (ca. 1 vol%; Fig. 6B) while the staurolite volume is highly increased (ca. 9-10 vol%; Fig. 6C). The increase of Fe and Mg contents and the decrease of Mn and Ca contents in Grt_2 toward its rim are in favour of higher *P–T* conditions. The smooth evolution of composition in Grt_2 suggests that garnet was affected by an intracrystalline diffusion process. The thin garnet rim (Grt_3) with high Mn and low Mg contents indicates *P–T* conditions at 545 °C and 0.45 GPa, similar to Grt_1. However, the Ca content does not confirm these P–T conditions.

The observed muscovite composition was compared to the composition of muscovite obtained through forward modelling. The results are presented in figure 5D using the model quality factor Q_{cmp} of Duesterhoeft & Lanari (2020). Highest values represent a good fit between modelled and observed muscovite composition, a value of 100 % represents a perfect match within uncertainty of the EPMA measurements. The elements considered for the comparison are K_2O, Na_2O, MgO, FeO, Al_2O_3 and SiO_2. The highest value reaches 82% with in a large *P–T* field showing the mineral assemblage defined by garnet inclusions (Fig. 6D).

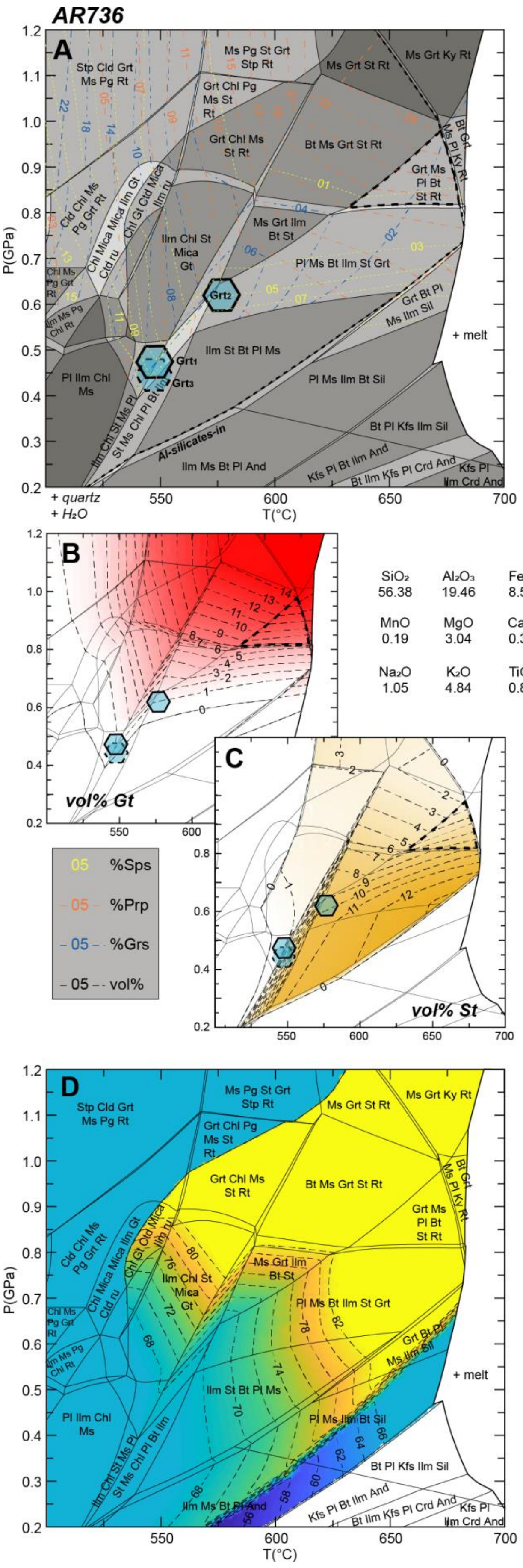
AR736
A
B
C
D
P(GPa)
T(°C)
+ quartz
+ H_2O
Stp Cld Grt Ms Pg Rt
Ms Pg St Grt Stp Rt
Ms Grt St Rt
Ms Grt Ky Rt
Grt Chl Pg Ms St Rt
Grt Chl Ms St Rt
Bt Ms Grt St Rt
Bt Grt Ms Pl Ky Rt
Grt Ms Pl Bt St Rt
Cld Chl Ms Pg Grt Rt
Chl Mica Mica Ilm Gt Ctd ru
Chl Gt Cld Mica Ilm ru
Ilm Chl St Mica Gt
Ms Grt Ilm Bt St
Pl Ms Bt Ilm St Grt
Grt Bt Pl Ms Ilm Sil
Chl Ms Pg Grt Rt
Ilm Ms Pg Chl Rt
Grt2
Grt1
Grt3
Ilm St Bt Pl Ms
Pl Ms Ilm Bt Sil
Pl Ilm Chl Ms
+ melt
Ilm Chl St Ms Pl
St Ms Chl Pl Bt Ilm
Al-silicates-in
Ilm Ms Bt Pl And
Bt Pl Kfs Ilm Sil
Kfs Pl Bt Ilm And
Bt Ilm Kfs Pl Crd And
Kfs Pl Ilm Crd And
vol% Gt
vol% St
SiO₂ 56.38
Al₂O₃ 19.46
FeO 8.54
MnO 0.19
MgO 3.04
CaO 0.35
Na₂O 1.05
K₂O 4.84
TiO₂ 0.81
05 %Sps
05 %Prp
05 %Grs
05 vol%

Figure 6 : Phases equilibrium results obtained for sample AR736. (A) P–T mineral assemblage diagram with isopleths of spessartine, grossular and pyrope contents in garnet and corresponding location of Grt1, Grt2 and Grt3 compositions. Note that the Grt3 location is only based on spessartine and pyrope content (see text). Dashed line indicates the mineral stability field defined by inclusions in garnet. Predicted modes expressed as vol% for (B) garnet and (C) staurolite. And: andalusite; Bt: biotite; Cld: chloritoid; Chl: chlorite; Crd: cordierite; Grt: garnet; Ilm: ilmenite; Kfs: K-feldspar; Ky: kyanite; Ms: muscovite; Pg: paragonite; Pl: plagioclase; Rt: rutile; Sil: sillimanite; St: staurolite; Stp: stilpomelane.

4.2.2. Lac Emosson micaschist (AR14)

The mineral assemblage during garnet growth is defined by garnet and its inclusions that consist of Qtz + Bt + Ms + Pl + Rt + Ap + Grt. This assemblage is predicted to be stable at pressure conditions above 0.78 GPa and at temperatures between 615-690 °C (Fig. 7A). At higher temperatures, melt is predicted to be stable whereas plagioclase only appear above 625 °C. At lower pressure conditions in the present model, rutile is replaced by ilmenite as observed in the matrix and staurolite appears in mineral assemblages. Under temperature conditions below 575 °C, biotite is progressively replaced by chlorite and staurolite is no longer present in the model (Fig. 7A).

The spessartine, grossular and pyrope isopleths corresponding to garnet core (Grt_I) intersect at 585 °C and 0.73 GPa. These *P–T* conditions plot in a field composed of Ms + Bt + Chl + Grt + Pg + Ilm + Qtz, close to the stability field of rutile and the disappearance of chlorite (Fig. 7A). These *P–T* conditions do not fit with the field of Qtz + Bt + Ms + Pl + Rt + Grt recognized as the mineral assemblage synchronous with the formation of garnet cores.

In the thin garnet rim (Grt_{II}), the decrease of Mg content indicates a decrease of temperature conditions while the increase of Mn content emphasizes a decompression path (Fig. 7A). The Grt_{II} isopleths intersect at 550 °C and 0.48 GPa, where the Ca content is almost similar to garnet core, which could explain the lack of Ca zoning. The breakdown of a small amount of staurolite predicted by the phase diagram at higher temperatures slightly increases the volume of garnet created (Fig. 7B) and thus could have induced the crystallization of the garnet rim. At these *P–T* conditions, the predicted assemblage is composed of Ilm + Chl + Pl + Bt + Ms + Grt.

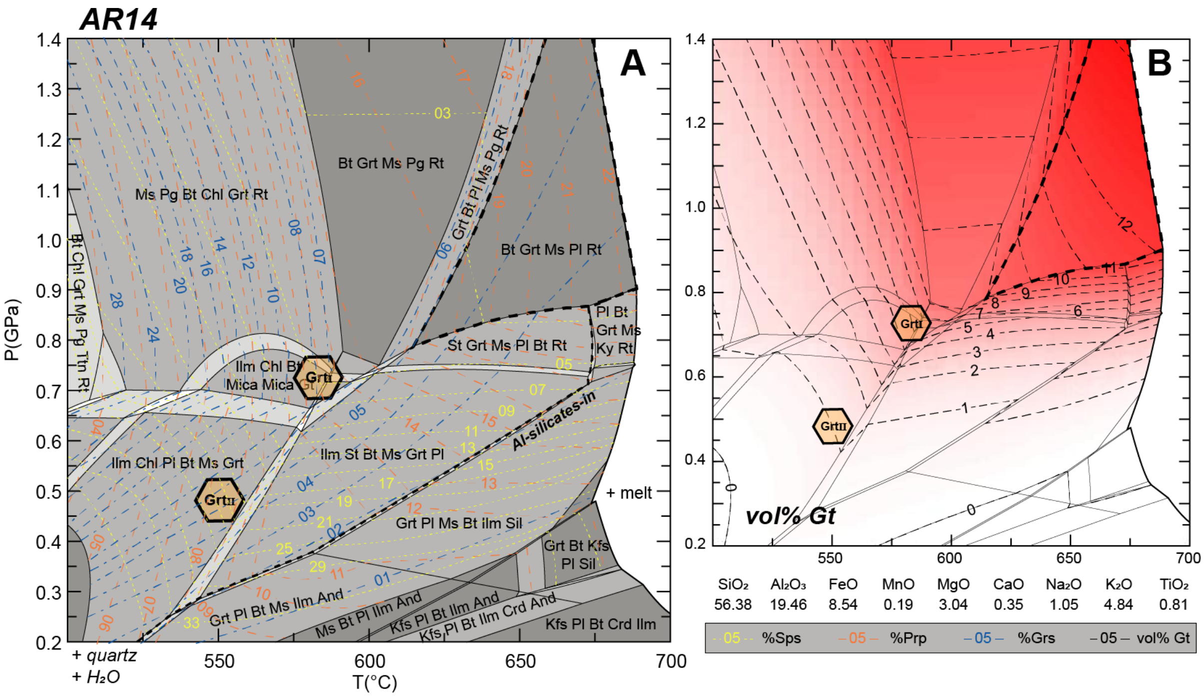

Figure 7 : Phases equilibrium results obtained for sample AR14. (A) P–T mineral assemblage diagram with isopleths of spessartine, grossular and pyrope contents in garnet and corresponding location of GrtI and GrtII compositions. Dashed line indicates the mineral stability field defined by inclusions in garnet. (B) Predicted garnet modes expressed as vol%. And: andalusite; Bt: biotite; Chl: chlorite; Crd: cordierite; Grt: garnet; Ilm: ilmenite; Kfs: K-feldspar; Ky: kyanite; Ms: muscovite; Pg: paragonite; Pl: plagioclase; Rt: rutile; Sil: sillimanite; St: staurolite; Ttn: titanite.

5. Monazite U-Pb geochronology

5.1.Analytical procedure

Monazite was analysed in-situ in thin section to preserve the textural relationships between the distribution of accessory minerals and the fabric. Before analysis, backscatter electron (BSE) images were acquired for all grains using a scanning electron microscope (SEM) to check spot positions with respect to the internal microstructures, inclusions, fractures or other physical defects (Fig. 8).

U-Pb geochronology on monazite was conducted by LA-ICPMS at the Laboratoire Magmas et Volcans, Clermont-Ferrand (France). The analyses involved ablation of grains with a Resonetics Resolution M-50 powered by an ultra-short pulse ATL Atlex Excimer laser system operating at a wavelength of 193 nm. The detailed analytical procedures are described in Paquette et al. (2014) and detailed in Hurai et al. (2010) and in the Supplementary material (Appendix 1 and Table S1). Data reduction was carried out with the GLITTER® software package from Macquarie Research Ltd (van Achterbergh et al., 2001). Dates and diagrams were generated using Isoplot/Ex v. 2.49 software package (Ludwig, 2001). All uncertainties are given at ±2σ.

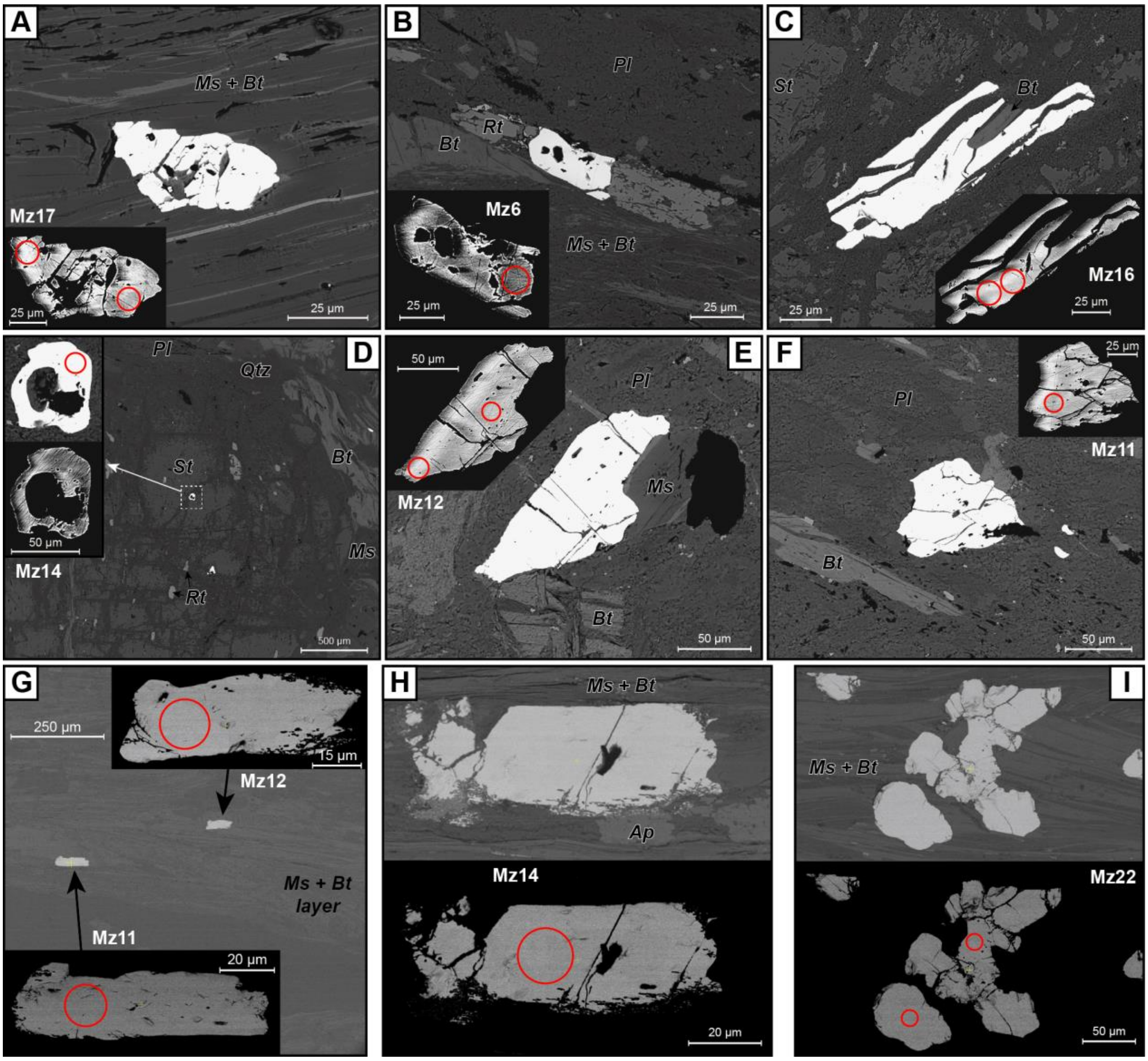

Figure 8 : Back-scattered electron images of monazite (Mz) from sample AR736 located in (A and B) Bt-Ms layers, in (C and D) staurolite and in (E and F) plagioclase. Back-scattered electron photos of monazite from sample AR14 with (G) elongated shapes in the foliation, (H) partially replaced by apatite and (I) shape perpendicular to the foliation. Red circles indicate the analytical spots locations. Numbers of monazite correspond to Table S2.

5.2. Results

5.2.1. Bellachat micachist (AR736)

Monazite occurs both in the biotite-muscovite layers (Mz1, 2, 4, 5, 6, 7, 8 and 17) (Fig. 8A-B) and as inclusions in staurolite (Mz grains 3, 14, 15 and 16) (Fig. 8C-D) and plagioclase (Mz

11, 12 and 18) crystals (Fig. 8E-F). No monazite grain was observed as inclusion in garnet but some were observed in staurolite. In the matrix monazite is abundant with anhedral grains ranging from 50 to 100 µm in size. Most grains have no zoning and are fractured as visible in BSE images (Fig. 8A, C, E and F). Monazite grains contain numerous inclusions of quartz, biotite, staurolite, plagioclase and muscovite (Fig. 8A-F). Twenty-two analyses on fifteen monazites were performed. They mostly show high to very high Pb, U and Th contents ~ 1300-2200 ppm, ~ 4000-6300 ppm and ~ 30000-55000 ppm, respectively and with Th/U ratios between 6.4 and 11.7 (Table S2). The Tera Wasserburg diagram displays a complex pattern with showing discordant data with a percentage of concordance ranging from 52 to 95 % and with a greatest dispersion of ^{206}Pb/^{238}U dates between ~ 350 and 300 Ma (Table S2; Fig. 9A). The figure 8B built only just from the least discordant data (% concordance > 82 %) indicates that there is a correlation between the ^{206}Pb/^{238}U dates and the textural position of the monazites. Amongst the eight monazites crystals from the biotite-muscovite layers, seven yields a mean ^{206}Pb/^{238}U date of 311 ± 5 Ma (MSWD = 0.03). The monazite Mz6 (spot #9), which is also a grain from the Bt-Ms layers and is located between two rutile grains (Fig. 8B) gives an older ^{206}Pb/^{238}U date of 335 ± 13 Ma. Eight analyses on four monazites included in staurolite were performed. Two monazite grains (Mz15 and Mz16 or spots #16, 17, 18 and 19) located in the staurolite core yield a mean of 333 ± 6 Ma (MSWD = 1.13; n = 4). The monazites Mz14 (# 15) and Mz3 (#3, 4 and 5) located in a fracture of a staurolite grain and on the rim of another smaller grain give a weighted average of ^{206}Pb/^{238}U dates is 311 ± 5 Ma (MSWD = 0.14; n = 4). Four analyses on three monazites (Mz11, 12 and 18) included in plagioclase determine a mean of 322 ± 12 Ma (MSWD = 1.6; n = 4).

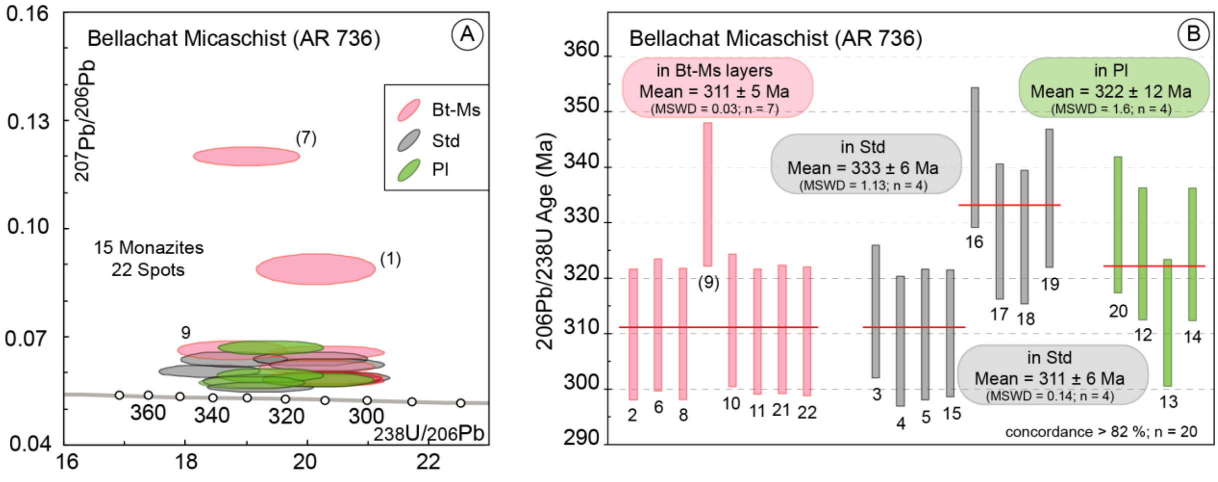

Figure 9 : (A) Monazite U-Pb Tera Wasserburg diagram obtained by LA-ICPMS on the Bellachat micaschist (AR736). (B) The diagram of weighted averages of ^{206}Pb/^{238}U dates as function of monazite textural location. Only

analyses with more than 82% of concordance agreement are taken into account. Error ellipses and uncertainties are ±2σ level. Bt-Ms: monazite in biotite-muscovite layers; Std: monazite in staurolite inclusion; Pl: monazite in plagioclase inclusion.

5.2.2. Lac Emosson micaschist (AR14)

All monazite grains lie in the biotite-muscovite layers and none of them were observed as inclusion in garnet. Monazite crystals are abundant, the majority are ~50 µm in size with a few up to ~100 µm. They are commonly subhedral (Fig. 8G), but with irregular boundaries, suggesting that these crystals could be resorbed crystals and replaced by apatite (Mz9, 7, 10, 14, 18, 21) (Fig. 8H). Most of the monazite grains are elongated parallel to the foliation (Fig. 8G-H). Alternatively, some of them form cluster perpendicular to the foliation (Fig. 8I). Most of monazite grains do not show fractures or internal deformation, which suggests that they are late or post-kinematic. The BSE images reveal that most grains show no zoning and are inclusion-poor (Fig. 8G-I) with few inclusions of quartz or biotite and muscovite. Twenty-seven analytical spots on 21 grains were analysed. Pb (~1400-2000 ppm), Th (~ 38220-63000 ppm) and U (2300-4400 ppm) contents and Th/U ratios (9.5-23.5) are similar to those observed for monazite of the samples AR736 (Table S2). All data have a discordant position with the percentage of concordant between 71% and 93% (Table S2). In the Tera Wasserburg diagram, these data define a regression line that yields by lower intercept a date of 311 ± 5 Ma (MSWD = 0.9; n = 27) (Fig. 10).

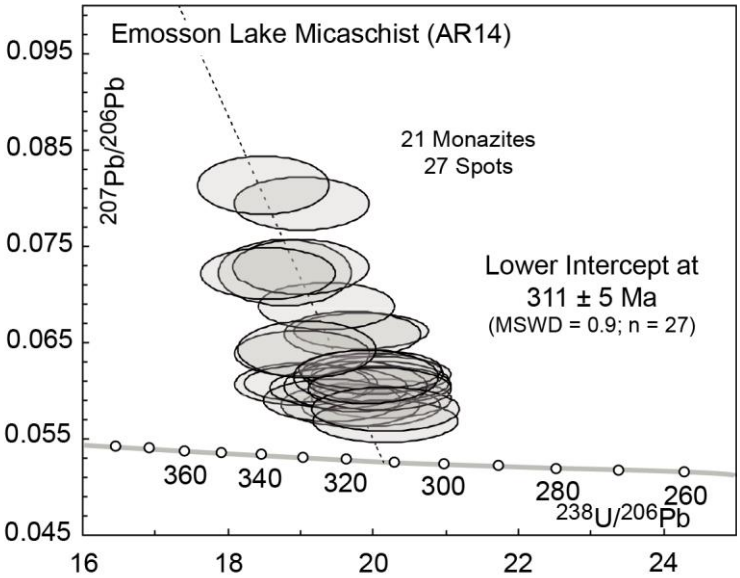

Figure 10 : Tera Wasserburg diagram for Monazite on the Lac Emosson micaschist (AR14). Error ellipses and uncertainties are ± 2σ level.

6. Discussion

6.1.Reconstruction of the P–T–t path

For sample AR736, the compositions of Grt_1 and Grt_2 and the inclusions contained in the external part of Grt_2 defined a prograde path from ca. 550 °C and 0.48 GPa to a *P-T* field at ca. 630-680°C and 0.82-0.97 GPa (Fig. 11A, data and *P–T* path in blue). This is consistent with an increase of garnet volume along such a prograde evolution (Fig. 6B). At higher temperature conditions, melt is predicted to be stable. The lack of evidence for partial melting in this sample supports peak conditions of 630-680 °C and 0.82-0.97 GPa. Inclusions in garnet from sample AR14 defined *P–T* conditions of the same magnitude (>0.78 GPa and 615-690 °C) also interpreted as reflecting peak metamorphism (Fig. 11A, data and *P–T* path in orange).

For sample AR14, the composition of Grt_I yields *P–T* conditions that could be interpreted either as prograde or retrograde metamorphism. Assuming that Grt_I constrains the retrograde metamorphism, the *P–T* conditions defined by the garnet inclusions and the two garnet compositions would form a *P–T* path that would remain within the kyanite stability field, which does not fit with previous mineralogical observations in the study area (von Raumer, 1983; Genier et al., 2008) nor in the whole ARM (von Raumer and Bussy, 2004). On the other hand, the *P–T* conditions defined by Grt_I fit the prograde path defined by sample AR736 (Fig. 11A). Therefore, we interpret Grt_I as to be formed during prograde metamorphism (Fig. 11B).

Aluminosilicates have not been observed in our samples, thus the aluminosilicates-in reaction roughly constrains the retrograde paths of both samples (Fig. 11A). These retrograde paths are also constrained by the compositions of Grt_{II} in sample AR14 and Grt_3 in sample AR736 around 550 °C and 0.48 GPa (Fig. 11A). However, in the Lac Emosson area, von Raumer (1983) described sillimanite and andalusite in some lithologies, which is consistent with our *P–T* paths crossing through or close to the sillimanite and andalusite fields (Fig. 11A). Additional forward thermodynamic models show that the presence of aluminosilicates in our phase diagrams is controlled by the amount of H_2O into the system (Fig. S3). Heterogeneous water fluxes along the transpressional EVSZ is reported with a strong impact on mineral equilibria (e.g. Genier et al., 2008). Similarly, water drainage along D2 vertical shear zones may account for local presence or absence of aluminosilicates in the Lac Emosson area. It is also likely that strong retrogression during retrograde HT-LP metamorphism due to intense aqueous fluid fluxing may lead to total replacement of sillimanite or andalusite by white micas.

Surprisingly, in these two samples, the garnet compositions do not record peak of metamorphism. The peak of metamorphism is defined by the inclusions located at the edge of the garnet grains and by the white mica compositions. Therefore, the edge of the garnet containing the inclusion have crystallized during the peak of metamorphism. Thus, the initial composition of the garnet edges coeval with the peak of metamorphism has been probably changed later on by intracrystalline diffusion or replacement (REF). In addition, during the retrograde path, the garnet volume is predicted to decrease at equilibrium, which is consistent with evidence of garnet resorption observed in both samples (Fig. 3B and 5B) that may have partially erased some garnet composition associated to peak metamorphism (Fig. 11B). However, the composition of the Grt_1 in sample AR736 indicate *P-T* conditions just above the garnet-in reaction, which indicate that potential diffusion processes have not modified significantly the growth composition of garnet cores.

The compositions of the narrow garnet rims in both samples (i.e. Grt_3 and Grt_{II}) are modelled close to the staurolite stability curve (Fig. 6A, 8A and C), which induces a slight increase in garnet volume (Fig. 6B and 8B). it is therefore possible that garnet overgrowth was caused by staurolite breakdown (Fig. 11B).

The absence of monazite inclusion in garnet indicates that monazite formed after garnet and therefore near the conditions of peak metamorphism. In sample AR736, the monazite U-Pb dates range from ca. 330 to 310 Ma depending on the textural position of the dated grains (Fig. 9). A date of 333 ± 6 Ma was obtained on two monazite grains included in the core of a large staurolite. Similarly, a monazite from the Bt-Ms layers but framed between two rutiles (Fig. 8B) also yielded a date at ca. 335 Ma. Phase equilibrium modelling suggests that rutile is stable for pressures above 0.8 GPa (Fig. 6A), conditions that are only reached close to peak metamorphism. Staurolite is also predicted to be stable at these conditions (Fig. 6A and C) and this is in line with the observation of numerous rutile inclusions (Fig. 3D). Therefore, we interpret this age of 333 ± 6 Ma as reflecting peak metamorphism (Fig. 11B). This age is consistent with the monazite U-Pb age at 327 ± 2 Ma (ID-TIMS) obtained on a metapelite from the Emosson area and interpreted the same way by Bussy et al. (2000). During the retrograde evolution, garnet is partially consumed. The crystallisation of monazite can be induced by the garnet breakdown reactions (Spear and Pyle, 2002; Kohn and Malloy, 2004; Gibson et al., 2004; Kelly et al., 2006; Rocha et al., 2017; Shrestha et al., 2019). Therefore, we propose that the crystallization of monazite grains as the result of garnet breakdown.

A younger date of 311 ± 6 Ma was recorded by two monazites located one included in a small staurolite without rutile inclusion and the other in a fracture of a larger staurolite crystal. This date reflects a minimum age of staurolite crystallization during cooling (Fig. 6C) and indicates that at ca. 310 Ma, the *P–T* conditions were still in the staurolite stability field and that the garnet rims (i.e. Grt_3) are thus later than 311 ± 6 Ma. Moreover, a similar date of 311 ± 5 Ma was obtained on monazite included in the micas-rich layers marking the dextral shearing deformation. Monazite included in plagioclase yields a poorly constrained date of 322 ± 12 Ma, which does not allow to date with precision the age of plagioclase crystallization during cooling between ca. 330 Ma and 310 Ma. However, it fits well with our phase diagram that predicts the stability of the plagioclase at the peak of metamorphism and during the retrograde path (Fig. 6).

Dating of monazite from the Bt-Ms layers of sample AR14 yields a date of 311 ± 5 Ma. Monazite in these layers does not record the stage at 330 Ma (Fig. 10). The Lac Emosson metapelite (Sample AR14) shows more intense D2 deformation than the Bellachat metapelite (AR736) collected in the southern part of the ARM gneissic basement (Fig. 1). The perpendicular and parallel orientations of monazites in the mylonitic foliation (Fig. 8A-C) suggest that the ca. 310 Ma date represents the age of dextral shearing in this sample (Fig. 11B). Moreover, a similar age was obtained on monazite grains included in the mica-rich layers of sample AR736 marking dextral shearing deformation.

Monazite may (re)-crystallize owing to fluid–rock interaction relatively late in the metamorphic history (e.g. Didier et al., 2014; Erikson et al., 2015; Roger et al., 2020; and references therein). Indeed, fluid-assisted dissolution-precipitation mechanisms are efficient at modifying the chemical and isotopic composition of monazite, even at low temperature (down to ~300 °C) (Hawkins and Bowring, 1997; Townsend et al., 2000). In the Lac Emosson area, partial melting is restricted to a 500 m-wide shear zone, and adjacent fertile metapelites remained apparently unmolten. To explain these observations, Genier et al. (2008) proposed that aqueous fluid circulation triggered melting, and that vertical transcurrent shear zones have tapped and channelled external water likely from tectonic units underlying the Emosson migmatites. Given the absence of aluminosilicates due to the high-water activity and the relationships between deformation strain-rate and the youngest monazite ages at 310 Ma, we propose that continued deformation-recrystallization and fluid flow within these shear zones probably induced monazite recrystallization in the mineral matrix.

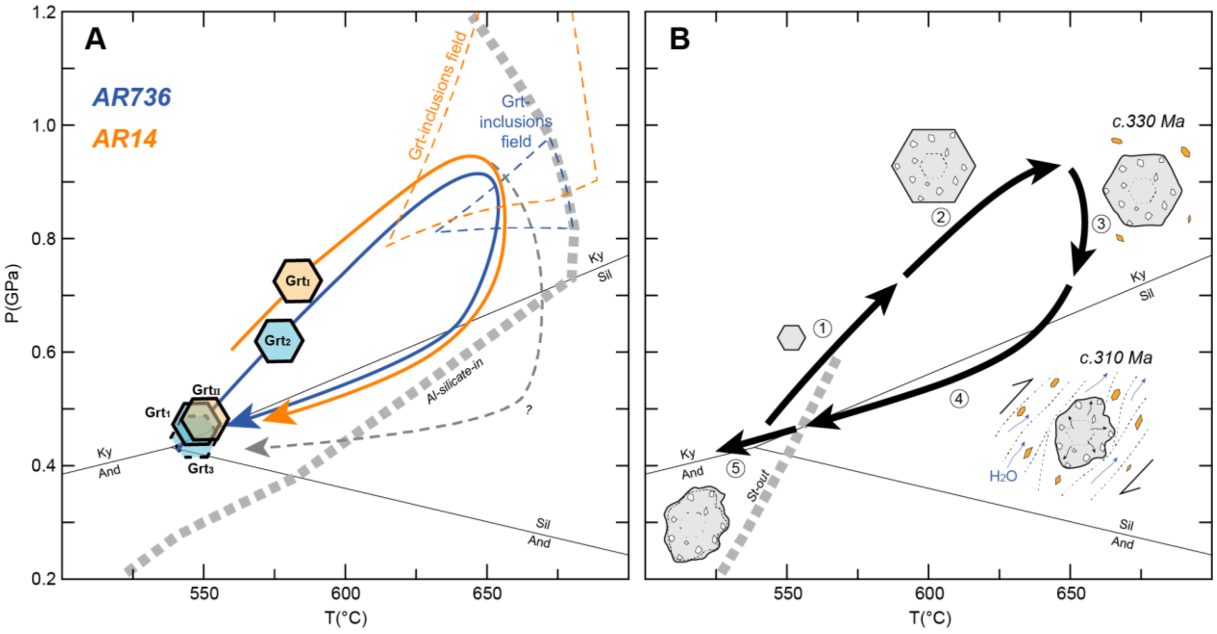

Figure 11 : (A) Reconstructed P–T paths for samples AR736 (blue) and AR14 (orange). (B) Simplified model showing the garnet evolution and its links with the crystallization of monazite and ages: (1) Nucleation of garnet; (2) main crystallization stage at the end of prograde metamorphism with incorporation of inclusions; (3) beginning of retrograde metamorphism associated with garnet resorption and crystallization of monazite starting at 333 ± 6 Ma; (4) Garnet breakdown and monazite crystallization continue and while dextral shearing partially or totally recrystallized older monazite grains until 310 Ma assisted by aqueous fluids; (5) Consumption of staurolite induces the crystallization of thin garnet rims.

6.2.Comparison with published data and tectonic implications

Our thermobarometric results from the gneissic basement of the south-western part of the Aiguilles-Rouges massif (i.e. sample AR736) do not record an anticlockwise *P–T* path as proposed by Dobmeier (1998) for the study area (Fig. 1A) but emphasize a clockwise *P–T* path similar to the central part of the Aiguilles-Rouges massif (i.e. sample AR14) (Fig. 11A). Also, our results do not fit with the LP-HT conditions (650 °C and 0.3 GPa) proposed by Genier et al. (2008) but are more consistent with retrograde *P–T* conditions calculated on metapelites from the Val Bérard and the Emosson areas (Fig. 1B) (Joye, 1989; Schulz and von Raumer, 1993, 2011). On the other hand, our prograde path displays a higher dT/dP gradient than those proposed by Schulz and von Raumer (1993, 2011) culminating at *P–T* conditions of ca. 1.1-1.3 GPa and 500-600 °C. An explanation for these differences could be find in the different thermobarometric approaches, i.e. empirical thermobarometry in Schulz and von Raumer (1993, 2011) and phase diagram modelling in our study. We cannot rule out that D2 transpression may have juxtaposed crustal segments with variable *P–T* records. Alternatively, our geochronological data fit well with previously published data suggesting that retrogression took place between 330 and 305 Ma (Bussy et al., 2000; Schulz and von Raumer, 2011; Simonetti et al., 2020a).

The retrograde *P–T* paths recorded in our samples is similar to the end of the retrograde path of the Lac Cornu eclogites (Fig. 12) (Vanardois et al., in review). The mafic eclogites represent the deep portion of an overthickened crust exhumed from ~60 km depth whereas there is a lack of evidence that the metapelite samples studied here were buried at depth deeper than ~35 km (Fig. 11). The similar slate retrograde *P–T* path segments recorded by the lower and upper crustal rocks suggest that these structural levels were juxtaposed during dextral transpression before to be finally exhumed together. The exhumation of our samples occurred during the dextral shearing between ca. 330 and 310 Ma (Fig. 11A) and the end of the exhumation of the eclogites is also induced by the dextral shearing at a similar period of time (Vanardois et al., in review). Therefore, the juxtaposition of lower and upper crust probably occurred at about 330 Ma before a final exhumation by dextral shearing until 311 ± 6 Ma and 311 ± 5 Ma in our samples and 298 ± 10 Ma in the eclogites (Vanardois et al., in review).

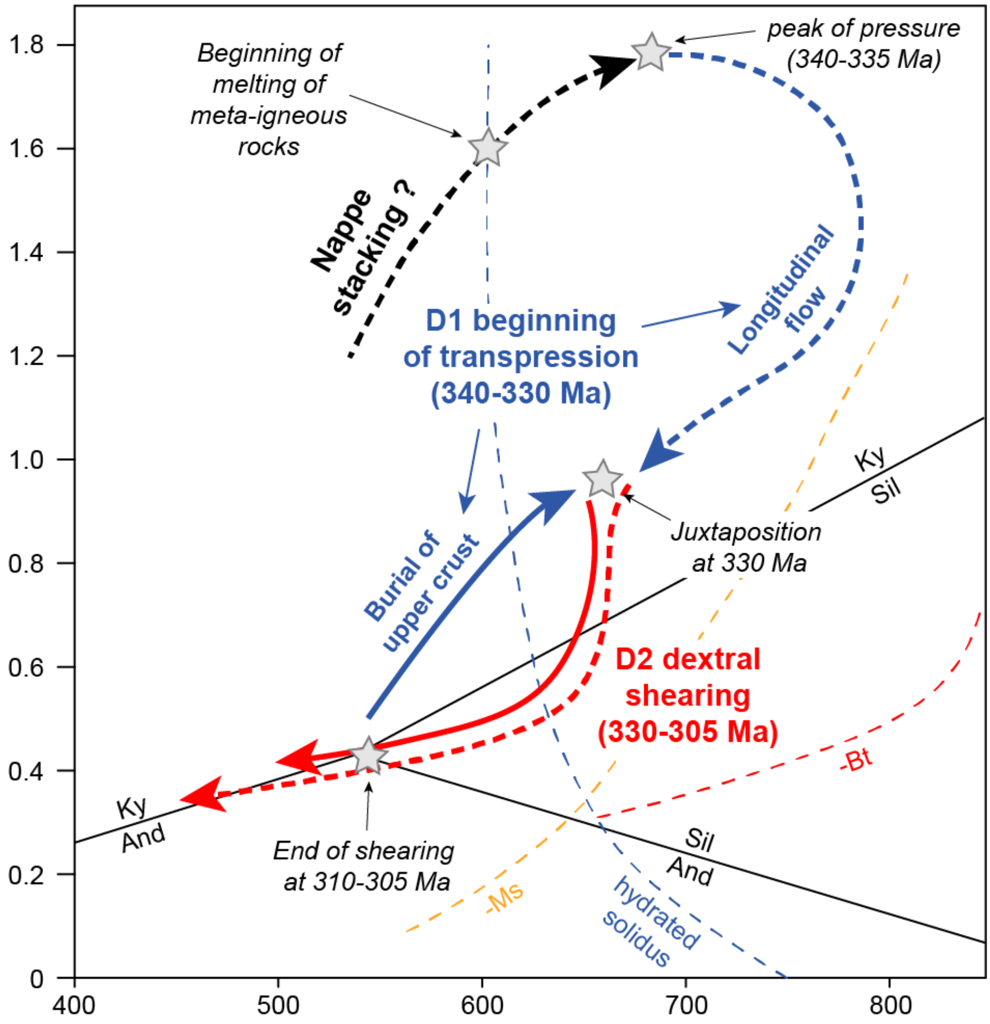

Figure 12: Comparison of P-T-t-D paths from the metasedimentary rocks from this study (thick arrows) and from the eclogites (dashed arrows) (Vanardois et al., in review).

Before juxtaposition at 330 Ma, supracrustal rocks were buried down while the lower material was exhumed (Fig. 12). A similar process with synchronous burial of supracrustal rocks and exhumation of lower crust before juxtaposition at the same crustal level is described in several Variscan massifs and thought to occur in transpressive settings (Giacomini et al., 2008; Rolland et al., 2009; Corsini & Rolland, 2009; Carosi et al., 2009; Pereira et al., 2017). EBSD data obtained on syn-exhumation minerals indicate that the beginning of exhumation of the lower crust was accommodated by shallow dip foliations interpreted as horizontal flow of a partially molten crust (Vanardois et al., in review). Recently, Cochelin et al. (2017, 2021) have highlighted that the transpression regime affecting the Variscan Pyrenees induced a longitudinal flow going along with exhumation of the partially molten lower crust. This scenario perfectly fits with the *P–T–t* paths from our samples and from the Lac Cornu eclogites (Vanardois et al., in review). Therefore, we propose that dextral transpression in the ARM started at ca. 340 Ma. At that time, strain was partitioned between vertical and horizontal fabrics that accommodated longitudinal flow and exhumation of the lower crust and burial of metasedimentary rocks in the meantime. Ongoing transpression led to the broadening of dextral shear zone and their coalescence in an anastomosed system where lower and upper crustal domains juxtaposed before final exhumation in the range 330–310 Ma (Fig. 12).

Eclogite remnants in ECMs have been interpreted either as an ancient subducted oceanic crust (Guillot et al., 2009; Guillot and Ménot, 2009; Rubatto et al., 2010; Jouffray et al., 2020) or as pieces of the lower thickened continental crust (Jacob et al., 2020; Vanardois et al., in review). The reconstitution of the prograde metamorphic paths of both studied samples (AR14 and AR736) highlight the absence of LT-HP conditions in the metapelites and is more consistent with intracontinental crustal thickening.

7. Conclusion

Petrological observations and models allowed us to constrain the conditions of peak metamorphism of two metapelites of the Aiguilles-Rouges massif at 630–680 °C and 0.82–0.97 GPa associated to monazite crystallisation with an age of 333 ± 6 Ma Ma. Garnet compositional mapping emphasizes successive growth stages followed by a partial resorption phase followed by the crystallization of a thin rim. Despite high strain deformations during the cooling and exhumation, the garnet core compositions preserved in both samples a record of prograde metamorphic conditions that are comparable. The thin rims constrained a retrograde stage. Petrological observations suggest that the crystallization of monazite is induced by garnet breakdown occurring during the early retrograde stages from 333 ± 6 Ma to 311 ± 5 Ma. The deformation and associated fluids drained in the large-scale dextral shear zone partially or totally recrystallized monazite and reset ages. Comparison with the P–T path previously obtained for the eclogitic lenses support a juxtaposition of the upper and lower crustal domains at 333 ± 6 Ma followed by a shared final exhumation during dextral transpression at 311 ± 5 Ma. Furthermore, our prograde metamorphic conditions are consistent with a continental collision and do not record any indications of a subduction stage.

Acknowledgements

This work was supported by the BRGM through the Référentiel Géologique de la France program (RGF program). Didier Convert-Gaubier provided generous support with thin section preparation.

Supplementary material

Tables S1 and S2 are presented in Annexe 3.

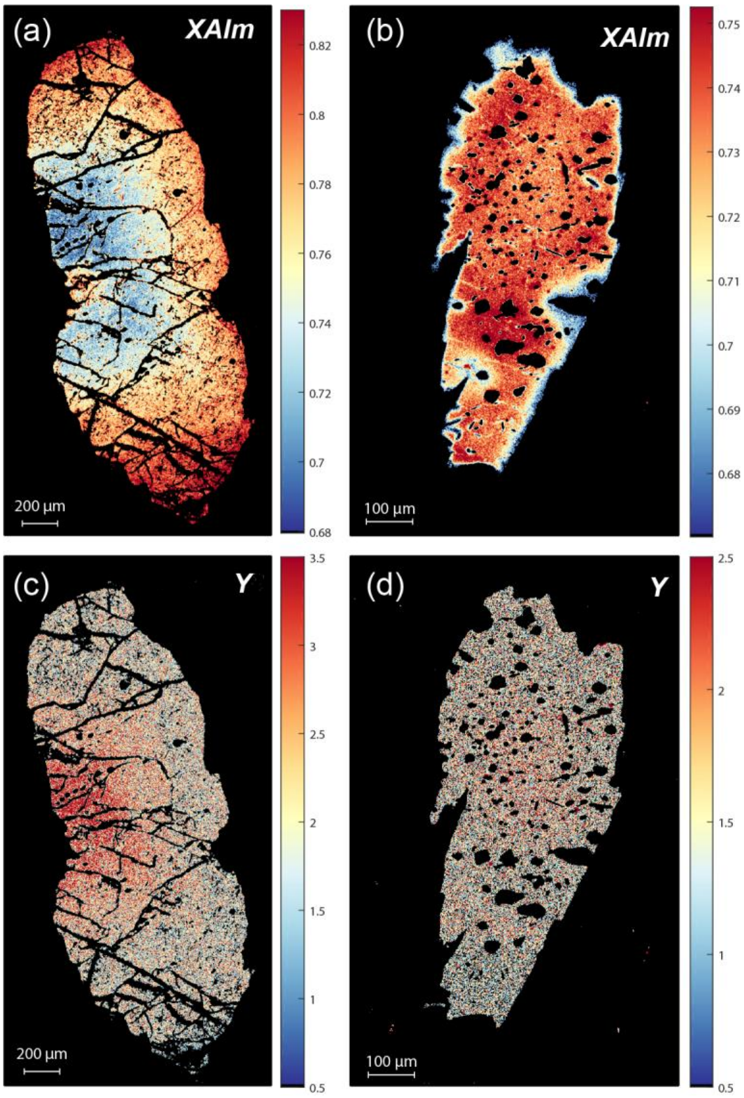

Figure S1 : Additional compositional maps acquired by electron probe microanalyser (EPMA) from samples AR736 (a-c) and AR14 (b-d). Compositional maps of garnets in function of their (a-b) almandine (Alm) and (c-d) yttrium (Y) contents. Yttrium maps are in WDS counts.

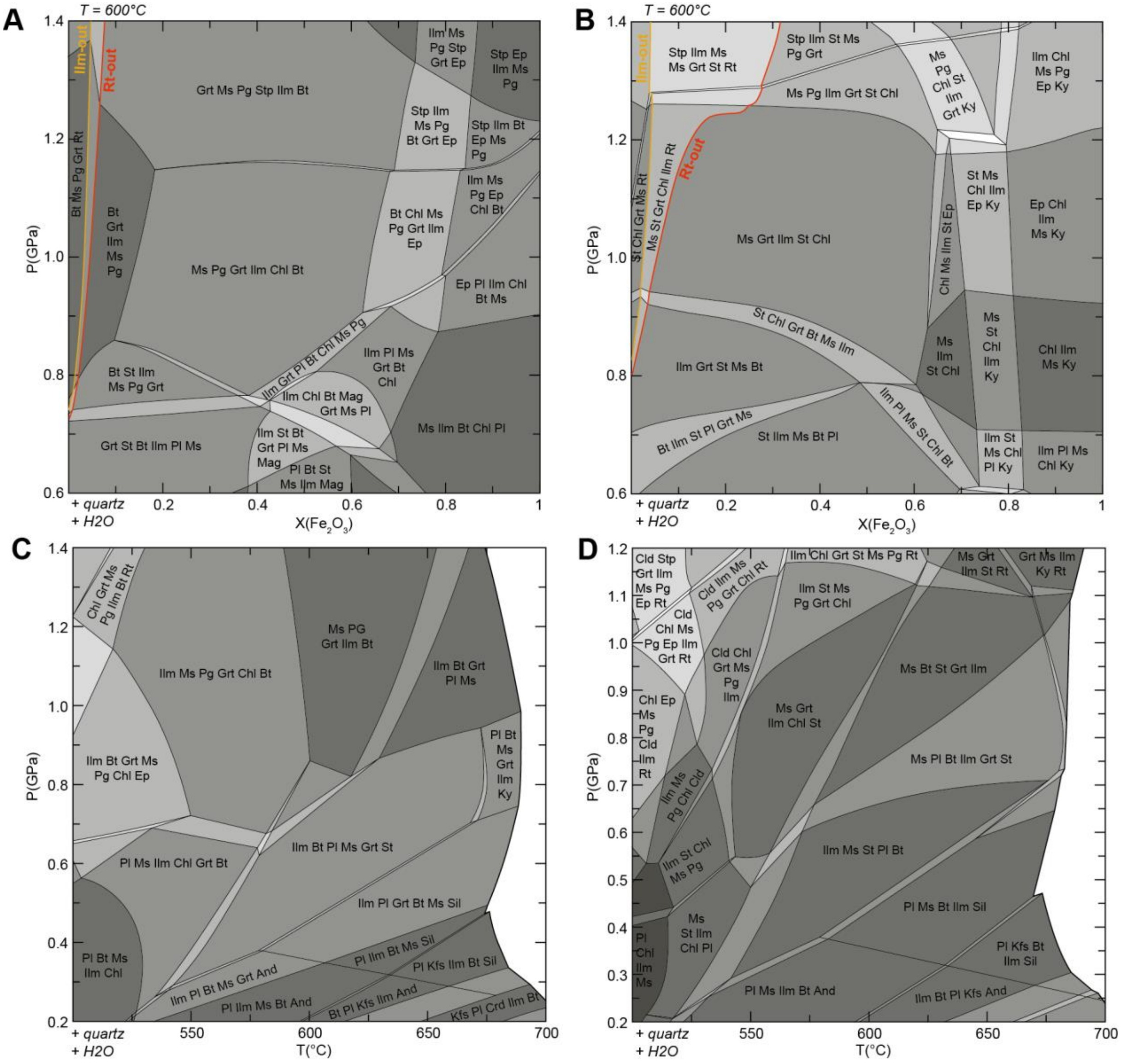

Figure S2 : Diagrams obtained from samples AR14 (A and C) and AR736 (B and D). (A and B) P-XFe2O3 diagrams at 600 °C showing the strong impact of Fe_2O_3 on the stability of rutile and ilmenite. (C and D) Phases diagrams with similar settings than in figures 5-6 with 10 mol% of Fe_2O_3. Note the absence of field without ilmenite. And: andalusite; Bt: biotite; Chl: chlorite; Cld: chloritoid; Crd: cordierite; Ep: epidote; Grt: garnet; Ilm: ilmenite; Kfs: K-feldspar; Ky: kyanite; Mag: magnetite; Ms: muscovite; Pg: paragonite; Pl: plagioclase; Rt: rutile; Sil: sillimanite; St: staurolite; Stp: stilpnomelane; Ttn: titanite. Epidote model is from Holland and Powell (2011) and magnetite model is from White et al. (2002).

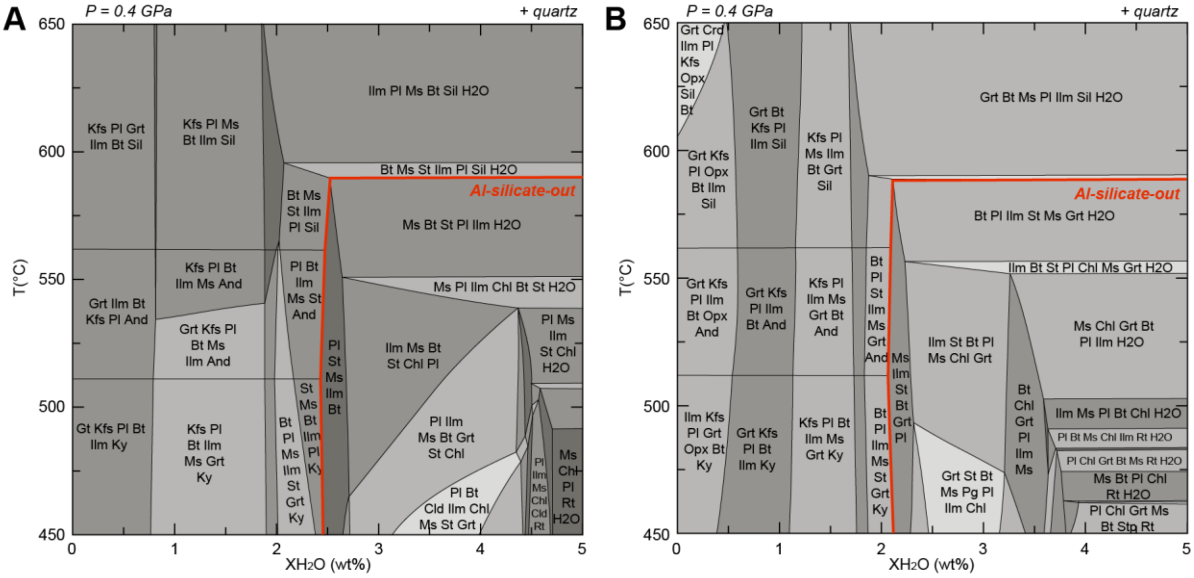

Figure S3 : Impact of H_2O content on the stability field of aluminosilicates for samples (A) AR736 and (B) AR14. And: andalusite; Bt: biotite; Cld: chloritoid; Chl: chlorite; Crd: cordierite; Grt: garnet; Ilm: ilmenite; Kfs: K-feldspar; Ky: kyanite; Ms: muscovite; Opx: orthopyroxene; Pg: paragonite; Pl: plagioclase; Rt: rutile; Sil: sillimanite; St: staurolite; Stp: stilpomelane.

Chapitre 6. Relations entre déformations, fusion hydratée et emplacement de granite dans une zone de cisaillement crustale.

Ce chapitre présente une étude structure sur l'ensemble du massif des Aiguilles-Rouges et une partie du massif du Mont-Blanc. Cette étude révèle que l'ensemble de ces massifs est principalement structuré par un réseau anastomosé de foliations et de zones de cisaillement formant de larges structures S-C-C' formées durant un régime transcurrent dextre (D2). Des foliations peu pentées antérieures au cisaillement dextre (D1) et une fabrique planaire subhorizontale postérieure à ces déformations (D3) complètent la structuration Varisque de ces massifs. L'analyse microstructurale des plutons ainsi que leur datation U-Pb LA-ICPMS sur leurs zircons et monazites nous permettent de contraindre l'évolution tectonique des massifs des Aiguilles-Rouges et du Mont-Blanc et de discuter de l'emplacement de ces plutons dans la croûte. Des datations supplémentaires sur de petits corps magmatiques issus de l'anatexie de la croûte (i.e. pegmatites, aplites) nous permettent de discuter de l'origine des magmas et de proposer un modèle intégrant la déformation, la fusion hydratée de la croûte et l'emplacement de larges plutons dans une zone de cisaillement crustale. Ce chapitre est présenté sous la forme d'un article en préparation pour une soumission à *Tectonophysics*.

Interplay between deformation, water-fluxed crustal melting and granite growth in a crustal-scale shear zone. The case of the East-Variscan Shear Zone in the Aiguilles-Rouges and Mont-Blanc massifs (French External Crystalline Massifs).

Jonas Vanardois[1]*, Pierre Trap[1], Françoise Roger[2], Jérémie Melleton[3], Didier Marquer[1], Jean-Louis Paquette[4], Philippe Goncalves[1], Florence Cagnard[3] and Benjamin Le Bayon[3]

jonas.vanardois@univ-fcomte.fr; pierre.trap@univ-fcomte.fr; francoise.roger@umontpellier.fr; didier.marquer@univ-fcomte.fr; j.l.paquette@opgc.univ-bpclermont.fr; f.cagnard@brgm.fr; b.lebayon@brgm.fr; j.melleton@brgm.fr

[1]UMR 6249 Chrono-environnement, Université de Bourgogne-Franche-Comté, 25030 Besançon, France.

[2]Géosciences Montpellier, Campus Triolet, Université Montpellier, CNRS, 34095 Montpellier Cedex 5, France.

[3]BRGM-French Geological Survey, 3 Avenue Claude Guillemin, 45100, Orléans, France.

[4]Laboratoire Magmas et Volcans (CNRS-UMR 6524), Campus Universitaire des Cézeaux, 63178 Aubière Cedex, France.

*Corresponding author: jonas.vanardois@univ-fcomte.fr +33(0)381666242 Present address: 16 route de Gray, 25030 Besançon.

Key points: External Crystalline Massifs, Variscan Belt, Transpression, Structural analysis, LA-ICMPS dating

Abstract

The Aiguilles-Rouges massif represents a segment of a crustal-scale transpressional shear zone named the Eastern Variscan Shear Zone (EVSZ) along which two plutonic pulses, i.e. early and late Carboniferous, occurred. The aim of this study is to constrain the relationships between the crustal-scale shear zone, emplacement mechanism of plutons in the crust and the source of the melts. We first present a structural analysis on the whole massif that highlights the detailed crustal-scale anastomosed network of the EVSZ. Microstructural observations and U-Pb LA-ICPMS dating of zircon from large plutons constrain the beginning of the transpression at 340 Ma. From 340 to 305 Ma, the EVSZ broadened and formed a 25 km-wide S-C-C' anastomosed network creating dilation zones acting as preferential paths for melt segregation and pluton growth. Additional U-Pb LA-ICPMS dating of zircon and monazite from small magmatic bodies (i.e. pegmatites, aplite and microgranite) yields a strong ordovician inheritance recorded in magmatic zircon grains. Considering the low temperature of melting (ca. 700°C), the zircon inheritance reveals that granitic melts are mainly derived from water-fluxed melting of Ordovician meta-igneous rocks. Gradually, the growth and broadening of the dextral anastomosed network facilitated the water-flux through the meta-igneous that increased the volume of anatectic melts and also favored the formation of large plutons. A comparison with zircon records from Variscan granitoids from the Armorican and the French Central Massif

suggest that the water-present melting of meta-igneous rocks could be a major source of melts in the whole Variscan belt.

1. Introduction

Continent-scale strike-slip shear zones are very efficient conduit along which ductile and brittle deformation drives the segregation and transport of melt from deep to shallow crustal levels where syn-kinematic plutons emplaced (e.g. D'Lemos et al., 1992; Tikoff and Teyssier, 1994; Tommasi et al., 1994; Brown and Solar, 1998; Brown, 2013). Large(continental)-scale shearing may last over tens of m.y. (Oriolo et al., 2018; Simonetti et al., 2020a) but may result from a succession of transient events located at specific spatial areas in a complex and dynamic network of anastomosed small(kilometer)-scale shear zones (e.g. Fossen and Cavalcante, 2017). The dynamics of granitic pluton construction is source controlled and large plutons (>103km3) have infilling rates of about 1-10 Ma (Brown, 2013; de Saint Blanquat et al., 2011). Duration and quantity of melt production could be very variable depending on the lithology and melting reaction. Recently, water-fluxed crustal melting was increasingly regarded as an important mechanism to trigger voluminous melting (Weinberg and Hasalovà, 2015) and produce large batholiths (Collins et al., 2016) as an alternative to dehydration melting of biotite or amphibole. A full understanding, from the genesis to the emplacement of granitic magma along crustal-scale shear zones necessitate reconciling the timing and rate of processes between shear deformation, melt production at depth, melt and aqueous fluid transfer and pluton growth.

The Aiguilles-Rouges and Mont-Blanc (AR-MB) massifs expose sections of middle and upper crust where migmatites and syn-kinematic carboniferous granitic plutons are in close spatial-temporal relationships with the continental-scale East-Variscan Shear Zone (EVSZ; Guillot et al., 2009; Simonetti et al, 2020a). Previous geochronological studies documented two magmatic events at ca. 340-330 Ma and ca. 310-300 Ma (von Raumer and Bussy, 2004 and references therein). This two-fold carboniferous plutonism is typical of the External Crystalline massifs of the variscan Alps (e.g. Debon and Lemmet, 1999) and other neighbour areas in the Variscan belt (Corsica-Sardinia: Paquette et al., 2003; Rossi et al., 2009; Vosges: Tabaud et al., 2014, 2015). The early carboniferous plutons are rather small and emplaced in the upper crust whereas the late-carboniferous plutons are large with an approximate area of ca. 20 to 200 km^2. Granitic melts are thought to have formed at depth in a thickened continental crust (Bussy, 1990; von Raumer and Bussy, 2004). However, the precise rock source of the related granitic magmas is elusive as well as the draining structural framework and deformation history.

Field relationship combined with a multiscale structural analysis allows the detailed strain pattern of the EVSZ in the AR-MB area to be drawn. LA-ICPMS dating gives new insights on emplacement and inheritance ages of small(pegmatites) and large(pluton) magmatic bodies and crustal anatexis. We integrate our field-based structural analysis and U-Th/Pb data to propose a model for the production, ascent and emplacement of silicic magma within the EVSZ. We emphasize the importance of water-fluxed crustal melting and appearance of large-scale dilative structures controlling melt transfer from migmatitic source to pluton sink.

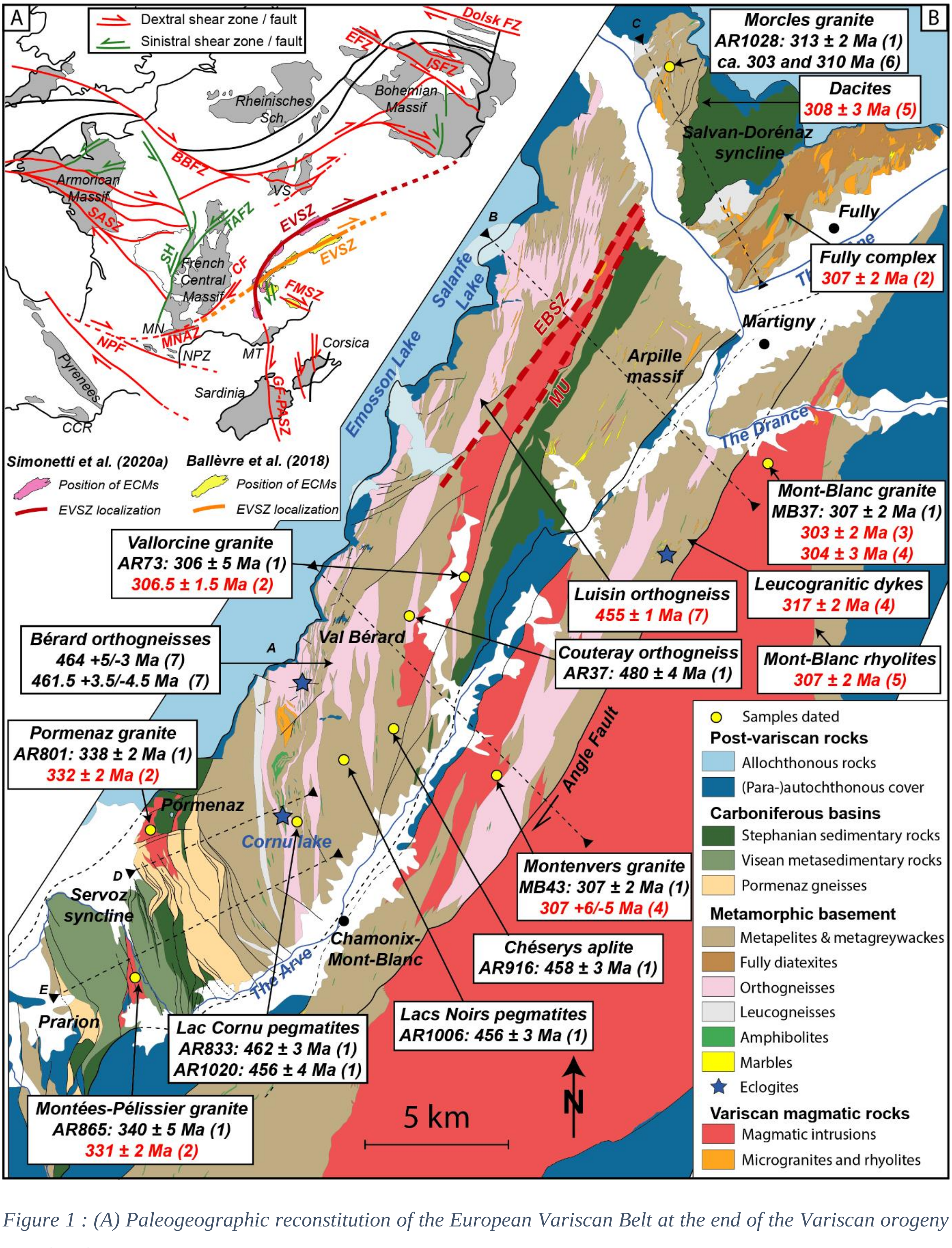

Figure 1 : (A) Paleogeographic reconstitution of the European Variscan Belt at the end of the Variscan orogeny modified from Franke et al. (2017). Sardinia and Corsica have the same position as the one used in Simonetti et al. (2020a). Models of the EVSZ are after Simonetti et al. (2020a) and Ballèvre et al. (2018). The position of ECMs is after Bellahsen et al. (2014) in the Ballèvre et al. (2018) model. BBFZ: Bristol Bray Fault Zone; CCR: Catalan Coastal Ranges; CF: Cévennes Fault; EFZ: Elbe Fault Zone; EVSZ: Eastern Variscan Shear Zone; FMSZ: Ferrière-Mollière Shear Zone; GF-PAL: Grimault Fault - Posada-Asinara Shear Zone; ISFZ: Intra-Sudetic Fault Zone; MN: Montagne Noire; MNAZ: Montagne Noire Axial Zone; NPF: North Pyrenean Fault; NPZ: North

Pyrenean Zone; SASZ: South Armorican Shear Zone; SH: Sillon Houiller; TAFZ: Taure-Aigueperse Fault Zone; VS: Vosges-Schwarzwald. (B) Geological map of the Aiguilles-Rouges and the Mont-Blanc Massifs. EBSZ: Emosson-Bérarde shear zone; MU: Miéville ultramylonite. U-Pb ID-TIMS (red) and LA-ICPMS (black) ages are obtained by (1) this study, (2) Bussy et al. (2000), (3) Bussy & von Raumer (1993), (4) Bussy & von Raumer (1994), (5) Capuzzo & Bussy (2000), (6) Bussien et al. (2017). Cross-sections A, B, C, D and E corresponding to those presented in Figures 3 and 7 are located on the map.

2. Geological setting

The AR-MB massifs belong to the External Crystalline Massifs of the Alps (ECMs) and represent an exhumed portion of the Variscan crust that recorded the history of high temperature deformation from ca. 340 to 300 Ma (e.g. von Raumer and Bussy, 2004; Vanardois et al., in review) (Fig. 1A, 1B). The AR massif has been documented as a dextral dominated transpressional domain and the Emosson-Bérard Shear Zone (EBSZ) interpreted as a part of the EVSZ (von Raumer et al., 2004 and reference therein; Simonetti et al., 2020a). However, the EVSZ width as well as the strain pattern of the AR-MB massifs and their integration in the Variscan belt reconstitution are still matters of discussion (Fig. 1A).

The AR-MB massifs are composed of a high-grade gneissic basement and two low-grade Carboniferous basins (Fig. 1B). The protoliths of the gneissic basement consist of a Protero-Paleozoic sedimentary and volcanoclastic sequence intruded by Ordovician laccoliths (Bussy et al., 2011; Paquette et al., 1989; Fig. 1B). A first middle to high pressure metamorphic event gave rise to garnet-kyanite bearing assemblage in micaschists and paragneisses and omphacite-bearing eclogitic assemblage within mafic lenses (von Raumer and Schwander, 1985, von Raumer and Bussy, 2004; Liégeois and Duchesne, 1981; Vanardois et al., in review). High-pressure conditions have been calibrated at 680-750°C and 1.6-1.85 GPa on the Lac Cornu eclogites (Vanardois et al., in review), and at 650-750°C and 1.3-1.5 GPa on the Val Bérard eclogites (Schulz & von Raumer, 1993, 2011). U-Pb LA-ICPMS analyses on zircon and rutile of an eclogite from the Lac Cornu date the HP metamorphism at 340-330 Ma and a protolith age at ca. 460 Ma (Paquette et al., 1989; Bussy et al., 2011; Vanardois et al., in review). The AR-MB massifs were subsequently affected by a high temperature-low pressure (HT-LP) metamorphism with peak temperature conditions at 650-700°C for pressures ranging between 0.2 and 0.6 GPa (Dobmeier, 1996, 1998; Schulz & von Raumer, 1993, 2011; von Raumer et al., 1996; Chiaradia, 2003; Marshall et al., 1997; Genier et al., 2008).

The main planar fabric reported in the AR massif is coeval with this HT-LP metamorphism and consists of N150 to N30 striking foliation holding a nearly horizontal mineral stretching lineation along which dextral kinematic indicators often occur (Bellière, 1958; von Raumer & Bussy, 2004; Simonetti et al., 2020a). Centimeter to kilometer size dextral mylonites are also reported (Genier et al., 2008; von Raumer & Bussy, 2004). The strain pattern has been interpreted as a dextral transpression (von Raumer & Bussy, 2004; Joye, 1989; Simonetti et al., 2020a). Relics of earlier planar fabrics are mentioned in several studies (Bellière, 1958; Joye, 1989; von Raumer, 1984; von Raumer & Bussy, 2004). In the Lac Cornu area, Vanardois et al. (in review) attributed an early flat-lying foliation as the result of near horizontal flow of the partially molten crust.

Widespread partial-melting over the whole AR-MB massifs started at the end of prograde metamorphism, at near peak pressure condition and lasted during decompression (von Raumer & Bussy, 2004; Genier et al., 2008; Vanardois et al., in review). The peak of temperature and the crystallization of the anatectic melts are dated at 327 ± 2 Ma and 320 ± 1 Ma respectively in Emosson metapelites (ID-TIMS on monazite, Bussy et al., 2000). The gneissic basement underwent several episodes of partial melting. A first anatexis is roughly constrained at ca. 330-315 Ma (Bussy et al., 2000; Bussy and von Raumer, 1994; Vanardois et al., in review). A second anatectic event took place at ca. 307 Ma in the Fully area that corresponds to cordierite-bearing migmatite (Krummenacher, 1959; Bussy et al., 2000) (Fig. 1B).

The upper crustal level consists of low-grade metamorphic rocks that record evidence of transcurrent shearing (Dobmeier, 1996, 1998; Bellière & Streel, 1980). The sequence shows metagreywackes, phyllites and the so-called “greenstones unit” at the bottom of the Servoz syncline and the underlying fine-grained Pormenaz gneisses (Fig. 1B) (Dobmeier et al., 1999). The uppermost portion of the Variscan crust is represented by unmetamorphosed fluvial and volcanic sediments (Pilloud, 1991; Capuzzo & Wetzel, 2004) that fill the upper part of the Servoz syncline and the Salvan-Dorenaz syncline that lie unconformably on the Variscan metamorphic rocks (Dobmeier & von Raumer, 1995; Lox & Bellière, 1993). Whereas some authors consider that these sedimentary rocks were not affected by Variscan deformation (Dobmeier & von Raumer, 1995), variscan folding is reported (Lox & Bellière, 1993) but its tectonic significance remains elusive (e.g. von Raumer & Bussy, 2004).

Along the EBSZ, the syn-kinematic Vallorcine granite emplaced at 306.5 ± 1.5 Ma (ID-TIMS on zircon and monazite; Bussy et al., 2000) during dextral transpression. Similar emplacement ages (ID-TIMS on zircons) at 307 +6/-5 Ma, 303 ± 2 Ma and 304 ± 3 Ma are proposed for the Montenvers and the Mont-Blanc granites, respectively (Bussy & von Raumer, 1993, 1994) (Fig. 1B). The Mont-Blanc and Montenvers granites show local and widespread solid-state vertical mylonites (Bussy, 1990; Bussy et al., 2000). In the MB massif, Bussy and von Raumer (1994) also dated leucogranitic injections within vertical shear zones at 317 ± 2 Ma (ID-TIMS on monazite). Several small-volume intrusions called Morcles microgranite dated at 302.5 ± 3 Ma, 303.6 ± 1.3 Ma and 310.9 ± 2.1 Ma (LA-ICPMS on zircon) are interpreted as the prolongation of the Vallorcine granite at shallow-level (Bussien et al., 2017) (Fig.1B). Furthermore, rhyolitic dykes in the MB massif and dacites in the Salvan-Dorenaz syncline have been dated at 307 ± 2 Ma and 308 ± 3 Ma, respectively (ID-TIMS on zircon; Capuzzo & Bussy, 2000) (Fig. 1B). The detailed temporal relationships between granite emplacement and shear zone networking remains unknown.

The weakly metamorphosed rocks of the upper crustal portion are intruded by the peraluminous Montées-Pélissier monzogranite and the metaluminous Pormenaz monzonite, dated at 331 ± 2 Ma and 332 ± 2 Ma (ID-TIMS on zircon; Bussy et al., 2000) (Fig. 1B). These two ca. 330 Ma granites represent a first magmatic impulse whose relationships with the strain field are not clearly documented. However, several authors proposed that the Pormenaz and Montées-Pélissier plutons are syn-tectonic granites related to the dextral shearing and intruding their surrounding country rocks along vertical shear zones (Bussy et al., 2000; Dobmeier, 1996, 1998). So far, only Bellière (1958) proposed a crustal-scale structural model but without considering strain partitioning and neither heterogeneous deformation nor supra/subsolidus deformation surfaces are documented at the scale of the whole AR-MB massifs.

3. Structural analysis

The AR and MB massifs are juxtaposed narrow NE trending Variscan inliers within the western Alpine external domain that are bounded by autochthonous or allochthonous Mesozoic sedimentary rocks (Fig. 1B). Alpine tectonic and metamorphic reworking are mainly located along low-grade metamorphic shear zones, formed under greenschist facies conditions, below the stability field of biotite (Marshall et al., 1998; Rolland et al., 2003; Rossi et al., 2005) and alpine metamorphism did not exceed 350°C in the surrounding Mesozoic cover (Boutoux et al., 2016). Alpine faulting with reactivation of inherited Variscan shear zone, as the Angle fault in the MB massif is easily depicted on the field (von Raumer and Bussy, 2004; Simonetti et al., 2020a). Alpine tectonics is also responsible for the pinch of the NE-SW elongated

Carboniferous Salvan-Dorenaz syncline (Fig. 1B) (Pilloud, 1991). The Variscan tectono-metamorphic features are confidently identified from the Alpine structures in this massif (e.g. Krummenacher, 1959; von Raumer & Bussy, 2004). Field relationships combined with the multiscale geodata set analysis suggest that the finite strain pattern of the AR-MB area results from the superposition of three deformation events (Fig. 2). In this contribution, D1, D2 and D3 are rather increments of a longer, progressive deformation than deformations phases described as separate events of characteristic external boundary conditions (Fossen et al., 2019). At the scale of the AR-MB area, the gneissic basement principally shows D2 transpressional fabrics that rework an early D1(Fig. 2 and 3), whereas the Servoz syncline shows D2 and D3 deformations. Details on the geometry and the kinematics of each deformation event are given by the following sections.

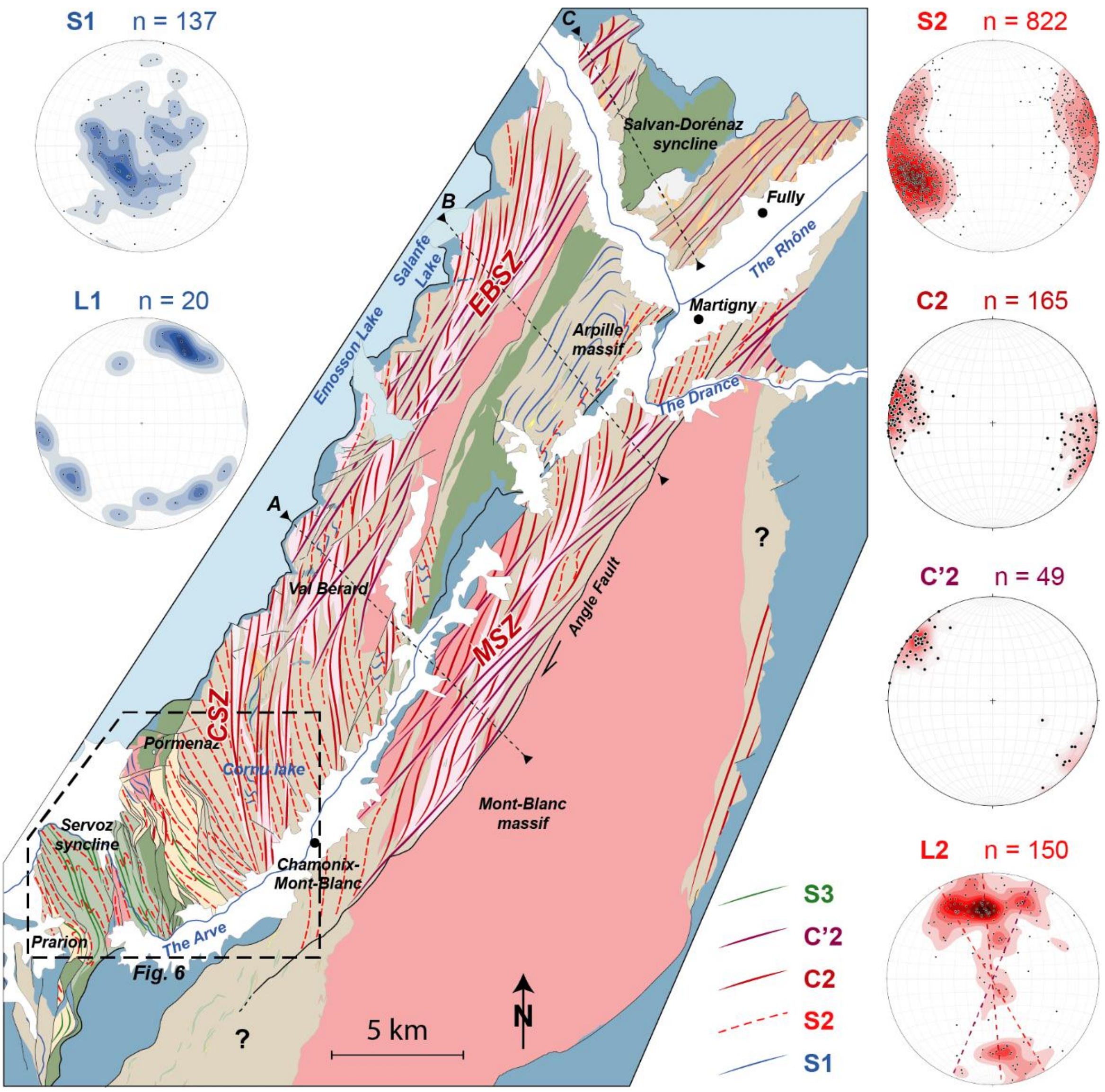

Figure 2 : Synthetic map showing the simplified foliation trajectories of D1, D2 and D3 deformation with poles of planar fabrics and lineations of D1 and D2 deformations (lower Wulf hemisphere stereograms). The areas corresponding to Figures 4 and 5 are indicated. CSZ: Cornu Shear Zone; EBSZ: Emosson Bérarde Shear Zone; MSZ: Montenvers Shear Zone. Poles of planar fabrics and corresponding mineral and stretching lineations for D1 and D2 deformations (lower Wulf hemisphere stereograms).

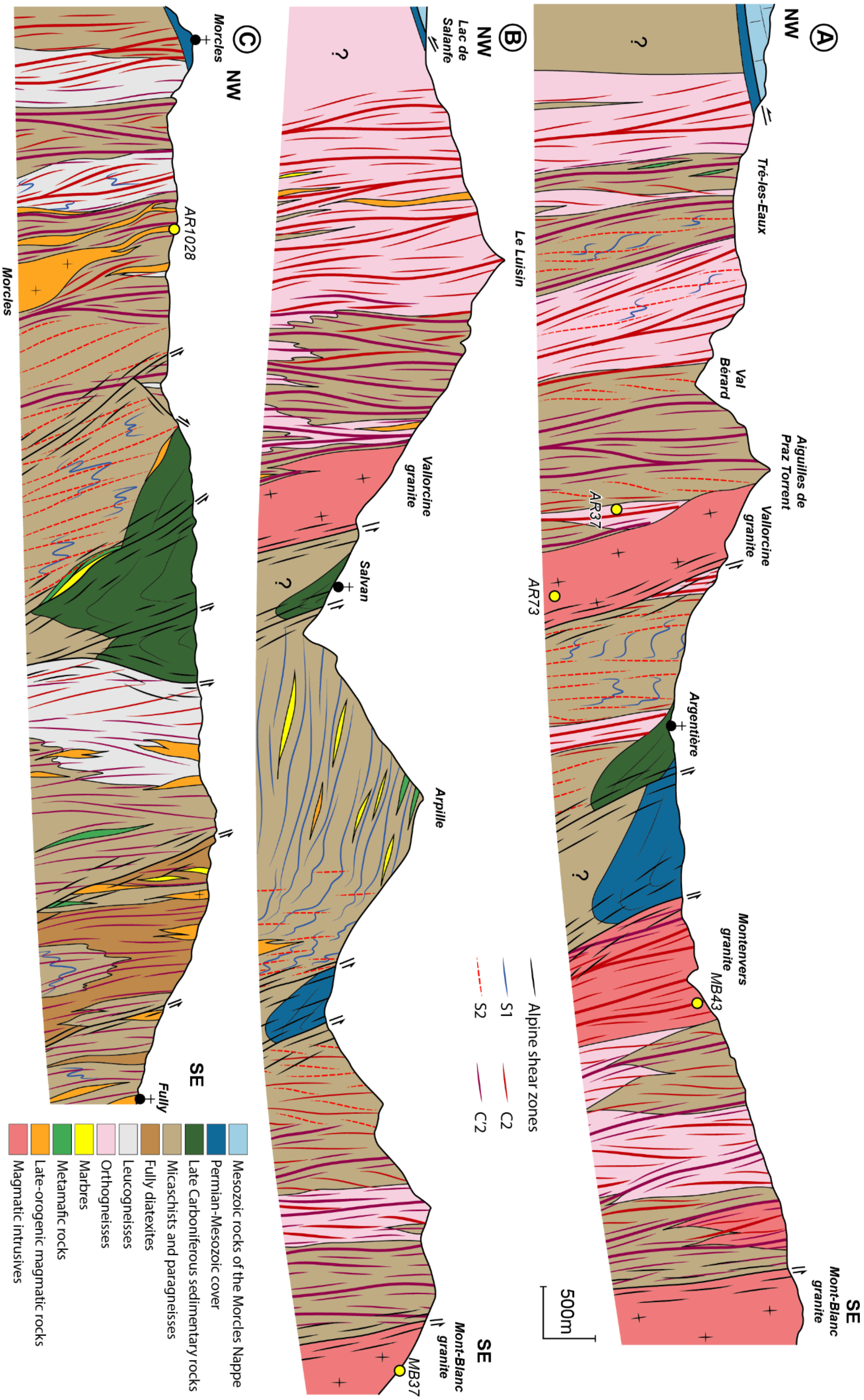
A
NW
?
Tré-les-Eaux
Val Bérard
Aiguilles de Praz Torrent
Vallorcine granite
AR37
AR73
Argentière
?
Montenvers granite
MB43
SE
Mont-Blanc granite
500m
B
NW
Lac de Salanfe
?
Le Luisin
Vallorcine granite
Salvan
?
Arpille
SE
Mont-Blanc granite
MB37
Alpine shear zones
S1
S2
C2
C'2
C
NW
Morcles
AR1028
Morcles microgranite
SE
Fully
Mesozoic rocks of the Morcles Nappe
Permian-Mesozoic cover
Late Carboniferous sedimentary rocks
Micaschists and paragneisses
Fully diatexites
Leucogneisses
Orthogneisses
Marbres
Metamafic rocks
Late-orogenic magmatic rocks
Magmatic intrusives

Figure 3 : E-W Cross-sections through the Aiguilles-Rouges and the Mont-Blanc Massifs (see location of sections on Figure 2).

3.1. D1 deformation

In low-D2 strain domains, D1 is typified by a sub-horizontal S1 foliation with a N20 trending mineral and stretching lineation (Fig. 2). With the increasing of D2 deformation, S1 foliation gets straightened up and folded (Figs. 3 and 4A to D). Because D2 is penetrative at the regional scale, the S1 is most of the time recognized in the hinge of isoclinal D2 folds. In the lower domain, the S1 foliation is made of migmatitic layering and is best recognized in the metapelites from the Arpille massif (Fig. 2 and 3). In the upper domain, a flat-lying foliation is well preserved in the Pormenaz area (Fig. 2). Sigmoids, mica-fishes and C-S structures indicate a top-to-the-NE kinematics (Fig. 4E to H). In metabasites, spectacular retrogressed evolution is visible from the core of boudins constituted of preserved eclogites bearing an early D1 fabric to amphibolites at the rim of the boudins in D2 domains.

It is important to note that the so-called “D1” in this contribution is probably not the first planar fabric deforming the rocks of the AR-MB massifs as attested by few isoclinal folds recognized in the D1 domains (Fig. 4C and F). This early deformation, named Dx in the following, cannot be simply considered as an initial stratigraphy due to the metamorphic minerals composing these ancient planar fabrics.

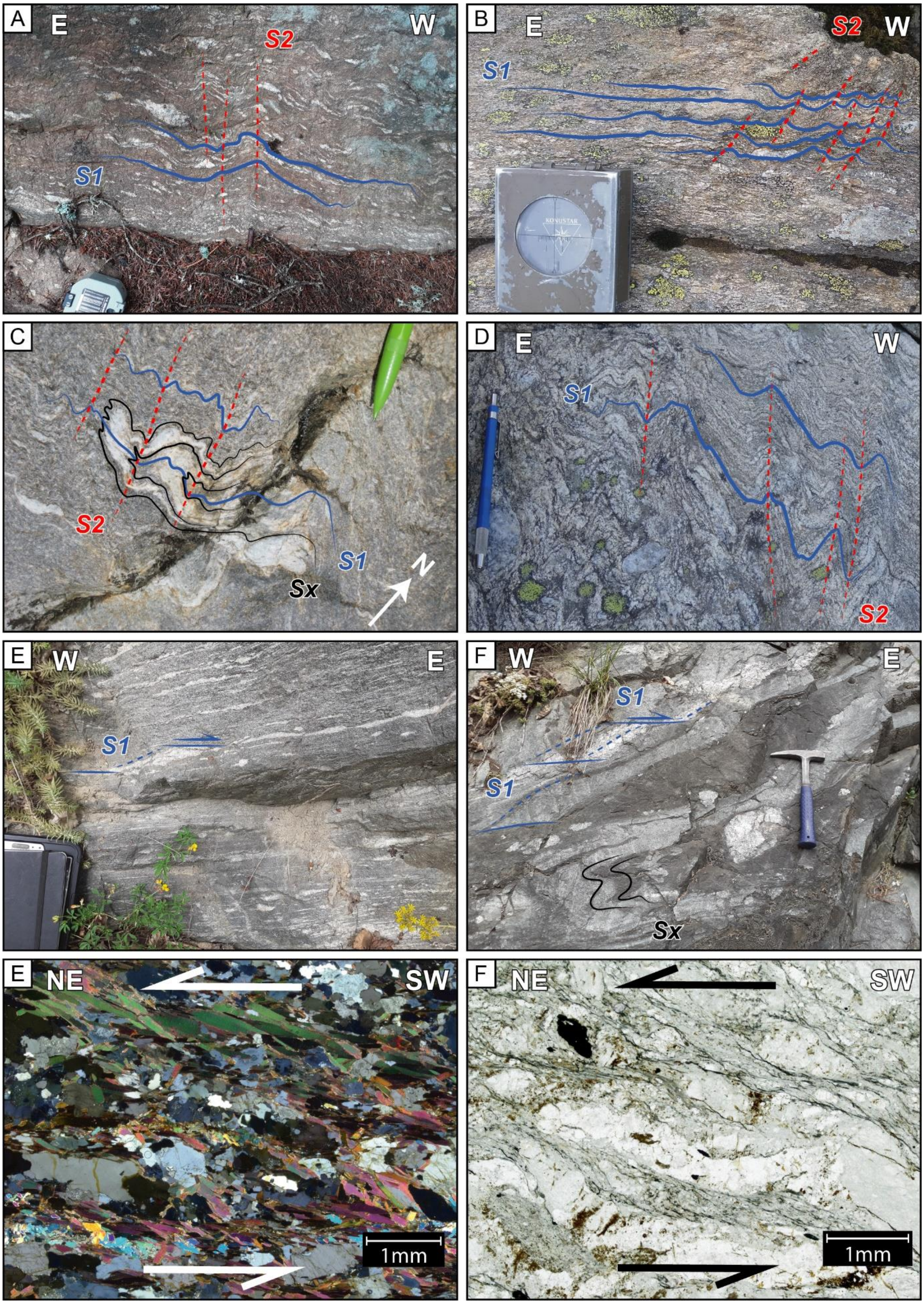

Figure 4 : D1 structural characteristics and D1/D2 relationships. (A) S1 flat foliation preserved in a weakly deformed lense in the Arpille massif. Preserved S1 foliation and appearance of a scarce S2 schistosity (A) in the

Arpille massif, (B) next to the Brévent location and (C) in the Cornu Lake area. (D) D1/D2 fold interference: a F1 fold folding a relic of an Sx foliation and the S1 foliation folded by the S2 schistosity, Val Bérard area. (E and F) Top-to-the-NE kinematics indicated by sigmoids in Prarion metabasites. (G) Top-to-the-NE kinematics indicated by biotite mica-fish forms, Arpille massif. (H) Top-to-the-NE C-S structures in a low-grade Pormenaz gneiss.

3.2. D2 deformation

The D2 deformation is heterogeneous but it is the most pervasive deformation at the scale of the AR-MB massifs (Fig. 2 and 3). It has already been described in several studies (e.g. Joye, 1989; Bellière, 1958; von Raumer & Bussy, 2004; Simonetti et al., 2020a). Our observations highlight a dextral S-C-C' structure at the scale of the whole massif with three main orientations: S2 (N150-170), C2 (N0-20) and C'2 (N20-40). It affects the gneissic basement and the Visean metasedimentary rocks of the Servoz syncline (Fig. 2). In low-D2 strain domains, S2 appears as a weak crenulation cleavage upon folded S1 by F2 folds. Progressive tightening of isoclinal F2 folds culminates in the transposition of S1 into S2 (Fig. 4). The F2 folds have axial planes parallel to the S2 foliation and their fold axes plunge either gently or deeply along the vertical N160 plane. S2 holds a weakly to moderately plunging stretching and mineral lineation that is conspicuously associated with a dextral kinematic as a result of bulk dextral transpression (von Raumer & Bussy, 2004; Simonetti et al., 2020a). In high-D2 strain domains, the increase of dextral shearing forms shear zones. We identified three main shear zones in the AR-MB massif: the Cornu shear Zone (CSZ) mainly formed of C2 planes and the Montenvers and Emosson-Bérarde shear zones (MSZ and EBSZ) composed of C2 and C'2 planar fabrics (Fig. 2). These three planar fabrics hold a L2 lineation gently dipping toward the north (Fig. 2).

Along S2 and C2 planes, leucosomes with no internal solid-state deformation indicate D2 dextral shearing synchronous to partial melting (Fig. 5A). D2 is best observed as sub-solidus fabrics that developed from peak temperature down to low-grade metamorphic conditions (Fig. 5D; Simonetti et al., 2020a; Vanardois et al., in review). In the Fully area, a cordierite-bearing migmatite shows both suprasolidus and subsolidus D2 folding and shearing along C'2 planes (Fig. 5D).

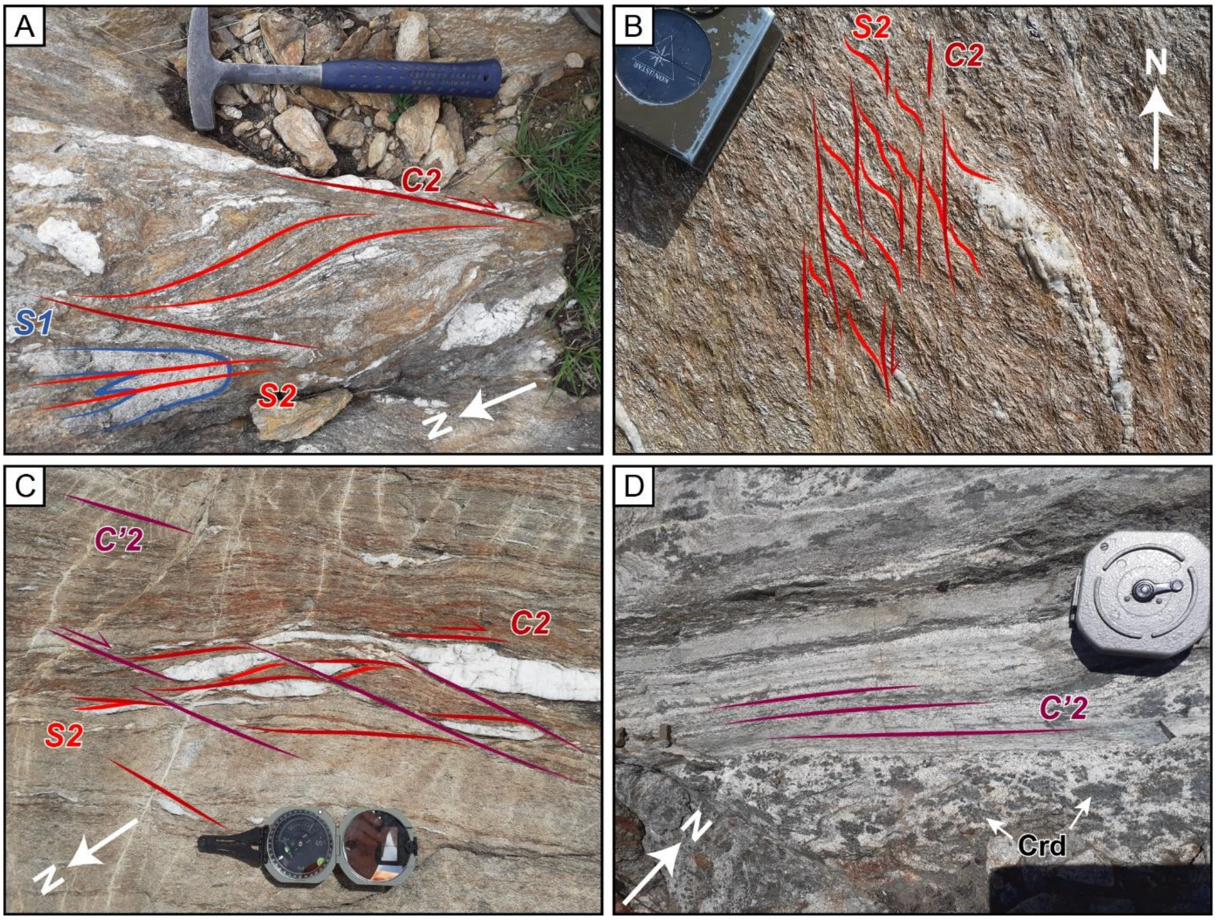

Figure 5 : D2 structural characteristics. S2-C2-C'2 structures in the Lac Emosson area (A and C) and near Chamonix-Mont-Blanc (B). (D) Fully cordierite-bearing migmatites with cordierite clots (Crd) oriented parallel with C'2 planes and affected by subsolidus C'2 shear bands.

3.3. D3 deformation

D3 has only been observed in the south-western part of the AR massif, within the Pormenaz gneisses and the Visean metasedimentary rocks, and is not well-recorded in the whole gneissic basement further north (Fig. 2, 6 and 7). D3 forms meter to decameter sized localized domains where D2 is reworked by open to tight F3 folds with a sub-horizontal S3 cleavage (Fig. 6, 7 and 8). S3 cleavage gently dips toward the East and F3 axial planes are parallel to S3. F3 axes are gently plunging toward N160. Only few lineations have been observed that mainly consist of intersections rather than stretching or mineral lineations (Fig. 6). So far, the kinematics of D3 deformation remains unknown. Few allochthonous injections of partial melting in the F3 hinges indicate that partial melting was still active in the deeper structural levels during D3 (Fig. 8C). The Variscan age of this deformation is inferred from its absence in the Late-Carboniferous sedimentary rocks (Fig. 6 & 7).

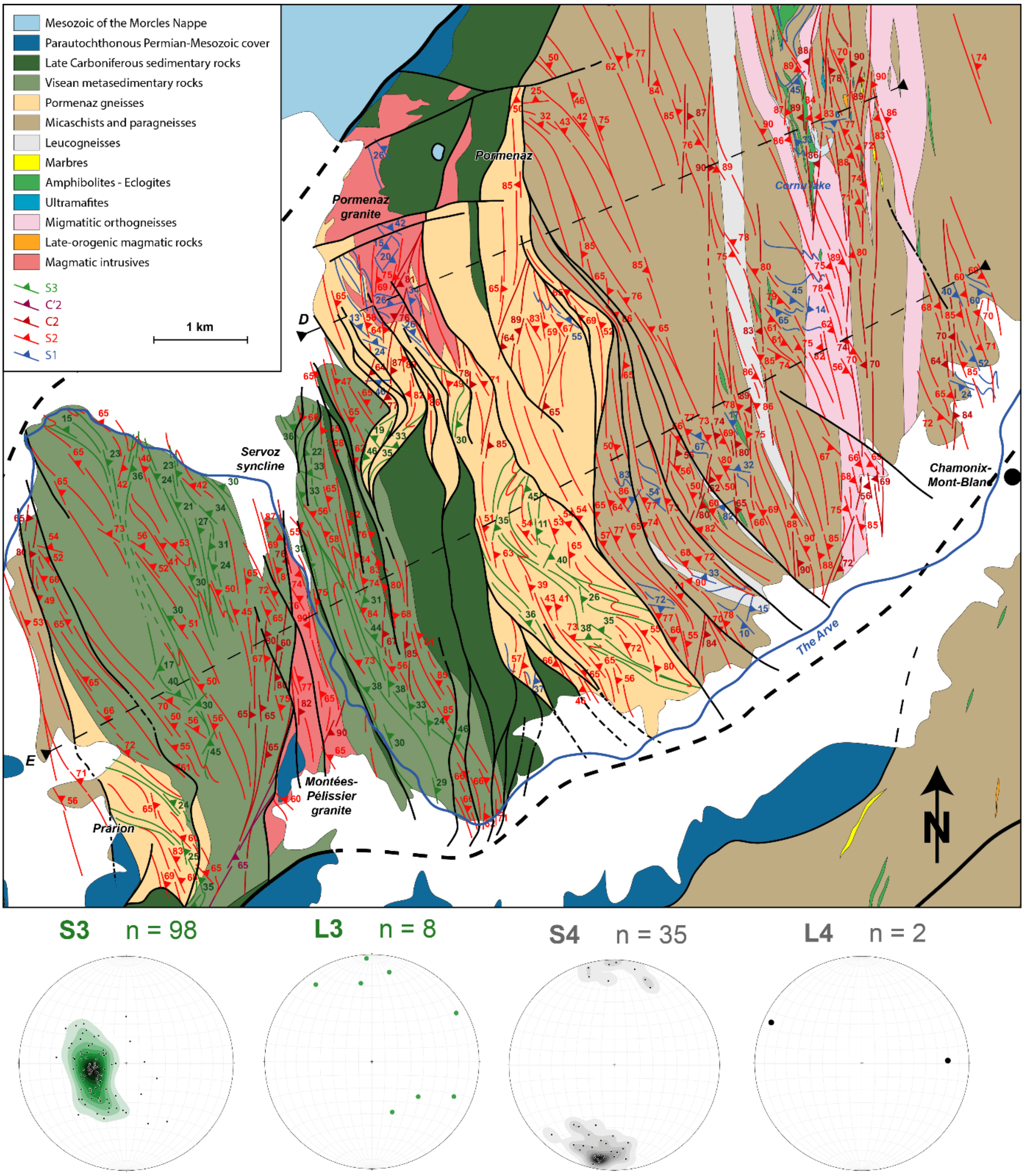

Figure 6 : Detailed map of the D1-D2-D3-D4 foliations and their trajectories in the southwestern part of the Aiguilles-Rouges Massif with poles of planar fabrics and lineations of D3 and D4 deformations (lower Wulf hemisphere stereograms). Locations of cross-sections D and E presented in Figure 6 are located.

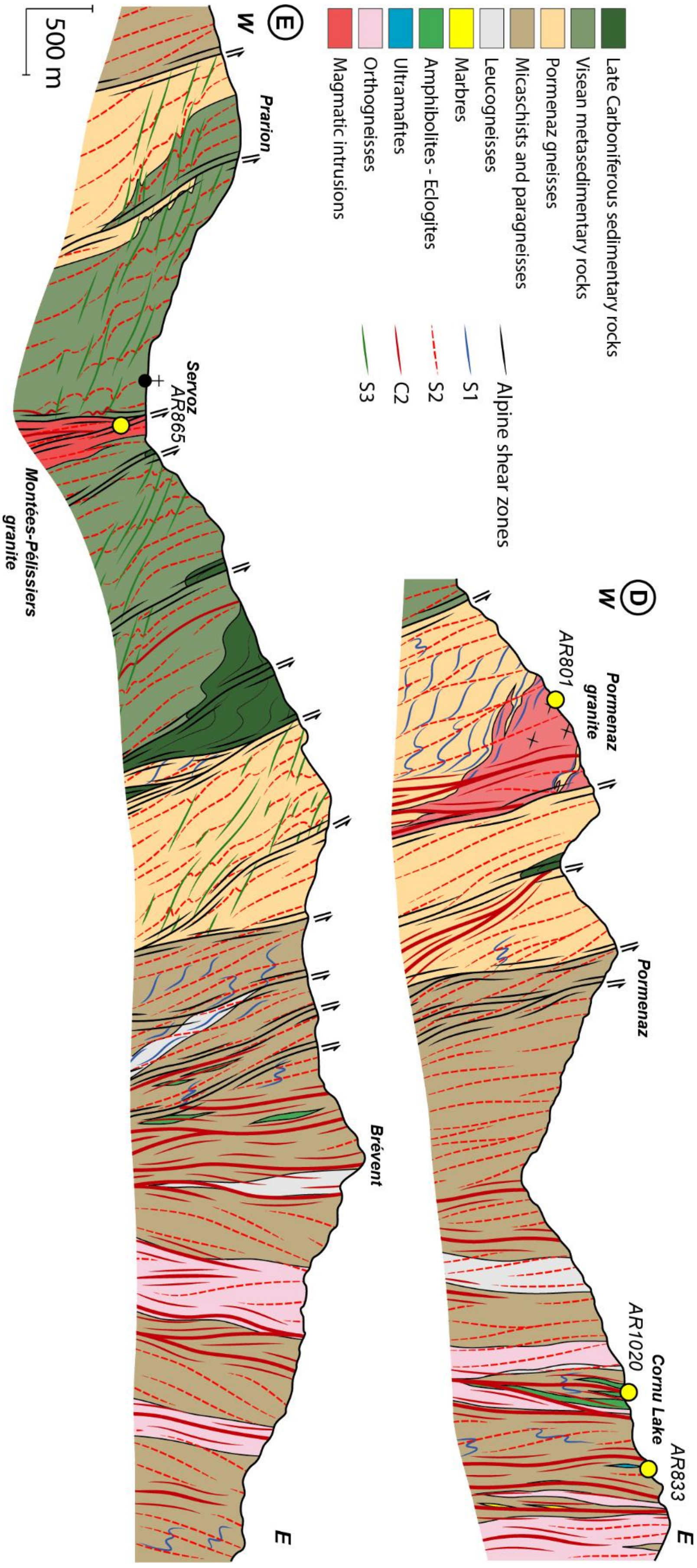
Late Carboniferous sedimentary rocks
Visean metasedimentary rocks
Pormenaz gneisses
Micaschists and paragneisses
Leucogneisses
Marbres
Amphibolites - Eclogites
Ultramafites
Orthogneisses
Magmatic intrusions
Alpine shear zones
S1
S2
C2
S3
500 m
E
W
Prarion
Servoz
AR865
Montées-Pélissiers granite
Brévent
E
D
W
AR801
Pormenaz granite
Pormenaz
AR1020
Cornu Lake
AR833
E

Figure 7 : E-W cross-sections at the southwestern extremity of the Aiguilles-Rouges Massif. (A) In the Pormenaz area and (B) through the Servoz syncline.

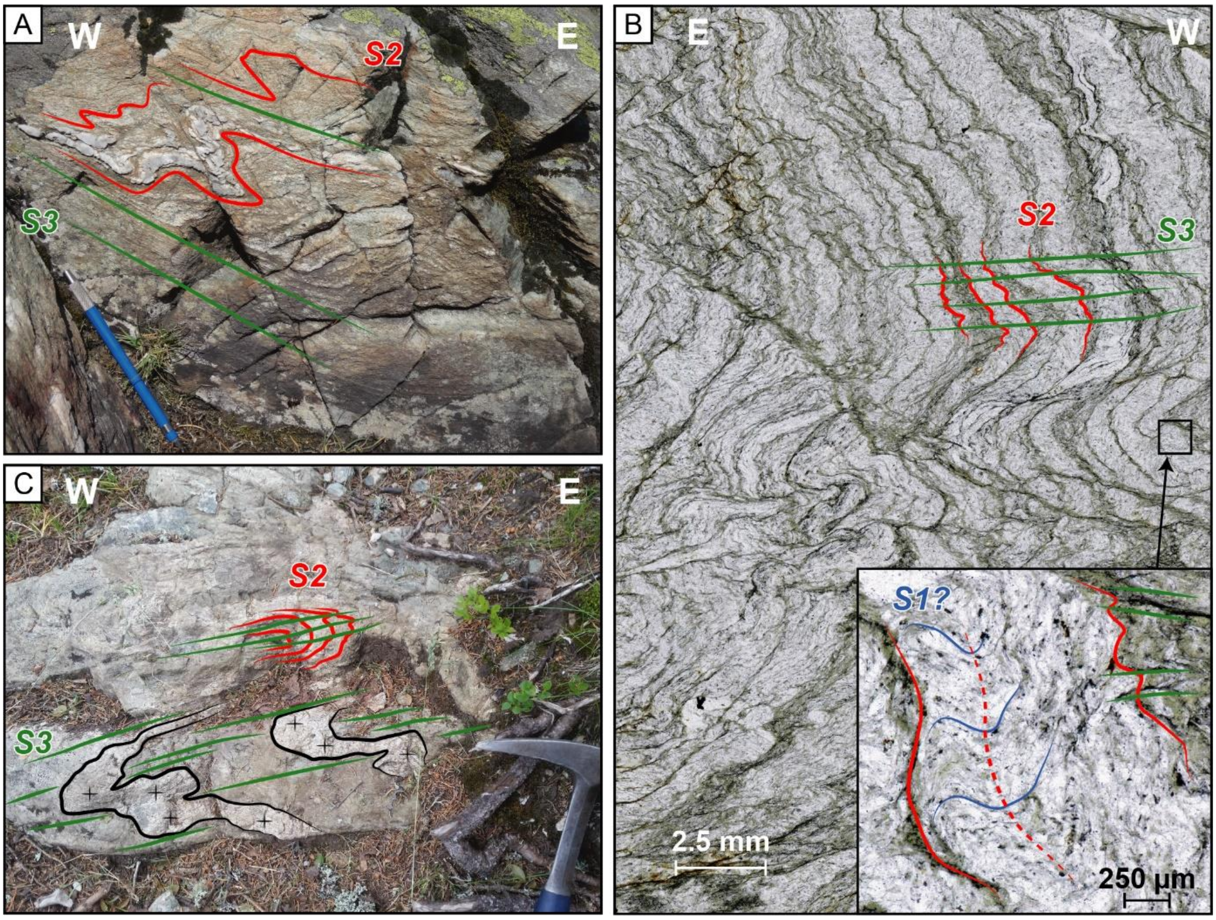

Figure 8 : Outcrops and microphotographs showing D3 characteristics. (A) F3 folds from the western side of the Servoz syncline, Prarion area. (B) Thin section showing the interference relationships of D1-D2-D3 planar fabrics in Visean greenschists. (C) Accumulation of weakly deformed allochthonous trondhjemtitic melts in F3 fold hinges.

4. Field relationships, strain features and U-Th/Pb dating of studied samples

Eleven samples have been dated that come from different locations of the plumbing system, from migmatitic rocks (migmatitic orthogneiss AR37) to plutonic bodies (Pormenaz granite AR801), Montées-Pélissier granite AR865, Vallorcine granite AR73, Montenvers granite MB43 and Mont-Blanc granite MB37) through veins complexes, i.e the Morcles microgranite sample (AR1028) and four pegmatitic and aplitic dykes (AR833, AR1020, AR1006 and AR916). Their field locations are detailed on Fig. 1 and Table 1. Field relationships and finite strain features of each magmatic rock, related to D1, D2 or D3 deformations, are given in the following paragraphs.

Table 1 : Localisation and description of samples

Sample	**Rock type**	**GPS location**	**Mineral dated**	**U-Th-Pb age (±2σ)**
AR801	Pormenaz granite	N45.949951 E06.789104	Zircon	338 ± 2 Ma
AR865	Montées-Pélissier granite	N45.917067 E06.77147	Zircon	340 ± 5 Ma
AR73	Vallorcine granite	N46.032901 E06.936665	Zircon	306 ± 5 Ma
MB43	Montenvers granite	N45.96768 E06.949665	Zircon	306 ± 3 Ma
MB37	Mont-Blanc granite	N46.063859 E07.08007	Zircon	305 ± 2 Ma
AR37	Courtenay orthogneiss	N46.019559 E06.907883	Zircon	587 ± 10 Ma 480 ± 4 Ma
AR1028	Morcles microgranite	N46.193943 E07.043689	Zircon Monazite	463 ± 10 Ma 312.5 ± 1.7 Ma
AR833	Lac Cornu Pegmatite	N45.956094 E06.853814	Zircon	462 ± 3 Ma 317 ± 6 Ma
AR1020	Lac Cornu Pegmatite	N45.958210 E06.846594	Zircon	456 ± 4 Ma
AR1006	Lac Noirs Pegmatite	N45.966231 E06.871656	Zircon	456 ± 3 Ma
AR916	Chéserys Pegmatite	N45.982963 E06.908710	Zircon	458 ± 3 Ma

Zircon and monazite U-Th-Pb dating of these samples was carried out using Laser Ablation-Inductively Coupled Plasma Mass Spectrometry (LA-ICP-MS) at the Laboratoire Magmas et Volcans, Clermont–Ferrand (France). Separated zircon and monazite grains were mounted in epoxy resin discs that were polished to reveal equatorial cross sections. Cathodoluminescence (CL) and Back-Scattered Electron (BSE) images were used to select points for analysis. The analyses involve the ablation of minerals with a Resonetics Resolution M-50 powered by an ultra-short pulse ATL Atlex Excimer laser system operating at a wavelength of 193 nm (detailed description in Müller et al., 2009). The detailed analytical procedures are described in Paquette and Tiepolo (2007), Hurai et al. (2010), and Paquette et al. (2014) and detailed in the Table S1. Data reduction was carried out with the GLITTER® software package developed by Macquarie Research Ltd (Jackson et al., 2004). The analytical data are provided in Table S1. Ages and diagrams were generated using the Isoplot/Ex v. 2.49 software package by Ludwig (2001). Only concordant data or discordant data fitting with the discordia line were taken into account in the age calculation. In the text and figures, all uncertainties in ages are given at ± 2σ level.

4.1. Early (ca. 330 Ma) plutons.

4.1.1. The Pormenaz granite (AR801)

The Pormenaz granite was emplaced in the gneisses of the eastern side of the Servoz syncline (Fig. 1) and is composed of quartz, K-feldspar, plagioclase and chloritized biotite. Field observations in the western part of pluton indicate that the magmatic fabric is marked by the alignment and orientation of euhedral K-feldspar megacrystals which defines a sub-horizontal planar fabric parallel to the S1 of the surrounding gneisses (Fig. 6 & 7) and a mineral lineation L1 that trends N20 (Fig. 9A), respectively. The D1 deformation is pervasive along the pluton's edges and weak in its core (Fig. 7A). In the eastern part, the S1 magmatic foliation is deformed by the D2 deformation and reoriented into a vertical foliation striking from N0 to N20 (Fig. 6 & 7). In this area, the K-feldspar megacrystals are plastically deformed as well as the surrounding matrix subsolidus conditions (Fig. 9B). The K-feldspar grains are fractured and quartz show undulose extinction and BLG recrystallization and none myrmeckite, GBM or SGR recrystalization or other high-temperature deformations are observed, which suggest that the D2 deformation affected the Pormenaz granite after its cooling. Based on these observations, the Pormenaz pluton is interpreted as syn-D1, and its eastern border suggests that this pluton was lately deformed by the vertical C2 shear zone at subsolidus conditions. Sample AR801 was collected in the western part of the Pormenaz pluton in a pervasive D1 domain (Fig. 7A) which also deformed the pluton at low-temperature conditions with SGR recrystallization of quartz.

Most of the zircon grains analysed are euhedral either prismatic with a shape ratio up to 2:1 or stubbier with a shape ratio of 1:1. They are pinkish, transparent to slightly opaque. CL imaging shows strong evidence of concentric or oscillatory igneous growth zoning as well as the presence of cores displaying either a sector-like zoning or patchy zoning textures surrounded by zoned rims (Fig. 10A). Seventy-five analyses were performed on sixty-five zircon crystals (Table S2). In the Tera Wasserburg diagram, excepted two inherited cores (#10 and 35) concordant around 650 Ma, all the data are scattered along the concordia curve between around 340 to 190 Ma with thirty-two data yielding a concordia age of 338 ± 2 Ma ($\mathrm{MSWD}_{(C+E)}$ = 1.4) (Fig. 11A). These data consist mainly of zoned cores (24 cores and 8 rims). The analysed grains have a various range of Pb (8.5-69 ppm), Th (most 55-281 ppm) and U (150-1526 ppm) contents and Th/U ratios (most 0.15-0.51) (Table S2). Other data (dotted ellipses) mainly composed of rims (34 rims and 7 cores) are characterized by similar Pb, Th and U contents and Th/U ratios (most 0.14-0.66) (Table S2). They are not taken into consideration for the age calculation because they are often discordant. These discordances are due to radiogenic Pb losses and common Pb contaminations.

Figure 9 : Deformation patterns in the magmatic rocks of the Aiguilles-Rouges and the Mont-Blanc Massifs. (A) L1 mineral lineation indicated by euhedral K-feldspars from the western part of the Pormenaz granite (AR801). (B) Pormenaz granite deformed by the D2 in the eastern side of the pluton. (C) Thin section in crossed light of the Montées-Pélissier granite (AR865) with feldspar mineral oriented parallel with the C2 planes. Orange arrows indicate microfractures in feldspar infilled by quartz suggesting high temperature sub-magmatic deformation. (D)

Undeformed Vallorcine granite (AR73) cross-cutting the C'2 planar fabrics of the EBSZ. (E) Montenvers granite deformed by the D2. (F) Thin section in crossed light of the Montenvers granite (MB43). Orange and yellow arrows indicate microfractures in feldspar infilled by quartz and quartz-polygonal blasts recrystallization suggesting high temperature sub-magmatic deformation, respectively. Blue arrows indicate quartz-polygonal blasts deformed at lower temperature. (G) Mont-Blanc granite (MB37) showing a magmatic foliation inferred by the alignment of K-feldspar that is parallel to C'2 orientation. (H) Couteray orthogneiss affected by a C2-C'2 shear zone with rare evidence of early partial melting (orange arrow). (I) Thin section in crossed light of the Morcles microgranite (AR1028) without mineral orientation.

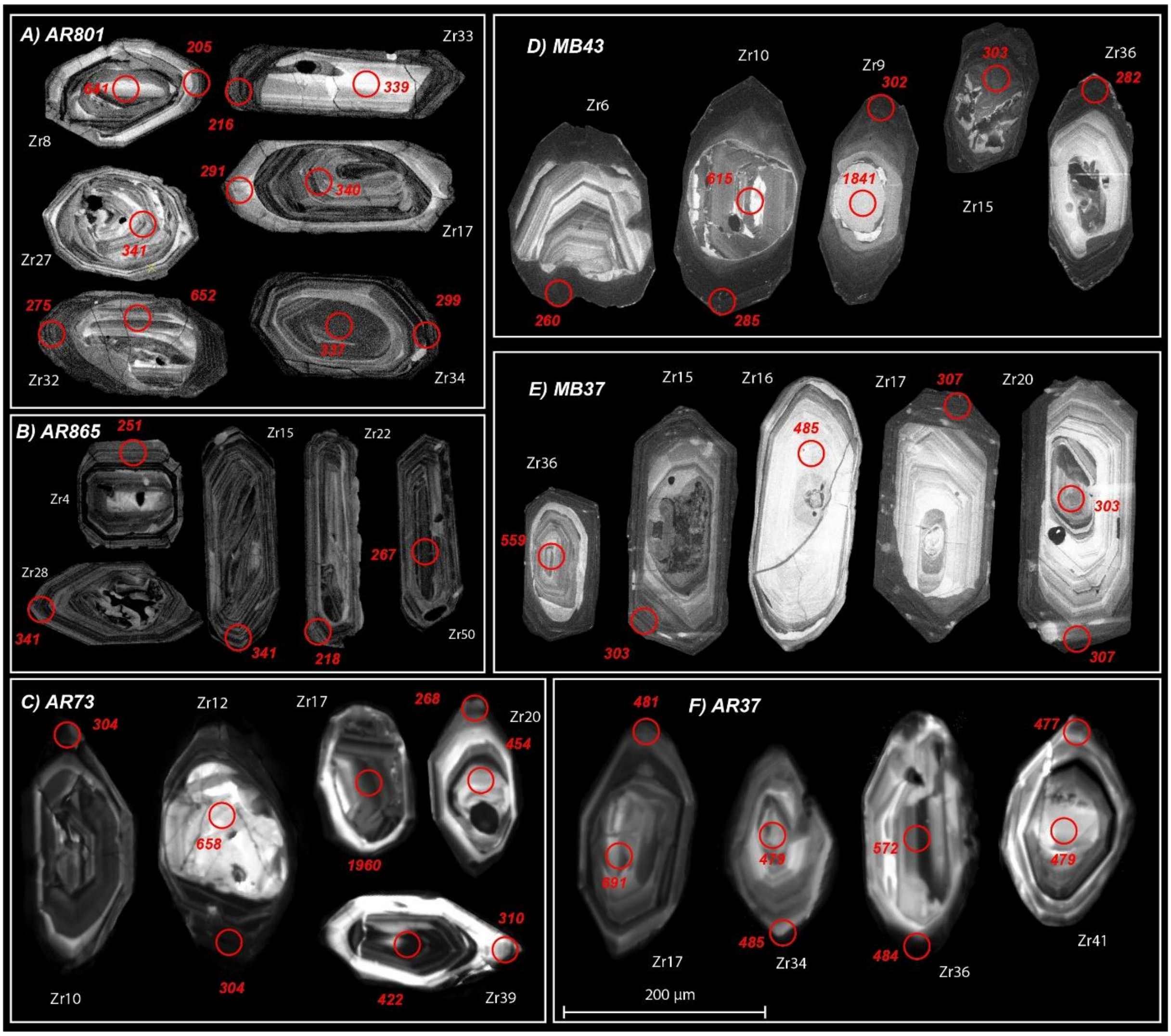

Figure 10 : *Cathodoluminescence images of zircon grains from: (A) the Pormenaz granite (sample AR 801); (B) the Montées Pélissier granite (AR865); (C) the Vallorcine granite (AR73); (D) the Montenvers granite (MB43); (E) the Mont Blanc granite (MB37); (F) the Couteray orthogneiss. Red circles indicate the analytical spots locations with the* ^{206}*Pb/*^{238}*U date without errors associated. Zr number corresponds to the zircon grain numbers reported in Tables S2.*

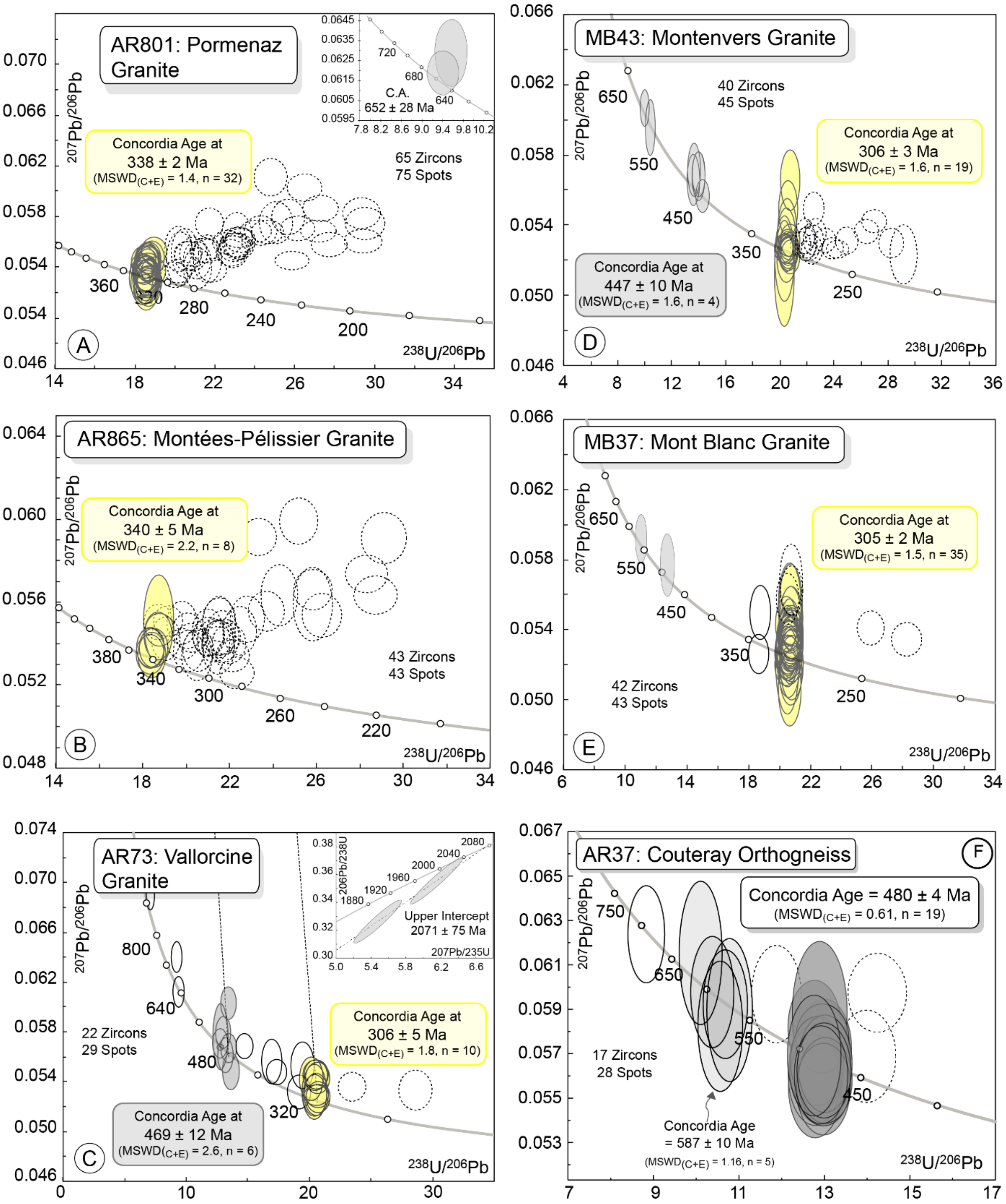

Figure 11 : Zircon U-Pb Tera Wasserburg diagrams obtained by LA-ICPMS on (A) the Pormenaz granite (AR801), (B) the Montées Pélissier granite (AR865), (C) the Vallorcine granite (AR73), (D) the Montenvers granite (MB43), (E) the Mont Blanc granite (MB37), (F) the Couteray orthogneiss. Error ellipses and uncertainties in ages are ± 2σ level. The discordance of dotted ellipses is due to radiogenic Pb losses and common Pb contaminations. Dotted and white ellipses are not taken into account for the age calculation (see text for detail).

4.1.2. The Montées-Pélissier granite (AR865)

The Montée-Pélissier pluton is a fine-grained monzogranite intruding the Visean metasedimentary rocks in the Servoz syncline (Fig. 1) composed of quartz, K-feldspar, plagioclase with few muscovite and chloritized biotite. The D2 deformation highly deformed this pluton and erased most of the original magmatic foliation. Nonetheless, in thin-section, it appears that feldspar crystals are oriented parallel with the C2 shear planes and show extensive microfractures filled by quartz (Fig. 9C), suggesting that the granite may have deformed under high temperature and sub-magmatic conditions (e.g. Hibbard, 1987; Bouchez et al., 1992; Pawley and Collins, 2002) before being highly deformed at lower temperatures. The Montée-Pélissier pluton is interpreted as a syn-D1 intrusion highly reworked during D2 transpression.

Zircons from sample AR865 are pinkish, transparent, eudrehal and elongated but often broken. CL imaging shows strong evidence of concentric or oscillatory igneous growth zoning (Fig. 10B). Forty-three analyses are obtained on rims or cores of 43 crystals and present Th/U ratios ranging between 0.04 and 1.02 (most 0.16-0.67) with homogeneous Pb content (most 21-64 ppm) and variable U (most 555–1450 ppm) and Th (most 90–347 ppm) contents (Table S2). In the Tera Wasserburg, the data are scattered along the concordia curve between around 350 to 210 Ma (Fig. 11B). The eight oldest data (# 2, 6, 7, 8, 12, 13, 22 and 34) form a cluster around 340-335 Ma that yields a concordia age of 340 ± 5 Ma ($\mathrm{MSWD}_{(C+E)}$ = 2.2). Other data (dotted ellipses), often discordant, show younger $^{206}\mathrm{Pb}/^{238}\mathrm{U}$ ages (Table S2; Fig. 11B). These data are not taken into account because they were probably affected by radiogenic Pb losses as well as common Pb contaminations.

4.2. Late (ca. 305 Ma) plutons

4.2.1. Vallorcine granite (AR73)

The Vallorcine granite is a NE-SW elongated pluton composed of quartz, K-feldspar, plagioclase and biotite that emplaced in the EBSZ (Fig. 3). Unlike Simonetti et al. (2020a), we have observed that the Vallorcine granite crosscuts the C’2 shear planes near the Emosson Lake (Fig. 9D) and is weakly deformed. Alternatively, it often shows a magmatic foliation parallel to the C’2 orientation (Joye, 1989; Bussy et al., 2000) as well as an elongated shape (Fig. 1B). In thin section, quartz is nested with undulose extinction, and small shear bands induce quartz Grain Boundary Recrystallization (GBM; Stipp et al., 2002). Thus, we propose that the Vallorcine granite emplaced through the C’2 EBSZ.

The zircon crystals from the Vallorcine granite (AR73) are transparent, pinkish and euhedral. Zircon ranges in shape from equant to elongate. These latter are often broken. CL images also show complex internal textures such as the presence of inherited cores and concentric oscillatory zoning and patchy zoning textures (Fig. 10C). Twenty-nine analyses were carried out on twenty-two zircons (Fig. 11C). Two data composed by two inherited cores (#4 and 25) are sub-concordant and yield an upper intercept at 2071 ± 75 Ma. These zircon cores have similar Pb (64-67 ppm), Th (31-59 ppm) and U (181-184 ppm) contents with Th/U ratios of 0.17 and 0.32 (Table S2). Three data obtained on inherited cores show Th/U ratios of ca. 0.3 and have also a sub-concordant position around 650 Ma (# 15 and 20) and 840 Ma (# 2) (Table S2). The other twenty data are scattered along the concordia curve between around ca. 840 to 220 Ma by forming two main distinct clusters: one very wide between 485 and 450 Ma (group 1) and the other more limited between 310 to 300 Ma (group 2). Group 1 dates (# 3, 5, 6, 10, 12, 18, 22) were determined from 5 cores and 2 rims. These seven analyses are characterized by variable Pb and Th contents ranging from 19 to 52 ppm and 11 to 183 ppm, respectively and by Th/U ratios from 0.04 to 0.54 (most 0.13-0.54) (Table S2). The linear regression on these seven data yields a lower intercept date of 468 ± 13 Ma (MSWD = 2). Amongst these data, six give a concordia age of 469 ± 12 Ma ($\mathrm{MSWD}_{(C+E)}$ = 2.5). Group 2 dates (# 7, 8, 11, 16, 19, 21, 23, 26, 27, 29) are obtained from 2 cores and 8 rims. Pb and Th contents ranging from 12-72 ppm and 11-201 ppm, respectively, and with Th/U ratios from 0.01 to 0.31 (most 0.1-0.31) characterize these data. These ten data yield a concordia age of 306 ± 5 Ma ($\mathrm{MSWD}_{(C+E)}$ = 1.8). The five data (white ellipses) between these two clusters are probably meaningless because they correspond to a mixed age. The two youngest data (dotted ellipses) may be the result of radiogenic Pb loss.

4.2.2. Montenvers granite (MB43)

The Montenvers granite intruded into anatectic paragneiss and orthogneiss of the MB massif (Fig. 1) and is composed of Qtz + Kfs + Pl + Ms + Bt + scarce Grt. The Montenvers granite and its host rocks are highly deformed by an anastomosed network of C2 and C'2 shear zones of the MSZ (Fig. 2, 3A & 9E). Microfractures in feldspar filled by quartz and quartz-polygonal blasts recrystallization observed in thin section (Fig. 9F) suggest high temperature and sub-magmatic deformation (e.g. Hibbard, 1987; Bouchez et al., 1992; Pawley and Collins, 2002; Kurse et al., 2001; Stipp et al., 2002; Passchier & Trouw, 2005; Owona et al., 2013). Later D2 deformation of quartz-polygonal aggregates forming NE-SW trending and steeply dipping planes indicate ongoing solid-state C'2 shear deformation during subsolidus cooling. Therefore, we propose that the Montenvers granite was emplaced within the C2-C'2 MSZ before being deformed by the latter C'2 shear zones.

Zircons from sample MB43 are pinkish, transparent. They have either a squat shape with a shape ratio up to 2:1 or a sub-eudrehal shape with prismatic or elongated fragments. CL imaging shows evidence of concentric or oscillatory igneous growth zoning as well as the presence of cores displaying either a sector-like zoning or patchy zoning textures surrounded by zoned rims with sometimes a thinner and CL-dark over-rim (Fig. 10D). Forty-five analyses are obtained on rims or cores of 40 crystals and present Th/U ratios ranging between <0.01 and 1.30 (most 0.01-0.82) with variable Pb (33-404 ppm), U (most 98–5721 ppm) and Th (most 29–869 ppm) contents (Table S2). In the Tera Wasserburg diagram, excepted the datum # 4 (no plotted) measured on the inherited core of the zircon Z9 showing a Th/U ratio of 1.30 and a discordant position around 1.8 Ga, all the other data are scattered along the concordia curve between around 620 to 220 Ma by forming a main cluster around 310-220 Ma and two others more limited around 600 Ma and 450 Ma (Fig. 11D). The cores of zircons Z10 (# 9) and Z19 (#19) have a Th/U ratio of 0.32 and 0.79 and give concordant data at 615 ± 16 Ma and 592 ± 16 Ma, respectively. The cluster at 450 Ma consisting of the analyses obtained on three tips (# 1, 35, 43; Th/U = 0.01-0.26) and two cores (# 29, 37; Th/U = 0.15-0.38) that yield a concordia age of 447 ± 10 Ma ($MSWD_{(C+E)}$ = 1.6, n = 4). Amongst of the thirty-eight youngest data, nineteen data constituted by 10 cores and 9 rims yield a concordia age of 306 ± 3 Ma ($MSWD_{(C+E)}$ = 1.6) (Fig. 11D). In the diagram, the dotted ellipses are obtained mainly on the metamict CL-dark rim and are characterized by very high U contents (1315-9763 ppm). They are not taken into consideration for the age calculation, their discordance is due to radiogenic Pb losses and common Pb contaminations.

4.2.3. Mont-Blanc granite (MB37)

The Mont-Blanc granite is a huge NE-SW elongated pluton forming the main part of the MB massif (Fig. 1) and is composed of Qtz + Kfs + Pl + Bt. The granite core is mostly weakly deformed and shows a magmatic foliation emphasized by the slight alignment of the K-feldspar, and biotite crystals and mafic enclaves striking N20-40 (Bussy, 1990), parallel with the C'2 shear planes (Fig. 9G). In its northern border, the pluton is deformed by the C'2 shear zones (Fig. 2). Therefore, we consider that the Mont-Blanc granite is not post-tectonic as proposed in several studies (e.g. Bussy et al., 2000; von Raumer & Bussy, 2004) but is rather a late-D2 intrusion.

The zircon crystals from the Mont Blanc granite (MB37) are transparent, pinkish and euhedral with an elongated shape with a shape ratio up to 3:1. CL imaging shows evidence of oscillatory igneous growth zoning as well as the presence of few cores displaying either a sector-like zoning surrounded by CL-dark zoned rims (Fig. 10E). Forty-three analyses were carried out forty-two zircons (Fig. 11E, Table S2). Among these data, two data (#15 and 34) composed by two inherited cores characterized by a concentric zoning and a Th/U ratio of 0.34 are concordant at ca. 485 Ma and ca. 558 Ma. And there are also two more data (# 1 and 10) obtained on a centre and a rim which are concordant to ca. 335 Ma with a Th/U around 0.3-0.4. Otherwise, thirty-seven data form a cluster characterized by Th/U ratios ranging between 0.2 and 0.86 and yield a concordia age of 305 ± 2 Ma ($MSWD_{(C+E)} = 1.5$, n = 35). Two discordant data (dotted ellipses) (#37 and 42) obtained on CL-dark rims show youngest $^{206}Pb/^{238}U$ dates which may be the result of radiogenic Pb loss as well as common Pb contamination.

4.3. Small intrusions, aplites and pegmatites

4.3.1. Morcles microgranite (AR1028)

Sample AR1028 comes from one of the dykes composing the Morcles microgranite, located in the northern part of the AR massif. It is mainly composed of quartz, K-feldspar and plagioclase with few muscovite and chloritized biotite grains. Minerals are not oriented, quartz grains do not show undulose extinction and are sometimes nested (Fig. 9H). No evidence of subsolidus deformations have been observed. Calcite partially replaced some feldspar grains and filled cracks, which probably indicates late fluid circulations (Fig. 9H). This microgranite has a main NE-SW orientation and sometimes cross-cuts C2 and C’2 shear zones. Its emplacement is therefore interpreted as late or posterior to the C’2 shear zones and D2 deformation in this area.

Zircons from sample AR1028 are not numerous, colourless to slightly pink and transparent. They have either a squat shape with a shape ratio up to 3:1 or ovoid or fragment-like. CL images show complex internal textures such as the presence of inherited cores and concentric oscillatory zoning and patchy zoning textures (Fig. 12A). A few monazite crystals were also found in this sample. They are euhedral, transparent, light yellow. CL imaging exhibits concentric oscillatory zoning or patchy zoning textures (Fig. 12A). Some crystals have metamict rims which could not be analysed because they are too rich in Pb common.

Twenty analyses were carried out on seventeen zircons and present Th/U ratios ranging between 0.08 and 0.62 (most 0.1-0.44) with variable Pb (3.9-118 ppm), U (40–2298 ppm) and Th (16–731 ppm) contents (Table S2). In the Tera Wasserburg diagram, except the data 5 and 8, the concordant to sub-concordant data are scattered between ca. 800 and ca. 450 Ma (Fig. 13A). The linear regression on ten data (# 1, 4, 6, 9, 10, 11, 14, 16, 17, 18) obtained on 5 centres and 5 rims yields a lower intercept date of 463 ± 10 Ma (MSWD = 2.9 Ma). Sixteen analyses were also performed on nine monazite crystals (Table S2). Excepted the datum # 11, the data form a cluster with a concordia age of 313 ± 3 Ma ($\mathrm{MSWD}_{(C+E)}$ = 0.49, n = 15) in the concordia diagram (Fig. 13B). The datum # 11 which has a discordant position around ca. 360 Ma, is probably meaningless, it may correspond to an analytical mixture between an old component (possibly Ordovician) and a Variscan component.

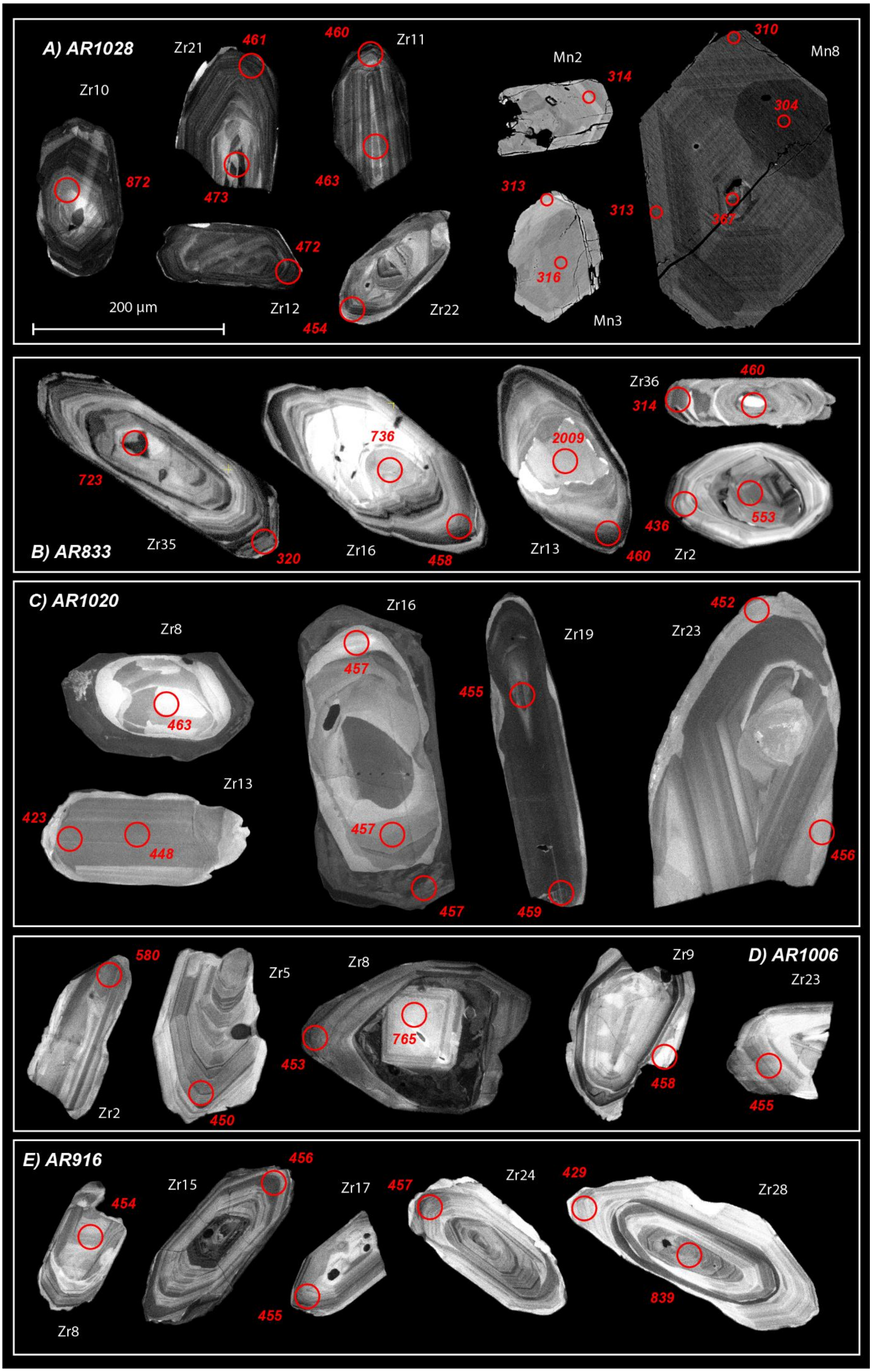
A) AR1028
Zr10
872
Zr21
461
473
460
Zr11
463
Zr12
472
454
Zr22
200 µm
Mn2
314
313
316
Mn3
310
Mn8
304
313
367
B) AR833
Zr35
723
320
Zr16
736
458
Zr13
2009
460
Zr36
314
460
Zr2
436
553
C) AR1020
Zr8
463
Zr13
423
448
Zr16
457
457
457
455
Zr19
459
Zr23
452
456
Zr2
580
Zr5
450
Zr8
453
765
Zr9
458
D) AR1006
Zr23
455
E) AR916
Zr8
454
Zr15
456
Zr17
455
457
Zr24
429
Zr28
839

Figure 12 : Cathodoluminescence and back-scattered electron images of zircon and monazite grains from: (A) the Morcles microgranite (AR1028); (B) a Lac Cornu pegmatite (AR833); (C) a Lac Cornu pegmatite (AR1020); (D) the Lacs Noirs pegmatite (AR1006); (E) the Chéserys aplite (AR916). Red circles indicate the analytical spots locations with the ^{206}Pb/^{238}U date or ^{208}Pb/^{232}Th date without errors associated for the zircons and the monazites, respectively. Zr (or Mn) number corresponds to the zircon (or monazite) grain numbers reported in Tables S2.

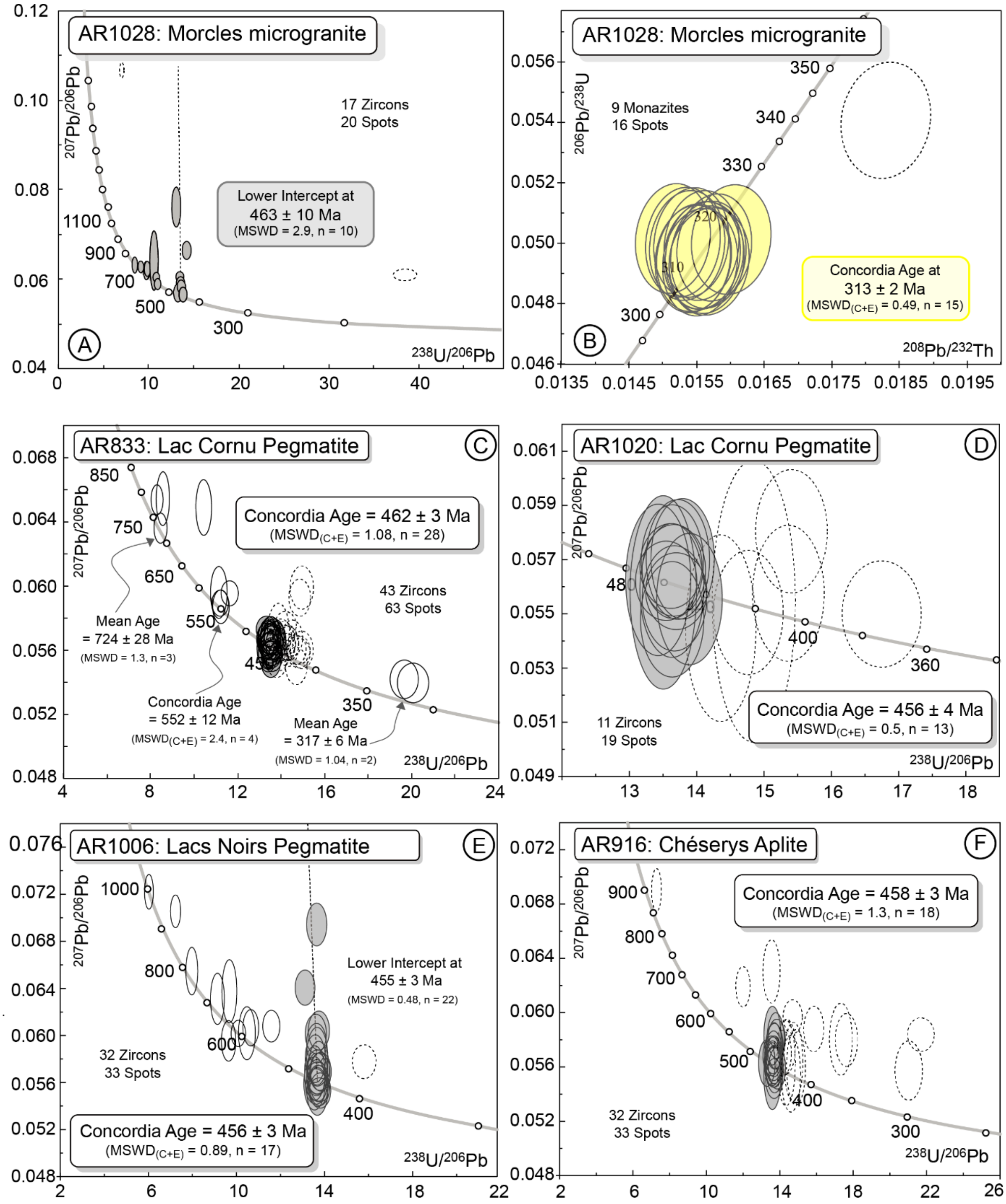

Figure 13 : Zircon U-Pb Tera Wasserburg diagrams and monazite U-Th-Pb concordia diagram obtained by LA-ICPMS on (A and B) the Morcles microgranite (AR1028), (C and D) the Lac Cornu pegmatites (AR833 and

AR1020), (E) the Lacs Noirs pegmatite (AR1006), (F) the Chéserys aplite (AR916) Error ellipses and uncertainties in ages are ± 2σ level. The discordance of dotted ellipses is due to radiogenic Pb losses and common Pb contaminations. Dotted and white ellipses are not taken into account for the age calculation (see text for detail).

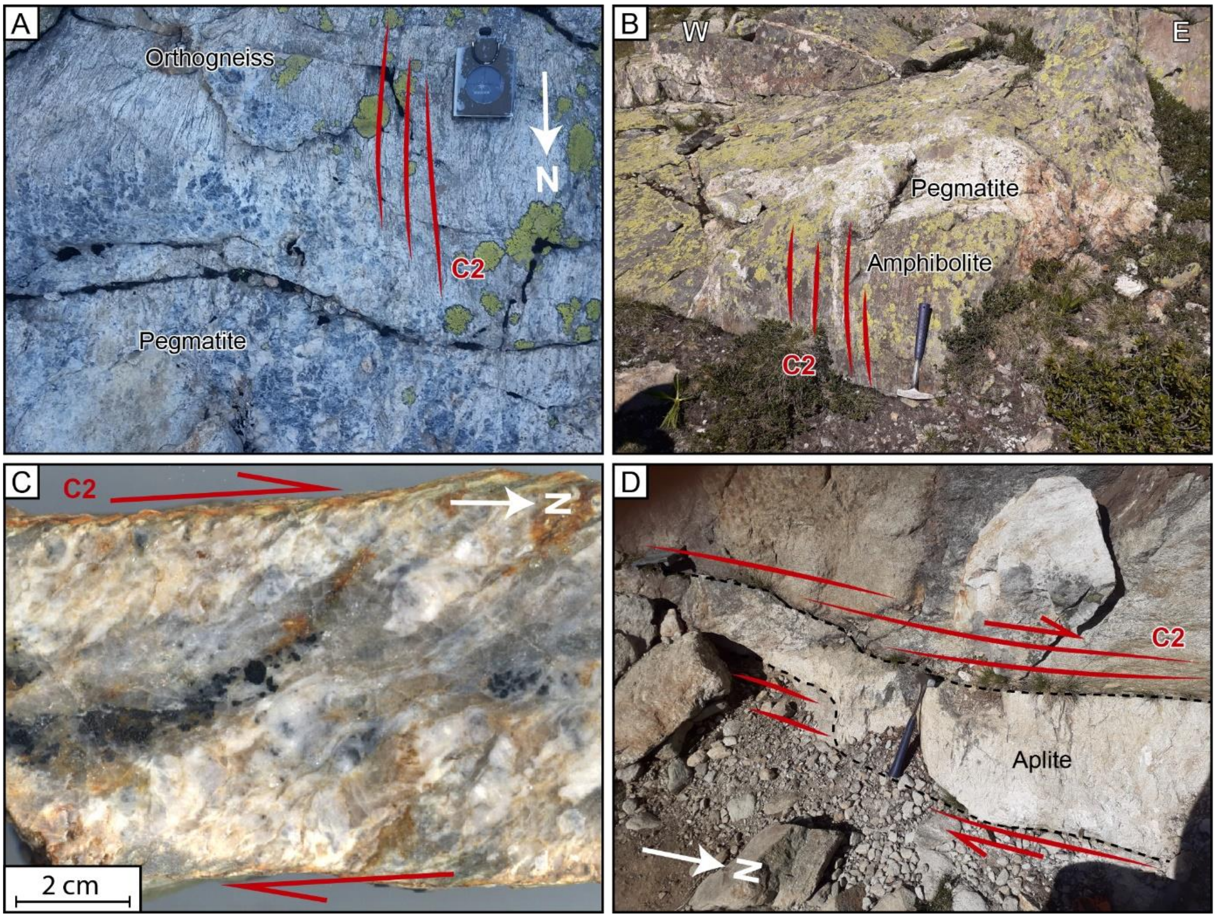

Figure 14 : Relationships with deformation patterns of the pegmatitic and aplitic samples. (A) Pegmatite AR833 from the Lac Cornu area embedded in a migmatitic orthogneiss with diffusive contacts. (B) Pegmatite AR1020 secant on the C2 planes of an amphibolitic boudin of the Lac Cornu area. (C) Section of the Lacs Noirs pegmatite (AR1006) showing C-S structures. (D) Chéserys aplite (AR916) emplaced in a C2 shear zone.

4.3.2. Lac Cornu pegmatites (AR833 and AR1020)

Pegmatites are numerous in the orthogneiss of the Lac Cornu area. The sample AR833 is one of these pegmatites which show a diffusive contact with the migmatitic orthogneiss (Fig. 14A). The migmatitic orthogneiss is structures by suprasolidus C2 planar fabrics also roughly recognized in the pegmatite by the mineral orientation. The pegmatite is composed of large K-feldspar, plagioclase, quartz and a few muscovite. Large K-feldspar grains are all surrounded by myrmeckites highlighting a high-temperature deformation. K-feldspar and plagioclase are partially replaced by white micas.

Zircon crystals from sample AR833 are euhedral, colourless and transparent. Their shapes evolved from elongated to rounded. CL images highlight various cores surrounded by rims with concentric and oscillatory zoning (Fig. 12B). Sixty-three analyses were carried out on forty-three zircon grains and are distributed into four clusters (Fig. 13C). Three data (#15, 20, 46) obtained on inherited cores with Th/U ratios between 0.16 and 0.23 yield a mean age at 724 ± 28 Ma (MSWD = 1.3). Four data (#2, 4, 22, 34) also obtained on inherited cores with similar Th/U ratios (0.19-0.28) display a concordia age at 552 ± 12 Ma ($MSWD_{(C+E)}$ = 2.4). The main cluster is composed of fifty-one analyses obtained on cores and rims with concentric and oscillatory zoning and lower Th/U ratios (mostly 0.04-0.15) that spread from ca. 465 Ma to 420 Ma. Among them, twenty-eight data yield a concordia age at 462 ± 3 Ma ($MSWD_{(C+E)}$ = 1.08). In addition, two sub-concordant data (#45, 48) obtained on rims with oscillatory and concentric zoning and low Th/U ratios (0.00-0.01) yield a mean age at 317 ± 6 Ma ($MSWD_{(C+E)}$ = 1.04). One datum (#16) from a zircon core is concordant at 2.0 GPa (Table S3).

The sample AR1020 is a pegmatite that cross-cuts the C2 planar fabric of an amphibolitic lense embedded in the Lac Cornu orthogneiss (Fig. 14B). The pegmatite does not show a mineral orientation. It is composed of non-oriented large quartz, K-feldspar and plagioclase grains. Quartz shows a slight undulose extinction and sometimes GBM recrystallisation. K-feldspar and plagioclase are highly sericitized.

Zircons from the pegmatite AR1020 are not numerous, often metamict and pinkish, others are transparent to milky. Their shapes are extremely heterogeneous from elongated to rounded. CL images reveal complex textures such as the presence of inherited cores surrounded by rims, concentric oscillatory zoning and patchy zoning textures (Fig. 12C). Nineteen analyses were performed on eleven grains (Table S2). Despite the various and complex zoning of these zircons and their scattered Th/U ratios (0.05-1.03), all the analyses spread between ca. 465 and 375 Ma with and thirteen yield a concordia age at 456 ± 4 Ma ($MSWD_{(C+E)}$ = 0.5) (Fig. 13D). Other analyses might reflect Pb loss or common Pb contamination.

4.3.3. Lacs Noirs pegmatite (AR1006)

The Lacs Noirs pegmatite is a small dyke within micaschists, which is highly deformed by the C2 dextral wrenching (Fig. 14C). It is composed of Qtz + Kfs + Tur + Ms. Quartz is highly deformed and shows a well-marked undulose extinction, and a recrystallization evolving from GBM to SGR state. The tourmaline grains are either oriented parallel to the foliations or are dismembered by the deformation. In high-strain zones, K-feldspar is highly replaced by muscovite.

Zircon grains from the pegmatite AR1006 are fragments of zircon crystals, colourless and transparent. CL images show that most of the grains have resorption structures affecting inherited cores and rims with oscillatory and concentric zoning (Fig. 12D). Thirty-three analyses were carried on thirty-two zircon grains (Fig. 13E). Twenty-two data with Th/U ratios ranging between 0.04 and 0.70 align and form a lower intercept at 455 ± 3 Ma (MSWD = 0.48). Among them, seventeen data yield a concordia age at 456 ± 3 Ma ($\mathrm{MSWD}_{(C+E)}$ = 0.89). Other analyses, except one (#14), are concordant or sub-concordant and spread from 535 to 997 Ma.

4.3.4. Chéserys aplite (AR916)

The sample AR916 comes from an aplitic dyke that emplaced within a C2 shear zone in metasedimentary rocks (Fig. 14D). The aplite is composed of small grains of quartz, plagioclase, K-feldspar, muscovite and rare tourmaline and garnet retrogressed into chlorite. The mineral assemblage does not show any mineral orientation nor deformation. Some plagioclase and K-feldspar are partially replaced by white micas.

Zircons from the aplite AR916 are not numerous and are mainly transparent and colourless fragments with elongated to ovoid shapes. CL images show mainly simple internal structures with concentric and oscillatory zoning (Fig. 12E). Few grains show an inherited core surrounded by a rim with oscillatory zoning. Some grains also display a small metamorphic rim. Thirty-three analyses were carried on thirty-two zircon grains (Fig. 13F). Most of the data form a cluster between 460 and 420 Ma. Among them, eighteen analyses on cores and rims with Th/U ratios between 0.04 and 0.95 yield a concordia age at 458 ± 3 Ma ($\mathrm{MSWD}_{(C+E)}$ = 1.3). One datum (#22) on an inherited core is sub-concordant at 839 Ma. Several discordant data show $^{206}\mathrm{Pb}/^{238}\mathrm{U}$ ages younger than 400 Ma that may be induced by Pb loss.

4.4. Couteray orthogneiss (AR37)

The Couteray orthogneiss is a N-S elongated meta-igneous body located in the Val Bérard next to the Vallorcine granite (Fig. 1B). This orthogneiss is composed of quartz, K-feldspar, plagioclase, muscovite and biotite. The sample AR37 shows a well pronounced N-S planar fabric (Fig. 9H) resulting mainly from a pure shear deformation with a slight dextral simple shear component. Some shear bands passing through large K-feldspar grains induce the crystallization of myrmeckites, suggesting a deformation at high-temperature conditions, although low-temperature deformation also affected this orthogneiss. In some places, it seems that the orthogneiss have been partially molten (Fig. 9H). Adjacent meta-sedimentary rocks show the same planar fabric with a more non-coaxial deformation interpreted as C2 shearing.

Zircons from the Couteray orthogneiss are transparent and euhedral. Zircon ranges in shape from equant to elongate. CL images show either the presence of inherited cores surrounded by rims with concentric oscillatory zoning, or uniform grain with concentric oscillatory zoning (Fig. 10F). Twenty-eight analyses were conducted on seventeen zircon crystals (Fig. 11F; Table S2). Analyses on inherited cores with concentric zoning and Th/U ratios between 0.18 and 0.99 (Table S2) yield one concordant datum at 691 Ma (#12) and five data (#8, 10, 18, 20, 25) forming a concordant cluster at 587 ± 10 Ma ($MSWD_{(C+E)}$ = 1.16) (Fig. 11F). Nineteen analyses on cores and rims with concentric zoning and Th/U ratios ranging between 0.01 and 0.76 (Table S2) yield a concordia age at 480 ± 4 Ma ($MSWD_{(C+E)}$ = 0.61, n = 19) (Fig. 11F).

5. Discussion

5.1. Ages and emplacements of silicic magma in the AR-MB area.

5.1.1. Early-Carboniferous plutonism

Consistently with Bussy et al. (2000), our zircon LA-ICPMS U-Pb results indicate an early-Carboniferous emplacement age for the Pormenaz and Montées-Pélissier granites. Most of the zircon grains analysed from these two plutons show magmatic growth zoning with Th/U ratios from 0.1 to 1.0 typical for an igneous zircon origin (Tiepel et al., 2004; Linnemann et al., 2011). The zircon concordia ages of 338 ± 2 Ma and 340 ± 5 Ma obtained on the Pormenaz (AR801) and Montées-Pélissier (AR865) granites, respectively, are similar in the error bars and are interpreted as the emplacement ages of these two plutons (Fig. 11A and B). These two samples exhibit many discordant data mainly obtained on zircon rims probably affected by radiogenic Pb losses due the successive Variscan and Alpine deformations affecting these plutons.

Our results argue that the two granites emplaced in the upper crust probably along the ductile-to-brittle transition. Considering their geochemical signature, authors suggest that these plutons probably originated from partial melting of the lower overthickened crust and occurrences of durbachites and lamprophyres are interpreted as evidence of a mantellic component (von Raumer and Bussy, 2004). Early-Carboniferous plutons are described in other

ECMs (e.g. Schaltegger and Corfu, 1992; Debon et al., 1994, 1998; Guerrot and Debon, 2000; Rubatto et al., 2001; Fréville et al., in prep) and show similar geochemical compositions interpreted as a mixing between crustal and mantellic components (review in Debon and Lemmet, 1999). The root zone of the visean plutons is not exposed and we do not know the number or shape of feeder structures. Considering the submagmatic deformations observed in the Montées-Pélissier granite (Fig. 9C), we propose that these granites emplaced through small vertical shear zones formed during the initiation of the transpression.

5.1.2. Late Carboniferous and voluminous plutonism

The concordia ages at 306 ± 5 Ma, 306 ± 3 Ma and 305 ± 2 Ma of the Vallorcine granite (AR73), Montenvers granite (MB43) and Mont-Blanc granite (MB37) are obtained on zircon cores and rims showing concentric and oscillatory zoning (Fig. 10C, D and E) with Th/U ratios mostly higher than 0.1 (Table S2) typical of igneous zircons (Tiepel et al., 2004; Linnemann et al., 2011) and are interpreted as emplacement ages (Fig. 11 C, D and E). Our results are identical with previous published ID-TIMS ages on zircon and monazite at ca. 305 Ma for these same plutons (Bussy et al., 2000; Bussy and von Raumer, 1993, 1994) (Fig. 1).

Our structural and microstructural analyses highlight that the growth of the Vallorcine, Montenvers and Mont-Blanc granites took place along crustal dextral shear zones (Fig. 2 and 9). In particular, the large plutons were emplaced in areas where broad C’2 shear zones are pervasive. We interpret the C’2 shear zones as large-scale dilation structures allowing the emplacement of huge volumes of melts within the crust. This interpretation is also consistent with the injections of diatexites through C’2 shear zones in the Fully area at ca. 307 Ma (Bussy et al., 2000; von Raumer and Bussy, 2004). These large plutons are surrounded by a network of leucogranitic, pegmatitic and aplitic dykes also often emplaced in shear zones (Fig. 14C and D) that may represent the feeder structures of these plutons. Microgranites and rhyolites may represent the prolongation of these plutons in the upper crust (Bussien Grosjean et al., 2017).

Several of these smaller magmatic bodies have been dated with only few data that yield a variscan age (Fig. 13). In the undeformed Morcles microgranite dyke (AR1028), the concordia age at 313 ± 2 Ma obtained on monazite is interpreted as the emplacement of this microgranite, and is consistent with the age at ca. 312-309 Ma proposed by Bussien et al. (2017) (Figs. 1 and 13B). Two sub-concordant analyses on zircon rims of the Lac Cornu pegmatite AR833 yield a mean ^{206}Pb/^{238}U age at 317 ± 6 Ma. These rims display oscillatory and concentric zoning and low Th/U ratios (0.00-0.01; Table S2), these features are reported for magmatic zircon in high-

SiO_2 and/or peraluminous granitoids (Lopez-Sanchez et al., 2016). Thus, this age is interpreted as the emplacement of the pegmatite AR833. It is consistent with the age at ca. 317 Ma obtained in anatectic leucogranitic dykes in the Mont-Blanc massif (Bussy and von Raumer, 1994).

5.2. Zircon inheritance and source of late-carboniferous magmas

The small magmatic bodies (i.e. microgranite, pegmatites and aplite) record a well-marked Ordovician zircon inheritance with ages in the range 460-450 Ma. The inherited component is obtained on zircon grains that display typical igneous origin with concentric zoning and high Th/U (Fig. 12; Table S2). They are slightly younger than the emplacement age of the magmatic protolith of the Couteray orthogneiss (i.e. ca. 480 Ma; Fig. 11F) but are very similar to other orthogneisses of the AR-MB massifs emplaced at ca. 465-455 Ma (Fig. 1B; Bussy and von Raumer, 1994; Bussy et al., 2011) and fall in the range 450-480 Ma ordovician event documented in the whole variscan belt. We suggest that the strong inheritance argues for a genetic link between the small magmatic bodies and the partially molten Ordovician orthogneisses. Considering the orthogneiss as a source for silicic melt is consistent with our field-observations; as for instance the pegmatite AR833 that is embedded in a migmatitic orthogneiss with diffuse boundaries (Fig. 14A) or the pervasive leucocratic vein complex and dykes intruding the migmatitic orthogneiss that surrounds the Mont Blanc granite (Vitel, 1965; Bussy and von Raumer, 1994). All the small magmatic bodies, dykes and pegmatites dated in this study may represent anatectic melts that crystallized during their ascent at the early stage of late-Carboniferous plutonism (ca. 320-310 Ma). It is worth to note that zircons from these small magmatic bodies do not record the Variscan magmatism, except pegmatite AR833 and the Morcles microgranite (Fig. 12 and 13C). Newly growth of zircon in an anatectic melt is considered to result solely from the dissolution of pre-existing zircon grains and reprecipitation of overgrowths or neograins directly from the melt (Watson, 1996; Yakymchuk and Brown, 2004; Bea et al., 2006; Kelsey et al., 2008; Mintrone et al., 2020). The solubility of zircon in silicate melts is dependent on the temperature (Kelsey et al., 2008), melt composition (Watson and Harrison, 1983; Boehnke et al., 2013) as well as the heating and cooling rates (Bea et al., 2007), that depends on the pluton's size (de Saint-Blanquat et al., 2011). In the AR-MB massifs, the range of metamorphic peak temperatures estimated in the partially molten gneissic basement is 650-750°C (Schulz and von Raumer, 1993, 2011; Chiaradia, 2003; Genier et al., 2008) and 750-800°C in the lower crust (Vanardois et al., in review). At these temperatures, biotite and amphibole dehydration melting does not occur. Considering the high melt fraction observed in the EVSZ, melt is produced through water-present melting reactions (White et al., 2005; Sawyer, 2010), as previously proposed by Genier et al. (2008) for migmatites in the Emosson area. Recently, Couzinié et al. (2021) highlighted water-fluxed melting of ordovician orthogneisses in the eastern French Massif Central. They show that low melting temperature including limited zircon solubility in the melt phase, occlusion of zircon in non-reacting source biotite and sluggish zircon dissolution kinetics prevent the crystallization of newly formed zircon in the anatectic melt. Therefore, we interpret the water-fluxed melting of orthogneiss as the main source of crustal melts forming the pegmatites, aplites and microgranites in the AR-MB massifs.

The Ordovician inheritance is also recorded in the Montenvers, Vallorcine and Mont-Blanc granites in inherited zircon cores with typical igneous origin (Fig. 10). These granites have peraluminous chemical compositions and a main crustal origin (von Raumer and Bussy, 2004). They are spatially associated to the migmatitic orthogneisses (Fig. 1B; Vitel, 1965). Thus, we propose that the major melt source of the Vallorcine, Montenvers and Mont-Blanc granites comes from the water-present melting of ordovician orthogneiss. Inheritance of Proterozoic and Cambrian zircons also suggests a supply form the metasedimentary rocks. The lower component of Ordovician inheritance than pegmatites and aplites may be attributed to the larger pluton sizes that reduce their cooling rates (de Saint-Blanquat et al., 2011) and therefore increase the dissolution of zircon grains (Bea et al., 2007).

The Early-Carboniferous plutons do not display any Ordovician inheritance. The occurrences of Mg-K rich durbachites and lamprophyres in the Pormenaz and Montées-Pélissiers granites and their metaluminous geochemical compositions suggest a mixing of mantellic magmas with anatectic melts form the lower crust (von Raumer and Bussy, 2004). This crustal component is confirmed by the inherited cores yielding ages at ca. 650 Ma in the Pormenaz pluton (Fig. 11A). Even if a crustal component may also come from the partial melting of Ordovician orthogneisses, the metaluminous melt compositions highly increase the dissolution of inherited zircon grains (Bea et al., 2006) and may have erased most of the Ordovician inheritance.

5.3. Melt drainage during shearing

The time scales of pluton formation in the middle and upper crust argue that deep-seated partial melting and segregation are the first controlling processes that relate directly to fertility and changes in the boundary conditions (de Saint Blanquat et al., 2011). Following the work of

Bea et al. (2007) we consider that fast melting and magma-transport rates may be inferred from the elevated zircon inheritance. We suggest that these elevated rates of crustal melting could have been caused by deformation enhanced water-fluxed melting. In addition, the short distance between the migmatitic orthogneissic source and the pluton sink may explain the high magma-transport rate, also increased through deformation dextral shearing.

Our results allow us to propose a temporal evolution of the tectono-magmatic system during carboniferous transpression, which emphasizes the role of shear zone growth and water-fluxed melting of orthogneiss (Fig. 15). In the AR-MB massifs, the Variscan magmatism starts at the end of the crustal thickening around 340-330 Ma with the emplacement of the Pormenaz and Montées-Pélissier granites (Fig. 11A and B; Bussy et al., 2000). Based on their major and trace elements contents, von Raumer and Bussy (2004) interpreted these granites as a mixing of mantellic melts and of crustal melts from the lower crust. The crustal component is consistent with the rare inherited zircon cores (Fig. 11A), and the mantle-derived contribution is confirmed by the mingling with durbachites and lamprophyres magmas. Considering that the temperature conditions stay below 800 °C (Schulz and von Raumer, 1993, 2011; Chiaradia, 2003; Genier et al., 2008; Vanardois et al., in review), the majority of the melts are thus produced by water-present melting reactions (Sawyer, 2010), especially in the fertile orthogneiss (Villaros et al., 2018). The water could be provided by the dehydration of surrounding metasedimentary rocks (e.g. White et al., 2005) and by the crystallization of mafic magmas (Wienberg and Hasalová, 2015).

At 340-330 Ma, the vertical dextral shear zones just initiated, which limited the vertical migration of fluids and melts, leading to small intrusions in the upper crust near the brittle-ductile transition (Fig. 15A). With the increase of dextral transpression the formation of numerous shear zones between 320-300 Ma (this study, Simonetti et al., 2020a) enhance aqueous fluid drainage in the orthogneiss, increasing the melt volume. The anatectic melts gathered in dilation areas created by the dextral shearing. In particular, at ca. 310-300 Ma, the formation of C’2 shear zones created large dilation zones and allowed the emplacement of large plutons (Fig. 15B). Few mafic intrusions in the Fully area (Krummenacher, 1959; Bussy et al., 2000) and mafic enclaves in the Mont-Blanc granite (Bussy, 1990) suggest the intrusion of mantle derived mafic magmas that may have elevated rates of crustal melting through heating (von Raumer and Bussy, 2004) or water supply (Wienberg and Hasalová, 2015). Melts migrating in the upper crust through the shear zones crystallized into microgranites and rhyolites, such as the Morcles microgranite and the Mont-Blanc rhyolites between 315 and 300 Ma (Fig. 13B; Bussien et al., 2017; Bussy et al., 2000).

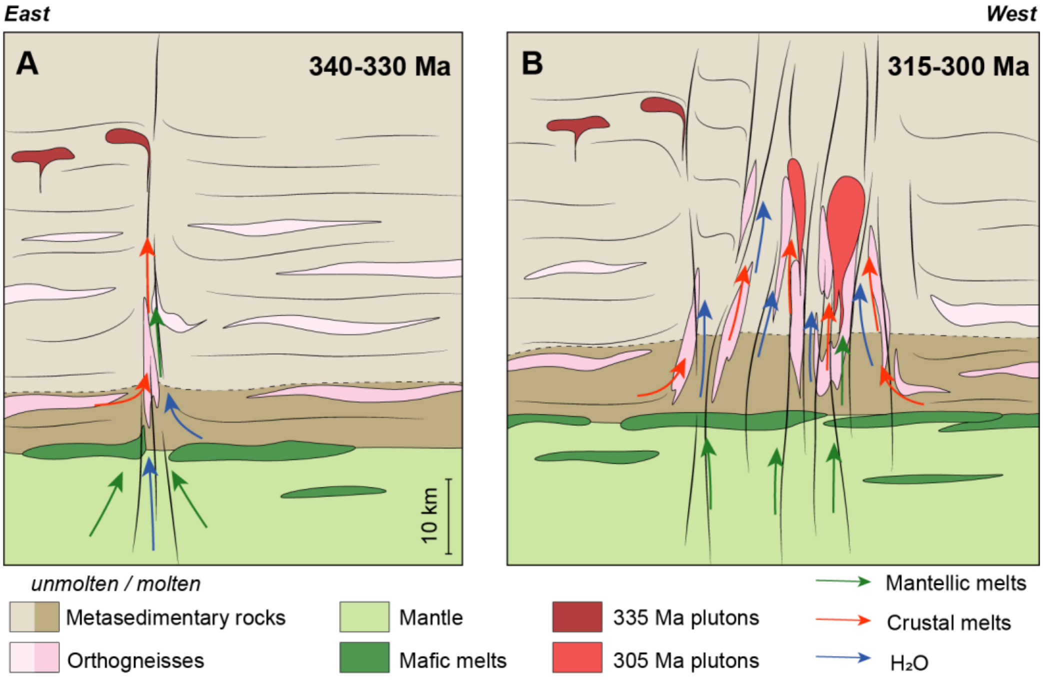

Figure 15 : Tectono-magmatic evolution of the AR-MB massifs. (A) Initiation of the dextral shearing after the nappe stacking. The fluids, anatectic melts of the lower crust and mantellic mafic melts are drained by these local shear zones and form small plutons in the upper crust. (B) Broadening of the shear zones drains more fluids that increase the partial melting of meta-igneous rocks. Dilation shear zones collect anatectic melts and the small mantellic supply to form large plutons.

6. Conclusion

Our structural analysis on the Variscan crust of the Aiguilles-Rouges and Mont-Blanc massifs highlights a crustal scale S-C-C' anastomosed network formed during a dextral transpressive setting. U-Pb LA-ICPMS dating of zircon from large plutons and their relationships with the dextral shearing allow us to constrain this deformation between ca. 340 and 305 Ma. During this time span, the EVSZ broadened and formed a regional-scale anastomosed system where C'-type shear zones acted as preferential dilation structures for pluton growth. Zircon inheritance indicates that granitic melts are mainly derived from water-fluxed melting of ordovician orthogneissic laccoliths. Over time, the growth of the dextral anastomosed network facilitated the water-flux through the orthogneiss that increased the volume of anatectic melts and also favored the formation of large plutons.

Acknowledgements

This work was supported by the BRGM through the Référentiel Géologique de la France program (RGF). We thank Cyprien Astoury for mineral separation. Didier Convert provided generous support with thin section preparation. The newly acquired and compiled structural data will be available on the RGF website (http://rgf.brgm.fr).

Supplementary material

Tables S1 and S2 are presented in Annexe 4.

Chapitre 7. La géodynamique du bassin de Servoz. Evidences d'un rifting ante-collision.

Jusqu'ici, nos études ont principalement portées sur le socle gneissique des Aiguilles-Rouges, i.e. la croûte profonde et moyenne. Or le massif des Aiguilles-Rouges possède encore un peu de sa croûte supérieure dans sa partie Sud-Ouest au niveau du synclinal de Servoz. Ce synclinal est composé de roches magmatiques et volcaniques bimodales et de roches sédimentaires métamorphisées au cours de l'orogénèse Varisque, mais aussi de roches sédimentaires post-orogéniques. Les granites Viséens de Pormenaz et de Montées-Pélissier se mettent en place dans ce synclinal. Nous avons donc étudié l'évolution géodynamique de ce bassin en investiguant son évolution thermique par Spectrométrie Raman sur Matière Carbonées (RSCM) et en ajoutant des contraintes temporelles par géochronologie U-Pb LA-ICPMS sur des zircons détritiques et sur une roche métavolcanique. Ces données nous permettent de contraindre le contexte géodynamique antérieur à la collision continentale Carbonifère.

Pre-collision high thermal gradient recorded in a Variscan orogenic basin (Servoz basin, Western Alps)

Jonas Vanardois[1*], Abdeltif Lahfid[2], Pierre Trap[1], Brice Lacroix[3], Françoise Roger[4], Laurent Guillou-Frottier[2], Didier Marquer[1], Jean-Louis Paquette[5], Jérémie Melleton[2]

jonas.vanardois@univ-fcomte.fr; a.lahfid@brgm.fr; pierre.trap@univ-fcomte.fr; francoise.roger@umontpellier.fr; didier.marquer@univ-fcomte.fr; j.l.paquette@opgc.univ-bpclermont.fr; j.melleton@brgm.fr; blacroix@ksu.edu

[1]UMR 6249 Chrono-environnement, Université de Bourgogne-Franche-Comté, 25030 Besançon, France.

[2]BRGM-French Geological Survey, 3 Avenue Claude Guillemin, 45100, Orléans, France.

[3]Department of Geology, Kansas State University, 108 Thompson Hall, Manhattan, KS 66506

[4]Géosciences Montpellier, Campus Triolet, Université Montpellier, CNRS, 34095 Montpellier Cedex 5, France.

[5]Laboratoire Magmas et Volcans (CNRS-UMR 6524), Campus Universitaire des Cézeaux, 63178 Aubière Cedex, France.

*Corresponding author: jonas.vanardois@univ-fcomte.fr +33(0)381666242 Present address: 16 route de Gray, 25030 Besançon.

Keywords: Intracontinental basin**,** RSCM thermometry, Numerical modelling, LA-ICPMS U-Th-Pb dating on zircon, Variscan belt

Abstract

In the Variscan basement of the Aiguilles-Rouges massif, a metavolcano-sedimentary sequence is described in the Servoz syncline. This sequence was usually described as (i) a volcanic unit of unknown age and elusive origin at the bottom of the basin, (ii) Late-Carboniferous sedimentary series highly affected by the Variscan orogeny and intruded by the Montées-Pélissier pluton, and (iii) a Late-Carboniferous post-orogenic sedimentary sequence. Field observations, Raman Spectrometry on Carbonaceous Materials analyses on forty-seven samples and LA-ICPMS U-Pb analyses on zircon from two samples enable us to revisit this lithostratigraphy sequence and to constrain the geodynamic evolution of the Servoz syncline but also of similar basins in other External Crystalline massifs of the Alpes. Our results allow us to distinct three sedimentary formations (F1, F2 and F3). The F1 formation is composed of metagreywackes and volcanic and magmatic rocks induced by a bimodal magmatism. This formation is formed during the opening of basin initiated between 370 and 350 Ma during an early rifting stage triggered by a back-arc geodynamic setting. This extensional regime induced a high thermal event nowadays yielding an apparent gradient of ca. 115 °C/km and a local anatexis of the basement dated at 351 ± 5 Ma. Then, the basin was inversed by the collision between 350 and 330 Ma during a transpressional setting forming dextral shear zones favouring the emplacements of several plutons at ca. 340-330 Ma inducing local metamorphisms. The

transcurrent regime evolved locally into transtension forming a pull-apart basin in the western part of the syncline during 330-310 Ma and allowing the deposition of F2 phyllites formation that was deformed by the Variscan orogeny at temperatures between 200 and 350 °C. Finally, at the end of the Variscan orogeny around 310-290 Ma, a slight orogenic collapse formed a post-orogenic basin (F3 formation). The alpine tectonics overprinted all temperatures beneath 350 °C. Similar openings of basin are recognized in other Variscan massifs, but the Servoz syncline is the first example recording all the orogenic steps.

1. Introduction

Understanding the paleotemperature conditions reached by metamorphic rocks from rifting to collisional stages is fundamental to evaluate the thermal evolution of orogens. In the inner part of orogen, that experienced significant deformation through subduction and collision processes, the reconstruction of pre-collision thermal evolution associated to the rifting stage is difficult to assess. In contrast, in the back-arc and foreland basins, recent studies highlight that thermal pre-collisional stage could be preserved (e.g., Saspiturry et al., 2019; Jammes & Huismans, 2012; Vacherat et al., 2014, 2016; Jourdon et al., 2019; Lahfid et al., 2019). Paleotemperature conditions recognitions are of major interest as recent studies shown a clear correlation between high thermal gradient that occurred during the incipient stage of basins, and the presence of energy resources such as gas (e.g. Saspiturry et al., 2020).

The Variscan orogen, which results from the collision between the Laurussia and Gondawana supercontinents (e.g. Matte, 1991, 1998; Lardeaux et al., 2014; Edel et al., 2018; Martinez-Catalan et al., 2021), is associated with the subduction of one or several oceanic domains during the Late-Devonian – Early-Carboniferous (i.e. 380-350 Ma; Franke et al., 2017; Paquette et al., 2017). This period of continental convergence generated contrasting tectonic and metamorphic processes in the active margins and back-arc zones. The active margin of the northern edge of the Moldanubian zone of the Variscan belt of Europe experienced syn-tectonic high-grade HP-LT conditions metamorphism during subduction (Schmädicke & Müller, 2000; Ballèvre et al., 2003; Massonne & Kopp, 2005; Berger et al., 2010; Lotout et al., 2018). This stage was followed by Barrovian metamorphism during the collisional stage and formation of the orogenic plateau (Schulmann et al., 2008b; Stipska et al., 2016; Vanderhaeghe et al., 2020; Benmammar et al., 2020). In contrast, the thermal evolution of the back-arc zone was controlled by Devonian – Carboniferous thermal rifting during the earliest phase of the Laurussia – Gondwana collision (Lardeaux et al., 2014), prior experiencing a tectono-thermal event related to compressional tectonics. The opening of several basins currently occurring in from the External Crystalline massifs of the Alps (ECMs) could be related to this early rifting stage. However, this hypothesis remains speculative considering that (i) syn- and late-orogenic basins described in the rest of the Variscan massifs show similarities with the basins from the ECMs, (ii) some microfossils from these basins indicate ages younger than the early rifting stage and (iii) the opening and geodynamic evolutions of these basins are poorly constrained, which avoid any attempts of correlation with preserved basins in other Variscan massifs.

In this study we document an example of a Devonian – Carboniferous basin from the ECMs: the Servoz syncline located in the Aiguilles-Rouges massif (ARM) (Fig. 1A). The syncline corresponds to Late-Devonian – Early-Carboniferous metasedimentary and metavolcanic rocks deposed on a Proterozoic – Cambrian basement and unconformably overlain by a Late-Carboniferous formation (e.g. Bellière and Streel, 1980; Dobmeier, 1998; Dobmeier et al., 1999). According to Dobmeier (1998), the metamorphic grade of Late-Devonian and Early-Carboniferous rocks ranges from amphibolite to greenschists facies. Similar formations have also been described in others ECMs (Fig. 1A) (Ménot, 1986, 1987; Guillot and Ménot, 2009; Fréville et al., 2018, in review) but their geodynamic interpretations vary from intracontinental rifting (e.g. Ménot, 1988b; Ménot et al., 1988a) to back-arc basins settings (e.g. Pin and Carme, 1987; Guillot et al., 2009).

Based on new geochronological data obtained on zircon from a metavolcano-sedimentaty rock and on detrital zircon from a microconglomerate as well as thermometric data (Raman Spectroscopy of Carboniferous Materials (RSCM)) from 47 samples, and propose a new quantitative reconstruction of pre- to post-orogenic thermal gradient. This thermal reconstruction suggests that the early inversion of the Servoz basin occurred during high heat flow conditions, presumably inherited from the Devonian rifting stage. Our results allow us to discuss the Variscan geodynamic evolution of the ECMs and to correlate it with similar rocks from others Variscan massifs.

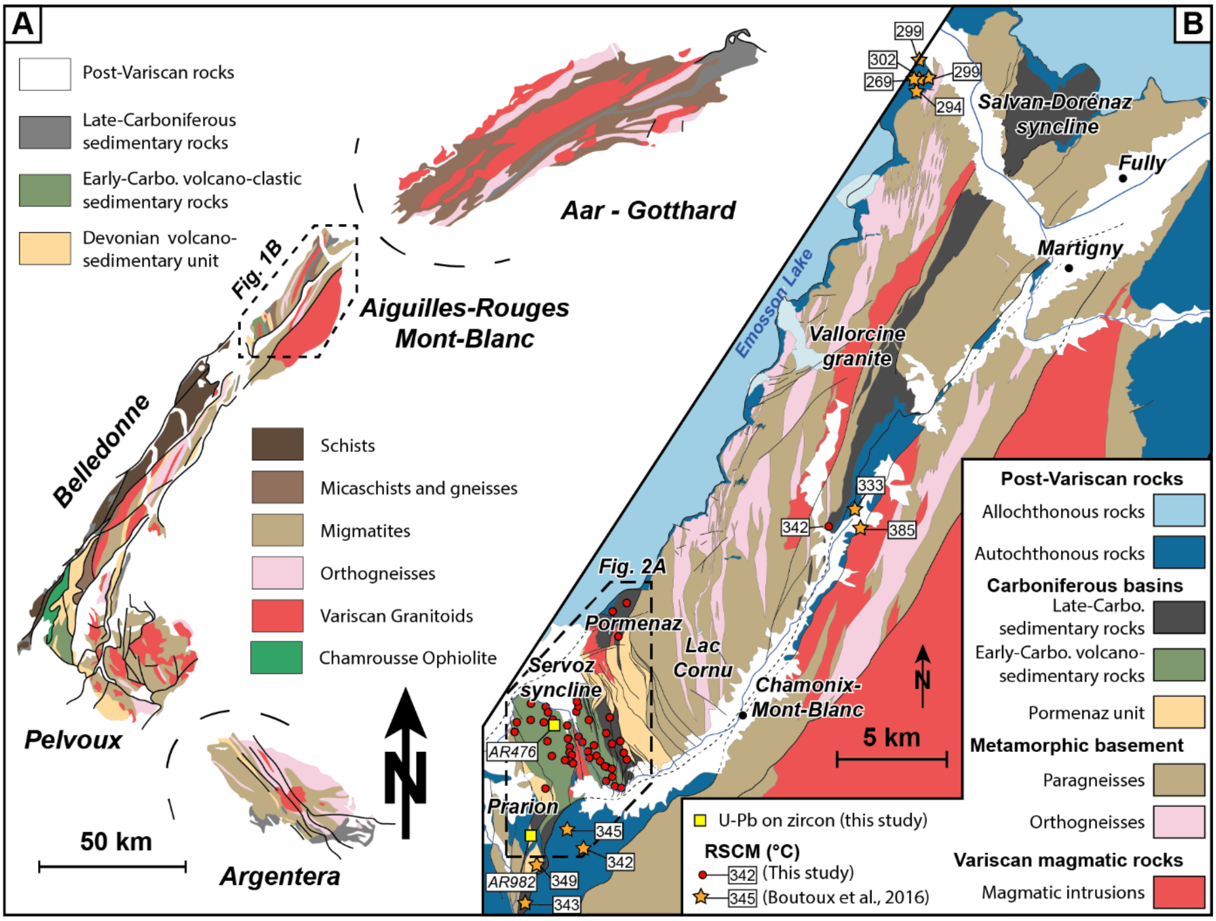

Figure 1 : (A) Geological map of the Variscan basement of the External Crystalline Massifs in the French and Swiss Alps. (B) Geological map of the Aiguilles-Rouges massif with locations of LA-ICPMS U-Pb dated samples AR476 and AR982 on zircon, and RSCM samples analysed in this study and those of Boutoux et al. (2016). Location of figure 2a is shown.

2. Geological setting

2.1.The Aiguilles-Rouges massif and Alpine deformation

The Aiguilles-Rouges massif (ARM) is a 45-km-long NE trending Variscan massif bounded by (para)autochthonous and allochthonous Mesozoic and Cenozoic sedimentary rocks (Fig. 1A). The ARM is formed of a gneissic basement composed of micaschists, paragneiss and Ordovician orthogneisses (Bussy et al., 2000), of a late-Carboniferous basin (Salvan-Dorenaz syncline) (Capuzzo and Bussy, 2000) and of a supposed Devonian to late-Carboniferous basin (i.e. Servoz syncline; Fig. 2) (Laurent, 1967; Dobmeier, 1996, 1998, Dobmeier et al., 1999).

Within the gneissic basement, the alpine deformation is localized into low-grade shear zones (e.g. von Raumer and Bussy, 2004) developed under greenschist facies metamorphic conditions similar to those reported in the Mont-Blanc massif (e.g. Marshall et al., 1998; Rolland et al., 2003; Rossi et al., 2005). Alpine metamorphism in the surrounding autochthonous Mesozoic sedimentary rocks is limited to temperature about 300-400 °C (RSCM temperatures, Boutoux et al., 2016) (Fig. 1B). A single RSCM temperature on a late-Carboniferous sedimentary rock yield a temperature at 343 ± 50 °C (Boutoux et al., 2016) (Fig. 1B). Alpine deformation forms a non-pervasive cleavage associated to open folds in the late-Carboniferous sedimentary rocks of the Servoz and Salvan-Dorenaz syncline (Pilloud, 1991; Lox and Bellière, 1993; Dobmeier and von Raumer, 1995).

2.2.Variscan tectono-metamorphic and magmatic evolution of the ARM

The ARM underwent a long lasting tectono-metamorphic history with a peak of high-pressure – high-temperature at ca. 340-330 Ma (Vanardois et al., in review, in prep), followed by a progressive decompression and then a high-temperature – mid-pressure metamorphism (Schulz and von Raumer, 1993, 2011; Vanardois et al., in review, in prep). The HP prograde metamorphism is related to a nappe stacking event between 350 and 340 Ma (Dobmeier, 1998). The decompression is accommodated by a D_1 horizontal flow of the lower crust associated to shallow dipping S_1 foliations (Vanardois et al., in review), and by coeval D_2 dextral transpressive shear zones forming both vertical S_2 foliations and large-scale crustal shear zones striking from N150 to N030 (e.g. Bellière, 1958; von Raumer and Bussy, 2004) (Fig. 2a). These transcurrent shear zones were active between 320 and 300 Ma (Simonetti et al., 2020a), although some authors reported syn-kinematic magmatic ages between 340 and 330 Ma (Bussy et al., 2000; Vanardois et al., in prep). A first Visean magmatic pulse has been recognized at 340-330 Ma with the emplacements of the Montées-Pélissier and Pormenaz granites (Bussy et al., 2000; Vanardois et al., in prep) (Fig. 2b). A second Late-Carboniferous pulse has been identified at 313-305 Ma with the emplacements of the Morcles and Vallorcine granites in the ARM, as well as with emplacements of the Mont-Blanc and Montenvers granites (Bussy and von Raumer, 1993, 1994; Bussy et al., 2000; Vanardois et al., in prep). These Late-Carboniferous granites emplaced through vertical dextral crustal shear zones (Dobmeier, 1998; Bussy et al., 2000; Vanardois et al., in prep). Finally, a third deformation (D_3) event has been described in the Servoz syncline and is associated with the development of a discrete S_3 gently dipping foliation (Vanardois et al., in prep). This fabric is generally discrete, forming a crenulation and open folds. However, it can be locally pervasive, and then partly transposing the S_2 foliation. The age of D_3 deformation is likely Late-Carboniferous, prior to the deposition of post-orogenic Late-Carboniferous – Permian sediments (Pilloud, 1991).

2.3.The Servoz syncline

The Servoz syncline is composed of a Devonian – Carboniferous volcanic and sedimentary series (Laurent, 1967; Dobmeier, 1996, 1998; Dobmeier et al., 1999) (Fig. 2a). The bottom of the Servoz syncline series is composed by volcanic rocks metamorphosed into epidote-bearing amphibolites and greenschists (Laurent, 1967) (Fig. 2b). In these volcanic rocks, SiO_2 content varies from 44 wt% to 73 wt% with a predominance of andesitic compositions (Dobmeier et al., 1999). Major and trace element contents define two magmatic suites, evolving during magmatic differentiation, subduction-related magmas and continental tholeiites ("Greenstones unit" from Dobmeier et al., 1999). The top of the series is composed of phyllites and metagreywackes. This formation is dated at ca. 335–325 Ma based on continental microflora analysis on phyllites (Bellière and Streel, 1980), but metagreywackes are intruded by the Montées-Pélissier granite, which has been dated at 340 ± 5 Ma (LA-ICPMS on zircon, Vanardois et al., in prep) and 332 ± 2 Ma (ID-TIMS U-Pb on zircon, Bussy et al., 2000) (Fig. 2b). Empirical thermobarometry on amphibole yields P–T conditions at 445 °C/0.32 GPa and 630 °C/0.67 GPa in the eastern and western sides, respectively (Dobmeier, 1998). This difference of metamorphic conditions is attributed to the presence of a Variscan dextral shear zone, the Arve fault, located in the axial plane of the Servoz syncline and which allows the emplacement of the Montées-Pélissier granite (Dobmeier et al., 1998; Bussy et al., 2000). However, the exact location of this fault remains enigmatic, as it is either described in the eastern or western border of the granite (Pairis et al., 1992; Dobmeier, 1998). Ar/Ar dating on muscovite from gneisses yield cooling ages of 337 ± 3 Ma and 331 ± 3 Ma on the western side and 316 ± 3 Ma on the eastern side of the Servoz syncline (Dobmeier, 1998), with peaks of P-T conditions estimated at 650 °C/1.0 GPa in the western side and 620 °C/0.8 GPa in the eastern side by empirical thermobarometry on metapelitic assemblages (Dobmeier, 1998).

All these lithologies are covered by unconformity by a sequence of nearly undeformed sandstones, shales and conglomerates (Lox and Bellière, 1983; Dobmeier and von Raumer, 1995; Dobmeier, 1996, 1998), with age estimated to ca. 305-300 Ma based on fossils analyses (Laurent, 1967) (Fig. 2b). Similar rocks from the Salvan-Dorenaz syncline (Fig. 1B) are dated by the U-Pb zircon method (ID-TIMS) from volcanic rocks at ca. 308 – 295 Ma (311-291 Ma if considering uncertainties; Capuzzo and Bussy, 2000) and are interpreted as fluvial and alluvial fans deposits (Capuzzo and Wetzel, 2004).

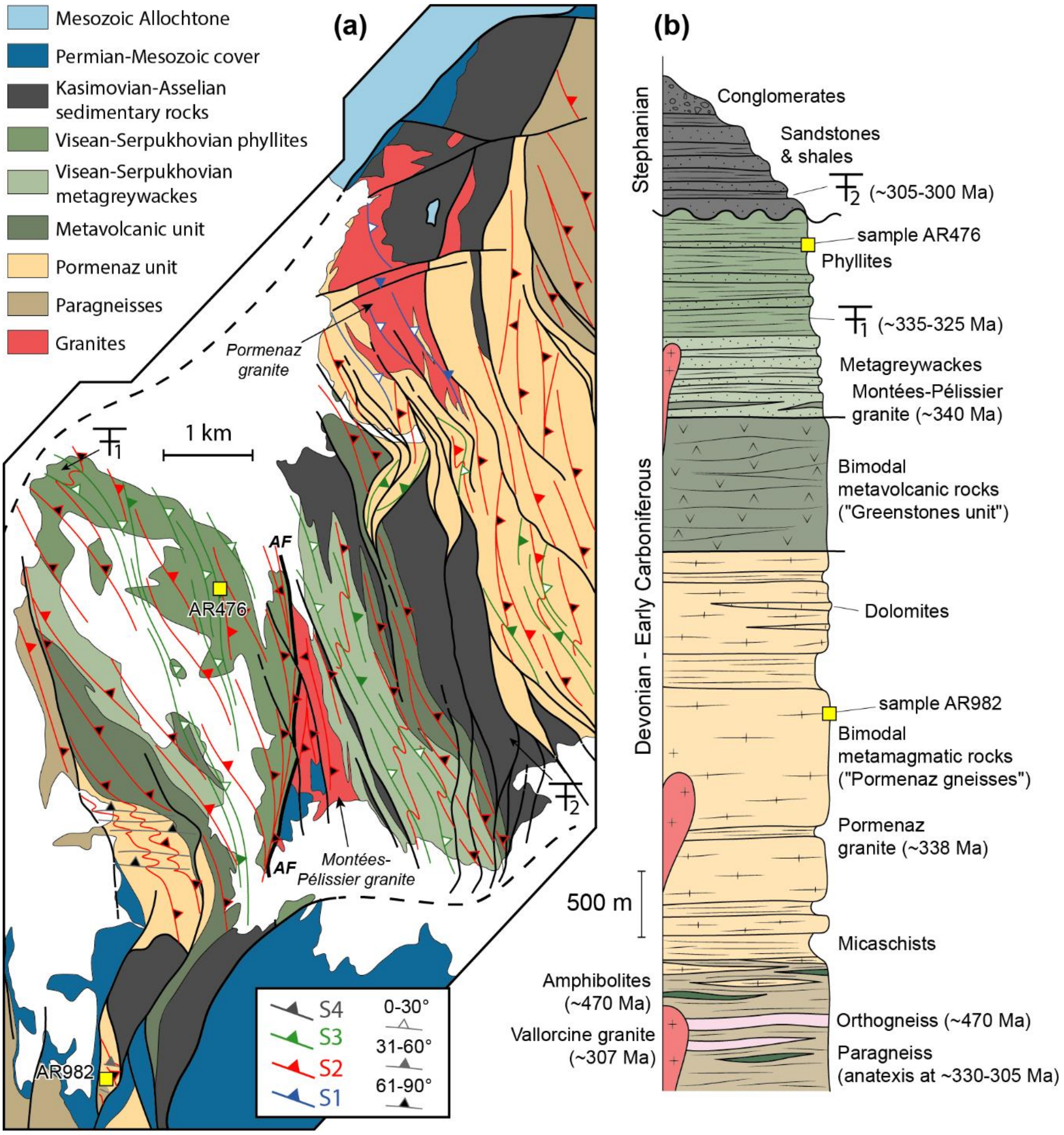

Figure 2 : (a) Map of the Servoz syncline, modified from Dobmeier (1996). (b) Synthetic LOG of the Servoz syncline, modified from Pairis et al. (1992), Dobmeier (1996) and Dobmeier et al. (1999). Fossils analyses are from Laurent (1967) and Bellière and Streel (1980). Age of meta-igneous rocks are from Bussy et al. (2000) and Vanardois et al. (in review, in prep). AF: Arve Fault.

3. Field observations and new lithostratigraphic subdivision

Based on field descriptions, observations and published data, we propose a new lithostratigraphic subdivision of the Servoz syncline that will be used for the rest of the study (Fig. 2b). The lithologies composing the Servoz syncline rest on a gneissic basement composed of paragneiss sometimes partially molten (Fig. 3A), Ordovician felsic orthogneisses and amphibolites (Fig. 3B). The bottom of the stratigraphic sequence is composed of magmatic and volcano-sedimentary rocks metamorphosed into fine-grained gneisses (Fig. 3C) associated with metapelites (Fig. 3D) and rare dolomitic layers (Dobmeier et al., 1999). These lithologies form the ca. 3-km-thick 'Pormenaz unit' (Fig. 2) and are intruded by the Pormenaz granite dated at 338 ± 2 Ma (LA-ICPMS U-Pb on zircon; Vanardois et al., in prep) and 332 ± 2 Ma (ID-TIMS U-Pb on zircon; Bussy et al., 2000). Its distribution embraces a part of the Greenstones unit of Dobmeier et al. (1999), the rest of the Greenstones unit forms the ca. 1-km-thick metavolcanic rocks composed of lower metamorphic grade than the Pormenaz unit (Fig. 3E). Both metavolcanics rocks and Pormenaz unit are derived from a bimodal magmatic suite ranging between acid (Fig. 3F) and basic (Fig. 3G) components (Dobmeier et al., 1999). These metavolcanic rocks are overlaid by at least ca. 1.5 km of Visean – Serpukhovian (?) metagreywackes and phyllites (Fig. 3H and I) with a predominance of metagreywackes at the bottom and phyllites at the top (Laurent et al., 1967). Based continental microflora analysis on phyllites, this sequence is dated at 335-325 Ma (Bellière and Streel, 1980) (Fig. 2b). The Montées-Pélissier granite intruded the metagreywackes (Fig. 3H) (Dobmeier, 1996, 1998; Bussy et al., 2000) at 340-330 Ma (Bussy et al., 2000; Vanardois et al., in prep) (Fig. 2). These lithologies are covered by unconformity by the undeformed Kasimovian – Asselian sedimentary rocks (Fig. 3J).

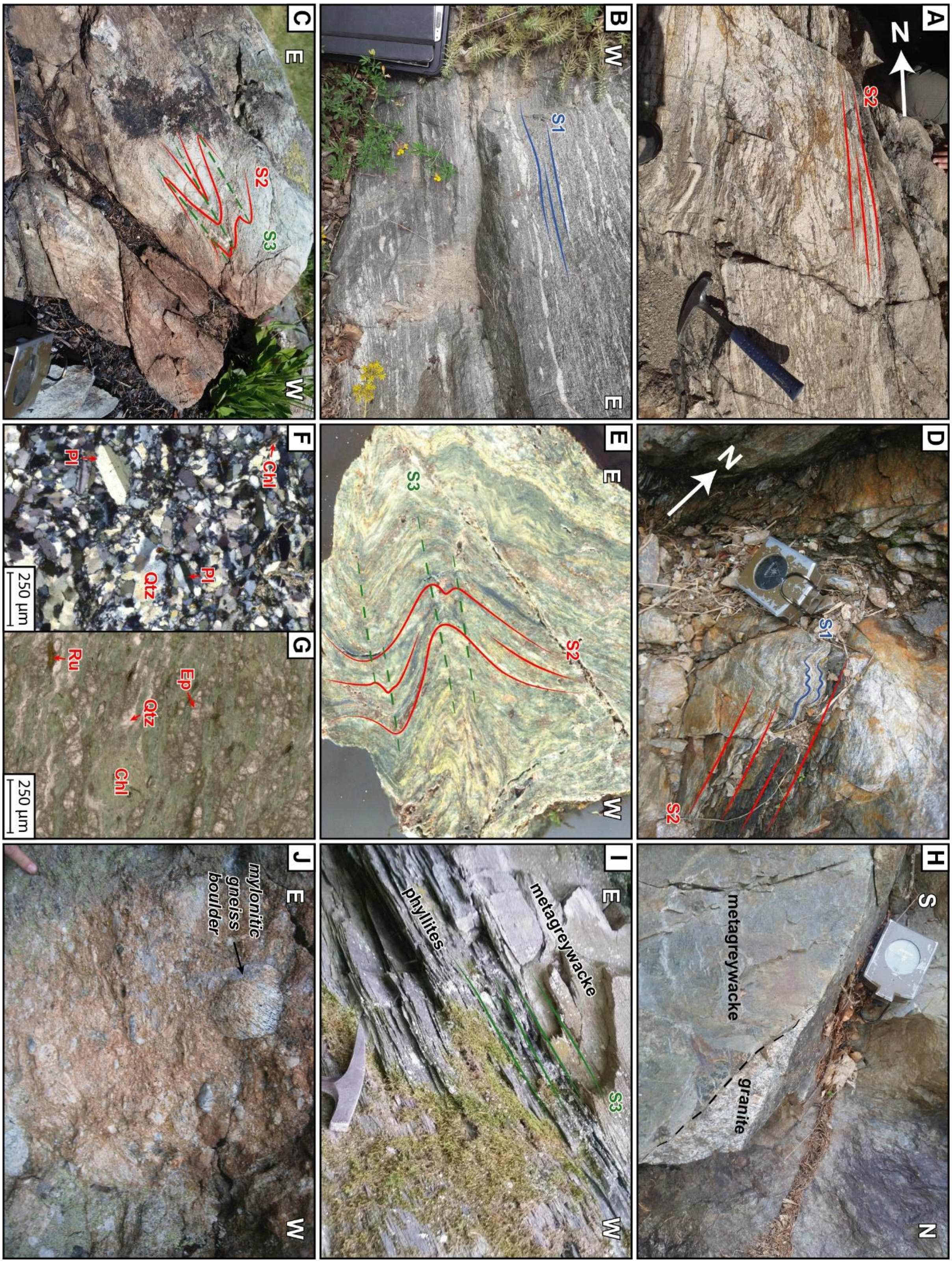

Figure 3 : Lithologies from the SW part of the Aiguilles-Rouges massif. (A) Migmatitic paragneiss of the gneissic basement structured by vertical S2 foliations from the eastern of the Servoz syncline, near the Lac Cornu. (B) Anatectic metavolcano-sedimentary rocks of the Pormenaz unit (AR982) from the western side of the Servoz syncline structured by shallowing dipping S1 foliations. (C) Fine-grained gneiss from the Pormenaz unit in the Prarion area with S3 foliations folding S2 foliations. (D) Micaschists from the Pormenaz unit structured by S2

foliations with relictual S1 foliations, eastern side of the Servoz syncline. (E) Metavolcanic rock with vertical S2 foliations and F3 open folds, western side of the Servoz syncline. (F) Acid and (G) basic rocks from the bimodal magmatic suite. (H) Intrusion of the Montées-Pélissier granite in Visean metagreywackes. (I) Visean phyllites and local metagreywacke layer structured by pervasive S3 foliations from the western side of the Servoz syncline. (J) Kasimovian-Asselian conglomerate with mylonitic gneiss boulder.

4. U-Pb LA-ICPMS results

In order to further constrain the timing of sedimentation within the Servoz syncline, U-Pb Laser-Ablation Inductively-Coupled Plasma Mass-Spectrometry (LA-ICPMS) analyses were performed on detrital zircons from a microconglomerate (AR476) of the upper structural levels of the phyllites (Fig. 2b) and on zircons from a volcano-sedimentary rocks (AR982) of the Pormenaz unit, both located in the western side of the Servoz syncline (Located on figures 1 and 2).

Zircon crystals were separated using conventional mineral separation method (Table S1). The selected grains were mounted in epoxy resin and polished down to expose their near equatorial sections. Before analysis, cathodoluminescence (CL) images were acquired for each grain using a scanning electron microscope (SEM). LA-ICPMS spot locations were selected based on the internal microstructures and to avoid inclusions, fractures and physical defects. U-Th-Pb isotope data of zircon were obtained at the Laboratoire Magmas & Volcans (LMV), Clermont-Ferrand, France by LA-ICPMS.

The analyses involved the ablation of minerals with a Resonetics M-50 laser system operating at a wavelength of 193 nm (Müller et al., 2009). The ablated material was carried in helium and then mixed with nitrogen and argon before injection into the plasma source of a Thermo Element XR Sector Field high-resolution ICP-MS. The alignment of the instrument and mass calibration were performed before every analytical session using the NIST SRM 612 reference glass, by inspecting the signal of ^{238}U and by minimising the ThO$^+$/Th$^+$ ratio (< 1%). Raw data were corrected for U-Pb fractionation during laser sampling and for instrumental mass bias by standard bracketing with repeated measurements of the GJ-1 zircon standard (Jackson et al., 2004). The reproducibility and accuracy of the corrections were controlled by repeated analyses of the 91500 zircon standard (Wiedenbeck et al., 1995) treated as unknown. Because of the non-negligible mercury content of the Ar gas creating an isobaric interference between 204Pb and 204Hg, no common Pb correction was applied prior to data reduction using the GLITTER® software package (van Achterbergh et al., 2001). The detailed analytical procedures are described in Paquette & Tiepolo (2007), Paquette et al. (2014) and detailed in Hurai et al. (2010) and in the supplementary material (Table S1). The calculated ratios were exported and ages and diagrams generated using Isoplot/Ex v. 2.49 software package (Ludwig, 2001). The decay constants used for the U-Pb system are those determined by Jaffey et al. (1971) and recommended by the IUGS (Steiger & Jäger, 1977). In the text, tables and figures, all uncertainties are given at 2σ level.

Discordant data analysed by the LA-ICPMS method are considered only if they allow the definition of discordia lines in the concordia or/and Tera Wasserburg diagrams, so that the age(s) by intercept (s) have a geologically meaningful. Otherwise, the interpretation of the discordant data remains too doubtful. In LA-ICPMS analyses, several factors that are difficult to detect from the inspection of the time-resolved signals might contribute to discordance (e.g. common Pb, by way of inclusions, mixture of two components of distinct age, small cracks). Thus, discordant data are typically excluded from detrital datasets (Gehrels, 2012). In this study, we use single-analysis concordant ages (Ludwig, 1998) to highlight the concordance of our detrital zircon data.

For the microconglomerate (AR 476), the maximum age of deposition was calculated as the concordia age (Ludwig, 1998) of the youngest group of at least 3 grains with a 2σ (standard deviation) age overlap, as proposed by Dickinson and Gehrels (2009).

4.1.Microconglomerate (AR476)

Detrital zircons grains extracted from sample AR476 show various shapes from rounded to sub-euhedralwith elongated ratios between 3:1 and 1:1 (Fig. 4A). The analysed grains range in size from 100 to 300 µm. In CL, most crystals (e.g. Zr36, Zr18) are characterized by oscillatory zonation that probably reflects magmatic growth but sometimes by faded oscillatory zoning (e.g. Zr 32). Moreover, a few grains have cores (e.g. Zr12, Zr56), which are CL-bright with patchy or sector-like zoning or oscillatory zoning and rims, which are dark and featureless (Fig. 4A). Sixty-two analyses were performed on 58 zircon grains. A very large majority of the Th/U ratios are between 0.11 and 0.89, only 13 values measured on rims or tips are less than 0.10 (Table S2), values that are considered typical for metamorphic zircon (e.g. Tiepel et al., 2004; Linnemann et al., 2011, Rubatto, 2017) (Fig. 4E). In the Tera Wasserburg diagram, most of the data are concordant (grey ellipses) and range from Neoproterozoic (Ediacarian) to Permo-Carboniferous ages with scattered concordant data at c.a 1Ga, 875 Ma, 750 Ma and 660 Ma as well as one sub-corcordant data at ca. 1.8 Ga (Fig. 4B). Only data that are a single-analysis concordia age and have single grain core-rim pairs, which give distinguishable dates at 2σ are considered and plotted in the histogram (Fig. 4C; Table S2). For the period between Ediacaran and Permian, the binned frequency histogram (coupled with a probability-density distribution) shows that at least 5 thermal events were recorded around ca. 610-540 Ma, 500-460 Ma, 350-320 Ma and 320-290 Ma with varying proportions of the aforementioned distinct events as well a few scattered date peaks at ca. 380 Ma and possibly at ca. 510 Ma (Fig. 4C). The Ediacaran date population is the most represented (~38%) with a date peak around 570 Ma. It is essentially obtained on zircon cores with oscillatory zoning and Th/U ratios higher than 0.17 (Fig. 4E). The early Paleozoic dates fall into two similar-sized populations (~10-13 %) around 480 Ma and 460 Ma that are composed of rims and zoned cores with Th/U ratios between 0.10 and 0.40 for the Cambro-Ordovician date population and between 0.02 and 0.24 for the Ordo-Silurian date population (Fig. 4E). And finally, the Carboniferous dates also seem to be divided into two similar—sized populations (~8-10 %), one of Visean age (a date peak at ca. 335 Ma) and the other Pennsylvanian age (a date peak at ca. 310 Ma) (Fig. 4B). The Visean dates were mainly obtained on cores and rims characterized by Th/U ratios between 0.11 and 0.30 except for a data at 0.02 obtained on a tip.

The youngest population (date peak at ca. 310 Ma) consisting of 4 dates obtained on 3 tips/rims and one on a grain core, is characterized by Th/U ratios less than 0.10 and yields a concordia age at 307 ± 9 Ma ($\mathrm{MSWD}_{(C+E)}$ = 3.1; n = 4) (Fig. 4D and E) and the youngest analysis has a single-grain age at 296.5 ± 8 Ma (Table S2).

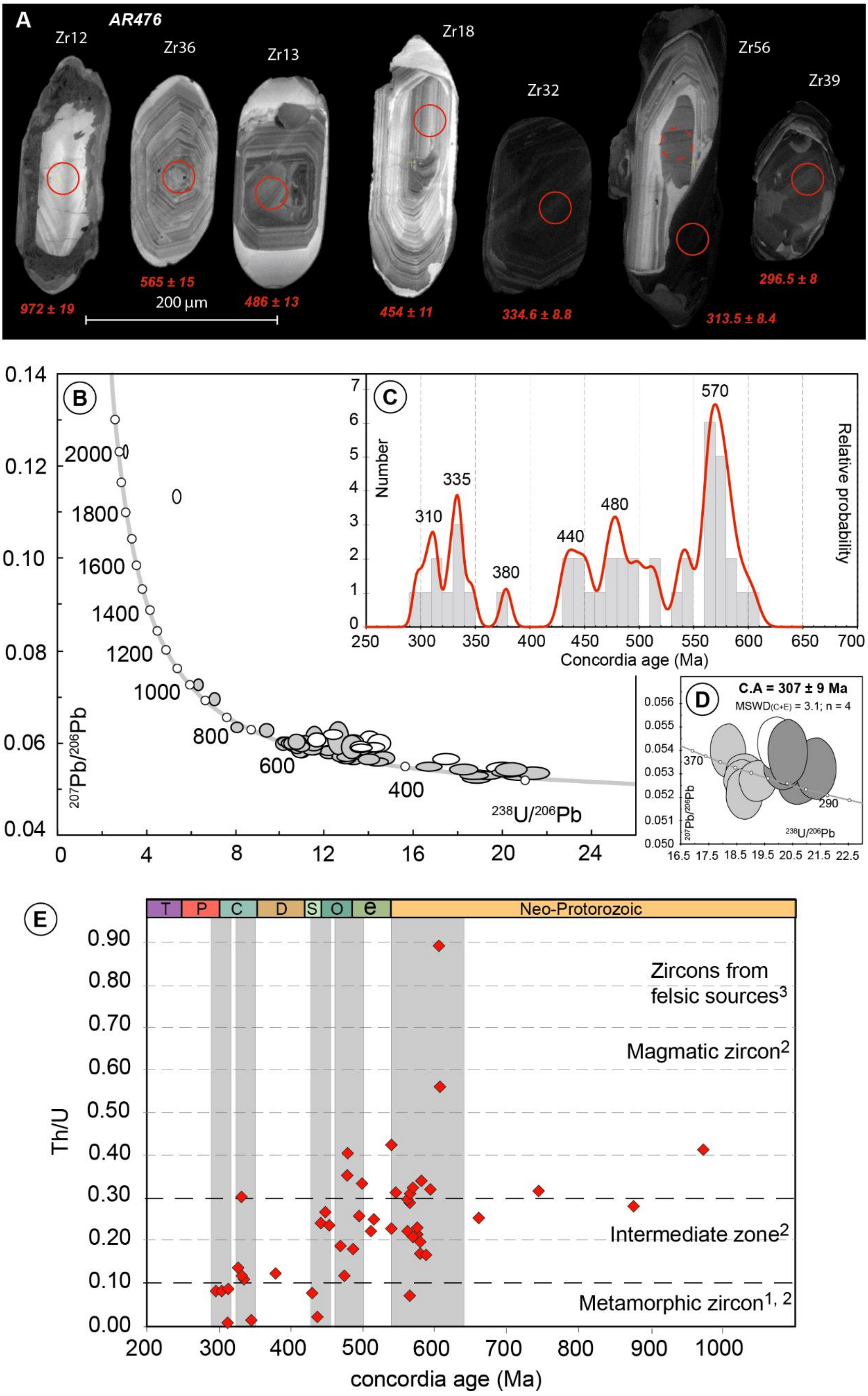

Figure 4 : U-Pb LA-ICPMS results on the microconglomerate AR476. (A) Cathodoluminescence photos of zircons with locations of laser spots and associated single-grain concordia ages. (B) Zircons U-Pb Tera Wasserburg

diagram. (C) Single-grain concordia ages histogram and probability distribution histogram were generated using a bin-width = 40 and a band-width = 10. Discordant ellipses (white ellipses) and concordant ellipses (grey ellipses) older than 650 Ma are not plotted in these diagrams. (D) Zoom of (B) on the youngest analyses. Only dark grey ellipses are used to calculate the concordia age. Error ellipses and uncertainties in ages are ± 2σ. (E) Zircon Th/U ratio vs. single-grain concordia age diagram. Th/U = 0.10 is the upper limit for metamorphic zircon after (1) and (2); 0.30 is the lower limit for the magmatic zircon after (2) and Th/U = 1 is the upper limit for the felsic zircon sources field after (3). (1): Rubatto, 2017; (2): Teipel et al. (2004) (3): Linnemann et al. (2011).

4.2.Prarion metavolcano-sedimentary rock (AR982)

This sample located in the southwestern extremity of the AR massif (Fig. 1 and 2) is composed of Qtz + Amph + Bt + Pl + Kfs + Ttn (Fig. 5A and B). The sample is stratified with layers mainly composed of Amph + Ttn alternating with layers mainly composed of Qtz + Kfs + Pl + Bt. This layering suggests a volcano-sedimentary protolith. In this area, the presence of leucosomes and the presence of small dihedral angles of interstitial phases, quartz filling pores and elongated interstitial plagioclases grains indicate that the volcano-sedimentary rocks were partially molten (Lee et al., 2018; Stuart et al., 2018) (Fig. 5B).

Zircons from sample AR982 are pinkish, transparent to slightly opaque. They are euhedral with a squat shape with a shape ratio up to 3:1. CL imaging shows oscillatory igneous growth zoning as well as the presence of cores displaying either a sector-like zoning or patchy zoning textures surrounded by zoned or convolute rims (Fig. 5C). Forty-seven analyses are obtained on rims or cores of 40 crystals (Fig. 5D, Table S2). In the Tera Wasserburg diagram, the data are scattered between ca. 485 Ma and ca. 220 Ma and part of them form two concordant clusters around ca. 475 Ma and 350 Ma. Amongst these data, fifteen analyses obtained on 10 cores (# 1, 7 13, 17, 20, 21, 40, 42, 43, 45) and 5 zoned tips (# 5, 10, 11, 19, 36) yield a weighted average of ^{206}Pb/^{238}U dates of 474 ± 3 Ma (MSWD = 0.7) and present Th/U ratios ranging between 0.24 and 0.39 with variable Pb (14-75 ppm), U (182–969 ppm) and Th (54–361 ppm) contents (Fig. 5D and E, Table S2). The other cluster is constituted by eight concordant data obtained on tips which are characterized by very low Th/U ratios (0.0-0.01) and low Th contents (1.9-8.7 ppm). The weighted average of ^{206}Pb/^{238}U dates is 351 ± 5 Ma (MSWD = 1.8) (Fig. 5D and E). In the diagram, the dotted ellipses are obtained mainly on the probably metamict tips which are characterized by very high U contents (most 651-2127 ppm). These data are not taken into consideration for the age calculation; their discordances are due to radiogenic Pb losses and common Pb contaminations.

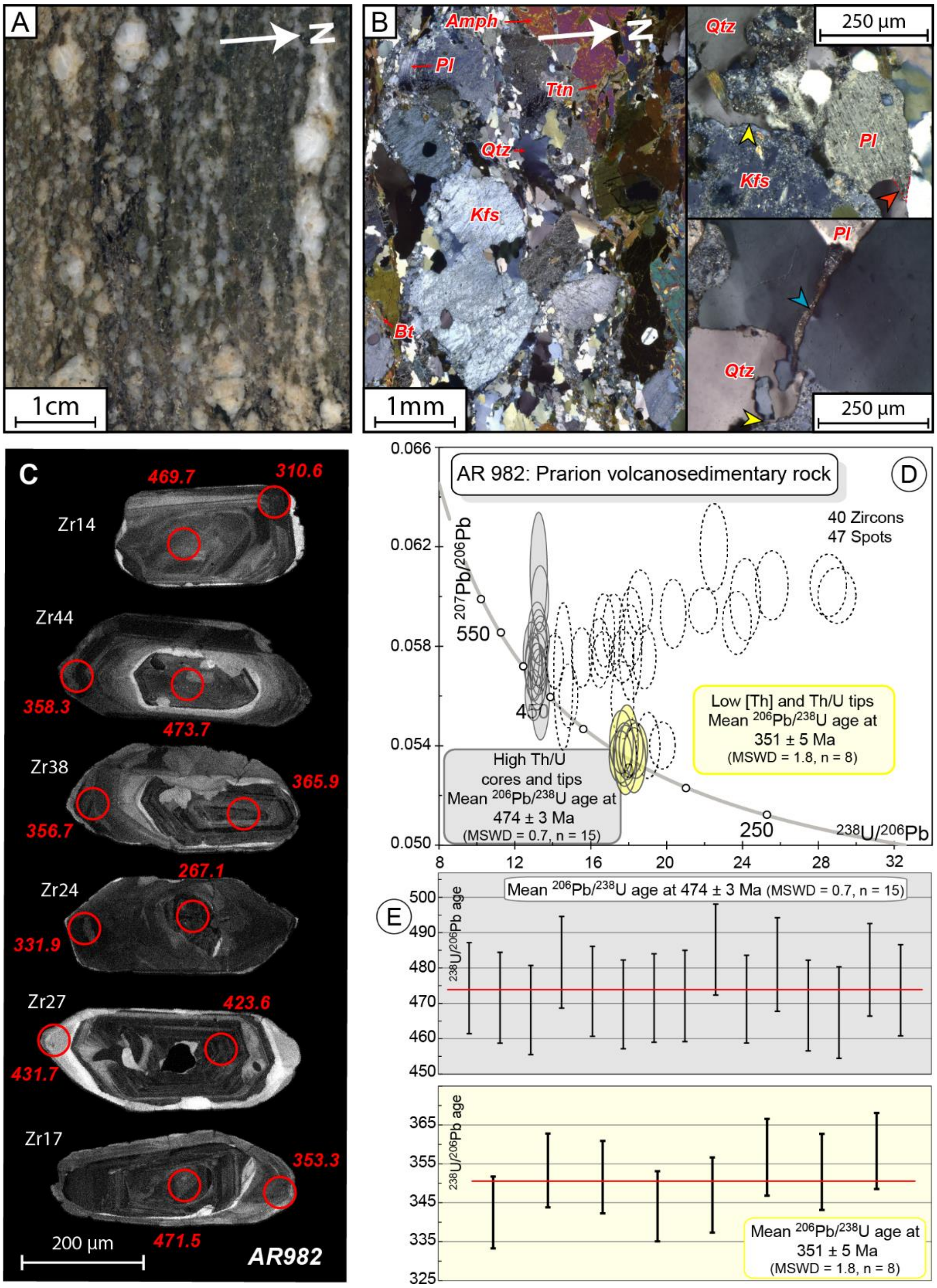

Figure 5 : Description and U-Pb LA-ICPMS results on the Prarion metavolcano-sedimentary rock AR982. (A) Photo of the sample AR982 showing distinct Kfs-Pl-Qtz and Amph-rich layers. (B) Thin section images of the a Kfs-Pl-Qtz layer showing presence of small dihedral angles of interstitial phases (orange arrow), quartz filling pores (yellow arrows) and elongated interstitial plagioclases grains (blue arrow) that indicate a partially melting event (Lee et al., 2018; Stuart et al., 2018). Amph: amphibole; Bt: biotite; Kfs: K-feldspar; Pl: plagioclase; Ttn: titanites. (C) Cathodoluminescence photos of zircons with locations of laser spots and associated ^{206}Pb/^{238}U dates. (D) Zircons U-Pb Tera Wasserburg diagram. Dotted ellipses are not taken into account for the calculation of the calculation of weighted average of ^{206}Pb/^{238}U age of the two populations (grey and yellow ellipses) because they

are affected by radiogenic Pb losses and/or common Pb contaminations. Error ellipses and uncertainties in ages are ± 2σ. (E) Diagrams of weighted average of $^{206}Pb/^{238}U$ age of the two populations (grey and yellow). Uncertainties in dates and ages are ± 2σ.

5. RSCM thermometry results

5.1.Thermometric method

5.1.1. Analytical method

Raman spectra of carbonaceous material (CM) have been acquired at BRGM using a Renishaw inVia Reflex microspectrometer and following the analytical procedure outlined in Delchini et al. (2016). The Diode Pumped Solid State (DPSS) green laser is focused on the sample with power lower than 1 mW at the thin section surface, through ×100 objective (numerical aperture = 0.90) of a Leica DM2500 microscope. After interaction between CM and laser beam, Raman signal was dispersed using 1800 lines/mm before being analyzed by a deep depletion Charge Coupled Device detector (1024 × 256 pixels).

At least 15 spectra were recorded for each sample to ensure CM homogeneity. Both instrument calibration and Raman measurements were performed using Renishaw Wire 4.1. Before each measurement session, the microspectrometer was calibrated using the 520.5 cm^{-1} line of internal silicon.

5.1.2. Thermometric approach: RSCM geothermometry

Temperature is the key parameter that controls the structure evolution of the natural carbonaceous material. This irreversible evolution can be quantified using Raman microspectroscopy (e.g. Wopenka and Pasteris, 1993; Yui et al., 1996; Beyssac et al., 2002; Lahfid et al., 2010). Consequently, a geothermometry approach has been developed, namely the Raman Spectroscopy of Carbonaceous Material (RSCM). This approach allows estimating rocks peak temperatures in the range 200-640°C (Beyssac et al., 2002; Lahfid et al. 2010). In the present study, all maximum temperatures determined by RSCM geothermometry, noted T_{RSCM}, were estimated using R2 parameter proposed by Beyssac et al., (2002).

5.2.Raman spectra evolution

Raman spectra obtained on CM from metasedimentary rocks that experienced hornfels/amphibolite facies conditions (Pormenaz, metavolcanics, metagreywackes and phyllites units) show some spectral variations (Fig. 6). All these samples present similar spectral features mainly composed of a G band located around 1580 cm^{-1} and defect bands D1 and D2 located around 1350 cm^{-1} and 1620 cm^{-1}, respectively (Fig. 6b to e). The values of Raman parameter R2 of these samples vary between 0.20 and 0.65 (Table 1), corresponding to T_{RSCM} between 550 and 350°C (Fig. 6b to e), respectively.

Raman spectra from Kasimovian – Asselian (post-orogenic) formation samples are similar to those observed for poorly ordered CM (e.g., Lahfid et al., 2010). The exhibit a broad G band located at ~1590 cm^{-1}, including the G band and the D2 band, and a very wide and more intense composite defect band around 1350 cm^{-1} (Fig. 6). The composite defect band includes D1 (wavenumber), D3 (around 1500 cm^{-1}) and D4 (around 1200 cm^{-1}) defect bands appeared in the spectra (Fig. 6). The values of Raman R2 vary between 0.60 and 0.67, corresponding to T_{RSCM} between 340 °C and 360 °C (Table 1).

In Pormenaz and metagreywackes units, the RSCM temperatures are consistent with the temperatures proposed by Dobmeier (1998), based on empirical thermometry on amphibole, which yields temperatures at 620 ± 50 °C in the western side, and 450 ± 50 °C in the eastern of the Arve fault (Fig. 6a). In the western side of the Arve fault, the T_{RSCM} increase from the bottom to the top of the sequence, whereas in the eastern side T_{RSCM} decrease toward the bottom of the sequence (Fig. 6). This inverse gradient could be induced by the intrusion of the Montées-Pélissier granite in the metagreywackes.

The T_{RSCM} have been plotted vs. the sample locations on the map and along cross-section (Fig. 7A and B), taking into account the estimated thickness of the formations. Due to the Arve fault, two zones were determined, and two diagrams are proposed (Fig. 7B): diagrams (1) concerns the western part of the fault, while diagram (2) represents the eastern part. In the western side of the Arve fault, T_{RSCM} measured in samples from Pormenaz and metagreywackes units vary from 400 °C to 550 °C and define an anomalously high geothermal gradient of ca. 115 °C/km (Fig. 6 and 7), whereas samples from phyllites yield constant T_{RSCM} at ca. 350 °C (Fig. 6 and 7).

In the eastern side of the Arve fault, metagreywackes samples of the metagreywackes unit display T_{RSCM} ranging from 530 °C to 420 °C and define a geotherm gradient of 30 °C/km (Fig. 6 and 7). Diagram (2) (Fig. 7B) shows that T_{RSCM} from the metagreywackes unit do not align along the same geotherm than the post-orogenic rocks. Furthermore, this geotherm is also different from the geotherm defined in the western part and is inversed compared to the facing of the sedimentary sequence. The T_{RSCM} measured in samples from the post-orogenic sedimentary rocks are constant with temperatures of ca. 350 °C (Fig. 6 and 7).

Table 1 : RSCM thermometer results

sample	Latitude	Longitude	Unit	n	R2	SD	T (°C)	SD	SE	method
AR175	45.923252	6.792117	Stephanian	15	0.63	0.02	361	10	3	Beyssac et al., 2002
AR185	45.916337	6.789523	Stephanian	13	0.65	0.02	351	9	2	Beyssac et al., 2002
AR203	45.922759	6.77952	Stephanian	12	0.65	0.01	354	5	1	Beyssac et al., 2002
AR303	45.914851	6.765488	Visean	13	0.65	0.02	354	7	2	Beyssac et al., 2002
AR305	45.911218	6.766686	Visean	13	0.65	0.01	353	7	2	Beyssac et al., 2002
AR307	45.909062	6.766462	Visean	19	0.65	0.02	353	9	2	Beyssac et al., 2002
AR308	45.907833	6.768025	Visean	20	0.64	0.01	355	4	1	Beyssac et al., 2002
AR309	45.905352	6.763706	Visean	20	0.65	0.01	353	7	1	Beyssac et al., 2002
AR311	45.907944	6.755221	Visean	16	0.51	0.05	414	20	5	Beyssac et al., 2002
AR356	45.92839	6.772924	Stephanian	13	0.60	0.04	375	19	5	Beyssac et al., 2002
AR357	45.930347	6.772509	Stephanian	17	0.65	0.01	351	7	2	Beyssac et al., 2002
AR371	45.915553	6.772666	Visean	13	0.33	0.04	496	20	5	Beyssac et al., 2002
AR372	45.905322	6.7664	Visean	17	0.64	0.02	355	10	2	Beyssac et al., 2002
AR374	45.904835	6.767961	Visean	16	0.65	0.01	352	6	1	Beyssac et al., 2002
AR447	45.893737	6.750608	Pormenaz gneiss	14	0.20	0.06	550	25	6	Beyssac et al., 2002
AR463	45.930882	6.744295	Visean	15	0.63	0.03	360	12	3	Beyssac et al., 2002
AR466	45.929253	6.752933	Visean	13	0.65	0.03	354	14	4	Beyssac et al., 2002
AR474	45.923449	6.756683	Visean	25	0.64	0.02	357	9	2	Beyssac et al., 2002
AR477	45.926493	6.754188	Visean	12	0.64	0.02	357	8	2	Beyssac et al., 2002
AR511	45.919218	6.733573	Visean	14	0.42	0.04	453	16	4	Beyssac et al., 2002
AR516	45.922847	6.735157	Visean	13	0.55	0.02	394	9	2	Beyssac et al., 2002
AR517	45.923757	6.74377	Visean	12	0.62	0.02	364	11	3	Beyssac et al., 2002
AR519	45.922216	6.751198	Visean	13	0.63	0.02	362	10	3	Beyssac et al., 2002
AR522	45.913968	6.753084	Visean	10	0.62	0.02	364	11	3	Beyssac et al., 2002
AR645	45.912895	6.797938	Stephanian	13	0.67	0.01	345	4	1	Beyssac et al., 2002
AR649	45.911918	6.79285	Stephanian	13	0.67	0.01	344	3	1	Beyssac et al., 2002
AR653	45.907766	6.799887	Stephanian	17	0.62	0.02	366	9	2	Beyssac et al., 2002
AR665	45.904612	6.801483	Stephanian	13	0.62	0.04	366	17	4	Beyssac et al., 2002
AR757	45.971587	6.805773	Stephanian	12	0.66	0.01	346	6	2	Beyssac et al., 2002
AR761	45.968368	6.797074	Stephanian	13	0.65	0.01	352	4	1	Beyssac et al., 2002
AR794	45.957586	6.799844	Stephanian	15	0.66	0.02	349	8	2	Beyssac et al., 2002
AR807	45.892676	6.796551	Visean	10	0.49	0.04	421	17	5	Beyssac et al., 2002
AR810	45.89351	6.792997	Visean	12	0.32	0.04	500	18	5	Beyssac et al., 2002
AR814	45.900854	6.791436	Visean	10	0.36	0.04	482	17	5	Beyssac et al., 2002
AR816	45.902241	6.788473	Visean	12	0.42	0.03	453	12	4	Beyssac et al., 2002
AR817	45.902698	6.787408	Visean	10	0.36	0.02	478	10	3	Beyssac et al., 2002
AR818	45.904459	6.784962	Visean	14	0.41	0.03	459	15	4	Beyssac et al., 2002
AR819	45.906975	6.78282	Visean	15	0.37	0.06	474	27	7	Beyssac et al., 2002
AR821	45.911684	6.781503	Visean	12	0.41	0.04	460	17	5	Beyssac et al., 2002
AR825	45.897451	6.791988	Visean	11	0.38	0.04	473	17	5	Beyssac et al., 2002

AR826	45.895966	6.787796	Visean	14	0.30	0.04	507	18	5	Beyssac et al., 2002
AR827	45.926299	6.771557	Visean	13	0.43	0.02	450	11	3	Beyssac et al., 2002
AR853	45.999586	6.929771	Stephanian	16	0.67	0.01	342	4	1	Beyssac et al., 2002
AR862	45.913239	6.774496	Stephanian	14	0.61	0.02	368	10	3	Beyssac et al., 2002
AR863	45.909229	6.777927	Visean	11	0.25	0.05	530	23	6	Beyssac et al., 2002
AR864	45.906481	6.778808	Visean	15	0.40	0.07	463	31	8	Beyssac et al., 2002
AR871	45.918963	6.767402	Visean	13	0.63	0.02	362	11	3	Beyssac et al., 2002

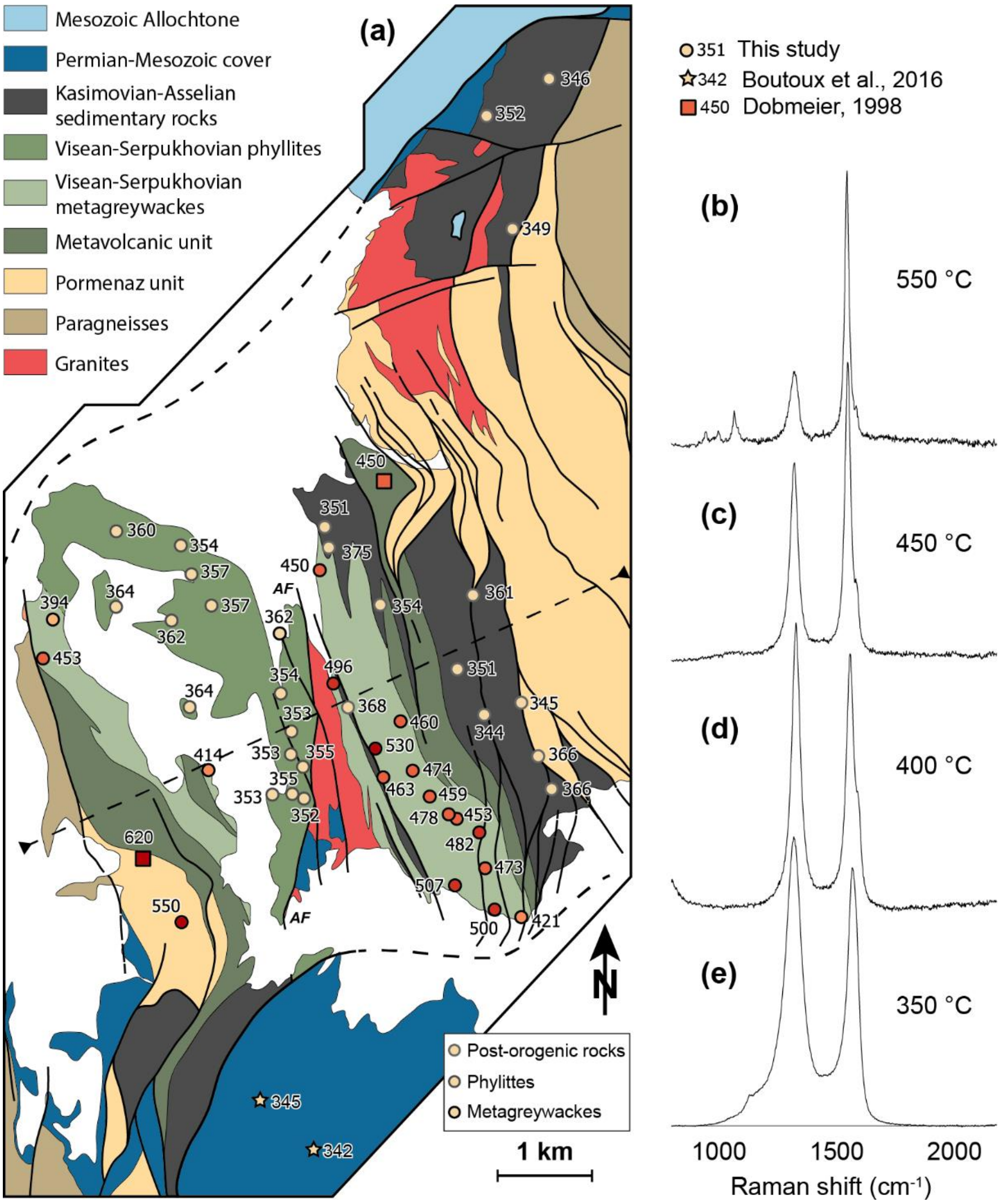

Figure 6 : Map of the Servoz syncline with mean foliations and T_{RSCM} temperatures, and representative Raman spectra of carbonaceous material of four samples with varied temperatures. Cross-section of Figure 7A is located. AF: Arve Fault.

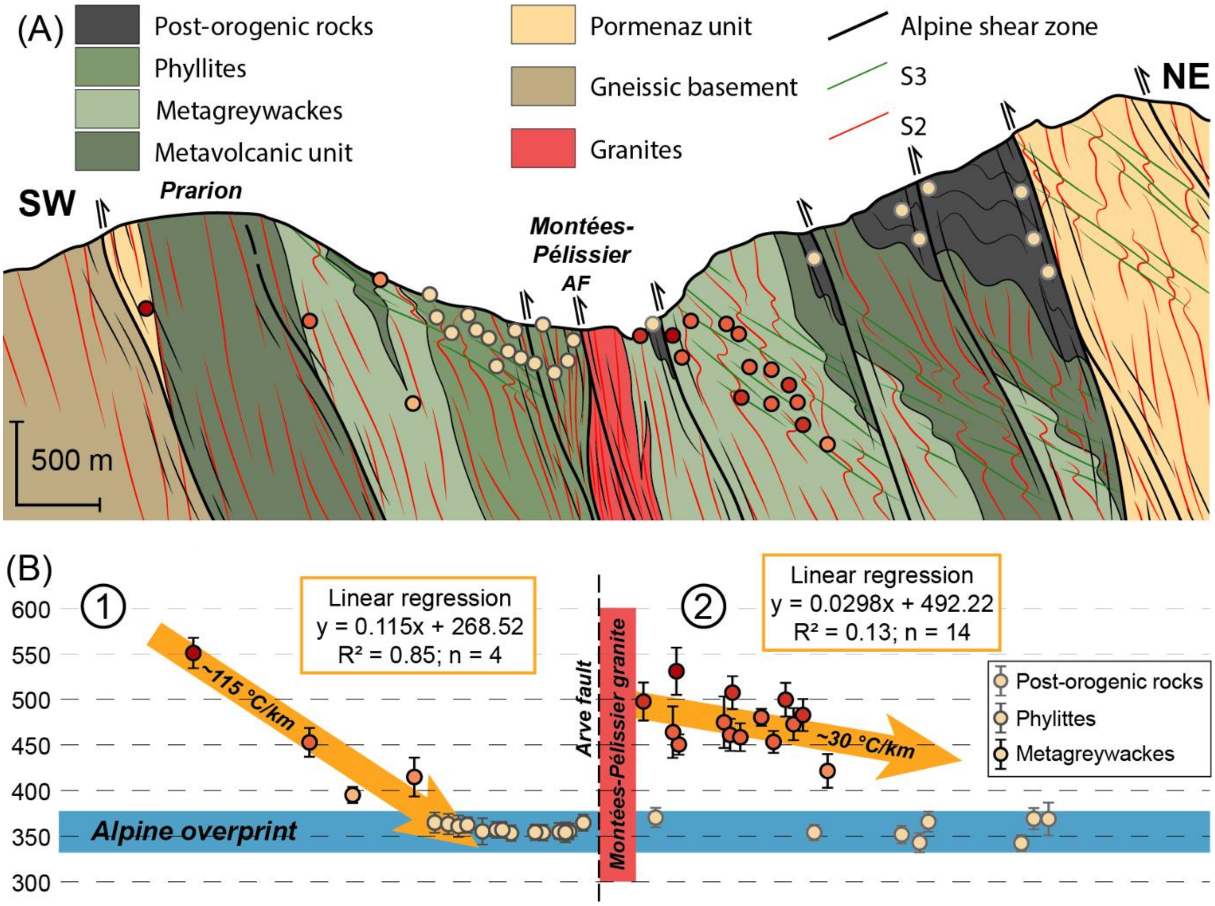

Figure 7 : (A) Cross-section in through the Servoz syncline with projected RSCM temperatures. AF: Arve Fault. (B) Apparent gradients from (1) western and (2) eastern side of the Servoz syncline calculated on Famennian – Early-Visean samples.

6. Numerical modelling

In the light of our RSCM thermometry results, the geotherm defined in the eastern part of the Servoz syncline is inversed compared to the facing of the sedimentary sequence (Fig. 6 and 7). This inverse gradient could be the effect of the intrusion of the Montées-Pélissier granite that could have induced a contact metamorphism in the metagreywackes from the western side of the Servoz syncline (Fig. 6 and 7). In order to test this hypothesis, we present a thermal numerical modelling of a vertical granitic intrusion within metasedimentary rocks using the heat equation:

$$\rho . Cp . \frac{\partial T}{\partial t} = \frac{\partial}{\partial z}\left(k . \frac{\partial T}{\partial z}\right) + H \tag{1}$$

Several studies on the thermal conductivity (k) as a function of temperature have demonstrated a strong temperature dependence of k (Zoth and Hänel, 1988; Seipold, 1998; Vosteen and Schellschmidt, 2003; Whittinghton et al., 2009; Nebalek et al., 2010, 2012; Miao et al., 2014; Wen et al., 2015). In this study, we used the relationship proposed by Vosteen and Schellschmidt (2003) to model the variation of *k* in function of the temperature for granitic and metasedimentary rocks. The thermo-dependent evolution of *k* is given by the following formulas:

$$k(T) = \frac{k(0)}{0.99 + T\left(a - \frac{b}{k(0)}\right)} \tag{2}$$

with a = 0.0030 ± 0.0015 and *b*= 0.0042 ± 0.0006 for crystalline rocks and *a*= 0.0034 ± 0.0015 and b = 0.0039 ± 0.0014 for sedimentary rocks with *k(0)* being calculated for these rocks, respectively as:

$$k_{cry}(0) = 0.53k(25) + \frac{1}{2}\sqrt{1.13k(25)^2 - 0.42k(25)} \tag{3}$$

$$k_{sed}(0) = 0.54k(25) + \frac{1}{2}\sqrt{1.16k(25)^2 - 0.39k(25)} \tag{4}$$

The values of *k(25)* (Table 2) are from Vosteen and Schellschmidt (2003). The density (ρ) and the heat capacity (*Cp*) also vary in function of the temperature but have a negligible effect on the temperature (e.g. Duprat-Oualid et al., 2015), thus typical fixed values were assigned (Table 2).

In equation (1), *H* corresponds to heat supplies such as mantellic or radiogenic heat flux. Based on the high structural level of the Servoz syncline, mantellic heat flux was disregarded. Radiogenic heat production (*A* (µW.m^{-3})) of the Montées-Pélissier granite was estimated by the relationship of Rybach (1988):

$$A = \rho\left(9.67C_U + 2.56C_{Th} + 2.89C_{K_2O}\right) \times 10^{-5} \tag{5}$$

Concentrations, *C*, of U and Th in ppm and K2O in wt% from Dobmeier (1996), leading to a mean value of 4 µW.m^{-3}. Due to the absence of geochemical analyses on the metagreywackes, their radiogenic production was fixed at 1 µW.m^{-3} (Hasterok et al., 2018) (Table 2).

Table 2 : Parameters used in the numerical models

Parameters	metagreywackes	granite
Crust density ρ (kg.m^{-3})	2700	2700
Heat capacity *Cp* (J.kg^{-1}.K^{-1})	1100	1100
Thermal conductivity at 25°C *k(25)* (W.m^{-1}.K^{-1})	2.9	3.1
Radiogenic heat production *A* (µW.m^{-3})	1	4

Intrusion of the granite was modelled with a temperature of 700 °C and a thickness of 1 km. The initial temperature of the metagreywackes cannot be superior to the T_{RSCM} of sample AR807 at 421 ± 17 °C (Fig. 6; Table 1). Therefore, initial temperature of the metagreywackes was fixed at 250 °C, 300 °C, 350 °C and 400 °C (Fig. 8).

Modelling of the one-kilometre thick granite sheet induces an inverse gradient within 50 ka (Fig. 8). However, temperatures induce by the contact metamorphism are too low compared to the T_{RSCM} measured for initial temperatures in the metagreywackes at 250 °C, 300 °C and 350 °C (Fig. 8). On the other hand, with an initial temperature of 400 °C in the metagreywackes, the intrusion of the Montées-Pélissier granite produced a contact metamorphism with temperatures fitting the T_{RSCM} (Fig. 8).

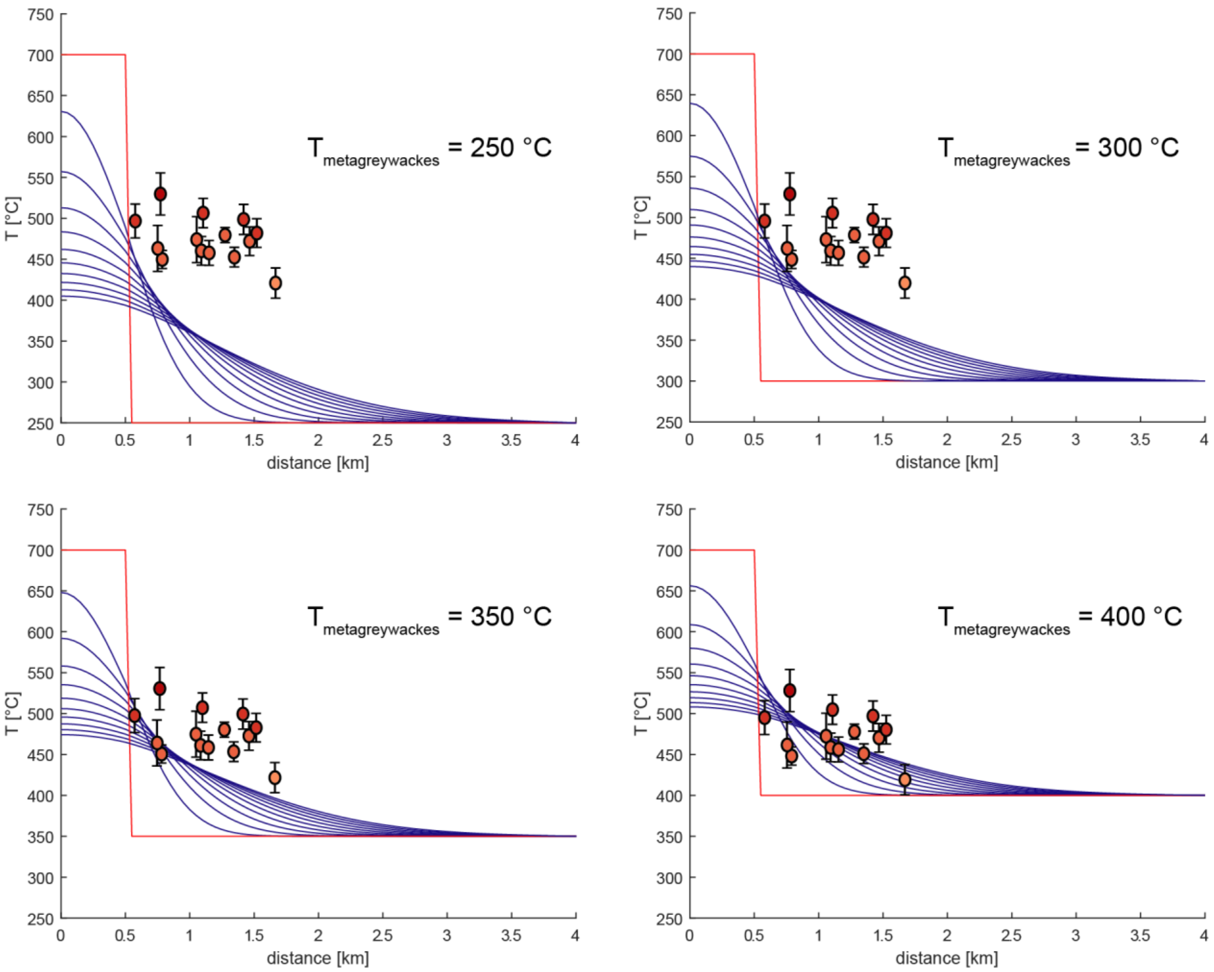

Figure 8 : Numerical models of the thermal diffusion of the Montées-Pélissier granite within metagreywackes at initial temperatures of 250, 300, 350 and 400 °C. Models last 50 ka. Red lines: initial geotherms; Blue lines: geotherms every 5 ka. RSCM temperatures from the western side of the Servoz syncline are projected.

7. Discussion

7.1.Time constraints on the Servoz formations

Historically, two distinct stratigraphic formations have been described in the Servoz syncline: the Late-Visean – Serpukhovian formation (i.e. 335 – 325 Ma) and the Kasimovian – Asselian formation (i.e. 305-295 Ma) (e.g. Bellière and Streel, 1980; Pairis et al., 1992; Dobmeier, 1996). However, based on published geochronological data (e.g. Ménot et al., 1987; Capuzzo and Bussy, 2000; Fréville et al., 2018), fossil analyses (Laurent, 1967; Bellière and Streel, 1980), as well as our recent results obtained by LA-ICPMS U-Th-Pb dating on zircon, we propose that the Servoz syncline is composed of three main formations (F1, F2 and F3; Fig. 9), as follow.

F1 formation:

The Montées-Pélissier granite intruded into the metagreywackes has been dated at 340 ± 5 Ma (Vanardois et al., in prep) and therefore defines a minimum age for the deposition of the metagreywackes and the deeper sedimentary and magmatic formations (i.e. metavolcanics and Pormenaz units) (Fig. 2b).

The Rioupéroux-Livet formation in the Belledonne and Pelvoux massifs, located at ca. 100 km from the studied area, is also composed of volcano-sedimentary rocks similar to the metavolcano-sedimentary rocks from the Pormenaz unit (Ménot, 1986; Dobmeier et al., 1999; Guillot and Ménot, 2009; Guillot et al., 2009; Fréville et al., 2018, in review; Fréville, 2016). The Rioupéroux-Livet magmatic event have been dated at ca. 370-350 Ma (Ménot et al., 1987, 1988a; Ménot, 1988a, 1988b; Fréville et al., 2018, in review). Based on this comparison with the Rioupéroux-Livet unit, an age between 370 and 350 Ma is proposed for the emplacement of metavolcanics and Pormenaz units. Therefore, the metagreywackes, metavolcanics and Pormenaz units form the F1 formation (370-350 Ma).

Zircon U-Th-Pb dating of the Prarion metavolcano-sedimentary sample (AR982) indicates the occurrence of two distinct populations (Fig. 5D). A population constituted by cores and tips with a magmatic origin (Th/U > 0.1 and oscillatory zoning) that yields a mean $^{206}Pb/^{238}U$ date of 474 ± 3 Ma and a younger population of tips characterized by low Th contents (<9 ppm) and very low Th/U ratios (0.0-0.01) that gives a mean $^{206}Pb/^{238}U$ date of 351 ± 5 Ma. The Ordovician date is obtained mainly on zircon cores showing internal structures and Th/U ratios >0.1 typical of magmatic zircon (Tiepel et al., 2004; Linnemann et al., 2011; Rubatto, 2017). The existence of an Ordovician magmatic event that affects the ECMs is well known (e.g. Bussy et al., 2011; Schaltegger et al., 2003; Paquette et al., 1989; Rubatto et al., 2001, 2010; Jacob et al., 2021; Vanardois et al. in review, in prep). On the other hand, the date at 351 ± 5 Ma is obtained on dark zircon rims displaying low Th/U ratios (0.00-0.01) often interpreted as a metamorphic origin (Tiepel et al., 2004; Linnemann et al., 2011; Rubatto, 2017). This interpretation is also suggested by the presence in the conglomerate (AR476) of a significant population (~20-25 %) of early Paleozoic detrital zircons. Indeed, measured Th/U ratios (0.10-0.40) on the Cambrian-Ordovician sub-population suggest that this detrital zircon population consists of grains likely from felsic igneous sources (Teipel et al., 2004; Linnemann et al., 2011). While, the Silurian-Ordovician date sub-population (Th/U = 0.02-0.24) is thought to be dominated by grains from felsic igneous sources and metamorphic sources (Teipel et al., 2004; Linnemann et al., 2011) (Fig. 4E). Therefore, we interpret the Ordovician date as the age of emplacement of the magmatic protolith and the date at 351 ± 5 Ma is very likely the age of the anatectic event affecting the sample AR982. This anatexis is therefore synchronous with the bimodal magmatism and highlights high thermal conditions during the F1 formation.

F2 formation:

Based on micropaleontological evidences, Bellière and Streel (1980) deduced a Late-Visean – Serpukhovian age (i.e. between ca. 335-325 Ma) for the bottom of the phyllites formation. The emplacement of the Montées-Pélissier granite, dated at 340 ± 5 Ma and 332 ± 2 Ma (Bussy et al., 2000; Vanardois et al., in prep), is anterior to the deposition of the F2 phyllites. Our geochronological results on detrital zircons from a microconglomerate (AR476) located at the top of the phyllites formation indicate the youngest detrital date obtained is 296.5 ± 8 Ma, this date is sometimes considered as a maximum limit for the age of deposition (e.g. Bingen et al., 2001), in fact the crystallization of the youngest detrital zircon within a sediment precedes deposition of the host sediment. But in some cases (i.e. Pb loss), this date may post-date the real maximum depositional age, so the youngest detrital date is interpreted as the minimum of the maximum depositional age (Spencer et al., 2016). To ensure a statistically more robust estimate of this age, the maximum age of deposition was calculated, the concordia age thus obtained is 307 ± 9 Ma (n=4), is similar within the error bars with the youngest detrital date, which implies that the sedimentation was still active at least 307 ± 9 Ma (Fig. 4). Considering the local origin of these sediments (Bellière and Streel, 1980), the presence in the microconglomerate of a Visean detrital zircon population characterized by Th/U ratios (> 0.1) typical of magmatic zircons suggests that the origin of these grains could come Visean high-K calc-alkaline to shoshonitic plutons such the Pormenaz and/or Montées-Pélissier granites (Bussy et al., 2000; Vanardois et al., in prep). This would suggest that at least one of these plutons, and their country rocks (i.e. the F1 formation), were already exhumed during the sedimentation of the phyllites, which may could the difference of thickness of the metagreywackes between the western (ca. 500 m) and the eastern (ca. 1000 m) sides of the Servoz syncline (Fig. 7A). Thus, we propose that the metagreywackes and the phyllites cannot belong to the same continuous sedimentation, which therefore implies an age between 330-300 Ma for the formation (F2) mainly composed of phyllites.

F3 formation:

Finally, the age of the post-orogenic deposits that uncomfortably overlays older formations (F1 and F2) has been estimated by ID-TIMS U-Pb on zircon from volcanic rocks in the Salvan-Dorenaz syncline between 311-291 Ma (with uncertainties; Capuzzo and Bussy, 2000). In the Servoz syncline, a fossil print from a sample at the bottom of the formation yields an age at ca. 305-300 Ma, which suggests an age between ca. 310 and 290 Ma for the post-orogenic sedimentary rocks (F3). Considering the unconformity between the F2 and F3 formation, if the F3 started to sediment at ca. 310 Ma, the F2 formation is thus anterior to 310 Ma and a has probably sediments between 330 and 310 Ma.

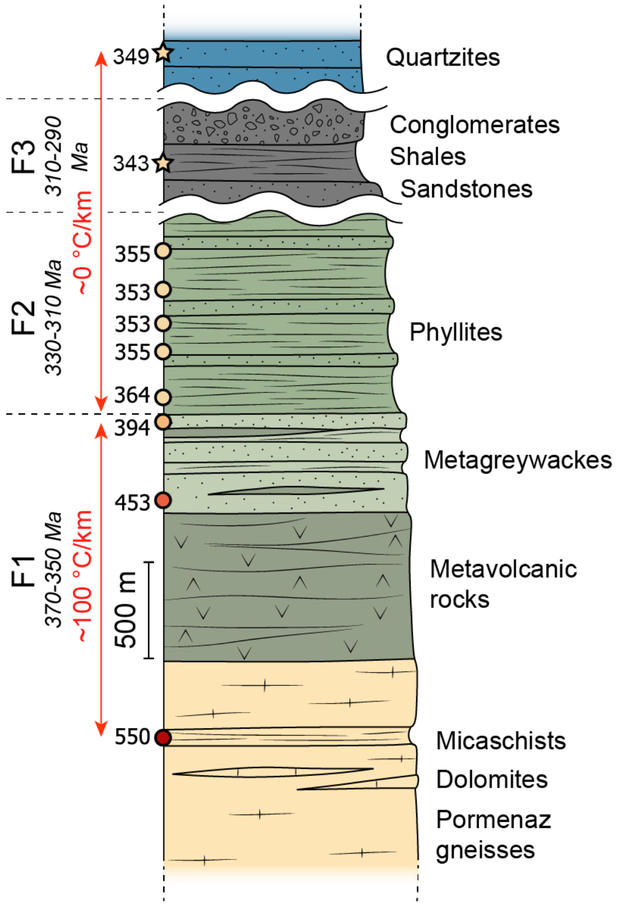

Figure 9 : LOG of the western side of the Servoz syncline showing the F1, F2 and F3 formations with representative T_{RSCM} from this study and from Boutoux et al. (2016) and associated geothermal gradients.

7.2.The T_{RSCM} recorded in the Servoz syncline

Carbonaceous Materials included in the forty-seven samples collected from the three formations presented above were analysed by Raman Spectrometry in order to estimate peak temperatures (T_{RSCM}).

In the western side of the Arve fault, T_{RSCM} measured in F1 samples vary from 400 °C to 550 °C with a high thermal gradient of ca. 115 °C/km (Fig. 6 and 7). Note that the isotherms of the high-temperature gradient are transposed by the dextral transpression deformation active between 340-305 Ma in the ECMs (Vanardois et al., in prep; Simonetti et al., 2020a) that is responsible of the folding of the basin (Dobmeier, 1996, 1998). Therefore, this anomalously high geothermal gradient is an apparent gradient that has probably increased by the posterior deformations. In the eastern side of the Arve fault, metagreywackes samples of the F1 formation display T_{RSCM} ranging from 530 °C to 420 °C (Fig. 6 and 7) with an inverse gradient of ca. 30 °C/km due to the Montées-Pélissier instrusion (Fig. 8). Our numerical models also suggest that the granite had to intrude rocks at temperatures higher than 350 °C to reach the measured T_{RSCM}

(Fig. 7), suggesting that the high geothermal gradient affecting the F1 is prior or coeval to the granite emplacement (ca. 340 Ma) (Vanardois et al., in prep).

In the ECMs, peak temperatures within the F1 have been attributed to the early Variscan nappe stacking phase (Dobmeier, 1998; Fréville et al., 2018, in review) ranging between ca. 350-340 Ma (Guillot and Ménot, 2009; Guillot et al., 2009; Fréville et al., 2018; Vanardois et al., in prep). Dobmeier (1998) estimated maximum of pressure conditions of 6.7 kbar in the western side of the Arve fault. Such conditions would be enough to produce the peak-temperature estimated in the F1 considering a common geothermal gradient of ~30 °C/km. However, in the western side of the Arve fault, considering the F1 metasedimentary rocks thickness, the high T_{RSCM} could not be recorded with a common gradient at 30 °C/km. Indeed, the T_{RSCM} could be reach only with a high thermal gradient of around 100 °C/km (Fig. 7B and 9), or a bit less if considering the impact of the transpressive deformation that probably brought isotherms closer. Our geochronological data on the Prarion volcano-sedimentary rock indicate a new age of ca. 351 Ma for the anatexis and the high thermal conditions affecting this sample, synchronously with the bimodal magmatism that is related to intracontinental extension (Dobmeier et al., 1999). Similar magmatism is described in the Belledonne and Pelvoux massifs (Fig. 1A) and is interpreted as a rifting stage between 370-350 Ma (Pin and Carme, 1987; Guillot and Ménot, 2009; Fréville et al., 2018). Moreover, high-gradients similar to the one measured in the F1, have been recorded in several other orogens, all characterized by a hot thermal anomaly linked to the rifting stage (Lahfid et al., 2019; Saspiturry et al., 2019; Vacherat et al., 2014). Therefore, we propose that this high-gradient is inherited from the extensional setting at 370-350 Ma.

From diagrams (1) and (2), it appears that the F2 and the F3 record the same maximal T_{RSCM} at ca. 350 °C. Note that the 350 °C isotherm is recorded in the post-orogenic F3 rocks from the Servoz syncline and from one sample (AR853; Table 1) of the Salvan-Dorenaz syncline (Fig. 1B), indicating a post-Variscan origin. Similar T_{RSCM} where measured in the surrounding Mesozoic rocks (Fig. 1B; Boutoux et al., 2016) emphasizing an Alpine origin for this thermal event probably related to the Alpine nappe stacking (e.g. Boutoux et al., 2016; Girault et al., 2020). However, F2 phyllites were affected by the Variscan deformations (Fig. 2A and 3I) (Bellière and Streel, 1980; Dobmeier, 1998; Vanardois et al., in prep) forming pervasive cleavage that can only develop with temperatures conditions above 250-300 °C (e.g. Elliott, 1976). Therefore, we propose that F2 phyllites were affected by the Variscan orogeny at temperatures below 350 °C that were overprinted later by the Alpine orogeny. Therefore, the three formations F1, F2 and F3 defined by geochronological constrains are also recognized by their thermal evolutions.

7.3.Pre, Syn and Post-orogenic evolution of the Servoz syncline within the Variscan belt

Based on our RSCM results, it appears that the F1 originated from a pre-orogenic rifting allowing the emplacement of bimodal magmatism (Fig. 10A). In the Belledonne and Pelvoux massifs, a pre-orogenic rifting event coeval with bimodal magmatism is also proposed (Ménot, 1988b; Ménot et al., 1988a; Pin and Carme, 1987; Guillot and Ménot, 2009; Fréville et al., 2018). However, this rifting and magmatic event is interpreted as a syn-collisional continental rifting (Ménot, 1988b; Ménot et al., 1988a), a back-arc basin opening (Pin and Carme, 1987; Guillot and Ménot, 2009; Guillot et al., 2009), or an oceanic arc coeval with continental extension (Dobmeier et al., 1999). Several recent studies on the ECMs highlighted that the collision initiated during Early-Carboniferous times (e.g. Guillot and Ménot, 2009; Guillot et al., 2009; Fréville et al., 2018; Jacob et al., 2020; Vanardois et al., in review, in prep), thus the scenario of a Devonian syn-collisional continental rifting can be excluded. The hypothesis of an oceanic arc coeval with continental extension seems reasonable within a back-arc setting. Similar Late-Devonian – Early-Carboniferous basins associated with bimodal magmatism are described in the Armorican massif (Paquette et al., 2017), French Central massif (Pin et al., 1982; Sider and Ohnenstetter, 1986; Faure et al., 1997; Pin and Paquette, 1998, 2002), Vosges massif (Pin & Carme, 1988; Pin, 1990; Skrzypek et al., 2012) and Bohemian massif (Schulmann et al., 2009; Žák et al. 2011). These volcanic basins are interpreted as back-arc basins related to the southward subduction of an oceanic domain located north of the Moldanubian domain (Lardeaux et al., 2014 and references therein). Therefore, we interpret the 370-350 Ma basins in the ECMs as pre-collisional back-arc basins opened by the subduction of an oceanic domain beneath the Moldanubian domain, and then inversed during Early-Carboniferous (Fig. 10B).

The presence of F2 confirms that the sedimentation was active after the crustal thickening event. Recent studies propose that this period was dominated by a transpressive regime with the formation of large strike-slip shear zones (Simonetti et al., 2018, 2020a; Fréville et al., in review; Vanardois et al., in prep) either in the ECMs than in the whole Variscan belt (e.g. Edel et al., 2018; Ballèvre et al., 2018) which formed intramountain pull-apart basins (e.g. Shelley and Bossière, 2001; Gumiaux et al., 2004; Faure et al., 2005). Several dextral strike-slip faults and shear zones affected the Servoz syncline, started prior the deposition of phyllites, and ended during the Late Carboniferous around ca. 305-300 Ma (Vanardois et al., in prep). Therefore, we propose that the Servoz syncline was reactivated as a syn-orogenic pull-apart basin allowing the deposition of the F2 phyllites (Fig. 10C).

Finally, the opening of late or post orogenic basins (F3) is documented in the others ECMs (e.g. Guillot and Ménot, 2009) and also in the French Central massif (Malavieille et al., 1990; Faure, 1995). The formation of these basins is attributed to a slight late-orogenic collapse of the Variscan belt (Malavieille et al., 1990; Faure, 1995; Guillot et al., 2009; Guillot and Ménot, 2009). This interpretation agrees with the presence of numerous gneissic and granitic boulders (Dobmeier and von Raumer, 1995; Lox and Bellière, 1983; Capuzzo et al., 2003) and few syn-sedimentary normal faults (Pilloud, 1991) in the Late-Carboniferous basins of the ARM, highlighting erosion of reliefs and opening of narrow intramountain basins (Capuzzo and Wetzel, 2004) suggesting a slight post-orogenic collapse (Ballèvre et al., 2018) (Fig. 10D).

Regarding the similarities with the Moldanubian massifs, we infer that the ECMs belong to the Moldanubian zone. Considering the relatively narrow and short-living back-arc basins in the ECMs (i.e. 370-350 Ma) compared to the large and long-living back-arc basin of Bohemian massif (ca. 380-345 Ma) (Lardeaux et al., 2014), and the similar narrow Late-Carboniferous basins in the ECMs and in the French Central Massif, we propose that the ECMs belong to the West-Moldanubian zone defined by Lardeaux et al. (2014).

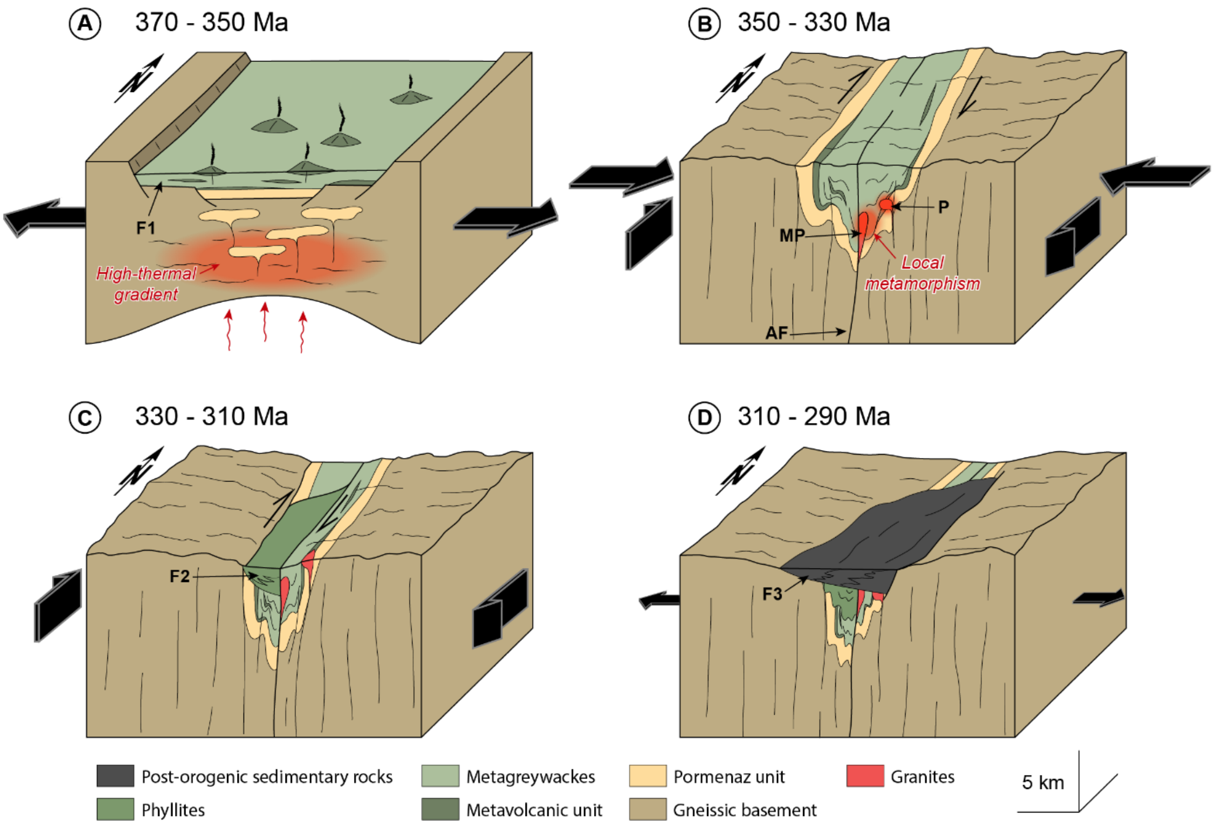

Figure 10: Geodynamic evolution of the Servoz basin. (A) 370-350 Ma: Back-arc rifting induced a crustal thinning and a high heat mantle flux leading to the partial melting of the crust, the formation of a bimodal magmatism and a high-thermal gradient in the metagreywackes forming the F1. (B) 350-330 Ma: Transpression during the continental collision inversed the basin and drained melts from the lower crust forming the Pormenaz (P) and Montées-Pélissier (MP) granites which induced local metamorphisms. (C) 330-310: The dextral transcurrence formed a pull-apart basin in the western side of the Arve fault (AF) allowing the sedimentation of the F2 phyllites while the eastern side is exhumed. (D) 310-290 Ma: Slight post-orogenic collapse forming the late basins and the F3.

8. Conclusion

Characterization of the thermal gradient and deposition ages of sediments and volcanic rocks from the Servoz syncline highlight a continuous record from pre-collision to post-orogenic evolution with three distinct sedimentary formations (F1, F2 and F3). The opening of basin initiated between 370 and 350 Ma during an early rifting stage triggered by a back-arc geodynamic setting. This extensional regime induced a high thermal gradient in the metagreywackes of the F1 formation associated with the bimodal magmatism. Then, the basin was inversed by the collision between 350 and 330 Ma during a transpressional setting forming large dextral shear zones favouring the emplacements of several plutons at ca. 340 Ma inducing local metamorphism. In the Servoz syncline, this transcurrent deformation formed a pull-apart basin in the western part of the syncline during 330-310 Ma and allowing the deposition of F2 phyllites formation. Finally, at the end of the Variscan orogeny around 310-290 Ma, a slight orogenic collapse formed a post-orogenic basin (F3 formation). Similar openings of basin are recognized in other Variscan massifs, but the Servoz syncline is the first example recording all the orogenic steps. The homogenisation of peak temperature at the scale of the Aiguilles-Rouges massifs in both Carboniferous and Mesozoic rocks suggests that the Variscan thermal imprint of the F2 and F3 formations was lately overprinted by the Alpine metamorphism.

Acknowledgements

This work was supported by the BRGM through the Référentiel Géologique de la France program (RGF program). We thank Cyprien Astoury for mineral separation and Didier Convert-Gaubier for his generous support with thin section preparation.

Supplementary material

Tables S1 and S2 presented in Annexe 5.

Chapitre 8. L’impact de l’anisotropie structurale sur la diffusion thermique dans la croûte orogénique.

Dans les chapitres précédents, nous avons montré le rôle majeur des zones de cisaillement dans l'advection de fluides et de liquides au sein de la croûte. Ces mouvements de matière chaude ont un impact majeur sur l'évolution thermique de la croûte. De plus, l'advection créée par l'épaississement ou l'amincissement au niveau de ces grands accidents tectoniques contrôle aussi l'évolution du géotherme dans la croûte. Or quelques études expérimentales ont aussi montré que les fabriquent planaires et linéaires dans les roches avaient un impact sur la conductivité thermique. Des zones de cisaillement crustale pourraient donc aussi avoir un impact majeur sur la diffusivité thermique au sein de la croûte. Nous avons donc décidé de modéliser ce phénomène pour connaitre son impact au niveau de zones de cisaillement crustales et contraindre les paramètres principaux le régissant. Ce chapitre 8 présente les résultats obtenus lors de ces modélisations.

1. Introduction

Les résultats des études structurales et microstructurales sur les socles gneissiques des massifs des Aiguilles-Rouges – Mont-blanc (Vanardois et al., in prep a) et du massif de l'Agly (Vanardois et al., 2020, in prep e) ont démontré l'importance des zones de cisaillements et des fabriques planaires sur l'advection de magmas et de fluides dans la croûte induisant des modifications du géotherme de la croûte de l'ordre d'une ou plusieurs centaines de degré (e.g. Depine et al., 2008 ; Siron et al., 2020). De telles zones de cisaillements induisent également des advections de matière majeures par amincissement ou par épaississement de la croûte (e.g. England and Thompson, 1986 ; Davy and Gillet, 1986 ; Gerbi et al., 2006). Cependant, quelques études expérimentales ont démontré que les fabriques planaires et linéaires ont aussi un impact sur la conductivité thermique (*k*) et influencent donc aussi la conductivité dans la croûte au niveau de ces anisotropies de déformation (Popov and Mandel, 1997 ; Vosteen and Schellschmidt, 2003 ; Nabelek et al., 2010). Le but de ce chapitre est d'estimer l'ordre de grandeur de l'impact de ces zones de cisaillement sur la conductivité et le régime thermique de la croûte.

Les quelques études expérimentales disponibles indiquent que les roches structurées par des fabriques planaires et linéaires peuvent avoir un tenseur de conductivité thermique perpendiculaire aux fabriques planes (*kz*) (e.g. schistosités et foliations) plus petits que leur tenseur parallèle à la linéation (*kx*) (Fig. 1a) (Vosteen and Schellschmidtn 2003). Dans ce cas, le tenseur *kz* est donc la droite normale aux plans de foliations et le tenseur *kx* est parallèle à la linéation d'étirement (Fig. 1a). Le rapport entre le tenseur kz et kx est appelé facteur d'anisotropie (a) :

$$a = \frac{kz}{kx} \tag{1}$$

Ce facteur peut varier entre 0.8 et 0.5 en fonction des lithologies et de la pétrologie dans des roches montrant une forte structure planaire et/ou linéaire (Popov and Mandel, 1997 ; Vosteen and Schellschmidt, 2003). Les données expérimentales sont pour l'instant trop peu nombreuses pour pouvoir pleinement comprendre comment évolue le facteur d'anisotropie. Cette étude est donc purement exploratoire.

Les structures planaires et linéaires influent donc sur la conductivité thermique (k) qui est l'un des paramètres contrôlant la diffusivité thermique (D) des roches avec la masse volumique (ρ) et la capacité calorifique (Cp) :

$$D = \frac{k}{\rho \times Cp} \tag{2}$$

D'autres études ont montré que la variation de la conductivité thermique (k) induite par la température (e.g. Seipold, 1998 ; Miao et al., 2014) peut avoir des implications majeures sur le géotherme de la croûte (Nabelek et al., 2010) et sur les processus de diffusion thermique liés à l'intrusion de corps magmatiques (Nabelek et al., 2012) ou de chevauchements crustaux (Whittington et al., 2009). Ce contrôle de l'évolution thermique de la croûte par les propriétés thermiques des roches (conductivité thermique, diffusivité thermique et capacité calorifique ; Fig. 1b) indique que la variation de la conductivité thermique induite par les fabriques structurales pourrait avoir un impact important sur l'évolution thermique de la croûte.

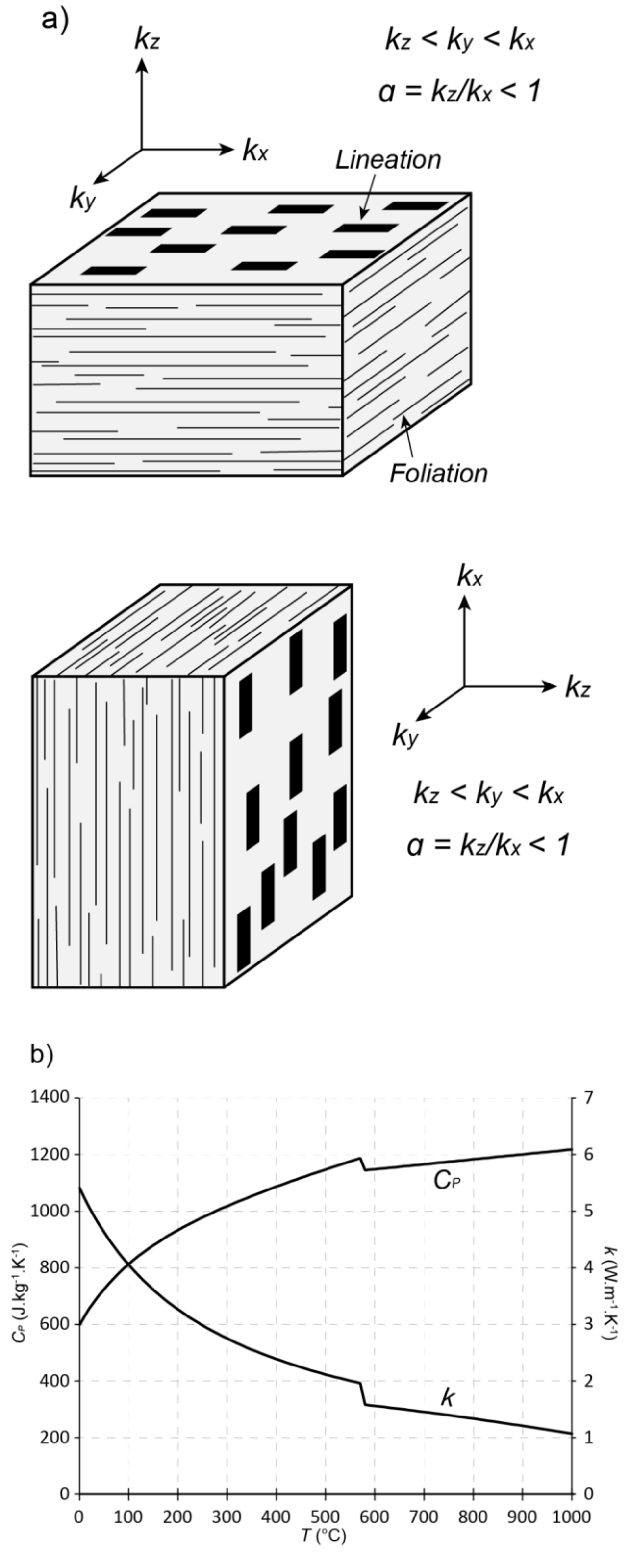

Figure 1: (a) Impacts of a horizontal and vertical structural anisotropy on the thermal conductivity (k). (b) Thermal dependences of the heat capacity (Cp) and thermal conductivity (k) modified from Whittington et al. (2009).

Dans ce chapitre, pour répondre à cette question, une modélisation numérique en 1D et 2D de structures induisant des variations des valeurs de la conductivité thermique dans une croûte initialement à l'équilibre est proposée. Dans un premier temps une étude paramétrique en 1D est présentée dans le but d'identifier les paramètres les plus influents sur l'évolution d'un géotherme d'une croûte continentale avec une anisotropie structurale (i.e. une zone de cisaillement) en utilisant et en faisant varier de larges gammes d'épaisseur de croûte, de flux mantellique, de facteur d'anisotropie, d'épaisseur d'anisotropie et de sa profondeur. Puis, cette étude paramétrique est complétée en utilisant un code numérique en 2D. Enfin, plusieurs géométries structurales observées dans la chaîne Varisque sont testées et discutées. Les résultats présentés dans ce chapitre sont préliminaires et auront besoin d'être approfondis ultérieurement.

2. Etude paramétrique en 1D

2.1.Equation de la chaleur et calcul du géotherme initial

L'évolution de la température en fonction du temps est régie par l'équation de la chaleur (e.g. Stüwe, 1995):

$$\rho.Cp.\frac{\partial T}{\partial t}=\frac{\partial}{\partial z}\left(k.\frac{\partial T}{\partial z}\right)+H \tag{3}$$

Dans laquelle *z* est la profondeur, *t* est le temps, *T* la température, ρ est la masse volumique, *Cp* est la capacité calorifique et *H* représente les apports de chaleur composés de la production de chaleur radiogénique, du shear heating et de la chaleur latente produite ou consommée par les réactions métamorphiques. Pour simplifier notre étude paramétrique et mettre en évidence l'impact des anisotropies structurales, le shear heating et la chaleur latente ne sont pas pris en compte et aucune advection ne sera implémentée. La production de chaleur radiogénique (*Hr*) peut être définie par l'équation suivante (Turcotte and Schubert, 2002) :

$$Hr(z)=Hr_0.\exp\left(\frac{-z}{z_r}\right) \tag{4}$$

Où Hr_0 est la production radiogénique en surface et z_r est une grandeur caractérisant la décroissance de la production radiogénique dans la croûte. Le géotherme initial avant l'introduction d'une anisotropie est défini par :

$$T_0(z)=\frac{Q_M}{k}z+\frac{Hr_0 z_r^2}{k}\left(1-\exp\left(\frac{-z}{z_r}\right)\right) \tag{5}$$

où Q_M est le flux mantellique. En raison de la dépendance thermique de la capacité calorifique et de la conductivité thermique (Fig. 1b), l'équilibre du géotherme n'est pas atteint par l'équation (4) qui est initialement définie par une valeur constante de la conductivité thermique et a donc besoin d'être affinée par une succession d'itérations de l'équation (2). L'évolution de la capacité calorifique en fonction de la température est définie par (Whittington et al., 2009) :

$$C_p(T < 846K) = 199.50 + 0.0857T - 5.0 \times 10^{-6}T^{-2} \tag{6}$$

$$C_p(T > 846K) = 229.32 + 0.0323T - 47.9 \times 10^{-6}T^{-2} \tag{7}$$

L'évolution de la conductivité thermique en fonction de la température est gouvernée par les équations (7) et (8) calculées à partir des équations des dépendances thermiques de la capacité calorifique et de la diffusivité thermique de Whittington et al. (2009):

$$k(T < 846K) = \rho \times 10^{-3} \times \left(31.521 + \frac{11317.35}{T} - \frac{0.0028365}{T^3} - 0.00531 \times T + \frac{3.1 \times 10^{-7}}{T^2}\right)/221.78 \tag{8}$$

$$k(T > 846K) = \rho \times 10^{-3} \times \left(167.86 - 0.007435 \times T - 4.36 \times 10^{-5} \times T^2 + \frac{6.47 \times 10^{-9}}{T^2}\right)/221.78 \tag{9}$$

La valeur de 846 K représente la transition entre le α-quartz et le β-quartz. Le géotherme initial est considéré comme étant à l'équilibre lorsque la variation maximale de température après un pas de temps (dT/dt) est inférieure à $1\text{x}10^{-6}$.

2.2.Ajout de l'anisotropie structurale et champs des valeurs testées

Dans notre modélisation en 1D, l'anisotropie structurale est définie par son épaisseur (h), sa profondeur (z_a) et son facteur d'anisotropie (a) (Fig. 2). Ce facteur d'anisotropie est défini par le rapport de la valeur de *kz* par la valeur de *kx* du tenseur de la conductivité thermique (équation 1 ; Fig. 1a). Dans le cas d'une zone de cisaillement horizontale, la valeur du tenseur vertical sera donc le plus faible, tandis qu'il sera le plus grand pour une zone de cisaillement verticale avec une linéation verticale (Fig. 1a). Dans notre modélisation en 1D, seul importe le vecteur de conductivité vertical (*kv*). Dans le cas d'une zone de cisaillement horizontale, au sein de l'anisotropie verticale ce facteur sera plus faible que dans le reste de la croûte, et il sera plus grand dans le cas d'une anisotropie structurale verticale. Dans ce modèle, l'impact de l'anisotropie structurale sera implémenté par un paramètre appelé *aniso* et calculé selon l'équation suivante :

$$aniso = \frac{kv}{k} \tag{10}$$

Où *kv* est donc la valeur du tenseur vertical de la conductivité dans l’anisotropie structurale et *k* est la valeur de la conductivité dans la croûte isotrope. Lorsque *aniso* est inférieur à 1 il représente une fabrique planaire ou linéaire horizontale (zone de cisaillement horizontale) dans laquelle le flux thermique vertical sera diminué selon *kz* = *kv*. A l’opposé, si aniso est supérieur à 1 il représente une fabrique planaire ou linéaire verticale (zone de cisaillement verticale) dans laquelle le flux thermique vertical sera augmenté avec *kx* = *kv*. Si *aniso* est égale à 1, il représente une zone isotrope. L’anisotropie structurale est implémentée dans le code en multipliant la valeur de la conductivité thermique (*k*) par le paramètre *aniso* pour chaque nœud se trouvant dans l’anisotropie structurale.

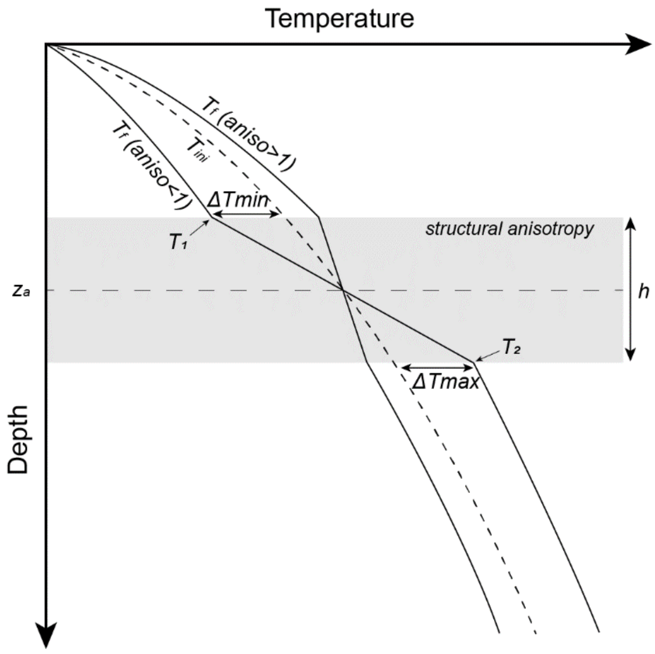

Figure 2: Scheme of the 1D numerical model. See text for explanations.

Les modélisations préliminaires indiquent que le géotherme perturbé par une anisotropie structurale n’évolue presque plus après 1 Ma. Notre étude paramétrique se basera donc sur des modélisations de 1 Ma. Les valeurs et gammes de valeurs testées dans cette étude sont compilées dans la Table 1. Les valeurs du paramètre *aniso* seront testées jusqu’à 0.5 et 2, ce qui représente les valeurs les plus extrêmes reportées dans les études expérimentales (Popov and Mandel, 1997). Pour chaque valeur de chaque paramètre, toutes les valeurs des autres paramètres ont été testées. Pour z_a, chaque valeur inférieure à l’épaisseur crustale (*Zc*) a été testée.

Table 1: Parameters used in the 1D numerical model

Symbol	***Parameter***	***Range of tested values***	***Unit***
ρ	crust density	2800	kg.m^{3}
Cp	heat capacity	equations (5) and (6)	J.kg^{-1}.K^{-1}
k	thermal conductivity	equations (7) and (8)	W.m^{-1}.K^{-1}
D	thermal diffusivity	k/(ρ.Cp)	m^{2}.s^{-1}
Q_M	Mantle heat flux	0.01 - 0.05	W.m^{-2}
Zc	crust thickness	10000 - 80000	m
aniso	anisotropy factor	0.5 - 2	
h	structural anisotropy thickness	500 - 5000	m
z_a	structural anisotropy depth	5000 - 750000	m

L'impact de la structure anisotrope est mesuré par trois paramètres : *Grad*, *ΔTmax* et *ΔTmin*. Le paramètre *Grad* est la différence de température aux extrémités de l'anisotropie structurale (T_1 et T_2) divisée par l'épaisseur de l'anisotropie (h) et est exprimé en °C/km (Fig. 2) :

$$Grad = \frac{T_1 - T_2}{h} \tag{11}$$

Les paramètres *ΔTmax* et *ΔTmin* sont respectivement la plus grande et la plus basse différence entre le géotherme initial et le géotherme final après 1 Ma divisée par la température initiale :

$$\Delta T = \frac{T_f - T_{ini}}{T_{ini}} \tag{12}$$

Ces paramètres *ΔTmax* et *ΔTmin* sont exprimés en %. Le paramètre *Grad* nous informe donc du gradient thermique dans l'anisotropie structurale et les paramètres *ΔTmax* et *ΔTmin* apportent des informations sur les écarts de température maximaux par rapport au géotherme stationnaire initial.

2.3.Résultats

Les résultats des 66000 modélisations sont compilés dans la Figure 3 sous forme de diagrammes boîtes à moustaches. Dans ces diagrammes, les valeurs absolues obtenues de ces modélisations n'ont pas vraiment de sens puisqu'elles comprennent des cas sans anisotropie (*aniso* = 1) par exemple. En revanche, leurs tendances et leurs évolutions fournissent des résultats intéressants.

Deux paramètres indépendants de la structure anisotrope, l'épaisseur de la croûte continentale (*Zc*) et le flux thermique mantellique (Q_M) (Fig. 3a et b), ont été testés dans cette étude et conditionnent le géotherme initial de la croûte, et trois paramètres intrinsèques de l'anisotropie structurale ont été investigués (son facteur d'anisotropie (*aniso*), son épaisseur (*h*) et sa profondeur (z_a)).

Sur les diagrammes concernant *Zc*, on peut observer que l'augmentation de l'épaisseur de la croûte tend à augmenter le gradient thermique (*Grad*) mais aussi à diminuer les différences de températures (ΔT). Cependant ces tendances restent faibles avec des moyennes de Grad évoluant de 14 °C/km pour une croûte de 10 km à 20 °C/km pour une croûte de 80 km. De plus, les données sont très dispersées, ce qui indiquent que l'impact de l'épaisseur de la croûte continentale n'est pas un paramètre prépondérant dans l'impact thermique d'une anisotropie structurale. Les diagrammes présentant l'évolution du paramètre Q_M (Fig. 3b) montrent une nette tendance croissante du gradient et des différences de températures avec l'augmentation du flux mantellique. Les données sont très groupées pour le gradient, ce qui indique un rôle de premier ordre dans l'impact qu'aura une anisotropie structurale sur le géotherme. Plus le flux mantellique sera élevé, plus le géotherme sera chaud et plus une anisotropie structurale telle qu'une zone de cisaillement aura un impact important sur le géotherme.

Les diagrammes du paramètre *aniso* montrent un fort contrôle du gradient thermique et des différences de températures au sein de l'anisotropie structurale (Fig. 3c). Des paramètres *aniso* inférieurs à 1 (représentant une anisotropie horizontale) auront tendance à augmenter le gradient thermique dans l'anisotropie avec des différences de températures positives élevées par rapport au géotherme standard, tandis que les paramètres *aniso* supérieurs à 1 (représentant une anisotropie verticale) vont former des gradients thermiques froids et vont favoriser les différences de températures négatives par rapport au géotherme standard. L'épaisseur de l'anisotropie structurale (*h*) n'a aucune influence sur le gradient thermique mais augmente les différences de températures aux limites de l'anisotropie (ΔT) (Fig. 3d). Enfin, la profondeur de l'anisotropie structurale (z_a) influence le gradient jusqu'à 40 km de profondeur et montre une légère tendance à diminuer les différences de températures avec l'augmentation de la profondeur (Fig. 3e).

Ces diagrammes illustrent un impact important du flux mantellique et donc plus généralement de l'état thermique de la croûte à l'état initial, et aussi du facteur d'anisotropie. Les autres paramètres ont un effet moins important.

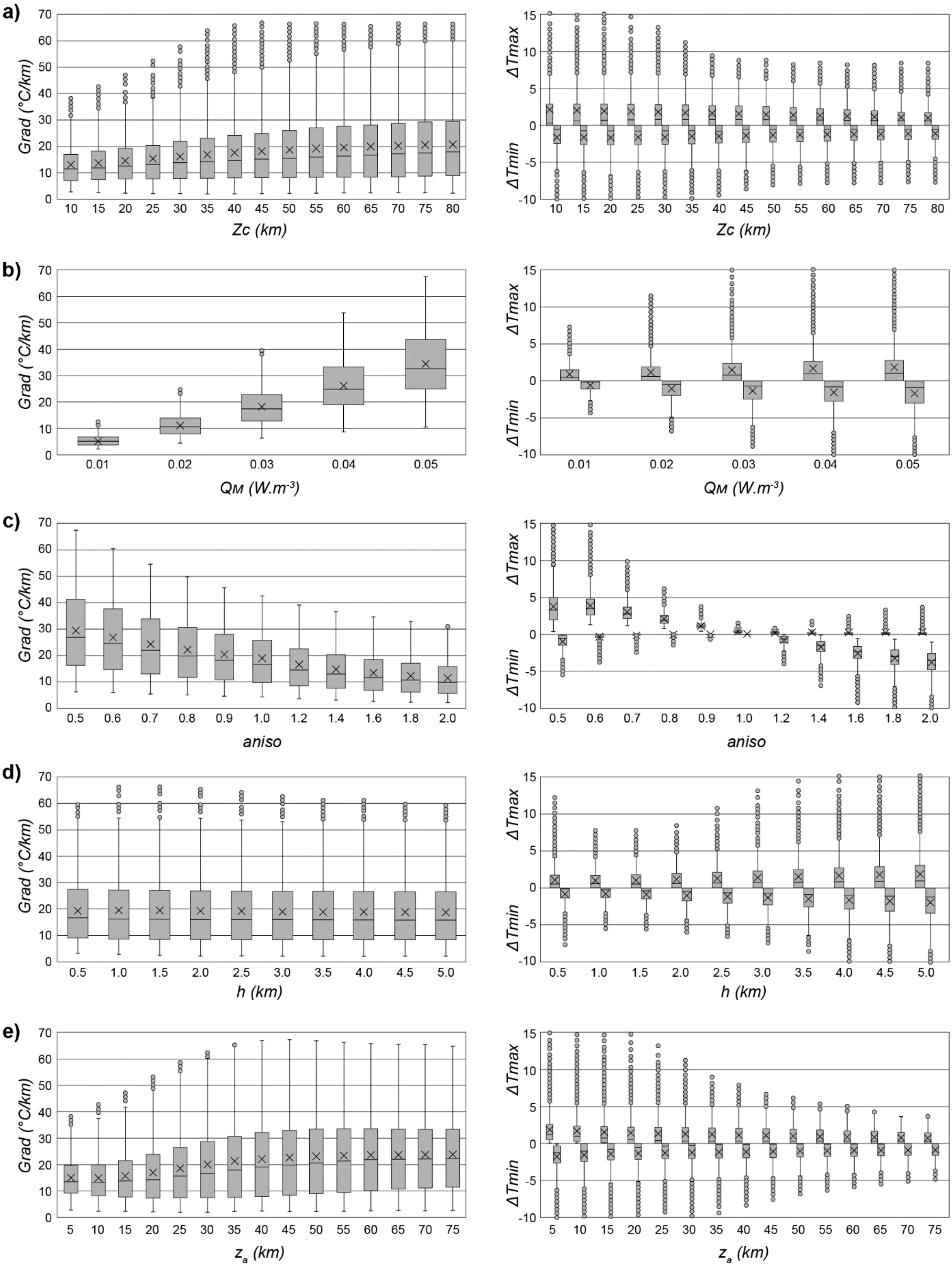

Figure 3: Results of the 1D parametric study for each parameter: a) crustal thickeness (Zc); b) heat mantle flux (Q_M); c) anisotropy parameter (aniso); d) anisotropy thickness (h); e) anisotropy depth (z_a). ΔTmax and ΔTmin are expressed in percent. In box plot, the cross represents the average and the line is the median. Circles are outliers.

3. Etude paramétrique en 2D

3.1.Paramétrage de l'étude

Pour compléter cette étude paramétrique et évaluer l'impact de structures verticales et horizontales telles que des zones de cisaillements sur le géotherme, nous avons paramétré un modèle en 2D avec une largeur (x) de 100 km et une épaisseur crustale (Zc) de 50 km (Fig. 4) en nous basant sur le code développé par Duprat-Oualid (2014) et Duprat-Oualid et al. (2013, 2015). Le flux mantellique (Q_M) a été défini à 0.03 W.m^{-3}. La profondeur de l'anisotropie structurale (z_a) a été fixée à 20 km pour une zone de cisaillement horizontale. L'anisotropie structurale a été modélisée avec une épaisseur (h) de 0.5, 2.5 et 5 km. L'impact de l'anisotropie a été modélisé avec des facteurs d'anisotropie (a) de 0.5 et 0.75. D'après Vosteen and Schellschmidt (2003), l'impact de structures linéaires est beaucoup plus faible que celui de structures planaires et donc pour simplifier le code, les tenseurs kx et ky seront considérés comme égaux (Fig. 4). Le facteur d'anisotropie (a) est calculé par ces équations :

$$\begin{cases} \dfrac{k_z}{k_x} = a \\ k_z = k \times \left(1 - \dfrac{2}{3}p\right) \\ k_x = k \times \left(1 + \dfrac{1}{3}p\right) \end{cases} \tag{13}$$

Où p est un paramètre sans dimension, utilisé dans le code du modèle. Dans les modèles avec une zone de cisaillement horizontale, le vecteur vertical de la conductivité thermique dans la zone de cisaillement kz est inférieur à celui du reste de la croûte et les vecteurs horizontaux kx et ky sont au contraire plus importants dans la zone de cisaillement que dans le reste de la croûte (Fig. 4). Dans les modèles avec une zone de cisaillement verticale, c'est le tenseur horizontal perpendiculaire à la zone de cisaillement kz qui est fortement diminué tandis que les deux autres tenseurs kx et ky sont augmentés (Fig. 4).

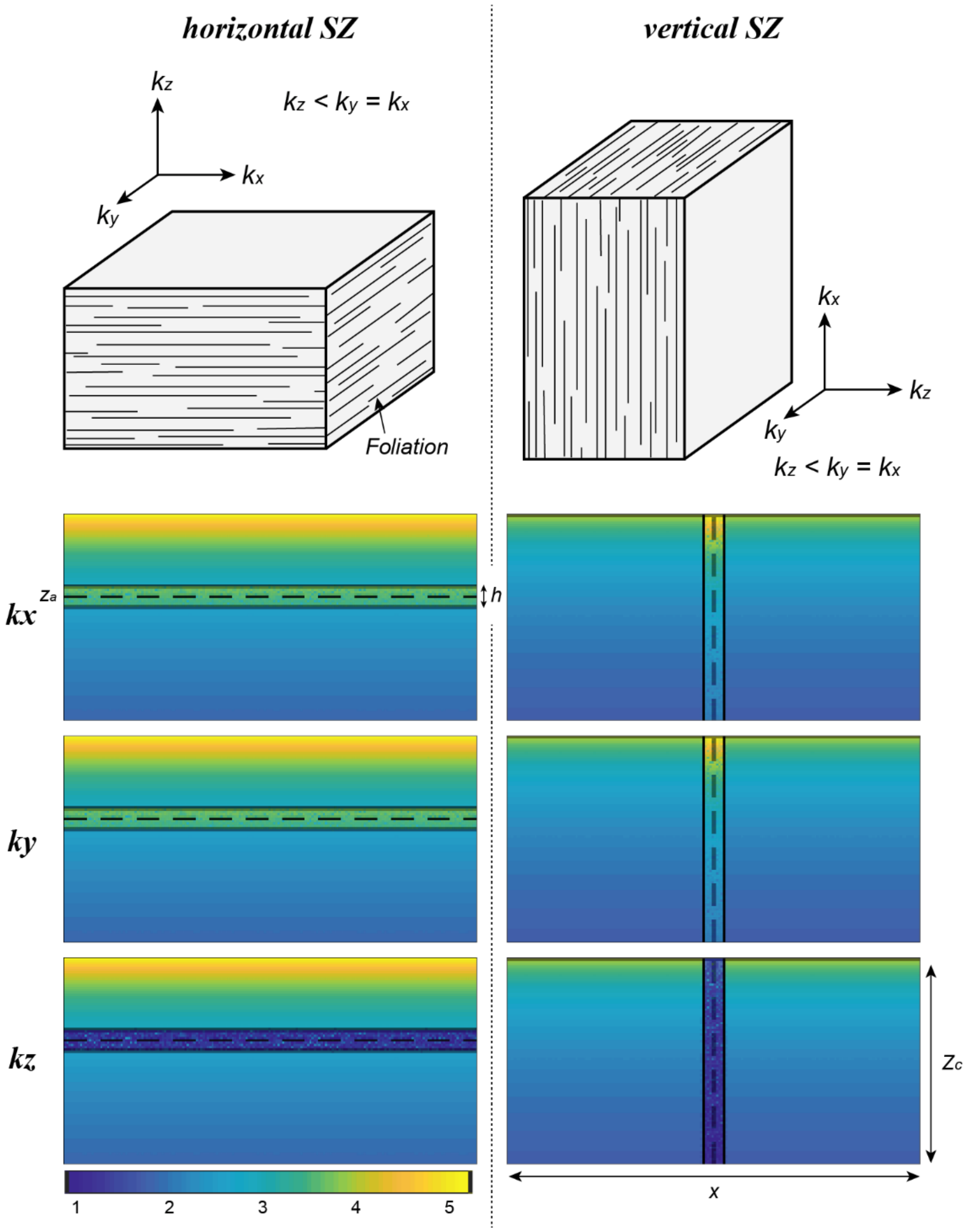

Figure 4 : Impact of the structural anisotropy right on the conductivity tensors after the formation of the shear zone in function of the orientation of the shear zone. Scale from 1 to 5 represent the value of the conductivity tensors.

Table 2: Parameters used in the 2D numerical model

Symbol	***Parameter***	***Range of tested values***	***Unit***
ρ	crust density	2800	$kg.m^3$
Cp	heat capacity	equations (5) and (6)	$J.kg^{-1}.K^{-1}$
k	thermal conductivity	equations (7) and (8)	$W.m^{-1}.K^{-1}$
D	thermal diffusivity	k/(ρ.Cp)	$m^2.s^{-1}$
Q_M	Mantle heat flux	0.03	$W.m^{-2}$
Zc	crust thickness	500000	m
a	anisotropy factor	0.5 - 0.75	
h	structural anisotropy thickness	500 -2500 - 5000	m
z_a	structural anisotropy depth	20000	m

Les modélisations sont effectuées sur 1 Ma. Les résultats des modélisations sont présentés avec la différence relative en pourcentage et la différence absolue en degré Celsius calculées pour chaque nœud selon les équations :

$$\Delta T_{relatif}\,(\%) = 100 \times \left(\frac{T_{finale} - T_{initiale}}{T_{initiale}}\right) \tag{14}$$

$$\Delta T_{absolue}\,(°C) = T_{finale} - T_{initiale} \tag{15}$$

3.2.Résultats

Nos modélisations montrent qu'une zone de cisaillement horizontale a pour effet de réchauffer les niveaux profonds et de refroidir les niveaux supérieurs de la croûte (Fig. 5). Quant aux zones de cisaillement verticales, elles auront tendances à refroidir localement la croûte (Fig. 6). Ces résultats sont cohérents avec les modélisations en 1D qui montrent aussi une tendance à refroidir avec des anisotropies verticales et à l'inverse à réchauffer avec des anisotropies horizontales (Fig. 3c). Dans la suite de ce chapitre, nous nous intéresserons à l'impact des différents paramètres sur l'évolution de la température dans une croûte avec une épaisseur initiale de 50 km et une profondeur d'anisotropie (zone de cisaillement) horizontale située à 20 km de profondeur.

3.2.1. Les caractéristiques de la zone de cisaillement

Dans un premier temps, les deux paramètres testés ont été le facteur d'anisotropie (a) et l'épaisseur de la zone de cisaillement (h). Les résultats des modélisations avec une zone de cisaillement horizontale et verticale sont représentés dans les Figures 5 et 6, respectivement.

Ces modélisations confirment que le facteur d’anisotropie (*a*) est l’un des paramètres prépondérants concernant l’impact d’une zone de cisaillement sur la diffusivité thermique dans la croûte. Que ce soit dans le cas d’une zone de cisaillement horizontale ou verticale, la diminution du facteur d’anisotropie de 0.75 à 0.5 double les effets thermiques de la zone de cisaillement (Fig. 5 et 6).

D’après ces modélisations, il apparaît aussi que l’épaisseur des zones de cisaillement (*h*) a aussi un impact proportionnel sur les différences de températures générées par les zones de cisaillements (Fig. 5 et 6). Cet impact est néanmoins moins important que celui du facteur d’anisotropie, une zone de cisaillement avec une épaisseur de 2.5 km et un facteur de 0.75 n’est que légèrement plus impactante qu’une zone de cisaillement de 500 mètres avec un facteur de 0.5 (Fig. 5 et 6).

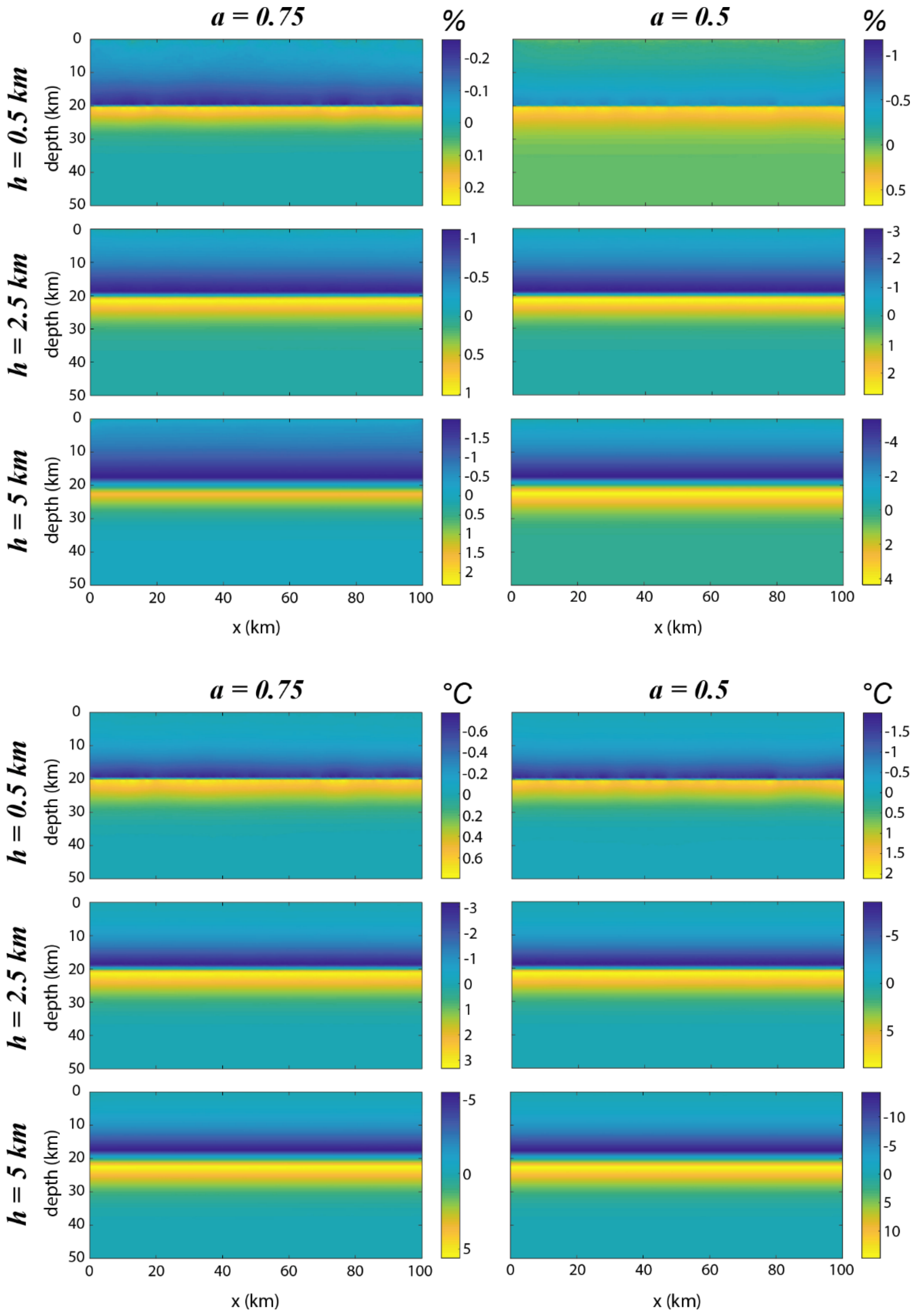

Figure 5: Diagrams showing the relative (%) and absolute (°C) difference between the steady-state geotherm and a geotherm affected by a horizontal shear zone with an anisotropic factor (a) of 0.5 and 0.75, and thickness (h) of 0.5, 2.5 and 5 km. $Q_M = 0.03$ W.m^{-3}; $z_a = 20$ km; $t = 1$ Ma.

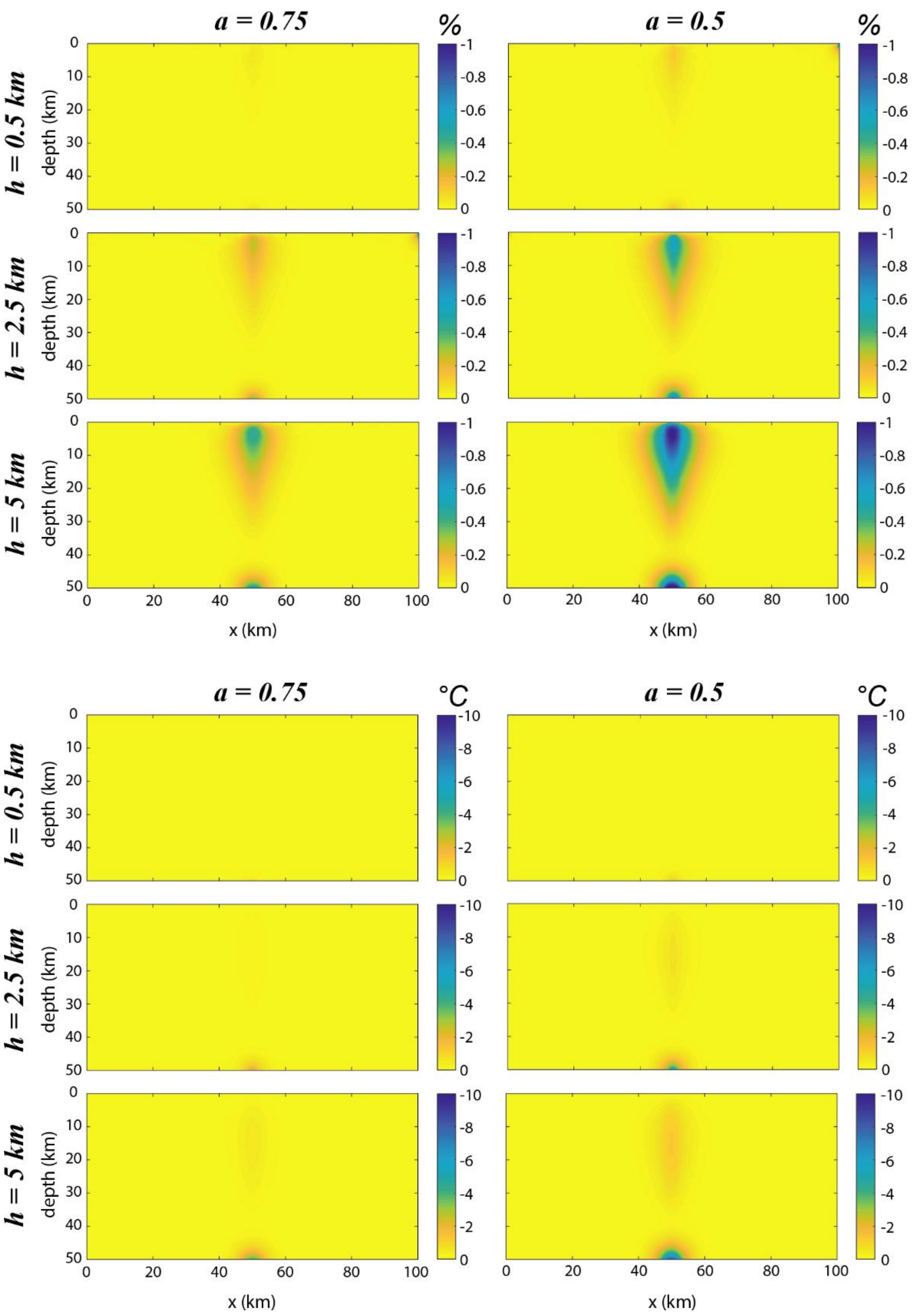

Figure 6: Diagrams showing the relative (%) and absolute (°C) difference between the steady-state geotherm and a geotherm affected by a vertical shear zone with an anisotropic factor (a) of 0.5 and 0.75, and thickness (h) of 0.5, 2.5 and 5 km. $Q_M = 0.03$ W.m^{-3}; $z_a = 20$ km ; t = 1 Ma.

Dans un second temps, deux profondeurs de zones de cisaillement (z_a = 20 km et 40 km) ont été testées avec des paramètres identiques (Fig. 7). L'impact relatif de la zone de cisaillement à 40 km de profondeur est légèrement inférieur à celui de la zone de cisaillement à 20 km. En valeurs absolues, l'impact est quasi similaire dans les deux cas et au maximum de l'ordre de 20°C d'un bord à l'autre de l'anisotropie planaire. Ces diagrammes indiquent donc que la profondeur d'une zone de cisaillement change peu son impact absolu sur le géotherme, mais que cet impact devient moins important comparé aux températures régnant à fortes profondeurs. En d'autres termes, la valeur de la température au sein d'un géotherme influe peu l'impact de l'anisotropie structurale. En revanche le gradient thermique de ce géotherme influencera cet impact (Q_M).

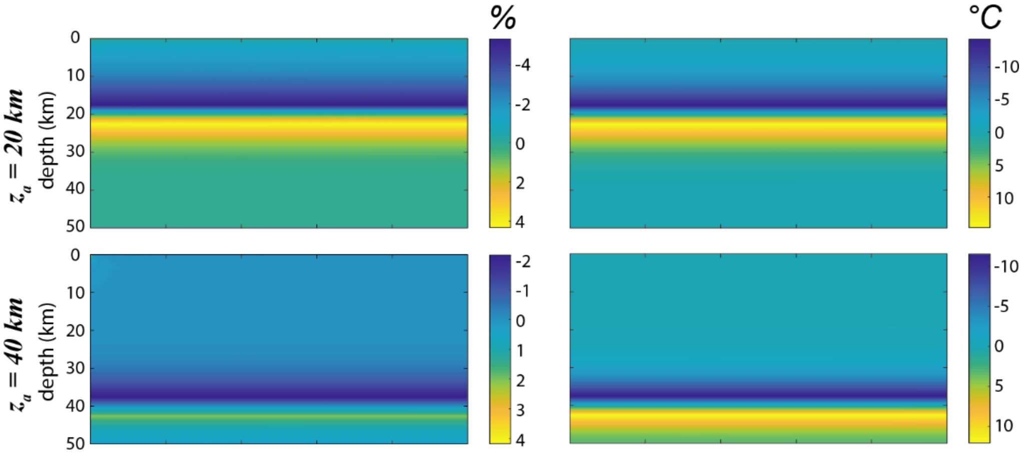

Figure 7: Diagrams showing the relative (%) and absolute (°C) difference between the steady-state geotherm and a geotherm affected by a horizontal shear zone with a depth (z_a) of 20 km and 40 km. $Q_M = 0.03$ W.m^{-3}; $a = 0.5$; $h = 5$ km; $t = 1$ Ma.

3.2.2. *Impact du géotherme initial*

Les résultats de l'étude en 1D ont montré que l'état thermique de la croûte à l'état initial influençait l'impact d'une anisotropie structurale dans une croûte orogénique (Fig. 3a et b), en particulier en ce qui concerne les valeurs du flux mantellique. Les impacts de l'épaisseur de la croûte et du flux mantellique ont donc été testés.

Dans un premier temps nous avons fait varier l'épaisseur de la croûte (*Zc*) avec des valeurs de 30 km, 50 km et 70 km (Fig. 8). Comme pour l'étude en 1D, les résultats en 2D montrent que l'épaisseur de la croûte n'influence pas ou très peu l'impact thermique d'une zone de cisaillement. Une légère augmentation des valeurs absolues peut être notée pour les zones de cisaillement horizontales, pouvant au maximum atteindre une variation de 40 °C d'un bord à l'autre de l'anisotropie planaire pour une épaisseur de croûte de 70Km.

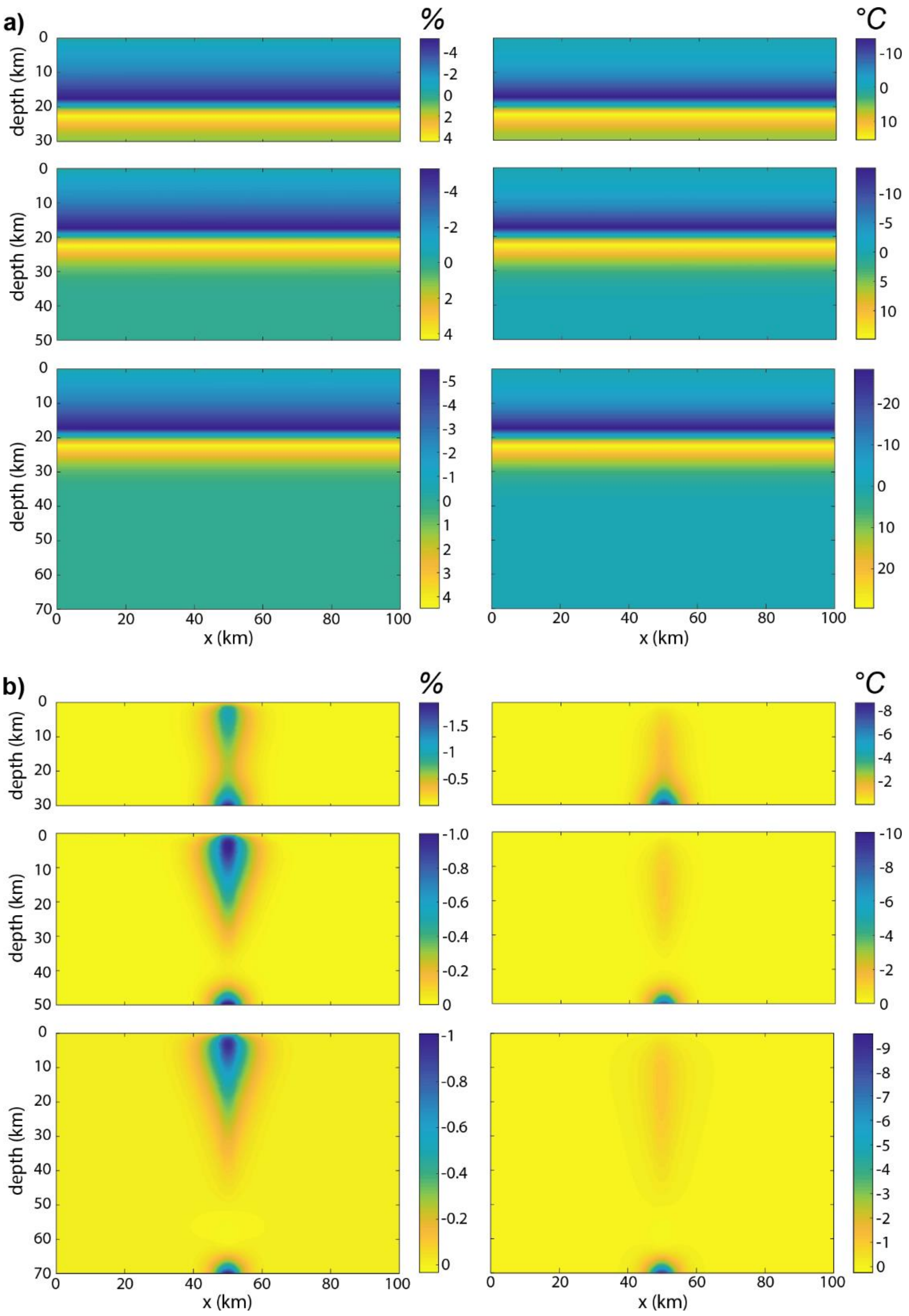

Figure 8: Diagrams illustrating the impact of the thickness of the crust (Zc) on geotherm disturbed by a) horizontal (a = 0.5) and b) vertical (a = 2) shear zones with values of 30, 50 and 70 km. Q_M = 0.03 W.m^{-3}. h = 5 km; z_a = 20 km ; t = 1Ma.

Ensuite, la même zone de cisaillement a été modélisée dans une croûte de 50 km avec des valeurs de flux mantellique (Q_M) de 0.01, 0.03 et 0.05 W.m^{-3}. L'impact de ce flux n'est pas ou peu visible sur les diagrammes montrant la différence de température relative à l'état initial

(Fig. 9), mais elle est en revanche bien marquée par les différences de température absolues. L'augmentation du flux mantellique va donc accentuer la différence de température de part et d'autre d'une zone de cisaillement horizontale de 15 °C à 40 °C pour des flux de 0.01 et 0.05 W.m^{-3}, respectivement (Fig. 9a).

Pour les zones de cisaillement verticales, l'impact de l'anisotropie est visible en base de croûte et dans la croûte supérieure (Fig. 6 et 9b). La variation du flux mantellique fait varier l'impact de la zone de cisaillement en base de croûte mais n'a finalement que peu d'influence sur la température de la croûte supérieure qui est probablement contrôlée par la température fixe en surface (Fig. 9b). La diminution de température en base de croûte atteint au maximum -15 °C pour un flux de 0.05 W.m^{-3} tandis qu'elle n'atteint que 2 °C pour un flux de 0.01 W.m^{-3}.

Ces résultats indiquent donc que l'impact d'une zone de cisaillement sur l'évolution thermique de la croûte dépend en partie de l'état thermique initial de la croûte. Une croûte initialement chaude sera donc plus influencée par une anisotropie structurale qu'une croûte initialement froide.

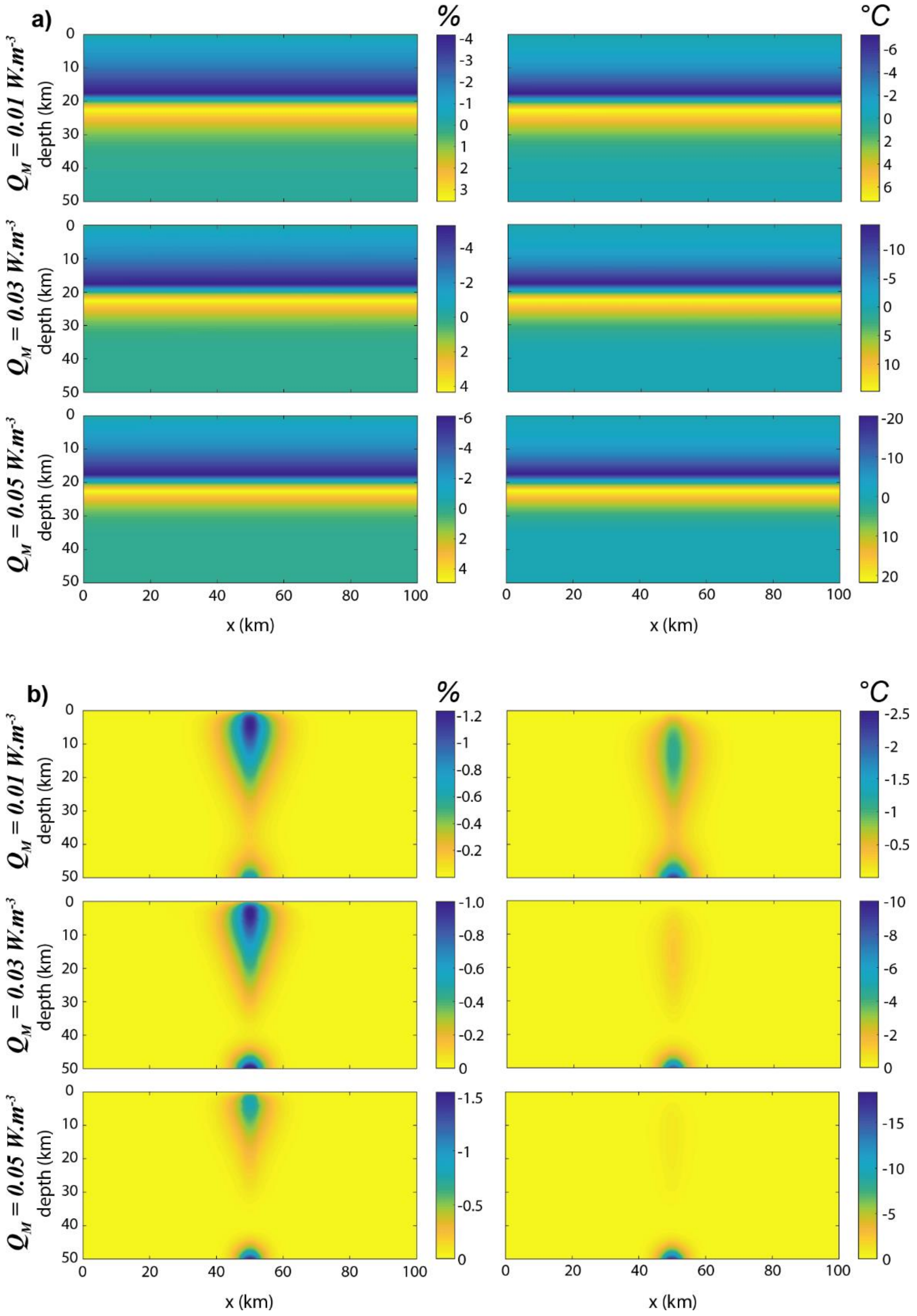

Figure 9: Diagrams illustrating the impact of the heat mantle flux (Q_M) on geotherm disturbed by a) horizontal (a = 0.5) and b) vertical (a = 2) shear zones with values of 0.01, 0.03 and 0.05 W.m^{-3}. h = 5 km; z_a = 20 km; t = 1 Ma.

3.2.3. Evolution sur le long terme

Toutes les modélisations précédentes ont été effectuées sur une durée d'un million d'année. Or, même si l'on envisage une activité d'une zone de cisaillement courte dans le temps, son anisotropie structurale acquise lors de sa formation continue d'influencer la diffusion thermique après la fin de la déformation. Nous avons donc effectué des modélisations sur 10 millions d'année (Fig. 10). La comparaison entre les résultats au bout d'un million et de 10 millions d'année montrent une légère augmentation des différences de température générées par les zones de cisaillements, mais démontrent surtout une augmentation de la zone d'influence de ces zones de cisaillements (Fig. 10).

Dans les zones de cisaillements horizontales, au bout d'un million d'année l'épaisseur de la croûte influencée est restreinte aux abords de la zone de cisaillement (Fig. 5, 9a et 10a). Pour un cisaillement de 5 km d'épaisseur, la zone influencée au bout d'un million d'année est d'environ 20 km d'épaisseur. En revanche, après 10 millions d'année, l'ensemble de la croûte sous la zone de cisaillement est réchauffé tandis que la croûte supérieure est refroidie (Fig. 10a). Dans le cas des zones de cisaillements verticales, l'influence d'un cisaillement de 5 km d'épaisseur affecte une largeur de la croûte d'environ 20 km, tandis qu'elle atteint environ 40 km au bout de 10 millions d'année (Fig. 10b).

Ces modélisations 2D montrent donc qu'au court du temps, l'impact d'une zone de cisaillement sur l'évolution thermique de la croûte va surtout se propager et influencer un plus grand domaine de la croûte. Néanmoins, les variations de températures sont de l'ordre de la vingtaine de degré, même après 10 Ma.

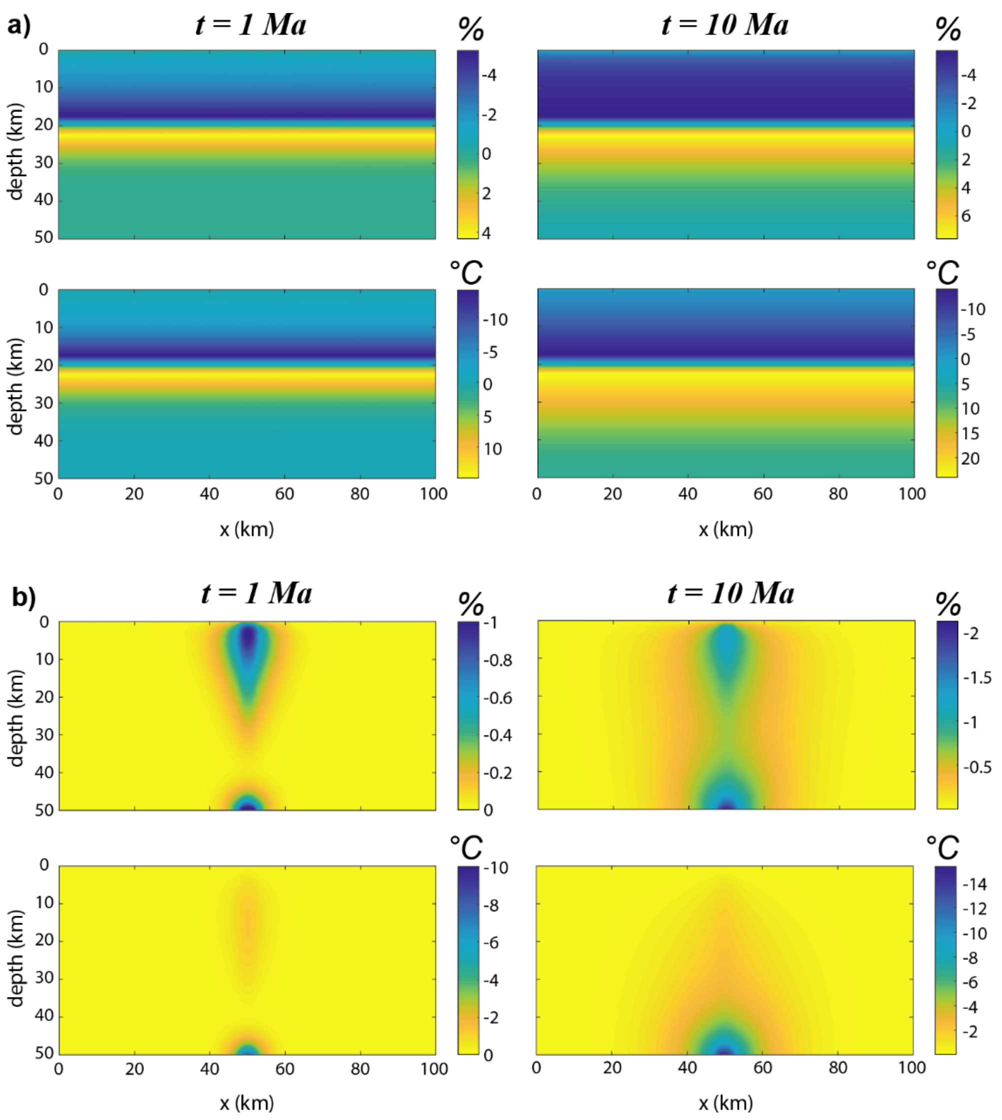

Figure 10: Comparison between geotherms disturbed by a) horizontal (a = 0.5) and b) vertical (a = 2) shear zones after 1 Ma and 10 Ma. Q_M = 0.03 W.m^{-3}; h = 5 km; z_a = 20 km.

3.2.4. Conclusions de l'étude paramétrique en 2D

Les résultats de l'étude en 2D sont majoritairement en accord avec l'étude paramétrique en 1D. Concernant les paramètres intrinsèques de la zone de cisaillement, la profondeur de la zone de cisaillement (z_a) influence très peu l'impact d'une zone de cisaillement (Fig. 7). Au contraire, son épaisseur (h) et surtout son facteur d'anisotropie (a) sont des paramètres exerçant une influence majeure sur cet impact (Fig. 5 et 6). Comme indiqué par l'étude paramétrique en 1D, le géotherme initial conditionne l'impact thermique sur une zone de cisaillement, en particulier le flux mantellique (Q_M) car plus le géotherme initial sera chaud plus l'impact de la zone de cisaillement sera important (Fig. 9). En revanche l'épaisseur de la croûte n'a pas d'effet direct sur cet impact (Fig. 8). Enfin le facteur temps influence peu les valeurs maximales générées par l'anisotropie structurale mais contrôle le volume de la croûte qui sera affecté (Fig. 10).

En conclusion, il apparaît que la connaissance de l'épaisseur et du facteur d'anisotropie d'une zone de cisaillement ainsi que le flux mantellique sont les paramètres principaux à prendre en compte dans la modélisation de l'impact sur la diffusivité thermique d'une anisotropie structurale, tandis que l'épaisseur de la croûte et la profondeur de cette anisotropie importent peu. Cependant il faut également retenir que les variations de températures sont de l'ordre de la dizaine de degré au sein des anisotropies et donc d'un facteur 10 par rapport aux valeurs des températures enregistrées au niveau du gradient géothermique considéré. Les autres phénomènes de modification de l'allure des gradients géothermiques (advection de matière, de fluides, de magmas…) qui induisent des modifications de l'ordre de la centaine de degrés en quelques millions d'années semblent donc plus influents sur le régime thermique de la croûte que la présence d'anisotropies horizontales ou verticales plurikilométriques au sein de la croûte.

4. Modélisation de structures naturelles

Dans cette section, nous présentons trois modélisations de structures naturelles observées dans les massifs Varisques. Le but est d'illustrer si des configurations structurales naturelles peuvent avoir un impact non négligeable sur la diffusion de la température dans une croûte initialement à l'équilibre. Nos modélisations ne permettent pas de discuter directement de l'évolution thermique dans ces massifs puisque certains d'entre eux sont régis par un *melt-enhanced geotherm* (Depine et al., 2008) tamponnant les températures au solidus à environ 720°C (Rabin et al., 2015 ; Trap et al., 2017 ; Siron et al., 2020) dans la croûte moyenne et inférieure. Les facteurs d'anisotropie ont été fixés à 0.5, le flux mantellique n'est pas connu, mais les modélisations avec un flux mantellique de 0.03 $W.m^{-3}$ dans une croûte de 50 km d'épaisseur indiquent des températures d'environ 700 °C en base de croûte, ce qui est cohérent avec les températures généralement mesurées. L'épaisseur des zones de cisaillement varie en fonction des massifs étudiés.

4.1. Une large zone de cisaillement ou un réseau anastomosé vertical (massifs des Aiguilles-Rouges – Mont-Blanc)

Comme présentées dans le chapitre 5, les structures des massifs des Aiguilles-Rouges et du Mont-Blanc sont essentiellement verticales avec de nombreuses zones de cisaillement (Fig.

11a). Cette structuration verticale forme une partie de l'Eastern Variscan Shear Zone qui est une zone de cisaillement crustale. Nous avons donc modélisé cette structure avec une anomalie structurale verticale large de 25 km (Fig. 11b). Trois zones de cisaillements proches de 5 km de largeur ont été modélisées pour représenter les zones de cisaillement du Lac Cornu, de Emosson-Bérarde et de Montenvers formant un réseau anastomosé cf. Chapitre 5).

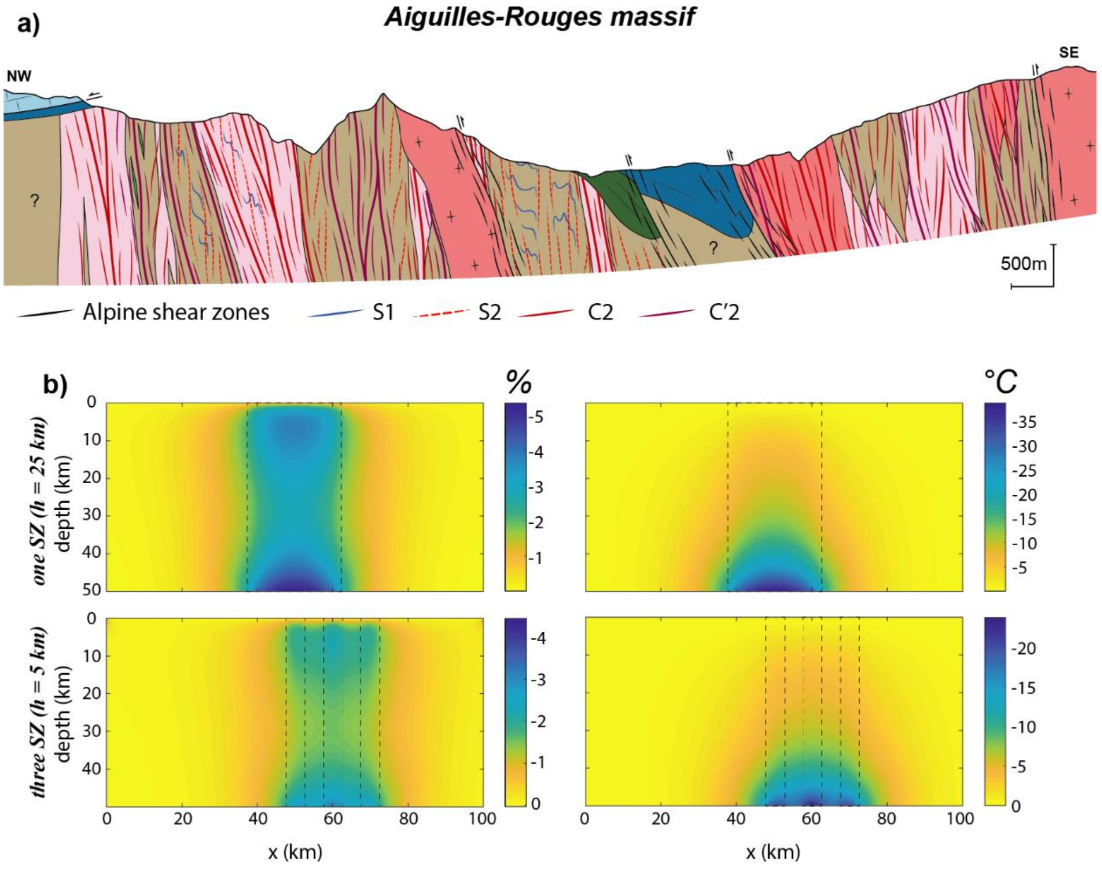

Figure 11: Modelling of a thick vertical shear zone and of several vertical shear zones corresponding to an anastomosed network, both representing the EVSZ in the Aiguilles-Rouges – Mont-Blanc massifs. (a) Cross-section through the massifs highlighting the vertical structures, from Vanardois et al. (in prep). (b) Diagrams illustrating the impact of a 25-km-thick shear zones and an anastomosed network of three 5-km-thick shear zones. $Q_M = 0.03$ W.m^{-3}; a = 0.5; h = 25 and 5 km; t = 10 Ma.

Les résultats indiquent qu'après 10 Ma, une large zone de cisaillement pourrait faire diminuer la température de ~5% en base croûte, soit environ 35°C pour une base de croûte à 700 °C, et aurait un impact assez limité dans la croûte supérieure. Les résultats pour le réseau anastomosé de zone de cisaillement ont un impact un peu plus faible que celui d'une large zone de cisaillement et pourraient faire diminuer la température en base de croûte de ~4%, soit 20 °C pour une base de croûte à 700 °C.

Ces résultats questionnent finalement sur la signification et les valeurs du facteur d'anisotropie (*a*) en fonction de la déformation. Dans cet exemple, les foliations verticales entre les zones de cisaillements ont-elles aussi un facteur d'anisotropie qui doit être pris en compte ? Si oui, le modèle le plus correct est celui d'une large zone de cisaillement de 25 km, sinon ce serait celui d'un réseau anastomosé de trois anisotropies verticales. Cependant, l'impact de ces deux modèles reste inférieur à 40 °C.

4.2.Une large zone de cisaillement horizontale (massif de l'Agly)

Notre analyse structurale du massif de l'Agly met en lumière une structuration essentiellement horizontale, mis à part au niveau de la Tournefort Diorite Zone (cf. Chapitre 7) (Fig. 12a). Nous avons donc modélisé une anisotropie structurale horizontale de 10 km d'épaisseur. L'épaisseur de la croûte (*Zc*) est assez mal connue dans le massif de l'Agly, mais ce paramètre a très peu d'influence sur l'impact de l'anisotropie structurale (Fig. 8). La profondeur de la zone de cisaillement a été fixée à 20 km, ce qui est cohérent avec les estimations structurales et thermobarométriques (Siron et al.,2020).

Les résultats indiquent qu'après 10 Ma une zone de cisaillement horizontale pourrait augmenter la température à sa base de ~10% et la diminuer de ~10% à son sommet, soit une augmentation d'environ 40 °C et une diminution de 20 °C, respectivement (Fig. 12b). Dans ce modèle, presque toute la croûte supérieure est refroidie tandis que la majorité de la croûte inférieure est réchauffée.

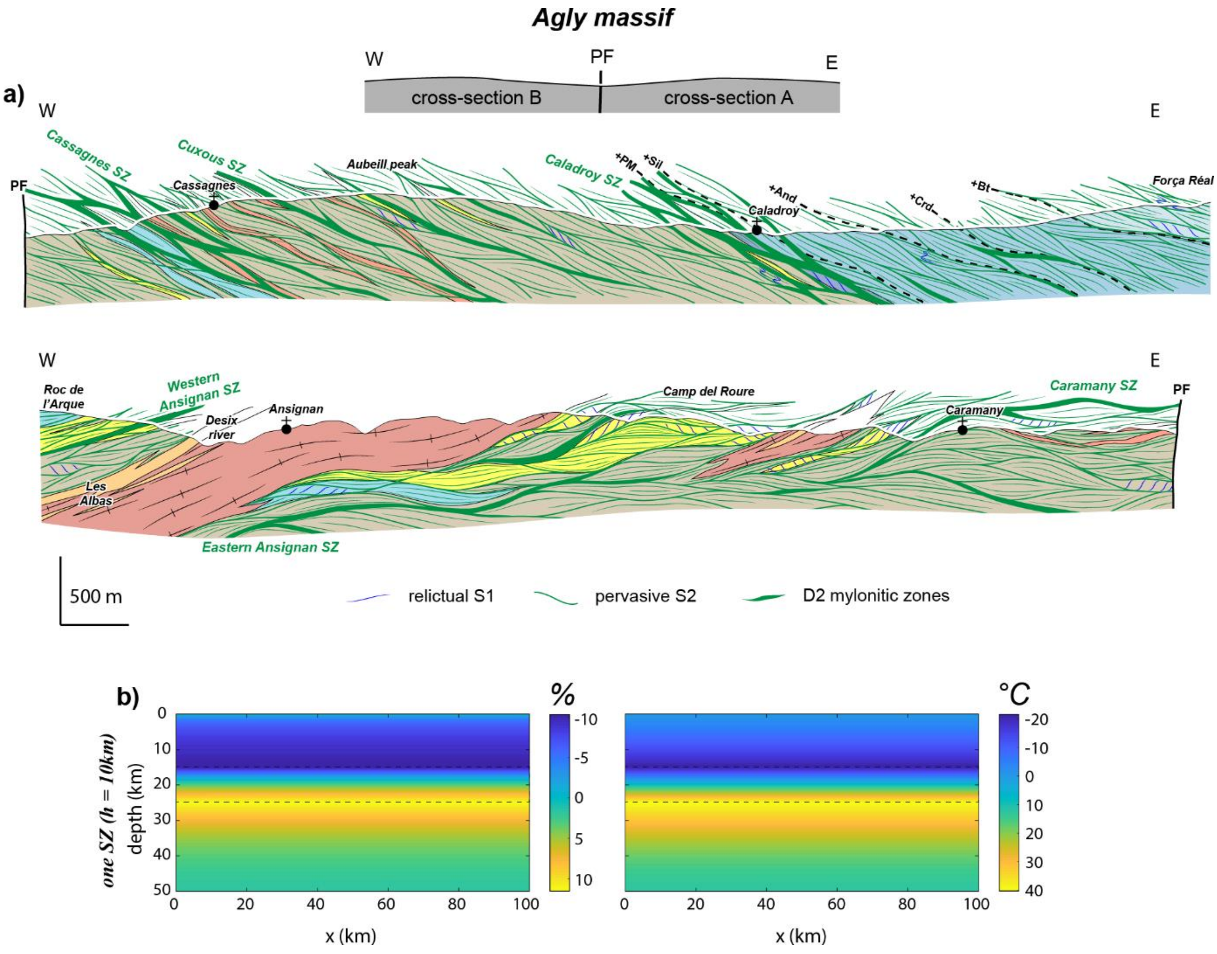

Figure 12: Modelling of a thick horizontal shear zone representing the horizontal structures in the Agly massif. (a) Cross-section through the Agly massif highlighting the horizontal structures, from Vanardois et al. (2020). (b) Diagrams illustrating the impact of a 10-km-thick horizontal shear zones. $Q_M = 0.03$ *W.m*$^{-3}$*; a = 0.5; h = 10 km;* z_a *= 20 km; t = 10 Ma.*

4.3.Zones de cisaillement horizontales et verticales synchrones (Montagne Noire)

En Montagne Noire, des études ont mis en évidence l'activité synchrone d'une zone de cisaillement horizontale avec un cisaillement vertical dans la croûte sous-jacente (Rabin et al., 2015 ; Whitney et al., 2015 ; Trap et al., 2017) (Fig. 13a). Pour simplifier les interprétations, nous avons fixé des épaisseurs de zones de cisaillements identiques (h = 5 km). Nos résultats indiquent que l'impact d'une zone de cisaillement verticale est négligeable comparé à celui d'un cisaillement horizontal avec des facteurs intrinsèques similaires (Fig. 13b).

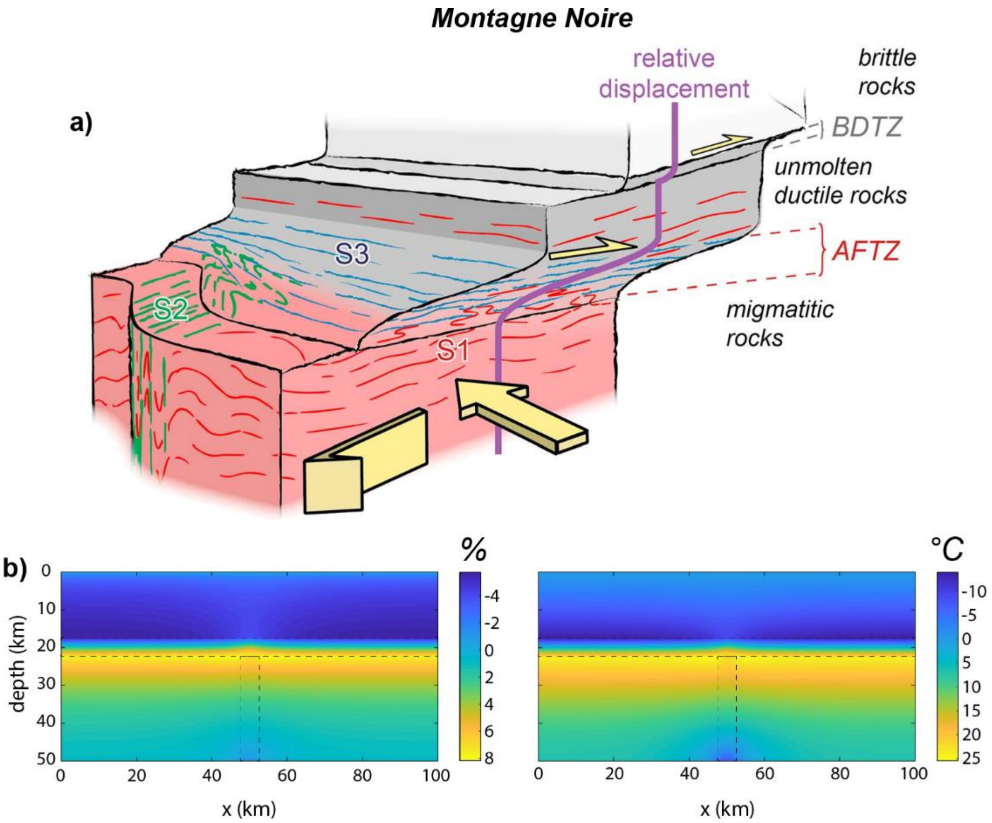

Figure 13: Modelling of a horizontal shear zone associated to a transcurrent shear zone in the lower crust representing the Montagne Noire. (a) 3D bloc diagram highlighting the horizontal and vertical structures, from Rabin et al. (2015). (b) Diagrams illustrating the impact of the association of a vertical and a horizontal 5-km-thick shear zones. $Q_M = 0.03$ W.m^{-3}; a = 0.5; h = 5 km; z_a = 20 km; t = 10 Ma.

5. Les anisotropies structurales ont-elles un impact négligeable ?

Nos modélisations indiquent que les anisotropies structurales ont un impact sur l'évolution thermique de la croûte, mais cet impact est-il assez conséquent pour devoir être pris en compte dans les modèles géodynamiques ?

En premier lieu, nos résultats montrent qu'une zone de cisaillement aura un impact de quelques dizaines de degré au maximum en ne considérant que la diffusion thermique, et ce même avec des facteurs d'anisotropie très important (*a* = 0.5). Même avec un facteur de 0.75, ce qui est supérieur pour la plupart des lithologies testées par Vosteen and Schellschmidt (2003), une zone de cisaillement horizontale de 5 km aura un impact d'une dizaine de degrés au bout d'un million d'année (Fig. 5), et un cisaillement vertical aura un impact inférieur à 5°C et seulement à la base de la croûte (Fig. 6). Dans les cas d'une zone de cisaillement kilométrique avec un facteur d'anisotropie de 0.5, l'influence d'une zone de cisaillement horizontale peut alors être de l'ordre de 40 °C sur le géotherme après 1 Ma, qu'il soit initialement froid ou chaud (Fig. 9). Une zone de cisaillement verticale aura un impact beaucoup plus restreint (Fig. 9).

Dans la croûte inférieure, une large zone de cisaillement ou un large réseau anastomosé vertical peut induire une diminution de la température d'une trentaine de degrés au maximum dans une croûte à 700 °C (Fig. 11). Dans ces conditions, une différence de 30 °C pourrait influencer la nature des réactions de fusion partielle de type fluide-absent impliquées dans l'anatexie crustale, ou pourrait contrebalancer le shear heating local induit par le cisaillement.

Les zones de cisaillement horizontales ont un impact plus important que celles verticales. L'impact d'une zone de cisaillement horizontale de 5 km avec un facteur d'anisotropie de 0.5 induira une différence de température d'environ 40 °C au niveau du cisaillement (Fig. 8a), réchauffera la croûte inférieure et refroidira la croûte supérieure. Néanmoins, ces impacts et influences restent faibles en comparaison avec les apports de chaleurs par l'advection causé par l'empilement de nappes ou bien l'advection de fluides chauds ou de magmas (e.g. Nabelek et al., 2010, 2012 ; Riel et al., 2016) ou bien par rapport au tamponnage de la température causé par la chaleur au point eutectique (e.g. Depine et al., 2008). Nos résultats suggèrent donc que l'impact des anisotropies planaires n'est pas un facteur de premier ordre dans l'évolution du géotherme mais nécessite des études plus approfondies pour caractériser son effet sur le *shear heating* par exemple.

6. Limites et perspectives

Ces résultats restent préliminaires et ont besoin d'être complétés par des modélisations complémentaires et plus abouties. Une première difficulté est d'obtenir des géothermes totalement stabilisés dans le temps. La thermo-dépendance des paramètres k et Cp rend l'équilibration du géotherme très longue voir impossible dans certains cas, principalement avec des flux mantelliques élevés. Pour les modèles en 2D, les géothermes présentés dans ce chapitre ont une variation de température inférieure à $1x10^{-5}$ °C/an, ce qui peut représenter une dizaine de degrés par million d'année et donc biaiser nos résultats.

La principale limite de cette étude est le peu de données disponibles sur le facteur d'anisotropie qui est le paramètre le plus important. En fonction des études et de la lithologie, la différence de valeur entre les tenseurs de la conductivité thermique peut être de 20% (Vosteen and Schellschmidt, 2003) ou de 100% (Popov and Mandel, 1997). De plus, l'évolution de ce facteur en fonction du taux de déformation est totalement inconnue. Est-ce qu'une foliation, une schistosité ou une stratigraphie peuvent induire un facteur d'anisotropie important, ou bien cela est-il restreint aux roches mylonitiques ? Quel est aussi le rôle de la pétrologie et de la minéralogie sur ce facteur ? Quel est le facteur d'anisotropie dans une métatexite possédant un rubanement biphasé solide-liquide ? Les inconnues sur ce facteur sont donc pour l'instant trop grandes pour pouvoir pleinement comprendre l'impact que peut avoir une anisotropie structurale sur l'évolution du géotherme. Il semble cependant que les variations de températures associées à ces anisotropies soient tout de même d'un ordre de grandeur inférieur aux modifications associées à d'autres processus de transfert de matière et de chaleur (chevauchement, amincissement, magmas, fluides…).

Pour aller plus loin dans nos modélisations sur les géothermes des massifs des Aiguilles-Rouges, de l'Agly et de la Montagne Noire, il faudrait ajouter aux modélisations d'autres composantes telles que le shear heating ou bien la chaleur latente, et surtout ajouter de l'advection de fluides et de liquides magmatiques dans les zones de cisaillement.

Chapitre 9. Evolution géodynamique des ECMs et reconstruction paléogéographique de la branche SE Varisque.

Ce chapitre est consacré à la corrélation des données acquises durant cette thèse avec les données de la littérature, dans le but d'améliorer la compréhension de la chaîne Varisque. Dans un premier temps, le contexte géodynamique propre aux Massifs Cristallins Externes sera discuté et un modèle tectonique depuis l'Ordovicien au Carbonifère sera proposé. Dans un second temps, le repositionnement de ces massifs mais aussi du reste de la branche SE Varisque sera investigué et une reconstruction paléogéographique de la branche SE Varisque sera proposée, offrant une nouvelle vision de la structuration de la chaîne varisque et de l'Eastern-Variscan Shear Zone.

Partie 1 : Evolution Géodynamique des Massifs Cristallins Externes

Dans les Massifs Cristallins Externes (ECMs), le dernier modèle géodynamique considérant l'ensemble des ECMs a été proposé par Guillot et al. (2009). Depuis, plusieurs études ont revisité ce modèle géodynamique via l'apport de données structurales, pétrologiques, géochronologiques et géochimiques. Ces études sont détaillées ci-après. Nous discutons dans un premier temps de l'évolution tectonique des Massifs des Aiguilles-Rouges et du Mont-Blanc (AR-MB) puis dans un second temps du modèle de l'évolution de l'Eastern Variscan Shear Zone (EVSZ). Enfin, un modèle géodynamique synthétique, concernant l'ensemble des ECMs sera proposé et intégré dans l'histoire globale de la chaîne Varisque.

1. Evolution tectonique des massifs des Aiguilles-Rouges et du Mont-Blanc

Dans les massifs des AR-MB, trois fabriques planaires (D1, D2 et D3) ont été identifiées (Vanardois et al., in review, en prép a). La déformation D1 forme une foliation S1 horizontale qui se produit à des conditions suprasolidus de HT-HP dans la croûte profonde (Vanardois et al., in review). Cette déformation a aussi été identifié dans la croûte supérieure au niveau du granite de Pormenaz. Considérant la géométrie de D1 et le métamorphisme M1 associé de haut-grade et la fusion partielle dans la croûte profonde, cette déformation peut être interprétée comme une phase d'empilement de nappe induisant des conditions de HP et de fusion partielle dans la croûte profonde, ou bien comme un fluage horizontal de la croûte partiellement fondue dans une croûte orogénique thermiquement mature succédant à la phase d'épaississement crustal. Un empilement de nappes a été proposé dans la croûte supérieur au niveau du synclinal de Servoz (Dobmeier, 1996, 1998) et dans les lithologies similaires du SW du massif de Belledonne (Fréville et al., 2018 ; Fernandez et al., 2002 ; Guillot & Ménot, 2009). Néanmoins, quelques plis F1 dans le socle gneissique attestent que la foliation S1 n'est pas la première fabrique planaire de ces massifs et que la déformation D1 est précédée par une déformation antérieure Dx. La foliation S1 porte une linéation minérale et d'étirement L1 orientée vers le N20, qui est parallèle aux linéations L2 observées dans les cisaillements dextres. De plus, les données EBSD des éclogites (Vanardos et al., in review) indiquent que la foliation S1 se développe durant la décompression de la croûte inférieure. Cette déformation D1 dans la croûte inférieure est donc interprétée comme un fluage longitudinal dans une croûte orogénique chaude. La déformation Dx, aussi reconnue dans les inclusions de minéraux dans les grenats des éclogites (Vanardois et al., in review), pourrait correspondre à l'épaississement crustal correspondant probablement à une phase précoce d'empilement de nappes. A quelques endroits, en particulier au niveau du granite de Pormenaz, des fabriques planaires sont préservées dans la croûte supérieure. Considérant la localisation supracrustale de ces foliations, il est peu probable qu'elles résultent du fluage de la croûte inférieure. Elles pourraient en revanche être le témoin d'une tectonique d'empilement de nappes identique à celle décrite dans le massif de Belledonne (Fréville et al., 2018). Considérant le pic de pression enregistré à 340-335 Ma dans les éclogites (Vanardois et al., in review), l'empilement de nappes est probablement antérieur à ca. 340 Ma et son commencement est postérieur au magmatisme bimodal du synclinal de Servoz daté à ca. 350 Ma (Vanardois et al., en prép b).

La déformation D2 correspond à un cisaillement dextre en transpression ou en transtension localement (von Raumer and Bussy, 2004 ; Simonetti et al., 2020a ; Vanardois et al., in prep c). Nos observations et les données de la littérature supportent l'hypothèse que les granites de Pormenaz et de Montées-Pélissier intrudent la croûte supérieure vers entre 340 et 330 Ma et que la migration des magmas pourrait s'effectuée à la faveur de zones de cisaillement dextres naissantes, en régime transpressif (Dobmeier, 1996, 1998 ; Bussy et al., 2000 ; Vanardois et al., in prep a). Il semble vraisemblable que la transpression dextre D2 et la formation des cisaillement C2 commencent aux alentours de 340 Ma en même temps que le fluage longitudinal D1. Après son initiation à 340 Ma, la transpression dextre D2 s'intensifie au cours du temps jusqu'à former un réseau anastomosé de zones de cisaillement venant transposer presque totalement la déformation D1. Les granites de Vallorcine, de Montenvers et du Mont-Blanc se mettent en place tardivement dans ces cisaillements dextres aux alentours de 305 Ma (Vanardois et al., in prep a ; Joye, 1989 ; Bussy et al., 2000 ; von Raumer and Bussy, 2004) et indiquent donc un âge inférieur pour la déformation D2 entre ca. 305-300 Ma. L'emplacement de rhyolite et de microgranites entre 307-303 Ma (Bussien Grosjean et al., 2017 ; Bussy et al., 2000) indique qu'à cette époque le socle gneissique était en cours d'exhumation avancée. Cette exhumation est aussi confirmée par la présence de blocs et galets de granite et de gneiss retrouvés dans le bassin de Salvan-Dorénaz dont le remplissage est daté entre ca. 308 et 293 Ma (Pilloud, 1991 ; Capuzzo and Bussy, 2000 ; Capuzzo et al., 2003 ; Capuzzo and Wetzel, 2004).

La déformation D3 est localisée dans la croûte supérieure au niveau du synclinal de Servoz et forme une schistosité subhorizontale S3 (Vanardois et al., in prep a). Des déformations tardives subhorizontales sont aussi décrites dans les massifs de Belledonne et du Pelvoux proches du front d'anatexie et sont interprétées comme l'effet d'un découplage entre la croûte inférieure partiellement fondue et la croûte supérieure à 305 Ma (Fréville et al., in review) ou bien comme des détachements tardifs (Guillot and Ménot, 1999, 2009 ; Fernandez et al., 2002). L'amincissement de la croûte est attesté par l'ouverture des bassins au Carbonifère supérieur entre 308 et 293 Ma (Capuzzo and Bussy, 2000). La déformation D3 pourrait donc être l'expression de l'amincissement à l'interface croûte supérieure/croûte moyenne, comme dans le massif du Pelvoux (Fréville et al., soumis), le massif de l'Agly (Siron et al., 2020) ou en Montagne Noire (Rabin et al., 2015), potentiellement lors de l'effondrement de la chaîne Varisque.

2. Implications pour le modèle de l'EVSZ

L'analyse structurale du réseau anastomosé de zone de cisaillement dextre (Vanardois et al., in prep) démontre quelques différences avec le modèle récent de l'EVSZ proposé par Simonetti et al. (2020a) dans le massif des Aiguilles-Rouges. Premièrement, le cisaillement dextre n'est pas seulement cantonné aux cisaillements NE-SW, i.e. l'Emosson-Bérard Shear Zone (EBSZ) et la Miéville Shear Zone, mais forme un réseau anastomosé de zones de cisaillement, large d'au moins 25 km avec une direction de cisaillement principale N-S dans les massifs des AR-MB.

Le timing de la transpression dextre, entre 340 et 300 Ma, est similaire à celui proposé dans le massif de l'Argentera (Simonetti et al., 2018). Nos résultats permettent de préciser que le cisaillement dextre ne commence pas seulement à basse pression, i.e. à la fin de l'anatexie (Genier et al., 2008 ; Simonetti et al., 2018) mais s'initie dans une croûte-épaisse et en contexte suprasolidus, comme enregistré dans les roches de HP-HT. La déformation dextre se poursuit après la cristallisation des liquides silicatés et au cours de l'exhumation puis du refroidissement de la croûte.

En extrapolant, nos résultats questionnent aussi les interprétations proposées sur la zone de cisaillement de Ferrière-Mollière (FMSZ) dans le massif de l'Argentera, aussi interprétée comme un segment de l'EVSZ (e.g. Guillot and Ménot, 2009 ; Guillot et al., 2009 ; Carosi et al., 2016 ; Simonetti et al., 2018, 2020a, 2020b). La déformation de la FMSZ est essentiellement décrite comme une déformation mylonitique s.s., en conditions subsolidus sans la présence de liquide silicaté dans les roches (Simonetti et al., 2018, 2021). Cependant, les orientations des foliations verticales structurant les migmatites de part et d'autre de la FMSZ varient entre N0 et N90 (e.g. Faure-Muret et al., 1967 ; Rouire et al., 1980). Nous interprétons cette variation des orientations des trajectoires de foliation comme étant liée à des structures S-C-C', formant un réseau anastomosé comme nous le décrivons pour les massifs des AR-MB. En définitive, l'orientation générale du cisaillement dextre dans le massif de l'Argentera pourrait ne pas être parallèle avec l'orientation de la FMSZ, laquelle représenterait une structure C'.

Enfin, nos résultats indiquent que l'EVSZ est un réseau anastomosé crustal de zones de cisaillements. Il est donc très probable que certaines branches de ce réseau affleurent dans des MCEs différents sans qu'il soit forcément nécessaire de les corréler ou relier chacunes entre elles. La majeure partie de la chaîne Varisque forme un large réseau anastomosé de zones de cisaillement dextre (Ballèvre et al., 2018 ; Edel et al., 2018). Il est donc possible que la branche de l'EVSZ dans les Aiguilles-Rouges ne rejoigne pas la FMSZ du massif de l'Argentera.

3. Nouveau modèle de l'évolution géodynamique des ECMs

Sur la base des résultats obtenus durant cette thèse et les données bibliographiques publiées, un nouveau modèle géodynamique des ECMs est présenté pour la période 480 et 300 Ma.

3.1.Magmatisme Ordovicien (480-450 Ma)

Entre ca. 480 et 450 Ma, la marge Nord du Gondwana est une croûte continentale en extension voyant la formation de nombreux rifts continentaux (e.g. Lardeaux et al., 2014 ; Vanderhaeghe et al., 2020). L'amincissement crustal s'accompagne de la mise en place de laccolithes felsiques datés entre 450 et 480 Ma (e.g. Melleton et al., 2010) et de tholéiites de type MORB (e.g. Paquette et al., 1989) qui induisent un métamorphisme de HT-BP (Schulz and von Raumer, 2011) (Fig. 1A). L'ophiolite de Chamrousse, datée à ca. 500 Ma (Ménot et al., 1985, 1988b) pourrait s'être formée quelques temps plus tôt. Cependant, les incertitudes sur ces âges permettent aussi de rattacher la formation de Chamrousse au rifting ordovicien affectant la marge Nord gondwanienne et entrainant la formation de bassins océaniques locaux. Entre ca. 450 et 370 Ma, les ECMs ne semblent pas enregistrer d'événements tectoniques, mise à part la potentielle obduction de l'ophiolite de Chamrousse (Guillot and Ménot, 2009 ; Fréville et al., 2018).

3.2.Formation du magmatisme bimodal dans les ECMs (370-350 Ma)

Les roches métavolcaniques du synclinal de Servoz dans les Aiguilles-Rouges sont semblables à celles de la partie SO du massif de Belledonne et à celles du Cortical Pelvoux (voir Vanardois et al., in prep pour une révision). Ce magmatisme bimodal est issu d'une phase de rifting intracontinental datée entre 370 et 350 Ma, en position d'arrière arc (Vanardois et al., in prep ; Fréville et al., 2018, in review; Fréville, 2016; Ménot et al., 1985, 1987; Ménot, 1986, 1988b). Les données géochimiques sur ce magmatisme bimodal semblent indiquer une origine de magmatisme d'arrière-arc ou d'arc (Dobmeier et al., 1999 ; Vivier et al., 1987). Ces formations peuvent être comparées avec l'arc magmatique du Morvan et le bassin d'arrière-arc de la Brévenne (Faure et al., 1997 ; Lardeaux et al., 2014) qui se sont aussi formés entre 370 et 350 Ma (Pin and Paquette, 1998, 2002). Ces données indiquent donc que le magmatisme bimodal des ECMs est relié à un contexte de bassin d'arrière-arc (Fig. 1B), potentiellement induit par la subduction d'une lithosphère océanique (océan Saxothuringien ?) sous la zone Moldanubienne (Lardeaux et al., 2014).

3.3.Epaississement crustal et empilement de nappes (350-340 Ma)

Le socle gneissique des massifs des AR-MB est affecté par un métamorphisme prograde jusqu'au pic de pression daté à ca. 340-335 Ma (Vanardois et al., in review ; Rubatto et al., 2010 ; Jacob et al., 2021). Les conditions P-T de ce métamorphisme prograde indiquent un gradient de MT-MP interprété comme l'épaississement crustal durant la collision continental (Vanardois et al., in prep c). Un empilement de nappes vers l'Est est décrit dans les parties SO des massifs de Belledonne et des Aiguilles-Rouges (Dobmeier, 1996, 1998 ; Fernandez et al., 2002 ; Fréville et al., 2018) et est probablement responsable d'une partie de l'épaississement crustal. Cette déformation pourrait correspondre à la déformation Dx décrite dans le massif des Aiguilles-Rouges dans les charnières de plis des déformations postérieures et enregistrée dans les inclusions des grenats des éclogites (Vanardois et al., in review, in prep). Cet épaississement crustal induit des conditions de HP dans la base de la croûte et forme les éclogites de HP-HT (Fig. 1C). Cet événement d'empilement de nappes est aussi décrit dans le Massif Central (e.g. Ledru et al., 2001 ; Faure et al., 2014b ; Vanderhaeghe et al., 2020) et est probablement induit par la collision continentale entre la zone Moldanubienne et les terrains du microcontinent Armorica.

3.4.Fluage horizontal et début du cisaillement dextre (340-330 Ma)

Au niveau du Lac Cornu, la déformation D1 procède de l'épaississement crustal qui culmine à ca. 340 Ma (Vanardois et al., in review). Cette déformation D1 est associée à la fusion partielle de la croûte profonde (Vanardois et al., in prep) laquelle est aussi documentée dans d'autres ECMs (e.g. Le Fort, 1973 ; Pecher, 1970 ; Fréville et al., 2018, in review ; Rubatto et al., 2001). Dans des croûtes épaissies, la fusion de la croûte moyenne-inférieure entraine généralement son fluage gravitaire (e.g. Beaumont et al., 2001 ; Vanderhaeghe, 2009 ; Rosenberg et al., 2007). Dans les AR-MB, la déformation D1 est interprétée comme le résultat du fluage horizontal de la croûte profonde partiellement fondue sous l'effet des forces de volumes (Fig. 1D). La plupart des roches de haut-grade observée dans les AR ne représente que la partie superficielle du chenal de fluage. La formation de ce fluage gravitaire est contemporaine de la nucléation et formation des premières zones de cisaillements dextres dans les Aiguilles-Rouges (Vanardois et al., in prep) ou du cisaillement senestre conjugué dans le massif du Pelvoux (Fréville et al., in review), mais aussi de l'enfouissement de la croûte supérieure dans les Aiguilles-Rouges (Vanardois et al., in prep). On peut donc interpréter la S1 observée dans la croûte partiellement fondue comme un fluage longitudinal de la croûte inférieure, contemporain d'un épaississement de la croûte supérieure, dans un régime global en transpression dextre.

Cette période (340-330 Ma) est aussi caractérisée par un magmatisme Mg-K (Debon and Lemmet, 1999) qui s'illustre par la mise en place de granites dans la croûte supérieure, comme les granites de Pormenaz et de Montées-Pélissier dans les Aiguilles-Rouges par exemple (Bussy et al., 2000 ; Vanardois et al., in prep), le granite des Sept-Laux dans le massif de Belledonne (Fréville et al., in prep), le granite du Rochail dans le Pelvoux (Fréville et al., in prep) ou une monzonite dans le massif de l'Argentera (Rubatto et al., 2001). Ce pulse magmatique est interprété comme la ségrégation des premiers liquides anatectiques dans la croûte inférieure, contaminés par des liquides à composante mantellique (Debon and Lemmet, 1999 ; von Raumer and Bussy, 2004). Dans les massifs Varisques voisins, l'apport de chaleur nécessaire à ce magmatisme est interprété comme étant induit par le panneau plongeant sous la zone moldanubienne (Schulmann et al., 2009 ; Tabaud et al., 2014 ; Guillot et al., 2020) ou bien par sa rupture (Faure et al., 2014a ; Li et al., 2014) (Fig. 1D).

3.5.La transpression dextre (330-305 Ma)

A partir de 330-320 Ma, la transpression dextre D2 devient peu à peu la déformation principale dans l'ensemble de la chaîne Varisque (e.g. Edel et al., 2018 ; Ballèvre et al., 2018). Dans les ECMs, le cisaillement dextre plisse la croûte supérieure (Dobmeier, 1998 ; Fréville et al., 2018) et forme localement des bassins en pull-apart (Vanardois et al., in prep d). Dans la croûte ductile, elle crée un large réseau anastomosé de zones de cisaillement telle que l'EVSZ (Simonetti et al., 2018, 2020a; Guillot & Ménot, 2009) et des cisaillements senestres conjugués dans le massif du Pelvoux (Strzerzynski et al., 2005; Fréville, 2016 ; Fréville et al., in review) (Fig. 1E). Ces zones de cisaillement exhument la croûte inférieure et moyenne et juxtaposent différents niveaux structuraux (Schulz and von Raumer, 1993 ; Vanardois et al., in prep).

3.6.Transtension et orogénique collapse (305-300 Ma)

Durant la transcurrence dextre, de nombreux plutons se mettent en place dans les zones de dilatance créées par les cisaillements verticaux, en particulier à ca. 305 Ma à la fin du cisaillement (Bussy et al., 2000 ; Fréville et al., in prep ; Vanardois et al., in prep). Cette activité magmatique est accompagnée d'une circulation de fluide aqueux (Genier et al., 2008 ; Vanardois et al., in prep) induisant localement de la fusion partielle BP-HT formant des migmatites à cordiérite au niveau de la zone de Fully (Krummenacher, 1959 ; Bussy et al., 2000) ou dans l'Inner Pelvoux (Barféty et al., 1984 ; Bogdanoff et al., 1991 ; Grandjean et al., 1996 ; Fréville et al., in review). Un léger amincissement crustal (D3 ?) est parfois observé dans les massifs de Belledonne, du Pelvoux et des Aiguilles-Rouges (Fréville et al., in review; Guillot & Ménot, 1999, 2009; Fernandez et al., 2002 ; Vanardois et al., in prep) et pourrait être associé à l'effondrement de la chaîne. Ces dernières déformations Varisques sont accompagnées de la formation de bassins étroits tardi-Carbonifères (Pilloud, 1991 ; Capuzzo and Bussy, 2000 ; Guillot and Ménot, 2009 ; Vanardois et al., in prep) (Fig. 1F).

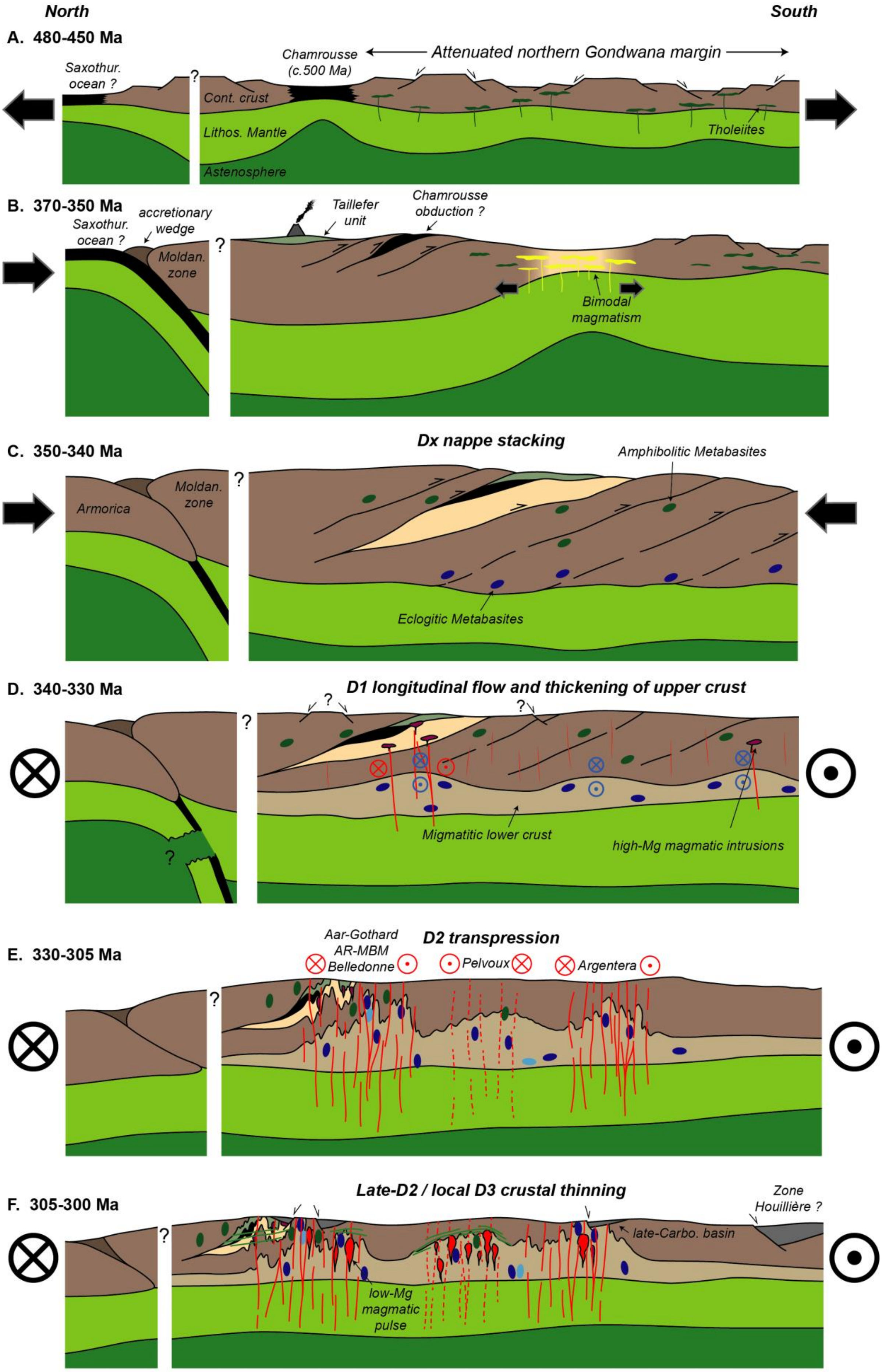
North
South
A. 480-450 Ma
Saxothur. ocean ?
?
Chamrousse (c.500 Ma)
Attenuated northern Gondwana margin
Cont. crust
Lithos. Mantle
Astenosphere
Tholeiites
B. 370-350 Ma
Saxothur. ocean ?
accretionary wedge
Moldan. zone
?
Taillefer unit
Chamrousse obduction ?
Bimodal magmatism
C. 350-340 Ma
Dx nappe stacking
Amphibolitic Metabasites
Armorica
Moldan. zone
?
Eclogitic Metabasites
D. 340-330 Ma
D1 longitudinal flow and thickening of upper crust
?
?
?
?
Migmatitic lower crust
high-Mg magmatic intrusions
E. 330-305 Ma
Aar-Gothard
AR-MBM
Belledonne
D2 transpression
Pelvoux
Argentera
?
F. 305-300 Ma
Late-D2 / local D3 crustal thinning
Zone Houillière ?
late-Carbo. basin
?
low-Mg magmatic pulse

Figure 1 : Model of the Geodynamic evolution of the ECMs. See section 3 for details on each stage.

Partie 2 : Reconstitution de la branche SE Varisque

1. Introduction

L'étude de la chaîne Varisque nous permet de mieux comprendre les processus orogéniques se déroulant dans la croûte moyenne et profonde des chaînes de montagnes actuelles (e.g. Maierová et al., 2016 ; Cochelin et al., 2021). Cependant, l'étude des processus de grande échelle affectant la chaîne Varisque peuvent être discutés et interprétés seulement si la structuration et l'organisation paléogéographique de la chaîne sont bien contraintes. Cette géométrie de la chaîne est relativement bien connue dans la partie Nord de la chaîne (e.g. Franke et al., 2017 ; Lardeaux et al., 2014), à l'Est (massif de la Bohème ; Schulman et al., 2008, Stipská et al., 2019) et dans sa partie Sud-Ouest (i.e. massif Ibérique ; voir Martinez-Catalan et al., 2021 pour une synthèse) (Fig. 2). En revanche, sa partie Sud-Est est très mal contrainte et les reconstitutions paléogéographiques diffèrent beaucoup d'une étude à l'autre. Cette méconnaissance de la structuration de la branche SE de la chaîne provient des nombreux mouvements tectoniques ayant affecté les terrains Paléozoïques après l'orogénèse Varisque au Permien (Edel et al., 2014, 2015), au Mésozoïque lors de l'ouverture de l'océan Téthysien (e.g. Lemoine et al., 1986 ; Haas et al., 2020) et au Cénozoïque durant la formation de la chaîne Alpine (e.g. Schmid et al., 2017). Une parfaite illustration de cette complexité est donnée par le nombre de modèles différents de la position du bloc Corse-Sardaigne-Maure-Tanneron (CSMT) qui est parfois placé dans la continuité des Massifs Cristallins Externes des Alpes (e.g. Rossi et al., 2009 ; Simonetti et al., 2020a), auprès des Pyrénées et des Catalan Coastal Ranges (e.g. Carreras and Druguet, 2014) ou bien entre le Massif Central et le massif de la Bohème (e.g. Edel et al., 2014, 2018) (Fig. 2).

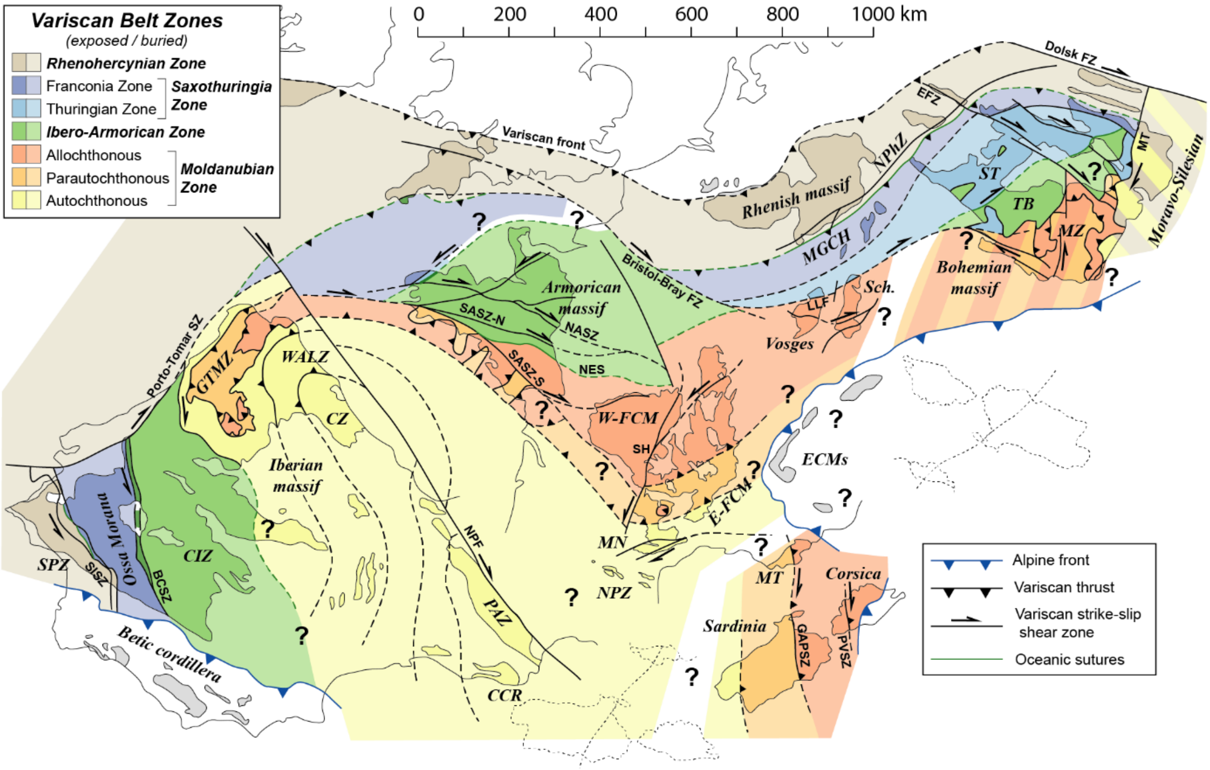

Figure 2: Sketch of the Variscan belt in an early Permian reconstruction at the end of the Variscan orogeny, based on Martinez-Catalan et al. (2021), Franke et al., (2017), Edel et al., (2018) and Lardeaux et al. (2014). ***Zones (Z):*** *CCR: Catalan Coastal Ranges; CIZ: Central Iberian; CZ: Cantabrian; ECMs: External Crystalline Massifs; E-FCM and W-FCM: French Central Massif (East and West); GTMZ: Galicia-Trás-os-Montes; MGCH: Mid German Crystalline High; MN: Montagne Noire; MZ: Moldanubian; NPhZ: Northern Phyllite; NPZ: North Pyrenean; PAZ: Pyrenean Axial; Sch: Schwarzwald; SPZ: South-Portugese; ST: Saxo-Thuringia; TB: Teplá-Barrandian block; WALZ: West Asturian-Leonese.* ***Shear Zones (SZ), Fault Zones (FZ) and Fault (F):*** *BCSZ: Badajoz-Corboda; EFZ: Elbe; GAPSZ: Grimaud-Asinara-Posada; LLF: Lalaye-Lubine; MT: Moldanubian Thrust; NASZ: Northern Armorican; NES: Nort-sur-Erdre segment; NPF: North Pyrenean; PVSZ: Porto Vecchio; SH: Sillon Houiller; SASZ: Southern Armorican (North and South); SISZ: Southern Iberian.*

Dans cette seconde partie de chapitre, une restauration de la structuration et de la paléogéographie de la branche SE est proposée sur la base de nos résultats et d'une compilation des données publiées. Cette restauration se concentre sur la Zone Axiale des Pyrénées (PAZ), la Zone Nord-Pyrénéenne (NPZ), les Catalan Coastal Ranges (CCR), la Corse, la Sardaigne, les massifs Cristallins Externes (ECMs) et les Maures-Tanneron (MT) (Fig. 3). Elle se base sur une comparaison avec le Massif Central de l'Ouest (W-FCM) et de l'Est (E-FCM), la Montagne Noire (MN) et les Vosges Centrales et du Sud qui sont considérés comme "fixes" n'ayant pas ou peu été affectés par les épisodes de tectonique post-Varisques et qui représentent la zone Moldanubienne. La compilation concerne (1) les données des conditions du métamorphisme de haute-pression (HP) illustrées par les reliques d'éclogite dans ces massifs, (2) l'âge des pulses magmatiques, (3) les épisodes de fusion partielle et leurs conditions pression-température (P-T), et (4) le timing de l'ouverture de basin en contexte d'arrière-arc affectant certains de ces massifs. Ces données nous permettent de discuter la structuration de la chaîne Varisque depuis le Dévonien au Carbonifère.

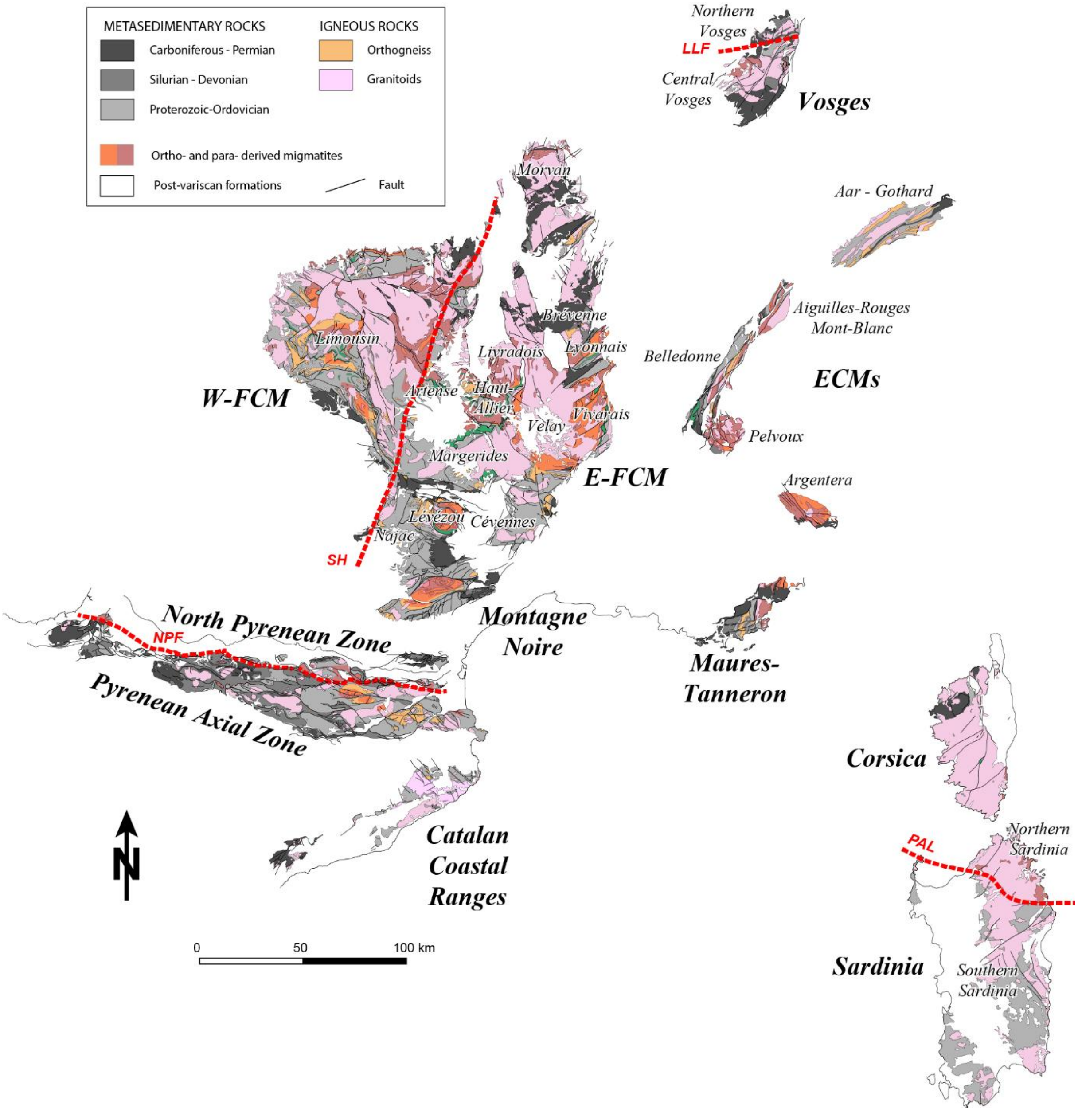

Figure 3: Geological map of the massifs of the SE Variscan branch in current position. E-FCM: Eastern French Central Massif; LLF: Lalaye-Lubine Fault; NPF: North Pyrenean Fault; PAL: Posada-Asinara Lineament; SH: Sillon Houiller; W-FCM: Western French Central Massif.

2. Compilations des événements dévoniens et carbonifères de la branche SE

Les données du Massif Central et des Vosges Moldanubiennes qui nous serviront de référentiels dans notre reconstitution.

Concernant la subdivision des massifs étudiés, la PAZ et la NPZ sont séparés par la Faille Nord-Pyrénéenne (NPF dans la Fig. 3). L'E-FCM et le W-FCM sont séparés par le Sillon Houiller (SH dans la Fig. 3). Les Vosges Moldanubiennes sont séparées des Vosges du Nord par la Faille de Lalaye-Lubine (LLF dans la Fig. 3).

2.1. Métamorphisme de haute-pression

Des témoins de paragénèses de haute-pression (HP) sont décrites dans tous les massifs étudiés dans ce chapitre à l'exception de la NPZ, la PAZ et des CCR (Fig. 4) dans lesquels l'épaississement Varisque a été limité (de Hoÿm de Marien et al., 2019 ; Reche Estrada and Martinez, 2002). Dans le Massif Central, la majorité des éclogites enregistrent des conditions de haute-pression-haute-température (HP-HT) comprises entre 1.5-2.0 GPa et 700-750 °C (Fig. 4). Les faibles gradients thermiques (HP-BT) typiques des zones de subductions sont rares et ont été reportées dans le W-FCM et les monts du Lyonnais avec des conditions d'ultra-haute pression (UHP) (Lardeaux et al., 2001 ; Berger et al., 2010), et dans le massif de Najac avec des conditions aux alentours de 570 °C/1.6 GPa (Lotout et al., 2018 ; Benmammar et al., 2020). Les conditions d'UHP n'ont pas été retrouvées dans les terrains adjacents qui indiquent des conditions de HP-HT similaires aux autres éclogites du Massif Central (Gardien and Lardeaux, 1991 ; Bellot and Roig, 2007). A l'exception des éclogites de Najac et de la MN, les éclogites du Massif Central subissent ensuite un métamorphisme granulitique de moyenne-pression (MP)-HT (Fig. 4). L'âge des conditions de HP a d'abord été considéré comme Silurien – Dévonien inf. sur la base de datations anciennes (ID-TIMS sur zircon et Sm-Nd sur grenat – roche totale ; Ducrot et al., 1983 ; Pin and Lancelot, 1982 ; Paquette et al., 1995). Dans le Limousin (W-FCM), Berger et al. (2010) ont obtenu deux âges sur des bordures de zircons d'une éclogite à 412 ± 6 Ma et 382 ± 7 Ma (LA-ICPMS sur zircon) et, par comparaison avec les âges Silurien – Dévonien inférieur obtenus dans le Massif Central, ont attribué l'âge à 412 Ma à l'événement d'UHP. Cependant, des études récentes dans le massif Armoricain (Paquette et al., 2017) et sur les éclogites du Massif Central (Lotout et al., 2018, 2020 ; de Hoÿm de Marien, 2020) remettent en cause la validité de ces âges et datent la HP entre ca. 380 et 360 Ma (LA-ICPMS on zircon, rutile and apatite).

Dans la MN, les éclogites sont retrouvées sous forme de boudins mafiques de quelques mètres emballés dans des migmatites felsiques. Elles enregistrent des conditions HP-HT de ca. 1.5-2.1 GPa/700-750 °C, similaires à celles du Massif Central, mais sont suivies d'une décompression isotherme sans le faciès granulitique (Whitney et al., 2015, 2020 ; Pitra et al., 2021). L'âge du métamorphisme de HP est interprété à 315 Ma (LA-ICPMS sur zircon ; Whitney et al., 2015, 2020) ou bien à 360 Ma (LA-ICPMS sur zircon et Sm-Nd sur grenat ; Pitra et al., 2021 ; Faure et al., 2014b).

Dans les Vosges Moldanubiennes, les conditions de HP sont enregistrées dans des péridotites à grenat, des boudins d'éclogites et des granulites felsiques de l'unité granulitique. Les modélisations thermodynamiques sur les péridotites indiquent des conditions d'UHP-UHT et ont été extrapolées aux éclogites (Altherr and Kalt, 1996 ; Altherr and Soder, 2018 ; Altherr, 2021). Dans le massif de Schwarzwald adjacent aux Vosges (Fig. 2), les modélisations thermodynamiques sur les granulites felsiques indiquent des conditions d'HP-UHT (Marschall et al., 2003) tandis que les boudins d'éclogites dans les migmatites enregistrent des conditions P-T entre 1.6-2.0 GPa et 670-750 °C datées à 340-330 Ma suivies d'une décompression isotherme jusqu'à ca. 0.5 GPa (Kalt et al., 1994 ; Altherr et al., 2021).

Les lentilles d'éclogites des ECMs sont très similaires, elles sont emballées dans des migmatites et enregistrent des conditions de pression et de température de 1.4-1.8 GPa/700-750 °C (Fig. 4) datées entre 340 et 330 Ma (LA-ICPMS sur zircon et rutile ; Rubatto et al., 2010 ; Jacob et al., 2021 ; Vanardois et al., soumis). Le pic de pression est parfois suivi d'un métamorphisme granulitique de moyenne ou basse pression (Grandjean et al., 1996 ; Jacob et al., 2021 ; Vanardois et al., soumis).

En Corse et Sardaigne, les paragénèses de HP sont aussi reconnues dans des boudins mafiques englobés dans des migmatites. En Corse, Cruciani et al. (2021) ont contraint les conditions de HP à 1.3-1.75 GPa/650-700 °C suivies d'un réchauffement de MP-HT. Plusieurs auteurs proposent un âge compris entre 365 et 345 Ma pour cet épisode de HP (e.g. Li et al., 2014 ; Massonne et al., 2018). Giacomini et al. (2008) rapportent des conditions de HP-UHT (1.4-1.8 GPa/900-1000 °C) dans des granulites felsiques datées à 361 ± 3 Ma (Fig. 4). Dans la partie Nord de la Sardaigne, de nombreuses études ont contraint les conditions de HP à ca. 1.5-2.1 GPa/650-750 °C suivies d'une évolution en faciès granulitique à ca. MP-HT (Fig. 4) (Cortesogno et al., 2004 ; Giacomini et al., 2005 ; Cruciani et al., 2011, 2012, 2015a, 2019, 2021). En revanche, l'âge de cet épisode de HP est très mal contraint et pourrait avoir lieu à ca.

400 Ma (Palmeri et al., 2004) ou bien aux alentours de 350-345 Ma (Di Vicenzo et al., 2004). Dans la zone Centrale de la Sardaigne, les conditions de pression enregistrées par les boudins mafiques sont plus faibles aux alentours de 1.0-1.5 GPa et 570-700 °C (Cortesogno et al., 2004 ; Scodina et al., 2021). Cruciani et al. (2013) rapportent aussi des conditions de HP-BT obtenues sur un schiste à chloritoïde incompatibles avec les conditions obtenues sur les boudins mafiques (Fig. 4).

Dans les MT massifs, le LAC n'enregistre pas de HP (Bellot et al., 2003) mise à part dans des lentilles de péridotite provenant d'une potentielle suture Cambrienne (Bellot et al., 2010). D'autres reliques d'HP sont identifiées sous forme de boudins mafiques enveloppées par des migmatites (Schneider et al., 2014) mais les conditions P-T n'ont pas été estimées. L'âge du métamorphisme prograde est potentiellement contraint entre 380 et 330 Ma (EPMA sur monazite ; Oliot et al., 2015).

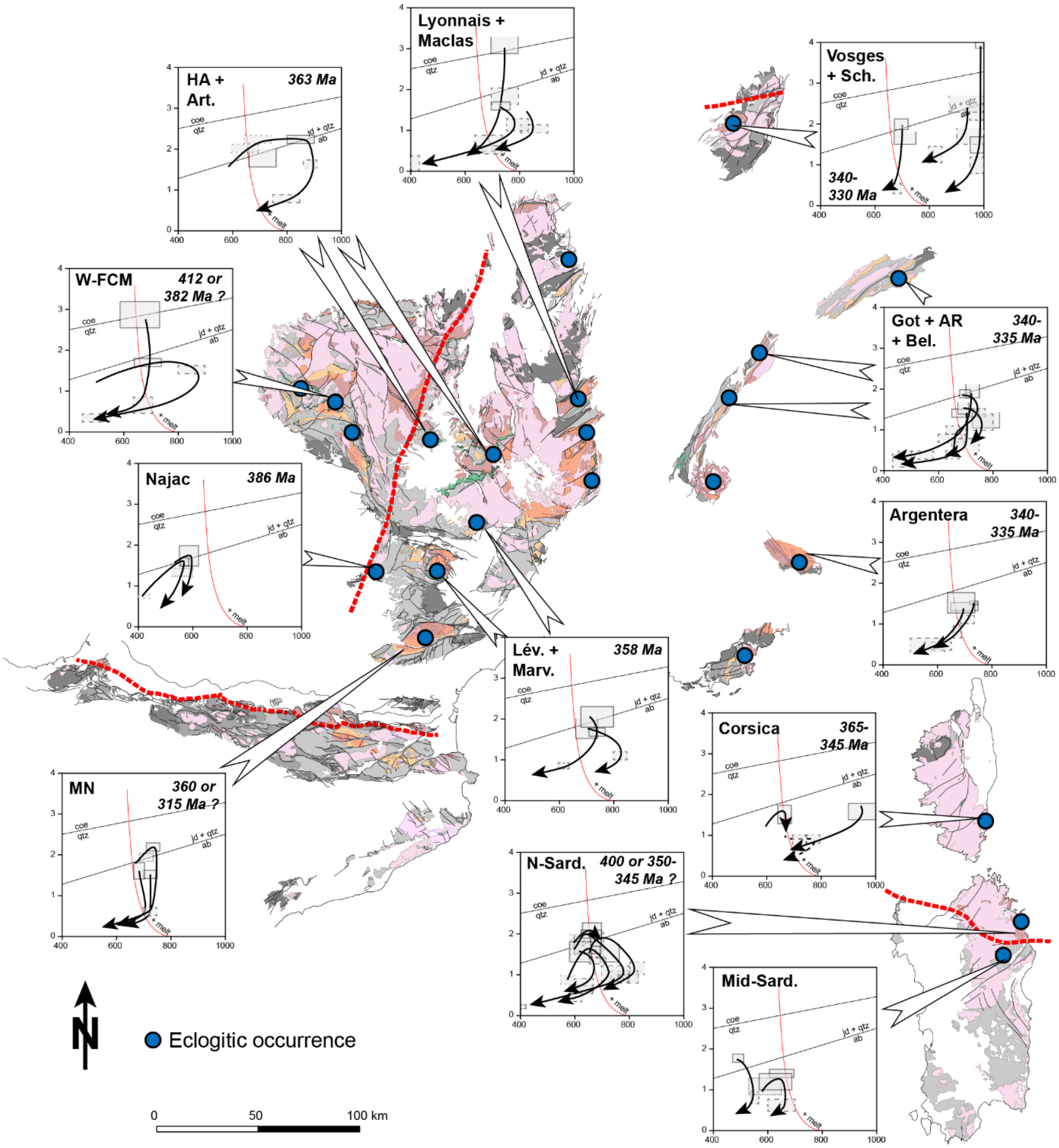

Figure 4: P-T-t constraints on the metamorphic history of the eclogitic relicts in the SE Variscan branch. Full squares = peak of HP metamorphism; dotted squares = prograde metamorphism; dashed squares = retrograde metamorphism. Got + AR + Bel. = Gottard, Aiguilles-Rouges and Belledonne; HA + Art. = Haut-Allier and Artense; Lév. + Marv. = Lévézou and Marvejols; MN = Montagne Noire; Sard. = Sardinia; Sch. = Schwarzwald; W-FCM = West French Central Massif. References are compiled in Table S1. P-T-t paths of eclogites in the Pelvoux massif (ECMs) and in the MT have not been constrained.

2.2. Magmatisme d'arcs et d'arrière-arc

Dans le Nord de l'E-FCM, l'ophiolite de la Brévenne a été interprétée comme le résultat de l'ouverture d'un bassin d'arrière-arc entre ca. 365 et 355 Ma (Pin and Paquette, 1998, 2002) tandis qu'un complexe volcanique dans le Morvan est interprété comme l'arc volcanique associé (Faure et al., 1997 ; Pin and Paquette, 1998, 2002). Ce contexte a donc été interprété comme la preuve de la subduction d'un océan (Saxothuringien, Rhénohercynien ou Rhéique en fonction des études) vers le Sud entre ca. 370 et 350 Ma (Faure et al., 1997 ; Lardeaux et al., 2014). Cet événement est aussi identifié par le magmatisme andésitique dans le Nord du Massif Central (Est et Ouest ; Pin and Paquette, 2002) et s'exprime aussi par l'ouverture d'un bassin d'arrière-arc dans les Vosges Moldanubiennes à ca. 372 Ma (Skrzypek et al., 2012) et par un rifting associé à un magmatisme bimodal dans les ECMs entre 370 et 350 Ma (Ménot, 1988b ; Fréville et al., 2018 ; Vanardois et al., en prép a, en prép b) (Fig. 5). En revanche, cet événement n'a pas été enregistré ou décrit dans les autres massifs de la branche SE Varisque.

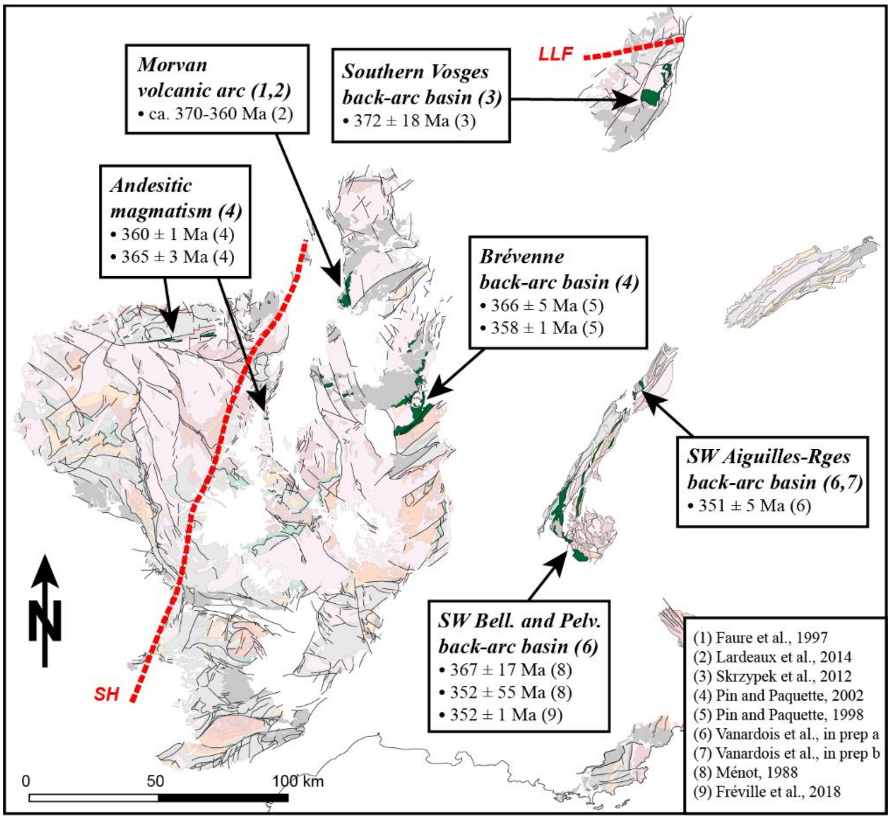

Figure 5: Review of arc and back-arc magmatism during Late-Devonian – Early-Carboniferous times.

2.3. Les épisodes magmatiques

Les données géochronologiques U-Pb (sans les données EPMA sur monazites) datant l'emplacement de corps magmatiques ont été compilées pour chaque massif (Les références sont disponibles dans la Table S2) et sont présentées dans la Figure 5 sous la forme d'histogramme et d'une aire KDE (traitement statistique additionnant les gaussiennes de chaque donnée sans tenir compte des erreurs analytiques pour éviter les artefacts ; Vermeersch, 2012). Ces histogrammes et les aires KDE sont bien sûr biaisés par le nombre d'analyses et l'échantillonnage reporté en fonction des zones mais permettent de dégager une tendance qualitative renseignant sur la chronologie du magmatisme dans chaque massif.

Dans le W-FCM, le magmatisme semble débuter aux alentours de 360-350 Ma avec la mise en place de corps andésitiques liés au contexte de supra-subduction (Pin and Paquette, 2002) discuté dans la section précédente. Puis deux pics d'activité sont enregistrés à 335 Ma et 319 Ma, le premier correspondant à l'emplacement de plutons (Rolin et al., 2008 ; Thiery, 2010) mais aussi de dykes et de roches volcaniques (Cartanaz et al., 2008 ; Bruguier et al., 1998), le second à l'emplacement de plutons et de leucogranites syn-tectoniques dans des zones de cisaillement transcurrentes d'échelle crustales (Gébelin et al., 2009 ; Thiery et al., 2009). Dans la partie Nord de l'E-FCM, les pics d'activité magmatiques sont similaires à ceux de l'W-FCM (i.e. 334 Ma and 313 Ma) dont principalement du magmatisme viséen et la mise en place de granites et de vaugnérites (Laurent et al., 2017). Les Vosges Moldanubiennes enregistrent aussi principalement un magmatisme viséen vers ca. 339 Ma avec une composition riche en Mg-K (Tabaud et al., 2015 ; Guillot et al., 2020) ainsi que quelques granites tardifs aux alentours de 320 Ma (Schaltegger et al., 1999 ; Kratinova et al., 2007 ; Tabaud et al., 2015). Aucun magmatisme tardi-carbonifère (310-290 Ma) n'est enregistré ou décrit dans les Vosges Moldanubiennes, le W-FCM et la partie Nord de l'E-FCM (Fig. 6).

A l'opposé, la MN, la NPZ et les CCR enregistrent un magmatisme depuis ca. 320 Ma jusqu'à 290 Ma avec un pic d'activité à ca. 301-305 Ma et ne présentent pas de magmatisme viséen (Fig. 6). Le Sud de l'E-FCM et la PAZ ont aussi un pic d'activité magmatique aux alentours de 307 Ma et 302 Ma, respectivement, mais ont aussi quelques traces d'un magmatisme viséen plus ancien (Pin, 1979 ; Mezger and Gerdes, 2016).

Les ECMs, les MT et la Corse enregistrent les deux magmatismes viséen et stéphanien (ca. 340-332 Ma et 305-303 Ma, respectivement) (Fig. 6). Dans les ECMs et en Corse, le magmatisme viséen est principalement représenté par une composition magmatique riche en

Mg-K tandis que l'épisode magmatique stéphanien est plus riche en Fe (Debon and Lemmet, 1999 ; Fréville et al., en prép ; Paquette et al., 2003). Dans ces massifs, le magmatisme aux alentours de 320 Ma est presque inexistant, au contraire de la Sardaigne qui enregistre un épisode magmatique à ca. 318 Ma continuant jusqu'à 300 Ma.

Un magmatisme Permien est enregistré en Corse et dans les massifs Basques de la PAZ (Fig. 6). Cet événement est aussi décrit sous forme de filons dans les CCR (Martinez-Catalan et al., 2014) et dans les ECMs (e.g. Laurent, 1992), mais aussi sous forme de roches volcaniques dans les MT (e.g. Zheng et al., 1992). Ce magmatisme d'affinité alcaline est habituellement attribué à un contexte anorogénique distensif (Poitrasson and Pin, 1998 ; Paquette et al., 2003), potentiellement lié à des décrochements (Denèle et al., 2012).

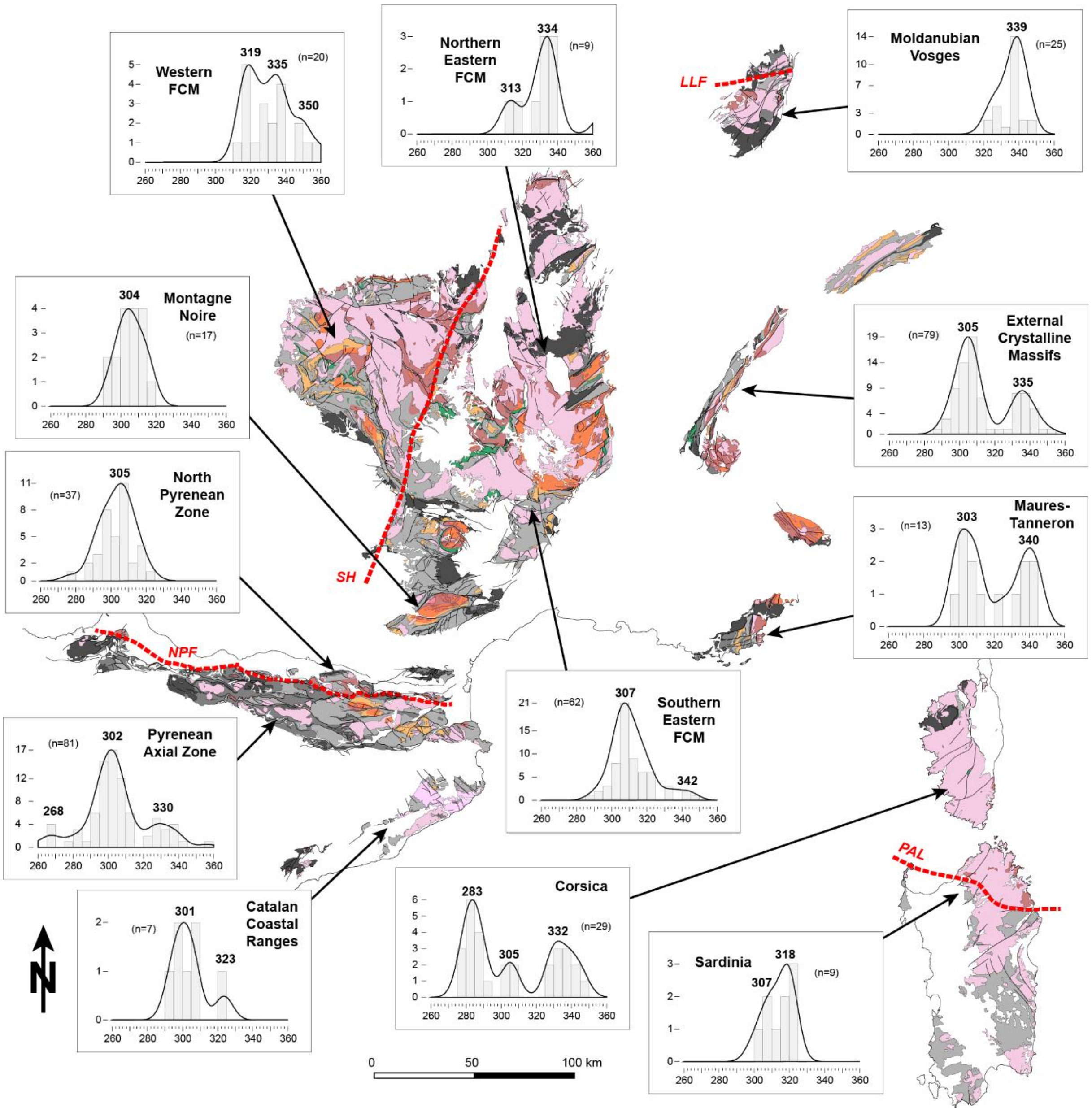

Figure 6: Review of U-Pb geochronological ages of magmatic corps illustrated by histograms and KDE statistical treatment (cf. Vermeesch, 2012; bandwith = 5; bin width = 5). Northern E-FCM comprised Artense, Haut-Allier, Livradois, Lyonnais, Brévenne and Morvan areas, Southern E-FCM comprised Vivarais, Velay, Margerides, Lévézou, Cévennes and Najac areas (cf. Fig. 3). References are available in Table S3. EPMA ages on monazite are not included due to uncertainty on the method (Poujol et al., 2017).

2.4. Episodes de fusion partielle

Dans le Massif Central, quatre épisodes de fusion partielle sont décrits (Faure et al., 2009 ; Barbey et al., 2015 ; Vanderhaeghe et al., 2020). Le premier est associé à l'exhumation de matériel crustal suivant son enfouissement durant la subduction d'un océan vers le Nord ou le Sud en fonction des interprétations des auteurs (e.g. Faure et al., 2009 ; Vanderhaeghe et al., 2020). Cet épisode est principalement décrit dans les terrains allochtones du Massif Central (UGU essentiellement (Faure et al., 2009 ; Vanderhaeghe et al., 2020)). L'âge de cet événement est daté entre 385-375 Ma (synthèse dans Faure et al., 2009) d'après des méthodes de datations maintenant controversées (Rb/Sr sur roche totale et EPMA sur monazite). De plus, ces conditions P-T sont mal connues et sont parfois incohérentes avec l'assemblage minéralogique (e.g. conditions de MP-MT estimées dans une migmatite montrant une paragénèse à cordiérite typique de conditions de BP (Duthou et al., 1994)). Récemment, Benmammar et al. (2020) ont estimé les conditions d'anatexie d'une amphibolite à ca. 1. GPa/700-750 °C et l'ont daté à 363 ± 3 Ma (LA-ICPMS on zircon), ce qui représente sûrement la meilleure estimation de ce premier épisode anatectique.

Le second épisode de fusion partielle dans le Massif Central est décrit dans le dôme du Velay avec la fusion partielle de la croûte moyenne dans des conditions BP-MT entre 325-315 Ma (Barbey et al., 2015) ou 330-310 Ma (Vanderhaeghe et al., 2020). Toujours dans le Velay, les troisième et quatrième épisodes sont caractérisés par une fusion intense à BP-HT puis par la mise en place de plutons issus de l'anatexie des niveaux plus profonds entre 305 et 295 Ma (Barbey et al., 2015). Ces trois épisodes de fusion partielle sont associés à l'effondrement du plateau orogénique (Vanderhaeghe et al., 2020). Dans l'W-FCM et la partie Nord de l'E-FCM, ces épisodes de fusion partielle ne sont pas décrits et la seule trace de fusion postérieure au premier épisode anatectique est la mise en place de leucogranites aux alentours de 315 Ma associées à des migmatites locales (Gébelin et al., 2009).

Dans le cœur du dôme de la MN, la fusion partielle est considérée comme continue entre 315 et 300 Ma en conditions BP-MT (Trap et al., 2017 ; Roger et al., 2020) ou bien deux épisodes sont identifiés à ca. 319 Ma et 298-295 Ma (Poujol et al., 2017). L'origine de la fusion partielle a été interprétée comme résultant d'un épaississement crustal suivi d'une exhumation (Faure et al., 2014b) ou bien d'un fluage de la croûte inférieure vers les zones externes (Whitney et al., 2015 ; 2020 ; Roger et al., 2020 ; Vanderhaeghe et al., 2020).

Dans la NPZ, les premières traces d'anatexie sont datées entre 325 et 315 Ma (Lemirre, 2016 ; Vanardois et al., en prép c). Lemirre (2016) propose ensuite un second épisode de fusion partielle entre 305 et 280 Ma, tandis que Vanardois et al. (en prép c) sont en faveur d'une fusion partielle continue entre ca. 325 – 295 Ma à BP-HT (Siron et al., 2020) se clôturant dans les niveaux profonds aux alentours de 290 Ma avec un pic d'intensité aux alentours de 305-300 Ma. Cette fusion commence potentiellement avec un faible épaississement crustal (Lemirre, 2016). Dans la PAZ, les premières traces de fusion partielle sont datées entre 340 et 320 Ma (Mezger and Gerdes, 2016) mais l'épisode principal est daté entre 310 et 300 Ma en conditions de BP-HT (synthèse dans Cochelin et al., 2021) et est peut-être liée à un fort flux mantellique (Denèle et al., 2014).

Dans les Vosges, la fusion partielle à lieu en conditions granulitiques entre 345-335 Ma et est induite par l'enfouissement des roches puis de leur exhumation (Skrzypek et al., 2012, 2014). Dans les ECMs, le premier épisode d'anatexie est lié à l'épaississement crustal en conditions de MP-MT entre 335 et 315 Ma (Fréville et al., soumis ; Rubatto et al., 2001 ; Bussy et al., 2000 ; Bussy and von Raumer, 1994). Un second épisode de fusion partielle affecte localement les ECMs entre 307-303 Ma et est caractérisé par des conditions de BP-HT (Barféty et al., 1984 ; Fréville et al., soumis ; Bussy et al., 2000 ; Krummenacher, 1959). Dans les MT, l'épisode anatectique est peu contraint mais est généralement estimé entre 330 et 310 Ma suite à l'épaississement crustal (Schneider et al., 2014). En Corse, la fusion partielle est interprétée comme résultant de l'exhumation de terrains enfouis dans le faciès granulitique à ca. 360 Ma (Giacomini et al., 2008) ou bien entre 345 et 330 Ma en MP-MT (Li et al., 2014, Faure et al., 2014a). En Sardaigne du Nord, la fusion partielle est aussi interprétée comme induite par l'exhumation de la croûte suite à la collision continentale potentiellement entre 360 et 320 Ma (Cruciani et al., 2015b). Le Sud de la Sardaigne et les CCR ne subissent pas d'épisode de fusion partielle mise à part localement, au contact de plutons entre 320 et 290 Ma (Reche Estrada and Martinez, 2002).

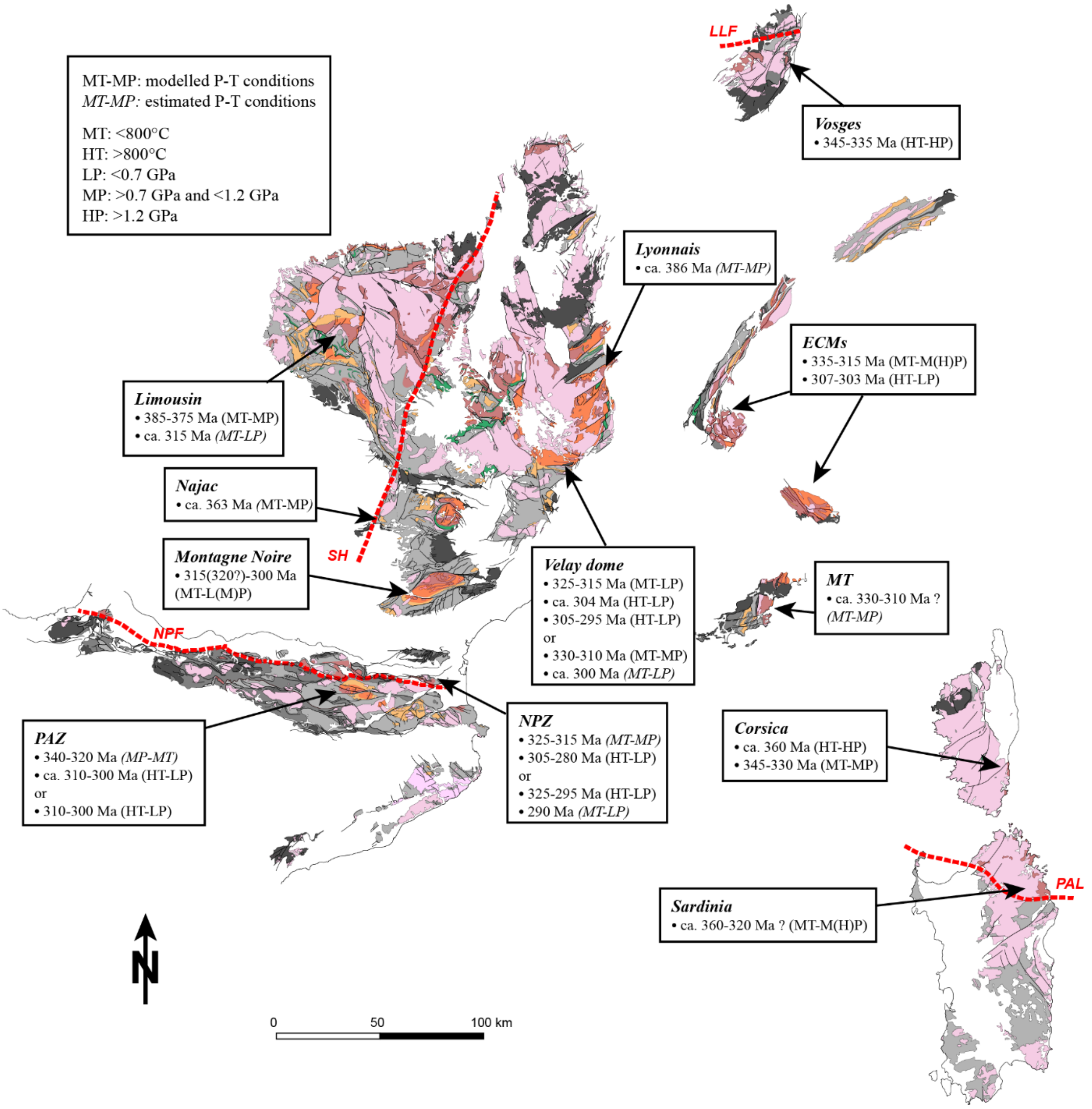

Figure 7: Review of P-T conditions and ages of partial melting events. Data are available in Table SX.

3. Corrélations entre les massifs et reconstitution paléogéographique

3.1.Les Massifs Cristallins Externes des Alpes

Les ECMs sont subdivisées en trois domaines juxtaposés par des zones de cisaillement décrochantes : Ouest, Central et Est (Guillot and Ménot, 2009 ; Ballèvre et al., 2018), ou quatre avec un domaine intermédiaire entre les domaines Central et Est (Fréville et al., en prép), sur la base des caractères du magmatisme, du métamorphisme et de la tectonique dans ces zones. Le domaine Ouest affleure dans la partie NW du massif de Belledonne et n'est que très faiblement métamorphisé et ne comporte pas de corps magmatique (Guillot and Ménot, 2009 ; Fréville et al., en prép). Il ne sera donc pas traité dans ce chapitre. En revanche, le domaine Central affleurant dans les secteurs Ouest des Aiguilles-Rouges, de Belledonne et du Pelvoux, est composé des terrains formés lors du rifting d'arrière-arc tardi-dévonien (Fig. 5) et de la majorité des corps magmatiques viséens. L'ouverture de bassins d'arrière-arc et le magmatisme associé à ce contexte de supra-subduction sont seulement décrits dans la partie Nord du Massif Central et dans les Vosges (Fig. 5 et 8A) (synthèse dans Lardeaux et al., 2014). Le magmatisme riche en Mg-K viséen est lui aussi principalement enregistré dans la partie Nord du Massif Central et dans les Vosges (Fig. 6 and 8B). Ces similitudes avec le Nord du Massif Central et les Vosges suggèrent que le domaine Central des ECMs faisait partie de l'allochtone Moldanubien.

Le domaine Est représente la plus grande superficie des ECMs. Ce domaine contient des lentilles d'éclogites plus jeunes que celles du Massif Central à l'exception de la Montagne Noire (Fig. 8A et B) et qui n'enregistrent pas le même trajet P-T (Fig. 4). En revanche, leurs trajets P-T sont similaires à ceux des éclogites de la Montagne Noire. Ce domaine enregistre un premier épisode de fusion partielle suite à l'épaississement crustal entre ca. 335-315 Ma, ce qui est assez similaire avec le début de la fusion partielle décrite dans le Velay (Ledru et al., 2001) et dans la Montagne Noire (Trap et al., 2017 ; Poujol et al., 2017) (Fig. 8C). Enfin, le domaine Est des ECMs est intrudé par de nombreux corps magmatique stéphanien et est affecté par un second épisode de fusion partielle en conditions BP-HT daté à ca. 305 Ma (Fig. 8D). Cet événement thermique stéphanien est bien enregistré dans la partie Sud du Massif Central (dôme du Velay par exemple) et dans la MN, alors qu'il est absent ou non décrit dans la partie Nord du Massif Central ou dans les Vosges (Fig. 8D). Considérant l'épaississement crustal relativement important et les quelques corps magmatiques viséens présents dans ce domaine, nous l'interprétons comme faisant partie des terrains para-autochtones. Nous proposons de rattacher le domaine Est des ECMs à la bordure Sud du plateau orogénique.

3.2.Le bloc Corse – Sardaigne – Maures-Tanneron

En Corse, au Nord de la zone de cisaillement de Porto Vecchio, un métamorphisme de HP-UHT est décrit dans des granulites felsiques à 360 Ma (Giacomini et al., 2008). Ces conditions sont suivies par une anatexie à MP-MT lors de l'exhumation de la croûte profonde entre 345 et 330 Ma (Giacomini et al., 2008 ; Li et al., 2014) associée à un magmatisme magnéso-potassique

(Mg-K) (Paquette et al., 2003 ; Faure et al., 2014a). Une évolution similaire est proposée dans les Vosges avec un métamorphisme de HP-UHT suivi d'une exhumation et d'une fusion partielle à ca. 340 Ma (Skrzypek et al., 2012) synchrones d'un magmatisme Mg-K (Tabaud et al., 2015 ; Guillot et al., 2020). Ces corrélations suggèrent que le Nord de la Corse faisait partie de l'allochtone Moldanubien et était probablement proche des Vosges.

La diminution du grade métamorphique depuis le Nord de la Corse vers le Sud de la Sardaigne et celui depuis la zone Interne vers la zone Externe des MT sont similaires à celui observé depuis le Nord vers le Sud du Massif Central et les nappes de la Montagne Noire, ce qui suggère une même position dans la partie Sud et externe du plateau orogénique. La partie Sud de la Corse, le Nord de la Sardaigne et la zone Interne des MT contiennent des lentilles d'éclogites emballées dans des migmatites felsiques, comme en MN ou dans les ECMs, mais ces éclogites enregistrent un trajet P-T similaire à ceux décrit par les éclogites de l'allochtone du Massif Central caractérisé par une décompression dans le faciès granulitique (Fig. 4). Le magmatisme de la Sardaigne est similaire à celui de la MN (Fig. 6) tandis que celui des MT ainsi que leur fusion partielle est semblable à ceux des ECMs (Fig. 8C). Il est donc difficile de définir l'appartenance de ces domaines aux zones autochtones, para-autochtones et allochtones Moldanubiennes, en particulier à cause du manque de données géochronologiques. Cette complexité résulte probablement des nombreuses zones de cisaillement décrochantes actives durant le Carbonifère (Simonetti et al., 2020a, 2020b, 2021 ; Giacomini et al., 2008 ; Carosi et al., 2012 ; Padovano et al., 2014) juxtaposant les différents domaines Moldanubiens comme dans les ECMs.

Le domaine Central et Sud de la Sardaigne et le domaine Externe des MT montrent le même métamorphisme de bas grade et la même structure en nappes que dans la MN et peuvent donc être rattachés à l'autochtone Moldanubien.

3.3. Les Pyrénées et les CCR

La NPZ montre un magmatisme similaire à celui de MN ainsi qu'un ou des épisodes de fusion partielle sensiblement identiques (Fig. 8C and D). Il semble donc logique d'attribuer la NPZ au domaine autochtone Moldanubien. La seule différence notable entre la NPZ et la MN est l'absence de relique éclogitique dans la NPZ (Fig. 4). Cette différence pourrait s'expliquer par la localisation de la MN en bordure du plateau orogénique tandis que la NPZ se situe dans l'avant-pays Sud de ce plateau orogénique et n'enregistre donc pas de HP. Pitra et al. (2021)

proposent même que les éclogites de la MN puissent avoir fluer depuis le nord et représenter un héritage d’une zone de subduction située au Nord du massif Central.

La PAZ a une évolution géodynamique très similaire à celle de la zone NPZ (Fig. 8 ; Cochelin et al., 2021) et l’absence de HP sont en faveur d’une appartenance à l’avant-pays Sud du plateau orogénique et à l’autochtone Moldanubien. En revanche, le magmatisme viséen dans cette zone est difficile à expliquer et à corréler avec les autres massifs (Fig. 8B).

Les CCR présentent des similarités avec le Sud de la Sardaigne avec des plis couchés et des chevauchements (Reche Estrada and Martinez, 2002), un magmatisme compris entre ca. 320 et 290 Ma (Fig. 6) et l’absence de fusion partielle régionale (Fig. 7) (Sebastian et al., 1990 ; Reche Estrada and Martinez, 2002). Plusieurs études corrèlent en effet ces massifs (Edel et al., 2014, 2015 ; Carreras and Druguet, 2014). Il est donc possible d’attribuer les CCR à l’autochtone Moldanubien.

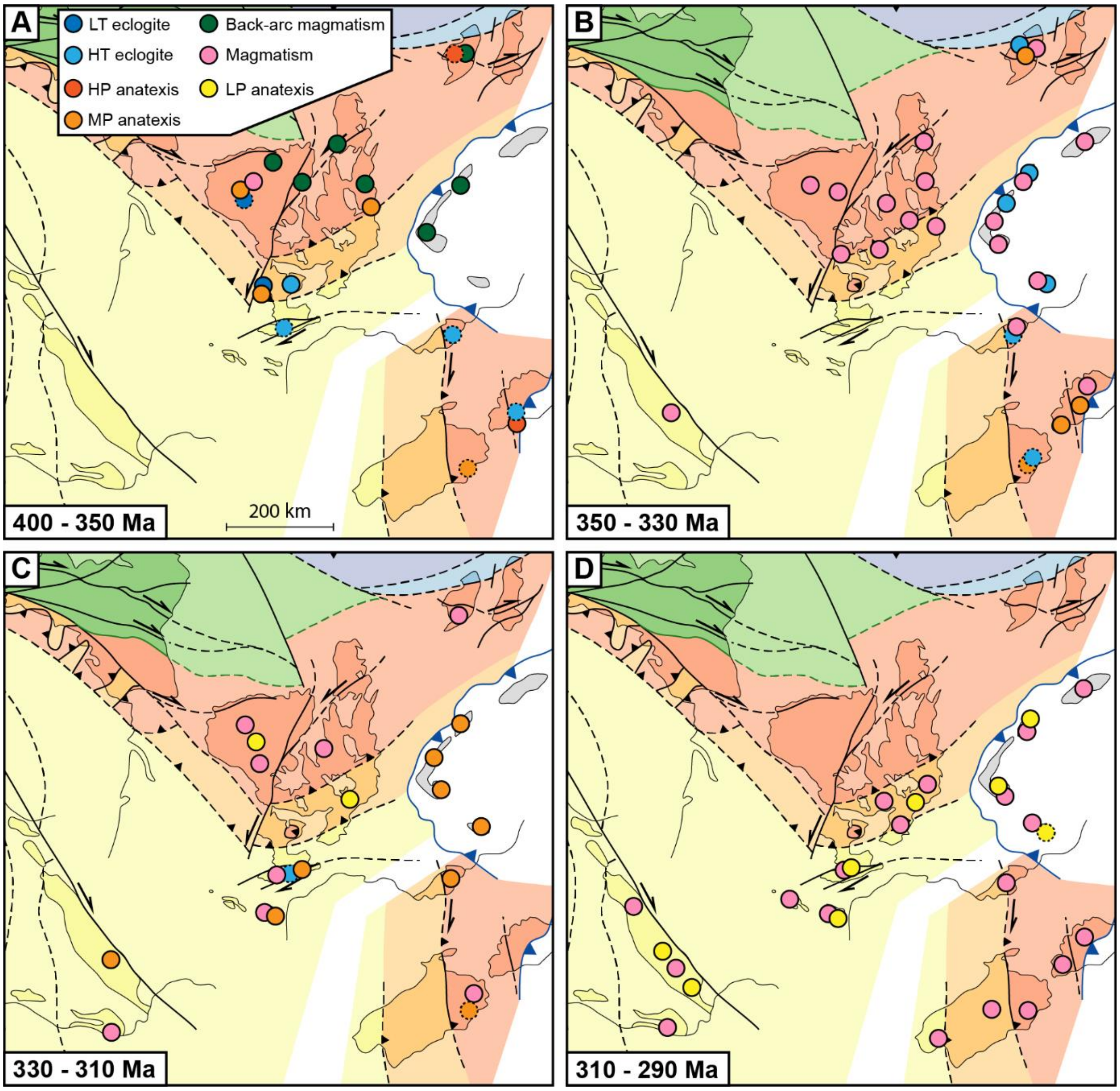

Figure 8: Evolution of metamorphic, magmatic and related back-arc setting stages of the SE Variscan branch replaced on map from Fig. 2. Dotted circles are questionable ages.

3.4.Proposition de reconstitution paléogéographique

La Figure 8 présente une proposition de nouvelle reconstitution paléogéographique toujours basée sur les reconstitutions de Lardeaux et al. (2014), Franke et al. (2017), Edel et al. (2018) et Martinez-Catalan et al. (2021). La Figure 9 reprend le principe de le Figure 7 avec la nouvelle reconstitution.

Au vu des corrélations entre (1) le Nord de la Corse et les Vosges et (2) de l’évolution du gradient métamorphique et du magmatisme vers le Sud de la Sardaigne similaire à celle observée dans le Massif Central, nous avons replacé le bloc Corse – Sardaigne – MT dans le prolongement Est du Massif Central et des Vosges, en accord avec les données paléomagnétiques d'Edel et al. (2014, 2018).

Les ECMs ont été replacés selon leur position ante-Cénozoïque proposée par Bellahsen et al. (2014). Les déformations Mésozoïques sur les ECMs forment des blocs basculés et leur impact est interprété comme assez faible (Lemoine et al., 1986). Quant aux mouvements permiens, importants pour le bloc CSMT, les données paléomagnétiques sur le massif de l'Argentera indiquent qu'ils sont faibles pour ce dernier (Bogdanoff and Schott, 1977 ; Sonnette et al., 2014). Nous interprétons donc la position ante-Cénozoïque comme proche de leur position tardi-Varisque.

Une fois ces massifs replacés, il devient assez évident de relier la zone de cisaillement Grimaud-Asinara-Posada (GAPSZ) passant en Sardaigne et dans les MT avec la zone de cisaillement Ferriere-Mollières (FMSZ) du massif de l'Argentera, comme cela est proposé dans de nombreuses études (e.g. Simonetti et al., 2018, 2020a, 2020b ; Guillot et al., 2009 ; Padovano et al., 2012). Nous proposons aussi de relier la zone de cisaillement Eastern Variscan (EVSZ) passant dans les massifs de Belledonne, des Aiguilles-Rouges et de l'Argentera avec la zone de cisaillement Porto Vecchio (PVSZ) en Corse (Fig. 9). Ces zones de cisaillement ne sont pas les seules décrites dans ces massifs, il est donc probable que cette partie de la chaîne Varisque soit composée d'un réseau anastomé de zones de cisaillement transcurrentes juxtaposant les différents domaines de la zone Moldanubienne. Cette reconstruction permet la continuité de la séquence allochtone, para-autochtone et autochtone depuis le Nord vers le Sud observée dans le Massif Central vers l'Est (Fig. 9), avec un potentiel décalage dextre au niveau de la faille des Cévennes (Chardon et al., 2020).

La bonne corrélation entre la MN et la NPZ indique que la NPZ était probablement dans une position proche de celle actuelle. En revanche, la position de la PAZ et des CCR est plus délicate à replacer dans la chaîne Varisque. Les données paléomagnétiques sur les CCR d'Edel et al. (2015) indiquent une rotation Permienne similaire à celle de la Corse et de la Sardaigne ce qui les placeraient proche de la Sardaigne (Fig. 9 option 1). En revanche, il n'y a pas de données paléomagnétiques sur les mouvements permiens de la PAZ. Une option est de considérer la PAZ et les CCR comme un bloc cohérent et donc de placer la PAZ dans la continuité de la Sardaigne (Edel et al., 2018) (Fig. 9 option 1), mais ce modèle est difficilement compatible avec les orientations des zones de cisaillement transcurrentes observées dans la PAZ et pose la question de la signification de la fusion partielle et du magmatisme ayant lieu aussi loin dans l’avant-pays de la chaîne Varisque. Une seconde option est de considérer que la PAZ était proche de l’Ibérie et de sa position actuelle (Fig. 9 option 2) mais n’explique pas les données paléomagnétiques des CCR.

Une troisième alternative est de ne pas considérer les CCR et la PAZ comme un bloc cohérent durant l’orogénèse Varisque. Les CCR peuvent donc être replacés à côté de la Sardaigne et la PAZ peut être placée dans une orientation cohérente avec les zones de cisaillement transcurrentes et dans une zone relativement proche du plateau orogénique pour pouvoir expliquer le magmatisme viséen et stéphanien (Fig. 9 option 3). Padel (2016) a montré grâce à des datations de zircons détritiques que la PAZ était initialement placée entre la Sardaigne et la MN (Fig. 9). Il est donc concevable que les CCR et la PAZ aient été juxtaposés l’un à l’autre et à l’Ibérie par les zones de cisaillement transcurrentes à la fin de l’orogénèse Varisque. De tels mouvements pourraient d’ailleurs être à l’origine de la formation de l’orocline Ibéro-Armoricain. Des données paléomagnétiques supplémentaires sur la PAZ seraient nécessaires pour étayer ou non cette hypothèse.

Cette reconstitution paléogéographique apporte une structure cohérente avec les zonations définies par les conditions métamorphiques, les ouvertures de bassins d’arrière-arc et les épisodes magmatiques (Fig. 10). Il nous faut néanmoins signaler que les déplacements engendrés par les zones de cisaillement transcurrentes restent inconnus et n’ont donc pas été représentés au cours du temps sur la Figure 9 malgré leur impact important sur l’emplacement des massifs de la branche SE Varisque. La Figure 9 ne peut donc pas être considérée comme une reconstitution de l’évolution paléogéographique au cours du temps mais permet d’illustrer une cohérence de la répartition spatio-temporelle du métamorphisme et du magmatisme dans la zonation de la chaîne.

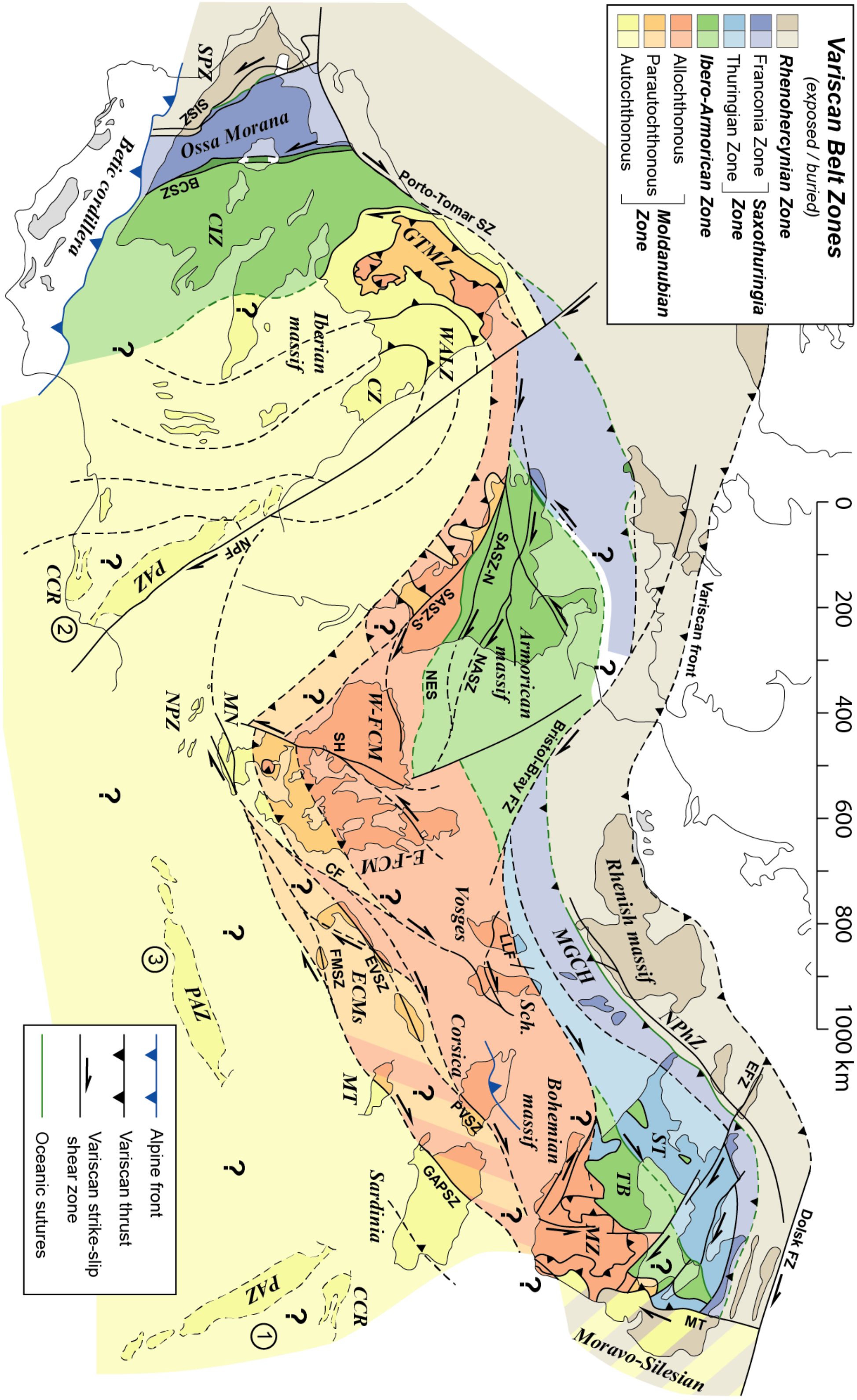

Figure 9: Sketch of the Variscan belt in an early Permian reconstruction at the end of the Variscan orogeny modified based on correlations discussed in the text. Positions of the PAZ and CCR remain elusive and the three options are discussed in the text. Abbreviations are the same than Fig. 2 except CF: Cévennes Fault; EVSZ: Eastern Variscan Shear Zone; FM: Ferriere-Mollières Shear Zone.

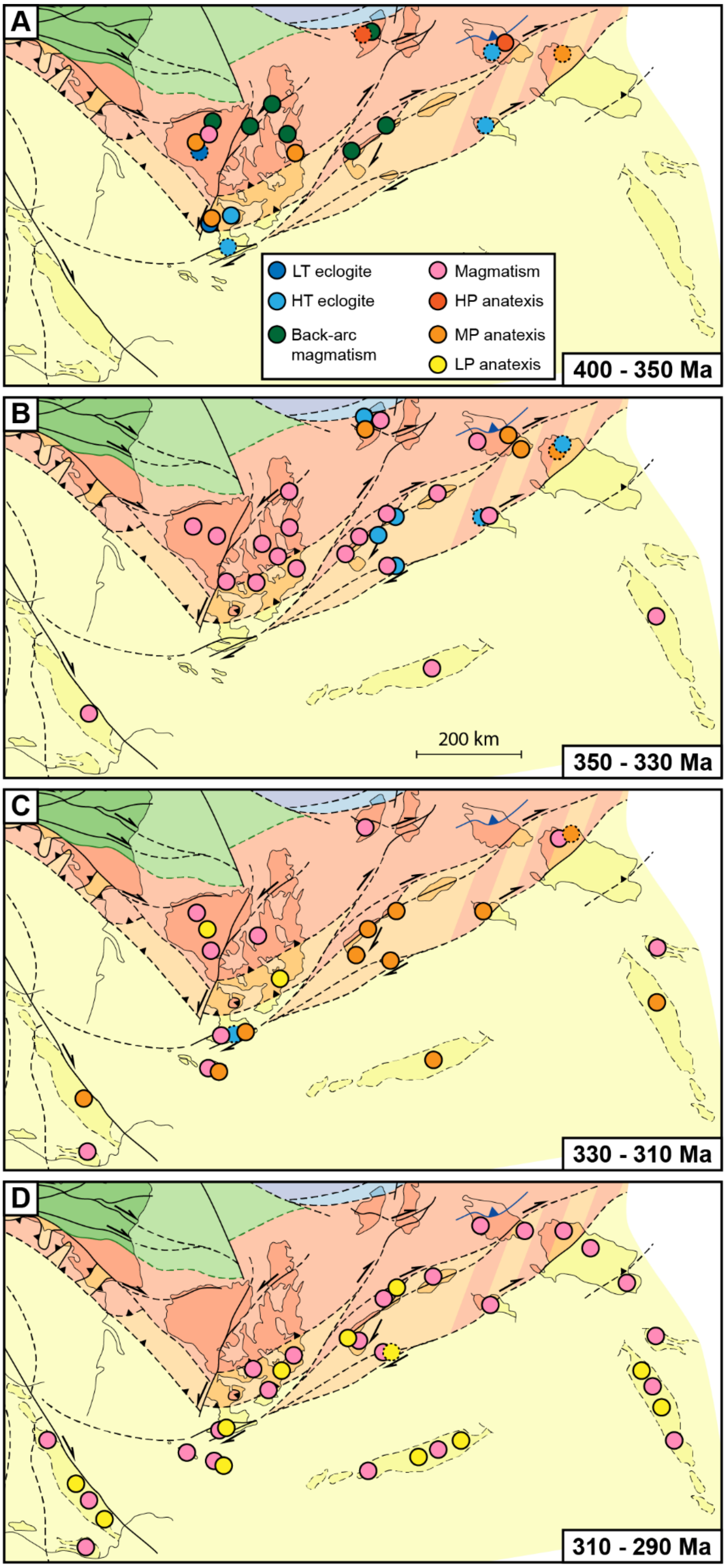
A
LT eclogite
HT eclogite
Back-arc magmatism
Magmatism
HP anatexis
MP anatexis
LP anatexis
400 - 350 Ma
B
200 km
350 - 330 Ma
C
330 - 310 Ma
D
310 - 290 Ma

Figure 10: Evolution of metamorphic, magmatic and related back-arc setting stages of the SE Variscan branch replaced on map from Fig. 9. Zoning of the metamorphic, magmatic and geodynamic events is continuous in this configuration than in the one in Fig. 8.

4. Implications pour la chaîne Varisque

4.1.Structure en double orocline et position de l'EVSZ

Le repositionnement du bloc CSMT comme proposé dans la Figure 8 rend caduque le modèle proposé par Matte (2001) impliquant une structure avec deux oroclines, l'un en Ibérie et l'autre au niveau des MT. Ce modèle était très souvent associé à celui de l'EVSZ passant à travers les ECMs et le bloc CSMT (e.g. Guillot et al., 2009 ; Padovano et al., 2012 ; Duchesne et al., 2013 ; Simonetti et al., 2018, 2020a, 2020b). Notre reconstruction paléogéographique ne remet pas en cause l'existence de l'EVSZ mais la replace dans une orientation plus cohérente avec les autres zones de cisaillement dextres de la chaîne Varisque formant un réseau anastomosé de zones de cisaillements crustales (e.g. Ballèvre et al., 2018) donc la direction est ici proche de l'orientation générale de la chaîne. Les zones de cisaillement ont très probablement joué un rôle important dans l'accommodation du fluage longitudinal de la croûte inférieure qui sera discuté dans le chapitre suivant.

4.2.Y a-t-il une suture océanique dans la branche SE ?

La localisation d'une ancienne suture océanique démembrée dans la branche SE Varisque a été invoquée dans de nombreuses études dont certaines sont très récentes (e.g. Schneider et al., 2014 ; Gerbault et al., 2018 ; Guillot and Ménot, 2009 ; Fréville et al., 2018 ; Jouffray et al., 2020 ; Regorda et al., 2019). Ces modèles se basent sur la présence de lentilles d'éclogites mafiques et de LAC, mais ils diffèrent significativement d'un massif à l'autre. Dans les ECMs, la HP a récemment été daté à 340-335 Ma (Rubatto et al., 2010 ; Jacob et al., 2021 ; Vanardois et al., soumis) ce qui est trop jeune pour être rattaché à la subduction océanique enregistrée dans le Nord du Massif Central et dans le Sud du massif Armoricain à la fin du Dévonien (Paquette et al., 2017 ; Lotout et al., 2018, 2020) et implique donc l'existence d'une nouvelle zone de subduction. Les conditions P-T obtenues sur ces lentilles d'éclogites indiquent des gradients anormalement chauds si l'on considère que ces roches proviennent d'une zone de subduction classique avec un gradient dP/DT faible (Jacob et al., 2021 ; Vanardois et al., soumis ; Ferrando et al., 2008). Jouffray et al. (2020) proposent un modèle de subduction d'une croûte océanique chaude. Or les protolithes de ces éclogites sont majoritairement interprétés comme étant des tholéiites continentales mises en place aux alentours de 460 Ma (e.g. Paquette et al., 1989 ; Schaltegger et al., 2003 ; Bussy et al., 2011 ; Vanardois et al., soumis ; Jacob et al., 2021), soit 120 Ma avant leur subduction ce qui leur laisse largement le temps de se refroidir. De plus, les éclogites des Aiguilles-Rouges n'étaient pas saturées en H_2O lors de leur enfouissement et le deviennent au cours de leur exhumation (Vanardois et al., soumis) au contraire des conditions habituelles en subduction classique (e.g. Faccenda et al., 2009; Angiboust and Agard, 2010; van Keken et al., 2011; Freundt et al., 2014) et les métasédiments associés n'enregistrent pas de gradient de HP-BT (Vanardois et al., en prép d). Il apparaît donc très peu probable que la HP carbonifère des ECMs soit liée à la subduction d'une ancienne croûte océanique. Alternativement, des processus de subduction intracontinentale ou d'épaississement crustal sont proposés dans la MN pour y expliquer les reliques d'éclogites (e.g. Faure et al., 2014b ; Whitney et al., 2015) et sont des solutions plus cohérentes avec les éclogites des ECMs. En MN, les pressions atteignent 1.4-2.0 GPa, soient ca. 50-70 km de profondeur en considérant une densité de 2800 kg.m^{-3}, ce qui est cohérent pour un plateau orogénique. Les températures en base de croûte y sont tamponnées aux alentours de 700-750 °C par la chaleur latente consommée lors de la fusion partielle des matériaux felsiques (e.g. Trap et al., 2017).

Dans le bloc CSMT, la GAPSZ est parfois considérée comme localisée sur une ancienne suture océanique (Rossi et al., 2009 ; Schneider et al., 2014 ; Casini et al., 2015). Certains auteurs proposent aussi la localisation de deux sutures en Corse (Faure et al., 2014a ; Li et al., 2014). Le manque de données géochronologiques sur la HP dans ces massifs empêche de la corréler avec les autres massifs Varisque. Néanmoins, la similarité entre les conditions de HP-HT dans ces éclogites avec celle des ECMs (Fig. 4) suggère une histoire commune. Certains auteurs proposent d'ailleurs une subduction intracontinentale d'une croûte initialement amincie (e.g. Giacomini et al., 2006, 2008). Il est aussi possible que l'extension Cambro-Ordovicienne affectant la marge Nord du Gondwana ait ouvert d'étroits bassins océaniques similaires à celui de Chamrousse dans les ECMs qui furent ensuite enfouis durant la collision continentale carbonifère, formant localement des LAC avec des paragénèses de HP dans ces massifs.

5. Conclusion

La reconstitution de l'évolution géodynamique des ECMs et la compilation de données sur l'évolution métamorphique, géodynamique et magmatique des massifs de la branche SE Varisque nous permettent de proposer une reconstitution de la chaîne Varisque qui prend en compte la Zone Nord Pyrénéenne, les Massifs Cristallins Externes des Alpes et nous permet aussi d'envisager des zones de cisaillement majeurs structurant la branche SE Varisque. Cette nouvelle reconstitution nous permet aussi de discuter des positions du bloc Corse – Sardaigne – Maures-Tanneron et de la Zone Axiale des Pyrénées entre 400 et 300 Ma. Cette reconstitution illustre une zonation depuis le Nord vers le Sud avec un magmatisme et un métamorphisme principalement viséen dans le Nord de la zone Moldanubienne et un métamorphisme de BP-HT stéphanien associé à un magmatisme abondant dans la partie Sud.

Données supplémentaires

Les Tables S1, S2 et S3 sont disponibles en Annexe 6.

Chapitre 10. Discussions des processus de fluage et de nucléation de zones de cisaillement

Dans ce dernier chapitre, les modalités du fluage de la croûte au niveau des ECMs est discuté et intégré à l'échelle de la chaîne Varisque. Une comparaison est proposée avec la chaîne Himalayenne-Tibétaine. Dans une deuxième partie, un modèle de nucléation et de croissance des zones de cisaillement d'échelle crustale dans la croûte migmatitique est proposé sur la base des observations de terrain et résultats présentés dans le chapitre 7.

Partie 1 : Le fluage de la croûte partiellement fondue

1. Le fluage dans la Chaîne Varisque

Le fluage de la croûte partiellement fondue est contrôlé par les forces tectoniques, les gradients de pressions et les contrastes de densité entre le liquide silicaté produit par la fusion partielle et les roches non fondues (e.g. Vanderhaeghe, 2009) (Fig. 1a). En fonction de l'équilibre de ces forces, le fluage de la croûte partiellement fondue peut être vertical, longitudinal (parallèle à la chaîne) ou latéral (perpendiculaire à la chaîne) (Fig. 1b).

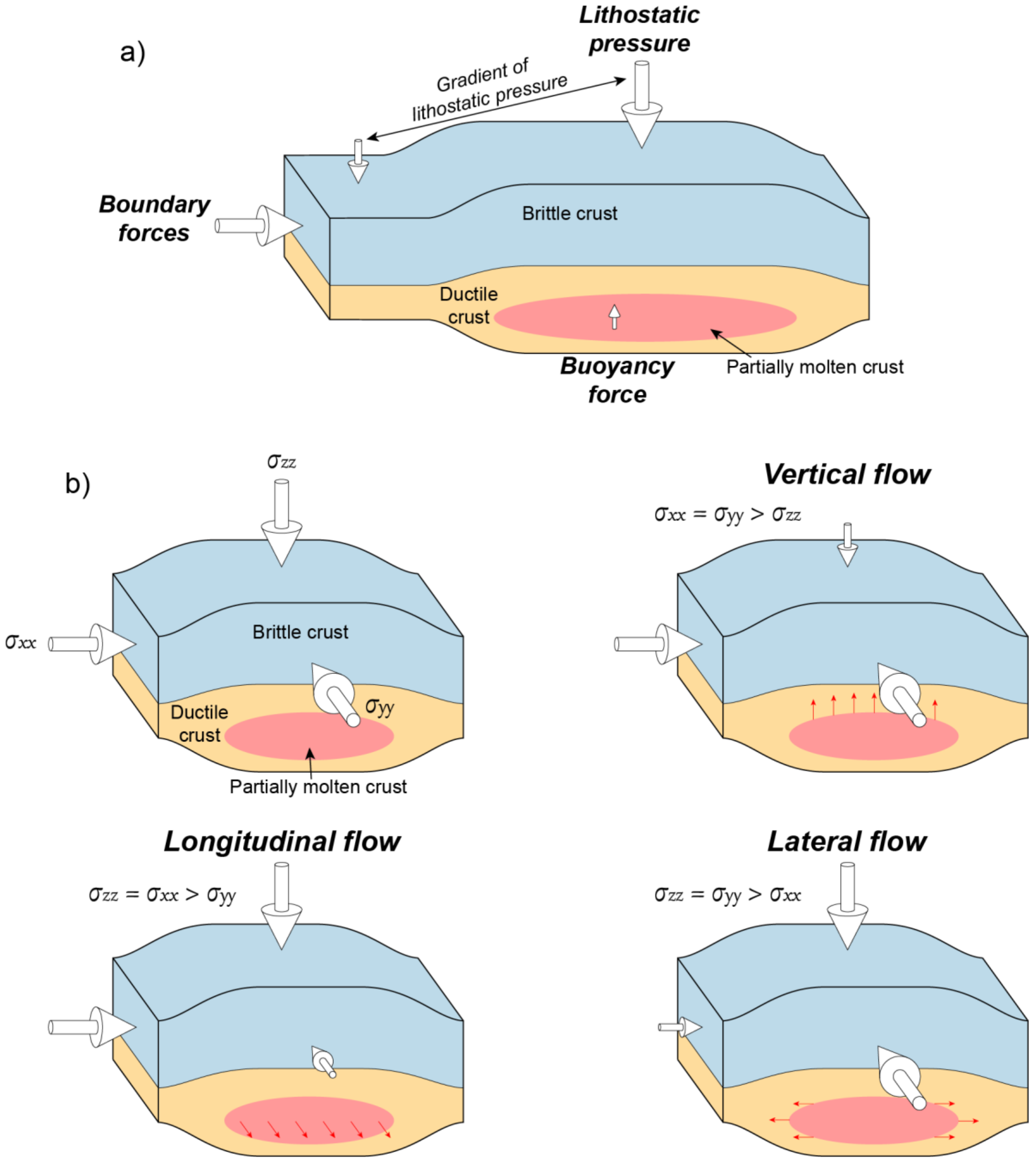

Figure 1: The three main direction of the flow of the molten crust controlled by the stress tensors. The vertical tensor (σ_{zz}) is composed of the gravity force and by the opposite stress of the buoyancy force.

1.1.Le fluage gravitaire latéral.

Des directions de fluage latéral ont été observées et décrites dans le Sud du massif de la Bohème (Schulmann et al., 2008, 2014), dans le massif Ibérique (Bento dos Santos et al., 2021) et dans la Zone Nord-Pyrénéenne (Vanardois et al., in prep c) (Fig. 4). Ces fluages latéraux sont induits par des gradients de pression lithostatique entre les zones internes et externes de la Chaîne Varisque. Ce fluage latéral à lieu entre ca. 355 Ma et 325 Ma dans le massif de la

Bohème (Schulmann et al., 2008, 2014) et environ entre 330 et 305 Ma dans le Massif Ibérique (Bento dos Santos et al., 2021).

Dans le Massif Central, Vanderhaeghe et al. (2020) proposent un modèle avec un fluage gravitaire latéral vers le Sud participant d'abord à la formation du plateau orogénique puis à l'effondrement de la chaîne synchrone du fluage de la croûte partiellement fondue dans l'avant-pays (i.e. Montagne Noire et Pyrénées). Ce fluage latéral serait aussi accompagné d'un fluage longitudinal depuis l'Ouest vers l'Est du Massif Central. La direction du fluage gravitaire serait induit par le retrait du panneau lithosphérique plongeant à vergence Nord vers le Sud entrainant un amincissement du manteau lithosphérique et de la croûte orogénique et formant donc un gradient de pression lithostatique vers le Sud, en plus d'être augmenté par la différence de pression lithostatique entre l'avant-pays et le plateau. Ce modèle se base sur un rajeunissement des âges magmatiques vers le Sud (Laurent et al., 2017) mais n'a pas été directement observé sur le terrain et ne considère peu l'impact des nombreux décrochements dextres structurant la croûte Varisque. Dans la continuité de ce modèle, le fluage latéral vers le Sud est aussi proposé en Montagne Noire avec l'avancée d'un front de fusion partielle depuis le Nord vers le Sud (Whitney et al., 2015 ; Roger et al., 2020), charriant potentiellement les éclogites de la Montagne Noire (Pitra et al., 2021). Nos données sur le massif de l'Agly (Zone Nord-Pyrénéenne) sont plutôt en accord avec la proposition d'un fluage latéral gravitaire depuis le plateau orogénique (i.e. Massif Central) vers l'avant-pays (i.e. Pyrénées et Montagne Noire) entre ca. 325-300 Ma (Vanardois et al., in prep c). En revanche, l'amincissement du manteau lithosphérique pourrait aussi entrainer une surrection du manteau asthénosphérique induisant une augmentation de la pression verticale (Göğüş & Pysklywec, 2008), et donc la pression « lithostatique », ce qui empêcherait ou limiterait le fluage gravitaire vers le Sud. En outre, Vanderhaeghe et al. (2020) proposent que l'effondrement gravitaire de la chaîne Varisque à la fin du Carbonifère est accommodé par des détachements formant des dômes migmatitiques en raison d'une extension finale environ N-S. Or nos résultats sur les Aiguilles-Rouges et les études traitants de la fin du Carbonifère dans la Zone Axiale des Pyrénées et dans la Montagne Noire indiquent plutôt une exhumation de la croûte profonde par des failles transcurrentes à la fin du Carbonifère (e.g. Vanardois et al., in review ; Cochelin et al., 2017, 2020 ; Chardon et al., 2020 ; Roger et al., 2015, 2020). Dans la Zone Nord-Pyrénéenne, l'extension tardi-Carbonifère est interprétée comme une accommodation des mouvements transcurrents dextres (Vanardois et al., in prep). Nous proposons donc que l'accommodation des instabilités gravitaires à la fin de l'orogénèse Varisque se fait principalement par des mouvements longitudinaux et transcurrents dans la partie Sud de la chaîne, et est accompagné d'ouverture de petits bassins dans la croûte supérieure (e.g. Servoz et Salvan Dorénaz dans les Aiguilles-Rouges).

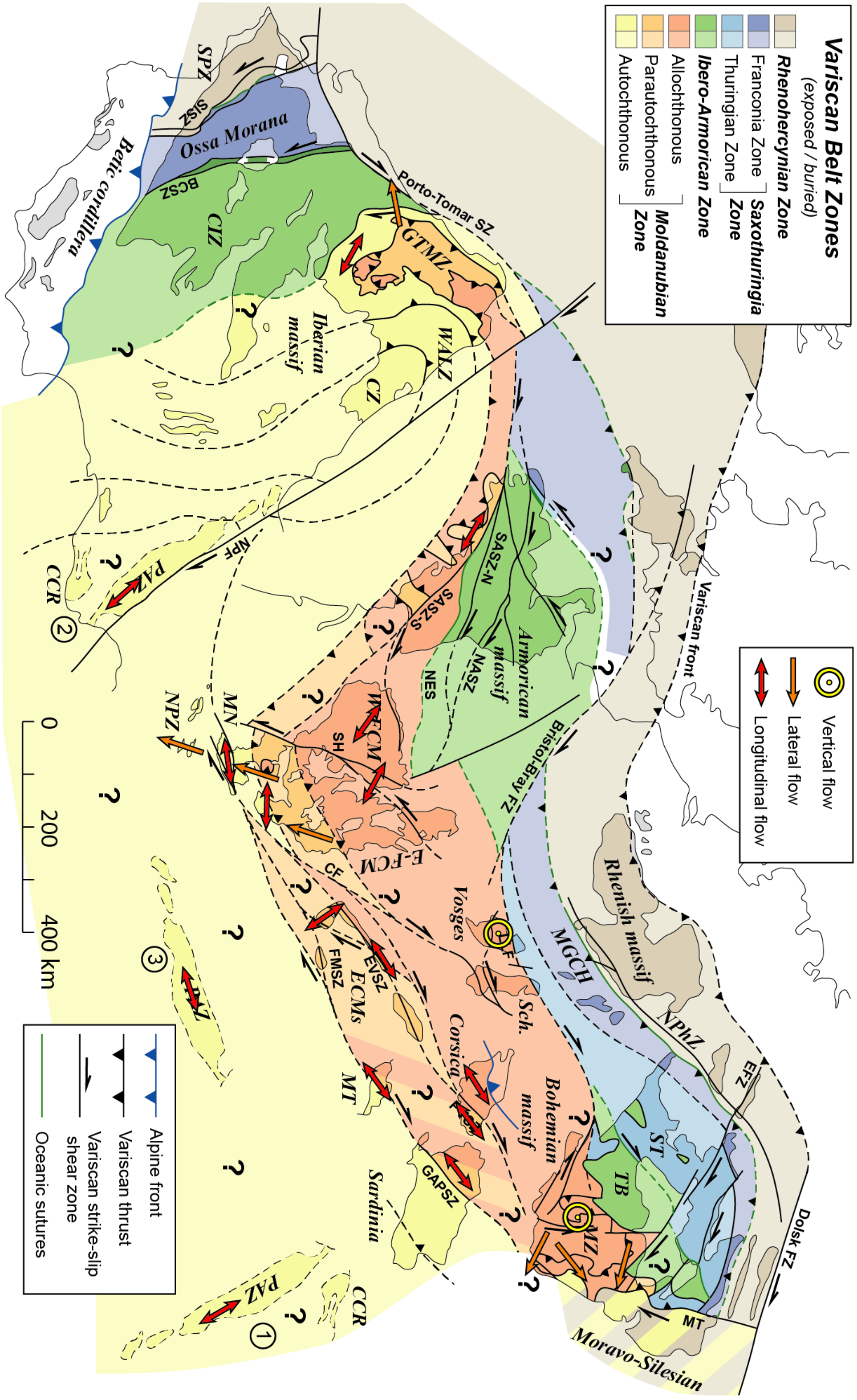

Figure 2 : Flow of the anatectic crust in the Variscan chain during Carboniferous. See figures 2 and 10 from Chapter 9 for abbreviations

1.2.Le fluage gravitaire longitudinal

Dans le massif des Aiguilles-Rouges, le fluage horizontal (mu par la gravité) de la croûte partiellement fondue est parallèle aux zones de cisaillements dextres qui s'initient vers 340 Ma (Vanardois et al., in prep). D'après notre reconstitution de la paléogéographie de la chaîne Varisque, cette direction de fluage est longitudinale. Nos modélisations thermodynamiques et nos données EBSD indiquent que ce fluage perdure au cours du début de l'exhumation (de ca. 60 km à 40 km) de la croûte inférieure entre ca. 330 et 315 Ma (Vanardois et al., in review). Au même moment dans la croûte supérieure, les décrochements dextres permettent l'ouverture d'un bassin en pull-apart au niveau du synclinal de Servoz (Vanardois et al., in prep). Cette exhumation de la croûte profonde et l'ouverture de ce bassin suggèrent un régime en transtension (Fig. 2). Cette transtention peut être très locale dans un régime transpressif de plus grande échelle (e.g. Eyal, 1988 ; D'Lemos et al., 1992). L'amincissement local créé au niveau de la transtension va localement diminuer la pression lithostatique, créant ainsi un gradient de pression lithostatique qui va induire le fluage de la croûte partiellement fondue vers cette dépression (Block and Royden, 1990 ; Kruse et al., 1991 ; Rey et al., 2009 ; Whitney et al., 2013). Ce fluage local dans les zones de dépression des zones de transtension forme des dômes migmatitiques allongés parallèlement à la direction de l'extension (Le Pourhiet et al., 2012). Ce mécanisme peut être comparé à l'exhumation de la croûte profonde du Sud du massif Armoricain aux environs de 300 Ma (Gapais et al., 2015) ou bien à la formation du dôme migmatitique de la Montagne Noire (Rey et al., 2011, 2017) et au développement associé d'un pull-apart dans un régime dextre transtensif entre 315 et 300 Ma (e.g. Franke et al., 2011 ; Roger et al., 2015 ; Trap et al., 2017 ; Chardon et al., 2020).

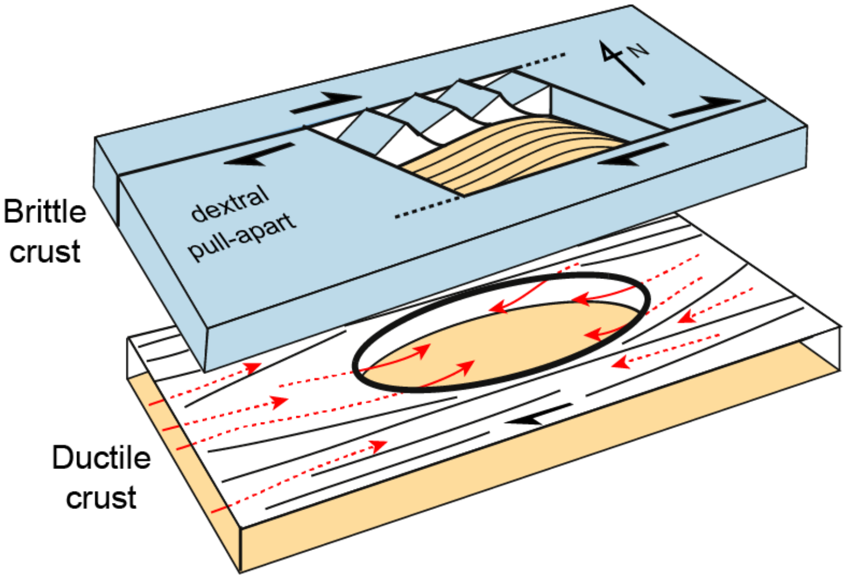

Figure 3: Longitudinal flow of the crust in a transtensive setting, modified from Roger et al. (2015)

Dans les Maures-Tanneron, la Corse, la Sardaigne et la Zone Axiale des Pyrénées, l’exhumation de la croûte partiellement fondue se fait dans un régime transpressif formant des zones de cisaillements crustales (e.g. Rolland et al., 2009 ; Corsini ad Rolland, 2009 ; Giacomini et al., 2008 ; Faure et al., 2014a ; Elter et al., 2010 ; Padovano et al., 2014 ; Cochelin et al., 2021). Une partie de cette exhumation est de l’extrusion verticale induite par les forces tectoniques compressives et par les contrastes de densité (e.g. Schneider et al., 2014 ; Gerbault et al., 2018) mais la direction de fluage de la croûte sera essentiellement longitudinale et contrôlée par les zones de cisaillements transcurrentes et les forces tectoniques compressives (Cochelin et al., 2021) (Fig. 3). Ce fluage longitudinal a lieu entre 340-320 Ma en Sardaigne (Elter et al., 2010), 320-300 Ma dans les Maures-Tanneron (Rolland et al., 2009) et entre 310 et 290 Ma dans la Zone Axiale des Pyrénées (Denèle et al., 2014 ; Cochelin et al., 2017, 2021). Dans le massif du Pelvoux, du fluage de la croûte partiellement fondue associé à des zones de cisaillements transcurrentes est aussi décrit entre 325 et 305 Ma (Fréville et al., soumis). Dans ces deux contextes, transpressif et transtensif, le fluage de la croûte est donc contrôlé par les mouvements transcurrents des zones de cisaillements crustales, par les contraintes tectoniques et par les gradients de pression lithostatique formés localement entre les zones en transpression et les zones en transtension.

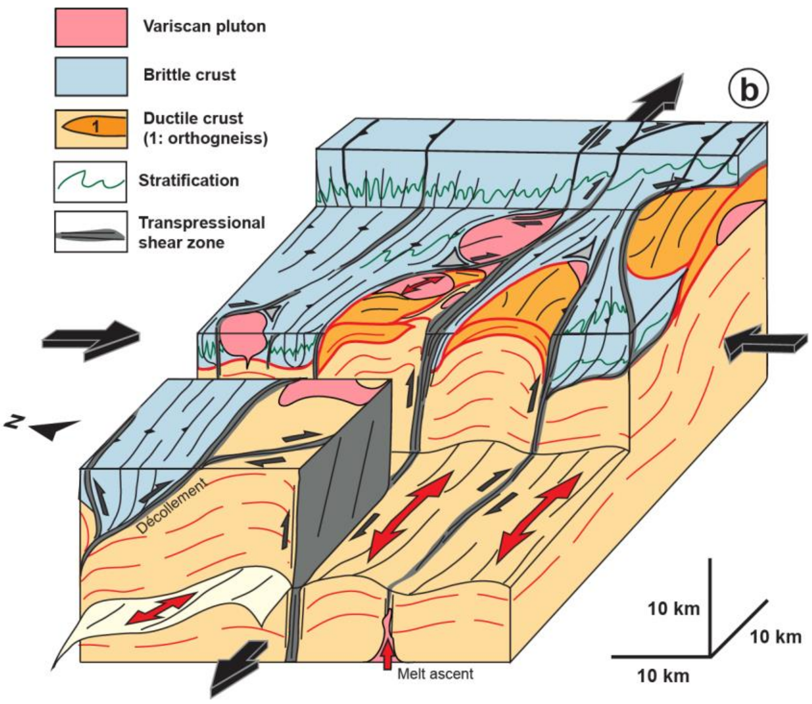

Figure 4: Longitudinal flow of the crust in a transpressive setting, modified from Cochelin et al. (2017).

1.3.Le fluage vertical

Du fluage essentiellement vertical induit par les forces tectoniques compressives et par les contrastes de densité est décrit dans les Vosges (Skrzypek et al., 2014) et le massif de la Bohème (Schulmann et al., 2008, 2014). Ces phénomènes d'extrusion verticale sont cantonnés au Nord de la Zone Moldanubienne (Fig. 4) et sont reliés à la subduction de la croûte Saxothuringienne sous la croûte Moldanubienne (Skzrypek et al., 2014 ; Schulmann et al., 2008, 2014 ; Stipská et al., 2019) (Fig. 5). De l'extrusion verticale est aussi proposée dans les massifs des Maures-Tanneron (Gerbault et al., 2018). Mis à part dans le massif de la Bohème et dans les Vosges, ce fluage vertical semble rare dans la chaîne Varisque.

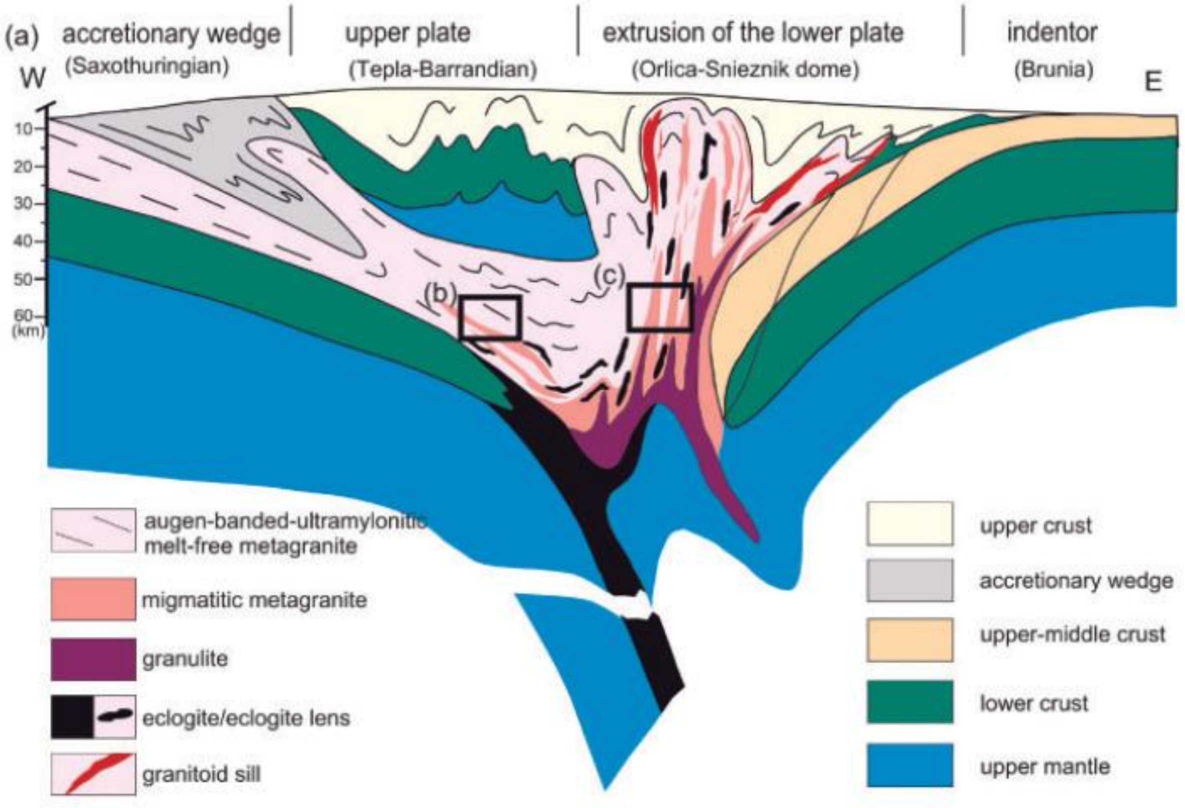

Figure 5: Vertical extrusion of the lower anatectic crust in the Bohemian massif, from Stipská et al. (2019).

2. Comparaison avec la Chaîne Himalayenne-Tibétaine

Un schéma sensiblement similaire est décrit dans la chaîne Himalayenne-Tibétaine avec des processus de fluage gravitaire latéral aux bords du plateau orogénique et un fluage général majoritairement longitudinal vers l'Est (Fig. 5) (Clark and Royden, 2000 ; Kemplerer, 2006 ; Bai et al., 2010), excepté au niveau de l'orocline du Pamir (e.g. Metzger et al., 2020). Bien que le fluage gravitaire vers le Sud soit l'objet le plus étudié dans la chaîne (e.g. Beaumont et al., 2001, 2004 ; Hollister and Grujic, 2006 ; Hodges, 2006 ; Godin et al., 2006), le fluage longitudinal de la croûte partiellement fondue vers l'Est de la chaîne est non négligeable (Fig. 5 ; Clark and Royden, 2000 ; Kemplerer, 2006) (Fig. 5). Comme dans la chaîne Varisque, ce fluage longitudinal est associé à de nombreuses failles et zones de cisaillement (Fig. 5) qui accommodent les déplacements de la croûte profonde (Yin and Taylor, 2011 ; Yuan Liu et al., 2014 ; Xu et al., 2015). Ce fluage longitudinal vers l'Est est dû aux forces compressives N-S et à un gradient de pression lithostatique vers l'Est (e.g. Tapponnier et al., 1982 ; Avouac and Tapponnier, 1993).

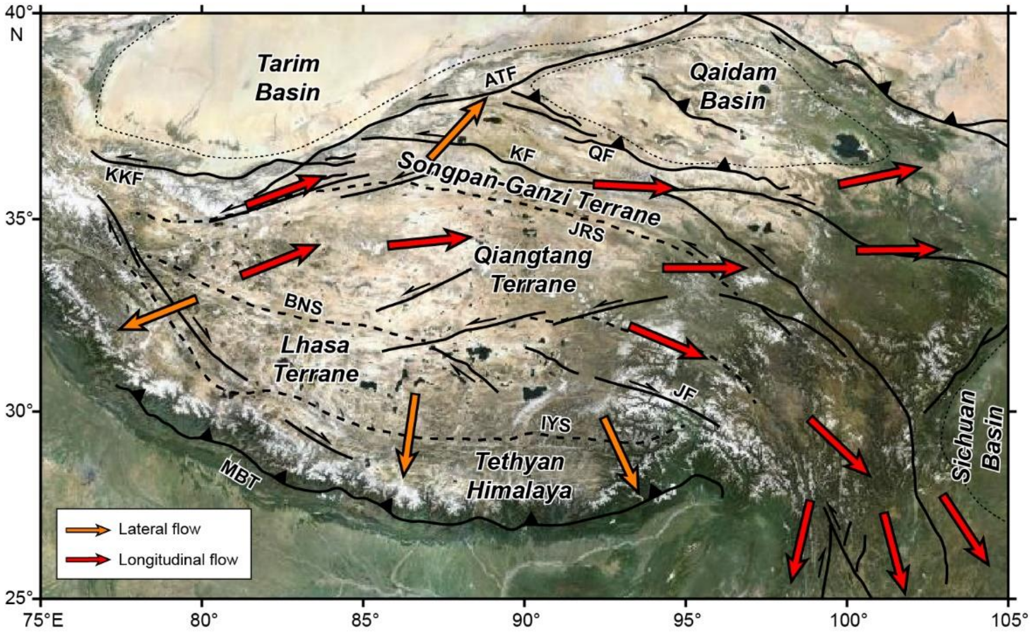

Figure 6: Main direction of middle and lower crustal channel flow in the Himalayan-Tibetan belt based on Clark and Royden (2000) and Kemplerer (2006). Main sutures, faults and kinematics are from Styron et al. (2010). Dashed line = sutures (BNS: Banggong – Nujiang suture; IYS: Indus – Yarlung suture; JRS: Jinsha River suture); black lines = faults (ATF: Altyn Tagh fault; JF: Jiali fault; KF: Kunlun fault; KKF: Karakax fault; MBT: Main Boundary thrust; QF: Qaidam Border fault).

D’après des modélisations numériques, Rey et al. (2010) soutiennent que la formation d’un plateau orogénique ne peut pas induire un fluage gravitaire latéral conséquent (de l’ordre de 1000 km) dans les zones externes en raison du refroidissement du channel flow dans l’avant-pays entrainant une augmentation de sa viscosité. Or dans le cas d’un fluage longitudinal, la température reste relativement élevée et constante au sein du plateau orogénique, favorisant donc le fluage sur de longues distances.

Dans la chaîne Varisque et Himalayenne-Tibétaine, le fluage au sein du plateau orogénique est principalement longitudinal en relation avec des failles et zones de cisaillements transcurrentes. Dans la chaîne Himalayenne-Tibétaine, le fluage semble être à sens unique vers la bordure Est du plateau orogénique (Fig. 5 and 6a). Dans la chaîne Varisque, le réseau anastomosé de zones de cisaillements forme localement des zones en transpression et d’autres en transtension induisant des gradients de pression lithostatique qui contrôlent probablement la direction du fluage (Fig. 6b), mais nous n’avons pas connaissance d’une direction préférentielle de fluage, mise à part dans la Zone Axiale des Pyrénées (Cochelin et al., 2021). Cette absence de direction préférentielle est peut-être liée à l’absence de gradient de pression lithostatique important dans les bordures Ouest et Est du plateau orogénique Varisque.

a) Himalayan-Tibetan belt

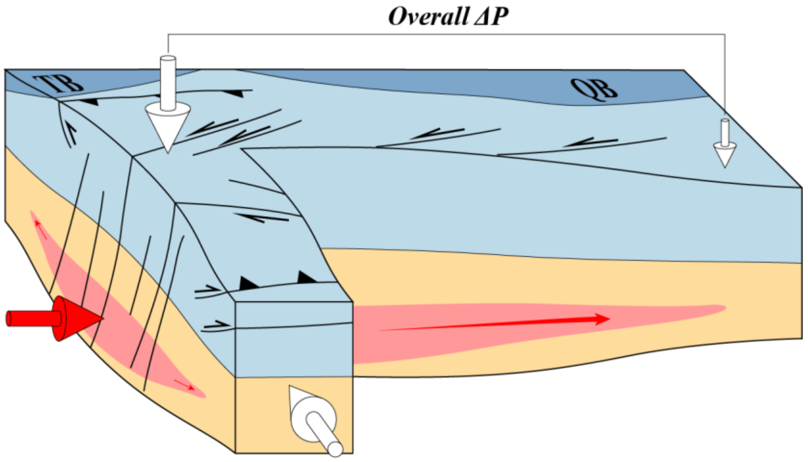

b) Variscan belt

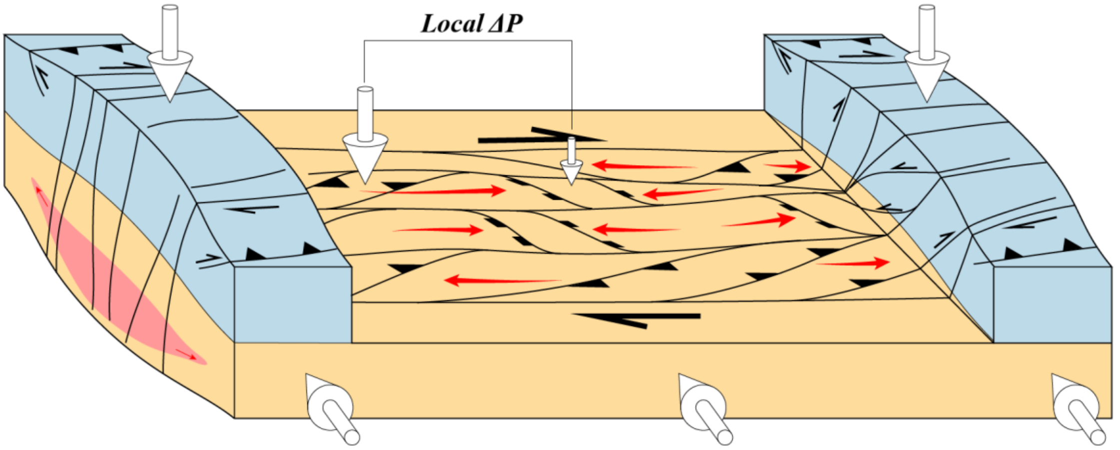

Figure 7: Sketch of the longitudinal flow in the (a) Himalayan-Tibetan and (b) Variscan belts. Red arrows represent the flow of the molten crust. White arrows represent stress tensors. ΔP = pressure gradient; QB: Qaidam basin; TB: Tarim basin.

Partie 2 : Nucléation et développement des zones de cisaillements transcurrentes d'échelle crustale

Cette seconde partie de ce chapitre est présentée sous la forme d'un article en préparation qui sera soumis à *Geology*.

Birth and growth of continental shear zones. The critical role of metagranite undergoing H_2O-present partial melting.

Jonas Vanardois[1], Pierre Trap[1], and Didier Marquer[1].

jonas.vanardois@univ-fcomte.fr; pierre.trap@univ-fcomte.fr; didier.marquer@univ-fcomte.fr.

[1]UMR 6249 Chrono-environnement, Université de Bourgogne-Franche-Comté, 25030 Besançon, France.

*Corresponding author: jonas.vanardois@univ-fcomte.fr +33(0)381666242 Present address: 16 route de Gray, 25030 Besançon.

Abstract

Where, when and why large-scale shear zones nucleate and propagate into the continental lithosphere is a critical issue that challenges the geological community. The East Variscan Shear Zone is an orogen scale, strike-slip fault that formed within the Variscan orogenic crust during late Carboniferous times. Field-based strain analysis and structural, microstructural and petrological observations demonstrate that suprasolidus high-strain deformation zones and metagranite intrusions are actually spatially related. Among the three dominant lithologies forming the studied orogenic middle crust in that part of the belt, i.e. metapelite, metagreywacke and metagranite, petrological observations and phase equilibrium modelling argue that the latter lithology is the most fertile and, in response to H2O-fluid-saturated melting, melts at lower

temperature in the course of regional Barrovian-type metamorphism. Our data and modelling suggest that the water-fluxed melting of metagranite has a primary control on the birth and growth of crustal-scale shear zones at depth of in the middle crust. Thus, granite intrusion distributions would be regarded as critical objects influencing the crustal rheological inheritance that governs the tectonic evolution and bulk strain localization in continental arcs, collisional orogens and continental rifts.

1. Introduction

Localized deformation along crustal or lithospheric-scale shear zones is the first process controlling the reorganization of continental masses along convergent plate boundaries and continental breakup in divergent settings. With depth, strain distribution varies from narrow brittle faults in the upper crust to a broad ductile shear zone and shear zone network in the deep crust and lithospheric mantle (Teyssier and Tikoff, 1998; Vauchez and Tommasi, 2003; Fossen and Cavalcante, 2017). Where and when large-scale shear zones nucleate and what governs the localization of shear at depth remains a matter of debate. Field-based studies of exhumed shear zones, numerical and experimental works describe several strain-weakening processes responsible for localization including fabric development, shear heating, metamorphic reactions, grain size reduction, melt-presence or fluid circulation. The roles and contributions of each of the strain-weakening parameters are readily identified from the micro- to meter-scale. By contrast, they are much more difficult to assess at the scale of the continental crust or lithosphere typified by rheological inheritance because of inherent structural and lithological complexities. Above all, a primary control given by mechanical heterogeneity (with weak vs strong phases) is needed to nucleate a shear zone regardless of the scale (e.g. Tommasi et al., 1995; Holyoke and Tullis, 2006; Cao et al., 2016; Gardner et al., 2017).

Into the mid- and lower-orogenic crust, the presence of melt is the main weakening parameter leading to drastic strength drop of the partially molten rock compared to its un-molten counterpart (e.g. Handy et al., 2001; Rosenberg and Handy, 2005; Rosenberg et al., 2007). Crustal melt content depends on melting reactions, P-T conditions, melt drainage or storage (e.g. Vielzeuf et al., 1990; Brown, 2001; Genier et al., 2008; Rennie et al., 2013; Diener and Fagereng, 2014; Lee et al., 2020) and is therefore strongly impacted by compositional and structural inheritance.

In the Aiguilles-Rouge massif (French Alps) (Fig. 1a), the East Variscan Shear Zone (EVSZ) gives the opportunity to learn more about where and when the nucleation of a crustal scale shear zone operates. This study also discuss how the EVSZ broadens and propagates inside the crust that recorded a typical orogenic evolution with burial and heating, partial melting at peak temperature conditions followed by exhumation and cooling. Through regional scale detailed field mapping, microstructural and petrological observations supported by phases equilibrium modelling, we highlight the critical role of metagranite acting as the target rock for diffusive H_2O-fluxed melting and the root cause for nucleation and shaping of orogen-scale shear zones.

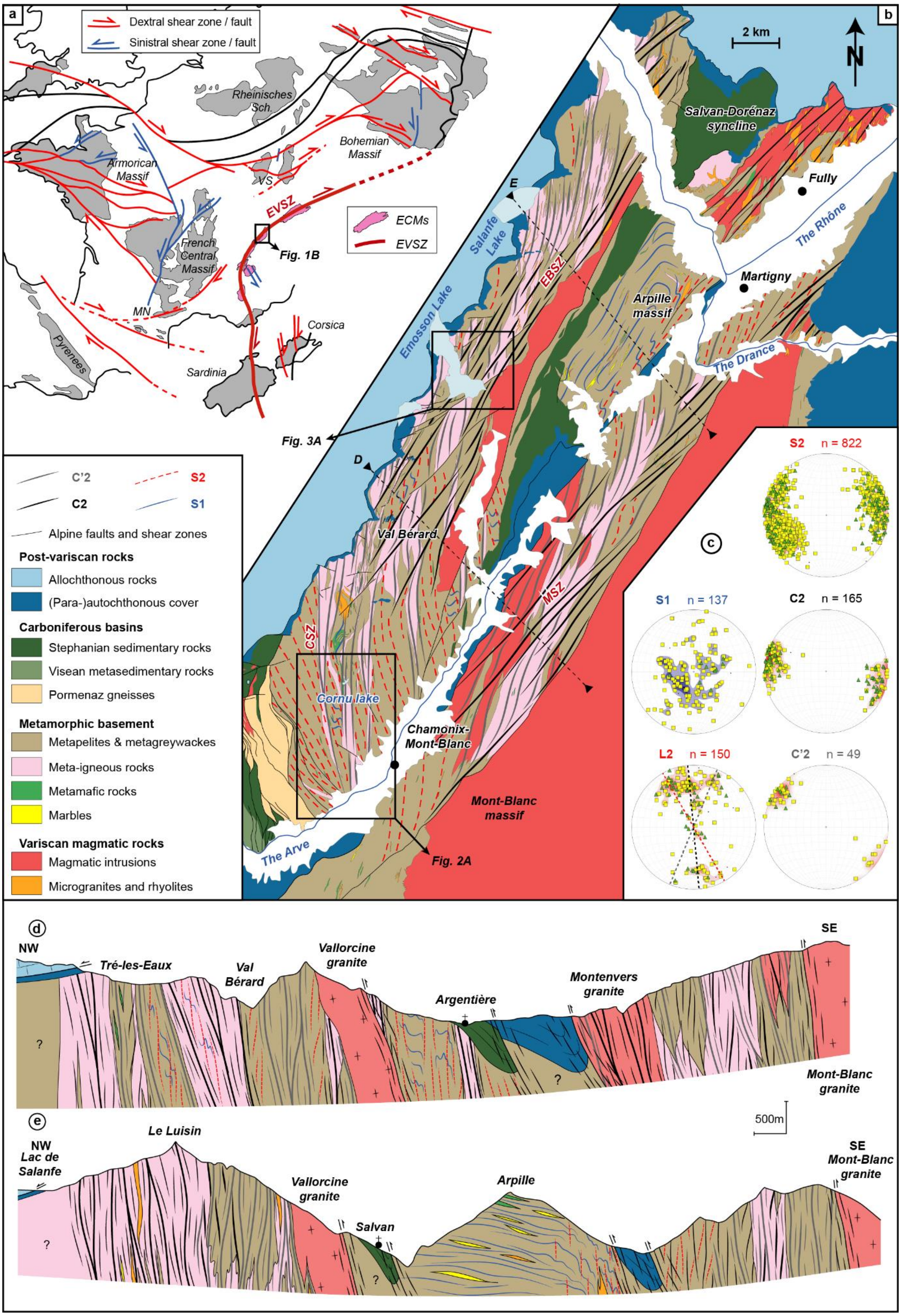
a
Dextral shear zone / fault
Sinistral shear zone / fault
Rheinisches Sch.
Bohemian Massif
Armorican Massif
VS
EVSZ
ECMs
EVSZ
French Central Massif
Fig. 1B
MN
Corsica
Pyrenees
Sardinia
b
2 km
N
Salvan-Dorénaz syncline
Fully
The Rhône
Martigny
Salanfe Lake
E
EBSZ
Arpille massif
The Drance
Emosson Lake
Fig. 3A
D
Val Bérard
MSZ
CSZ
Cornu lake
Chamonix-Mont-Blanc
Mont-Blanc massif
The Arve
Fig. 2A
C'2
S2
C2
S1
Alpine faults and shear zones
Post-variscan rocks
Allochthonous rocks
(Para-)autochthonous cover
Carboniferous basins
Stephanian sedimentary rocks
Visean metasedimentary rocks
Pormenaz gneisses
Metamorphic basement
Metapelites & metagreywackes
Meta-igneous rocks
Metamafic rocks
Marbles
Variscan magmatic rocks
Magmatic intrusions
Microgranites and rhyolites
c
S2 n = 822
S1 n = 137
C2 n = 165
L2 n = 150
C'2 n = 49
d
NW
Tré-les-Eaux
Val Bérard
Vallorcine granite
Argentière
Montenvers granite
SE
Mont-Blanc granite
?
?
e
500m
NW
Lac de Salanfe
Le Luisin
Vallorcine granite
Salvan
Arpille
SE
Mont-Blanc granite
?
?

Figure 1: (A) Paleogeographic reconstitution of the European Variscan Belt at the end of the Variscan orogeny modified from Franke et al. (2017). Localization of the EVSZ is from Simonetti et al. (2020a). EVSZ: Eastern Variscan Shear Zone; MN: Montagne Noire; VS: Vosges-Schwarzwald. (B) Geological map of the Aiguilles-Rouges and the Mont-Blanc Massifs (ARMBM) with simplified foliation trajectories of S1, S2, C2 and C'2 with (C) poles of planar fabrics and lineations (lower Wulf hemisphere stereograms); yellow square = metasedimentary rocks; green triangles = orthogneiss; black dots = other rocks. (D and E) SE-NW Cross-sections through the ARMBM (see location of sections on Figure 1B). Areas corresponding to Figures 2A and 3A are indicated. CSZ: Cornu Shear Zone; EBSZ: Emosson Bérarde Shear Zone; MSZ: Montenvers Shear Zone.

2. Geological setting

The EVSZ is a 10 km wide and 600 km long, strike-slip shear zone recognized in the migmatitic crust of the Variscan External Crystalline Massifs (ECMs; Fig. 1a) and beautifully exposed in the Aiguilles-Rouges and Mont-Blanc massifs, in the French Alps (ARMBM; Fig. 1b; Guillot et al., 2009; Simonetti et al., 2020a). The strain pattern of the main the ARMBM is defined by a subvertical foliation striking from N150 to N30 that holds a moderately plunging mineral stretching lineation along which dextral kinematics is conspicuous and interpreted as a bulk dextral transpression that lasted *ca*. 20 Ma at least (von Raumer & Bussy, 2004 and references therein; Simonetti et al., 2020a). As the Alpine deformation was limited to low grade shear zones where metamorphism does not exceed 450°C (von Raumer and Bussy, 2004 and references therein), the high-grade variscan tectono-metamorphic features are confidently identified. The ARMBMs expose a typical collisional mid-lower crust composed of high-grade metapelites, metagreywackes and meta-igneous intrusions, i.e. orthogneisses and leucogneisses (Fig. 1b). Orthogneisses are mainly Bi-K-feldspar augengneisses with granodiorite to monzogranite compositions. The climax of Barrovian-type metamorphism reached P-T conditions of 600-750 °C/0.8-1.5 GPa (von Raumer and Bussy, 2004 and references therein) followed by a nearly isothermal decompression down to 600-700 °C/0.2-0.6 GPa (Genier et al., 2008; von Raumer and Bussy, 2004 and references therein). Very low melt fraction in the metasedimentary rocks argues for limited partial melting in comparison to the meta-igneous rocks (mainly orthogneisses) that show a high melt fraction (von Raumer and Bussy, 2004). Melt fraction in the migmatitic orthogneisses often reaches 20-30 vol%. Such high volumes of melts in metagranite migmatites are usually attributed to water-flux melting (Sawyer, 2010; White et al., 2005; Weinberg and Hasalová, 2015). These observations argue that migmatization in the ARMBM was predominantly controlled by water-present melting reactions that consume quartz, feldspar and H2O, for the four different lithologies, consistently with the P-T conditions. Advection of water-rich fluid along the Emosson-Bérard Shear Zone (EBSZ, Simonetti et al., 2020a; Fig. 1) promoted partial melting of metagreywacke near the Lac Emosson (Genier et al., 2008). In line with that view we present a detailed field-based structural analysis that highlights the spatial relationships between shear zone development and H_2O-fluxed melting depending on the lithological nature of the protolith, at the regional scale.

3. Crustal-scale shear zones network

Our detailed mapping revealed that the EVSZ is actually made of a complex strain pattern developed during D2 dextral transpression. A steep NNW-SSE trending transpression-related foliation (S2) resulted from folding and transposition of an initially shallowly dipping lithological and metamorphic layering S1 (Fig. 1b-e). In low-D2 strain areas, the early flat-lying S1 is best recognized through stromatic layering in migmatitic orthogneisses. The regularly NNW-SSE trending S2 foliation is deflected and offset by three bands of higher strain striking N-S to NE-SW (Fig. 1b): the Cornu Lake Shear Zone (CLSZ), the Emosson-Bérard Shear Zone (EBSZ) and the Montenvers Shear Zone (MSZ). These high-strain corridors are 2-5 km wide and typified by sub-vertical shear foliation and mylonites with sub-horizontal to moderately plunging lineations (Fig.1c-e). Along the shear zone boundaries, a D2 strain gradient ranges from open to tight doubly plunging meter-scale F2 folds to rootless F2 hinges with S2 axial plane. In these high-strain zones, the S1-2 foliation is sheared by C2 and C’2 shear zones oriented N-S and NE-SW (Figs. 1b and 1c). At the regional scale, our data argue that the C2 shear zones are markedly localized in and nearby the meta-igneous rocks i.e. orthogneisses (Figs. 1b, 1d, 1e, 2a). In the following we describe the appearance and distribution of the syn-melt and solid-state deformation in the aforementioned regional strain pattern we highlighted.

4. Melt-present and solid-state deformation

In low D2-strain domains, the S1 migmatitic layering in orthogneisses and metasedimentary rocks indicates that melt was present before the onset of D2. Leucosomes with absent or subordinate plastic strain are conspicuously observed in S2, C2 and C’2 planes and inside F2 axial planes emphasizing suprasolidus conditions during ongoing of D2 transpression (Fig. 2). In the orthogneisses, high-strain domains are typified by well-foliated stromatic migmatites where recognisable leucosomes form pluricentimer-scale elongated seams (Fig. 2b-c). The mesosome of the orthogneisses shows mm to cm melt pockets with soft edges. Microstructures of the mesosome include myrmekite around large K-feldspar (Fig. 2d), elongated interstitial quartz and feldspar grains (Fig. 2e), fine grained K-feldspar-bearing aggregates, small quartz-feldspar bearing shear bands and dykelets that indicate the former presence of melt homogeneously distributed in the orthogneiss before movement of melt in the deformed rock. A high melt fraction (>10%) may be estimated from macro- and microscopic observations. While reworked by subsolidus deformation, suprasolidus shearing along C2 is also recognized in the orthogneiss of the MSZ and EBSZ with in-situ leucogranite seams and crystallized melt injections in shear bands as previously described by von Raumer & Bussy (2004) and (Genier et al., 2008). Solid-state mylonites are conspicuous in the C’2 shear zones (i.e. EBSZ and MSZ; Fig. 3) and affect both meta-igneous and metasedimentary rocks (Fig. 3b and c) with higher shear strain in metasedimentary rocks than meta-igneous rocks, especially in mica-rich metapelites.

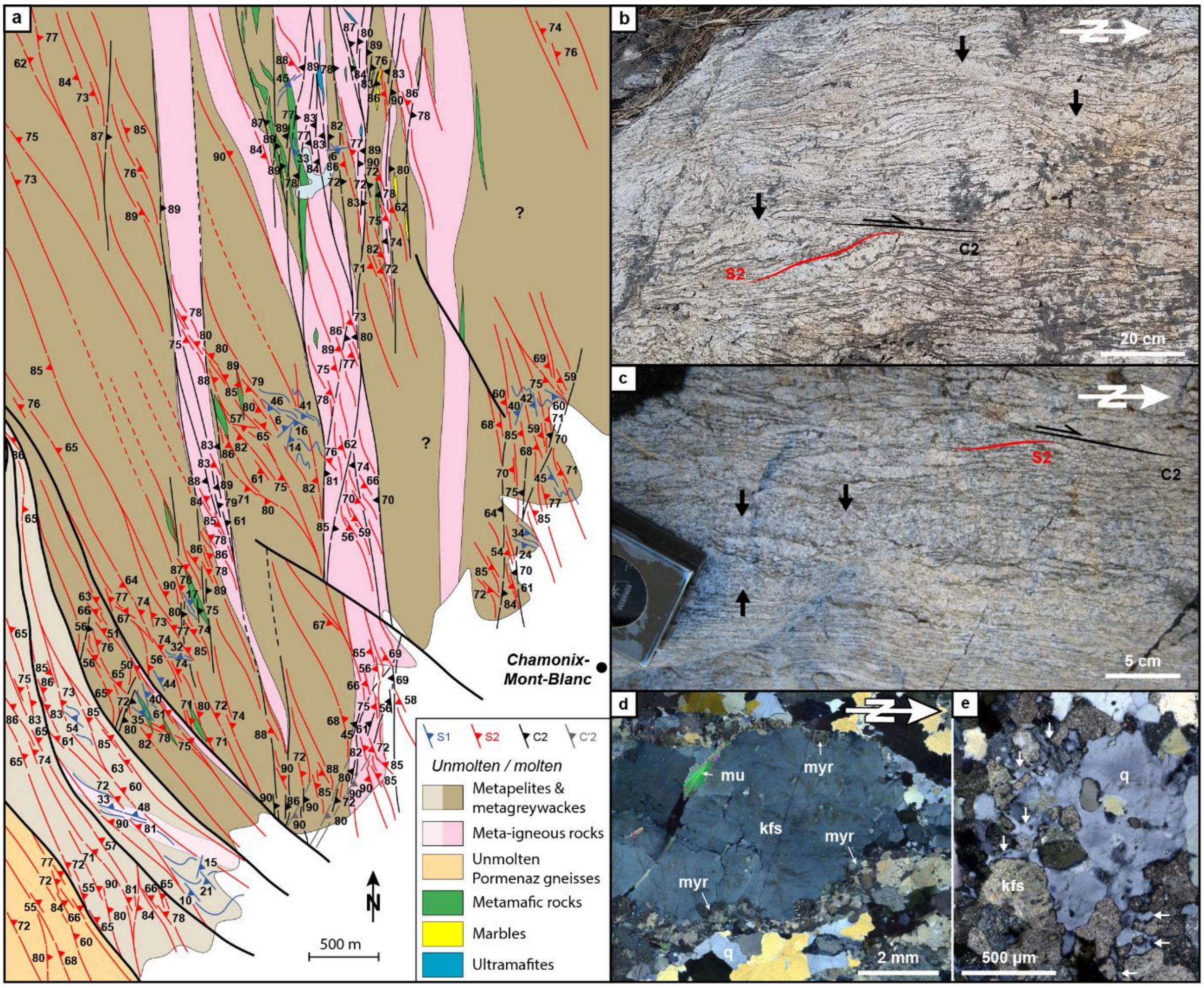

Figure 2: Field and microstructural features of the suprasolidus CSZ. (a) Detailed map of the S1-S2-C2 foliations and their trajectories. In partially molten area, C2 shear zones are mainly located in meta-igneous rocks whereas they are absent in unmolten domain. Relictual S1 foliations are restricted to metasedimentary rocks except in unmolten areas. (b, c) Migmatitic orthogneiss with S2-C2 structures. Black arrows indicate melt injections into

shear planes highlighting suprasolidus conditions of the C2 shearing. (d, e) Photomicrographs of leucosomes injected in C2 shear zones from meta-igneous rocks featuring suprasolidus shearing with (d) quartz (q)-plagioclase myrmekite (myr) surrounding large K-feldspar (kfs) grain and (e) interstitial quartz melt infilling pore space.

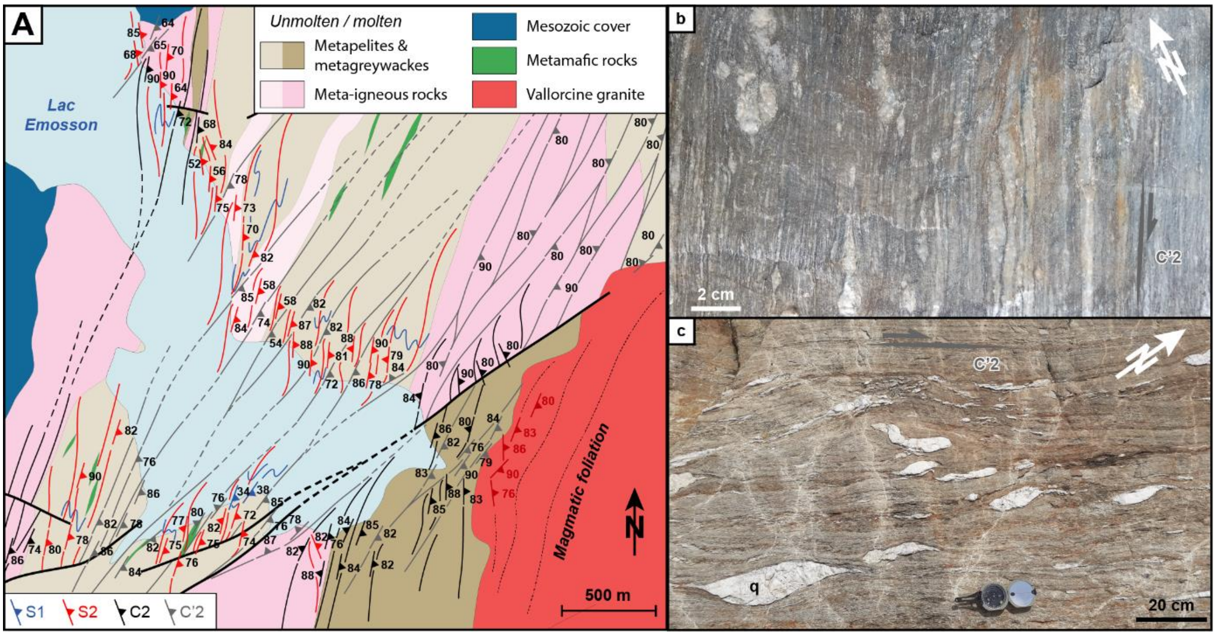

Figure 3: Field features of the subsolidus Emosson-Bérard Shear Zone (EBSZ). (a) The detailed map of the S1-S2-C2-C'2 trajectories display reworking of the syn-melt C2 shear zones by solid-state C'2 shear zones. C2 shear zones are also located in molten rocks whereas C'2 shear zones affect both molten and unmolten rocks. Vallorcine granite locally cross-cuts C'2 shear planes and displays a weak vertical magmatic foliation striking N-S to NE-SW. (b) Former partially molten meta-igneous rocks affected by high-strain C'2 shearing in subsolidus conditions. (c) High-strain C'2 shearing inferred in unmolten metapelites by quartz exudates.

5. Incipient melting and rock fertility

Our results argue that in the ARMBM, the crustal scale shearing is preferentially located in the partially molten metagranite (i.e. orthogneiss) rather than its surrounding. Its eutectic mineralogical composition makes the orthogneiss the first target rock for H_2O-fluxed melting. Considering the peak-temperature conditions at 700 °C and pressure between 0.8-1.6 GPa (Genier et al., 2008; Simonetti et al., 2020a; von Raumer and Bussy, 2004 and references therein; Vanardois et al., in press), mineral equilibrium modelling shows that at H_2O saturated conditions, incipient melting is restricted to the orthogneiss (Fig. 4a and b) and that orthogneiss produced higher amount of melt than metagreywackes and micaschists (Fig. 4c). A reverse trend is evident for H_2O below 3 wt.%, at these conditions incipient melting is restricted to micaschists (Fig. 4b and c). Finally, during retrogression, the orthogneisses and the metagreywackes stay in suprasolidus conditions until pressure reaches a value around 0.4 GPa, then, all the lithologies are in subsolidus conditions (Fig. 4d). At this PT stage, the strain localization is controlled by the amount of micas which is the softest mineralogical phase (Handy, 1994; Hunter et al., 2016). During this retrograde path, the mica modal proportion is generally higher in micaschists rather than in orthogneisses and in metagreywackes. At MP-MT conditions (Fig. 4d path 1), the mica modal proportions are about 40% in the orthogneisses and the metagreywackes, and is about 45-50% in the micaschists. At LP-MT conditions (Fig. 4d path 2), the difference is much higher with mica modal proportions that are around 5-10% in the orthogneisses and metagreywackes but around 20% in the micaschists.

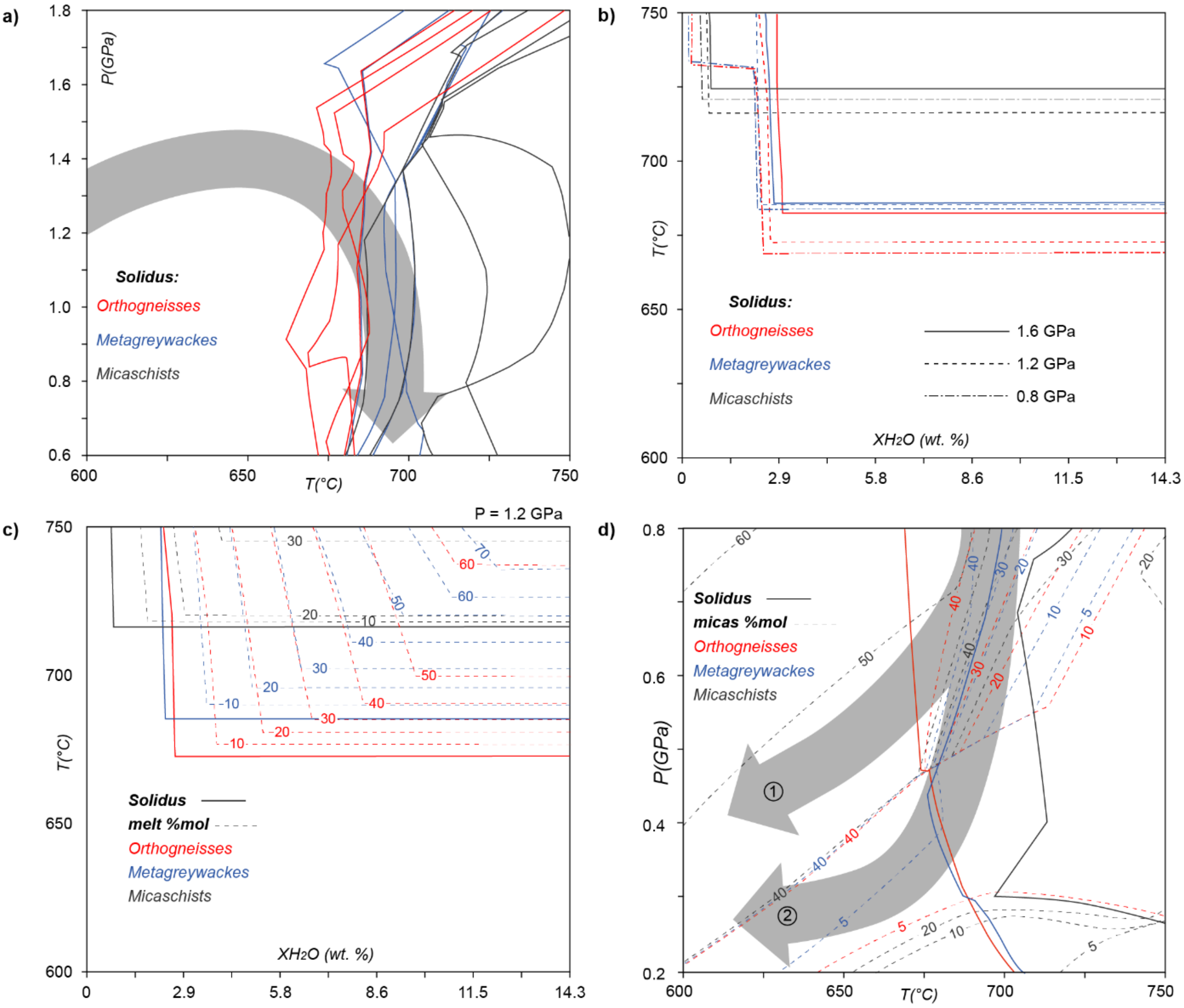

Figure 4: Thermodynamic modelling of (a) solidus reactions in four orthogneisses, four metagreywackes and four metapelites. (b) T-XH_2O diagram of one sample of each lithology at 0.8, 1.2 and 1.6 GPa. (c) Similar T-XH_2O diagram than (b) at 1.2 GPa with melt fraction. (d) micas modal proportion in one sample of each lithology. Bulk rock compositions are from von Raumer and Bussy (2004) (DR1). Modelling parameters are detailed in DR2. The fluid content in (a) and (d) was chosen to be saturated to reproduce hydrated fusion observed in the field. The micas fractions combined the muscovite, biotite and chlorite fractions. The grey arrows represent P-T paths from Schulz and von Raumer (1993, 2011) in (a) and two possible P-T paths are presented in (d) : path 1 is from Vanardois et al. (in review, in prep) and path 2 pass through P-T conditions of Genier et al. (2008).

6. Discussion and conclusion

Numerous studies describe the drastic weakening effect of melt on strain weakening (e.g. Rosenberg and Handy, 2005; Rosenberg et al., 2007; Piazolo et al., 2020). Strength contrast between partially melted granite and its surrounding drive strain localization as can be observed at grain scale when a high-phase strength contrast drives a positive interaction between strain and reaction to produce a narrow ductile shear zone (Holyoke and Tullis, 2006).

If positive feedback between strain localization and melt presence leads to progressive weakening, the syn-melt shearing can also favour melt migration and extraction leading to strength hardening (Brown, 2004; Rushmer, 2001; Diener and Fagereng, 2014). In this study however, a significant amount of melt was not extracted but rather remained in-situ as already described in other active shear zones (e.g. Lee et al., 2018; Torvela and Kurhilka, 2020). Furthermore, crystallization of in-situ anatectic melts can also induce a strain hardening leading to higher rheological properties than initial rheologies (Handy et al., 2001; Druguet and Carreras, 2006; Diener and Fagereng, 2014). Syn-melt shear zones do not necessarily induce a grain-size reduction (e.g. Lee et al., 2020), which could have influenced the localization of high-strain zones after crystallization of anatectic melts (Stenvall et al., 2019). We suggest that strain hardening of the orthogneiss is mainly due to crystallisation of melt during the cooling path (see Handy et al., 2001; Diener and Fagereng, 2014). After the crystallization of anatectic melt, rheology of metamorphic rocks is controlled by weak phases other than melt (i.e. micas) (e.g. Hunter et al., 2016; Diener and Fagereng, 2014). In the metagreywackes and metapelites, the limited anatexis was not sufficient to lead to melt extraction, that would have led to strength increase due to higher amounts of garnet and feldspar proportions (Diener and Fagereng, 2014). During the retrogression a MT-LP subsolidus conditions, micaschists contain a higher mica modal proportion than meta-igneous rocks (Fig. 4d path 2). With a retrograde path at slightly higher pressure conditions (Fig. 4d path 1), the mica modal proportion is still higher in the micaschists than in the meta-igneous rocks. Therefore, in the study area, the transcurrent deformation forms subsolidus C’2 shear zones mainly localized within the metapelites, even if the metagreywackes and meta-igneous rocks are probably also affected by this sub-solidus deformation. This change in the nature of the weakest phase, starting with melt in metagranites and followed by micas in metasedimentary rocks, controls the progressive localization and broadening of the crustal scale shear zones in the gneissic basement of the ARMBM during the clockwise P-T-t path (grey arrows in Fig. 4).

Our petrological modelling emphasises the role of meta-granite as a critical heterogeneity impacting rheological inheritance of the orogenic crust. The proposed mechanism is likely to occur in any continental crust in which sufficient pervasive water influx impacts isolated fertile meta-granite bodies under appropriate P-T conditions. Since the onset of melting follows prograde metamorphism, influx of metamorphic water originated from the dehydration of nearby metapelitic rocks with a higher solidus temperature is likely (Sawyer, 2010; White et al., 2005; Weinberg and Hasalová, 2015). Our thermodynamic modelling indicates that an amount of ca. 3 wt.% is needed to produce the incipient partial melting in orthogneiss, which is coherent with the value of H_2O in the lower crust proposed by Braga and Massone (2012).

Given the depth emplacement of granitic intrusions, related to the depth dependence of the temperature of wet solidus, we should expect strain localization to preferentially occur in the mid-lower crust. Our results point to an evolving understanding of thermo-mechanical behaviour of the hot and partially molten crust, leading to a reappraisal of well-studied geological objects. For instance, Neves et al. (2021) emphasized a strong spatial relationship between the lithospheric-scale Pernambuco shear zone (NE-Brazil) and the alignment of orthogneiss bodies. They suggested that the regional alignment of the magmatic protoliths may reflect the presence of a cryptic rift-related crustal scale fault that acted as an inherited structure on which the crustal scale shear zone initiated. Our results may lead to an alternative view considering that incipient H_2O-fluxed melting of the orthogneiss may have strongly contributed to the nucleation of the Pernambuco shear zone. Another example might be provided by the controversial Montagne Noire massif, where a crustal-scale steep high-strain zone that separates two migmatitic domes might be the result of upward flow of the partially molten crust in response to upper crustal stretching (Rey et al., 2011). Detailed field work argues that the high-strain zone corresponds to a dextral shear zone that is contained to a partially-molten K-feldspar orthogneisses (Rabin et al., 2015).

Burri et al. (2005) observed in the internal Alps that granitoids near a vertical shear zone produced large amount of melt due to water-assisted partial melting whereas smaller leucosome-fraction was found in the metasedimentary rocks. They proposed that the vertical shear zone triggered episodic injection of fluids, which induced water-assisted partial melting in granitoids. We go further saying the starting point is diffusive flow of H_2O that trigger melt and enhance shear zone nucleation. This mechanism promotes nucleation of crustal-scale shear zone in response to melt-related strain weakening in the heterogenous mid-lower crust.

Acknowledgements

This work was financially supported by the French Geological Survey (BRGM) through the Référentiel Géologique de la France program (RGF). The newly acquired and compiled structural data will be available on the RGF website (http://rgf.brgm.fr).

Supplementary materials

Table DR1: Bulk compositions used for phase diagram modelling, from von Raumer and Bussy (2004)

wt%	**Ortho1**	**Ortho3**	**Ortho9**	**Ortho10**	**1684**	**1694**	**SDU6**	**KS156**	**1388D**	**1584**	**V93**	**1394**
SiO2	69.4	66.19	66.94	64.44	70.31	74.1	68.32	64.95	51.73	65.05	55.19	48.83
TiO2	0.53	0.75	0.69	0.69	0.38	0.8	0.88	1.04	1	0.76	1.09	3.58
Al2O3	15.26	16.14	15.29	16.38	15.6	11.57	15.04	16.4	23.27	16.41	22.67	18.24
Fe2O3	0.92	0.9	1.06	1.32	0.65	0.69	5.66	6.87	1.96	0.98	1.14	1.86
FeO	2.57	3.82	3.54	2.96	1.85	3.87			6.86	4.17	7.41	11.19
MnO	0.05	0.07	0.07	0.07	0.03	0.08	0.09	0.08	0.12	0.07	0.17	0.14
MgO	1.23	1.72	1.41	1.43	0.72	2.05	2.59	2.87	3.05	2.56	2.62	4.1
CaO	1.12	1.69	1.84	2.28	1.56	1.37	1.55	1.78	4.4	1.8	0.43	4.87
Na2O	3.25	2.99	3.08	2.89	3.79	2.02	3.53	3.54	3.23	2.79	1.39	2.03
K2O	4.38	4.47	4.02	4.55	3.67	1.34	2.13	2.28	1.78	3.35	3.7	1.16

Table DR2: Phase diagram modelling method

$MnO-Na_2O-CaO-FeO-MgO-Al_2O_3-SiO_2-H_2O-TiO_2-Fe_2O_3$	
Perple_X software (Connolly, 2005)	
Dataset from Holland and Powell, 2011 (hp62ver.dat)	
Solution models	**reference**
Bi(W)	White et al., 2014
Mica(W)	
Gt(W)	
St(W)	
Crd(W)	
Opx(W)	
melt(W)	
Chl(W)	
Ctd(W)	
Ilm(WPH)	
Sp(WPC)	White et al., 2012
feldspar	fuhrman & lindsley, 1988; Haselton et al., 1983
Ep(HP11)	Holland and Powell, 2011
Omph(GHP)	Green et al., 2007
cAmph(G)	Green et al., 2016

Perspectives

Ce travail a permis d'apporter un certain nombre de réponse aux problématiques que nous avons exposées dans les deux premiers chapitres mais soulève aussi de nouvelles questions qu'il serait intéressant d'investiguer par la suite :

- Il faudrait aller vérifier notre modèle concernant la nucléation des zones de cisaillement verticales dans les méta-granites en raison de la fusion hydratée dans d'autres massifs Variques et d'autres orogènes.
- La fusion partielle formant des diatextites à 307 Ma dans la zone Nord-Est des Aiguilles (Fully) nécessite d'être étudiée conjointement avec les migmatites à cordiérite du massif du Pelvoux pour déterminer leur formation. Sont-elles issues d'un apport de chaleur à basse pression, si oui quel est son origine, ou bien peuvent-elles être uniquement produites par une fusion hydratée à basse pression ?
- Les massifs de l'Aar-Gothard méritent d'être réinvestigués. Ces massifs n'ont presque pas été étudiés depuis le début des années 2000, ils contiennent pourtant de nombreuses occurrences de roches mafiques et ultramafiques qui pourraient être corrélées avec l'ophiolite de Chamrousse.
- Les études récentes sur le massif de l'Argentera se sont concentrées sur la déformation subsolidus, qu'en est-il des déformations suprasolidus ?
- Des contraintes géochronologiques sur la haute-pression et la fusion partielle dans les Maures-Tanneron, la Corse et la Sardaigne sont nécessaires pour pouvoir comprendre l'évolution de la branche SE Varisque.
- Il serait particulièrement intéressant d'aller travailler sur les éclogites du Nord du Massif Central pour pouvoir les comparer avec celles plus au Sud et voir si elles pourraient provenir de la subduction de l'océan Saxothuringien. Des données géochronologiques sont aussi nécessaires sur le premier épisode de fusion partielle dans le Nord du Massif Central. Ces migmatites sont-elles vraiment dévoniennes ?
- Ce travail n'a pas intégré le socle Varisque des Alpes Internes, ce qu'il faudra donc faire dans le futur.

References

Abrecht, J. 1980. Zur Bildung migmatitischer Schollenamphibolite aus dem Altkristallin des Aarmassivs. Geol Rundsch 69: 695-725.

Abrecht, J., & Biino, G. 1994. The metagabbros of the Kastelhorn area (Gotthard massif, Switzerland): Their metamorphic history inferred from mineralogy and texture. Schweizerische Mineralogische und Petrographische Mitteilungen, 74, 53–68.

Abrecht, J., Biino, G. G., Mercolli, I., & Stille, P. 1991. Mafic-ultramafic rock associations in the Aar, Gotthard and Tavetsch massifs of the Helvetic domain in the Central Swiss Alps: markers of ophiolitic pre-Variscan sutures, reworked by polymetamorphic events? Schweizerische Mineralogische und Petrographische Mitteilungen, 71, 295–300.

Aguilar C, Liesa M, Castiñeiras P, Navidad M. 2013. Late Variscan metamorphic and magmatic evolution in the eastern Pyrenees revealed by U–Pb age zircon dating. J Geol Soc London 171:181–192.

Aguilar C, Liesa M, Štípská P, Schulmann K, Muñoz JA, Casas JM. 2015. P–T–t–d evolution of orogenic middle crust of the Roc de Frausa Massif (Eastern Pyrenees): A result of horizontal crustal flow and Carboniferous doming? J Metamorph Geol 33: 273–294.

Aleinikoff, J. N., Wintsch, R. P., Fanning, C. M., & Dorais, M. J. 2002. U-Pb geochronology of zircon and polygenetic titanite from the Glastonbury Complex, Connecticut, USA: An integrated SEM, EMPA, TIMS, and SHRIMP study. Chemical Geology, 188, 125–147, doi:10.1016/S0009-2541(02)00076-1.

Alexandrov P, Cheilletz A, Deloule É, Cuney M. 2000. 319 ± 7 Ma crystallization age for the Blond granite (northwest Limousin, French Massif Central) obtained by U/Pb ion-probe dating of zircons. Comptes Rendus Académie Sci. – Ser. IIA-Earth Planet. Sci. 330: 617–622.

Altherr, R. 2021. Retrograded garnet peridotites from Col des Bagenelles and Crébimont in the Variscan Vosges Mountains (NE France). 176: https://doi.org/10.1007/s00410-021-01811-7

Altherr R, Kalt A. 1996. Metamorphic evolution of ultrahigh-pressure garnet peridotites from the Variscan Vosges Mts. (France). Chem. Geol. 134: 27–47.

Altherr R, Soder CG. 2018. Sapphirine as a breakdown product of garnet in a Variscan UHP/HT peridotite from the Vosges Mountains (France)—an indication of near-isothermal decompression. J Petrol 59:2221–2243. https:// doi. org/ 10. 1093/ petro logy/ egy096

Altherr, R., Hepp, S., Klein3, H., Hanel, M. 2021. Metabasic rocks from the Variscan Schwarzwald (SW Germany): metamorphic evolution and igneous protoliths. 110:1293–1319

Althoff F, Barbey P, Pons J. 1994. La charnockite d'Ansignan et le granite de Saint-Arnac, témoins d'une extension crustale d'âge hercynien dans le massif de l'Agly (Pyrénées Orientales, France). C R Acad Sci Paris 319: 239–246.

Andrieux P. 1982a. Conditions de cristallisation et évolution paragénétique d'une charnockite hercynienne : le complexe granulitique d'Ansignan (massif de l'Agly, Pyrénées-Orientales). B Minéral 105: 253–266.

Andrieux P. 1982b. La charnockite d'Ansignan (Massif d'Agly, Pyrénées Orientales). Mise en place et évolution paragénétique. Introduction à l'étude des équilibres grenat-orthopyroxène. 3rd Cycle Thesis, Clermont-Ferrand (France), Univ. Blaise Pascal.

Angiboust, S., Agard, P. 2010. Initial water budget: the key to detaching large volumesof eclogitized oceanic crust along the subduction channel? Lithos 120, 453–474.

Annen C, Sparks RSJ. 2002. Effects of repetitive emplacement of basaltic intrusions on thermal evolution and melt generation in the crust. Earth Planet. Sci. Lett. 203: 937–955.

Antolín-Tomás B, Román-Berdiel T, Casas-Sainz A, Gil-Peña I, Oliva B, Soto R. 2009. Structural and magnetic fabric study of the Marimanha granite (Axial Zone of the Pyrenees). Int J Earth Sci 98: 427–441.

Arenas, R., Sánchez Martínez, S., Díez Fernández, R., Gerdes, A., Abati, J., Fernández-Suárez, J., Andonaegui, P., González Cuadra, P., López Carmona, A., Albert, R., Fuenlabrada, J.M., Rubio Pascual, F.J., 2016.

Allochthonous terranes involved in the Variscan suture of NW Iberia: A review of their origin and tectonothermal evolution. Earth Sci. Rev. 161, 140–178. https://doi.org/10.1016/j.earscirev.2016.08.010.

Arzi, A. A, 1978. Critical phenomena in the rheology of partially melted rocks. Tectonophysics 44, 173-184.

Aubele, K., Bachtadse, V., Muttoni, G., Ronchi, A., Durand, M., 2012.A paleomagneticstudy of Permian and Triassic rocks from the Toulon–Cuers Basin, SE France: evidence for intra-Pangea block rotations in the Permian. Tectonics 31, TC3015.

Auréjac JB, Gleizes G, Diot H, Bouchez JL. 2004. Le complexe granitique de Quérigut (Pyrénées, France) ré-examiné par la technique de l’ASM: un pluton syntectonique de la transpression dextre hercynienne. Bull Soc geol Fr 175: 157–174.

Avouac JP, Tapponnier P. 1993. Kinematic model of active deformation in central Asia. Geophys. Res. Lett. 20:895–98

Ayora C, Liesa M, Delgado J. 1993. Low-thermal-gradient Hercynian metamorphismin the eastern Pyrenees. J MetamorphGeol 11:49–58. Azambre B, Guitard G. 2001. Disthène et staurotide reliques dans les métapélites du Canigou (Pyrénées orientales). Relations avec les épisodes hercyniens de basses et moyennes pressions. C R Acad Sci Paris 333: 601–609.

Azambre B, Ravier J. 1978. Les écailles de gneiss du faciès granulite du Port de Saleix et de la région de Lherz (Ariège), nouveaux témoins du socle profond des Pyrénées. Bull Soc geol Fr 7: 221–228.

Badertscher, N., & Burkhard, M. 1998. Inversion alpine du graben Permo-Carbonifère de Salvan-Dorénaz et sa relation avec le chevauchement de la nappe de Morcles sus-jacente. Eclogae Geologicae Helvetiae, 91, 359–373.

Bai, D., Unsworth, M.J., Meju, M.A., Ma, X., Teng, J., Kong, X., Sun, Y., Sun, J., Wang, L., Jiang, C., Zhao, C., Xiao, P., Liu, M., 2010. Crustal deformation of the easternTibetan plateau revealed by magnetotelluric imaging. Nat. Geosci. 3, 358–362, http://dx.doi.org/10.1038/ngeo830.

Bakos, F., Del Moro, A., & Visonà, D. 1990. The Hercynian volcano-plutonic association of Ganna (Lake Lugano, central Southern Alps, Italy). European Journal of Mineralogy, 2, 373–383.

Ballèvre, M., Pitra, P., and Bohn, M., 2003. Lawsonitegrowth in the epidote blueschist from the Ile de Groix (Armorican Massif, France): A potential geobarometer. Journal of Metamorphic Geology, v. 21, p. 723–735.

Ballèvre M, Martínez Catalán JR, López-Carmona A, Pitra P, Abati J, Fernández RD, et al. 2014. Correlation of the nappe stack in the Ibero-Armorican arc across the Bay of Biscay: a joint French–Spanish project. Geol. Soc. Lond. Spec. Publ. 405: 77–113. https://doi.org/10.1144/SP405.13.

Ballèvre, M., Manzotti, P., & Dal Piaz, G. V. 2018. Pre-Alpine (Variscan) inheritance: A key for the location of the future Valaisan Basin (Western Alps). Tectonics, 37, 786–817.

Banzet, G., Rouer, O., & Lapierre, H. 1984. Nouvelles données pétrographiques, stratigraphiques et structurales sur le volcanisme carbonifère du col de la Croix-de-Fer (Alpes externes). Bulletin de la Société Géologique de France, 16(6), 1269–1280.

Banzet, G., Lapierre, H., Le Fort, P., & Pêcher, A. 1985. Le volcanisme Carbonifère-supérieur du massif des Grandes Rousses (Zone dauphinoise-Alpes externes françaises): Un magmatisme à affinités shoshonitiques lié à la fracturation crustale tardi-varisque. Géologie Alpine, 61, 33–60.

Barbarin, B., Gerbe, M-C., Vitel, G., Gonord, H., Couette, F., Lebret, P. 2012 Notice feuille de Firminy, 1/50000, 747.

Barbey P, Villaros A, Marignac C, Montel JM. 2015. Multiphase melting, magma emplacement and P-T-time path in late-collisional context: The Velay example (Massif Central, France). Bull Soc geol Fr 186: 93–116.

Barfety J.C, Bordet P, Carme F, Debelmas J, Meloux M, Montjuvent, G., Sarrot-Reynaud, J., 1972. Notice feuille de Vizille, 1/50000, 797.

Barféty, J.-C., Blaise, J., Fourneaux, J.-C., & Méloux, J. 1984. Notice explicative de la feuille La Rochette à 1/50 000, BRGM, Orléans, p. 45.

Bachtadse V., Aubele K., Muttoni G., Ronchi A., Kirscher U. & Kent D.V. 2018 - New early Permian paleopoles from Sardinia confirm intra-Pangea mobility. Tectonophysics, 749: 21-34.

Bea, F., Montero, P., Ortega, M., 2006. A LA-ICP-MS evaluation of Zr reservoirs in common crustal rocks: Implications for Zr and Hf geochemistry, and zircon-forming processes. Can. Mineral. 44, 693–714.

Bea, F., Montero, P., Gonzalez-Lodeiro, F. & Talavera, C. 2007. Zircon inheritance reveals exceptionally fast crustal magma generation processes in central Iberia during the Cambro-Ordovician. Journal of Petrology 48, 2327-2339.

Beaumont, C., Jamieson, R.A., Nguyen, M.H., Lee, B. 2001. Himalayan tectonics explained by extrusion of a low-viscosity crustal channel coupled to focused surface denudation. Nature, 414, 738–742.

Beaumont C, Jamieson RA, Nguyen MH, Medvedev S 2004 Crustal channel flows: 1. Numerical models with applications to the tectonics of the Himalayan-Tibetan orogen. J Geophysic Res 109, B06406. DOI: 10.1029/2003JB002809.

Bellahsen, N., Jolivet, L., Lacombe, O., Bellanger, M., Boutoux, A., Garcia, S., Mouthereau, F., Le Pourhiet, L., Gumiaux, C., 2012. Mechanisms of margin inversionin the external Western Alps: implications for crustal rheology. Tectonophysics 560–561, 62–83. http://dx.doi.org/10.1016/j.tecto.2012.06.022.

Bellahsen, N., Mouthereau, F., Boutoux, A., Bellanger, M., Lacombe, O., Jolivet, L., & Rolland, Y. 2014. Collision Kinematics in the Western External Alps. Tectonics, 33. https://doi.org/10.1002/2013TC003453Bellière, 1958

Bellanger, M., Bellahsen, N., Jolivet, L., Baudin, T., Augier, R., & Boutoux, A. 2014. Basement shear zones development and shortening kinematics in the Ecrins Massif, Western Alps. Tectonics, 33, 84–111.

Bellière, J. 1958. Contribution à l'étude pétrogénétique des schistes cristallins du massif des Aiguilles Rouges. Annales de la Société géologique de Belgique, 81, 1–198.

Bellière J, Streel M. 1980. Roches d'âge viséen supérieur dans le massif des Aiguilles Rouges (Haute-Savoie). C.R. Acad. Sci. Paris 290:1341-1343.

Bellot, J.-P., 2005. The Palaeozoic evolution of theMauresMassif (France) and its potential correlation with other areas of the Variscan belt: a review. J. Virtual Explor. 19, 1–24 (Paper 4).

Bellot, J.-P., Triboulet, C., Laverne, C. & Bronner, G. 2003. Evidence for two burial/exhumation stages during the evolution of the Variscan belt, as exemplified by P–T–t–d paths of metabasites in distinct allochthonous units of the Maures massif (SE France). International Journal of Earth Sciences, 92, 7–26.

Bellot J-P, Roig J-Y. 2007. Episodic exhumation of HP rocks inferred from structural data and PT paths from the southwestern Massif Central (Variscan belt, France). J. Struct. Geol. 29: 1538–1557.

Bellot, J.-P., Triboulet, C., Laverne, C. & Bronner, G. 2003. Evidence for two burial/exhumation stages during the evolution of the Variscan belt, as exemplified by P–T–t–d paths of metabasites in distinct allochthonous units of the Maures massif (SE France). International Journal of Earth Sciences, 92, 7–26.

Bellot, J.-P., Laverne, C. & Bronner, G. 2010. An early Palaeozoic supra-subduction lithosphere in the Variscides: new evidence from the Maures massif. International Journal of Earth Sciences, 99, 473–504.

Benmammar, A., Berger, J., Triantafyllou, A., Duchene, S., Bendaoud, A., Baele, J.M., … Diot, H. 2020. Pressure-temperature conditions and significance of Upper Devonian eclogite and amphibolite facies metamorphisms in southern French Massif central. Bulletin de la Société géologique de France, 191. doi.org/10.1051/bsgf/2020033

Bento dos Santos, T., Rodrigues, J.F., Castro, P., Cotrim, B., Pereira, I., Ferreira, J.A., Meireles, C., Ferreira, N., Ferreira, P., Ribeiro, A., Guimarães, F. 2021. Exhumation of an anatectic complex by channel flow and extrusion tectonics: structural and metamorphic evidence from the Porto–Viseu Metamorphic Belt, Central-Iberian Zone. International Journal of Earth Sciences, 110, 2179–2201

Berger GM, Fonteilles M, Leblanc D, Clauzon G, Marchal JP, Vautrelle C. 1993. Notice de la carte géologique de la France, feuille Rivesaltes (1090), scale 1:50 000. Orléans : BRGM.

Berger, A., Burri, T., Alt-Epping, P., & Engi, M. 2008. Tectonically controlled fluid flow and water-assisted melting in the middle crust: an example from the Central Alps. Lithos, 102(3-4), 598-615

Berger, J., Féménias, O., Ohnenstetter, D., Bruguier, O., Plissart, G., Mercier, J.-C.C., Demaiffe, D. 2010. New occurrence of UHP eclogites in Limousin (French Massif Central): age, tectonic setting and fluid-rock interactions. Lithos, 118, 365–382.

Berger, A., Mercolli, I., Herwegh, M., & Gnos, E. 2017. Geological map of the Aar Masif, Tavetsch and Gotthard Nappes. Geol. Spec. Map 1:100 000, explanatory notes 129. Federal Office of Topography Swisstopo

Bertotti G, Picotti V, Bernoulli D, Castellarin A 1993 From rif-ting to drifting: tectonic evolution of the South-Alpine uppercrust from the Triassic to the Early Cretaceous. Sediment Geol 86: 53-76

Bertrand, J.-M., & Leterrier, J. 1997. Granitoïdes d'âge Paléozoïque inférieur dans le socle de Vanoise méridionale: Géochronologie U-Pb du métagranite de l'Arpont (Alpes de Savoie, France). Comptes Rendus de l'Académie des Sciences Paris, II, 325, 839–844.

Bertrand, J.-M., Guillot, F., Leterrier, J., Perruchot, M.-P., Aillères, L., & Macaudière, J. 1998. Granitoïdes de la zone houillère briançonnaise en Savoie et en Val d'Aoste (Alpes occidentales): Géologie et géochronologie U–Pb sur zircon. Geodinamica Acta, 11, 33–49.

Bertrand, J.-M., Pidgeon, R. T., Leterrier, J., Guillot, F., Gasquet, D., & Gattiglio, M. 2000. SHRIMP and IDTIMS U-Pb zircon ages of the pre-Alpine basement in the Internal Western Alps (Savoy and Piemont). Schweizerische Mineralogische und Petrographische Mitteilungen, 80, 225–248.

Besson M. 1974. Présence de disthène dans les gneiss du massif de l'Aston. Bull Soc Fr Minéral Cristallogr 97: 487–490.

Beyssac, O., Rouzaud, J.-N., Goffé, B., Brunet, F., Chopin, C. 2002: Graphitization in a high-pressure, low-temperature metamorphic gradient: a Raman microspectroscopy and HRTEM study. Contrib. Mineral. Petrol., 143, 19–31.

Biino, G. G. 1994. The pre-Late Ordovician metamorphic evolution of the Gotthard-Tavetsch massifs (Central Alps): From lawsonite to kyanite eclogites to granulite retrogression. Schweizerische Mineralogische und Petrographische Mitteilungen, 74, 87–104.

Biino, G. 1997. Pre-Variscan evolution of the eclogitised mafic rocks from the Helvetic basement of the central Alps. European Journal of Mineralogy, 7, 57–70.

Biino, G. G., & Meisel, T. 1993. Geochemistry of Polymetamorphic Ultramafics (Major, Trace, Noble and Rare Earth Elements): an Example From the Helvetic Basement, Central Alps, Switzerland. Mineralogy and Petrology, 49, 189-212.

Biino, G., Marquer, D., Nussbaum, C. 1997. Alpine and Pre-Alpine subduction events in polycyclic basements of the Swiss Alps. Geology, 25 (8), 751–754.

Bingen B, Austrheim H, Whitehouse M 2001 Ilmenite as a source of zirconium during high-grade metamorphism? Textural evidence from the Caledonides of Western Norway and implications for zircon geochronology. J Petrol 42:355–375

Block, L., and Royden, L.H., 1990, Core complex geometries and regional scale flowin the lower crust: Tectonics, v. 9, p. 557–567.

Bodinier J-L, Burg J-P. 1981. Evolution métamorphique et tectonique des séries cristallophylliennes du Rouergue occidental : mise en évidence d'un chevauchement dans la région de Najac (Aveyron). Bull BRGM I: 315–339

Boehnke, P., Watson, E.B., Trail, D., Harrison, T.M., Schmitt, A.K., 2013. Zircon saturation rerevisited. Chem. Geol. 351, 324–334.

Bogdanoff. S. and Schott, J.J., 1977. Etude paleomagnetique et analyse tectonique dans les schistes rouges permiens du Sud de I'Argentera. Bull. Sot. Geol. Fr., 19: 815-824.

Bogdanoff S, Menot R.P, Vivier G, 1991. Les Massifs cristallins externes des Alpes occidentales francaises, un fragment de la zone interne varisque. Extern. Cryst. Massifs Fr. West. Alps Part Intern. Variscan Zone 44: 237–285.

Bons, P.D., Arnold, J., Elburg, M.A., Kalda, J., Soesoo, A., van Milligen, B.P., 2004. Melt extraction and accumulation from partially molten rocks. Lithos 78, 25e42.

Bons, P.D., Druguet, E., Castaño, L.M., Elburg, M.A., 2008. Finding what is not there anymore: recognizing missing fluid and magma volumes. Geology 36, 851e854.

Bordet, P., & Bordet, C. 1963. Belledonne-Grandes Rousses et Aiguilles Rouges-Mont Blanc: Quelques données nouvelles sur leurs rapports structuraux. Livre à la mémoire du Professeur Paul Fallot, Société Géologique de France, II, 309–316.

Bossart, P. J., Meier, M., Oberli, F. & Steiger, R.H. 1986. Morphology versus U–Pb systematics in zircon: a high-resolution isotopic study of a zircon population from a Variscan dike in the Central Alps. Earth and Planetary Science Letters 78, 339–354.

Bouchardon J-L, Santallier D, Briand B, Ménot R-P, Piboule M. 1989. Eclogites in the French Palaeozoic Orogen: geodynamic significance. Tectonophysics 169: 317–332.

Bouchez JL, Gleizes G. 1995. Two stage deformation of the Mont-Louis-Andorra granite pluton (Variscan Pyrenees) inferred from magnetic susceptibility anisotropy. J Geol Soc 152: 669–679.

Bouchez JL, Delas D, Gleizes G, Nedelec A, Cuney M. 1992. Submagmatic microfractures in granites. Geology 20:35–38.

Bouchez JL, Nguema TMM, Esteban L, Siqueira R, Scrivener R. 2006. The tourmaline-bearing granite pluton of Bodmin (Cornwall, UK): Magnetic fabric study and regional inference. J Geol Soc 163:607–616.

Bouhallier H, Choukroune P, Ballevre M. 1991. Evolution structurale de la croûte profonde hercynienne : exemple du massif de l'agly (pyrenees-orientales, france). C R Acad Sci Paris 312: 647–654.

Boulvais P. 2016. Fluid generation in the Boucheville Basin as a consequence of the North Pyrenean Metamorphism. C R Geosci 348: 301–311.

Bousquet, R., Engi, M., Gosso, G., Oberhänsli, R., Berger, A., Spalla, M.I., Goffé, B., 2004.Explanatory notes to the map: metamorphic structure of the Alps, transition fromthe Western to the Central Alps. Mitteilungen der Österreichischen MineralogischenGesellschaft 149, 145–156

Boutoux, A., Bellahsen, N., Nanni, U., Pik, R., Verlaguet, A., Rolland, Y., & Lacombe, O. 2016. Thermal and Structural Evolution of the External Western Alps: Insights from (U–Th–Sm)/He Thermochronology and RSCM Thermometry in the Aiguilles Rouges/Mont Blanc Massifs. Tectonophysics, 683, 109 23. https://doi.org/10.1016/j.tecto.2016.06.010.

Bracciali, L., Parrish, R.R., Horstwood, M.S.A., Condon, D.J., & Najman, Y. 2013. U-Pb LA-(MC)-ICP-MS dating of rutile: New reference materials and applications to sedimentary provenance. Chemical Geology, 347, 82-101.

Braga, R., Massonne, H.-J., 2012. H2O content of deep-seated orogenic continental crust: the Ulten Zone, Italian Alps. International Geology Review 54, 633–641

Briand B, Piboule M, Bouchardon JL. 1988. Diversite geochimique des metabasites des groupes leptyno-amphiboliques du Rouergue et de Marvejols (Massif Central) ; origine et implications. Bull. Société Géologique Fr. 4: 489–498.

Briand B, Duthou J-L, Guerrot C, Chenevoy M. 2002. Les « granites à tablettes d'orthose » du Vivarais, témoins d'un magmatisme postépaississement d'âge Dinantien inférieur ; identification d'une unité géologique Nord-Ouest-Vivarais. Comptes Rendus Geosci. 334: 741–747

Brichau S, Respaut J-P, Monié P. 2007. New age constraints on emplacement of the Cévenol granitoids, South French Massif Central. Int. J. Earth Sci. 97: 725–738.

Brown, M., 1994. The generation, segregation, ascent and emplace-ment of granite magma: the migmatite-to-crustally-derived granite connection in thickened orogens. Earth-Sci. Rev. 36,83–130.

Brown, M. Orogeny, migmatites and leucogranites: a review. Journal of Earth System Science, 110(4), 313-336.2001

Brown, M. 2004, The mechanism of melt extraction from the lower continental crust of orogens, Trans. R. Soc. Edinburgh, 95, 35–48

Brown, M. 2007, Crustal melting and melt extraction, ascent and emplacement in orogens: mechanisms and consequences, Journal of the Geological Society, London, 164, 709–730

Brown, M. 2010. The spatial and temporal patterning of the deepcrust and implications for the process of melt extraction. Philo-sophical Transactions of the Royal Society of London, Series A,368: 11–51. doi:10.1098/rsta.2009.0200.

Brown, M., 2013. Granite: From genesis to emplacement. Bulletin of the Geological Society of America 125, 1079–1113.

Brown, M., & Solar, G. S. 1998. Shear-zone systems and melts: feedback relations and self-organization in orogenic belts. Journal of structural geology, 20(2-3), 211-227.

Bruguier O, Becq-Giraudon JF, Bosch D, Lancelot JR. 1998. Late Visean hidden basins in the internal zones of the Variscan belt: U-Pb zircon evidence from the French Massif Central. Geology 26:627–630.

Burg JP, Vanderhaeghe O. 1993. Structures and way-up criteria in migmatites, with application to the Velay dome (French Massif Central). J Struct Geol 15: 1293–1301.

Burg JP, Van Den Driessche J, Brun JP. 1994. Syn- to post-thickening extension in the Variscan Belt of Western Europe: Modes and structural consequences. Géologie de la France 3: 33–51.

Burri, T., Berger, A., & Engi, M. 2005. Tertiary migmatites in the Central Alps: regional distribution, field relations, conditions of formation, and tectonic implications. Schweizerische Mineralogische und Petrographische Mitteilungen, 85(2-3), 215-232

Bussien Grosjean D, Meisser N, May-Leresche S, Ulianov A, Vonlanthen, P. 2017. The Morcles microgranite (Aiguilles Rouges, Swiss Alps): Geochronological and geochemical evidences for a common origin with the Vallorcine intrusion. Swiss J. Geosci. 110:35–49. https://doi.org/10.1007/s00015-017-0282-3

Bussy F. 1990. Pétrogenèse des enclaves micro-grenues associées aux granitoïdes calco-alcalins: Exemple des massifs varisques du Mont-Blanc (Alpes occidentales) et miocène du Monte Capanne (Ile d'Elbe, Italie). Mém. Géol. Lausanne, 7:1–309.

Bussy, F., von Raumer, J.F. 1993. U–Pb dating of Paleozoic events in the Mont-Blanc crystalline massif, Western Alps. Terra Nova, 5, 382.

Bussy, F., & von Raumer, J.F. 1994. U–Pb geochronology of Palaeozoic magmatic events in the Mont-Blanc Crystalline Massif, Western Alps. Schweizerische Mineralogische und Petrographische Mitteilungen, 74, 514–515.

Bussy, F., Sartori, M. and Thélin, Ph. 1996: U–Pb zircon dating in the middle Penninic basement of the Western Alps (Valais, Switzerland). Schweiz. Mineral. Petrogr. Mitt. 76, 81–84.

Bussy, F., Delitroz, D., Fellay, R., & Hernandez, J. 1998. The Pormenaz Monzonite (Aiguilles Rouges, western Alps): An additional evidence for a 330 Ma-old magnesio-potassic magmatic suite in the Variscan. Schweizerische Mineralogische und Petrographische Mitteilungen, 78, 193–194.

Bussy, F., Hernandez, J., & von Raumer, J.F. 2000. Bimodal magmatism as a consequence of the post-collisional re-adjustment of the thickened Variscan continental lithosphere (Aiguilles Rouges/Mont-Blanc Massifs, western Alps). Transactions of the Royal Society of Edinburgh–Earth Sciences, 91, 221–233.

Bussy, F., Péronnet, V., Ulianov, A., Epard, J.L., & von Raumer, J. 2011. Ordovician magmatism in the External French Alps: witness of a peri-Gondwanan active continental margin. In Gutiérrez-Marco, J.C., Rábano, I., & García-Bellido, D., eds., The Ordovician of the World: Madrid, Instituto Geológico y Minero de España, Cuadernos del Museo Geominero, v. 14, p. 75–82.

Cagnard, F., Durrieu, N., Gapais, D., Brun, J.-P., & Ehlers, C. 2006. Crustal thickening and lateral flow during compression of hot lithospheres, with particular reference to Precambrian times. Terra Nova, 18, 72–78. https://doi.org/10.1111/j.1365-3121.2005.00665.x

Calignano, E., Sokoutis, D., Willingshofer, E., Brun, J.-P., Gueydan, F., Cloetingh, S., 2017.Oblique contractional reactivation of inherited heterogeneities: cause for arcuateorogens. Tectonics 36:542–558. http://dx.doi.org/10.1002/2016TC00442

Cao, S., & Neubauer, F. 2016. Deep crustal expressions of exhumed strike-slip fault systems: Shear zone initiation on rheological boundaries. Earth-Science Reviews, 162, 155-176

Capuzzo N, Bussy F. 2000. High-precision dating and origin of synsedimentary volcanism in the late Carboniferous Salvan-Dorenaz basin (Aiguilles-Rouges Massif, western Alps): Schweiz Miner Petrog 80:147–167.

Capuzzo N, Wetzel A. 2004. Facies and basin archi-tecture of the late Carboniferous Salvan-Dorenaz continental basin (western Alps, Switzerland/France). Sedimentology 51:675–697. doi:10.1111/j.1365-3091.2004.00642.x.

Capuzzo, N., Handler, R., Neubauer, F., & Wetzel, A. 2003. Post-collisional rapid exhumation and erosion during continental sedimentation: The example of the late-Variscan Salvan-Dorenaz basin (western Alps). International Journal of Earth Sciences, 92, 364–379. doi:10.1007/s00531-003-0332-0.

Carme, F., 1965. Sur deux formations, d'origine volcanique, des schistes cristallins antéhouillers de la chaîne de Belledonne (Alpes Francaise). C R Acad Sc Paris 260, 6401–6404.

Carmignani, L., Oggiano, G., Funedda, A., Conti, P., Pasci, S., 2015. The Geological Map ofSardinia (Italy) at 1:250,000 Scale. Journal of Maps http://dx.doi.org/10.1080/17445647.2015.1084544

Carosi, R., Frassi, C., & Montomoli, C. 2009. Deformation during exhumation of medium- and high-grade metamorphic rocks in the Variscan chain in northern Sardinia (Italy). Geological Journal 44, 280–305.

Carosi, R., Montomoli, C., Tiepolo, M., & Frassi, C. 2012. Geochronological constraints on post-collisional shear zones in the Variscides of Sardinia (Italy). Terra Nova, 24, 42–51.

Carosi R, D’addario E, Mammoliti E, Montomoli C, Simonetti M 2016 Geological map of the northwestern portion of the Ferriere-Mollieres shear zone, Argentera Massif, Italy. J Maps 12:466–475

Carreras J, Capella I. 1994. Tectonic levels in the Palaeozoic basement of the Pyrenees: A review and a new interpretation. J Struct Geol 16: 1509–1524.

Carreras J, Druguet E. 2014. Framing the tectonic regime of the NE Iberian Variscan segment. Geol Soc Spec Publ London 405. https://doi.org/10.1144/SP405.7.

Cartannaz C, Rolin P, Cocherie A, Marquer D, Legendre O, Fanning CM, et al. 2007b. Characterization of wrench tectonics from dating of syn-to post-magmatism in the north-western French Massif Central. Int. J. Earth Sci. 96: 271–287.

Cartannaz C, Rolin P, Cocherie A, Henry P, Rossy M. 2007a. Notice Feuille Aubusson, 667 p.

Casas JM, Palacios T. 2012. First biostratigraphical constraints on the pre-Upper Ordovician sequences of the Pyrenees based on organic walled microfossils. C R Geosci 344: 50–56.

Casas JM, Fernández O, Domingo F. 2007. Carboniferous normal faults in the Eastern Pyrenees: Evidences and age constrains of synorogenic Variscan extension. Geodin Acta 20: 385–392.

Casini, L., Cuccuru, S., Maino, M., Oggiano, G., Tiepolo, M., 2012.Emplacement of theArzachena Pluton (Corsica–Sardinia Batholith) and the geodynamics of incomingPangaea. Tectonophysics 544-545, 31–49.

Casini, L., Cuccuru, S., Puccini, A., Oggiano, G., Rossi, P., 2015. Evolution of the Corsica–Sar-dinia Batholith and late-orogenic shearing of the Variscides. Tectonophysics 646,65–78

Chardon D, Gapais D, Cagnard F. 2009. Flow of ultra-hot orogens: a view from the Precambrian, clues for the Phanerozoic. Tectonophysics 477: 105–118.

Chardon, D., Jayananda, M., Peucat, J.-J., 2011. Lateral constrictional flow of hotorogenic crust: insights from the Neoarchean of South India, geological andgeophysical implications for orogenic plateaux. Geochemistry, Geophysics, Geosystems 12, Q02005,http://dx.doi.org/10.1029/2010GC003398.

Chardon D, Aretz M, Roques D 2020 Reappraisal of Variscan tectonics in the southern French Massif Central. Tectonophysics 787, 228477.Charles, N., Faure, M., & Chen, Y. 2009. The Montagne Noire migmatite dome emplacement (French Massif Central): New insights from petro fabric and AMS studies. Journal of Structural Geology, 31, 1423–1440. doi:10.1016/j.jsg.2009.08.007.

Chelalou R. 2015. Formation et évolution du bassin de Boucheville, implication sur l'évolution tectonique, métamorphique et sédimentaires des bassins sédimentaires mésozoïques du Nord-Est des Pyrénées. PhD thesis, Rennes (France), Univ. Rennes 1.

Chelalou R, Nalpas T, Bousquet R, Prevost M, Lahfid A, Poujol M, et al. 2016. New Sedimentological, Structural and Paleo-Thermicity Data in the Boucheville Basin (Eastern North Pyrenean Zone, France). C R Geosci 348: 312–321.

Chelle-Michou C, Laurent O, Moyen JF et al 2017 Pre-Cadomian to late-Variscan odyssey of the eastern Massif Central, France: Formation of the West European crust in a nutshell. Gondwana Res. 46:170-190.

Chiaradia, M. 2003. Formation and Evolution Processes of the Salanfe W–Au–As-Skarns (Aiguilles Rouges Massif, Western Swiss Alps). Mineralium Deposita, 38, 154 68. https://doi.org/10.1007/s00126-002-0296-1

Chopin, C. 1984. Coesite and pure pyrope in high-grade blueschists of the western Alps: a first record and some consequence. Contribution to Mineralogy and Petrology, 86, 107–118.

Clark, M.K., Royden, L.H., 2000. Topographic ooze: building theeastern margin of Tibet by lower crustal flow. Geology 28,703–706.

Clemens, J.D., Mawer, C.K., 1992. Granitic magma transport byfracture propagation. Tectonophysics 204, 339–360.

Clemens, J.D., Vielzeuf, D., 1987. Constraints in melting and magma production in the crust. Earth and Planetary Science Letters 86, 287–306.

Clemens, J.D., Petford, N., Mawer, C.K., 1997. Ascent mechanismsof granitic magmas: causes and consequences. In: Holness, M.(Ed.), Deformation-Enhanced Fluid Transport in the Earth'sCrust and Mantle. Chapman & Hall, London, pp. 144–171.

Clerc C. 2012. Évolution du domaine nord-pyrénéen au Crétacé. Amincissement crustal extrême et thermicité élevée : un analogue pour les marges passives. PhD thesis, Paris (France), Univ. Pierre et Marie Curie – Paris VI.

Clerc C, Lagabrielle Y. 2014. Thermal control on the modes of crustal thinning leading to mantle exhumation: Insights from the Cretaceous Pyrenean hot paleomargins. Tectonics 33: 1340–1359.

Clerc C, Lagabrielle Y, Neumaier M, Reynaud JY, St Blanquat M. 2012. Exhumation of subcontinental mantle rocks: Evidence from ultramafic-bearing clastic deposits nearby the Lherz peridotite body, French Pyrenees. Bull Soc geol Fr 183: 443–459.

Clerc C, Boulvais P, Lagabrielle Y, Blanquat M. 2013. Ophicalcites from the northern Pyrenean belt: A field, petrographic and stable isotope study. Int J Earth Sci 103: 141–163.

Clerc C, Lahfid A, Monié P, Lagabrielle Y, Chopin C. 2015. High temperature metamorphism during extreme thinning of the continental crust: A reappraisal of the North Pyrenean passive paleomargin. Solid Earth 6: 643–668.

Clerc C, Lagabrielle Y, Labaume P, Ringenbach JC, Vauchez A, Nalpas T, et al. 2016. Basement – Cover decoupling and progressive exhumation of metamorphic sediments at hot rifted margin. Insights from the Northeastern Pyrenean analog. Tectonophysics 686: 82–97.

Cochelin B. 2016. Champ de déformation du socle paléozoïque des Pyrénées. PhD thesis, Toulouse (France), Univ. Paul Sabatier.

Cochelin B, Chardon D, Denèle Y, Gumiaux C, Le Bayon B. 2017. Vertical strain partitioning in hot Variscan crust: Syn-convergence escape of the Pyrenees in the Iberian-Armorican syntax. Bull Soc geol Fr 188. https://doi.org/10.1051/bsgf/2017206.

Cochelin, B., Lemirre, B., Denèle, Y., & de Saint Blanquat, M. 2021. Strain partitioning within bending orogens, new insights from the Variscan belt (Chiroulet-Lesponne domes, Pyrenees). Tectonics, 40, e2020TC006386. https://doi.org/10.1029/2020TC006386

Cocherie A, Baudin T, Autran A, Guerrot C, Fanning CM, Laumonier B. 2005. U-Pb zircon (ID-TIMS and SHRIMP) evidence for the early ordovician intrusion of metagranites in the late Proterozoic Canaveilles Group of the Pyrenees and the Montagne Noire (France). Bull. Société Géologique Fr. 176: 269–282.

Cogné, J. P., Perroud, H. 1985, Strain removal applied to paleomag-netic directions in an orogenic belt: The Permian red slates of the AlpsMaritimes, France, Earth Planet. Sci. Lett.,72, 125–140

Collins, W.J., Huang, H.Q., Jiang, X.Y., 2016. Water-fluxed crustal melting produces Cordilleran batholiths. Geology 44, 143–146.

Collombet M, Thomas JC., Chauvin A, Tricart P, Bouillin JP, Gra-tier JP 2002 Counterclockwise rotation of the western Alps since the Oligocene: New insights from paleomagnetic data. Tectonics 21(4):1032. https://doi.org/10.1029/2001T C9010 16

Colombo, F., Compagnoni, R., & Lombardo, B. 1994. Le rocce eclogitiche dei Laghi del Frisson (Argentera sud-orientale, Alpi Marittime). Atti Ticinensi di Scienze della Terra (Pavia), Serie Speciale, 1, 75–82.

Compagnoni, R., & Rolfo, F. 2003. UHPM units in the Western Alps. In D. A. Carswell & R. Compagnoni (Eds.), Ultrahigh pressure metamorphism, Eur. Mineral. Union Notes Mineral. (Vol. 5, pp. 13–49). Budapest: Eötvös Loránd University.

Connolly, J.A.D. 2005. Computation of phase equilibria by linear programming: a tool for geodynamic modeling and its application to subduction zone decarbonation. Earth Planetary Science Letters, 236, 524–541.

Corfu, F., Hanchar, J. M., Hoskin, P. W. O., & Kinny, P. 2003. Atlas of zircon textures. In: Hanchar, J. M. & Hoskin, P. W. O. (eds) Zircon. Mineralogical Society of America, Reviews in Mineralogy and Geochemistry, 53, 469-500.

Corre B, Boulvais P, Boiron MC, Lagabrielle Y, Marasi L, Clerc C. 2018. Fluid circulations in response to mantle exhumation at the passive margin setting in the north Pyrenean zone, France. Mineral Petrol 112: 1–24.

Corsini, M., & Rolland, Y. 2009. Late evolution of the southern European Variscan belt: exhumation of the lower crust in a context of oblique convergence. Comptes Rendus Geosciences, 341, 214–223.

Cortesogno, L., Gaggero, L., & Capelli, C. 1997. Petrology of pre-Alpine eclogites and amphibolites from the Ligurian Briançonnais basement. Atti Ticinensi di Scienze della Terra, 39, 3–29.

Cortesogno, L., Gaggero, L., Oggiano, G., & Paquette, J. L. 2004. Different tectono-thermal evolutionary paths in eclogitic rocks from the axial zone of the Variscan chain in Sardinia (Italy) compared with the Ligurian Alps. Ofioliti, 29, 125–144.

Couzinié S, Moyen JF, Villaros A, Paquette JL, Scarrow JH, Marignac C 2014 Temporal relationships between Mg-K mafic magmatism and catastrophic melting of the Variscan crust in the southern part of Velay Complex (Massif Central, France). J Geosci 59:1-18.

Couzinié S, Laurent O, Moyen JF, Zeh A, Bouilhol P, Villaros A. 2016. Post-collisional magmatism: Crustal growth not identified by zircon Hf–O isotopes. Earth Planet Sci Lett 456: 182–195.

Couzinié, S., Bouilhol, P., Laurent, O., Marko, L., & Moyen, J. F. 2021. When zircon drowns: Elusive geochronological record of water-fluxed orthogneiss melting in the Velay dome (Massif Central, France). Lithos, 384, 105938.

Crowley, Q.G., Floyd, P.A., Winchester, J.A., Franke, W., Holland, J.G., 2000. Early Palaeozoic rift-related magmatism in VariscanEurope: fragmentation of the Armorican Terrane Assemblage.Terra Nova 12, 171–180.

Cruciani G., Franceschelli M., Caredda A.M. Carcangiu G.,2001. Anatexis in the Hercynian basement of NE Sardinia, Italy: a case study of the migmatite of Porto Ottiolu. Mineral. Petrol., 71: 195-233

Cruciani, G., Franceschelli, M., & Groppo, C. 2011. P–T evolution of eclogite-facies metabasite from NE Sardinia, Italy: insights into the prograde evolution of Variscan eclogites. Lithos, 121(1), 135–150.

Cruciani, G., Franceschelli, M., Groppo, C., & Spano, M. E. 2012. Metamorphic evolution of non-equilibrated granulitized eclogite from Punta de li Tulchi (Variscan Sardinia) determined through texturally controlled thermodynamic modelling. Journal of Metamorphic Geology, 30, 667–685.

Cruciani, G., Franceschelli, M., Massonne, H. J., Carosi, R. & Montomoli, C. 2013. Pressuretemperature and deformational evolution of highpressure metapelites from Variscan NE Sardinia, Italy. Lithos, 175–176, 272–284.

Cruciani, G., Franceschelli, M., Langone, A., Puxeddu, M., & Scodina, M. 2015a. Nature and age of pre-Variscan eclogite protoliths from the Low-to Medium-Grade Metamorphic Complex of north–central Sardinia (Italy) and comparisons with coeval Sardinian eclogites in the northern Gondwana context. Journal of Geological Society, 172(6), 792–807.

Cruciani, G., Montomoli, C., Carosi, R., Franceschelli, M., Puxeddu, M., 2015b. Continental collision from two perspectives: a review of Variscan metamorphism and deformation in northern Sardinia. Periodico di Mineralogia 84, 657–699.

Cruciani, G., Franceschelli, M., Scodina, M., Puxeddu, M., 2019. Garnet zoning in kyanite bearing eclogite from Golfo Aranci: new data on the early prograde P–T evolution in NE Sardinia, Italy. Geol. J. 54, 190–205.

Cruciani, G., Franceschelli, M., Massonne, H.J., Musumeci, G. 2021. Evidence of two metamorphic cycles preserved in garnet from felsic granulite in the southern Variscan belt of Corsica, France. Lithos, 380–381, 105919.

Cruden, A.R., 1990. Flow and fabric development during the diapiric rise of magma. Journal of Geology, 98, 681–698.

Cugeronne A, Roger F, Cenki-Tok B, Oliot E, Paquette JL. in press. Variscan U-Th-Pb age for stratabound Pb-Zn mineralization in the Bossòst dome (Pyrenean Axial Zone), Ore Geology Reviews , in press, doi:https://doi.org/10.1016/j.oregeorev.2021.104503

D'Lemos, R.S., Brown, M. and Strachan, R.A., 1992. The relationship between granite and shear zones: magma gen- eration, ascent and emplacement within a transpressional orogen. J. Geol. Soc. London, 149: 487-490.

Dale, J. & Holland, T. J. B. 2003. Geothermobarome-try, P – T paths and metamorphic field gradients of high-pressure rocks from the Adula Nappe, Central Alps. Journal of Metamorphic Geology, 21, 813 – 829.

Davy, P., Gillet, P. 1986. The stacking of thrust slices in collision zones and its thermal consequences, Tectonics, 5, 913-929

De Hoÿm de Marien, 2019. Évolution pression-température-temps des unités varisques de haute-pression de l'est du Massif Central : implications géodynamiques. PhD thesis, Rennes (France), Univ. Rennes 1.

de Hoÿm LM, Pitra P, Cagnard F, Le Bayon B 2020 Prograde and retrograde P-T evolution of a Variscan high-temperature eclog-ite, French Massif Central. Haut-Allier Earth Sci Bull 191:14

de Hoÿm de Marien L, Le Bayon B, Pitra P, Van Den Driessche J, Poujol M, Cagnard F. 2018. Two-stage Variscan metamorphism in the Canigou massif: Evidence for crustal thickening in the Pyrenees. J Metamorph Geol 37: 863–888.

de Saint Blanquat M. 1989. La faille normale ductile du massif du Saint Barthélémy. Age et signification de l'extension crustale dans le zone Nord-pyrénéenne. PhD thesis, Montpellier (France), Univ. Montpellier 2.

de Saint Blanquat M. 1993. La faille normale ductile du massif de Saint-Barthélémy. Évolution hercynienne des massifs nord pyrénéens catazonaux considérée du point de vue de leur histoire thermique. Geodin Acta 6: 59–77.

de Saint Blanquat M., Lardeaux JM, Brunel M. 1990. Petrological arguments for high-temperature extensional deformation in the Pyrenean Variscan crust (Saint Barthélémy Massif, Ariège, France). Tectonophysics 177: 245–262.

de Saint Blanquat, M., Horsman, E., Habert, G., Morgan, S., Vanderhaeghe, O., Law, R., Tikoff, B., 2011. Multiscale magmatic cyclicity, duration of pluton construction, and the paradoxical relationship between tectonism and plutonism in continentalarcs. Tectonophysics 500, 20–33. doi:10.1016/j.tecto.2009.12.009.

Debon F, Lemmet M. 1999. Evolution of Mg/Fe ratios in late Variscan plutonic rocks from the external crystalline massif of the Alps (France, Italy, Switzerland). J. Petrol. 40:1151–1185.

Debon, F., Cocherie, A., Ménot, R.-P., Vivier, G., & Barféty, J.-C. 1994. Datation du plutonisme magnésien varisque des massifs cristallins externes des Alpes: l'exemple du granite des Sept Laux (massif de Belledonne, France). Comptes Rendus de Academie des Sciences Paris Serie II, 318, 1497–1504.

Debon, F., Guerrot, C., Ménot, R.-P., Vivier, G., & Cocherie, A. 1998. Late Variscan granites in the Belledonne massif (French Western Alps): An Early Visean magnesian plutonism. Schweizerische Mineralogische und Petrographische Mitteilungen, 78, 67–85.

Debroas EJ, Canérot J, Bilotte M. 2010. Les Brèches d'Urdach, témoins de l'exhumation du manteau pyrénéen dans un escarpement de faille vraconnien-cénomanien inférieur (zone nord pyrénéenne, Pyrénées-Atlantiques, France). Geol Fr 2: 53–64.

Delaperrière E, de Saint-Blanquat M, Brunel M, Lancelot JR. 1994. Geochronologie U-Pb sur zircons et monazites dans le massif du Saint Barthelemy (Pyrenees, France) ; discussion des âges des évènements varisques et pré-varisques. Bull Soc geol Fr 165: 101–112.

Delay F. 1989. Le massif nord-pyrénéen de l'Agly (Pyrénées orientales) : Évolution tectono-métamorphique et exemple d'un amincissement crustal polyphasé. PhD thesis, Lille (France), Univ. Lille 1.

Delchini, S., Lahfid, A., Plunder, A., Michard, A. 2016: Applicability of the RSC geothermometry approach in a complex tectono-metamorphic context: the Jebilet massif case study (Variscan Belt, Morocco). Lithos, 256–257, 1–12.

Delor C, Leyreloup A, Bodinier J-L, Burg J-P. 1986. Découverte d'éclogites à glaucophane dans la klippe de Najac (Massif Central, France): nouveaux témoins océaniques d'un stade haute pression dans la chaîne de collision varisque. Comptes Rendus Académie Sci. Sér. 2 Mécanique Phys. Chim. Sci. Univers Sci. Terre 302: 739–744.

Delvolvé, J.-J., & Perret, M.-F. 1989. Variation de l'âge des sediments calcaires et "Culm" carbonifère dans la chaine varisque du sud de la France: Migration de l'orogenèse varisque. Geodinamica Acta, 3, 117–126. https://doi.org/10.1080/09853111.1989.11105179

Demoux, A., Schärer, U., and Corsini, M., 2008, Variscan evolu-tion of the Tanneron Massif, SE France, examined throughU-Pb monazite ages: Journal of the Geological Society, 165, 467–478.

Denèle, Y., 2007. Formation des dômes gneissiques hercyniens dans les Pyrénées : exemple du massif de l'Aston-Hospitalet. Université Toulouse III - Paul Sabatier.

Denèle Y, Olivier P, Gleizes G, Barbey P. 2009. Decoupling between the Middle and Upper Crust during Transpression-Related Lateral Flow: Variscan Evolution of the Aston Gneiss Dome (Pyrenees, France). Tectonophysics 477: 244–261.

Denèle, Y., Paquette, J.-L., Olivier, P., Barbey, P., 2012. Permian granites in the Pyrenees: the Aya pluton (Basque Country). Terra Nov. 24, 105–113.

Denèle Y, Laumonier L, Paquette JL, Olivier P, Gleizes G, Barbey P. 2014. Timing of granite emplacement, crustal flow and gneiss dome formation in the Variscan segment of the Pyrenees. Geol Soc London Spec Publ 405: 265–287.

Depine, G. V, Andronicos, C.L., Phipps-Morgan, J., 2008. Near-isothermal conditions in the middle and lower crust induced by melt migration. Nature 452, 80–83. https://doi.org/10.1038/nature06689

Dewey JF. 1988. Extensional collapse of orogens. Tectonics 7: 1123–1139.

Di Vincenzo, G., Carosi, R. & Palmeri, R. 2004. The relationship between tectono-metamorphic evolution and argon isotope records in white mica: constraints from in situ 40Ar-39Ar laser analysis of the Variscan Basement of Sardinia. Journal of Petrology, 45, 1013–1043.

di Paola, S., and M. I. Spalla 2000, Contrasting tectonic records in pre-Alpine metabasites of the southern Alps (Lake Como, Italy). J. Geodyn.,30, 167–189.

Di Rosa, M., Frassi, C., Meneghini, F., Marroni, M., Pandolfi, L., De Giorgi, A., 2020. Tectonometamorphic evolution of the European continental margin involved in the Alpine subduction: new insights from Alpine Corsica, France. Compt. Rendus Geosci. 351, 384–394.

Dickinson, W.R., Gehrels, G.E., 2009. Use of UePb ages of detrital zircons to infer maximum depositional ages of strata: a test against a Colorado Plateau Mesozoic database. Earth and Planetary Science Letters 288 (1-2), 115e125. http://dx.doi.org/10.1016/j.epsl.2009.09.013.

Didier A, Bosse V, Boulvais P, Bouloton J, Paquette J-L, Montel J-M, et al. 2013. Disturbance versus preservation of U–Th–Pb ages in monazite during fluid–rock interaction: textural, chemical and isotopic in situ study in microgranites (Velay Dome, France). Contrib. Mineral. Petrol. 165: 1051–1072.

Diener, J.F.A. & Fagereng, A., 2014. The influence of melting and melt drainage on crustal rheology during orogenesis. Journal of Geophysical Research: Solid Earth,119,6193–6210

Dobmeier C. 1996. Geodynamische Entwicklung dessüdwestlichen Aiguilles-Rouges Massivs (West-alpen, Frankreich). Mém. Géol. Lausanne 29:1-198.

Dobmeier, C. 1998. Variscan P-T deformation paths from the southwestern Aiguilles Rouges Massif (External massif, western Alps) and their implication for its tectonic evolution. Geologische Rundschau, 87, 107–123, doi:10.1007/s005310050193.

Dobmeier C, von Raumer JF. 1995. Significance of latest – Variscan and Alpine deformation for the evolution of Montagne de Pormenaz (southwestern Aiguilles-Rouges massif, western Alps). Eclogae Geol. Hel. 88:267–279.

Dobmeier C, Pfeifer HR, von Raumer JF. 1999. The newly defined “Greenstone Unit” of the Aiguilles-Rouges massif (western Alps); remnant of an early Palaeozoic oceanic island-arc. Schweiz Miner Petrog 79:263–276.

Dörr W, Zulauf G. 2010. Elevator tectonics and orogenic collapse of a Tibetan-style plateau in the European Variscides: The role of the Bohemian shear zone. Int J Earth Sci 99: 299–325.

Droop, G.T.R., 1983. Pre-Alpine eclogites in the Pennine basement complex of the eastern Alps. J. Metamorph. Geol. 1, 3-12

Druguet E. 1997. The structure of the NE Cap de Creus NE peninsula. Relationships with metamorphism and magmatism. PhD thesis, Barcelona (Spain), Univ. Autónoma de Barcelona.

Druguet E. 2001. Development of High Thermal Gradients by Coeval Transpression and Magmatism during the Variscan Orogeny: Insights from the Cap de Creus (Eastern Pyrenees). Tectonophysics 332: 275–293.

Druguet, E., Carreras, J., 2006. Analogue modelling of syntectonic leucosomes inmigmatitic schists. Journal of Structural Geology 28, 1734e1747.

Druguet E, Castro A, Chichorro M, Pereira MF, Fernández C. 2014. Zircon geochronology of intrusive rocks from Cap de Creus, Eastern Pyrenees. Geol Mag 151: 1095–1114.

Duchene, S., Lardeaux, J.M., & Albarède, F. 1997. Exhumation of eclogites: insights from depth–time path analysis. Tectonophysics 280 (1–2), 125–140.

Duchesne, J.-C., Liégeois, J.-P., Bolle, O., Vander Auwera, J., Bruguier, O., Matukov, D. I., & Sergeev, S. A. 2013. The fast evolution of a crustal hot zone at the end of a transpressional regime: The Saint-Tropez peninsula granites and related dykes (Maures Massif, SE France). Lithos, 162–163, 195–220.

Ducoux M. 2017. Structure, thermicité et évolution géodynamique de la Zone Interne Métamorphique des Pyrénées. PhD thesis, Orléans (France), Univ. d’Orléans.

Ducrot J, Lancelot JR, Marchand J. 1983. Datation U-Pb sur zircons de l’eclogite de la Borie (Haut-Allier, France) et consequences sur l’evolution ante-hercynienne de l’Europe occidentale. Earth Planet. Sci. Lett. 62: 385–394.

Dumond G, Goncalves P, Williams ML, Jercinovic MJ 2015 Monazite as a monitor of melting, garnet growth and feldspar recrystallization in continental lower crust. J Metamorph Geol 33:735–762, doi:10.1111/jmg.12150

Duesterhoeft, E., & Lanari, P. 2020. Iterative thermodynamic modelling—Part 1: A theoretical scoring technique and a computer program (Bingo-Antidote). Journal of Metamorphic Geology, 8, 527–551.

Dufour E. 1985. Granulite facies metamorphism and retrogressive evolution of the Monts du Lyonnais metabasites (Massif Central, France). Lithos 18: 97–113.

Duprat-Oualid, S. 2014. Évolution thermique et mécanique des zones de cisaillement : approche analytique et numérique, et confrontation aux données de terrain. PhD thesis, Rennes (France), Univ. Rennes 1.

Duprat-Oualid S, Yamato P, Pitra P 2013 Major role of shear heating on intracontinental inverted metamorphism: inferencefrom a thermo-kinematic parametric study. Tectonophysics 608:812–831

Duprat-Oualid S, Yamato P, Schmalholz SM 2015 A dimensional analysis to quantify the thermal budget around lithospheric-scale shear zones. Terra Nova 27:163–168

Duthou JL, Chenevoy M, Gay M. 1994. Rb-Sr middle Devonian age of cordierite bearing migmatites from Lyonnais area (French Massif Central). Comptes Rendus Acad. Sci. Ser. 2 Sci. Terre Planetes 319: 791–796.

Edel, J.B., 2000, Hypothèse d'une ample rotation horaire tardi-varisque en blocMaures-Estérel-Corse-Sardaigne: Géologie de la France, v. 1, p. 3–19.

Edel, J.B., Casini, L., Oggiano, G., Rossi, P., Schulmann, K., 2014. Early Permian 90°clockwise rotation of the Maures-Estérel-Corsica-Sardinia block confirmed by newpalaeomagnetic data and followed by a Triassic 60° clockwise rotation. Geol. Soc.Spec. Publ. 1–29.

Edel, J.B., Schulmann, K., Lexa, O., Diraison, M., Géraud, Y., 2015. Permian clockwiserotations of the Ebro and Corso-Sardinian blocks during Iberian-Armorican oroclinalbending: preliminary paleomagnetic data from the Catalan Coastal Range (NE Spain). Tectonophysics 657, 172–186

Edel JB, Schulmann K, Lexa O, Lardeaux JM. 2018. Late Palaeozoic palaeomagnetic and tectonic constraints for amalgamation of Pangea supercontinent in the European Variscan belt. Earth Sci Rev 177: 589–612.

Egli, D., Müller, W., & Mancktelow, N. 2016. Laser-cut Rb-Sr microsampling dating of deformational events in the Mont Blanc-Aiguilles Rouges region (European Alps). Terra Nova, 28, 35–42.

Egli, D., Mancktelow, N., & Spikings, R. 2017. Constraints from 40Ar/39Ar geochronology on the timing of Alpine shear zones in the Mont Blanc-Aiguilles Rouges region of the European Alps. Tectonics, 36, 730–748. https://doi.org/10.1002/2016TC004450

Eisele, J., Geiger, S., & Rahn, M. 1997. Chemical characterization of metabasites from the Turtmann valley (Valais, Switzerland): Remnant of an early Palaeozoic oceanic island arc? Schweizerische Mineralogische und Petrographische Mitteilungen, 77, 403–418

Elliott, D., 1976, The energy balance and deformation mechanisms of thrust sheets: Royal Soc. London Philos. Trans., ser. A, 283, 289–312.

Elter, F.M. & Pandeli, E. 2005. Structural-metamorphic correlations between three variscan segments in Southern Europe: Maures Massif (France), Corsica (France)–Sardinia (Italy), and Northern Appennines (Italy). Journal of the Virtual Explorer, 9.

Elter, F. M., Corsi, B., Cricca, P. & Muzio, G. 2004. The south-western Alpine foreland: correlation between two sectors of the Variscan chain belonging to 'stable Europe': Sardinia–Corsica and the Maures Massif (south-eastern France). Geodinamica Acta, 17, 31–40.

Elter, F. M., Padovano, M. & Kraus, R. K. 2010. The emplacement of Variscan HT metamorphic rocks linked to the interaction between Gondwana and Laurussia: structural constraints in NE Sardinia (Italy). Terra Nova, 22, 369–377

England, P.C., Thompson, A., 1986. Some thermal and tectonic models for crustal melting in continental collision zones. Geol. Soc. London, Spec. Publ. 83–94.

Esteban, J.J., Aranguren, A., Cuevas, J., Hilario, A., Tubía, J.M., Larionov, A., Sergeev, S., 2015. Is there a time lag between the metamorphism and emplacement of plutons in the Axial Zone of the Pyrenees? Geol. Mag. 152, 935–941. https://doi.org/10.1017/S001675681500014X

Eyal, Y., 1988, Sandstone dikes as evidence of localized transtension in a transpressive regime, Bir Zreir area, eastern Sinai: Tectonics 7, 1279–1289.

Faccenda, M., T. V. Gerya, and L. Burlini 2009, Deep slab hydration induced by bending-related variations in tectonic pressure, Nature Geosciences, 2, 790–793.

Fallourd S, Poujol M, Boulvais P, Paquette JL, de Saint Blanquat M, Rémy P. 2014. In Situ LA-ICP-MS U–Pb titanite dating of Na–Ca metasomatism in orogenic belts: The North Pyrenean example. Int J Earth Sci 103: 667–682.

Fancello, D., Cruciani, G., Franceschelli, M., Massonne, H.-J., 2018.Trondhjemiticleucosomes in paragneisses from NE Sardinia: Geochemistry and P-T conditions ofmelting and crystallization. Lithos 304–307, 501–517.

Faryad, S.W., Melcher, F., Hoinkes, G., Puhl, J., Meisel, T., Frank, W. 2002. Relics of eclogite facies metamorphism in the Austro-alpine basement, Hochgro ̈ßen (Speik Complex), Austria. Min-eral. Petrol. 74, 49–73

Faure M. 1995. Late orogenic carboniferous extensions in the Variscan French Massif Central. Tectonics 14: 132–153.

Faure, M., & Cottereau, N. 1988. Données cinématiques sur la mise en place du dôme migmatitique carbonifère moyen de la zone axiale de la Montagne Noire (Massif Central, France). Comptes Rendus Académiques scientifiques de Paris, 307, 1787–1794.

Faure M, Leloix C, Roig J-Y. 1997. L'évolution polycyclique de la chaîne hercynienne. Bull. Société Géologique Fr. 168: 695–705.

Faure, M., Bé Mezème, E., Duguet, M., Cartier, C. & Talbot, J. Y. 2005. Palaeozoic tectonic evolution of Medio-Europa from the example of the French Massif Central and Massif Armoricain. Journal of the Virtual Explorer, 19, 1–26.

Faure M, Bé Mézème E, Cocherie A, Rossi P, Chemenda A, Boutelier D. 2008. Devonian geodynamic evolution of the Variscan Belt, insights from the French Massif Central and Massif Armoricain. Tectonics 27.

Faure M, Lardeaux JM, Ledru P. 2009. A review of the pre-Permian geology of the Variscan French Massif Central. C R Geosci 341: 202–213.

Faure M, Cocherie A, Mézème EB, Charles N, Rossi P. 2010. Middle Carboniferous crustal melting in the Variscan Belt: New insights from U–Th–Pbtot. monazite and U–Pb zircon ages of the Montagne Noire Axial Zone (southern French Massif Central). Gondwana Res. 18: 653–673. https://doi.org/10.1016/j.gr.2010.02.005.

Faure M, Rossi P, Gaché J, Melleton J, Frei D, Li X, Lin W. 2014a. Variscan orogeny in Corsica: new structural and geochronological insights, and its place in the Variscan geodynamic framework. Int. J. Earth Sci. 103: 1533–1551.

Faure, M., Cocherie, A., Gaché, J., Esnault, C., Guerrot, C., Rossi, P., … Qiuli, L. 2014b. Middle Carboniferous intracontinental subduction in the Outer Zone of the Variscan Belt (Montagne Noire Axial Zone, French Massif Central): multi-method geochronological approach of polyphase metamorphism. In: Schulmann, K., Martinez Catalan, J.R., Lardeaux, J.M., Janousek, V., Oggiano, G. (Eds.), The Variscan Orogeny: Extent, Timescale and the Formation of the European Crust. Geological Society of London, Special Publication, 405. http://dx.doi.org/10.1144/SP405.2.

Faure-Muret, A., Fallot, P., Lanteaume, M. 1967. Carte Géologique de la France à 1:50.000, Feuille St-Martin-Vésubie–Le Boréon (947). Bureau de Recherches Géologiques et Minières, Orléans.

Fernandez, A., Guillot, S., Ménot, R.-P., & Ledru, P. 2002. Late Paleozoic polyphased tectonics in the SW Belledonne massif (external crystalline massifs, French Alps). Geodinamica Acta, 15, 127–139.

Ferrando, S., Lombardo, B., & Compagnoni, R. 2008. Metamorphic history of HP mafic granulites from the Gesso-Stura Terrain (ArgenteraMassif, Western Alps, Italy). European Journal of Mineralogy, 20, 777–790.

Filippi M, Zanoni D, Lardeaux J-M, Spalla MI, Gosso G 2020 Evi-dence of Tethyan continental break-up and Alpine collision in the Argentera-Mercantour Massif. Western Alps Lithos 372–373:105653. https:// doi. org/ 10. 1016/j. lithos. 2020. 105653

Fonteilles M. 1970. Géologie des terrains métamorphiques et granitiques du massif hercynien de l'Agly (Pyrénées orientales). Bull BRGM 3: 1–54.

Fonteilles M. 1976. Essai d'interprétation des compositions chimiques des roches d'origine métamorphique et magmatique du massif hercynien de l'Agly (Pyrénées Orientales). State thesis, Paris (France), Univ. Paris VI.

FonteillesM, Guitard G. 1971.Disthène relique et disthène hystérogène dans les terrains métamorphiques hercyniens des Pyrénées orientales franco-espagnoles. C R Acad Sci Paris 272: 361–363.

Fonteilles M, Guitard G, Raguin E. 1964. Sur la présence de gneiss à disthène et cordiérite dans le massif du Saint-Barthélémy (Pyrénées de l'Ariège). C R Acad Sci Paris 258: 3524–3525.

Fonteilles M, Leblanc D, Clauzon G, Vaudin JL, Berger GM. 1993. Carte géologique de la France, feuille Rivesaltes (1090), scale 1:50 000. Orléans : BRGM.

Fossen H, Tikoff B. 1993. The deformation matrix for simultaneous simple shearing, pure shearing and volume change, and its application to transpression-transtension tectonics. J Struct Geol 15: 413–422.

Fossen, H., Cavalcante, G.C.G., 2017. Shear zones–a review. Earth Sci. Rev. 171,434–455.

Fossen, H., Cavalcante, G.C.G., Pinheiro, R.V.L., Archanjo, C.J., 2019. Deformation - Progressive or multiphase? J. Struct. Geol 125, 82-99.

Franceschelli, M., Puxeddu, M., Cruciani, G. & Utzeri, D. 2007. Metabasites with eclogite facies relics from Variscides in Sardinia, Italy: a review. International Journal of Earth Sciences, 96, 795–815.

Franke W, Doublier MP, Klama K, Potel S, Wemmer K. 2011. Hot metamorphic core complex in a cold foreland. Int J Earth Sci 100:753–785.

Franke, W., Cocks, L. R. M., & Torsvik, T. H. 2017. The Palaeozoic Variscan oceans revisited. Gondwana Research, 48, 257-284.

Franz, L., & Romer, R. L. 2007. Caledonian high-pressure metamorphism in the Strona-Ceneri Zone (Southern Alps of southern Switzerland and northern Italy). Swiss Journal of Geosciences, 100, 457–467.

Freundt, A., Grevemeyer, I., Rabbel, W., Hansteen, T.H., Hensen, C., Wehrmann, H., … Frische, M. 2014. Volatile (H2O, CO2, Cl, S) budget of the Central American subduction zone. International Journal of Earth Science, 103, 2101–2127.

Fréville, K. 2016. The variscan orogeny in the external crystalline massifs of Belledonne and Pelvoux (French Western Alps): the role of partial melting and plutonism on the structuration of the continental crust, (Doctoral dissertation). Retrieved from HAL (https://tel.archives-ouvertes.fr/tel-01968058/). Orléans, France, Université de Orléans.

Fréville K, Cenki-Tok B, Trap P, Rabin M, Leyreloup A, Régnier JL, et al. 2016. Thermal interaction of middle and upper crust during gneiss dome formation: Example from the Montagne Noire (French Massif Central). J Metamorph Geol 34: 447–462.

Freville, K., Trap, P., Faure, M., Melleton, J., Li, X.H., Lin, W., Blein, O., Bruguier, O., Poujol, M. 2018. Structural, metamorphic and geochronological insights on the Variscan evolution of the Alpine basement in the Belledonne Massif (France). Tectonophysics, 726, 14–42.

Fréville, K., Trap, P., Vnardois, J., Melleton, J., Faure, M., Bruguier, O., Poujol, M., Lach, P. in review. Carboniferous tectono-metamorphic evolution of the Variscan crust in the Belledonne-Pelvoux area. Bulletin Géologique de la France, in review.

Fréville, K., Vanardois, J., Trap, P., Faure, M., Bruguier, O., Poujol, M., Lach, P. Timing of magmatism and partial melting during orogeny: clues from the Variscan Alpine External Massifs (Belledonne-Pelvoux area, French Alps). In prep.

Frost, B.R., Chamberlain, K.R., & Schumacher, J.C. 2000. Sphene(titanite): phase relations and role as a geochronometer. Chemical Geology, 172, 131–148.

Gaggero, L., Cortesogno, L., & Bertrand, J.-M. 2004. The pre-Namurian basement of the Ligurian Alps: A review of the lithostratigraphy, pre-Alpine metamorphic evolution, and regional comparisons. Periodico di Mineralogia, 73, 85–96.

Ganne, J., Bertrand, J.-M., Fudral, S., Marquer, D., & Vidal, O. 2007. Structural and metamorphic evolution of the Ambin massif (western Alps): Towards a new alternative exhumation model for the Briançonnais domain. Bulletin de la Société Géologique de France, 178, 437–458.

Gapais D, Potrel A, Machado N 2005 Kinematics of long-lasting Paleoproterozoic transpression within the Thompson Nickel Belt, Manitoba, Canada. Tectonics 24, TC3002. doi:10.1029/2004TC001700.

Gapais, D., Brun, J.-P., Gumiaux, C., Cagnard, F., Ruffet, G., Le Carlier De Veslud, C., 2015. Extensional tectonics in the Hercynian Armorican belt (France). An overview. Bull. la Société Géologique Fr. 186, 117–129. https://doi.org/10.2113/gssgfbull.186.2-3.117

García-Sansegundo, J., Poblet, J., Alonso, J. L., & Clariana, P. 2011. Hinterland–foreland zonation of the Variscan orogen in the Central Pyrenees: Comparison with the northern part of the Iberian Variscan Massif. Geological Society - Special Publications, 349, 169–184. https://doi.org/10.1144/SP349.9

Gardien V. 1993. High to medium Pressure relics in the eastern Vivarais series (Eastern part of the French Massif-Central). Comptes Rendus Académie Sci. Sér. II 316: 1247–1254.

Gardien V, Lardeaux J-M. 1991. Découverte d'éclogites dans la synforme de Maclas: extension de l'unité supérieure des gneiss à l'Est du Massif Central. Comptes Rendus Académie Sci. Sér. 2 Mécanique Phys. Chim. Sci. Univers Sci. Terre 312: 61–68.

Gardien, V., Reusser, E. & Marquer, D. 1994. Pre-Alpine metamorphic evolution of the gneisses from the Valpelline series 1986. Schweizerische Mineralogische und Petrographische Mitteilungenand garnet granulites 74, 489–502.

Gardien V, Vanderhaeghe O, Arnaud N, Cocherie A, Grange M, Lécuyer C. 2011. Thermal maturation and exhumation of a middle orogenic crust in the Livradois area (French Massif Central). Bull. Société Géologique Fr. 182: 5–24.

Gardner, R., Piazolo, S., Evans, L., & Daczko, N. 2017. Patterns of strain localization in heterogeneous, polycrystalline rocks–a numerical perspective. Earth and Planetary Science Letters, 463, 253-265

Garuti, G., Bea, F., Zaccarini, F., & Montero, P. 2001. Age, geochemistry and petrogenesis of the ultramafic pipes in the Ivrea Zone, NW Italy. Journal of Petrology, 42, 433–457.

Gauthiez, L., Bussy, F., Gouffon, Y., & Sartori, M. 2011. Ordovician mafic magmatism in the Métailler Formation of the Mont-Fort nappe (Middle Penninic domain, Western Alps)—Geodynamic implications. 9th Swiss Geoscience Meeting (Zürich), Abstract Volume, 110–111.

Gebauer, D., Quadt, A., Compston, W., Williams, I. S., & Grünenfelder, M. 1988. Archaean zircons in a retrograded, Caledonian eclogite of the Gotthard Massif (Central Alps, Switzerland). Schweizerische Mineralogische und Petrographische Mitteilungen, 68, 485–490.

Gébelin A, Brunel M, Monié P, Faure M, Arnaud N. 2007. Transpressional tectonics and Carboniferous magmatism in the Limousin, Massif Central, France: Structural and 40Ar/39Ar investigations. Tectonics 26. https://doi.org/10.1029/2005TC001822.

Gébelin A, Roger F, Brunel M. 2009. Syntectonic crustal melting and high-grade metamorphism in a transpressional regime, Variscan Massif Central, France. Tectonophysics 477: 229–243.

Gehrels, G., 2012. Detrital zircon U-Pb geochronology: current methods and new opportunities, in tectonics of sedimentary basins. In: Busby, C., Azor, A. (Eds.), Recent Advances. Wiley-Blackwell Publishing, pp. 47-62.

Genier, F., Bussy, F., Epard, J.L, & Baumgartner, L. 2008. Water-Assisted Migmatization of Metagraywackes in a Variscan Shear Zone, Aiguilles-Rouges Massif, Western Alps. Lithos, 102, 575 97. https://doi.org/10.1016/j.lithos.2007.07.024.

Gerbault, M., J. Martinod, and G. Herail 2005, Possible orogeny-parallellower crustal flow and thickening in the central Andes, Tectonophysics,399, 59–72, doi:10.1016/j.tecto.2004.12.015.

Gerbault, M., Schneider, J., Reverso-Peila, A., & Corsini, M. 2018. Crustal exhumation during ongoing compression in the Variscan Maures-Tanneron Massif, France - geological and thermo-mechanical aspects. Tectonophysics, 746, 439–458.

Gerbi, C.C., Johnson, S.E, Koons, P.O., 2006. Controls on low-pressure anatexis. J. Metamorph. Geol. 24, 107–118

Getsinger, A.J., & Hirth, G. 2014. Amphibole fabric formation during diffusion creep and the rheology of shear zones. Geology, 42, 535–538. doi:10.1130/G35327.1

Giacomini, F., Bomparola, R.M., & Ghezzo, C. 2005. Petrology and geochronology of metabasites with eclogite facies relics from NE Sardinia: constraints for the Palaeozoic evolution of Southern Europe. Lithos, 82(1), 221–248.

Giacomini, F., Braga, R., Tiepolo, M., Tribuzio, R. 2007. New constraints on the origin and age of Variscan eclogitic rocks (Ligurian Alps, Italy). Contribution to Mineralogy and Petrology, 153(1), 29–53.

Giacomini, F., Dallai, L., Carminati, E., Tiepolo, M., & Ghezzo, C. 2008. Exhumation of a Variscan orogenic complex: insights into the composite granulitic–amphibolitic metamorphic basement of south-east Corsica (France). Journal of Metamorphic Geology, 26, 403–436.

Gibergy, P., 1968. Découverte de “grès à trous” renfermant des schistes noirs de Valbonnais (série cristallophyllienne des Massifs Cristallins Externes dans les Alpes française). C R Acad Sc Paris 267, 1251–1254.

Gibson R. 1991. Hercynian low-pressure-high-temperature regional metamorphism and subhorizontal foliation development in the Canigou massif, Pyrenees, France – Evidence for crustal extension. Geology 19: 380–383.

Gidon, M. 2001. Les massifs cristallins externes des Alpes occidentales françaises sont-ils charriés? Géologie Alpine, 77, 23–38.

Gillcrist, R., Coward, M., & Mugnier, J.-L. 1987. Structural inversion and its controls: Examples from the Alpine foreland and the French Alps. Geodinamica Acta, 1, 5–34.

Giorgis, D., Thélin, P., Stampfli, G., & Bussy, F. 1999. The Mont-Mort metapelites: Variscan metamorphism and geodynamic context (Briançonnais basement, Western Alps, Switzerland). Schweizerische Mineralogische und Petrographische Mitteilungen, 79, 381–398.

Girault, J.B., Bellahsen, N., Boutoux, A., Rosenberg, C.L., Nanni, U., Verlaguet, A., Beyssac, O., 2020. The 3-D thermal structure of the Helvetic Nappes of the European Alps: implications for collisional processes. Tectonics 39, 1–20. https://doi.org/10.1029/2018TC005334.

Gleizes G, Bouchez JL, Lespinasse P, Roux L. 1992. Structure du granite de Lacourt (Arize occidentale) : une signature syntectonique de phase 2 dans l’Hercynien des Pyrénées. Bull Soc Hist Nat Toulouse 128: 53–57.

Gleizes G, Leblanc D, Bouchez JL. 1997. Variscan Granites of the Pyrenees Revisited: Their Role as Syntectonic Markers of the Orogen. Terra Nova 9: 38–41.

Gleizes G, Leblanc D, Bouchez JL. 1998a. The main phase of the Hercynian orogeny in the Pyrenees is a dextral transpression. Geol Soc London Spec Publ 135: 267–273.

Gleizes G, Leblanc D, Santana V, Olivier O, Bouchez JL. 1998b. Sigmoidal structures featuring dextral shear during emplacement of the Hercynian granite complex of Cauterets–Panticosa (Pyrenees). J Struct Geol 20: 1229–1245.

Gleizes G, Leblanc D, Olivier P, Bouchez JL. 2001. Strain partitioning in a pluton during emplacement in transpressional regime: The Example of the Néouvielle Granite (Pyrenees). Int J Earth Sci 90: 325–340.

Gleizes G, Crevon G, Asrat A, Barbey P. 2006. Structure, age and mode of emplacement of the Hercynian Bordères-Louron pluton (Central Pyrenees, France). Int J Earth Sci 95: 1039–1052.

Godard, G., Martin, S., Prosser, G., Kienast, J. R. & Morten, L. 1996. Variscan migmatites, eclogites and garnet-peridotites of the Ulten zone, Eastern Austroalpine system. Tectonophysics, 259, 313–341

Godin L, Grujic D, Law RD, Searle MP 2006 Channel flow, ductile extrusion and exhumation in continental collision zones: an introduction. In: Law RD, Searle MP, Godin L (eds) Channel flow, ductile extrusion and exhumation in continental collision zones, vol 268. Geological Society, London, Special Publications, pp 1–23

Göğüş, O.H. & Pysklywec, R.N. 2008. Near-surface diagnostics of dripping or delaminating lithosphere, J. geophys. Res., 113(B11), B11404.

Golberg JM, Leyreloup AF. 1990. High temperature-low pressure Cretaceous metamorphism related to crustal thinning (Eastern North Pyrenean Zone, France). Contrib Mineral Petrol 104:194–207.

Goncalves, P., Nicollet, C., Montel, J.-M. 2004. Petrology and in situ U-Th-Pb monazite geochronology of ultrahigh-temperature metamorphism from the Andriamena mafic unit, north-central Madagascar. Significance of a petrographical P-T path in a poly-metamorphic context: Journal of Petrology, 45, 1923–1957.

Goncalves, P., Oliot, E., Marquer, D., Connolly, J.A.D., 2012.Role of chemical processes onshear zone formation: an example from the Grimsel metagranodiorite (Aar massif, Central Alps). Journal of Metamorphic Geology 30, 703–722.

Gonçalves, G.O., Lana, C., Scholz, R., Buick, I.S., Gerdes, A., Kamo, S.L., Corfu, F., Marinho, M.M., Chaves, A.O., Valeriano, C., Nalini, A.Jr. 2016 An assessment of monazite from the Itambé pegmatite district for as U-Pb isotope reference material for microanalysis and implications for the origin of the “Moacyr” monazite. Chemical Geology, 424, 30-50.

Grauert B, Arnold A. 1968. Deutung diskordanter Zirkonalter der Silrettadecke und des Gotthardsmassivs (SchweizerAlpen). Contrib Mineral Petrol 20:34-56

Grandjean V, Guillot S, Pecher A. 1996. Un nouveau témoin de l’évolution métamorphique BP-HT post-orogénique hercynienne : l’unité de Peyre-Arguet (Haut-Dauphiné). Comptes Rendus Académie Sci. Sér. 2 Sci. Terre Planètes 322: 189–195.

Green, E. C. R., Holland, T. J. B. & Powell, R. 2007. An order-disorder model for omphacitic pyroxenes in the system jadeite-diopside-hedenbergite-acmite, with applications to eclogitic rocks. American Mineralogist, 92, 1181–1189.

Green, E.C.R., White, R.W., Diener, J.F.A., Powell, R., Holland, T.J.B. & Palin, R.M. 2016. Activity–composition relations for the calculation of partial melting equilibria in metabasic rocks. Journal of Metamorphic Geology, 34, 845–869.

Greene D, Schweickert R. 1995. The Gem Lake shear zone: Cretaceous dextral transpression in the Northern Ritter Range pendant, eastern Sierra Nevada, California. Tectonics 14: 945–961.

Grujic, D 2006 Channel flow and continental collision tectonics: an overview. In: Law RD, Searle MP, Godin L (eds) Channel Flow, Ductile Extrusion and Exhumation in Continental Collision Zones. Geological Society, London, Special Publications, 268, 25-37.

Grujic, D., Mancktelow, N.S. 1998. Melt-bearing shear zones: analogue experiments and comparison with examples from southern Madagascar. Journal of Structural Geology, 20, 673-680

Guernina, S., Sawyer, E.W., 2003. Large-scale melt-depletion in granulite terranes: an example fromthe Archaean Ashuanipi subprovince of Quebec. Journal of Metamorphic Geology 21, 181–201.

Guerrot, C. 1998. Résultats de datation U–Pb par dissolution sur zircons pour deux e´chantillons du massif du Pelvoux, Alpes. Massif du Rochail (RO 1) —Massif de Turbat-Lauranoure (TL 1). Rapport SMN/PEA/ISO 146/98 CG/NB. Orléans: Bureau de Recherches Géologiques et Minières, 6 pp.

Guerrot, C., & Debon, F. 2000. U-Pb zircon dating of two contrasting Late Variscan plutonic suites from the Pelvoux massif (French Western Alps). Schweizerische Mineralogische und Petrographische Mitteilungen, 80, 249–256.

Guillot, S., & Ménot, R.P. 2009. Paleozoic evolution of the External Crystalline Massifs of the Western Alps. Comptes Rendus Geosciences, 341(2-3), 253-265. https://doi.org/10.1016/j.crte.2008.11.010

Guillot, F., Liégeois, J.-P., & Fabre, J. 1991. Des granophyres du Cambrien terminal dans le Mont Pourri (Vanoise, zone briançonnaise): Première datation U-Pb sur zircon d'un socle des zones internes des Alpes françaises. Comptes Rendus de l'Académie des Sciences Paris, II, 313, 239–244.

Guillot, S., Ménot, R.-P., & Lardeaux, J.-M. 1992. Tectonique intra-océanique distensive dans l'ophiolite paléozoïque de Chamrousse (Alpes occidentales). Bulletin de la Société Géologique de France, 163, 229–240.

Guillot S, Ménot R.P, 1999. Nappe stacking and first evidence of late Variscan extension in the Belledonne Massif (External Crystalline Massifs, French Alps). Geodin. Acta 12: 19–111

Guillot, F., Schaltegger, U., Bertrand, J.M., Deloule, E. and Baudin, T. 2002: Ordovician magmatism in the Ruitor Massif (Internal W-Alps), U–Pb on zircon geochronology of polycyclic crustal granites. Int. J. Earth Sci. 91, 964–978.

Guillot, S., di Paola, S., Ménot, R.P., Ledru, P., Spalla, M., Gosso, G., & Schwartz, S. 2009. Suture zones and importance of strike-slip faulting for Variscan geodynamic reconstructions of the external crystalline massifs of the Western Alps. Bulletin de la Société géologique de France, 180, 483–500.

Guillot, F., Averbuch, O., Dubois, M., Durand, C., Lanari, P., Gauthier, A., 2020. Zircon age of vaugnerite intrusives from the Central and Southern Vosges crystalline massif (E France): contribution to the geodynamics of the European Variscan belt. BGSF – Earth Sci. Bull. 191, 26

Guitard G, Vielzeuf D, Martinez F. 1996. Le métamorphisme hercynien. In: Chiron JC, Barnolas A, eds. Synthèse géologique et géophysique des Pyrénées. Orléans (France) : Bureau de Recherches Géologiques et Minières, vol. 1, pp. 501–584.

Gumiaux C., Gapais D, Brun JP, Chantraine J, Ruffet G. 2004. Tectonic history of the Hercynian Armorican Shear belt (Brittany, France), Geodin. Acta 17 289–307.

Haas, I., Eichinger, S., Haller, D., Fritz, H., Nievoll, J., Mandl, M., et al. 2020. Gondwana fragments in the Eastern Alps: A travel story from U/Pb zircon data. Gondwana Research,77, 204–222.

Handy, M. R. 1994. Flow laws for rocks containing two non-linear viscous phases: a phenomenological approach. Journal of Structural Geology, 16(3), 287-301.

Handy, M. R., A. Mulch, M. Rosenau, and C. L. Rosenberg 2001, The role of fault zone and melts as agents of weakening, hardening and differentiation of the continental crust: A synthesis, in Nature and Tectonic Significance of Fault Zone Weakening, Geol. Soc. London Spec. Publ., vol. 186, edited by R. E. Holdsworth et al., pp. 305–332, London, U. K.

Hart NR, Stockl, DF, Hayman NW. 2016. Provenance evolution during progressive rifting and hyperextension using bedrock and detrital zircon U-Pb geochronology, Mauléon Basin, western Pyrenees. Geosphere 12: 1166–1186.

Hasalová P, Schulmann K, Lexa O, Štípská P, Hrouda F, Ulrich S, et al. 2008a. Origin of migmatites by deformation-enhanced melt infiltration of orthogneiss: A new model based on quantitative microstructural analysis. J. Metamorph. Geol. 26: 29–53.

Hasalová, P., Štípská, P., Powell, R., Schulman, K., Janoušek, V., Lexa, O., 2008b. Transforming mylonitic metagranite by open-system interactions during melt flow. Journal of Metamorphic Geology 26, 55–80.

Hasalová, P., Janoušek, V., Schulmann, K., Štípská, P., Erban, V., 2008c. From orthogneiss to migmatite: geochemical assessment of the melt infiltration model in the Gföhl Unit (Moldanubian Zone, Bohemian Massif). Lithos 102,508–537

Hasterok, D., Gard, M., and Webb, J.: On the radiogenic heat production of metamorphic, igneous, and sedimentary rocks, Geosci. Front., 9, 1777–1794, https://doi.org/10.1016/j.gsf.2017.10.012, 2018.

Haudour, J., & Sarrot-Reynauld, J. 1964. Le Carbonifère des zones externes des Alpes françaises, Cinquième congrès international de stratigraphie et de géologie du Carbonifère (Paris, 9–12 septembre 1963), I, 119–138.

Hauzenberger, C.A., Höller, W., Hoinkes, G., 1996. Transition fromeclogite to amphibolite-facies metamorphism in the Austroal-pine Ulten Zone. Mineral. Petrol. 58, 111–130.

Henk, A., Franz, L., Teufel, S., & Oncken, O. 1997. Magmatic underplating, extension, and crustal reequilibration: Insights from a cross-section trough the Ivrea Zone and Strona-Ceneri Zone, Northern Italy. Journal of Geology, 105, 367–377.

Hibbard MJ. 1987. Deformation of incompletely crystallized magma systems: Granitic gneisses and their implications. J Geol 95:543–561.

Hilario Orus A. 2004. Relación entre magmatismo y deformación en la transversal de Benasque a Luchon (Zona Axial del Pirineo). Tesis Doctoral, Leioa (Spain), Univ. del País Vasco.

Hodges, K.V., 2006. A synthesis of the channel-flow-extrusion hypothesis as devel-oped for the Himalayan–Tibetan orogenic system. Geological Society, LondonSpecial Publications 268, 71–90.

Holland, T., & Blundy, J. 1994 Non-ideal interactions in calcic amphiboles and their bearing on amphibole-plagioclase thermometry. Contributions to Mineralogy and Petrology, 116, 433–447. doi:10.1007/BF00310910.

Holland, T.J.B., & Powell, R. 2011. An improved and extended internally consistent thermodynamic dataset for phases of petrological interest, involving a new equation of state for solids. Journal of Metamorphic Geology, 29, 333–383.

Hollister L. S. 1993 The role of melt in the uplift and exhumationof orogenic belts.Chem. Geol.108, 31–48.

Hollister, L. S. & Grujic, D. 2006. Pulsed channel flow in Bhutan. In: Law, R. D., Searle, M. P. & Godin, L. (eds) Channel Flow, Ductile Extrusion and Exhumation in Continental Collision Zones. Geological Society, London, Special Publications, 268, 415-423.

Holyoke, C. W., & Tullis, J. 2006. Formation and maintenance of shear zones. Geology, 34(2), 105-108

Horstwood, M.S.D., Foster, G.L., Parrish, R.R., Noble, G.M., 2003. Commun-Pb corrected in situ U–Pb accessory mineral geochronology by LA-MC-ICP-MS. J. Anal. At. Spectrom. 18, 837–846.

Hoskin, P.W.O., & Schaltergger, U. 2003. The composition of zircon and igneous and metamorphic petrogenesis. Review of Mineral Geochemistry, 53, 27–62.

Hunter, N. J., Hasalová, P., Weinberg, R. F., & Wilson, C. J. 2016. Fabric controls on strain accommodation in naturally deformed mylonites: The influence of interconnected micaceous layers. Journal of Structural Geology, 83, 180-193.

Hurai, V., Paquette, J.L., Huraiová, M., & Konečný, P. 2010. Age of deep crustal magmatic chambers in the intra-Carpathian back-arc basin inferred from LA-ICPMS U-Th-Pb dating of zircon and monazite from igneous xenoliths in alkali basalts. Journal of Volcanology and Geothermal Research, 198, 275-287.

Hunziker, J. C., & Zingg, A. 1980. Lower Palaeozoic amphibolite to granulite facies metamorphism in the Ivrea zone. Schweizerische Mineralogische und Petrographische Mitteilungen, 60, 181–213.

Husson L, Sempere T 2003 Thickening the Altiplano crust by grav-ity-driven crustal channel flow. Geophys Res Lett 30(5): doi10.1029/2002GL016877

Irvine, T.N., Barragar, W.R.A. 1971. A guide to the chemical classification of the common volcanic rocks. Canadian Journal of Earth Sciences, 8, 523–548.

Izquierdo-Llavall E, Román-Berdiel T, Casas AM, Oliva-Urcia B, Gil-Peña I, Soto R, et al. 2012. Magnetic and structural study of the Eaux-Chaudes intrusion: Understanding the Variscan deformation in the Western Axial Zone (Pyrenees). Int J Earth Sci 101: 1817–1834.

Jackson, M. D., Cheadle, M. J. & Atherton, M. P. 2003. Quantitative modelling of granitic melt generation and segregation in the continental crust. Journal of Geophysical Research 108, 2332.

Jackson, S.E., Pearson, N.J., Griffin, W.L., & Belousova, E.A. 2004. The application of laser ablation-inductively coupled plasma-mass spectrometry to in situ U–Pb zircon geochronology. Chemical Geology, 211, 47-69.

Jacob, J-B., Guillot, S., Thiéblemont, D., Vanardois, J., Trap, P., Faure, M., Marquer, D. in press. Paleozoic evolution and Variscan inheritance in the Alps. In press.

Jacob, J-B., Guillot, S., Rubatto, D., Janots, E., Melleton, J., & Faure, M. 2021. Carboniferous high-pressure metamorphism and deformation in the Belledonne Massif (Western Alps). Journal of Metamorphic Geology, doi:10.1111/jmg.12600.

Jaffey, A.H., Flynn, K.F., Glendenin, L.E., Bentley, W.C., & Essling, A.M. 1971. Precision measurement of half-lives and specific activities of 235U and 238U. Physical Review C, 4, 1889-1906.

Jamieson, R. A., Unsworth, M. J., Harris, N. B., Rosenberg, C. L., & Schulmann, K. 2011. Crustal melting and the flow of mountains. Elements, 7(4), 253-260.

Jackson, M. D., Cheadle, M. J. & Atherton, M. P. 2003. Quantitativemodeling of granitic melt generation and segregation in thecontinental crust.Journal of Geophysical Research108, article number2332.

Jammes, S. & Huismans, R.S. 2012: Structural styles of mountain building: controls of lithospheric rheologic stratification and extensional inheritance. J. Geophys. Res., 117, B10403. DOI:10.1029/2012JB009376.

Jammes S, Manatschal G, Lavier LL, Masini E. 2009. Tectonosedimentary evolution related to extreme crustal thinning ahead of a propagating ocean: Example of the western Pyrenees. Tectonics 28. https://doi.org/10.1029/2008TC002406.

Jouffray, F., Spalla, M.I., Lardeaux, J.M., Filippi, M., Rebay, G., Corsini, M., … Gosso, G. 2020. Variscan eclogites from the Argentera-Mercantour Massif (External Crystalline Massifs, SW Alps): a dismembered cryptic suture zone. International Journal of Earth Sciences, 109, 1273–1294. https://doi.org/10.1007/s00531-020-01848-2.

Jourdon, A., Le Pourhiet, L., Mouthereau, F., Masini, E. 2019: Role of rift maturity on the architecture and shortening distribution in mountain belts. Earth Planet. Sci. Lett., 512, 89–99.

Joye, J.B. 1989. L'évolution pression-température-déformation dans le massif des Aiguilles Rouges, massif externe alpin, (Doctoral dissertation). Retrieved from HAL (https://tel.archives-ouvertes.fr/tel-00822947/). Fribourg, Switzerland, Université de Fribourg.

Kalt A, Hanel M, Schleicher H, Kramm U 1994 Petrology and geochronology of eclogites from the Variscan Schwarzwald (F.R.G.). Contrib Mineral Petrol 115:287–302

Kelsey, D.E., Clark, C., Hand, M., 2008. Thermobarometric modelling of zircon and monazite growth in melt-bearing systems: examples using model metapelitic and metapsammitic granulites. J. Metamorph. Geol. 26, 199–212.

Klemperer, S., 2006, Crustal flow in Tibet: Geophysical evidence for the physical state of Tibetan lithosphere, and inferred patterns of active fl ow, in Law, R., et al., eds., Channel fl ow, ductile extrusion and exhumation in continental collision zones: Geological Society of London Special Publication 268, 39–70, doi: 10.1144/GSL.SP.2006.268.01.03.

Kilzi, M., 2014. Roches ultramafiques de Gavarnie et de Castillon. Phd thesis, Université de Toulouse. https://doi.org/10.1163/187122099X00065

Kilzi, M.A., Grégoire, M., Bosse, V., Benoît, M., Driouch, Y., de Saint Blanquat, M., Debat, P., 2016. Geochemistry and zircon U–Pb geochronology of the ultramafic and mafic rocks emplaced within the anatectic series of the Variscan Pyrenees: The example of the Gavarnie–Heas dome (France). Comptes Rendus Geosci. 348, 107–115. https://doi.org/10.1016/J.CRTE.2015.06.014

Kim, J. & Jung, H. 2019. New crystal preferred orientation of amphibole experimentally found in simple shear. Geophysical Research Letters, 46, 12996–13005. https://doi.org/10.1029/2019GL085189

Klötzli, U. S., Singoi, S., Quick, J. E., Demarchi, G., Tassinari, C. C. G., Sato, K., & Günes, Z. 2014. Duration of igneous activity in the Sesia Magmatic System and implications for high-temperature metamorphism in the Ivrea-Verbano deep crust. Lithos, 206–207, 19–33.

Ko, B., & Jung, H. 2015. Crystal preferred orientation of an amphibole experimentally deformed by simple shear. Nature Communication, 6, doi:10.1038/ncomms7586.

Konzett, J., Yang, H. & Frost, D. J. 2005. Phase relations and stabilityof magnetoplumbite- and crichtonite-series phases under upper-mantleP^Tconditions: an experimental study to 15 GPa with im-plications for LILE metasomatism in the lithospheric mantle. Journal of Petrology 46, 749-781.

Konzett, J., Rhede, D., & Frost, D.J. 2012 The high-PT stability of apatite and Cl partitioning between apatite and hydrous potassic phases in peridotite: An experimental study to 19 GPa with implications for the transport of P, Cl and K in the upper mantle. Contributions to Mineralogy and Petrology, 163, 277–296. doi: 10.1007/s00410-011-0672-x.

Kratinová Z, Schulmann K, Edel J-B., Jezek J, Schaltegger U. 2007. Model of successive granite sheet emplacement in transtensional setting: integrated microstructural and anisotropy of magnetic susceptibility study. Tectonics 26: TC6003. https://doi.org/6010.1029/2006TC002035.

Kroner, A., & Romer, R.L. 2013. Two plates – many subduction zones: the Variscan orogeny reconsidered. Gondwana Research, 24(1), 298–329.

Krummenacher, D. 1959. Le cristallin de la région de Fully (Valais). Schweizerische Mineralogische und Petrographische Mitteilungen, 39, 151-266.

Krummenacher, D., Bordet, P. And Le Fort, P., 1965. Les massifs externes alpins et leurs séries métamorphiques, Schweiz. Mineral. Petrog. Mitt., 45: 855-874.

Kruiver, P.P., Dekkers, M.J., Langereis, C.G., 2000. Secular variation in Permian red bedsfrom Dôme de Barrot, SE France. Earth Planet. Sci. Lett. 179, 205–217.

Kruse, S., McNutt, M., Phipps-Morgan, J., Royden, L., Wernicke, B. 1991 Lithospheric extension near Lake Mead, Nevada: A model forductile flow in the lower crust. J. Geophys. Res. 96, 4435–4456.

Kunz, B. E., Manzotti, P., von Niederhäusern, B., Engi, M., Darling, J. R., Giuntoli, F., & Lanari, P. 2018. Permian high-temperature metamorphism in the Western Alps (NW Italy). International Journal of Earth Sciences, 107, 203–229. https://doi.org/10.10007/s00531-017-1485-6

Kurse R, Stünitz H, Kunze K. 2001. Dynamic recrystallization processes in plagioclase porphyroclasts. J. Struct. Geol. 23, 1781-1802.

Kurz, W., and H. Fritz 2003, Tectonometamorphicevolution of the Austroalpine nappe complex inthe central Eastern Alps–Consequences for theeo-Alpine evolution of the Eastern Alps, Int. Geol.Rev.,45, 1100–1127.

Lafon J-M, Respaut J-P. 1988. Géochronologie U-Pb et leucogranites varisques: cas des massifs de Grandrieu (Lozère) et de la Porcherie (Limousin), Massif Central français. Bull. Minéralogie 111: 225–237.

Lagabrielle Y, Bodinier JL. 2008. Submarine reworking of exhumed subcontinental mantle rocks: Field evidence from the Lherz peridotites, French Pyrenees. Terra Nova 20: 11–21.

Lagabrielle Y, Labaume P, St Blanquat M. 2010. Mantle exhumation, crustal denudation, and gravity tectonics during Cretaceous rifting in the Pyrenean realm (SW Europe): Insights from the geological setting of the lherzolite bodies. Tectonics 29. https://doi.org/10.1029/2009TC002588.

Lagabrielle Y, Clerc C, Vauchez A, Lahfid A, Labaume P, Azambre B, et al. 2016. Very High Geothermal Gradient during Mantle Exhumation Recorded in Mylonitic Marbles and Carbonate Breccias from a Mesozoic Pyrenean Palaeomargin (Lherz Area, North Pyrenean Zone, France). C R Geosci 348:290–300.

Lahfid, A., Beyssac, O., Deville, E., Negro, F., Chopin, C., Goffé, B. 2010: Evolution of the Raman spectrum of RSCM thermometry of carbonaceous material in low-grade metasediments of the Glarus Alps (Switzerland). Terra Nova, 22, 354–360.

Lahfid, A., Baidder, L., Ouanaimi, H., Soulaimani, A., Hoepffner, C., Farah, A., et al. 2019. From extension to compression: Highgeothermal gradient during the earliest Variscan phase of the Moroccan Meseta; afirst structural and RSCM thermometric study.European Journal of Mineralogy,31(4), 695–713. https://doi.org/10.1127/ejm/2019/0031-2882

Lanari, P., Riel, N., Guillot, S., Vidal, O., Schwartz, S., Pêcher, A., Hattori, K.H. 2013. Deciphering high-pressure metamorphism in collisional context using microprobe mapping methods: application to the Stak eclogitic massif (northwest Himalaya). Geology, 41(2), 111–114. https://doi.org/10.1130/g33523.1.

Lanari, P., Vidal, O., de Andrade, V., Dubacq, B., Lewin, E., Grosch, E., & Schwartz, S. 2014. XMapTools: a MATLAB-based program for electron microprobe X-ray image processing and geothermobarometry. Computers & Geosciences, 62, 227–240.

Lanari, P., & Engi, M. 2017. Local bulk composition effects on metamorphic mineral assemblages. Reviews in Mineralogy and Geochemistry, 83, 55–102.

Lanari, P., Vho, A., Bovay, T., Airaghi, L., & Centrella, S., 2019. Quantitative compositional mapping of mineral phases by electron probe micro-analyser. Geological Society of London, Special Publications, 478, 39-63.

Lardeaux, J.M., Gosso, G., Kienast, J.R., Lombardo, B., 1982. Metamorphism anddeformation in Sesia–Lanzo site (Western Alps) and eclogitization of continen-tal-crust. Bulletin De La Societe Geologique De France 24 (4), 793–800.

Lardeaux, J.M., Spalla, M.I., 1991. From granulites to eclogites inthe Sesia Zone (Italian Western Alps): a record of the openingand closure of the Piemont Ocean. J. Metamorph. Geol. 9,35–59.

Lardeaux, J.M., Ledru, P., Daniel, I., Duchene, S. 2001. The Variscan French Massif Central – a new addition to the ultra-high pressure metamorphic ‘club’: exhumation processes and geodynamic consequences. Tectonophysics, 332, 143–167.

Lardeaux JM, Schulmann K, Faure M et al. 2014. The Moldanubian Zone in the French Massif Central, Vosges/Schwarzwald and Bohemian Massif revisited: differences and similarities. In: Schulmann K, Martinez Catalan JR, Lardeaux JM, Janousek V, Oggiano G. (Eds.), The Variscan Orogeny: Extent, Timescale and the Formation of the European Crust. Special publications. Geological Society, London.

Latouche, L., & Bogdanoff, S. 1987. Evolution précoce du massif de l’Argentera: Apport des éclogites et des granulites. Géologie Alpine, 63,151–164.

Laumonier B. 1998. Les Pyrénées centrales et orientales au début du Paléozoique (Cambrien s.l.) : évolution paléogéographique et géodynamique. Geodin Acta 11: 1–11.

Laumonier B, Marignac C, Kister P. 2010. Polymétamorphisme et évolution crustale dans les Pyrenees Orientales pendant l’orogénèse Varisque au Carbonifère supérieur. Bull Soc geol Fr 181:411–428.

Laumonier, B., Calvet, M., Autran, A., Rossi, P. & Guennoc, P. 2013. Notice explicative, Carte géologique de France (1/50 000), feuille Argelès-sur-Mer-Cerbère (1097). BRGM, Orléans.

Laurent R 1967 Étude géologique et pétrographique de l’extrémité méridionale du massif des Aiguilles Rouges (Haute Savoie, France). Arch Sci Genève 2 (20): 221–353

Laurent, JC. 1992. Les épisodes magmatiques filoniens basiques du massif des Ecrins-Pelvoux entre Carbonifère et Lias. PhD Thesis, Grenoble (France). Univ. Joseph-Fourier.

Laurent, O., Couzinié, S., Zeh, A., Vanderhaeghe, O., Moyen, J.F., Villaros, A., … & Chelle-Michou, C. 2017. Protracted, coeval crust and mantle melting during Variscan late orogenic evolution: U–Pb dating in the eastern French Massif Central. International Journal of Earth Sciences, 106, 421-451.

Le Bas, M.J., Le Maitre, R.W., Streckeisen, A., & Zanettin, B. 1986. A chemical classification of volcanic rocks based on the total alkali-silica diagram. Journal of Petrology, 27, 445-450.

Le Bayon, B., & Ballèvre, M. 2006. Deformation history of a subducted continental crust (Gran Paradiso, Western Alps): Continuing crustal shortening during exhumation. Journal of Structural Geology, 28, 793–815.

Le Bayon B, Cochelin, B 2020 Anatomy of an extensional shear zone leading to the exhumation of the middle crust within the Canigou dome (Eastern Pyrenees, Axial Zone). J Struct Geol 141. doi.org/10.1016/j.jsg.2020.104200

Le Bayon, B., Pitra, P., Ballèvre, M., & Bohn, M. 2006. Reconstructing P-T paths during continental collision using multi-stage garnet (Gran Paradiso nappe, Western Alps). Journal of Metamorphic Geology, 24, 477–496.

Le Fort, P. 1973. Géologie du Haut-Dauphiné cristallin (Alpes françaises). Etude pétrologique et structurale de la partie occidentale, Mémoires des Sciences de la Terre (Nançy), 25, 375 p.

Le Pourhiet, L., Huet, B., May, D., Labrousse, L., Jolivet, L., 2012. Kinematic interpretation ofthe 3D shapes of metamorphic core complexes. Geochem. Geophys. Geosyst. 13 (9), Q09002. http://dx.doi.org/10.01029/02012GC004271.

Leake, B.E., Woolley, A.R., Arps, C.E.S., Birch, W.D., Gilbert, M.C., Grice, J.D., … Youzhi, G. 1997. Nomenclature of amphiboles: report of the subcommittee on amphiboles of the International Mineralogical Association Commission on New Minerals and Mineral Names. Mineral Magazine, 61, 295–321.

Leblanc D, Gleizes G, Lespinasse P, Olivier P, Bouchez JL. 1993. The Maladeta granite polydiapir, Spanish Pyrenees: A detailed magnetostructural study. J Struct Geol 16: 223–235.

Leblanc D, Gleizes G, Roux L, Bouchez JL. 1996. Variscan dextral transpression in the French Pyrenees: New data from the Pit des Trois-Seigneurs granodiorite and its country rocks. Tectonophysics 261: 331–345.

Ledru P, Courrioux G, Dallain C, Lardeaux JM, Montel JM, Vanderhaeghe O, et al. 2001. The Velay dome (French Massif Central): Melt generation and granite emplacement during orogenic evolution. Tectonophysics 342: 207–237.

Lee, A.L., Torvela, T., Lloyd, G.E. and Walker, A.M. 2018. Melt organisation and strain partitioning in the lower crust. Journal of Structural Geology, 113, 188–199, https://doi.org/10.1016/j.jsg.2018.05.016

Lee, A.L., Lloyd, G.E., Torvela, T., Walker, A.M., 2020. Evolution of a shear zone before, during and after melting. J. Geol. Soc. London.https://doi.org/10.1144/jgs2019-114.

Lejeune, A.-M., Richet, P. 1995 Rheology of crystal-bearing silicate melts: an experimental study at high viscosities. J. Geophys. Res.,100, 4215-4229.

Lemirre B. 2016. Origine et développement de la thermicité dans les Pyrénées varisques. PhD thesis, Toulouse (France), Univ. Toulouse.

Lemirre, B., Cochelin, B., Duchene, S., de Saint Blanquat, M., Poujol, M., 2019. Origin andduration of late orogenic magmatism in the foreland of the Variscan belt (Lesponne—Chiroulet—Neouvielle area, french Pyrenees). Lithos 336-337, 183–201. https://doi.org/10.1016/j.lithos.2019.03.037.

Lemoine, M. 1985. Structuration jurassique des Alpes occidentales et palinspastique de la Téthys ligure. Bulletin de la Société Géologique de France, 1(8), 126–137.

Lemoine, M., & Trümpy, R. 1987. Pre-oceanic rifting in the Alps. Tectonophysics, 133, 305–320.

Lemoine, M., Gidon, M., & Barféty, J.-C. 1981. Les massifs cristallins externes des Alpes Occidentales: D’anciens blocs basculés nés au Lias lors du rifting téthysien. Comptes Rendus de l’Académie des Sciences Paris, II, 292, 917–920.

Lemoine, M., Bas, T., Arnaud-Vanneau, A., Arnaud, H., Dumont, T., Gidon, M., et al. 1986. The continental margin of the Mesozoic Tethys in the Western Alps. Marine and Petroleum Geology, 3, 179–199.

Li, X.H., Faure, M., Lin, W., 2014. From crustal anatexis to mantle melting in the Variscan orogen of Corsica (France): SIMS U–Pb zircon age constraints. Tectonophysics 634, 19–30

Liati, A., Skarpelis, N., Pe-Piper, G., 2009. Late Miocene magmatic activity in theAttic–Cycladic Belt of the Aegean (Lavrion, SE Attica, Greece): implicationsfor the geodynamic evolution and timing of ore deposition. Geol. Mag. 146(5), 732–742.http://dx.doi.org/10.1017/S0016756809006438.

Libourel, G., & Vielzeuf, D. 1988. Isobaric cooling at high pressure: the example of Corsican high pressure granulites. Terra Cognita, 8, 268.

Liégeois, J.-P., & Duchesne, J.-C. 1981. The Lac Cornu retrograded eclogites (Aiguilles Rouges massif, Western Alps, France): Evidence of crustal origin and metasomatic alteration. Lithos, 14, 35–48.

Liermann H-P, Isachsen C, Altenberger U, Oberhänsli R 2002 Behaviour of zircon during high-pressure, low-temperature metamorphism: Case study from the Internal Unit of the Sesia Zone (Western Italian Alps). Eur JMineral 14:61-71

Linnemann U, Gerdes A, Drost K, Buschmann B. 2007. The continuum between Cadomian orogenesis and opening of the Rheic Ocean: Constraints from LA-ICP-MS U-Pb zircon dating and analysis of platetectonic setting (Saxo-Thuringian zone, northeastern Bohemian Massif, Germany). Spec. Pap. – Geol. Soc. Am. 423: 61.

Linnemann, U., Ouzegane, K., Drareni, A., Hofmann, M., Becker, S., Gärtner, A., & Sagawe, A. 2011. Sands of West Gondwana: anarchive of secular magmatism and plate interactions - a case study from the Cambro-Ordovician section of the Tassili Ouan Ahaggar (Algerian Sahara) using U–Pb LA-ICP-MS detrital zircon ages. Lithos, 123, 188–203.

Linnemann U, Gerdes A, Hofmann M, Marko L 2014 The Cadomian Orogen: Neoproterozoic to Early Cambrian crustal growth and orogenic zoning along the periphery of the West African Craton — Constraints from U–Pb Zircon Ages and Hf isotopes (Schwarzburg Antiform, Germany). Precambrian Res 244:236–278.

Liu, M., and Y. Yang. 2003. Extensional collapse of the Tibetan Plateau: Results of three-dimensional finite element modelling. J. Geophys. Res.,108(B8), 2361, doi:10.1029/2002JB002248

Liu Q Y, van der Hilst R D, Li Y, et al 2014. Eastward expansion of the Tibetan Plateau by crustal flow and strain partitioning across faults. Nature Geosci 7: 361–365

Lobjoie, C. 2018. Comportement rhéologique de la croûte continentale en conditions HT/UHT : Étude tectono-métamorphique de la ceinture paléoprotérozoïque de la ceinture de Khondalite (Craton de Chine du Nord). PhD thesis, Besançon (France), Univ. Besançon.

Lopez-Sanchez MA, Aleinikoff JN, Marcos A, Martínez FJ, Llana-Fúnez S 2016 An example of low-Th/U zircon overgrowths of magmatic origin in a late orogenic Variscan intrusion: the San Ciprián massif (NW Spain). J Geol Soc 173:282–291.

Lopez-Sanchez, M. A., García-Sansegundo, J., & Martínez, F. J. 2018. The significance of early Permian and early Carboniferous U-Pb zircon ages in the Bossòst and Lys-Caillaouas granitoids (Pyrenean Axial Zone). Geological Journal. https ://doi.org/10.1002/gj.3283

Lotout, C., Pitra, P., Poujol, M., Anczkiewicz, R., & Van Den Driessche, J. 2018. Timing and duration of Variscan high-pressure metamorphism in the French Massif central: a multimethod geochronological study from the Najac Massif. Lithos, 308–309, 381–394.

Lotout, C., Poujol, M., Pitra, P., Anczkiewicz, R., & Van Den Driessche, J. 2020. From Burial to Exhumation: Emplacement and Metamorphism of Mafic Eclogitic Terranes Constrained Through Multimethod Petrochronology, Case Study from the Lévézou Massif (French Massif Central, Variscan Belt). Journal of Petrology, doi: 10.1093/petrology/egaa046

Lox A, Bellière J. 1993. Le Silésien (Carbonifère Supérieur) de Pormenaz (Massif des Aiguilles-Rouges): lithologie et tectonique. Eclogae Geol. Hel. 86:769–783.

Ludwig, K.R. 1998. On the treatment of concordant uranium–leadages. Geochimica et Cosmochimica Acta,62: 665–676

Ludwig, K.R., 2001. User manual for Isoplot/Ex rev. 2.49. A geochronological toolkit for Microsoft Excel. Berkeley Geochronology Center Special Publication, 1a, 1–56.

Maierová P, Schulmann K, Lexa O, Guillot S, Štípská P, Janousek V, et al. 2016. European Variscan orogenic evolution as an analogue of Tibetan-Himalayan orogen: Insights from petrology and numerical modeling. Tectonics 35: 1760–1780.

Malavieille J, Guihot P, Costa S, Lardeaux JM, Gardien V. 1990. Collapse of a thickened Variscan crust in the French Massif Central: Mont-Pilat extensional shear zone and Saint-Etienne Upper Carboniferous basin. Tectonophysics 177: 139–149.

Mancktelow, N. 2002. Finite-element modelling of shear zone development in viscoelastic materials and its implications for localisation of partial melting. Journal of Structural Geology, 24(6–7):1045–1053.

Manzotti, P., & Zucali, M. 2013. The pre-Alpine tectonic history of the Austroalpine continental basement in the Valpelline unit (Western Italian Alps). Geological Magazine, 150, 153–172.

Manzotti, P., Ballèvre, M., Zucali, M., Robyr, M., & Engi, M. 2014. The tectonometamorphic evolution of the Sesia–Dent Blanche nappes (internal Western Alps): Review and synthesis. Swiss Journal of Geosciences, 107, 309–336

Manzotti, P., Pitra, P., Langlade, J., & Ballèvre, M. 2015. Constraining P-T conditions during thrusting of a higher pressure unit over a lower pressure one (Gran Paradiso, Western Alps). Journal of Metamorphic Geology, 33, 981–1002.

Manzotti, P., Ballèvre, M., Poujol, M., 2016. Detrital zircon geochronology in the Dora- Maira and Zone Houillère: a record of sediment travel paths in the carboniferous. Terra Nova 28 (4), 279–288.

Manzotti, P., Ballèvre, M., & Dal Piaz, G. V. 2017a. Continental gabbros in the Dent Blanche Tectonic System (Western Alps): From the pre-Alpine crustal structure of the Adriatic palaeo-margin to the geometry of an alleged subduction interface. Journal of the Geological Society of London, 174, 541–556. https://doi.org/10.1144/jgs2016-071

Manzotti, P., Rubatto, D., Zucali, M., El Korh, A., Cenki-Tok, B., Ballèvre, M., & Engi, M. 2017b. Permian magmatism and metamorphism in the Dent Blanche nappe: Constraints from field observations and geochronology. Swiss Journal of Geosciences. https://doi.org/10.1007/s00015-017-0284-1

Marmo V. 1971. Granite petrology and the granite problem: Amsterdam: Elsevier, 244 p.

Marquer, D., Challandes N., and Schaltegger U., 1998, Early Permian magmatism in Briançonnais terranes: the Truzzo graniteand Roffna rhyolite (Eastern Penninic nappes, Swiss and ItalianAlps),Schweiz. Mineral. Petrogr. Mitt.78: 397–415

Marschall, H. R., Kalt, A. & Hanel, M. 2003. P-T evolution of a Variscan lower-crustal segment: a study of granulites from the Schwarzwald, Germany. Journal of Petrology, 44, 227–253.

Marshall D, Kirschner D, Bussy F. 1997. A variscan pressure–temperature–time path for the N–E Mont Blanc massif. Contrib Mineral Petrol 126:416–428

Marshall D, Pfeifer HR, Hunziker JC, Kirschner D. 1998. A pressure-temperature-time path for the NE Mont-Blanc massif: Fluid-inclusion, isotopic and thermobarometric evidence. Eur. J. Mineral. 10:1227–1240.

Martínez, F.J., Reche, J. & Iriondo, A. 2008. U-Pb Shrimp-RG zircon ages of Variscan igneous rocks from the Guilleries massif (NE Iberia pre-Mesozoic basement). Geological implications. C.R. Geoscience, 340, 223-232.

Martínez, F. J., C. Dietsch, J. Aleinikoff, J. Cirés, M. L. Arboleya, J. Reche, and D. Gómez-Gras 2015, Provenance, age, and tectonic evolution ofVariscanflysch, southeastern France and northeastern Spain, based on zircon geochronology. Geol. Soc. Am. Bull.,128(5–6), 842–859

Martínez Catalán, J.R., Arenas, R., Abati, J., Sánchez Martínez, S., Díaz García, F., Fernández-Suárez, J., González Cuadra, P., Castiñeiras, P., Gómez Barreiro, J., Díez Montes, A., González Clavijo, E., Rubio Pascual, F.J., Andonaegui, P., Jeffries, T.E., Alcock, J.E., Díez Fernández, R., López Carmona, A., 2009. A rootless suture and the loss of the roots of a mountain chain: the Variscan belt of NW Iberia. Compt. Rendus Geosci. 341 (2–3), 114–126. https://doi.org/10.1016/j.crte.2008.11.004.

Martínez Catalán JR, Schulmann K, Ghienne JF. 2021. The Mid-Variscan Allochthon: Keys from correlation, partial retrodeformation and platetectonic reconstruction to unlock the geometry of a non-cylindrical belt. Earth-Science Reviews, https://doi.org/10.1016/j.earscirev.2021.103700

Masini E, Manatschal G, Tugend J, Mohn G. 2014. The tectonosedimentary evolution of a hyper-extended rift basin: The example of the Arzacq-Mauléon rift system (Western Pyrenees, SW France). Int J Earth Sci 103: 1565–1596.

Massonne, H.-J. & Kopp, J. 2005. A low-variance mineral assem-blage with talc and phengite in an eclogite from the SaxonianErzgebirge, central Europe, and itsP^Tevolution.Journal ofPetrology46, 355^375.

Massonne, H.-J., Cruciani, G., Franceschelli, M., Musumeci, G., 2018. Anticlockwise pressure–temperature paths record Variscan upper-plate exhumation: example from micaschists of the Porto Vecchio region, Corsica. J. Metamorph. Geol. 36, 55–77.

Matte P. 1986. Tectonics and plate tectonics model for the Variscan belt of Europe. Tectonophysics 126: 329–374.

Matte, P. 1991. Accretionary history of the Variscan belt in western Europe. Tectonophysics, 196, 309–337.

Matte, P. 1998. Continental subduction and exhumation of HP rocks, in Paleozoic orogenic belts: Uralides and Variscides. GFF, Vol. 120 (Pt. 2, June), pp. 209–222. Stockholm. ISSN 1103-5897.

Matte P. 2001. The Variscan collage and orogeny (480–290 Ma) and the tectonic definition of the Armorica microplate: a review. Terra Nova 13: 122–128.

Matte P. 2002. Les plis hercyniens kilométriques couchés vers l'ouest-sud-ouest dans la région du pic du Midi d'Ossau–col du Somport (zone axiale des Pyrénées occidentales). C R Geosci 334:773–779.

Maurel O, Monié P, Respaut JP, Leyreloup AF, Maluski H. 2003. Premetamorphic 40Ar/39Ar and U-Pb ages in HP metagranitoids from the Hercynian belt (France). Chem. Geol. 193: 195–214.

Maurel, O., Respaut, J.P., Monié, P., Arnaud, N. & Brunel, M. 2004. U-Pb emplacement and 40Ar/39Ar cooling ages of the Mont-Louis granite massif (Eastern Pyrenees, France). C.R. Geoscience, 336, 1091-1098

McKerrow, W.S., Niocall, C.M., Dewey, J.F., 2000. The Caledonianorogeny rede®ned. Journal of the Geological Society, London 157,1144±1154.

Mecklenburgh, J., Rutter, H.E. 2003, On the rheology of partiallymolten synthetic granite. J. Struct. Geol.,25, 1575–1585.

Melleton, J., Cocherie, A., Faure, M., Rossi, P. 2010. Precambrian protoliths and Early Paleozoic magmatism in the French Massif Central: U–Pb data and the North Gondwana connection in the west European Variscan belt. Gondwana Research, 17, 13–25.

Ménot, R.-P., 1986. Les formations plutono-volcaniques dévoniennes de Rioupéroux-Livet (massifs cristallins externes des Alpes françaises): nouvelles définitions lithostratigraphique et pétrographique. Schweiz. Mineral. Petrogr. Mitt. 66, 229–258.

Ménot, R.P., 1987. Magamtisme Paléozoïques et Structuration Carbonifère de Massif de Belledonne (Alpes Française). Contraintes Nouvelles Pour le Schémas D'évolution de la Chaîne Varisque Ouest-Européenne. Université de Rennes.

Ménot, R.-P., 1988a. An overview of the geology of the Belledonne Massif (external crystalline massifs of Western Alps). Schweiz. Mineral. Petrogr. Mitt. 70, 33–53.

Ménot, R.-P., 1988b. Magmatisme Paléozoïque et Structuration Carbonifère du Massif de Belledonne (Alpes Françaises). Contraintes Nouvelles Pour les Schémas D'évolution de la Chaîne Varisque Ouest-Européenne (Mémoire et documents du centre armoricain d'étude structural des socles). Rennes.

Ménot, R.-P., & Paquette, J.-L. 1993. Geodynamic significance of basic and bimodal magmatism, in the External domain. in von Raumer, J.F., and Neubauer, F., eds., The Pre-Mesozoic Geology in the Alps: Heidelberg, Germany, Springer-Verlag, p. 241–254.

Ménot, R.-P., Peucat, J.-J., Piboule, M., Scarenzi, D., 1985. Cambro-Ordovician age for theophiolitic complex of Chamrousse-Tabor (Belledonne massif, french external alpine domain). Ofioliti 10, 527.

Ménot, R.-P., Bonhomme, M.G., Vivier, G., 1987. Structuration tectono-métamorphique carbonifère dans le massif de Belledonne (Alpes occidentales françaises): apport de la géochronologie K/Ar des amphiboles. Schweiz. Mineral. Petrogr. Mitt. 67, 273–284.

Ménot, R.-P., Peucat, J.-J., Paquette, J.-L., 1988a. Les associations magmatiques acide-basique paléozoiques et les complexes leptyno-amphiboliques : les correlations hasardeuses. Exemples du massif de Belledonne Alpes occidentales. Bull. Soc. Geol. Fr. 6, 917–926.

Ménot, R.-P., Peucat, J.J., Scarenzi, D., Piboule, M., 1988b. 496 my age of plagiogranites in the Chamrousse ophiolite complex (external crystalline massifs in the French Alps): evidence of a Lower Paleozoic oceanization. Earth Planet. Sci. Lett. 88, 82–92. http://dx.doi.org/10.1016/0012-821X(88)90048-9.

Mercier L, Johan V, Lardeaux JM, Ledru P 1989 Découverte d'éclogites dans l'Artense (M.C.F.). Implications pour la définition des nappes à l'est du Sillon Houiller. C. R. Acad. Sci., Paris, 308:315-320.

Meschede, M. 1986. A method of discriminating between different types of mid-ocean ridge basalts and continental tholeiites with the Nb–Zr–Y diagram. Chemical Geology, 56, 207–218.

Messiga, B., Tribuzio, R., & Caucia, F. 1992. Amphibole evolution in Variscan eclogite-amphibolites from the Savona crystalline massif (western Ligurian Alps, Italy): Controls on the decompressional P–T–t path. Lithos, 27, 215–230.

Metzger, S., Ischuk, A., Deng, Z., Ratschbacher, L., Perry, M., Kufner, S.-K., et al. 2020. Dense GNSS profiles across the northwestern tip of the India-Asia collision zone: Triggered slip and westward flow of the Peter the First Range, Pamir, into the Tajik Depression. Tectonics, 39, e2019TC005797. https://doi.org/10.1029/2019TC005797

Mezger J, Gerdes A. 2016. Early Variscan (Visean) granites in the core of central Pyrenean gneiss domes: Implications from laser ablation U-Pb and Th-Pb studies. Gondwana Res 29: 181–198.

Mezger J, Passchier C. 2003. Polymetamorphism and ductile deformation of staurolite–cordierite schist of the Bossost dome: Indication for Variscan extension in the Axial Zone of the central Pyrenees. Geol Mag 140: 595–612.

Miao, S.Q., Li, H.P., Chen, G., 2014.Temperature dependence of thermal diffusivity, specificheat capacity and thermal conductivity for several types of rocks. Journal of ThermalAnalysis and Calorimetry 115, 1057–1063

Miller, C., & Thöni, M. 1995. Origin of eclogites from the Austro-alpine basement (Tirol, Austria): geochemistry and Sm–Nd vs. Rb–Sr isotope systematics. Chemical Geology, 122, 199–225.

Mintrone, M., Galli, A., Laurent, O., Chelle-Michou, C., Schmidt, M.W., 2020. Quantifying frozen melt in crustal rocks: a new melt-o-meter based on zircon rim volumes. Chem. Geol. 551.

Monié, P. 1990. Preservation of Hercynian 40Ar/39Ar ages through high-pressure low-temperature Alpine metamorphism in the Western Alps. European Journal of Mineralogy, 2, 343–361.

Monié P, Respaut JP, Brichau S, Bouchot V, Faure M, Roig JY. 2000. 40Ar/39Ar and U-Pb geochronology applied to Au-W-Sb metallogenesis in the Cévennes and Châtaigneraie districts (Southern Massif Central, France). Orog. Gold Depos. Eur. Doc BRGM 297: 77–79.

Monjoie, P., Bussy, F., Schaltegger, U., Mulch, A., Lapierre, H., & Pfeifer, H.-R. 2007. Contrasting magma types and timing of intrusion in the Permian layered mafic complex of Mont Collon (Western Alps, Valais, Switzerland): Evidence from U/Pb zircon and 40Ar/39Ar amphibole dating. Swiss Journal of Geosciences, 100, 125–135.

Mosca, P., Borghi, A., & Gattiglio, M. 2008. Storia pre-alpina ed alpina nel Massicio di Ambin (Alpi Occidentali). Rendiconti Online della Società Geologica Italiana, 12008, 129–131.

Mougeot R, Respaut J-P, Ledru P, Marignac C. 1997. U-Pb chronology on accessory minerals of the Velay anatectic dome (French Massif Central). Eur. J. Mineral. 9: 141–156.

Moussavou, M. 1998. Contribution a` l'histoire thermotectonique Varisque du Massif des Maures, par la typologie du zircon et la ge´ochronologie U/Pb sur minéraux accessoires. Unpublished Thesis, University of Montpellier, France.

Müller, B., Klötzli, U., Schaltegger, U. Flisch, M. 1996. Early Cambrian oceanic plagiogranite in the Silvretta Nappe, eastern Alps: geochemical, zircon U-Pb and Rb-Sr data from garnet-hornblende-plagioclase gneisses. Geologische Rundschau 85, 822---831.

Müller, W., Shelley, M., Miller, P. & Broude, S. 2009. Initial performance metrics of a new custom-designed ArF excimer LA-ICPMS system coupled to a two-volume laser-ablation cell. Journal of Analytical Atomic Spectrometry, 24, 209-214.

Nance RD, Gutiérrez-Alonso G, Keppie JD, Linnemann U, Murphy JB, Quesada C, et al. 2010. Evolution of the Rheic ocean. Gondwana Res. 17: 194–222.

Nabelek, P.I., Whittington, A.G., Hofmeister, A.M., 2010. Strain heating as a mechanism for partial melting and ultrahigh temperature metamorphism in convergent orogens: implications of temperature-dependent thermal diffusivity and rheology. J. Geophys. Res. 115, B12417

Nabelek, P.I., Hofmeister, A.M., Whittington, A.G., 2012. The influence of temperature-dependent thermal diffusivity on the conductive cooling rates ofplutons and temperatureetime paths in contact aureoles. Earth and PlanetaryScience Letters 317, 157e164.

Neves, S. P., Vauchez, A., & Archanjo, C. J. 1996. Shear zone-controlled magma emplacement or magma-assisted nucleation of shear zones? Insights from northeast Brazil. Tectonophysics, 262(1-4), 349-364.

Neves, S. P., Bezerra, J. P., Bruguier, O., & França, R. H. 2021. Evidence for Early Tonian (Ca. 1000-940 Ma) continental rifting in southern Borborema Province (NE Brazil): tectonic inheritance and shear zone nucleation during assembly of West Gondwana. International Geology Review, 63(7), 851-865

Nussbaum, C., Marquer, D., Biino, G.G., 1998. Two subductionevents in a polycyclic basement: Alpine and pre-Alpine high-pressure metamorphism in the Suretta nappe, Swiss EasternAlps. J. Metamorph. Geol. 16, 591–605.

O'Brien, P.J. 1997. Garnet zoning and reaction textures in overprinted eclogites, Bohemian Massif, European Variscides: a record of their thermal history during exhumation. Lithos 41,119–133.

O'Brien, P.J., Zotov, N., Law, R., Khan, M.A., Jan, & M.Q. 2001. Coesite in Himalayan eclogite and implications for models of India–Asia collision. Geology, 29, 435–438.

Oberli, F., Meier, M., & Biino, G. G. 1994. Time constraints on the pre-Variscan magmatic/metamorphic evolution of the Gotthard and Tavetsch units derived from U-Pb results. Schweizerische Mineralogische und Petrographische Mitteilungen, 74, 483–488.

Odlum ML, Stockli DF. 2019. Thermotectonic evolution of the North Pyrenean Agly Massif during Early Cretaceous hyperextension using multi-mineral U-Pb thermochronometry. Tectonics 38. https://doi.org/10.1029/2018TC005298.

Oggiano, G., Cherchi, G.P., Aversano, A., Di Pisa, A., Ulzega, A., Orrù, P., Pintus, C., 2005.Note Illustrative della Carta Geologica d'Italia alla scala 1:50000, Foglio 428, Arzachena, Firenze.

Oggiano, G., Casini, L., Mameli, P., Rossi, P., 2007.Long lived dextral strike-slip tectonics inthe southern Variscan Belt: evidence from two syn-kynematic intrusions in northSardinia. Géol. Fr. 2, 142.

Olsen, S.N., Johnson, C.M., Beard, B. and Baumgartner, L. 2000: New U–Pb zircon data and constraints on the age and mode of migmatization in the Aar Massif, Central Alps. Eur. J. Mineral. 12, 1245–1260.

Oliot, E., Melleton, J., Schneider, J., Corsini, M., Gardien, V., Rolland, Y. 2015. Variscan crustal thickening in the Maures-Tanneron massif (South Variscan belt, France): new in situ monazite U-Th-Pb chemical dating of high-grade rocks. Bulletin de la Société géologique de France, 186, 145–169.

Olivet JL. 1996. La cinématique de la plaque Ibérique. Bull Cent Rech Explor Prod Elf Aquitaine 20: 131–195.

Olivier, P. 2013. Comment on "Preorogenic exhumation of the North Pyrenean Agly Massif (eastern Pyrenees-France)" by A. Vauchez et al. Tectonics, 32, 821–822. https://doi.org/10.1002/tect.20049

Olivier, P., 2015. Comment on "Thermal control on the modes of crustal thinning leading to mantle exhumation: Insights from the Cretaceous Pyrenean hot paleomargins" by Clerc and Lagabrielle. Tectonics 34, 2271–2274. https://doi.org/10.1002/2014TC003755

Olivier P, Améglio L, Richen H, Vadeboin F. 1999. Emplacement of the Aya Variscan granitic pluton (Basque Pyrenees) in a dextral transcurrent regime inferred from a combined magneto-structural and gravimetric study. J Geol Soc London 156: 991–1002.

Olivier P, Gleizes G, Paquette JL. 2004. Gneiss domes and granite emplacement in an obliquely convergent regime: New interpretation of the Variscan agly massif (eastern pyrenees, france). Geol Soc Am sp pap 380: 229–240.

Olivier P, Gleizes G, Paquette JL, Muñoz Sáez C. 2008. Structure and U–Pb dating of the Saint-Arnac pluton and the Ansignan Charnockite (Agly Massif): A cross-section from the upper to the middle crust of the Variscan Eastern Pyrenees. J Geol Soc 165: 141–52.

Olivier P, Druguet E, Castaño L M, Gleizes G. 2016. Granitoid emplacement by multiple sheeting during Variscan dextral transpression: The Saint-Laurent– La Jonquera pluton (Eastern Pyrenees). J Struct Geol 82: 80–92.

Oriolo, S., Wemmer, K., Oyhantçabal, P., Fossen, H., Schulz, B., Siegesmund, S., 2018. Geochronology of shear zones–A review. Earth Sci. Rev. 185, 665–683.

Otamendi, J.E., Patiño Douce, A.E., 2001. Partial melting of aluminous metagreywackes in the northern Sierra de Comechingones, central Argentina. Journal of Petrology 42, 1751–1772

Ouimet, W.B., Cook, K.L., 2010. Building the central Andes through axial lower crustal flow. Tectonics 29 (3).

Owona S, Mvondo Ondoa J, Ratschbacher L, Ekodeck GE. 2013. Evidence of quartz dynamic recrystalliza-tions in SW Cameroon: Implications on post-archean-eburnean and late-panafrican deformations over 250-750℃. Sciences, Technologies et Développement 14:48-58

Padel, M. 2016. Influence cadomienne dans les séries pré-sardes des Pyrénées Orientales: Approche géochimique, stratigraphique etgéochronologique. PhD thesis, Lille 1.

Padovano, M., Elter, F. M., Pandeli, E., & Franceschelli, M. 2012. The East Variscan Shear Zone: new insights into its role in the Late Carboniferous collision in southern Europe. International Geology Review, 54(8), 957-970.

Padovano, M., Dörr, W., Elter, F. M., & Gerdes, A. 2014. The East Variscan Shear Zone: Geochronological constraints from the Capo Ferro area (NE Sardinia, Italy). Lithos, 196–197, 27–41.

Pairis JL, Bellière J, Rosset J. 1992. Notice explicative. Carte géologique de France (1/50 000), feuille Cluses (679). Éditions Bureau des Recherches Géologiques et Minières, 1–89.

Palmeri, R., Fanning, M., Franceschelli, M., Memmi, I. & Ricci, C. A. 2004. SHRIMP dating of zircons in eclogite from the Variscan basement in north-eastern Sardinia (Italy). Neues Jahrbuch fu¨r Mineralogie-Monatshefte, 6, 275–288.

Papapavlou, K., Darling, J.R., Storey, C.D., Lightfoot, P.C., Moser, D.E., & Lasallea, S. 2017. Dating shear zones with plastically deformed titanite: New insights into the orogenic evolution of the Sudbury impact structure (Ontario, Canada). Precambrian Research, 291, 220–235.

Pape, J., Mezger, K., & Robyr, M. 2016. A systematic evaluation of the Zr-in-rutile thermometer in ultra-high temperature (UHT) rocks. Contribution to Mineralogy and Petrology, 171, 1–20.

Paquet J, Delay F. 1989. Analyse en microscopie électronique des textures et des phases des mylonites nord-pyrénéennes des massifs de St-Barthélémy et de l'Agly et discussion des âges. Bull Soc geol Fr 8: 1111–1122.

Paquet J, Mansy JL. 1991. The structure of the Eastern Pyrenees (transect of the Agly massif): An example of crustal thinning. C R Acad Sci Paris 312: 913–919.

Paquet J, Mansy JL. 1992. Evolution alpine du massif nord-pyrénéen de l'Agly (Pyrénées-Orientales). C R Acad Sci Paris 315: 487–494.

Paquette, J.L., & Tiepolo, M. 2007. High resolution (5 µm) U-Th-Pb isotopes dating of monazite with excimer laser ablation (ELA)-ICPMS. Chemical Geology, 240, 222-237.

Paquette, L., Ménot, R.P., & Peucat, J.J. 1989. REE, Sm-Nd and U-Pb zircon study of eclogites from the Alpine External massifs (Western Alps): Evidence for crustal contamination. Earth and Planetary Science Letters, 96, 181–198.

Paquette J-L, Monchoux P, Couturier M. 1995. Geochemical and isotopic study of a norite-eclogite transition in the European Variscan belt: Implications for U/Pb zircon systematics in metabasic rocks. Geochim. Cosmochim. Acta 59: 1611–1622.

Paquette, J.L., Gleizes, G., Leblanc, D. & Bouchez, J.L. 1997. Le granite de Bassiès (Pyrénées) : un pluton syntectonique d'âge westphalien. Comptes Rendus Académie des Sciences, Paris, 324, 387-392.

Paquette, J.L., Ménot, R.P., Pin, C., Orsini, J.B., 2003. Episodic and short-lived granitic pulses in a post-collisional setting: evidence from precise U-Pb zircon dating through a crustal cross-section in Corsica. Chem. Geol. 198, 1–20.

Paquette, J.L., Piro, J.L., Devidal, J.L., Bosse, V., & Didier, A. 2014. Sensitivity enhancement in LA-ICP-MS by N2 addition to carrier gas: application to radiometric dating of U–Th-bearing minerals. Agilent ICP-MS Journal, 58, 4–5.

Paquette, J.-L., Ballèvre, M., Peucat, J.-J., & Cornen, G. 2017. From opening to subduction of an oceanic domain constrained by LA-ICP-MSU–Pb zircon dating (Variscan belt, Southern Armorican Massif, France). Lithos, 294–295, 418–437.

Paquette, J-L., Barbey, P., Olivier, P. 2021. Âge ordovicien moyen et caractéristiques chimiques du gneiss de la Rivérole (Massif de l'Agly, Pyrénées orientales). Bull. Soc. Hist. nat. Toulouse 156, 111-119

Pascal ML, Fonteilles M, Guitard G. 1976. Contribution à l'étude géométrique des plissements superposés hercyniens des Pyrénées orientales : Paléozoïque épizonal du massif de l'Agly. Bull Soc geol Fr 18:1471–1487.

Passchier CW, Trouw RAJ. 1996. Microtectonics. Springer, Berlin, p. 289.

Pawley MJ, Collins WJ. 2002. The development of contrasting structures during the cooling and crystallisation of a syn-kinematic pluton. J Struct Geol 24: 469–483.

Pearce, J.A. 1996. A user's guide to basalt discrimination diagrams. In: Wyman DA (ed) Trace element geochemistry of volcanic rocks: applications for massive sulphide exploration, vol 12. Geological Association of Canada, Short Course Notes, Newfoundland, pp 79–113.

Pecher A. 1970. Etude pétrographique de la partie orientale du massif des Ecrins-Pelvoux: le socle ancien - Alpes françaises. (Theses). Faculté des Sciences de l'Université de Grenoble.

Pennacchioni, G., Cesare, B., 1997. Ductile-brittle transition in pre-Alpine amphibolite facies mylonites during evolution from water-present towater-deficient conditions (Mont Mary Nappe, Italian Western Alps). Journal of Metamorphic Geology 15, 777 – 791.Pereira et al., 2014

Pereira, M.F., El Houicha, M., Chichorro, M., Armstrong, R., Jouhari, A., El Attari, A., Ennih, N., Silva, J.B., 2015. Evidence of a Paleoproterozoic basement in the MoroccanVariscan Belt (Rehamna Massif, Western Meseta). Precambrian Research 268, 61–73.

Pereira, I., Dias, R., Bento dos Santos, T., & Mata, J. 2017. Exhumation of a migmatite complex along a transpressive shear zone: inferences from the Variscan Juzbado–Penalva do Castelo Shear Zone (Central Iberian Zone). Journal of Geological Society of London, 174, 1004–1018. https://doi.org/10.1144/jgs2016-159

Peressini, G., Quick, J. E., Sinigoi, S., Hofmann, A. W., & Fanning, M. 2007. Duration of a large mafic intrusion and heat transfer in the lower crust: A SHRIMP U-Pb zircon study in the Ivrea-Verbano Zone (Western Alps, Italy). Journal of Petrology, 48, 1185–1218.

Petford, N., Cruden, A.R., McCaffrey, K.J.W., Vigneresse, J.-L., 2000, Granite magma formation, transport and emplacement in the Earth's crust: Nature, v. 408, p. 669–673.

Pfeiffer, H.R., Biino, G., Ménot, R-P., Stille, P. 1993. Ultramafic ricks in the Pre-Mesozoic basement of the Central and External Alps. in von Raumer, J.F., and Neubauer, F., eds., The Pre-Mesozoic Geology in the Alps: Heidelberg, Germany, Springer-Verlag, p. 241–254.

Piazolo, S., Daczko, N. R., Silva, D., & Raimondo, T. 2020. Melt-present shear zones enable intracontinental orogenesis. Geology, 48(7), 643-648.

Pilloud C. 1991. Structure de déformation alpines dans le synclinal de Permo-Carbonifère de Salvan-Dorenaz, (massif des Aiguilles Rouges, Valais). Mém. Géol. Lausanne 9:1-101.

Pin C. 1979. Géochronologie U-Pb et microtectonique des séries métamorphiques anté-stéphaniennes de l'Aubrac et de la région de Marvejols (Massif Central). PhD Thesis, Université Montpellier IISciences et Techniques du Languedoc.

Pin, C. 1986. Datation U–Pb sur zircon à 285 M.a. du complexe gabbro-dioritique du Val Sesia-Val Mastallone et âge tardi-hercynien du métamorphisme granulitique de la zone Ivrea-Verbano (Italie). Comptes Rendus de l'Académie des Sciences Paris, II, 303, 827–830.

Pin, C., 1990. Variscan oceans – ages, origins and geodynamic implications inferred from geochemical and radiometric data. Tectonophysics 177, 215–227.

Pin, C., & Carme, F. 1987. A Sm-Nd isotopic study of 500 Ma old oceanic crust in the Variscan belt of western Europe: The Chamrousse ophiolite complex, Western Alps (France). Contributions to Mineralogy and Petrology, 96, 406–413.

Pin C, Carme F 1988 Ecailles de matèriaux d'origine océaniquedans le charriage hercynien de la «Ligne des Klippes», Vosgesme´ridionales (NE France). Comptes Rendus de l'Acade´mie desSciences 306:217–222

Pin C, Lancelot J. 1982. U-Pb dating of an early Paleozoic bimodal magmatism in the French Massif Central and of its further metamorphic evolution. Contrib. Mineral. Petrol. 79: 1–12.

Pin C, Marini F. 1993. Early Ordovician continental break-up in Variscan Europe: Nd Sr isotope and trace element evidence from bimodal igneous associations of the Southern Massif Central, France. Lithos 29: 177–196.

Pin C, Paquette J-L. 1998. A mantle-derived bimodal suite in the Hercynian Belt: Nd isotope and trace element evidence for a subduction-related rift origin of the Late Devonian Brévenne metavolcanics, Massif Central (France). Contrib. Mineral. Petrol. 129: 222–238.

Pin C, Paquette JL. 2002. Sr-Nd isotope and trace element evidence for a Late Devonian active margin in northern Massif-Central (France). Geodin. Acta 15: 63–77.

Pin, C., Dupuy, C. & Peterlongo, J. M. 1982. Répartition des terres rares dans les roches volcaniques basiques dévono-dinantiennes du Nord-Est du Massif central. Bulletin de la Société Géologique de France, 7, 669–676.

Pinarelli, L., & Boriani, A. 2007. Tracing metamorphism, magmatism and tectonics in the southern Alps (Italy): Constraints from Rb-Sr and Pb–Pb geochronology, and isotope geochemistry. Periodico di Mineralogia, 76, 5–24.

Pinarelli, L., Boriani, A., & Del Moro, A. 1988. Rb-Sr geochronology of the Lower Permian plutonism in Massiccio dei Laghi, Southern Alps (NW Italy). Rendiconti della Società Italiana di Mineralogia e Petrologia, 43, 411–428.

Pistone, M., Müntener, O., Ziberna, L., Hetényi, G., & Zanetti, A. 2017. Report on the ICDP workshop DIVE (Drilling the Ivrea-Verbano zonE). Scientific Drilling, 23, 47–56.

Pitra P, Poujol M, Van Den Driessche J, Poilvet JC, Paquette JL. 2012. Early Permian extensional shearing of an Ordovician granite: The Saint-Eutrope "C/S-like" orthogneiss (Montagne Noire, French Massif Central). C R Geosci 344: 377–384.

Pitra, P., Poujol, M., Van Den Driessche, J., Bretagne, E., Lotout, C., & Cogné, N. 2021. Late Variscan (315 Ma) subduction or deceiving zircon REE patterns and U-Pb dates from migmatite-hosted eclogites? (Montagne Noire, France). Journal of Metamorphic Geology, in press. https://doi.org/10.1111/jmg.12609

Pohl, F., Froitzheim, N., Obermüller, G., Tomaschek, F., Schröder, O., Nagel, T.J., Sciunnach, D., Heuser, A., 2018. Kinematics and age of syn-intrusive detachmentfaulting in the Southern Alps: evidence for Early Permian crustal extension andimplications for the Pangea A versus B controversy. Tectonics 37.https://doi.org/10.1029/2018TC004974

Poilvet J-C, Poujol M, Pitra P, Van den Driessche J, Paquette J-L. 2011. The Montalet granite, Montagne Noire, France: An Early Permian syn-extensional pluton as evidenced by new U-Th-Pb data on zircon and monazite. Comptes Rendus Géoscience 343: 454–461

Poitrasson, F., Pin, C., 1998. Extreme Nd isotope homogeneity in alarge rhyolitic province: the Este´rel massif, southeast France.Bull. Volcanol. 60, 213–223

Poitrasson, F., Paquette, J.L., Montel, J.M., Pin, C., Duthou, J.L., 1998. Importance of late-magmatic and hydrothermal fluids on the Sm–Nd isotope mineral systematics of hypersolvus granites. Chem. Geol. 146, 187– 203.

Poitrenaud, T., Poujol, M., Augier, R., Marcoux, E., 2020. The polyphase evo-lution of a late-Variscan W/Au deposit (Salau, French Pyrenees): Insights from REE and U/Pb LA-ICP-MS analyses. Mineral. Deposita 30, 111–128

Popov Y, Mandel A 1997 Geothermal study of anisotropic rockmasses. Izv Phys Solid Earth 34(11):903–915

Postaire B. 1982. Systématique Pb commun et U-Pb sur zircons : applications aux roches de haut grade métamorphique impliquées dans la chaîne hercynienne (Europe de l'ouest) et aux granulites de Laponie (Finlande). Mémoires de la société géologique et minéralogique de Bretagne 15: 29–72.

Poujol M, Boulvais P, Kosler J. 2010. Regional-Scale Cretaceous Albitization in the Pyrenees: Evidence from in situ U-Th-Pb Dating of Monazite, Titanite and Zircon. J Geol Soc 167: 751–767.

Poujol M, Pitra P, Van Den Driessche J, Tartèse R, Ruffet G, Paquette JL, et al. 2017. Two-stage partial melting during the Variscan extensional tectonics (Montagne Noire, France). Int J Earth Sci 106: 477–500.

Powell, R., 1983. Processes in granulite–facies metamorphism. In: Atherton, M.P., Gribble, C.D. (Eds.), Migmatites, Melting and Metamorphism. Shiva, Cheshire, pp. 27–139.

Quick, J.E., Sinigoi, S., Peressini, G., Demarchi, G., Wooden, J.L., Sbisà, A., 2009. Magmaticplumbing of a large Permian caldera exposed to a depth of 25 km. Geology 37,603–606.

Rabin M, Trap P, Carry N, Fréville K, Cenki-Tok B, Lobjoie C, et al. 2015. Strain partitioning along the anatectic front in the Variscan Montagne Noire massif (Southern French Massif Central). Tectonics 34: 1709–1735.

Rahn, M. 1991. Eclogites from the Minugrat, Siviez-Mischabel nappe (Valais, Switzerland). Schweizerische Mineralogische und Petrographische Mitteilungen, 71, 415–426.

Raimondo T, Collins AS, Hand M, Walker-Hallam A, Smithies RH, Evins PM, Howard HM 2009 Ediacaran intracontinental channel flow. Geology 37, 291:294.

Reche-Estrada, J. Martinez, F.J. 2002. – Evolution of bulk composi-tion, mineralogy, strain style and fluid flow during a HT-LP me-tamorphic event : sillimanite zone of the Catalan Coastal RangesVariscan basement, NE Iberia. –Tectonophysics,348, 111-134

Regorda, A., Lardeaux, J.M., Roda, M., Marotta, A. M., & Spalla, M. I. 2020. How many subductions in the Variscan orogeny? Insights from numerical models. Geosciences Frontiers, 11(3), 1025-1052.

Renna, M.R., Tribuzio, R., Tiepolo, M., 2007. Origin and timing of the post-Variscan gab-bro–granite complex of Porto (Western Corsica). Contributions to Mineralogy andPetrology 154, 493–517.

Rennie, S.F., Fagereng, Å., Diener, J.F.A., 2013. Strain distribution within a km-scale, mid-crustal shear zone: the kuckaus mylonite zone, Namibia. J. Struct. Geol. 56,57e69.

Respaut JP, Lancelot JR. 1983. Datation de la mise en place synmétamorphe de la charnockite d'Ansignan (massif de l'Agly) par la méthode U/Pb sur zircons et monazites. Neues Jahrb Mineral Abh 147: 21–34.

Rey PF, Teyssier C, Whitney DL. 2009. The role of partial melting and extensional strain rates in the development of metamorphic core complexes. Tectonophysics 477: 135–144. https://doi.org/10.1016/j.tecto.2009.03.010.

Rey, P.F., Teyssier, C., Whitney, D.L., 2010. The limit of channel flow in orogenic plateaux. Lithosphere 2: 328–332.

Rey, P.F., Teyssier, C., Kruckenberg, S.C., & Whitney, D.L. 2011. Viscous collision in channel explains double domes in metamorphic core complexes. Geology, 39, 387–390.

Rey, P.F., Mondy, L., Duclaux, G., Teyssier, C., Whitney, D.L., Bocher, M., & Prigent, C. 2017. The origin of contractional structures in extensional gneiss domes. Geology, 45 (3), 263–266.

Riel, N., Mercier, J., Weinberg, R., 2016. Convection in a partially molten metasedimentary crust? Insights from the El Oro complex (Ecuador). Geology 44, 31–34. https://doi.org/10.1130/G37208.1

Roberts, M.P., Pin, C., Clemens, J.D., Paquette, J., 2000. Petrogenesis of Mafic to Felsic Plutonic Rock Associations: the Calc-alkaline Querigut Complex, French Pyrenees. J. Petrol. 41, 809–844.

Rodriguez-Méndez, L., Cuevas, J., Tubia, J.M., 2014. Post-Variscan basin evolution in the central Pyrenees: Insights from the Anayet basin.

Roger F, Respaut JP, Brunal M, Matte P, Paquette JL 2004 Première datation U–Pb des orthogneiss oeillés de la zone axiale de la Montagne noire (Sud du Massif central) : nouveaux témoins du magmatisme ordovicien dans la chaîne Varisque. CR Geosci 336:19-28.

Roger F, Maluski H, Lepvrier C, Van Vu T, Paquette JL 2012 LAICPMS zircons U/Pb dating of Permo–Triassic and Cretaceous magmatisms in Northern Vietnam—geodynamical implications. J Asian Earth Sci 48:72–82. doi:10.1016/j.jseaes.2011.12.012

Roger F, Teyssier C, Respaut JP, Rey PF, Jolivet M, Whitney DL, et al. 2015. Timing of formation and exhumation of the Montagne Noire double dome, French Massif Central. Tectonophysics 640–641: 53–69.

Roger, F., Teyssier, C., Whitney, D.L., Respaut, J.P., Paquette, J.L., & Rey, P.F. 2020. Age of metamorphism and deformation in the Montagne Noire dome (French Massif Central): Tapping into the memory of fine-grained gneisses using monazite U-Th-Pb geochronology. Tectonophysics, 776. doi.org/10.1016/j.tecto.2019.228316

Rolland, Y., Cox, S., Boullier, A.M., Pennacchioni, G., & Mancktelow, N. 2003. Rare earth and trace element mobility in mid-crustal shear zones: Insights from the Mont Blanc Massif (western Alps), Earth Planetary Science Letters, 214, 203–219.

Rolland, Y., Corsini, M., and Demoux, A., 2009, Metamorphicand structural evolution of the Maures-Tanneron Massif (SE Variscan chain): Evidence of doming along a transpressional margin: Bulletin de la Societe Geologique de France, 3, 217–230.

Rolin, P., Cartannaz, C., Henry, P., Rossy, M., Cocherie, A., Salen, F., Delwaulle, B., Mauroux, B. 2006. Notice Feuille Saint-Sulpice-Les-Champs, 667 p.

Rolin, P., Thiéry, V., Cartannaz, C., Cocherie, A., Rossy, M., Henry, P., Constant, J. 2008. Notice Feuille Felletin, 667 p.

Román-Berdiel T, Casas AM, Oliva-Urcia B, Pueyo EL, Rillo C. 2004. The main Variscan deformation event in the Pyrenees: New data from the structural study of the Bielsa granite. J Struct Geol 26: 659–677.

Román-Berdiel T, Casas AM, Oliva-Urcia B, Pueyo EL, Liesa C, Soto R. 2006. The Variscan Millares granite (central Pyrenees): Pluton emplacement in a T fracture of a dextral shear zone. Geodin Acta 19: 197–211.

Rosenberg, C. L., and M. R. Handy 2005, Experimental deformation of partially melted granite revisited: Implications for the continental crust, J. Metamorph. Geol., 23, 19–28.

Rosenberg, C. L., Medvedev, S., & Handy, M. R. 2007. Effects of Melting on faulting and Continental Deformation. In Handy, M. R., Hirth, G. & Hovious, N. (eds). Tectonic Faults, agents of change on a dynamic Earth: Report of the 95th Dahlem Workshop on the Dynamics of Fault Zones, Berlin, January 16-21, 2005.

Rossi, M., Rolland, Y., Vidal, O., & Cox, S. 2005. Geochemical variations and element transfer during shear zone development and related episyenites at middle crust depths: Insights from the Mont-Blanc granite (French-Italian Alps). In D. Brunh & L. Burlini (Eds.), High Strain Zones: Structure and Physical Properties, Geological Society, London, Special Publication, 245, 373-396. https://doi.org/10.1144/GSL.SP.2005.245.01.18

Rossi, P., Oggiano, G., Cocherie, A., 2009. A restored section of the “southern Variscan realm” across the Corsica–Sardinia microcontinent. Comptes Rendus Géosciences, Mécanique de l’orogénie varisque : Une vision moderne de la recherche dans le domaine de l’orogénie 341, 224–238. https://doi.org/10.1016/j.crte.2008.12.005

Rouire, J., Autran, A., Prost, A., Rossi, P., Rousset, C., 1980. Carte géologique de laFrance à l’échelle du deux-cent-cinquante millième (1/250.000ème), feuille deNice (40). Bureau de Recherche Géologique et Minière, Orléans, France.

Roux L. 1977. L’évolution des roches du faciès granulite et le problème des ultramafites dans le massif de Castillon (Ariège). State thesis, Toulouse (France), Univ. Toulouse.

Rybach, L., 1988. Determination of heat production rate. In: Hänel, R., Rybach, L., Stegena, I. (Eds.), Terrestrial Handbook of Heat-flow Density Determination. Kluwer Academic Publishers, Dordrecht, 125-142. Chapter 4.2.

Rubatto, D. 2002. Zircon trace element geochemistry: distribution coefficients and the link between U–Pb ages and metamorphism. Chemical Geology, 184, 123–138.

Rubatto, D. 2017. Zircon: The metamorphic mineral. Reviews in Mineralogy and Geochemistry, 83, 261–295.

Rubatto D, Gebauer D 1999 Eo/Oligocene (35 Ma) high-pressure metamorphism in the Gornergrat Zone (MonteRosa, Western Alps): Implications for paleogeography. Swiss Bull Mineral Petrol 79:353-362

Rubatto D, Gebauer D, Fanning M 1998 Jurassic formation and Eocene subduction of the Zermatt-Saas-Feeophiolites: Implications for the geodynamic evolution of the Central and Western Alps. Contrib Mineral Petrol132:269-287

Rubatto, D., Schaltegger, U., Lombardo, B., Colombo, F., & Compagnoni, R. 2001. Complex Paleozoic magmatic and metamorphic evolution in the Argentera Massif (Western Alps) resolved with U-Pb dating. Schweizerische Mineralogische und Petrographische Mitteilungen, 81, 213–228.

Rubatto, D., Ferrando, S., Compagnoni, R., & Lombardo, B. 2010. Carboniferous high-pressure metamorphism of Ordovician protolith in the Argentera Massif (Italy), Southern European Variscan Belt. Lithos, 116, 65–76.

Rushmer, T. 2001. Volume change during partial melting reactions: implications for melt extraction, melt geochemistry and crustal rheology. Tectonophysics, 342, 389–405, https://doi.org/10.1016/S0040-1951(01)00172-X

Rutter, E.H., Neumann, D.H.K., 1995. Experimental deformation of partially molten Westerly granite under fluid-absent conditions, with implications for the extraction of granitic magmas. Journal of Geophysical Research 100 (B8), 15697–15715.

Sartori, M. 1990. L'unité du Barrhorn (Zone pennique, Valais, Suisse). Mémoires de Géologie Lausanne, 6, 156 p.

Saspiturry, N., Razin, P., Baudin, T., Serrano, O., Issautier, B., Lasseur, E., Allanic, C., Thinon, I., Leleu, S. 2019: Symmetry vs. asymmetry of a hyper-thinned rift: example of the Mauléon Basin (Western Pyrenees, France). Mar. Petrol. Geol., 104, 86–105.

Saspiturry, N., Lahfid, A., Baudin, T., Guillou-Frottier, L., Razin, P., Issautier, B., Le Bayon, B., Serrano, O., Lagabrielle, Y., & Corre, B. 2020. Paleogeothermal gradients across an inverted hyperextended rift system: Example of the Mauléon Fossil Rift (Western Pyrenees). Tectonics, 39(10), e2020TC006206. https://doi.org/10.1029/2020T C006206

Sawyer, E.W., 2001. Melt segregation in the continental crust: distribution and movement of melt in anatectic rocks. Journal of Metamorphic Geology 19, 291–309.

Sawyer, E. W. 2010. Migmatites formed by water-fluxed partial melting of a leucogranodiorite protolith: Microstructures in the residual rocks and source of the fluid. Lithos, 116(3-4), 273-286.

Sawyer, E. W., Cesare, B. & Brown, M. 2011. When the continental crust melts. Elements 7, 229–234

Scaillet, B. & Searle, M. P. 2006. Mechanisms and timescales of felsicmagma segregation, ascent and emplacement in the Himalaya.InLaw, R. D., Searle, M. P. & Godin, L. (eds)Channel Flow, DuctileExtrusion and Exhumation in Continental Collision Zones. Geologi-cal Society, London, Special Publications268, 293–308. Bath, UK:The Geological Society Publishing House.Schaltegger, U. 1990. The Central Aar granite: Highly differentiated calc-alkaline magmatism in the Aar massif (Central Alps, Switzerland). European Journal of Mineralogy, 2, 245–259.

Schaltegger, U. 1993: The evolution of the polymetamorphic basement of the Central Alps unravelled by precise U–Pb zircon dating. Contrib. Mineral. Petrol. 113, 466–478.

Schaltegger, U. 1994. Unravelling the pre-Mesozoic history of Aar and Gotthard Massifs (Centreal Alps, Switzerland) by isotopic dating. Schweizerische Mineralogische und Petrographische Mitteilungen, 74, 41–51.

Schaltegger, U. and Corfu, F. 1992: The age and source for late Hercynian magmatism in the Central Alps: Evidence from precise U–Pb ages and initial Hf isotopes. Contrib. Mineral. Petrol. 111, 329–344.

Schaltegger, U., & von Quadt, A. 1990. U–Pb zircon dating of the Central Aar granite (Aar Massif, Switzerland). Schweizerische Mineralogische und Petrographische Mitteilungen, 70, 361–371.

Schaltegger U, Schneider J-L, Maurin J-C, Corfu F. 1996. Precise U–Pb chronometry of 345–340 Ma old magmatism related to synconvergence extension in the Southern Vosges/Central Variscan Belt. Earth and Planetary Science Letters 144: 403–419.

Schaltegger, U., Fanning, C. M., Gunther, D., Maurin, J. C., Schulmann, K., & Gebauer, D. 1999. Growth, annealing and recrystallization of zircon and preservation of monazite in high-grade metamorphism: Conventional and in-situ U-Pb isotope, cathodoluminescence and microchemical evidence. Contributions to Mineralogy and Petrology, 134, 186–201. https://doi.org/10.1007/s004100050478

Schaltegger U, Gebauer D. 1999. Pre-Alpine geochronology of the central, western and southern Alps. Schweiz. Mineral. Petrogr. Mitteilungen 79: 79–87.

Schaltegger, U., Abrecht, J., Corfu, F. 2003. The Ordovician orogeny in the Alpine basement: constraints from geochronology and geochemistry in the Aar Massif (Central Alps). Schweizerische mineralogische und petrographische Mitteilungen, 83, 183-195.

Schildgen, T. F. and Hoke, G. D. 2018 The topographic evolu-tion of the central Andes. Elements, 14, 231–236

Schmädicke, E. & Müller, W. F. 2000. Unusual exsolution phenom-ena in omphacite and partial replacement of phengite by phlogopi-teþkyanite in an eclogite from the Erzgebirge.Contributions toMineralogy and Petrology139, 629^642.

Schmid, S. M., Fügenschuh, B., Kissling, E., & Schuster, R. 2004. Tectonic map and overall architecture of the Alpine orogen. Eclogae Geologicae Helvetiae, 97, 93–117.

Schmid, S. M., A. Scharf, M. R. Handy, and C. Rosenberg 2013, The Tauern Window (Eastern Alps. Austria): A new tectonic map, with cross-sections and a tectono metamorphic synthesis. Swiss J. Geosci., 175–194, doi:10.1007/s00015-013-0123-y, in press

Schmid, S. M., Kissling, E., Diehl, T., van Hinsbergen, D. J. J., & Molli, G. 2017. Ivrea mantle wedge, arc of the Western Alps, and kinematic evolution of the Alps-Apennines orogenic system. Swiss Journal of Geosciences, 110, 581–612.

Schnapperelle S, Mezger JE, Stipp M, Hofmann M, Gärtner A, Linnemann U 2020 Polyphase magmatic pulses along the Northern Gondwana margin: U-Pb zircon geochronology from gneiss domes of the Pyrenees. Gondwana Res 81:291-311.

Schneider, J., Corsini, M., Reverso, P.A., & Lardeaux, J.-M. 2014. Thermal and mechanical evolution of an orogenic wedge during Variscan collision: an example in the Maures-Tanneron Massif (SE France). Geological Society of London, Special Publication, 405, 313-331.Schulmann et al., 2014

Schulmann K, Schaltegger U, Jezek J, Thompson AB, Edel J-B. 2002. Rapid burial and exhumation during orogeny: thickening and synconvergent exhumation of thermally weakened and thinned crust (Variscan orogen in western Europe). American Journal of Science 302: 856–879.

Schulmann, K., Kröner, A., Hegner, E., Wendt, I., Konopasek, J., Lexa, O., & Štípská, P. 2005 Chronological constraints on the pre-orogenic history, burial and exhumation of deep-seated rocks along the eastern margin of the Variscan orogen, Bohemian Massif, Czech Republic. American Journal of Science 305:407–448

Schulmann, K., Lexa, O., Štípská, P., Racek, M., Tajcmanova, L., Konopasek, J., … Lehmann, J. 2008. Vertical extrusion and horizontal channel flow of orogenic lower crust: key exhumation mechanisms in large hot orogens? Journal of Metamorphic Geology, 26, 273–297.

Schulmann, K., Konopásek, K., Janousek, V., Lexa, O., Lardeaux, J.-M., Edel, J.-B., Štípská, P. and Ulrich, S. 2009. An Andean type Palaeozoic convergence in the Bohemian Massif. Comptes Rendus Geoscience, 341, 266-286. https://doi.org/10.1016/j.crte.2008.12.006.

Schulmann K, Catalán JRM, Lardeaux JM, Janousek V, Oggiano G. 2014. The Variscan orogeny: extent, timescale and the formation of the European crust. Geol. Soc. Lond. Spec. Publ. 405: 1–6.

Schulz, B., & von Raumer, J.F. 1993. Syndeformational Uplift of Variscan High-pressure Rocks (Col de Bérard, Aiguilles Rouges Massif, Western Alps). Zeitschrift der Deutschen Geologischen Gesellschaft, 144, 104 20.

Schulz, B., & von Raumer, J. 2011. Discovery of Ordovician–Silurian metamorphic monazite in garnet metapelites of the Alpine External Aiguilles Rouges Massif. Swiss Journal of Geosciences, 104, 67–79. doi:10.1007/s00015-010-0048-7.

Schuster, R., & Stüwe, K. 2008. Permian metamorphic event in the Alps. Geology, 36, 603–606.

Schuster, R., Scharbert, S., Abart, R., & Frank, W. 2001. Permo-Triassic extension and related HT/LP metamorphism in the Austroalpine-Southalpine realm. Mitteilungen der Gesellschaft der Geologie und Bergbaustudenten in Oesterreich, 45, 111–141.

Scodina, M., Cruciani, G., Franceschelli, M., Massonne, H.-J., 2021. Multilayer corona textures in the high-pressure ultrabasic amphibolite of Mt. Nieddu, NE Sardinia (Italy): equilibrium versus disequilibrium. Periodico di Mineralogia 89, 169–186.

Sebastian, A., Reche, J. & Duran, H., 1990. Hercynian meta-morphism in the Catalonian coastal ranges. Acta geologicahispanica, 255, 31–32.

Sergeev, S. and Steiger, R.H. 1995: Improving the resolution of single-grain U/Pb dating by use of zircon extracted from feldspar: application to the Variscan magmatic cycle in the Central Alps. Earth Planet. Sci. Lett. 134, 37–51.

Seipold, U. 1998. Temperature dependence of thermal transport properties of crystalline rocks —a general law. Tectonophysics, 291(1–4):161–171.

Shelley, D. & Bossiere, G. 2001. The Ancenis Terrane: an exotic duplex in the Hercynian belt of Armorica, western France. Journal of Structural Geology, 23, 1597–1614.

Sibuet JC, Srivastava SP, Spakman W. 2004. Pyrenean orogeny and plate kinematics. J Geophys Res Solid Earth 109. https://doi.org/10.1029/2003JB002514.

Sider H, Ohnenstetter M. 1986. Field and petrological evidence for the development of an ensialic marginal basin related to the Hercynian orogeny in the Massif Central, France. Geol. Rundsch. 75: 421–443.

Siletto GB, Spalla MI, Tunesi A, Lardeaux JM, Colombo A 1993Pre-Alpine structural and metamorphic histories in the Orobicsouthern Alps, Italy. In: Raumer J von, Neubauer F (eds) The pre-Mesozoic geology in the Alps. Springer, Berlin Heidelberg NewYork, pp 585–598

Simeon, Y., 1979. Etude Petrologique, Geochimique et Structurale des Terrains Cristallins de Belledonne Entre l'Arc et L'Isere (Alpes Françaises). Université de Grenoble.

Simonetti M, Carosi R, Montomoli C, Langone A, D’Addario E, Mammoliti E. 2018. Kinematic and geochronological constraints on shear deformation in the Ferriere-Mollières shear zone (Argentera-Mercantour Massif, Western Alps): implications for the evolution of the Southern European Variscan Belt. Int. J. Earth Sci. 107:2163–2189. https://doi.org/10.1007/s00531-018-1593-y

Simonetti, M., Carosi, R., Montomoli, C., Cottle, J. M., & Law, R. D. 2020a. Transpressive Deformation in the Southern European Variscan Belt: New Insights From the Aiguilles Rouges Massif (Western Alps). Tectonics, 39. https://doi.org/10.1029/2020TC006153

Simonetti, M., Carosi, R., Montomoli, C., Corsini, M., Petroccia, A., Cottle, J. M., & Iaccarino, S. 2020b. Timing and kinematics of flow in a transpressive dextral shear zone, Maures Massif (Southern France). International Journal of Earth Sciences, 109, 2261–2285. https://doi.org/10.1007/s00531-020-01898-6

Simonetti, M., Carosi, R., Montomoli, C., Lawd, R.D., Cottle, J.M. Unravelling the development of regional-scale shear zones by a multidisciplinary approach: The case study of the Ferriere-Mollières Shear Zone (Argentera Massif, Western Alps). Journal of Structural Geology 149, 104399

Siron G, Goncalves P, Marquer D. 2012. The origin of high geothermal gradient: Post-orogenic extension or large intrusion in the middle crust? A case study from the Agly Massif, French Pyrenees. Abstract, Variscan 2012 meeting, Sassari, Italy.

Siron G, Goncalves P, Marquer D, Pierre T, Paquette JL, Vanardois J. 2020. Contribution of magmatism, partial melting buffering and localized crustal thinning on the late-Variscan thermal structure of the Agly massif (French Pyrenees). J Metamorph Geol 38:799-829. https://doi.org/10.1111/jmg.12549.

Skrzypek, E., Tabaud, A.-S., Edel, J.-B., Schumann, K., Cocherie, A., Guerrot, C., Rossi, P., 2012. The significance of Late Devonian ophiolites in the Variscan orogeny: a record from the Vosges Klippen Belt. Int. J. Earth Sci. 101, 951–972.

Skrzypek E, Schulmann K, Tabaud A-S, Edel J-B. 2014. Palaeozoic evolution of the Variscan Vosges mountains. Geol. Soc. Lond. Spec. Publ. 405: 45–75.

Soliva J. 1992. Les déformations ductiles dans la zone axiale des Pyrénées-Orientales : la convergence varisque, la mise en place des granites tardi-hercyniens, la convergence pyrénéenne. PhD thesis, Montpellier (France), Univ. Montpellier 2.

Sonnette, L., Humbert, F., Aubourg, C., Gattacceca, J., Lee, J.-C., Angelier, J., 2014.Significant rotations related to coveresubstratum decoupling: example of theD^ome de Barr^ot (Southwestern Alps, France). Tectonophysics 629, 275e289.

Soula, J.C., Debat, P., Brusset, S., Bessiere, G., Christophoul, F., Deramond, J. 2001. Thrust-related, diapiric, and extensional doming in a frontal orogenic wedge: example of the Montagne Noire, southern French Hercynian Belt. Journal of Structural Geology, 23,1677–1699.

Spalla, M.I., Lardeaux, J.M., Dal Piaz, G.V., Gosso, G., & Messiga, B. 1996. Tectonic significance of Alpine eclogites. Journal of Geodynamics, 21 (3), 257–285

Spencer, C.J., Kirland, C.L., Taylor, R.J.M.. 2016. Strategies towards statistically robust interpretations of in situ U-Pb zircon geochronology, Geosciences Frontiers, 7, 581-589

Stacey, J.S., & Kramers, J.D. 1975. Approximation of terrestrial lead isotope evolution by a two-stage model. Earth Planetary Science Letters, 26, 207–226.

Stampfli, G. M., von Raumer, J. F., & Borel, G. D. 2002. Paleozoic evolution of pre-Variscan terranes:From Gondwana to the Variscan collision. Geological Society of America Special Paper, 364: 263-280.

Stampfli, G. M., Hochard, C., Vérard, C., Wilhem, C., & von Raumer, J. 2013. The formation of Pangea. Tectonophysics, 593, 1-19.

Steiger, R.H., & Jäger, E. 1977. Subcommission on geochronology: convention on the use of decay constants in geo- and cosmochronology. Earth Planetary Science Letters, 36, 359–362.

Stenvall, C. A., Fagereng, Å., & Diener, J. F. A. 2019. Weaker than weakest: On the strength of shear zones. Geophysical Research Letters, 46, 7404–7413. https://doi.org/10.1029/2019GL083388

Stephan, T., Kroner, U., Romer, R.L. 2019. The pre-orogenic detrital zircon record of the Peri-Gondwanan crust. Geol. Mag. 156(2), 281–307. https://doi.org/10.1017/s0016756818000031.

Stern, R.A. 1997. The GSC sensitive high resolution ion micro-probe (SHRIMP): analytical techniques of zircon U–Th–Pb age determinations and performance evaluation. Radiogenic Age and Isotopic Studies. Geological Survey of Canada, Current Research, 10, 1–31.

Stipp M, Stunitz H, Heilbronner R, Schmid SM. 2002. The eastern Tonale fault zone: a 'natural laboratory' for crystal plastic deformation of quartz over a temperature range from 250 °C to 700 °C. J. Struct. Geol. 24:1861- 1884.

Štípská, P., Powell, R., Hacker, B.R., Holder, R. & Kylander-Clark, A.R.C., 2016. Uncoupled U/Pb and REE response inzircon during the transformation of eclogite to mafic andintermediate granulite (Blansky les, Bohemian Massif). Journal of Metamorphic Geology, 34, 551–572.

Štípská, P., Hasalová, P., Powell, R., Závada, P., Schulmann, K., Racek, M., ... Chopin, F. 2019. The effect of melt infiltration on meta-granitic rocks: The Snieznik dome, Bohemian Massif. Journal of Petrology, 60, 591–618.

Strzerzynski P, Guillot S, Courrioux G, Ledru P, 2005. Modélisation géométrique 3D des granites stéphaniens du massif du Pelvoux (Alpes, France). C R Geosci. 337: 1284–1292.

Stuart, C. A., Piazolo, S., & Daczko, N. R. 2018. The recognition of former melt flux through high-strain zones. Journal of Metamorphic Geology, 36(8), 1049-1069.

Stüwe, K., 1995. Thermal buffering effects at the solidus. Implications for the equilibration of partially melted metamorphic rocks. Tectonophysics 248, 39–51. https://doi.org/10.1016/0040-1951(94)00282-E

Styron, R., M. Taylor, and M. Murphy 2011, Oblique convergence, arc-parallel extension, and the role of strike-slip faulting in the High Himalaya, Geosphere,7, 582–596.

Sun, S.S., & McDonough, W.F. 1989. Chemical and isotopic systematics of oceanic basalts: implications for mantle composition and processes. In: Saunders AD, Norry MJ (eds) Magmatism in the Ocean Basins, vol 42. Geological Society of London, Special Publication, 313–345.

Sun, J.F., Yang, J.H., Wu, F.Y., Xie, L.W., Yang, Y.H., Liu, Z.C., Li, X.H. 2012. In situ U–Pb dating of titanite by LA–ICPMS. Chinese Science Bulletin, 57(20), 2506–2516.

Tabaud A-S, Whitechurch H, Rossi P, Schulmann K, Guerrot C, Cocherie A. 2014. Devonian-Permian magmatic pulses in the northern Vosges Mountains (NE France): result of continuous subduction of the Rhenohercynian Ocean and Avalonian passive margin. Geological Society, London, Special Publications 405: 197–223.

Tabaud A-S, Janouzek V, Skrzypek E, Schulmann K, Rossi P, Whitechurch H, et al. 2015. Chronology, petrogenesis and heat sources for successive Carboniferous magmatic events in the Southern-Central Variscan Vosges Mts (NE France). Journal of the Geological Society, London 172: 87–102.

Tapponnier P, Peltzer G, Le Dain AY, ArmijoR, Cobbold P. 1982. Propagating extrusion tectonics in Asia: new insights from simple experiments with plasticine. Geology 10:611–616

Tedeschi, M., Lanari, P., Rubatto, D., Pedrosa-Soares, A., Hermann, J., Dussin, I., … Baumgartner, L. 2017. Reconstruction of multiple P-T-t stages from retrogressed mafic rocks: Subduction versus collision in the Southern Brasília orogen (SE Brazil). Lithos, 294-295, 283-303. http://doi.org/10.1016/j.lithos.2017.09.025.

Teipel, U., Eichhorn, R., Loth, G., Rohrmüller, J., Höll, R., & Kennedy, A. 2004. U–Pb SHRIMP and Nd isotopic data from the western Bohemian Massif (Bayerischer Wald, Germany): implications for Upper Vendian and Lower Ordovician magmatism. International Journal of Earth Sciences, 93, 782–801.

Ternet, Y., Majeste-Menjoulas, C., Canerot, J., Baudin, T., Cocherie, A., Guerrot, C. & Rossi, P. 2004. Notice explicative, Carte géologique de France (1/50 000), feuille Laruns-Somport (1069). BRGM, Orléans, 192p.

Teyssier, C., Tikoff, B. 1998. Strike-slip partitioned transpression of the San Andreas fault system: a lithospheric-scale approach. Geological Society, London, Special Publications, 135(1), 143-158.

Teyssier C, Whitney DL, Rey P. 2008. Dynamic coupling and coeval contraction/extension in and around orogenic plateaux. American Geophysical Union, Fall Meeting 2008, Abstract #T23C–2040.

Ternois S, Odlum M, Ford M, Pik R, Stockli D, Tibari B, et al. 2019. Thermochronological evidence of early orogenesis, eastern Pyrenees, France. Tectonics 38: 1308–1336.

Thélin, P., Sartori, M., Lengeler, R., & Schaerer, J.-P. 1990. Eclogites of Paleozoic or early Alpine age in the basement of the Penninic Siviez-Mischabel nappe, Wallis, Switzerland. Lithos, 25, 71–88.

Thiébaut J. 1964. Étude géologique du Massif de la forêt de Castillon. Bull Soc Hist Nat Toulouse 99: 363–389.

Thiéry V. 2010. Métamorphismes et déformations des séries cristallophylliennes du Chavanon, de la Sioule et d'Ussel (Massif Central français). Discussion du modèle de nappes du Massif Central. PhD Thesis, Université de Franche-Comté.

Thiéry V, Rolin P, Marquer D, Cocherie A, Fanning CM, Rossi P. 2009. Visean sinistral wrench faulting along the Sillon Houiller in the French Massif Central: Late Variscan tectonic implications. Bull. Société Géologique Fr. 180: 513–528.

Thompson, A.B., 1983. Fluid-absent metamorphism. Journal of the Geological Society 140, 533–547.

Thöni, M. 2002. Sm–Nd isotope systematics in garnet fromdifferent lithologies (Eastern Alps): age results, andan evaluation of potential problems for garnet Sm–Ndchronometry.Chemical Geology185, 255–81.

Tiepolo M, 2003 In situ Pb geochronology of zircon with laser ablation-inductively coupled plasma-sector field mass spectrometry. Chem. Geol. 141, 1-19.

Tikoff B, Greene D. 1997. Stretching lineations in transpressional shear zones: An example from the Sierra Nevada Batholith, California. J Struct Geol 19: 29–39.

Tikoff B, Teyssier C. 1994. Strain modeling of displacement-field partitioning in transpressional orogens. J Struct Geol 16: 1575–1588.

Tikoff B, Teyssier C, Waters C. 2002. Clutch tectonics and the partial attachment of lithospheric layers. EGU Stephan Mueller Spec. Publ. Ser., 1: 57–73.

Tikoff, B., Russo, R., Teyssier, C. Tomassi, A. 2004. Mantle-driven deformation of orogenic zonesand clutch tectonics. In: Grocott, J., Mccaffrey, K. J. W., Yaylor, G.&Tikoff, B. (eds)VerticalCoupling and Decoupling in the Lithosphere. Geologi-cal Society, London, Special Publications,227, 41 – 64.

Tomascak, P. B., E. J. Krogstad, and R. J. Walker 1996, U-Pb monazite geochronology of granitic rocks from Maine: Im- plications for Late Paleozoic tectonics in the northern Appa- lachians, J. Geol., 104, 185–195.

Tomkins, H.S., Powell, R., & Ellis, D.J. 2007. The pressure dependence of the zirconium-in-rutile thermometer. Journal of Metamorphic Geology, 25, 703–713.

Tommasi, A., Vauchez, A., Fernandes, L.A.D., Porcher, C.C.,1994. Magma assisted strain localization in an orogen-parallel transcurrent shear zone of southern Brazil. Tectonics 13,421–437.

Tommasi, A., Vauchez, A., & Daudré, B. 1995. Initiation and propagation of shear zones in a heterogeneous continental lithosphere. Journal of Geophysical Research: Solid Earth, 100(B11), 22083-22101.

Torvela, T., Kurhila, M., 2020. How does orogenic crust deform? Evidence of crustal- scale competent behaviour within the partially molten middle crust during orogenic compression. Precambr. Res. 342, 105670

Tournaire Guille B, Olivier P, Paquette JL, Bosse V, Guillaume D. 2019. Evolution of the middle crust of the Pyrenees during the Paleozoic: New data on the plutonic rocks from the North Pyrenean Agly Massif. Int J Earth Sci 108: 245–265.

Trap, P., Faure, M., Lin, W., Augier, R., Fouassier, A. 2011. Syn-collisional channel flow and exhumation of Paleoproterozoic High Pressure rocks in the Trans-North China Orogen: the critical role of partial-melting and orogenic bending. Gondwana Research, 20, 498–515.

Trap P, Roger F, Cenki-Tok B, Paquette JL. 2017. Timing and duration of partial melting and magmatism in the Variscan Montagne Noire gneiss dome (French Massif Central). Int J Earth Sci 106: 453–476.

Tugend J, Manatschal G, Kusznir NJ. 2015. Spatial and temporal evolution of hyperextended rift systems: Implication for the nature, kinematics, and timing of the Iberian-European plate boundary. Geology 43: 15–18.

Tumiati, S., Thöni, M., Nimis, P., Martin, S., Mair, V., 2003. Mantle-crust interactions during Variscan subduction in the Eastern Alps (Nonsberg–Ulten Zone): geochronology and new petrological constraints. Earth and Planetary Science Letters 210, 509–526.

Turcotte, D. and Schubert, G. 2002. Geodynamics, 2nd edition. Cambridge University Press.

Vacherat, A., Mouthereau, F., Pik, R., Bernet, M., Gautheron, C., Masini, E., Le Pourhiet, L., Tibari, B., Lahfid, A. 2014: Thermal imprint of rift-related processes in orogens as recorded in the Pyrenees. Earth Planet. Sci. Lett., 408, 296–306.

Vacherat, A., Mouthereau, F., Pik, R., Bellahsen, N., Gautheron, C., Bernet, M., Daudet, M., Balansa, J., Tibari, B., Jamme, R.P., Radal, J. 2016: Rift-to-collision transition recorded by tectonothermal evolution of the northern Pyrenees. Tectonics, 35, 907–933.

Vacherat A, Mouthereau F, Pik R et al 2017 Rift-to-collision sediment routing in the Pyrenees: A synthesis from sedimentological, geochronological and kinematic constraints. Earth Sci Rev 172:43-72.

van Achterbergh, E., Ryan, C.G., Jackson, S.E., & Griffin, W.L., 2001. Data reduction software for LA-ICP-MS. In Laser ablation-ICPMS in the earth science. P. Sylvester ed. Mineralogical Association of Canada, 29, 239-243

Van Den Driessche J, Brun JP. 1992. Tectonic evolution of the Montagne Noire (French Massif Central): A model of extensional gneiss dome. Geodin Acta 5: 85–97.

Van der Molen, I., and M. S. Paterson, Experimental defor- mation of partially-melted granite, Contrib. Mineral. Petrol., 70, 299-318, 1979.

Van Hinsbergen DJ, Torsvik TH, Schmid SM, Maţenco LC, Maffione M, Vissers RL, Gürer D, Spakman W 2019 Orogenic architec-ture of the Mediterranean region and kinematic reconstruction of its tectonic evolution since the Triassic. Gondwana Res 81, 79-229

van Keken, P.E., Hacker, B.R., Syracuse, E.M., Abers, G. 2011. Subduction factory: 4. Depth-dependent flux of H2O from subducting slabs worldwide. Journal of Geophysical Research 116, B01401.

Van Lichtervelde, M., Grand'Homme, A., Saint Blanquat, M., Olivier, P., Gerdes, A., Paquette, J.-L., Melgarejo, J.C., Druguet, E., Alfonso, P., 2017. U-Pb geochronology on zircon and columbite-group minerals of the Cap de Creus pegmatites, NE Spain. Mineral. Petrol. 111, 1–21.

Vanardois J, Trap P, Goncalves P et al 2020 Kinematics, deformation partitioning and late Variscan magmatism in the Agly massif, Eastern Pyrenees, France. Bull Soc Geol Fr 191. doi.org/10.1051/bsgf/2020009

Vanardois J, Roger F, Trap P et al. in review. Exhumation of deep continental crust in a transpressive regime: the example of Variscan eclogites from Aiguilles-Rouges Massif (Western Alps). J. Metamorph. Geol

Vanardois J, Trap P, Roger F, Goncalves P, Marquer D, Paquette J-L, Siron G, Baudin T. Gravity-driven channel flow in the Variscan foreland revealed by U-Th-Pb dating of metamorphism, magmatism and deformation (Agly Massif, eastern Pyrenees). In prep.

Vanardois J, trap P, Goncalves P, Roger F, Marquer D, Paquette J-L, Lanari P, Melleton J. Subduction vs crustal thickening? Insights on early-Variscan tectonics from metapelites of the Aiguilles-Rouges massif (External Crystalline Massifs, Western Alps). In prep.

Vanardois J, Trap P, Roger F, Melleton J, Marquer D, Paquette J-L, Goncalves P, Cagnard F, Le Bayon B. Interplay between deformation, water-fluxed crustal melting and granite growth in a crustal-scale shear zone. The case of the East-Variscan Shear Zone in the Aiguilles-Rouges and Mont-Blanc massifs (French External Crystalline Massifs). In prep.

Vanardois J, Lahfid A, Trap P, Lacroix B, Roger F, Guillou-Frottier L, Marquer D, Paquette J-L, Melleton J. Pre-collision high thermal gradient recorded in a Variscan orogenic basin (Servoz basin, Western Alps). In prep.

Vanardois J, Trap P, Marquer D. Birth and growth of continental shear zones. The critical role of metagranite undergoing H2O-present partial melting. In prep.

Vanderhaeghe, O. 2009. Migmatites, granites and orogeny: flow modes of partially-molten rocks and magmas associated with melt/solid segregation in orogenic belts. Tectonophysics, 477, 119–134.

Vanderhaeghe O, Teyssier C. 2001. Partial melting and flow of orogens. Tectonophysics 342: 451–472.

Vanderhaeghe O, Burg JP, Teyssier C. 1999. Exhumation of migmatites in two collapsed orogens: Canadian Cordillera and French Variscides. Geological Society Special Publication 154: 181–204.

Vanderhaeghe, O., Laurent, O., Gardien, V., Moyen, J.F., Gébelin, A., Chelle-Michou, C., … Bellanger, M. 2020. Flow of partially molten crust controlling construction, growth and collapse of the Variscan orogenic belt: the geologic record of the French Massif Central. Bulletin de la Société géologique de France, 191, doi.org/10.1051/bsgf/2020013.

Vauchez, A., & Tommasi, A. 2003. Wrench faults down to the asthenosphere: Geological and geophysical evidence and thermomechanical effects. Geological Society, London, Special Publications, 210(1), 15-34.

Vauchez A, Clerc C, Bestani L, Lagabrielle Y, Chauvet A, Lahfid A, et al. 2013a. Preorogenic exhumation of the North Pyrenean Agly massif (Eastern Pyrenees, France). Tectonics 32: 95–106.

Vauchez, A., Chauvet, A., Lagabrielle, Y., Mainprice, D., Bestani, L., Clerc, C., & Lahfid, A. 2013b. Reply to comment by P. Olivier on“Preorogenic exhumation of the North Pyrenean Agly Massif (Eastern Pyrenees, France)”.Tectonics,32, 823–826. https://doi.org/10.1002/tect.20061

Vermeesch, P. 2012. On the visualisation of detrital age distributions. Chemical Geology, 312-313, 190-194.

Vernon RH. 1991. Interpretation of microstructures of microgranitoid enclaves. In: Didier J, Barbarin B, eds. Enclaves and granite petrology. Developments in petrology 13. Amsterdam: Elsevier, pp. 277–291.

Vernon RH. 2000. Review of microstructural evidence of magmatic and solid-state flow. Electron Geosci 5: 1–23.

Vielzeuf D. 1980. Orthopyroxene and cordierite secondary assemblages in the granulitic paragneisses from Lherz and Saleix (French Pyrenees). Bull Mineral 103: 66–78.

Vielzeuf D. 1984. Relations de phases dans le faciès granulite et implications géodynamiques. L’exemple des granulites des Pyrénées. State thesis, Clermont-Ferrand (France), Univ. Blaise Pascal.

Vielzeuf D, Pin C 1991 Granulites orthodérivées d’âge tardi-hercynien; exemple de la norite de Treilles, Corbières (Aude, France). Bull la société géologique Fr 162:1057–1066

Vielzeuf, D., Clemens, J. D., Pin, C., & Moinet, E. 1990. Granites, granulites, and crustal differentiation. In Granulites and crustal evolution (59-85). Springer, Dordrecht.

Vielzeuf D, Paquette JL, Clemens JD, Stevens G, Gannoun A, Suchorski K, Saúl A 2021 Age, duration and mineral markers of magma interactions in the deep crust: an example from the Pyrenees. Contrib Mineral Petrol. doi.org/10.1007/s00410-021-01789-2

Vilà M, Pin C, Liesa M, Enrique P. 2007. LPHT metamorphism in a late orogenic transpressional setting, Albera Massif, NE Iberia: Implications for the geodynamic evolution of the Variscan Pyrenees. J metamorph Geol 25: 321–347.

Villaros, A., Laurent, O., Couzinié, S., Moyen, J.F., Mintrone, M., 2018. Plutons and domes: the consequences of anatectic magma extraction—example from the southeastern French Massif Central. Int. J. Earth Sci. 107, 2819–2842.

Vissers R. 1992. Variscan extension in the Pyrenees. Tectonics 11: 1369–1384.

Vitel, G. 1965. Etude pétrographique du tunnel du Mont-Blanc (partie française) et recherches géologiques complémentaires dans le massif Mont-Blanc - Aiguilles-Rouges. PhD Thesis, University of Grenoble, France.

Vivier, G., Ménot, R.-P., Giraud, P., 1987. Magmatismes et structuration orogenique paleozoiques de la chaine de Belledonne (massifs cristallins externes alpins) le domaine nord-oriental. Geol. Alps 63, 25–53.

von Raumer J.F. 1984. The external massifs, relics of Variscan basement in the Alps. Geol. Rundsch. 73:1–31.

von Raumer JF, Schwander HW. 1985. Garnet evolution in pre-Variscan pelitic rocks from the Lake Emosson area, Aiguilles Rouges Massif, Western Alps. J. Metamorph. Geol. 3:467–479.

von Raumer, J.F., & Bussy, F. 2004. Mont-Blanc and Aiguilles-Rouges: Geology of their polymetamorphic basement (External massifs, France-Switzerland): Mémoires de Géologie (Lausanne), 42, 1–203.

von Raumer, J., Stampfli, G.M., 2008. The birth of the Rheic Ocean–Early Paleozoicsubsidence patterns and tectonic plate scenarios. Tectonophysics 461, 9–20.

von Raumer, J.F., Galetti, G., Oberhansli, R., & Pfeifer, H.R. 1990. Amphibolites from Lac Emosson/Aiguilles Rouges, Switzerland: tholeiitic basalts at a transition zone between continental and oceanic crust. Schweizerische Mineralogische und Petrographische Mitteilungen, 703, 419–435.

Von Raumer, J., Bussy, F. & Sharp, Z. D. 1996. Lac Cornu revisited: the evolution from lower to upper crust (Aiguilles Rouges Massif, Western Alps). Schweizerische Mineralogische und Petrographische Mitteilungen 76, 120-1.

Von Raumer, J. F. 1998. The Palaeozoic evolution in the Alps: from Gondwana to Pangea. Geologische Rundschau 87, 407-35

Von Raumer, J.F., Stampfli, G.M., Borel, G. and Bussy, F. 2002: Organization of pre-Variscan basement areas at the north-Gondwanan margin. Int. J. Earth Sci. 91, 35–52.

Von Raumer, J.F., Bussy, F., Stampfli, G.M., 2009. The Variscan evolution in the external massifs of the Alps and place in their Variscan framework. Comptes Rendus Geosci., Mécanique de l'orogénie varisque: Une vision moderne de le recherche dans le domaine de l'orogénie Mechanics of Variscan Orogeny: A modern view on orogenic research 341, 239–252. http://dx.doi.org/10.1016/j.crte.2008.11.007.

Von Raumer, J.F., Bussy, F., Scaltegger, U., Schulz, B., Stampfli, G.M., 2013. Pre-Mesozoic Alpine basements? Their place in the European Paleozoic framework. GSA Bull. 125, 89–108.

von Raumer, J. F., Stampfli, G. M., Arenas, R., & Sánchez Martínez, S. 2015. Ediacaran to Cambrian oceanic rocks of the Gondwana margin and their tectonic interpretation. International Journal of Earth Sciences, 104, 1107-1121. https://doi.org/10.1007/s00531-015-1142-x

Vosteen, H.-D., Schellschmidt, R. 2003, Influence of temperature onthermal conductivity, thermal capacity and thermal diffusivity for differ-ent types of rock, Phys. Chem. Earth,28, 499–509.

Waters, D. 2003. P-T path from Cpx-Hbl-Pl symplectites, updated 22 February 2003: http://www.earth.ox.ac.uk/~davewa/research/eclogites/symplectites.html (July 2012).

Waters, D.J., Whales, C.J., 1984. Dehydration melting and the granulite transition in metapelites from southern Namaqualand, S. Africa. Contributions to Mineralogy and Petrology 88, 269–275.

Watson, E.B., 1996. Dissolution, growth and survival of zircons during crustal fusion: kinetic principals, geological models and implications for isotopic inheritance. Trans. R. Soc. Edinburgh 87, 43–56.

Watson, E.B., Harrison, T.M., 1983. Zircon saturation revisited: temperature and composition effects in a variety of crustal magma types. Earth Planet. Sci. Lett. 64, 295–304.

Wen H, Lu JH, Xiao Y 2015 Temperature dependence of thermal con-ductivity, diffusion and specific heat capacity for coal and rocks from coalfield. Thermochim Acta 619:41–47

Wiedenbeck, M., Allé, P., Corfu, F., Griffin, W.L., Meier, M., Oberli, F., von Quadt, A., Roddick, J.C. and Spiegel, W., 1995 Three natural zircon standards for U-Th-Pb, Lu-Hf, trace element and REE analyses. Geostand. Newsl. 19/1, 1-23.

Weinberg, R. F., & Hasalová, P. 2015. Water-fluxed melting of the continental crust: A review. Lithos, 212, 158-188.

White, R.W., Powell, R., Holland, T.J.B. & Worley, B.A. 2000. The effect of TiO2 and Fe2O3 on metapelitic assemblages at greenschist and amphibolite facies conditions: mineral equilibria calculations in the system K2O-FeO-MgO-Al2O3-SiO2-H2O-TiO2-Fe2O3. Journal of Metamorphic Geology, 18, 497–511.

White, R. W., Powell, R. & Clarke, G. L., 2002. The inter-pretation of reaction textures in Fe-rich metapelitic granulitesof the Musgrave Block, central Australia: Constraints frommineral equilibria calculations in the system K2O–FeO–MgO–Al2O3–SiO2–H2O–TiO2–Fe2O3. Journal of Metamorphic Geology, 20, 41–55.

White, R.W., Powell, R., Clarke, G.L., 2003. Prograde metamorphic assemblage evolution during partial melting of metasedimentary rocks at low pressures: migmatites from Mt. Stafford, Central Australia. Journal of Petrology 44, 1937–1960

White, R. W., Pomroy, N. E., & Powell, R. 2005. An in situ metatexite–diatexite transition in upper amphibolite facies rocks from Broken Hill, Australia. Journal of Metamorphic Geology, 23(7), 579-602.

White, R.W., Powell, R., Holland, T.J.B., Johnson, T.E. & Green, E.C.R. 2014. New mineral activity–composition rela-tions for thermodynamic calculations in metapelitic systems. Journal of Metamorphic Geology, 32, 261–286.

Whitney DL, Teyssier C, Rey P, Buck WR. 2013. Continental and oceanic core complexes. Bulletin 125: 273–298.

Whitney DL, Roger F, Teyssier C, Rey PF, Respaut JP. 2015. Syncollapse eclogite metamorphism and exhumation of deep crust in a migmatite dome: The P–T–t record of the youngest Variscan eclogite (Montagne Noire, French Massif Central). Earth Planet Sci Lett 430: 224–234

Whitney, D. L., Hamelin, C., Teyssier, C., Raia, N. H., Korchinski, M. S., Seaton, N. C. A., ... & Rey, P. F. 2020. Deep crustal source of gneiss dome revealed by eclogite in migmatite (Montagne Noire, French Massif Central). Journal of Metamorphic Geology, 38, 297–327.

Whittington, A., Hofmeister, A., Nabelek, P. 2009. Temperature-dependent thermal diffusivity of the Earth's crust and implications for magmatism. Nature, 458(7236):319–321.

Wickham, S. M., & Oxburgh, E. R. 1985. Continental rifts as a setting for regional metamorphism. Nature, 318(6044), 330–333.

Wickham, S. M. & Oxburgh, E. R., 1986. A rifted tectonic setting for Hercynian high thermal gradient in the Pyrentes. Tectonophysics, 129, 53-69.

Wickham, S. M., Oxburgh, E. R., Reading, H. G., & Vissers, R. L. M. 1987. Low-pressure regional metamorphism in the pyrenees and its implications for the thermal evolution of rifted continental crust [and discussion]. Philosophical Transactions of the Royal Society A: Mathematical, Physical and Engineering Sciences, 321(1557), 219–242.

Wiedenbeck, M., Allé, P., Corfu, F., Griffin, W.L., Meier, M., Oberli, F., … Spiegel, W. 1995 Three natural zircon standards for U-Th-Pb, Lu-Hf, trace element and REE analyses. Geostandards Newsletter, 19(1), 1-23.

Wopenka, B. & Pasteris, J. D., 1993. Structural characterization of kerogens to granulite-facies graphite: Applicability of Raman microprobe spectroscopy. American Mineralogist,78,533–557

Xu ZQ, Wang Q, Cai ZH et al 2015 Kinematics of the Tengchong Terrane in SE Tibet from the late Eocene to early Miocene: insights from coeval mid-crustal detachments and strike-slip shear zones. Tectonophysics 665:127-148. doi.org/10.1016/j.tecto.2015.09.033.

Yakymchuk, C., Brown, M., 2014. Behaviour of zircon and monazite during crustal melting. J. Geol. Soc. Lond. 171, 465–479.

Yakymchuk, C., Siddoway, C.S., Fanning, C.M., McFadden, R., Korhonen, F., and Brown, M., 2013, Anatectic reworking and differentiation of continental crust along the active margin of Gondwana: A zircon Hf-O perspective from West Antarctica, in Harley, S.L., Fitzsimons, I.C.W., and Zhao, Y., eds, Antarctica and Supercontinent Evolution: Geological Society of London Special Publication 383, doi:10.1144/SP383.7.

Yin A, Taylor MH 2011 Mechanics of V-shaped conjugate strike-slip faults and the corresponding continuum mode of continental deformation. Geol Soc Am Bull 123:1798–1821. doi.org/10.1130/B30159.1.

Yui, T.F., Huang, E., Xu, J. 1996: Raman spectrum of carbonaceous material: a possible metamorphic grade indicator for low-grade metamorphic rocks. J. Metamorphic Geol., 14, 115–124.

Žák J., Kratinová, Z., Trubač, J., Janoušek, V., Sláma, J. & Mrlina, J. 2011a. Structure, emplacement, and tectonic setting of Late Devonian granitoid plutons in the Teplá-Barrandian Unit, Bohemian Massif. International Journal of Earth Sciences, 100, 1477–1495.

Zeh, A., Gerdes, A., 2010. Baltica and Gondwana derived sediments in the Mid-GermanCrystalline Rise (Central Europe): implications for the closure of the Rheic Ocean.Gondwana Research 17 (2-3), 254–263.

Zhang, G.B., Ellis, D., Christy, A., Zhang, L.F., & Song, S.G. 2010. Zr-in-rutile thermometry in HP/UHP eclogites from Western China. Contributions to Mineralogy and Petrology, 160, 427–439.

Zheng, J.S., Mermet, J.F., Toutin-Morin, N., Hanes, J., Gondolo, A., Morin, R., Feraud, G., 1991. Datation 40Ar/39Ar du magmatisme et de filons mineralises permiens en Provence orientale France. Geodin. Acta 5, 203–215.

Zingg, A. 1990. The Ivrea crustal cross-section (Northern Italy and Southern Switzerland). In M. H. Salisbury & D. M. Fountain (Eds.), Exposed cross-sections of the continental crust, NATO ASI Series C (Vol. 317, pp. 1–19). Dordrecht, Netherlands: Kluwer Academic.

Zoth, G. and Haenel, R. 1988. Thermal conductivity. In Haneal, R., Rybach, L., Stegena, L., eds.: Handbook of Terrestrial Heat-Flow Density Determination, p. 449–468. Springer.

Zurbriggen, R., Franz, L. and Handy, M.R. 1997: Pre-Variscan deformation, metamorphism and magmatism in the Strona-Ceneri Zone (southern Alps of northern Italy and southern Switzerland). Schweiz. Mineral. Petrogr. Mitt. 77, 361–380

Zurbriggen, R. 2015. Ordovician orogeny in the Alps: A reappraisal. International Journal of Earth Sciences, 104, 335–350.

ANNEXES

ANNEXE 1: supplementary materials of Chapter 3

Table S1: Operating conditions and instrument settings for U-Pb analyses

Laboratory & Sample Preparation		
Laboratory name	Laboratoire Magmas & Volcans, Clermont-Ferrand, France	
Sample type/mineral	Zircon and Monazite	
Sample preparation	Conventional mineral separation, 1 inch resin mount, 0.25µm polish to finish and thin section (Université Montpellier)	
Imaging	CL, FEI QUANTA 450w, 15 kV, 19mm working distance (Université Bourgogne-Franche Comté)	
Laser ablation system		
Make, Model & type	Resonetics/M-50E 193nm, Excimer	
Ablation cell & volume	Laurin Cell ® two volumes cell, Laurin Technic Ltd., volume ca. 1-2 cm^3	
Laser wavelength	193 nm	
Pulse width	< 4 ns	
Fluence	*Zircon :* 4 $J.cm^{-2}$; 3.5 $J.cm^{-2}$	*Monazite :* 9 $J.cm^{-2}$; 5 $J.cm^{-2}$
Repetition rate	3 Hz	1 Hz
Spot size	27 µm or 33µm	12 µm
Sampling mode / pattern	Single spot	
Carrier gas	100% He, Ar make-up gas and N_2 combined using the Squid® device from RESOlution Instruments.	
Background collection	30 secs	
Ablation duration	60 secs	
Wash-out delay	30 secs	
Cell carrier gas flow	0.75 l/min	
ICP-MS Instrument		
Make, Model & type	Agilent 7500cs, Q-ICP-MS	
Sample introduction	Via conventional tubing	
RF power	1350W	
Make-up gas flow	0.87 l/min Ar	
Detection system	Single collector secondary electron multiplier	
Masses measured	204, 206, 207, 208, 232, 238	
Integration time per peak	10 ms	
Total integration time per reading	130 ms *(should represent the time resolution of the data)*	
Sensitvity / Efficiency	20000 cps/ppm ^{238}U (44µm, 10Hz)	
Dead time	35 ns	
Data Processing		
Gas blank	30 second on-peak	
Calibration strategy	*Zircon :* GJ-1 used as primary reference material, 91500 used as secondary reference material (Quality Control)	*Monazite*: Trebilcock used as primary reference material, Itambé and Bananeira used as secondary reference materials (Quality Control)
Reference Material info	*Zircon:* 91500 (Wiedenbeck et al., 1995) GJ1 (Jackson et al., 2004)	*Monazite*: Trebilcock (Tomascak, 1996) Itambé (Gonçalves et al., 2016) Bananeira (Gonçalves et al., 2016)

Data processing package used / Correction for LIEF	GLITTER ® (van Achterbergh et al., 2001)
Mass discrimination	Standard-sample bracketing with ^{207}Pb/^{206}Pb and ^{206}Pb/^{238}U normalized to reference material GJ-1 or Trebicock
Common-Pb correction, composition and uncertainty	No common-Pb correction. Analyses discarded when discordance >10%
Uncertainty level & propagation	Ages are quoted at 2sigma absolute, propagation is by quadratic addition according to Horstwood et al. (2003). Reproducibility and age uncertainty of reference material are propagated.
Quality control / Validation	Zircon : 91500: Concordia age = 1065.3 ± 4.5 (2SD; MSWD$_{(C+E)}$ = 0.29; N=36) Concordia age = 1064.1 ± 5.1 Ma (2SD, MSWD$_{(C+E)}$ = 0.18, N = 39) Monazite : Itambé: Concordia age = 509.3 ± 2.6 Ma (2SD; MSWD$_{(C+E)}$ = 0.86; N=24) Bananeira: Concordia age = 506.4 ± 2.6 Ma (2SD; MSWD$_{(C+E)}$ = 0.97; N=24) Concordia age = 506.8 ± 3.6 Ma (2SD, MSWD$_{(C+E)}$ = 1.3, N= 27)
Other information	For detailed method description see Tiepolo (2003), Paquette and Tiepolo (2007), Hurai et al. (2010) and Roger et al. (2012, 2015). For detailed laser technical description see Müller et al. (2009).

Table S2: Analytical results of LA-ICPMS U-Th-Pb dating on monazite. Mn: monazite; R: rim; C: centre. Errors quoted in absolute values.

		Concentration (ppm)				Raw ratios					Apparent age (Ma)	
#		Pb	Th	U	Th/U	^{208}Pb/^{232}Th	±2σ	^{206}Pb/^{238}U	±2σ	Rho	^{208}Pb/^{232}Th	±2σ
	Ag57											
1	Mn1-1-b	1634	18394	11425	1.6	0.01455	0.00051	0.04664	0.00165	0.1	292	10
2	Mn1-2-c	1901	67855	2104	32.2	0.01483	0.00051	0.04820	0.00171	0.1	298	10
3	Mn6-c	1811	62849	2380	26.4	0.01490	0.00051	0.04738	0.00168	0.1	299	10
4	Mn3	1731	52266	4590	11.4	0.01439	0.00048	0.04652	0.00165	0.1	289	10
5	Mn4-1-b	1831	58588	3118	18.8	0.01533	0.00051	0.04794	0.00168	0.1	307	10
6	Mn4-2-c	2116	72381	3057	23.7	0.01490	0.00051	0.04648	0.00162	0.1	299	10
7	Mn8-1-c	1356	23734	7292	3.3	0.01503	0.00051	0.04638	0.00162	0.1	302	10
8	Mn8-2-b	1772	60112	2091	28.7	0.01536	0.00054	0.04963	0.00174	0.1	308	10
9	Mn11-c	1874	60990	3514	17.4	0.01487	0.00051	0.04675	0.00162	0.1	298	10
10	Mn12-1-b	1966	68066	2077	32.8	0.01530	0.00051	0.05004	0.00174	0.1	307	10
11	Mn12-2-c	1426	39005	4338	9.0	0.01505	0.00051	0.04678	0.00162	0.1	302	10
12	Mn13-c	1673	57269	2341	24.5	0.01493	0.00051	0.04767	0.00168	0.1	300	10
13	Mn15	2011	65242	3391	19.2	0.01525	0.00051	0.04670	0.00162	0.1	306	10
14	Mn20	1614	42543	5773	7.4	0.01458	0.00051	0.04522	0.00156	0.1	293	10
15	Mn19	1992	65928	3113	21.2	0.01515	0.00051	0.04707	0.00162	0.1	304	10
16	Mn26	1404	28592	6477	4.4	0.01534	0.00054	0.04671	0.00162	0.1	308	10
17	Mn38-1-c	1718	41615	6914	6.0	0.01473	0.00051	0.04535	0.00156	0.1	296	10
18	Mn38-2-b	1939	52619	6059	8.7	0.01500	0.00051	0.04642	0.00159	0.1	301	10
19	Mn36-1-c	2147	75616	3084	24.5	0.01457	0.00051	0.04587	0.00159	0.1	292	10

20	Mn36-2-b	1467	46054	3732	12.3	0.01433	0.00048	0.04428	0.00153	0.1	288	10
21	Mn41-c	1695	50896	3805	13.4	0.01526	0.00051	0.04725	0.00162	0.1	306	10
22	Mn40-1-b	1741	56953	2468	23.1	0.01552	0.00054	0.04905	0.00168	0.1	311	11
23	Mn40-2-c	1736	61887	1847	33.5	0.01491	0.00051	0.04864	0.00168	0.1	299	10
24	Mn39-1-c	2152	65347	4299	15.2	0.01555	0.00054	0.04772	0.00162	0.1	312	11
25	Mn39-2-b	2129	72619	3089	23.5	0.01494	0.00051	0.04683	0.00162	0.1	300	10
26	Mn42	1927	63450	3149	20.2	0.01515	0.00051	0.04642	0.00159	0.1	304	10
27	Mn43-1-b	1888	65102	2146	30.3	0.01526	0.00051	0.04917	0.00168	0.1	306	10
28	Mn43-2-c	1908	41315	8069	5.1	0.01523	0.00051	0.04696	0.00159	0.1	306	10
	Ag3B											
1	Mn8-1	1869	47499	6303	7.5	0.01547	0.00054	0.04694	0.00162	0.1	310	11
2	Mn8-2	1927	55157	6111	9.0	0.01438	0.00051	0.04559	0.00159	0.1	289	10
3	Mn11-1	2627	79851	7793	10.2	0.01417	0.00048	0.04385	0.00153	0.1	284	10
4	Mn11-2	2723	80990	7212	11.2	0.01481	0.00051	0.04627	0.00162	0.1	297	10
5	Mn4	2134	58376	6828	8.5	0.01483	0.00051	0.04615	0.00159	0.1	298	10
6	Mn10-1	2182	63600	5900	10.8	0.01488	0.00051	0.04690	0.00162	0.1	299	10
7	Mn10-2	1975	55849	6062	9.2	0.01464	0.00051	0.04599	0.00159	0.1	294	10
8	Mn3	1511	44280	3879	11.4	0.01502	0.00051	0.04734	0.00165	0.1	301	10
9	Mn41-1	1321	45617	1925	23.7	0.01473	0.00051	0.04668	0.00162	0.1	296	10
10	Mn41-2	1313	44741	2283	19.6	0.01438	0.00048	0.04710	0.00162	0.1	289	10
11	Mn31	2426	65739	7593	8.7	0.01482	0.00051	0.04669	0.00162	0.1	297	10
12	Mn32	2095	42058	10068	4.2	0.01485	0.00051	0.04628	0.00159	0.1	298	10
13	Mn34	2248	47365	9917	4.8	0.01487	0.00051	0.04772	0.00165	0.1	298	10
14	Mn35	2172	47824	10876	4.4	0.01389	0.00048	0.04312	0.00147	0.1	279	10
15	Mn36	2448	70021	7505	9.3	0.01430	0.00048	0.04559	0.00156	0.1	287	10
16	Mn39-1	1511	47173	3189	14.8	0.01498	0.00051	0.04554	0.00156	0.1	301	10
17	Mn39-2	1901	59572	5789	10.3	0.01362	0.00048	0.04296	0.00147	0.1	273	9
18	Mn28	2292	64724	7131	9.1	0.01461	0.00051	0.04539	0.00156	0.1	293	10
19	Mn5	1746	35693	9023	4.0	0.01413	0.00048	0.04504	0.00153	0.1	284	10
20	Mn37	2104	60390	6316	9.6	0.01454	0.00051	0.04558	0.00156	0.1	292	10
21	Mn9-1	2235	66244	6299	10.5	0.01446	0.00048	0.04548	0.00156	0.1	290	10
22	Mn9-2	2381	48272	12112	4.0	0.01443	0.00048	0.04511	0.00153	0.1	290	10
23	Mn38-1	2644	56696	12881	4.4	0.01443	0.00048	0.04448	0.00150	0.1	290	10
24	Mn38-2	3672	118463	8230	14.4	0.01432	0.00048	0.04580	0.00156	0.1	287	10
25	Mn27	1408	44398	3706	12.0	0.01416	0.00048	0.04262	0.00144	0.1	284	10
26	Mn2	1084	37360	1587	23.5	0.01464	0.00051	0.04725	0.00162	0.1	294	10
27	Mn10-1	1409	49187	1643	29.9	0.01490	0.00051	0.04921	0.00168	0.1	299	10
28	Mn24	1318	37393	4107	9.1	0.01458	0.00051	0.04337	0.00147	0.1	293	10
29	Mn26	1345	43439	3243	13.4	0.01400	0.00048	0.04402	0.00150	0.1	281	10
30	Mn23	2512	49196	13009	3.8	0.01442	0.00048	0.04449	0.00150	0.1	289	10
21	Mn47-1	2157	44865	10412	4.3	0.01463	0.00051	0.04428	0.00150	0.1	294	10
32	Mn47-2	2308	64611	7206	9.0	0.01446	0.00048	0.04503	0.00153	0.1	290	10
33	Mn17	2427	62242	8738	7.1	0.01461	0.00051	0.04505	0.00150	0.1	293	10

34	Mn16	3782	117865	8231	14.3	0.01477	0.00051	0.04583	0.00153	0.1	296	10
35	Mn18	2879	61674	13134	4.7	0.01463	0.00051	0.04528	0.00153	0.1	294	10
36	Mn19	2782	76205	8801	8.7	0.01477	0.00051	0.04576	0.00153	0.1	296	10
37	Mn7	1892	49933	6213	8.0	0.01506	0.00051	0.04562	0.00153	0.1	302	10
	Ag03											
1	Mn1	9940	202543	49007	4.13	0.01444	0.00048	0.04509	0.00141	0.1	290	9
2	Mn2-1	8067	86035	58120	1.48	0.01451	0.00048	0.04477	0.00141	0.1	291	10
3	Mn2-2	6607	89027	45256	1.97	0.01402	0.00045	0.04361	0.00138	0.1	282	9
4	Mn3	8519	109045	62300	1.75	0.01376	0.00045	0.04216	0.00132	0.1	276	9
5	Mn4-1	8217	69843	62775	1.11	0.01443	0.00048	0.04550	0.00144	0.1	290	10
6	Mn4-2	9366	84559	68207	1.24	0.01475	0.00048	0.04673	0.00147	0.1	296	10
7	Mn5	5443	83506	34697	2.41	0.01408	0.00048	0.04382	0.00138	0.1	283	9
8	Mn6	9662	74912	72337	1.04	0.01475	0.00048	0.04733	0.00150	0.1	296	10
9	Mn7	10332	164996	61773	2.67	0.01490	0.00048	0.04562	0.00144	0.1	299	10
10	Mn8	10120	82592	77302	1.07	0.01450	0.00048	0.04714	0.00150	0.1	291	10
11	Mn9-1	9624	87124	70850	1.23	0.01467	0.00048	0.04753	0.00150	0.1	294	10
12	Mn9-2	7658	70595	57840	1.22	0.01453	0.00048	0.04618	0.00147	0.1	292	10
13	Mn10	8819	269584	29933	9.01	0.01352	0.00045	0.04317	0.00138	0.1	272	9
14	Mn11	8558	85375	64950	1.31	0.01417	0.00048	0.04531	0.00144	0.1	284	9
15	Mn12	8526	54501	70646	0.77	0.01440	0.00048	0.04580	0.00144	0.1	289	10
16	Mn14	9592	46617	80764	0.58	0.01454	0.00048	0.04700	0.00150	0.1	292	10
17	Mn15	11201	58527	91157	0.64	0.01427	0.00048	0.04694	0.00150	0.1	286	9
18	Mn16	9101	69817	72118	0.97	0.01415	0.00048	0.04503	0.00144	0.1	284	9
19	Mn17	13712	102282	105937	0.97	0.01426	0.00048	0.04648	0.00147	0.1	286	9
20	Mn18	7510	80228	54493	1.47	0.01427	0.00048	0.04483	0.00141	0.1	286	9
21	Mn19	11614	57791	91566	0.63	0.01477	0.00048	0.04863	0.00156	0.1	296	10
22	Mn20	8790	93991	62547	1.50	0.01413	0.00048	0.04589	0.00147	0.1	284	9
23	Mn28	6394	113493	37163	3.05	0.01404	0.00048	0.04399	0.00141	0.1	282	9
24	Mn27	12014	60893	96254	0.63	0.01466	0.00048	0.04781	0.00153	0.1	294	10
25	Mn25	9531	75686	72705	1.04	0.01434	0.00048	0.04644	0.00147	0.1	288	10
26	Mn24	9180	91363	66825	1.37	0.01430	0.00048	0.04581	0.00147	0.1	287	10
	Ag38											
1	Mn1-1	8310	54752	69757	0.78	0.01432	0.00048	0.04616	0.00153	0.1	287	10
2	Mn1-2	11167	53262	96955	0.55	0.01459	0.00048	0.04676	0.00156	0.1	293	10
3	Mn2-1	10431	58163	89995	0.65	0.01417	0.00048	0.04620	0.00153	0.1	284	9
4	Mn2-2	10945	59284	93597	0.63	0.01446	0.00048	0.04663	0.00153	0.1	290	10
5	Mn3-1	9850	64677	81187	0.80	0.01427	0.00048	0.04676	0.00153	0.1	287	10
6	Mn3-2	11080	54410	95397	0.57	0.01449	0.00048	0.04669	0.00153	0.1	291	10
7	Mn4-1	10295	54001	89040	0.61	0.01426	0.00048	0.04612	0.00150	0.1	286	10
8	Mn4-2	11558	48152	101992	0.47	0.01446	0.00048	0.04640	0.00153	0.1	290	10
9	Mn5-1	10010	56346	85123	0.66	0.01430	0.00048	0.04660	0.00153	0.1	287	10
10	Mn5-2	9485	42259	83650	0.51	0.01428	0.00048	0.04626	0.00150	0.1	287	10
11	Mn6	9224	53584	77927	0.69	0.01450	0.00048	0.04642	0.00153	0.1	291	10

12	Mn7	9407	43858	97429	0.45	0.01283	0.00042	0.03954	0.00129	0.1	258	9
13	Mn8-1	4640	50320	37633	1.34	0.01412	0.00048	0.04192	0.00135	0.1	283	9
14	Mn8-2	5638	70496	41898	1.68	0.01387	0.00045	0.04373	0.00141	0.1	278	9
15	Mn9-1	9381	64851	75173	0.86	0.01457	0.00048	0.04713	0.00153	0.1	292	10
16	Mn9-2	9709	66555	78325	0.85	0.01466	0.00048	0.04675	0.00150	0.1	294	10
17	Mn10	8402	70688	59967	1.18	0.01516	0.00051	0.04804	0.00156	0.1	304	10
18	Mn11	10425	74445	79384	0.94	0.01447	0.00048	0.04726	0.00153	0.1	290	10
19	Mn12	8369	58845	76374	0.77	0.01341	0.00045	0.03994	0.00129	0.1	269	9
20	Mn13	9056	51979	75892	0.68	0.01392	0.00045	0.04486	0.00144	0.1	279	9
21	Mn14	3773	65364	22009	2.97	0.01401	0.00048	0.04428	0.00144	0.1	281	9
22	Mn15-1	7389	79612	50750	1.57	0.01459	0.00048	0.04643	0.00150	0.1	293	10
23	Mn15-2	9231	92063	64037	1.44	0.01472	0.00048	0.04699	0.00150	0.1	295	10
24	Mn16-1	9138	50042	73454	0.68	0.01428	0.00048	0.04662	0.00150	0.1	287	9
25	Mn16-2	10350	47682	85118	0.56	0.01436	0.00048	0.04655	0.00150	0.1	288	10
26	Mn17	11109	57158	90521	0.63	0.01416	0.00048	0.04638	0.00147	0.1	284	9
	Ag08											
1	Mn2-1	2309	77703	3275	23.7	0.01519	0.00057	0.04644	0.00195	0.1	305	12
2	Mn2-2	1603	55544	2084	26.7	0.01493	0.00057	0.04670	0.00198	0.1	300	11
3	Mn3-1	5761	177320	13419	13.2	0.01480	0.00057	0.04627	0.00189	0.1	297	11
4	Mn3-2	5662	173562	12455	13.9	0.01514	0.00057	0.04609	0.00189	0.1	304	11
5	Mn4r	2869	81772	8417	9.7	0.01478	0.00057	0.04572	0.00189	0.1	297	11
6	Mn4c	2495	75533	5995	12.6	0.01491	0.00057	0.04612	0.00192	0.1	299	11
7	Mn7	6456	197350	15229	13.0	0.01519	0.00057	0.04618	0.00189	0.1	305	11
8	Mn12r	4169	107664	15262	7.1	0.01494	0.00057	0.04590	0.00189	0.1	300	11
9	Mn12c	4114	108507	13767	7.9	0.01534	0.00057	0.04594	0.00189	0.1	308	12
10	Mn17-1	4540	147320	8957	16.4	0.01502	0.00057	0.04611	0.00189	0.1	301	11
11	Mn8	5144	177680	7681	23.1	0.01497	0.00057	0.04599	0.00189	0.1	300	11
12	Mn15c	5847	190088	11158	17.0	0.01510	0.00057	0.04616	0.00189	0.1	303	11
13	Mn15b	6714	194567	22166	8.8	0.01460	0.00054	0.04211	0.00174	0.1	293	11
14	Mn14	5982	174258	15431	11.3	0.01523	0.00057	0.04608	0.00192	0.1	306	12
15	Mn13	1211	53778	949	56.6	0.01229	0.00048	0.04713	0.00207	0.1	247	9
	Ag06											
1	Mn7	1996	72421	669	108.3	0.01586	0.00060	0.04940	0.00219	0.1	318	12
2	Mn8	2275	85205	797	107.0	0.01553	0.00060	0.04770	0.00207	0.1	311	12
3	Mn10	1834	73334	626	117.2	0.01454	0.00054	0.04740	0.00210	0.1	292	11
4	Mn12	1841	69832	506	138.0	0.01544	0.00060	0.04777	0.00213	0.1	310	12
5	Mn13	2486	93697	726	129.0	0.01550	0.00060	0.04764	0.00207	0.1	311	12
6	Mn4	2093	78593	845	93.0	0.01538	0.00060	0.04660	0.00204	0.1	309	12
7	Mn5	2122	79204	720	110.0	0.01556	0.00060	0.04832	0.00210	0.1	312	12
8	Mn14r	3058	109787	2759	39.8	0.01522	0.00057	0.04650	0.00198	0.1	305	12
9	Mn14c	2802	105325	1077	97.8	0.01524	0.00057	0.04777	0.00213	0.1	306	12
10	Mn15	2129	77343	1268	61.0	0.01540	0.00060	0.04730	0.00201	0.1	309	12
11	Mn16r	2421	88584	1829	48.4	0.01502	0.00057	0.04719	0.00204	0.1	301	11

12	Mn16c	4029	140262	5351	26.2	0.01477	0.00057	0.04669	0.00195	0.1	296	11
13	Mn19r	1896	68097	607	112.1	0.01601	0.00060	0.04959	0.00231	0.1	321	12
14	Mn19c	1767	65331	620	105.4	0.01552	0.00060	0.04814	0.00222	0.1	311	12
15	Mn22r	2011	63319	4121	15.4	0.01491	0.00057	0.04634	0.00195	0.1	299	11
16	Mn22c	2393	89397	823	108.6	0.01537	0.00057	0.04726	0.00207	0.1	308	12
17	Mn24b	2336	57646	8494	6.8	0.01516	0.00057	0.04644	0.00192	0.1	304	11
18	Mn24c	2309	90878	878	103.5	0.01462	0.00057	0.04648	0.00216	0.1	293	11
19	Mn36r	2738	71304	9127	7.8	0.01500	0.00057	0.04687	0.00195	0.1	301	11
20	Mn36c	2440	90258	1645	54.9	0.01505	0.00057	0.04657	0.00198	0.1	302	11
21	Mn35	*1889*	*60674*	*3656*	*16.6*	0.01486	0.00057	0.04671	0.00195	0.1	298	11
22	Mn34	*1776*	*65420*	*687*	*95.2*	0.01556	0.00060	0.04820	0.00210	0.1	312	12
23	Mn25	2914	110692	1427	77.6	0.01493	0.00057	0.04675	0.00207	0.1	300	11
24	Mn23	1578	37498	6035	6.2	0.01518	0.00057	0.04651	0.00195	0.1	305	11
25	Mn33	2447	90296	1067	84.6	0.01541	0.00057	0.04798	0.00213	0.1	309	12
26	Mn31	2045	77228	622	124.1	0.01527	0.00057	0.04762	0.00213	0.1	306	12
	Ag48											
1	Mn5	2160	63234	5261	12.02	0.01526	0.00054	0.04744	0.00177	0.1	306	11
2	Mn4-1	2276	72548	4418	16.42	0.01502	0.00051	0.04714	0.00174	0.1	301	10
3	Mn4-2	2493	77406	5030	15.39	0.01522	0.00054	0.04756	0.00177	0.1	305	11
4	Mn3	2367	72632	4987	14.56	0.01521	0.00054	0.04750	0.00177	0.1	305	11
5	Mn2	2245	74471	3871	19.24	0.01487	0.00051	0.04636	0.00171	0.1	298	10
6	Mn10	2076	63954	4155	15.39	0.01536	0.00054	0.04716	0.00174	0.1	308	11
7	Mn7-1	2340	72302	5019	14.41	0.01502	0.00051	0.04701	0.00171	0.1	301	10
8	Mn7-2	2238	70043	4536	15.44	0.01511	0.00051	0.04649	0.00171	0.1	303	10
9	Mn6	2408	82801	3688	22.45	0.01540	0.00054	0.04737	0.00174	0.1	309	11
10	Mn14-1	3516	106600	8450	12.62	0.01535	0.00054	0.04726	0.00171	0.1	308	11
11	Mn14-2	2920	95923	5775	16.61	0.01518	0.00051	0.04647	0.00168	0.1	305	10
12	Mn13	3299	114273	5005	22.83	0.01529	0.00054	0.04751	0.00174	0.1	307	11
13	Mn13-2	2716	87638	5345	16.40	0.01534	0.00054	0.04763	0.00174	0.1	308	11
14	Mn12-1	2480	80684	5265	15.32	0.01500	0.00051	0.04610	0.00168	0.1	301	10
15	Mn12-2	2781	93153	5232	17.80	0.01504	0.00051	0.04660	0.00168	0.1	302	10
16	Mn19	2896	105700	3391	31.17	0.01521	0.00051	0.04680	0.00168	0.1	305	10
17	Mn20	2289	71053	4765	14.91	0.01526	0.00054	0.04659	0.00168	0.1	306	11
18	Mn22	2568	78974	5780	13.66	0.01513	0.00051	0.04585	0.00165	0.1	303	10
19	Mn24-1	2553	73564	6676	11.02	0.01531	0.00054	0.04650	0.00168	0.1	307	11
20	Mn24-2	5805	195033	7731	25.23	0.01537	0.00054	0.04756	0.00171	0.1	308	11
21	Mn24-3	2493	68040	7409	9.18	0.01530	0.00054	0.04663	0.00165	0.1	307	11
22	Mn34-1	3400	98949	8618	11.48	0.01525	0.00054	0.04664	0.00165	0.1	306	10
23	Mn34-2	2820	87899	5270	16.68	0.01553	0.00054	0.04656	0.00165	0.1	312	11
24	Mn36-1	2751	83978	6002	13.99	0.01525	0.00054	0.04634	0.00165	0.1	306	10
25	Mn36-2	2311	74460	4104	18.14	0.01521	0.00051	0.04635	0.00165	0.1	305	10
26	Mn54-1	2344	72511	5208	13.92	0.01495	0.00051	0.04643	0.00165	0.1	300	10
27	Mn54-2	2408	74433	5053	14.73	0.01509	0.00051	0.04624	0.00165	0.1	303	10

28	Mn53	2248	73594	3698	19.90	0.01510	0.00051	0.04622	0.00162	0.1	303	10
	Ag51											
1	Mn1-1	3892	101503	13553	7.5	0.01464	0.00048	0.04605	0.00147	0.1	294	10
2	Mn1-2	3158	96481	7998	12.1	0.01440	0.00048	0.04663	0.00150	0.1	289	10
3	Mn2	3123	81897	10781	7.6	0.01468	0.00048	0.04584	0.00147	0.1	295	10
4	Mn3	3021	98985	5958	16.6	0.01457	0.00048	0.04628	0.00147	0.1	292	10
5	Mn4	3603	93207	12708	7.3	0.01461	0.00048	0.04639	0.00147	0.1	293	10
6	Mn5-1	2611	75731	7305	10.4	0.01467	0.00048	0.04613	0.00147	0.1	294	10
7	Mn5-2	3698	107708	10809	10.0	0.01440	0.00048	0.04563	0.00147	0.1	289	10
8	Mn6	2933	87637	8104	10.8	0.01442	0.00048	0.04536	0.00144	0.1	289	10
9	Mn7	3847	92986	14794	6.3	0.01458	0.00048	0.04598	0.00147	0.1	293	10
10	Mn8	3188	91031	9644	9.4	0.01441	0.00048	0.04543	0.00147	0.1	289	10
11	Mn9	2990	97843	5985	16.3	0.01447	0.00048	0.04624	0.00150	0.1	290	10
12	Mn10	4672	147318	10726	13.7	0.01447	0.00048	0.04576	0.00147	0.1	290	10

Table S3: Analytical results of LA-ICPMS U-Pb dating on zircon. Zr: zircon; R: rim; C: centre

		Concentration (ppm)				Raw ratios					Apparent age		Concordia	
#		Pb	Th	U	Th/U	$^{207}Pb/^{235}U$	± 2σ	$^{206}Pb/^{238}U$	± 2σ	Rho	$^{206}Pb/^{238}U$	± 2σ	Age (Ma)	± 2σ
	Ag57													
1	Zr8b	11	35	134	0.26	0.6683	0.0390	0.08412	0.00312	0.64	521	19	520	18
2	Zr8c	8	22	68	0.33	0.9306	0.0477	0.10878	0.00396	0.71	666	23	666	22
3	Zr3b	29	61	334	0.18	0.7424	0.0329	0.08803	0.00315	0.81	544	19	/	
4	Zr3c	90	344	873	0.39	0.8416	0.0314	0.10081	0.00354	0.94	619	21	621	17
5	Zr11b	16	22	290	0.07	0.4646	0.0196	0.05906	0.00210	0.84	370	13	/	
6	Zr11c	11	40	95	0.43	0.9155	0.0493	0.10740	0.00390	0.67	658	23	658	22
7	Zr18b	21	42	256	0.16	0.6592	0.0303	0.08197	0.00291	0.77	508	17	510	17
8	Zr18c	21	55	228	0.24	0.7719	0.0312	0.09452	0.00330	0.86	582	19	581	18
9	Zr17b	31	19	434	0.04	0.6215	0.0259	0.07485	0.00261	0.84	465	16	/	
10	Zr17c	24	78	199	0.39	1.0108	0.0401	0.11651	0.00405	0.88	711	23	709	20
11	Zr20b	23	196	504	0.39	0.3810	0.0160	0.04885	0.00171	0.83	307	10	/	
12	Zr20c	47	135	505	0.27	0.7672	0.0288	0.09403	0.00324	0.92	579	19	/	
13	Zr23b	22	54	272	0.20	0.6588	0.0263	0.08091	0.00279	0.86	502	17	578	16
14	Zr23c	63	335	617	0.54	0.7784	0.0327	0.09510	0.00330	0.83	586	19	585	18
15	Zr31b	19	34	199	0.17	0.8302	0.0349	0.09674	0.00333	0.82	595	20	605	19
16	Zr31c	52	161	461	0.35	0.9133	0.0339	0.10793	0.00366	0.91	661	21	658	18
17	Zr32b	31	215	289	0.74	0.7273	0.0281	0.08962	0.00303	0.87	553	18	555	16
18	Zr32c	36	347	284	1.22	0.8110	0.0334	0.09675	0.00330	0.83	595	19	600	18
19	Zr33b	30	44	321	0.14	0.8053	0.0319	0.09708	0.00327	0.85	597	19	599	18
20	Zr33c	34	128	332	0.39	0.8204	0.0332	0.09882	0.00333	0.83	608	20	608	18
21	Zr41b	11	17	217	0.08	0.4130	0.0210	0.05354	0.00183	0.67	336	11	337	11
22	Zr41c	5	13	46	0.29	0.9704	0.0488	0.11273	0.00387	0.68	689	22	689	22
23	Zr52b	21	241	136	1.77	0.9076	0.0521	0.10767	0.00378	0.61	659	22	658	21

24	Zr52c	18	145	141	1.03	0.8731	0.0362	0.10396	0.00348	0.81	638	20	637	19
25	Zr51b	26	58	281	0.21	0.7629	0.0379	0.09302	0.00318	0.69	573	19	574	18
26	Zr51c	18	49	149	0.33	0.9977	0.0404	0.11423	0.00381	0.82	697	22	701	20
27	Zr56b	20	27	281	0.10	0.5920	0.0262	0.07616	0.00255	0.76	473	15	473	15
28	Zr56c	12	128	85	1.50	0.8937	0.0416	0.10472	0.00351	0.72	642	20	644	20
29	Zr50b	29	143	256	0.56	0.8795	0.0368	0.10323	0.00342	0.79	633	20	637	19
30	Zr50c	43	254	337	0.75	0.9705	0.0390	0.11227	0.00369	0.82	686	21	688	20
31	Zr57b	15	16	337	0.05	0.3567	0.0176	0.04860	0.00162	0.68	306	10	306	10
32	Zr58b	81	31	899	0.03	0.7975	0.0290	0.09546	0.00309	0.89	588	18	595	16
33	Zr59b	56	58	527	0.11	0.9578	0.0365	0.11052	0.00357	0.85	676	21	681	19
34	Zr49b	32	113	350	0.32	0.7318	0.0299	0.08835	0.00288	0.80	546	17	551	16
35	Zr53b	45	19	541	0.04	0.7418	0.0285	0.08978	0.00291	0.84	554	17	550	16
36	Zr43b	10	12	200	0.06	0.4131	0.0191	0.05414	0.00177	0.71	340	11	341	11
37	Zr42b	8	4	180	0.02	0.3819	0.0184	0.04943	0.00162	0.68	311	10	/	
38	Zr40b	214	42	2598	0.02	0.7355	0.0256	0.08949	0.00285	0.91	553	17	561	15
39	Zr44b	44	7	997	0.01	0.3512	0.0132	0.04846	0.00153	0.84	305	9	305	9
40	Zr39b	10	5	108	0.05	0.8635	0.0437	0.09395	0.00309	0.65	579	18	/	
41	Zr37b	38	77	329	0.23	0.9881	0.0384	0.11334	0.00360	0.82	692	21	696	19
42	Zr47b	16	26	209	0.12	0.6032	0.0272	0.07651	0.00246	0.71	475	15	476	14
43	Zr36b	18	54	207	0.26	0.6965	0.0308	0.08584	0.00276	0.73	531	16	533	16
44	Zr34b	6	3	121	0.02	0.4097	0.0242	0.05148	0.00171	0.56	324	10	/	
45	Zr27b	22	15	440	0.03	0.4038	0.0176	0.05395	0.00171	0.73	339	10	340	10
	Ag03													
1	Zr2b	249	119	1069	0.11	3.3265	0.1132	0.22894	0.00729	0.94	1329	38	/	
2	Zr2c	81	168	214	0.78	4.6273	0.1595	0.31047	0.00987	0.92	1743	49	1762	22
3	Zr4b	59	20	1008	0.02	0.5079	0.0181	0.06459	0.00204	0.89	404	12	/	
4	Zr4c	40	45	529	0.09	0.6401	0.0263	0.08070	0.00258	0.78	500	15	501	15
5	Zr14c	143	33	2760	0.01	0.4496	0.0154	0.05616	0.00174	0.91	352	11	/	
6	Zr16	124	6	2804	0.00	0.3529	0.0120	0.04816	0.00150	0.92	303	9	306	9
7	Zr7	122	4	2732	0.00	0.3559	0.0122	0.04851	0.00150	0.90	305	9	307	9
8	Zr9b	1002	40	22272	0.00	0.3465	0.0114	0.04877	0.00150	0.93	307	9	302	9
9	Zr9c	894	33	19784	0.00	0.3459	0.0114	0.04881	0.00150	0.93	307	9	/	
10	Zr11	877	32	20111	0.00	0.3450	0.0113	0.04888	0.00150	0.93	308	9	/	
11	Zr15	102	5	1993	0.00	0.4262	0.0144	0.05690	0.00174	0.90	357	11	359	10
12	Zr17	113	48	2532	0.02	0.3687	0.0128	0.04905	0.00150	0.88	309	9	/	
13	Zr25	174	10	3838	0.00	0.3814	0.0128	0.04975	0.00150	0.90	313	9	/	
14	Zr29	154	12	3525	0.00	0.3472	0.0119	0.04763	0.00141	0.87	300	9	301	9
15	Zr35	160	13	3568	0.00	0.3509	0.0117	0.04838	0.00144	0.89	305	9	305	9
16	Zr39	119	9	2722	0.00	0.3502	0.0118	0.04875	0.00144	0.88	307	9	306	9
17	Zr41	135	12	3091	0.00	0.3512	0.0122	0.04865	0.00144	0.86	306	9	306	9
18	Zr49	124	9	2849	0.00	0.3470	0.0116	0.04819	0.00141	0.87	303	9	303	8
19	Zr50	106	6	2425	0.00	0.3460	0.0124	0.04801	0.00138	0.80	302	9	302	8
20	Zr44	165	30	3698	0.01	0.3654	0.0122	0.04824	0.00138	0.86	304	9	/	

21	Zr26	330	13	7356	0.00	0.3521	0.0118	0.04849	0.00138	0.85	305	9	306	8
22	Zr22b	1195	49	26687	0.00	0.3391	0.0111	0.04841	0.00138	0.87	305	8	/	
23	Zr22c	1044	45	24262	0.00	0.3382	0.0110	0.04825	0.00138	0.88	304	8	/	
24	Zr20c	125	132	2828	0.05	0.3702	0.0128	0.04883	0.00138	0.82	307	9	/	
25	Zr20b	110	8	2542	0.00	0.3501	0.0119	0.04819	0.00135	0.83	303	8	304	8
	Ag38													
1	Zr8	580	8.3	13399	0.00	0.3395	0.0110	0.04707	0.00144	0.94	297	9	297	8
2	Zr7b	364	5.3	8422	0.00	0.3431	0.0112	0.04696	0.00144	0.94	296	9	299	8
3	Zr6c	279	4.1	6266	0.00	0.3543	0.0115	0.04948	0.00150	0.93	311	9	308	9
4	Zr4	220	73	5166	0.01	0.3370	0.0110	0.04674	0.00141	0.93	295	9	295	8
5	Zr9	361	8.1	8417	0.00	0.3407	0.0109	0.04698	0.00141	0.94	296	9	298	8
6	Zr10b	330	4.2	7666	0.00	0.3482	0.0112	0.04677	0.00141	0.94	295	9	/	
7	Zr12	342	4.5	7874	0.00	0.3438	0.0110	0.04703	0.00141	0.94	296	9	299	8
8	Zr17	294	6.1	6922	0.00	0.3393	0.0109	0.04725	0.00141	0.93	298	9	297	8
9	Zr21	402	6.2	9422	0.00	0.3428	0.0110	0.04726	0.00141	0.93	298	9	299	8
10	Zr22	256	5.2	5956	0.00	0.3479	0.0112	0.04722	0.00141	0.93	297	9	/	
11	Zr31	445	6.4	10286	0.00	0.3527	0.0113	0.04704	0.00138	0.91	296	9	/	
12	Zr29c	287	3.2	6330	0.00	0.3689	0.0118	0.04930	0.00144	0.91	310	9	/	
13	Zr29b	322	3.2	7382	0.00	0.3499	0.0113	0.04733	0.00138	0.91	298	9	/	
14	Zr59	489	9.3	11213	0.00	0.3502	0.0112	0.04714	0.00138	0.92	297	8	/	
15	Zr33c	281	3.2	6624	0.00	0.3366	0.0108	0.04728	0.00138	0.91	298	8	296	8
16	Zr33b	281	3.2	6593	0.00	0.3387	0.0109	0.04729	0.00138	0.91	298	8	297	8
17	Zr37	375	4.6	8747	0.00	0.3432	0.0111	0.04732	0.00138	0.90	298	8	299	8
18	Zr52	431	6.4	10016	0.00	0.3368	0.0108	0.04732	0.00135	0.89	298	8	296	8
19	Zr51	339	4.6	7846	0.00	0.3475	0.0112	0.04705	0.00135	0.89	296	8	299	8
20	Zr54	402	4.3	9280	0.00	0.3399	0.0110	0.04734	0.00135	0.89	298	8	298	8
21	Zr52	505	6.8	11671	0.00	0.3336	0.0108	0.04727	0.00135	0.88	298	8	295	8
22	Zr61	250	5.3	5784	0.00	0.3407	0.0111	0.04692	0.00135	0.89	296	8	297	8
23	Zr58	103	2.3	2395	0.00	0.3502	0.0125	0.04741	0.00135	0.80	299	8	300	8
24	Zr34	175	15	4132	0.00	0.3344	0.0112	0.04711	0.00135	0.86	297	8	295	8
	Ag47													
1	Zr1-1	95	54	1212	0.04	0.6833	0.0217	0.08440	0.00240	0.90	522	14	528	13
2	Zr1-2	34	39	431	0.09	0.6767	0.0230	0.08525	0.00243	0.84	527	14	526	14
3	Zr1-3	76	69	1038	0.07	0.6212	0.0202	0.07854	0.00222	0.87	487	13	490	12
4	Zr2-1	125	1.1	2845	0.00	0.3506	0.0113	0.04841	0.00138	0.89	305	8	305	8
5	Zr5-1	144	1.9	3295	0.00	0.3502	0.0114	0.04794	0.00135	0.87	302	8	303	8
6	Zr5-2	68	1.1	1453	0.00	0.3705	0.0125	0.05139	0.00147	0.85	323	9	322	9
7	Zr6-1	92	0.9	2125	0.00	0.3431	0.0111	0.04732	0.00135	0.88	298	8	299	8
8	Zr6-2	75	0.8	1735	0.00	0.3372	0.0120	0.04730	0.00135	0.80	298	8	297	8
9	Zr6-3	84	1.5	1920	0.00	0.3446	0.0113	0.04783	0.00135	0.86	301	8	301	8
10	Zr7-1	167	1.5	3900	0.00	0.3393	0.0110	0.04720	0.00135	0.88	297	8	297	8
11	Zr7-2	129	1.0	2671	0.00	0.3822	0.0125	0.05309	0.00150	0.87	334	9	331	9
12	Zr10-1	111	2.8	2567	0.00	0.3440	0.0115	0.04726	0.00135	0.86	298	8	299	8

13	Zr10-2	110	1.2	2567	0.00	0.3400	0.0113	0.04732	0.00135	0.86	298	8	298	8
14	Zr11-1	163	1.0	3776	0.00	0.3404	0.0113	0.04756	0.00135	0.86	300	8	299	8
15	Zr11-2	144	1.9	3309	0.00	0.3514	0.0120	0.04743	0.00135	0.83	299	8	300	8
	Ag08													
1	Zr11r	108	271	2388	0.11	0.3432	0.0158	0.04703	0.00189	0.87	296	12	298	11
2	Zr11c	23	112	207	0.54	0.8315	0.0415	0.09910	0.00402	0.81	609	24	612	22
3	Zr12r	100	277	2244	0.12	0.3374	0.0152	0.04666	0.00189	0.90	294	12	295	11
4	Zr12c	17	131	313	0.42	0.3669	0.0193	0.05150	0.00210	0.78	324	13	322	13
5	Zr13r	59	59	1350	0.04	0.3420	0.0164	0.04747	0.00192	0.84	299	12	299	12
6	Zr14	17	47	333	0.14	0.3863	0.0198	0.05283	0.00213	0.79	332	13	332	13
7	Zr15r	81	168	1695	0.10	0.3630	0.0161	0.05003	0.00201	0.90	315	12	315	12
8	Zr15c	22	68	430	0.16	0.3734	0.0186	0.05164	0.00210	0.82	325	13	324	13
9	Zr16c	27	83	383	0.22	0.5285	0.0256	0.06954	0.00282	0.84	433	17	432	16
10	Zr17r	24	142	465	0.31	0.3665	0.0182	0.05070	0.00204	0.81	319	13	318	12
11	Zr23r	55	118	1131	0.10	0.3677	0.0168	0.05095	0.00204	0.88	320	13	319	12
12	Zr23c	32	84	538	0.16	0.4794	0.0230	0.06171	0.00249	0.84	386	15	390	15
13	Zr25r	67	352	1396	0.25	0.3476	0.0172	0.04691	0.00189	0.81	296	12	297	12
14	Zr25c	20	111	384	0.29	0.3743	0.0196	0.05169	0.00210	0.78	325	13	324	13
15	Zr27r	110	274	2455	0.11	0.3393	0.0164	0.04668	0.00189	0.84	294	12	295	11
16	Zr27c	12	44	244	0.18	0.3686	0.0213	0.05140	0.00210	0.71	323	13	322	13
17	Zr29r	85	152	1608	0.09	0.4151	0.0188	0.05624	0.00225	0.88	353	14	353	13
18	Zr29c	14	87	242	0.36	0.3799	0.0254	0.05320	0.00222	0.62	334	14	333	13
19	Zr30r	12	36	241	0.15	0.3743	0.0214	0.05164	0.00210	0.71	325	13	324	13
20	Zr30c	20	85	377	0.23	0.3769	0.0196	0.05202	0.00210	0.78	327	13	326	13
21	Zr34r	66	85	1529	0.06	0.3365	0.0164	0.04654	0.00186	0.82	293	12	294	11
22	Zr34c	10	49	199	0.25	0.3766	0.0233	0.05009	0.00204	0.66	315	13	316	12
23	Zr40r	123	31	2901	0.01	0.3396	0.0154	0.04645	0.00186	0.88	293	11	294	11
24	Zr45r	225	48	5254	0.01	0.3681	0.0168	0.04643	0.00186	0.88	293	11	/	
25	Zr47r	155	82	3641	0.02	0.3528	0.0164	0.04623	0.00186	0.87	291	11	/	
26	Zr50r	152	49	3597	0.01	0.3478	0.0164	0.04628	0.00186	0.85	292	11	/	
27	Zr52r	168	35	3974	0.01	0.3460	0.0159	0.04631	0.00186	0.87	292	11	/	
	Ag06													
1	Zr1r	61	203	1297	0.16	0.3726	0.0150	0.04783	0.00186	0.96	301	11	/	
2	Zr1c	65	199	1302	0.15	0.4411	0.0178	0.04959	0.00192	0.96	312	12	/	
3	Zr24r	118	664	2257	0.29	0.4420	0.0178	0.05027	0.00195	0.97	316	12	/	
4	Zr28c	92	318	1977	0.16	0.3581	0.0146	0.04773	0.00186	0.96	301	11	/	
5	Zr6r	89	304	1901	0.16	0.3736	0.0150	0.04796	0.00186	0.97	302	11	/	
6	Zr6c	56	132	1227	0.11	0.3699	0.0155	0.04747	0.00186	0.93	299	11	/	
7	Zr7r	69	237	1485	0.16	0.3419	0.0142	0.04736	0.00183	0.93	298	11	299	11
8	Zr8c	143	434	3094	0.14	0.3561	0.0143	0.04776	0.00186	0.97	301	11	/	
9	Zr10r	117	446	2509	0.18	0.3523	0.0142	0.04737	0.00183	0.96	298	11	/	
10	Zr32r	128	666	2694	0.25	0.3432	0.0138	0.04701	0.00183	0.97	296	11	302	10
11	Zr32c	43	232	895	0.26	0.3392	0.0148	0.04719	0.00183	0.89	297	11	297	11

12	Zr34r	96	311	2112	0.15	0.3430	0.0139	0.04722	0.00183	0.96	297	11	300	10
13	Zr35r	180	739	3796	0.19	0.3634	0.0148	0.04778	0.00186	0.96	301	11	/	
14	Zr36r	146	423	3218	0.13	0.3495	0.0142	0.04716	0.00183	0.96	297	11	/	
15	Zr39r	125	620	2648	0.23	0.3428	0.0139	0.04695	0.00183	0.96	296	11	301	10
16	Zr40r	161	913	3345	0.27	0.3443	0.0142	0.04709	0.00183	0.94	297	11	300	11
17	Zr40c	77	844	1443	0.58	0.3485	0.0145	0.04693	0.00183	0.94	296	11	/	
18	Zr15r1	114	624	2433	0.26	0.3476	0.0142	0.04687	0.00180	0.94	295	11	/	
19	Zr15r2	42	594	891	0.67	0.3903	0.0173	0.04829	0.00189	0.88	304	12	/	
20	Zr17r	70	258	1458	0.18	0.3988	0.0163	0.04855	0.00189	0.95	306	12	/	
21	Zr17c	51	94	1108	0.08	0.3795	0.0158	0.04809	0.00186	0.93	303	11	/	
22	Zr19r	154	745	3296	0.23	0.3400	0.0140	0.04672	0.00180	0.94	294	11	297	11
23	Zr41r	66	157	1482	0.11	0.3386	0.0141	0.04677	0.00180	0.92	295	11	296	11
24	Zr41c	107	300	2361	0.13	0.3525	0.0145	0.04697	0.00183	0.95	296	11	/	
25	Zr44r	195	1134	4076	0.28	0.3384	0.0138	0.04671	0.00180	0.94	294	11	296	11
26	Zr44c	68	422	1397	0.30	0.3453	0.0147	0.04670	0.00180	0.91	294	11	298	11
27	Zr22r	124	625	2618	0.24	0.3533	0.0146	0.04709	0.00183	0.94	297	11	/	
28	Zr23r	37	114	807	0.14	0.3492	0.0165	0.04711	0.00183	0.82	297	11	298	11
	Ag48													
1	Zr1b	28	18	632	0.03	0.3601	0.0125	0.04886	0.00138	0.82	308	9	309	8
2	Zr1-c	47	84	546	0.15	0.7281	0.0250	0.08984	0.00255	0.83	555	15	555	14
3	Zr10b	38	34	560	0.06	0.5611	0.0188	0.07185	0.00204	0.85	447	12	450	12
4	Zr10C	34	37	401	0.09	0.7225	0.0256	0.09002	0.00255	0.80	556	15	554	14
5	Zr2B	22	12	496	0.02	0.3521	0.0137	0.04862	0.00138	0.73	306	9	306	8
6	Zr2C	53	80	645	0.12	0.6844	0.0220	0.08547	0.00240	0.87	529	14	529	13
7	Zr5B	90	40	1161	0.03	0.6686	0.0216	0.08386	0.00237	0.87	519	14	520	13
8	Zr5C	11	34	113	0.30	0.7971	0.0319	0.09671	0.00279	0.72	595	16	595	16
9	Zr6B	22	13	498	0.03	0.3567	0.0132	0.04817	0.00138	0.77	303	8	304	8
10	Zr6C	25	42	361	0.12	0.5545	0.0207	0.07153	0.00204	0.76	445	12	446	12
11	Zr17B	56	21	830	0.03	0.5844	0.0189	0.07369	0.00207	0.87	458	12	463	12
12	Zr17C	16	38	165	0.23	0.7995	0.0303	0.09719	0.00276	0.75	598	16	597	16
13	Zr18B	21	14	436	0.03	0.3846	0.0141	0.05107	0.00144	0.77	321	9	323	9
14	Zr18C	22	27	274	0.10	0.6693	0.0239	0.08343	0.00237	0.80	517	14	518	14
15	Zr21B	46	36	664	0.05	0.6079	0.0211	0.07485	0.00210	0.81	465	13	/	
16	Zr21C	167	73	568	0.13	6.1487	0.1921	0.28400	0.00795	0.90	1612	40	/	
17	Zr27B	19	12	333	0.04	0.4794	0.0179	0.06225	0.00177	0.76	389	11	391	11
18	Zr27C	27	26	304	0.08	0.7820	0.0273	0.09543	0.00267	0.80	588	16	587	15
19	Zr27C	28	20	331	0.06	0.7237	0.0256	0.08977	0.00252	0.79	554	15	554	14
20	Zr22B	29	18	697	0.03	0.3363	0.0121	0.04594	0.00129	0.78	290	8	290	8
21	Zr31B	21	13	412	0.03	0.4047	0.0153	0.05472	0.00153	0.74	343	9	344	9
22	Zr31C	23	26	275	0.10	0.7195	0.0269	0.08957	0.00252	0.75	553	15	552	14
23	Zr34B	103	38	1458	0.03	0.6064	0.0198	0.07679	0.00213	0.85	477	13	479	12
24	Zr34C	61	39	112	0.34	12.2500	0.3992	0.48697	0.01365	0.86	2558	59	/	
25	Zr38B	31	8	700	0.01	0.3481	0.0125	0.04748	0.00132	0.78	299	8	300	8

26	Zr38C	23	58	316	0.18	0.5870	0.0220	0.07575	0.00213	0.75	471	13	470	12
27	Zr45B	158	58	2088	0.03	0.6570	0.0216	0.08219	0.00228	0.84	509	14	511	13
28	Zr39B	25	13	556	0.02	0.3669	0.0160	0.04877	0.00138	0.65	307	9	308	9
29	Zr9C	18	48	196	0.25	0.7388	0.0303	0.09277	0.00264	0.69	572	16	569	15
30	Zr45B	62	41	758	0.05	0.7086	0.0256	0.08803	0.00246	0.77	544	15	544	14
31	Zr45C	74	300	713	0.42	0.8230	0.0286	0.09924	0.00276	0.80	610	16	610	15
32	Zr57B	20	13	464	0.03	0.3574	0.0139	0.04753	0.00132	0.71	299	8	300	8
33	Zr57C	23	148	246	0.60	0.7001	0.0272	0.08607	0.00243	0.73	532	14	534	14
34	Zr66B	22	5	503	0.01	0.3529	0.0137	0.04741	0.00132	0.72	299	8	300	8
35	Zr66C	33	77	371	0.21	0.7298	0.0272	0.09011	0.00252	0.75	556	15	556	14
36	Zr59C	11	25	131	0.19	0.7084	0.0327	0.08854	0.00255	0.62	547	15	546	15
	Ag51													
1	Zr8b	70	16	1638	0.01	0.3599	0.0133	0.04636	0.00156	0.91	292	10	/	
2	Zr12b	40	10	963	0.01	0.3354	0.0130	0.04604	0.00156	0.87	290	10	292	9
3	Zr12c	49	157	537	0.29	0.7336	0.0274	0.08968	0.00303	0.90	554	18	559	16
4	Zr13b	44	10	1039	0.01	0.3550	0.0135	0.04618	0.00156	0.89	291	10	/	
5	Zr13c	34	196	755	0.26	0.3273	0.0159	0.04591	0.00159	0.71	289	10	289	10
6	Zr17c	82	290	1838	0.16	0.3315	0.0130	0.04628	0.00156	0.86	292	10	291	9
7	Zr18c	60	85	1394	0.06	0.3361	0.0131	0.04541	0.00153	0.87	286	9	289	9
8	Zr22b	41	5	967	0.01	0.3374	0.0127	0.04559	0.00153	0.89	287	9	/	
9	Zr24c	78	156	929	0.17	0.7000	0.0254	0.08680	0.00288	0.91	537	17	539	15
10	Zr29b	47	5	1105	0.00	0.3569	0.0133	0.04605	0.00153	0.89	290	9	/	
11	Zr35	109	129	2525	0.05	0.3465	0.0129	0.04623	0.00153	0.89	291	9	/	
12	Zr34c	172	199	3612	0.06	0.4009	0.0145	0.05016	0.00165	0.91	316	10	/	
13	Zr32b	36	4	868	0.00	0.3469	0.0136	0.04529	0.00150	0.85	286	9	/	
14	Zr36b	57	311	1238	0.25	0.3356	0.0136	0.04650	0.00153	0.81	293	9	293	9
15	Zr36c	5	20	45	0.43	0.9540	0.0684	0.11213	0.00402	0.50	685	23	684	23
16	Zr42b	78	19	1883	0.01	0.3399	0.0125	0.04521	0.00147	0.89	285	9	/	
17	Zr43b	39	7	931	0.01	0.3351	0.0130	0.04585	0.00150	0.84	289	9	290	9
18	Zr40b	37	6	857	0.01	0.3612	0.0140	0.04591	0.00150	0.84	289	9	/	
19	Zr49b	41	4	987	0.00	0.3393	0.0130	0.04522	0.00147	0.85	285	9	/	
20	Zr45b	48	5	1166	0.00	0.3224	0.0122	0.04517	0.00147	0.86	285	9	284	9
21	Zr57b	30	6	737	0.01	0.3381	0.0138	0.04527	0.00147	0.80	285	9	287	9
22	Zr50b	43	4	1038	0.00	0.3270	0.0126	0.04569	0.00150	0.85	288	9	288	9

ANNEXE 2: supplementary materials of Chapter 4

Table S1: Major and Trace element contents.

	AR 481C	AR 483
Major elements (wt. %)		
SiO_2	51.71	50.05
TiO_2	2.08	2.13
Al_2O_3	13.29	12.99
FeO	13.37	14.17
MnO	0.24	0.25
MgO	6.94	7.91
CaO	8.74	9.05
Na_2O	2.29	2.68
K_2O	0.32	0.17
P_2O_5	0.20	0.23
Cr_2O_3	0.02	0.01
NiO	0.01	0.01
LOI	0.19	0.10
Total	100.86	101.33
Traces (ppm)		
Sc	48.3	47.7
V	423.5	404.4
Cr	111.2	85
Mn	1658.7	1729.6
Co	44.6	46.2
Ni	50.9	47.5
Cu	49.8	61.6
Zn	118.2	128.4
Ga	19.5	21.1
Ge	1	-
As	3.4	-
Se	-	-
Br	-	-
Rb	10.8	2.5
Sr	82.8	79.5
Y	46	52.4
Zr	117.9	160
Nb	1.9	3.7
Mo	-	-
Ag	-	-
Cd	-	-
Sn	3.5	4.3
Sb	-	-
Te	-	-
I	-	-
Cs	2.2	3
Ba	35.2	27.8
La	-	-
Ce	20.6	23.7
Nd	16.4	17.8
Sm	5.7	3.7
Yb	4	3.7

Hf	3.2	5.9
Ta	-	-
W	-	2.8
Hg	-	-
Tl	-	-
Pb	2.9	2.1
Bi	-	-
Th	1.2	1
U	-	-

Table S2: Mineral compositions from samples AR483 and AR481. Amph1: amphibole within symplectite. Amph2: amphibole within corona. Amph3: amphibole within corona in direct contact with garnet. Amph4: large amphibole crystal.

	AR483								AR481			
	Cpx$_1$	Cpx$_{2a}$	Cpx$_{2b}$	Grt$_1$	Grt$_2$	Amph$_2$ sympl.	Amph$_2$ corona	Pl$_2$	Amph$_3$	Pl$_3$	Grt$_1$	Grt$_2$
Al_2O_3	8.35	6.89	2.73	21.81	21.82	8.71 – 9.96	11.28 – 16.88	21.12	11.58	25.84	21.15	21.33
CaO	14.75	17.07	21.93	8.87	6.40	11.02 – 10.59	10.60 – 10.56	2.34	11.96	7.17	8.88	6.79
FeO	7.99	8.77	7.95	25.85	27.37	15.67 – 16.18	15.16 – 15.85	0.00	17.72	0.00	25.37	26.62
K_2O	0.29	0.30	0.29	0.02	0.02	0.21 – 0.26	0.29 – 0.31	0.09	0.01	0.09	0.00	0.00
MgO	8.28	9.17	11.81	5.75	6.33	13.03 – 12.50	12.90 – 11.53	0.00	10.37	0.00	5.65	6.29
MnO	0.07	0.11	0.13	0.39	0.62	0.09 – 0.09	0.14 – 0.16	0.00	0.24	0.00	0.44	0.53
Na_2O	5.88	4.45	1.59	0.12	0.11	1.97 – 2.40	2.61 – 3.22	9.96	0.13	8.01	0.07	0.08
TiO_2	0.28	0.33	0.39	0.09	0.08	1.91 – 1.31	1.22 – 0.46	0.00	0.82	0.00	0.08	0.08
SiO_2	54.62	53.62	54.22	38.66	38.43	45.52 – 44.84	43.85 – 38.64	65.80	44.74	60.27	38.22	38.67
Total	100.50	100.71	101.03	101.57	101.19	98.13 – 98.13	98.05 – 97.62	99.31	97.57	101.39	99.85	100.39
Si	1.97	1.95	1.99	2.96	2.96	6.72 – 6.65	6.48 – 5.75	2.90	6.56	2.67	2.98	3.00
Al	0.36	0.32	0.13	1.97	1.98	1.51 – 1.74	1.97 – 2.96	1.10	2.00	1.35	1.94	1.95
Ca	0.57	0.66	0.81	0.73	0.53	1.74 – 1.68	1.68 – 1.68	0.12	1.88	0.34	0.74	0.56
Fe^{2+}	0.16	0.20	0.24	1.60	1.70	1.91 – 2.08	1.88 – 1.53	0.00	1.51	0.00	1.59	1.67
Fe^{3+}	0.08	0.07	0.05	0.06	0.06	0.02 – 0.00	0.00 – 0.44	0.00	0.66	0.00	0.08	0.06
K	0.00	0.00	0.00	0.00	0.00	0.04 – 0.05	0.05 – 0.06	0.00	0.00	0.01	0.00	0.00
Mg	0.45	0.48	0.61	0.66	0.74	2.87 – 2.76	2.84 – 2.56	0.00	2.27	0.00	0.66	0.73
Mn	0.00	0.00	0.00	0.03	0.04	0.01 – 0.01	0.02 – 0.02	0.03	0.00	0.00	0.03	0.03
Na	0.41	0.32	0.16	0.00	0.00	0.57 – 0.69	0.75 – 0.93	0.83	0.04	0.56	0.00	0.00
Ti	0.00	0.00	0.00	0.01	0.00	0.21 – 0.15	0.14 – 0.05	0.00	0.09	0.00	0.00	0.00
Total	4.00	4.00	3.98	8.01	8.02	15.60 – 15.81	15.82 – 15.99	4.99	15.00	4.93	8.01	8.01
XJd	0.33	0.25	0.11									
XAlm				0.52	0.55						0.51	0.54
XPrp				0.21	0.24						0.21	0.24
XGrs				0.24	0.17						0.24	0.18
XSps				0.01	0.01						0.01	0.01
XMg						0.6 – 0.57	0.6 – 0.63		0.6			
XAb								0.87		0.62		

Table S3: Zr-in-rutile thermometer results. AR483: 1 to 80; AR481: 81 to 120.

n°	SiO_2	Cr_2O_3	ZrO_2	TiO_2	FeO	Al_2O_3	Total		localisation	Zr (ppm)	T°C (1.5 Gpa)
1	0.15	0.02	0.58	98.90	0.33	0.02	100.01	std-1		4322.87	957
2	0.06	0.04	0.60	98.61	0.38	0.01	99.71	std-2		4453.82	961
3	0.07	0.04	0.61	98.39	0.40	0.02	99.52	std-3		4490.07	963
4	0.07	0.03	0.63	98.74	0.36	0.02	99.85	std-4		4655.06	968
5	0.10	0.03	0.62	98.73	0.38	0.01	99.88	std-5		4603.27	966
6	0.11	0.05	0.60	97.75	0.35	0.02	98.89	std-6		4438.28	961
7	0.01	0.06	0.06	99.66	0.18	0.01	99.98	Rt-1	Matrix	427.63	701
8	0.01	0.06	0.05	99.15	0.19	0.01	99.48	Rt-2	Matrix	392.85	694
9	0.01	0.08	0.07	99.20	0.16	0.01	99.52	Rt-3	Matrix	496.43	715
10	0.01	0.06	0.06	99.29	0.34	0.04	99.80	Rt-4	Grenat	422.45	700
11	0.01	0.06	0.06	99.36	0.27	0.02	99.78	Rt-5	Grenat	444.64	705
12	0.02	0.06	0.07	98.43	0.59	0.02	99.18	Rt-6	Grenat	497.91	715
13	0.00	0.06	0.06	99.19	0.35	0.01	99.67	Rt-7	Grenat	446.12	705
14	0.01	0.07	0.05	99.05	0.33	0.03	99.54	Rt-8	Grenat	368.44	688
15	0.01	0.15	0.06	99.32	0.14	0.01	99.68	Rt-9	Matrix	447.60	705
16	0.04	0.08	0.06	99.54	0.34	0.01	100.05	Rt-10	Matrix	432.07	702
17	0.04	0.14	0.09	99.31	0.31	0.01	99.89	Rt-11	Matrix	644.40	739
18	0.04	0.18	0.06	98.97	0.20	0.02	99.47	Rt-12	Matrix	445.38	705
19	0.04	0.11	0.06	98.97	0.65	0.01	99.84	Rt-13	Grenat	455.74	707
20	0.03	0.10	0.06	99.33	0.64	0.02	100.18	Rt-14	Grenat	426.89	701
21	0.05	0.20	0.06	98.78	0.24	0.01	99.33	Rt-15	Matrix	458.70	707
22	0.02	0.11	0.06	99.53	0.26	0.01	99.98	Rt-16	Matrix	457.22	707
23	0.04	0.11	0.06	99.63	0.23	0.01	100.08	Rt-17	Matrix	446.86	705
24	0.00	0.03	0.06	99.86	0.25	0.03	100.23	Rt-18	Grenat	435.76	703
25	0.01	0.04	0.06	99.70	0.25	0.01	100.08	Rt-19	Matrix	450.56	706
26	0.02	0.05	0.05	99.55	0.26	0.01	99.95	Rt-20	Matrix	392.11	694
27	0.02	0.13	0.06	99.76	0.18	0.02	100.16	Rt-21	Matrix	468.32	709
28	0.02	0.13	0.06	99.73	0.15	0.02	100.10	Rt-22	Matrix	431.33	702
29	0.01	0.04	0.07	99.48	0.32	0.01	99.93	Rt-23	Grenat	489.03	713
30	0.02	0.06	0.07	100.09	0.27	0.01	100.53	Rt-24	Matrix	535.64	721
31	0.02	0.07	0.06	99.63	0.31	0.01	100.10	Rt-25	Matrix	427.63	701
32	0.01	0.11	0.05	100.04	0.15	0.01	100.36	Rt-26	Matrix	360.30	686
33	0.02	0.10	0.04	100.03	0.18	0.01	100.39	Rt-27	Matrix	327.01	678
34	0.01	0.04	0.05	99.53	0.48	0.04	100.16	Rt-28	Grenat	403.95	696
35	0.00	0.05	0.06	99.97	0.36	0.01	100.45	Rt-29	Grenat	407.65	697
36	0.02	0.05	0.06	99.91	0.23	0.01	100.27	Rt-30	Matrix	418.75	699
37	0.01	0.06	0.06	99.89	0.21	0.01	100.24	Rt-31	Matrix	455.74	707
38	0.02	0.09	0.06	99.45	0.16	0.02	99.80	Rt-32	Matrix	407.65	697
39	0.02	0.09	0.06	98.81	0.18	0.01	99.17	Rt-33	Matrix	425.41	701
40	0.02	0.06	0.07	99.51	0.52	0.02	100.19	Rt-34	Grenat	500.87	715
41	0.02	0.06	0.05	98.92	0.27	0.01	99.32	Rt-35	Matrix	374.36	690
42	0.01	0.07	0.04	97.16	0.18	0.02	97.48	Rt-36	Matrix	308.51	673
43	0.00	0.07	0.05	88.74	0.29	0.01	89.16	Rt-37	Matrix	341.80	682
44	0.00	0.06	0.05	99.68	0.36	0.02	100.17	Rt-38	Grenat	378.80	691
45	0.04	0.08	0.06	100.31	0.34	0.01	100.84	Rt-39	Matrix	452.04	706
46	0.00	0.05	0.04	99.87	0.41	0.01	100.38	Rt-40	Grenat	311.47	674
47	0.01	0.05	0.03	99.40	0.22	0.03	99.75	Rt-41	Grenat	256.72	659
48	0.02	0.05	0.05	100.65	0.21	0.00	100.99	Rt-42	Matrix	371.40	689
49	0.02	0.04	0.08	98.87	0.40	0.01	99.42	Rt-43	Matrix	571.89	727
50	0.01	0.04	0.05	99.65	0.24	0.01	100.01	Rt-44	Matrix	387.67	693
51	0.00	0.04	0.05	100.20	0.29	0.00	100.59	Rt-45	Matrix	404.69	696
52	0.01	0.03	0.05	98.86	0.29	0.02	99.26	Rt-46	Matrix	379.54	691

53	0.02	0.04	0.05	98.80	0.44	0.01	99.36	Rt-47	Matrix	404.69	696
54	0.01	0.10	0.07	100.14	0.13	0.01	100.44	Rt-48	Matrix	487.55	713
55	0.02	0.08	0.06	100.00	0.18	0.01	100.33	Rt-49	Matrix	417.27	699
56	0.01	0.08	0.07	99.68	0.22	0.01	100.08	Rt-50	Matrix	524.54	719
57	0.03	0.04	0.05	99.91	0.44	0.01	100.47	Rt-51	Matrix	400.25	695
58	0.01	0.06	0.06	99.64	0.24	0.01	100.03	Rt-52	Grenat	469.80	710
59	0.01	0.06	0.08	99.85	0.21	0.05	100.26	Rt-53	Grenat	565.98	726
60	0.01	0.08	0.06	99.06	0.19	0.01	99.41	Rt-54	Matrix	406.91	697
61	0.00	0.07	0.06	99.90	0.18	0.01	100.23	Rt-55	Matrix	469.80	710
62	0.00	0.08	0.06	100.19	0.18	0.01	100.52	Rt-56	Grenat	463.88	708
63	0.00	0.08	0.07	100.32	0.25	0.01	100.73	Rt-57	Grenat	489.03	713
64	0.01	0.05	0.06	99.37	0.42	0.01	99.93	Rt-58	Matrix	426.89	701
65	0.02	0.08	0.06	100.00	0.26	0.01	100.43	Rt-59	Matrix	443.16	704
66	0.02	0.09	0.07	100.30	0.23	0.01	100.72	Rt-60	Matrix	487.55	713
67	0.01	0.05	0.04	88.59	9.64	0.02	98.35	Rt-61	Grenat	300.37	671
68	0.02	0.06	0.07	99.65	0.38	0.01	100.20	Rt-62	Grenat	554.14	725
69	0.00	0.06	0.06	100.18	0.23	0.00	100.55	Rt-63	Grenat	450.56	706
70	0.03	0.10	0.05	98.93	0.16	0.01	99.28	Rt-64	Matrix	378.80	691
71	0.03	0.10	0.05	99.06	0.16	0.01	99.41	Rt-65	Matrix	378.06	691
72	0.02	0.04	0.07	100.32	0.29	0.01	100.75	Rt-66	Matrix	483.11	712
73	0.01	0.11	0.06	99.30	0.19	0.01	99.68	Rt-67	Matrix	452.78	706
74	0.02	0.05	0.05	99.97	0.44	0.01	100.54	Rt-68	Grenat	353.64	685
75	0.01	0.16	0.05	99.88	0.11	0.01	100.22	Rt-69	Matrix	389.89	693
76	0.05	0.04	0.06	99.32	0.67	0.01	100.14	Rt-70	Matrix	409.13	697
77	0.01	0.11	0.06	100.23	0.22	0.01	100.65	Rt-71	Matrix	438.72	704
78	0.01	0.10	0.04	99.96	0.24	0.01	100.37	Rt-72	Matrix	321.83	677
79	0.01	0.11	0.03	100.40	0.27	0.00	100.83	Rt-73	Grenat	244.89	655
80	0.02	0.08	0.05	99.91	0.56	0.01	100.64	Rt-74	Grenat	378.80	691
81	0.00	0.06	0.07	99.96	0.29	0.03	100.40	Rt-75	Grenat	483.11	712
82	0.01	0.11	0.05	100.40	0.55	0.01	101.14	Rt-76	Grenat	352.90	685
83	0.02	0.08	0.07	99.96	0.36	0.01	100.50	Rt-77	Matrix	542.30	723
84	0.03	0.09	0.07	100.18	0.31	0.01	100.68	Rt-78	Matrix	535.64	721
85	0.01	0.12	0.06	99.94	0.25	0.03	100.40	Rt-79	Matrix	436.50	703
86	0.02	0.12	0.07	100.74	0.27	0.01	101.23	Rt-80	Matrix	485.33	712
87	0.04	0.11	0.08	99.76	0.15	0.00	100.14	Rt-81	Matrix	568.20	727
88	0.01	0.09	0.08	99.74	0.14	0.01	100.06	Rt-82	Matrix	590.39	730
89	0.03	0.09	0.10	99.50	0.14	0.01	99.88	Rt-83	Matrix	728.74	750
90	0.02	0.06	0.07	99.69	0.21	0.01	100.07	Rt-84	Matrix	551.92	724
91	0.02	0.05	0.05	99.70	0.19	0.03	100.04	Rt-85	Grenat	366.22	688
92	0.06	0.05	0.05	98.69	0.19	0.05	99.09	Rt-86	Grenat	345.50	683
93	0.02	0.07	0.04	100.09	0.31	0.01	100.54	Rt-87	Grenat	305.55	673
94	0.02	0.07	0.04	99.69	0.40	0.02	100.24	Rt-88	Grenat	286.32	667
95	0.03	0.07	0.08	99.43	0.43	0.01	100.05	Rt-89	Grenat	581.51	729
96	0.01	0.09	0.07	99.91	0.22	0.01	100.30	Rt-90	Matrix	489.77	713
97	0.02	0.05	0.06	99.71	0.28	0.01	100.13	Rt-91	Matrix	412.83	698
98	0.02	0.07	0.07	99.56	0.16	0.01	99.88	Rt-92	Matrix	528.24	720
99	0.02	0.07	0.06	99.65	0.22	0.01	100.03	Rt-93	Matrix	463.88	708
100	0.08	0.12	0.08	99.58	0.10	0.00	99.96	Rt-94	Matrix	557.10	725
101	0.04	0.10	0.07	99.96	0.20	0.01	100.38	Rt-95	Matrix	534.16	721
102	0.05	0.06	0.06	99.20	0.28	0.01	99.67	Rt-96	Matrix	462.40	708
103	0.01	0.14	0.07	99.78	0.15	0.00	100.16	Rt-97	Matrix	516.41	718
104	0.03	0.07	0.06	99.85	0.36	0.03	100.40	Rt-98	Grenat	413.57	698
105	0.03	0.07	0.05	99.74	0.51	0.03	100.42	Rt-99	Grenat	393.59	694
106	0.03	0.16	0.04	99.73	0.40	0.01	100.38	Rt-100	Grenat	311.47	674
107	0.04	0.07	0.08	99.72	0.28	0.01	100.20	Rt-101	Matrix	614.80	734
108	0.02	0.12	0.06	100.67	0.14	0.01	101.03	Rt-102	Matrix	438.72	704
109	0.04	0.17	0.07	98.89	0.21	0.01	99.38	Rt-103	Matrix	499.39	715
110	0.02	0.07	0.05	99.63	0.51	0.01	100.29	Rt-104	Grenat	398.77	695

111	0.01	0.09	0.05	100.10	0.41	0.01	100.68	Rt-105	Grenat	397.29	695
112	0.08	0.07	0.06	99.75	0.54	0.01	100.52	Rt-106	Grenat	466.10	709
113	0.01	0.05	0.04	99.73	0.24	0.01	100.08	Rt-107	Grenat	279.66	665
114	0.01	0.14	0.06	100.44	0.12	0.01	100.79	Rt-108	Matrix	450.56	706
115	0.00	0.14	0.06	99.72	0.14	0.01	100.07	Rt-109	Matrix	452.78	706
116	0.03	0.20	0.08	99.32	0.15	0.01	99.79	Rt-110	Matrix	571.15	727
117	0.01	0.09	0.04	100.06	0.31	0.01	100.52	Rt-111	Grenat	291.50	669
118	0.02	0.08	0.05	100.29	0.35	0.01	100.81	Rt-112	Grenat	387.67	693
119	0.00	0.09	0.06	100.29	0.19	0.01	100.64	Rt-113	Matrix	434.28	703
120	0.03	0.09	0.06	99.51	0.21	0.02	99.91	Rt-114	Matrix	443.90	705
121	0.03	0.15	0.05	100.10	0.12	0.01	100.46	Rt-115	Matrix	355.86	685
122	0.03	0.06	0.06	99.96	0.42	0.02	100.54	Rt-116	Matrix	471.28	710
123	0.01	0.06	0.04	100.49	0.26	0.01	100.88	Rt-117	Grenat	295.20	670
124	0.01	0.09	0.07	100.25	0.29	0.01	100.71	Rt-118	Grenat	491.99	714
125	0.02	0.08	0.06	100.22	0.27	0.01	100.65	Rt-119	Matrix	472.76	710
126	0.02	0.11	0.06	99.68	0.21	0.01	100.10	Rt-120	Matrix	472.02	710

Table S4: Local compositions in %mol extracted from XMapTools software.

	AR483 whole map	AR483 without garnet cores and inclusions
Al_2O_3	5.31	4.45
CaO	13.65	14.14
FeO	7.79	6.38
Fe_2O_3	0.21	0.17
MgO	10.71	10.89
Na_2O	2.99	3.26
TiO_2	0.92	0.91
SiO_2	57.42	59.06
Total	99.01	99.25

Tableau 4: Operating conditions and instrument settings for U-Pb analyses

Laboratory & Sample Preparation	
Laboratory name	Laboratoire Magmas & Volcans, Clermont-Ferrand, France
Sample type/mineral	*Zircon:* grain mounts *Rutile:* grain mounts and in thin section *Titanite:* in thin section
Sample preparation	Conventional mineral separation: heavy liquids, Frantz magnetic separator, handpicking under binocular microscope 1 inch Epotek® resin mount, 0.25um polish to finish (Université Montpellier). Thin section (Université Bourgogne-Franche Comté)
Imaging	CL, FEI QUANTA 450w, 15 kV, 19mm working distance (Université Bourgogne-Franche Comté)
Laser ablation system	
Make, Model & type	Resonetics/M-50E 193nm, Excimer

Ablation cell & volume	Laurin Cell ® two volumes cell, Laurin Technic Ltd., volume ca. 1cm^3		
Laser wavelength	193 nm		
Pulse width	< 4 ns		
Fluence	*Zircon* 2.5 J/cm^2	*Rutile* 3.5 J/cm^2	*Titanite* 2.5 J/cm^2
Repetition rate	3 Hz	5 Hz	3 Hz
Spot size	33 µm	67 µm	40 µm
Sampling mode / pattern	Single spot		
Carrier gas	100% He, Ar make-up gas and N_2 combined using the Squid® device from Resolution Instruments.		
Background collection	30 secs		
Ablation duration	60 secs		
Wash-out delay	30 secs		
Cell carrier gas flow	0.70 l/min He		
ICP-MS Instrument			
Make, Model & type	Element XR SF-ICP-MS		
Sample introduction	Via conventional tubing		
RF power	1200W		
Make-up gas flow	0.98 l/min Ar		
Detection system	Single collector secondary electron multiplier (Faraday cup)		
Masses measured	204, 206, 207, 208, 232, 238		
Integration time per peak	20 ms		
Sensitivity / Efficiency	150 000 cps/ppm ^{238}U (47µm, 10Hz, 3.5J/cm^2)		
Dead time	6 ns		
Data Processing			
Gas blank	30 second on-peak		
Calibration strategy	*Zircon and Titanite:* GJ-1 used as primary reference material, 91500 used as secondary reference material (Quality Control) *Rutile:* Sugluk-4 used as primary reference material PCA-S207 used as secondary reference material		
Reference Material info	*Zircon* 91500 (Wiedenbeck et al., 1995) GJ-1 (Jackson et al., 2004) *Rutile* Sugluk and PCA-S207 (Bracciali et al., 2013)		
Data processing package used / Correction for LIEF	GLITTER ® (van Achterbergh et al., 2001)		
Mass discrimination	Standard-sample bracketing with ^{207}Pb/^{206}Pb and ^{206}Pb/^{238}U normalized to reference material GJ-1		
Common-Pb correction, composition and uncertainty	No common-Pb correction. Analyses discarded of the age calculation when discordance >20%		
Uncertainty level & propagation	Ages are quoted at 2sigma absolute, propagation is by quadratic addition according to Horstwood et al. (2003). Reproducibility and age uncertainty of reference material are propagated.		
Quality control / Validation	91500: Concordia age = 1066.4 ± 2.1 Ma (2SD, MSWD$_{(C+E)}$ = 0.57, N = 61) PCA-S207: Lower intercept age = 1869 ± 15 Ma (2SD, MSWD = 0.3, N = 12)		
Other information	For detailed method description see Hurai et al. (2010). For detailed laser technical description see Müller et al. (2009).		

Tables S6. U-Pb LA-ICPMS results on zircon, rutile and titanite from samples AR483 and AR481.

U-Pb LA-ICPMS results on zircon

#	# Zircon	Pb ppm	Th ppm	U ppm	Th/U	Pb^{207}/U^{235}	±2σ	Pb^{206}/U^{238}	±2σ	Rho	Pb^{206}/U^{238} age	±2σ
	AR483											
1	Zr1	9.7	31	147	0.21	0.5818	0.0142	0.07431	0.00066	0.36	462.0	3.9
2	Zr2	8.0	28	123	0.23	0.5935	0.0165	0.07475	0.00072	0.35	464.7	4.3
3	Zr3	4.1	14	46	0.31	0.5746	0.0201	0.07421	0.00084	0.32	461.4	5.0
4	Zr4	5.1	21	58	0.37	0.6053	0.0194	0.07453	0.00081	0.34	463.4	4.9
5	Zr5	6.3	22	76	0.29	0.5958	0.0211	0.07414	0.00087	0.33	461.0	5.3
6	Zr6	9.2	36	120	0.30	0.5866	0.0237	0.07095	0.00093	0.32	441.9	5.6
7	Zr7	7.9	37	112	0.33	0.5709	0.0255	0.07157	0.00105	0.33	445.6	6.3
8	Zr8	7.9	27	112	0.24	0.5902	0.0278	0.07640	0.00117	0.33	474.6	7.1
9	Zr10	13	52	189	0.28	0.5795	0.0294	0.07513	0.00123	0.32	467.0	7.4
10	Zr11 center	7.6	30	117	0.25	0.5871	0.0348	0.07417	0.00138	0.31	461.2	8.4
11	Zr11 rim	1.2	0.3	14	0.02	0.9205	0.0712	0.06294	0.00165	0.34	393.5	9.9
12	Zr12	7.9	26	90	0.29	0.5671	0.0398	0.07593	0.00165	0.31	471.8	9.9
13	Zr13	5.4	14	64	0.21	0.6143	0.0257	0.07771	0.00108	0.33	482.5	6.5
14	Zr15	3.6	12	54	0.21	0.4390	0.0159	0.05823	0.00075	0.36	364.9	4.5
15	Zr17	20	114	247	0.46	0.5676	0.0093	0.07335	0.00072	0.60	456.3	4.3
16	Zr18	12	62	146	0.43	0.5723	0.0122	0.07326	0.00075	0.48	455.8	4.5
17	Zr19 rim	1.8	1.3	31	0.04	0.4918	0.0362	0.06255	0.00135	0.29	391.1	8.2
18	Zr20	12	46	155	0.30	0.6000	0.0325	0.07516	0.00132	0.32	467.1	7.9
19	Zr21	7.7	20	103	0.20	0.5870	0.0328	0.07514	0.00135	0.32	467.1	8.0
20	Zr23 center	1.1	0.2	21	0.01	0.4660	0.0440	0.05353	0.00144	0.28	336.2	8.8
21	Zr24	3.9	9.3	53	0.18	0.5811	0.0363	0.07554	0.00147	0.31	469.4	8.8
22	Zr25 center	16	67	215	0.31	0.5761	0.0347	0.07436	0.00141	0.32	462.4	8.5
23	Zr26	4.2	14	57	0.25	0.5857	0.0394	0.07400	0.00153	0.31	460.2	9.2
24	Zr27	7.0	22	96	0.23	0.5796	0.0386	0.07033	0.00144	0.31	438.1	8.7
25	Zr63 center	7.8	26	142	0.19	0.4138	0.0291	0.05503	0.00117	0.30	345.3	7.1
26	Zr30	13	51	167	0.30	0.5790	0.0393	0.07389	0.00153	0.31	459.6	9.3
27	Zr33	6.9	23	91	0.26	0.5724	0.0407	0.07459	0.00162	0.31	463.7	9.7
28	Zr36	12	43	153	0.28	0.5946	0.0445	0.07598	0.00171	0.30	472.1	10.3
29	Zr37	12	55	154	0.36	0.5747	0.0433	0.07384	0.00168	0.30	459.2	10.1
30	Zr39	7.7	19	106	0.18	0.5735	0.0446	0.07448	0.00174	0.30	463.1	10.5
31	Zr40	15	81	194	0.42	0.5828	0.0454	0.07449	0.00174	0.30	463.2	10.5
32	Zr41 center	6.4	24	84	0.28	0.5827	0.0473	0.07406	0.00180	0.30	460.6	10.8
33	Zr42	3.2	7.6	44	0.18	0.5826	0.0502	0.07450	0.00189	0.29	463.2	11.4
34	Zr43	4.9	14	66	0.21	0.5781	0.0509	0.07428	0.00192	0.29	461.9	11.6
35	Zr44 center	7.0	21	95	0.22	0.5708	0.0529	0.07377	0.00201	0.29	458.8	12.1
36	Zr45	6.4	21	88	0.24	0.5735	0.0543	0.07318	0.00204	0.29	455.3	12.2
37	Zr46 center	4.8	15	66	0.23	0.5831	0.0566	0.07446	0.00210	0.29	462.9	12.7
38	Zr44 rim	4.7	15	63	0.24	0.5688	0.0567	0.07373	0.00213	0.29	458.6	12.9

39	Zr47	11	41	141	0.29	0.5761	0.0575	0.07413	0.00216	0.29	461.0	13.0
40	Zr48	9.7	33	129	0.25	0.5677	0.0578	0.07371	0.00219	0.29	458.4	13.1
41	Zr49	8.1	20	111	0.18	0.5747	0.0598	0.07420	0.00225	0.29	461.4	13.5
42	Zr50	15	67	198	0.34	0.5686	0.0626	0.07413	0.00237	0.29	461.0	14.2
43	Zr51	6.4	24	86	0.29	0.5745	0.0659	0.07371	0.00243	0.29	458.4	14.6
44	Zr52 rim	2.4	1.8	49	0.04	0.3935	0.0466	0.05384	0.00183	0.29	338.1	11.1
45	Zr52 center	1.6	0.7	33	0.02	0.4425	0.0549	0.05387	0.00189	0.28	338.2	11.6
46	Zr52 rim	1.9	0.3	36	0.01	0.4745	0.0590	0.05376	0.00192	0.29	337.6	11.7
47	Zr53	6.3	20	84	0.24	0.5695	0.0693	0.07414	0.00258	0.29	461.0	15.5
48	Zr54	4.4	13	60	0.22	0.5729	0.0730	0.07324	0.00267	0.29	455.6	16.0
49	Zr55	9.3	42	121	0.35	0.5718	0.0724	0.07372	0.00267	0.29	458.5	16.1
50	Zr64	5.4	17	72	0.23	0.5824	0.0775	0.07476	0.00285	0.29	464.8	17.0
51	Zr56	9.0	21	124	0.17	0.5811	0.0786	0.07478	0.00288	0.28	464.9	17.3
52	Zr57	8.6	38	113	0.34	0.5707	0.0786	0.07423	0.00291	0.28	461.6	17.5
53	Zr58	9.1	35	124	0.28	0.5687	0.0794	0.07315	0.00291	0.28	455.1	17.5
54	Zr59 center, dark	8.7	27	118	0.23	0.5683	0.0188	0.07326	0.00216	0.89	455.7	13.0
55	Zr59 rim, bright	1.9	4.3	32	0.14	0.8564	0.0341	0.05136	0.00159	0.78	322.8	9.7
56	Zr60 center, dark	10	36	133	0.27	0.5754	0.0188	0.07398	0.00219	0.91	460.1	13.1
57	Zr60 rim, bright	4.8	11	71	0.16	0.5837	0.0222	0.06815	0.00204	0.79	425.0	12.3
58	Zr61	7.9	22	105	0.21	0.5793	0.0198	0.07509	0.00222	0.86	466.7	13.3
59	Zr62	5.1	18	67	0.26	0.5796	0.0209	0.07427	0.00222	0.83	461.8	13.2
60	aZr1 center	6.8	22	92	0.24	0.5809	0.0205	0.07408	0.00219	0.84	460.7	13.2
61	aZr1 rim	11	31	156	0.20	0.5749	0.0188	0.07368	0.00216	0.89	458.3	13.0
62	aZr2 center	5.6	20	74	0.27	0.5775	0.0219	0.07415	0.00222	0.79	461.1	13.3
63	aZr2 rim	6.0	12	83	0.14	0.5749	0.0197	0.07418	0.00219	0.86	461.3	13.2
64	aZ3 center, dark	12	23	166	0.14	0.5771	0.0206	0.07349	0.00219	0.83	457.2	13.1
65	aZr3 rim, bright	1.1	0.2	22	0.009	0.4018	0.0198	0.05406	0.00165	0.62	339.4	10.1
66	aZr3 rim, bright	1.1	0.2	23	0.007	0.3947	0.0191	0.05211	0.00159	0.63	327.5	9.8
68	aZr3 rim, bright	1.7	0.3	35	0.008	0.3983	0.0174	0.05330	0.00162	0.69	334.8	9.9
69	aZr3 rim, bright	0.9	0.1	18	0.008	0.4008	0.0216	0.05308	0.00165	0.58	333.4	10.1
70	aZr3 rim, bright	0.9	0.1	19	0.007	0.3883	0.0198	0.05331	0.00165	0.61	334.8	10.0
71	aZr4 center, dark	9.2	24	124	0.20	0.5762	0.0200	0.07500	0.00222	0.85	466.2	13.3
72	aZr4 rim	9.1	19	125	0.15	0.5824	0.0194	0.07501	0.00222	0.89	466.3	13.3
73	aZr5 rim	7.5	30	107	0.28	0.5224	0.0179	0.06875	0.00204	0.87	428.6	12.2
74	aZr6 center	6.0	21	81	0.25	0.5741	0.0209	0.07381	0.00219	0.82	459.0	13.2
75	aZr6 rim	4.7	13	65	0.19	0.5755	0.0205	0.07403	0.00219	0.83	460.4	13.2
	AR481											
1	Zr1 center	10	22	142	0.16	0.5733	0.0192	0.07473	0.00222	0.89	464.6	13.2
2	Zr2 center	29	63	402	0.16	0.5838	0.0181	0.07503	0.00219	0.94	466.4	13.2
3	Zr3 center	10	21	146	0.14	0.5837	0.0190	0.07401	0.00219	0.91	460.3	13.1
4	Zr3 rim, bright	6.8	13	94	0.14	0.5929	0.0202	0.07393	0.00219	0.87	459.8	13.1
5	Zr4 center	12	25	164	0.15	0.5772	0.0194	0.07402	0.00219	0.88	460.3	13.1
6	Zr5 center	12	34	168	0.20	0.5957	0.0196	0.07455	0.00219	0.89	463.5	13.2

7	Zr6 center	12	36	160	0.22	0.5642	0.0182	0.07370	0.00216	0.91	458.4	13.0
8	Zr7 center	8.6	22	118	0.18	0.5752	0.0191	0.07427	0.00219	0.89	461.8	13.1
9	Zr7 rim, bright	4.9	11	69	0.16	0.5810	0.0211	0.07370	0.00219	0.82	458.4	13.1
10	Zr8 center	7.9	22	107	0.21	0.5784	0.0193	0.07479	0.00222	0.89	464.9	13.2
11	Zr9 center	12	27	160	0.17	0.5727	0.0185	0.07429	0.00219	0.91	461.9	13.1
12	Zr10 center	2.7	6.2	37	0.17	0.5758	0.0244	0.07429	0.00225	0.71	462.0	13.4
13	Zr10 tip	8.1	15	114	0.14	0.5782	0.0193	0.07374	0.00219	0.89	458.7	13.1
14	Zr11 center	11	27	148	0.18	0.5708	0.0188	0.07394	0.00219	0.90	459.9	13.1
15	Zr13 rim, bright	5.7	11	79	0.14	0.5781	0.0224	0.07450	0.00222	0.77	463.2	13.4
16	Zr13 center	13	32	178	0.18	0.5805	0.0186	0.07421	0.00219	0.92	461.5	13.1
17	Zr14 center	11	33	150	0.22	0.5780	0.0189	0.07383	0.00219	0.91	459.2	13.1
18	Zr14 rim bright	11	30	150	0.20	0.5848	0.0192	0.07445	0.00219	0.90	462.9	13.2
19	Zr15 tip, zoning	11	22	157	0.14	0.5802	0.0187	0.07474	0.00219	0.91	464.6	13.2
20	Zr16 center	13	30	180	0.17	0.5798	0.0186	0.07449	0.00219	0.92	463.1	13.1
21	Zr17 center	31	88	426	0.21	0.5775	0.0179	0.07470	0.00219	0.95	464.4	13.2
22	Zr18 center	12	31	163	0.19	0.5704	0.0186	0.07366	0.00216	0.90	458.2	13.0
23	Zr18 rim, bright	7.2	15	100	0.15	0.5955	0.0207	0.07425	0.00219	0.85	461.7	13.2
24	Zr19 center	11	28	148	0.19	0.5782	0.0188	0.07402	0.00219	0.91	460.3	13.1
25	Zr20 center	6.7	20	91	0.21	0.5843	0.0202	0.07378	0.00219	0.86	458.9	13.1
26	Zr21 center	8.3	23	114	0.20	0.5705	0.0196	0.07366	0.00219	0.86	458.1	13.1
27	Zr22 center	8.4	28	114	0.24	0.5769	0.0195	0.07361	0.00216	0.87	457.8	13.1
28	Zr22 rim, bright	1.8	1.7	32	0.05	0.4735	0.0209	0.06225	0.00189	0.69	389.3	11.4
29	Zr23 center	8.0	26	109	0.24	0.5683	0.0190	0.07357	0.00216	0.88	457.6	13.1
30	Zr24 center	19	66	256	0.26	0.5693	0.0183	0.07412	0.00219	0.92	460.9	13.1
31	Zr24 rim	8.7	20	121	0.16	0.5863	0.0200	0.07376	0.00219	0.87	458.8	13.1
32	Zr25 center	14	33	191	0.17	0.5779	0.0185	0.07385	0.00216	0.91	459.3	13.1
33	Zr26 center	11	28	153	0.18	0.5753	0.0187	0.07391	0.00219	0.91	459.6	13.1
34	Zr27 center	14	38	193	0.20	0.5694	0.0184	0.07375	0.00216	0.91	458.7	13.1
35	Zr28 center	9.4	30	128	0.23	0.5763	0.0191	0.07386	0.00219	0.90	459.4	13.1
36	Zr29 center, dark	8.3	24	128	0.19	0.5078	0.0174	0.06636	0.00201	0.88	414.2	12.1
37	Zr29 rim, bright	1.4	0.3	28	0.010	0.4363	0.0254	0.05344	0.00174	0.56	335.6	10.6
38	Zr29 rim, bright	1.3	0.1	27	0.005	0.4432	0.0249	0.05345	0.00171	0.57	335.7	10.5
39	Zr29 rim, bright	1.4	0.1	30	0.003	0.3982	0.0196	0.05326	0.00165	0.63	334.5	10.2
40	Zr30 center	9.1	27	125	0.22	0.5697	0.0195	0.07362	0.00222	0.88	457.9	13.3
41	Zr31 center	21	52	283	0.19	0.5832	0.0188	0.07490	0.00225	0.93	465.6	13.5
42	Zr32 center	73	169	1000	0.17	0.5760	0.0177	0.07497	0.00225	0.98	466.0	13.4
43	Zr32 tip, bright	7.5	16	103	0.16	0.5778	0.0200	0.07470	0.00225	0.87	464.4	13.5
44	Zr33 center	13	36	176	0.21	0.5711	0.0186	0.07382	0.00222	0.92	459.1	13.3
45	Zr34 center	5.3	9.2	74	0.12	0.5789	0.0207	0.07442	0.00225	0.85	462.7	13.4
46	Zr36 center, zoning	7.1	17	99	0.18	0.5717	0.0204	0.07388	0.00222	0.84	459.5	13.4
47	Zr37 dark zone	21	57	285	0.20	0.5738	0.0185	0.07459	0.00222	0.92	463.8	13.4
48	Zr38 rim, dark	12	29	163	0.17	0.5821	0.0197	0.07481	0.00225	0.89	465.1	13.4
49	Zr39 center, dark	15	34	206	0.16	0.5694	0.0184	0.07352	0.00219	0.92	457.3	13.2
50	Zr39 tip	7.9	18	108	0.16	0.5817	0.0200	0.07450	0.00222	0.87	463.2	13.4

51	Zr40 dark zone	15	42	211	0.20	0.5736	0.0184	0.07381	0.00219	0.93	459.1	13.2
52	Zr41 center, zoning	13	40	173	0.23	0.5794	0.0189	0.07446	0.00222	0.91	463.0	13.3
53	Zr42 tip, zoning	6.5	14	90	0.16	0.5753	0.0204	0.07423	0.00222	0.84	461.6	13.4
54	Zr43 center	10	38	148	0.26	0.5403	0.0206	0.07023	0.00213	0.80	437.5	12.8
55	Zr44 center, zoning	15	43	197	0.22	0.5740	0.0184	0.07397	0.00219	0.92	460.0	13.2
56	Zr46 center	8.5	21	118	0.18	0.5737	0.0193	0.07370	0.00219	0.88	458.4	13.2
57	Zr45 center	17	28	241	0.12	0.5755	0.0184	0.07443	0.00222	0.93	462.8	13.2
58	Zr47 center	9.9	24	135	0.18	0.5827	0.0197	0.07428	0.00222	0.89	461.9	13.3
59	Zr48 center, zoning	7.3	19	100	0.19	0.5856	0.0206	0.07402	0.00222	0.85	460.3	13.3
60	Zr49 center, dark	12	26	169	0.15	0.5730	0.0189	0.07441	0.00222	0.90	462.7	13.2
61	Zr50 center, dark	11	36	142	0.25	0.5757	0.0197	0.07430	0.00222	0.88	462.0	13.3
62	Zr51 center	15	44	202	0.22	0.5726	0.0186	0.07456	0.00219	0.91	463.5	13.2
63	Zr51 rim, dark	8.4	16	117	0.13	0.5754	0.0212	0.07384	0.00219	0.80	459.3	13.2
64	Zr52 center, zoning	8.8	32	116	0.27	0.5781	0.0206	0.07437	0.00222	0.84	462.4	13.3
65	Zr53 center, zoning	9.0	18	125	0.14	0.5776	0.0200	0.07472	0.00222	0.86	464.5	13.3
66	Zr54 center	9.6	26	130	0.20	0.5839	0.0197	0.07436	0.00219	0.88	462.3	13.2
67	Zr55 center	11	40	158	0.26	0.5279	0.0183	0.06777	0.00201	0.85	422.7	12.1
68	Zr55 tip, dark	15	32	218	0.15	0.5568	0.0181	0.07188	0.00213	0.91	447.5	12.7

U-Pb LA-ICPMS results on rutile

#	#grain	Pb ppm	U ppm	Pb^{207}/U^{235}	±2σ	Pb^{206}/U^{238}	±2σ	Rho	Pb^{206}/U^{238} age	±2σ
	AR483									
1	Rt1	0.2	5.4	0.3857	0.0317	0.05300	0.00195	0.45	332.9	12.0
2	Rt2	0.1	5.5	0.3936	0.0334	0.05241	0.00198	0.45	329.3	12.1
3	Rt4	0.2	5.8	0.7002	0.0431	0.05640	0.00207	0.60	353.7	12.6
4	Rt6	0.2	5.5	0.3960	0.0383	0.05219	0.00204	0.40	328.0	12.5
5	Rt7	0.4	6.2	2.7069	0.1344	0.06814	0.00264	0.78	424.9	15.9
6	Rt8	0.2	5.6	0.4311	0.0384	0.05201	0.00201	0.43	326.9	12.3
7	Rt9	0.4	11.7	0.5544	0.0339	0.05373	0.00192	0.58	337.4	11.7
8	Rt10	0.2	7.3	0.4038	0.0371	0.05274	0.00201	0.42	331.3	12.2
9	Rt11	0.3	7.1	1.7840	0.1015	0.06252	0.00246	0.69	391.0	14.9
10	Rt12	0.2	5.9	0.4015	0.0380	0.05300	0.00204	0.41	332.9	12.5
11	Rt13	0.2	8.4	0.3904	0.0327	0.05254	0.00195	0.44	330.1	11.9
12	Rt14	0.2	7.2	0.3838	0.0348	0.05216	0.00195	0.41	327.8	12.0
13	Rt15	0.2	7.8	0.4198	0.0322	0.05299	0.00192	0.47	332.9	11.8
14	Rt17	0.2	8.9	0.4088	0.0364	0.05258	0.00198	0.42	330.4	12.2
15	Rt18	0.2	7.8	0.3819	0.0369	0.05148	0.00198	0.40	323.6	12.2
16	Rt19	0.2	5.8	0.4330	0.0399	0.05260	0.00198	0.41	330.5	12.2
17	Rt20	0.2	8.2	0.3973	0.0363	0.05256	0.00198	0.41	330.2	12.2
18	Rt21	0.2	6.1	0.3806	0.0370	0.05167	0.00198	0.39	324.8	12.1
19	Rt22	0.3	10.3	0.4105	0.0401	0.05245	0.00204	0.40	329.5	12.5
20	Rt24	0.2	7.8	0.3996	0.0316	0.05148	0.00186	0.46	323.6	11.4
21	Rt26	0.3	9.7	0.4140	0.0346	0.05216	0.00192	0.44	327.7	11.8

22	Rt27	0.1	5.4	0.3879	0.0390	0.05178	0.00198	0.38	325.5	12.1
23	Rt28	0.2	8.9	0.4084	0.0291	0.05304	0.00186	0.49	333.2	11.4
24	Rt29	0.2	8.0	0.3818	0.0325	0.05230	0.00189	0.42	328.6	11.6
25	Rt30	0.2	7.7	0.3902	0.0309	0.05168	0.00183	0.45	324.8	11.3
26	Rt32	0.2	7.6	0.3894	0.0385	0.05215	0.00201	0.39	327.7	12.3
27	Rt33	0.2	8.2	0.4067	0.0313	0.05301	0.00186	0.46	333.0	11.5
28	Rt34	0.2	8.4	0.3893	0.0377	0.05252	0.00198	0.39	329.9	12.1
29	Rt35	0.2	7.0	0.4606	0.0356	0.05317	0.00189	0.46	333.9	11.7
30	Rt36	0.2	8.2	0.4040	0.0314	0.05263	0.00186	0.46	330.6	11.4
31	Rt37	0.1	4.0	0.3951	0.0281	0.05371	0.00195	0.51	337.3	11.9
32	Rt38	0.1	3.2	0.4133	0.0309	0.05222	0.00192	0.49	328.1	11.7
33	Rt41	0.1	4.2	0.7843	0.0424	0.05617	0.00201	0.66	352.3	12.2
34	Rt42	0.3	9.5	0.4096	0.0274	0.05329	0.00189	0.53	334.7	11.6
35	Rt43	0.3	8.8	0.7888	0.0426	0.05596	0.00198	0.66	351.0	12.2
36	Rt44	0.2	8.9	0.4037	0.0273	0.05325	0.00189	0.52	334.4	11.5
37	Rt45	0.2	6.9	0.4135	0.0310	0.05380	0.00195	0.48	337.8	11.9
38	Rt46	0.2	8.0	0.4041	0.0288	0.05513	0.00195	0.50	346.0	12.0
39	Rt47	0.2	8.6	0.3954	0.0273	0.05247	0.00186	0.51	329.7	11.3
40	Rt48	0.2	8.6	0.4056	0.0288	0.05247	0.00186	0.50	329.7	11.4
41	Rt49	0.2	6.4	0.4038	0.0308	0.05312	0.00192	0.47	333.6	11.7
42	Rt50	0.3	9.7	0.3808	0.0252	0.05243	0.00183	0.53	329.4	11.2
43	Rt51	0.2	7.7	0.3867	0.0284	0.05271	0.00186	0.48	331.1	11.4
44	Rt52	0.3	11.8	0.3870	0.0391	0.05220	0.00204	0.39	328.0	12.5
45	Rt53	0.2	7.4	0.3656	0.0351	0.05214	0.00195	0.39	327.7	12.0
46	Rt55	0.2	6.0	0.3968	0.0353	0.05312	0.00195	0.41	333.6	11.9
47	Rt56	0.3	10.1	0.3919	0.0319	0.05220	0.00189	0.44	328.0	11.6
48	Rt57	0.3	9.4	0.4031	0.0283	0.05271	0.00183	0.49	331.1	11.3
49	Rt58	0.3	10.2	0.3866	0.0265	0.05177	0.00180	0.51	325.4	11.0
50	Rt59	0.3	9.7	0.3667	0.0267	0.05174	0.00180	0.48	325.2	11.0
51	Rt60	0.2	9.3	0.4066	0.0411	0.05234	0.00204	0.39	328.9	12.4
	AR481 isolated grains									
1	Rt1	0.2	6.3	0.6072	0.0524	0.05299	0.00207	0.45	332.8	12.6
2	Rt5	0.2	6.4	0.4385	0.0381	0.05199	0.00189	0.42	326.8	11.6
3	Rt6	0.3	10.1	0.4078	0.0351	0.05139	0.00189	0.43	323.1	11.6
4	Rt11	0.1	3.9	0.4501	0.0534	0.05235	0.00216	0.35	328.9	13.3
5	Rt13	0.5	18.9	0.4795	0.0278	0.05273	0.00177	0.58	331.2	10.8
6	Rt16	0.3	11.5	0.3893	0.0324	0.05163	0.00186	0.43	324.5	11.3
7	Rt17	0.2	7.7	0.6313	0.0430	0.05378	0.00192	0.52	337.7	11.7
8	Rt17	0.2	7.1	0.3901	0.0373	0.05288	0.00195	0.39	332.2	11.9
9	Rt23	0.1	4.3	0.3878	0.0430	0.05273	0.00201	0.34	331.3	12.3
10	Rt25	0.3	10.7	0.3930	0.0274	0.05270	0.00177	0.48	331.1	10.9
11	Rt26	0.1	5.0	0.4138	0.0418	0.05191	0.00195	0.37	326.2	12.0
12	Rt28	0.1	2.1	0.6196	0.0788	0.05328	0.00246	0.36	334.7	15.1

13	Rt29	0.3	11.5	0.4002	0.0341	0.05256	0.00189	0.42	330.2	11.5
14	Rt32	0.3	10.7	0.3720	0.0342	0.05286	0.00189	0.39	332.0	11.6
15	Rt34	0.1	1.7	0.5142	0.0784	0.05272	0.00252	0.31	331.2	15.5
16	Rt35	0.1	2.4	0.9982	0.0979	0.05777	0.00258	0.46	362.0	15.8
17	Rt36	0.3	12.4	0.4005	0.0310	0.05178	0.00177	0.44	325.4	10.9
18	Rt38	0.5	18.5	0.3903	0.0225	0.05205	0.00168	0.56	327.1	10.2
19	Rt41	0.4	13.7	0.3914	0.0338	0.05150	0.00183	0.41	323.7	11.2
	AR481 in situ									
1	Rt1	0.24	5.0	1.7883	0.1019	0.06316	0.00243	0.68	394.8	14.8
2	Rt2	0.22	5.0	1.4869	0.0734	0.06166	0.00222	0.73	385.7	13.4
3	Rt3	0.37	4.8	3.5791	0.1715	0.07570	0.00291	0.80	470.4	17.5
4	Rt4	0.22	4.1	2.0815	0.1667	0.06602	0.00318	0.60	412.1	19.2
5	Rt7	0.20	5.2	1.1146	0.0998	0.05779	0.00261	0.50	362.2	15.9
6	Rt6	0.12	3.3	0.7264	0.0663	0.05678	0.00234	0.45	356.0	14.3
7	Rt8	0.29	3.4	1.1272	0.0955	0.05995	0.00261	0.51	375.3	15.8
8	Rt9	0.15	3.7	1.1578	0.0712	0.05940	0.00225	0.62	372.0	13.6
9	Rt11	0.12	4.3	0.4159	0.0371	0.05386	0.00201	0.42	338.1	12.4
10	Rt12	0.23	4.6	1.7735	0.0958	0.06284	0.00237	0.70	392.8	14.4
11	Rt14-1	0.06	2.3	0.4066	0.0305	0.05424	0.00192	0.47	340.5	11.8
12	Rt14-2	0.08	2.8	0.3882	0.0283	0.05451	0.00192	0.48	342.2	11.8
13	Rt14-3	0.07	2.4	0.4266	0.0313	0.05514	0.00195	0.48	346.0	12.0
14	Rt14-4	0.06	1.9	0.6872	0.0634	0.05675	0.00234	0.45	355.8	14.3
15	Rt14-5	0.08	1.0	4.2649	0.2505	0.08074	0.00360	0.76	500.5	21.6
16	Rt14-6	0.04	1.1	0.8691	0.0755	0.05712	0.00237	0.48	358.1	14.5
17	Rt14-7	0.03	1.0	0.5453	0.0637	0.05372	0.00234	0.37	337.3	14.4
18	Rt14-8	0.02	0.5	0.7251	0.0841	0.05541	0.00255	0.40	347.7	15.6
19	Rt15	0.08	2.1	1.1499	0.0598	0.05934	0.00210	0.68	371.6	12.8
20	Rt16	0.06	2.2	0.4493	0.0343	0.05472	0.00198	0.47	343.4	12.2

U-Pb LA-ICPMS results on titanite

#	# Ttn	Pb ppm	Th ppm	U ppm	Th/U	Pb^{207}/U^{235}	±2σ	Pb^{206}/U^{238}	±2σ	Rho	Pb^{206}/U^{238} Ma	±2σ
	AR481											
1	Ttn-1	0.8	0.4	1.7	0.25	14.60	0.58	0.1673	0.0061	0.91	997	34
2	Ttn-2	1.0	0.3	1.5	0.18	21.23	0.78	0.2198	0.0076	0.94	1281	40
3	Ttn-3	0.9	0.2	1.7	0.11	17.26	0.66	0.1871	0.0067	0.93	1106	36
4	Ttn-4	1.1	0.1	4.6	0.03	7.33	0.26	0.1056	0.0035	0.91	647	20
5	Ttn-5-1	0.8	0.2	2.5	0.08	9.54	0.35	0.1225	0.0041	0.91	745	24
6	Ttn-5-2	2.0	0.1	1.8	0.07	38.07	1.37	0.3631	0.0125	0.96	1997	59
7	Ttn-6a	1.0	0.1	1.7	0.07	19.50	0.71	0.2068	0.0071	0.94	1212	38
8	Ttn-6b	0.9	0.0	1.0	0.04	30.55	1.16	0.2986	0.0107	0.95	1685	53
9	Ttn-6c	0.8	0.1	1.2	0.08	22.58	1.14	0.2326	0.0106	0.90	1348	56
10	Ttn-7	0.7	0.3	1.7	0.15	13.60	0.74	0.1594	0.0075	0.86	953	42

11	Ttn-8	0.8	0.5	1.7	0.29	14.01	0.60	0.1628	0.0062	0.89	972	35
12	Ttn-9	1.0	0.2	1.6	0.13	20.25	0.75	0.2138	0.0074	0.94	1249	39
13	Ttn-10	1.0	0.2	1.9	0.12	16.43	0.68	0.1806	0.0068	0.91	1070	37
14	Ttn-11	0.7	0.2	2.4	0.09	9.39	0.47	0.1222	0.0051	0.84	743	30
15	Ttn-13	0.7	0.7	1.5	0.51	15.60	0.61	0.1754	0.0062	0.91	1042	34
16	Ttn-14-1	0.9	1.9	2.1	0.91	12.79	0.63	0.1509	0.0065	0.87	906	36
17	Ttn-14-2	1.5	0.4	2.8	0.15	17.12	0.71	0.1856	0.0071	0.91	1097	38
18	Ttn-15	0.9	0.1	1.3	0.10	23.64	0.88	0.2399	0.0084	0.94	1386	44
19	Ttn-17	1.4	0.4	1.5	0.28	29.39	1.04	0.2872	0.0096	0.95	1627	48

Tableau 5: REE contents in zircons.

Sample	**AR483**														**AR481**	
Analyse	**Zr 11 core**	**Zr 11 rim**	**Zr 15 core**	**Zr 19 core**	**Zr 19 rim**	**Zr 23**	**Zr 52/1**	**Zr 52/2**	**Zr59 core**	**Zr 59 rim**	**Zr60 core**	**aZr2 core**	**aZr3 core**	**aZr3 rim**	**Zr29 rim**	**Zr 30 core**
Age	*462 Ma*	*393 Ma*	*364 Ma*	*460 Ma*	*390 Ma*	*336 Ma*	*338 Ma*	*338 Ma*	*456 Ma*	*323 Ma*	*460 Ma*	*461 Ma*	*457 Ma*	*330 Ma*	*335 Ma*	*458 Ma*
REE in ppm																
La139	0.0068	0.0338	0.0287	0.0278	0.0336	0.0109	<0.0123	0.0299	0.012	0.0165	0.0072	<0.0066	<0.0073	<0.0115	<0.0103	0.0171
Ce140	2.127	1.089	2.9	2.407	0.795	1.411	1.817	2.09	1.497	0.218	2.74	1.887	2.014	0.761	0.538	2.482
Pr141	0.006	0.0159	0.0269	0.0067	0.0254	0.0081	0.0172	0.0224	0.0082	0.0112	0.0129	0.0071	0.0065	<0.0061	0.0081	0.0074
Nd146	0.149	0.329	0.474	0.181	0.213	0.425	0.371	0.421	0.17	0.146	0.24	0.142	0.146	0.173	0.279	0.151
Sm147	0.371	0.405	0.933	0.416	0.773	3.53	1.749	2.58	0.267	0.205	0.637	0.314	0.266	0.375	1.336	0.405
Eu153	0.251	0.4	0.563	0.25	0.659	3.03	1.503	2.409	0.163	0.212	0.452	0.235	0.1813	0.39	1.451	0.255
Gd157	3.16	3.7	5.23	3.26	6.14	28.67	13.06	20.48	1.943	2.373	4.96	2.666	2.83	3.63	12.64	3.19
Tb159	1.261	1.134	1.794	1.333	1.306	6	3.06	4.55	0.793	0.744	1.998	1.082	1.246	0.986	3.53	1.276
Dy163	20.11	9.91	24.1	20.69	8.83	37.05	20.94	28.02	12.9	7.37	28.95	16.55	21.23	8.44	31.85	19.55
Ho165	8.91	3.05	10.11	9.43	1.92	7.92	4.79	5.82	5.81	1.821	12.29	7.25	10.35	2.491	8.66	8.65
Er166	51.19	13.82	54.75	54.31	6.83	26.61	17.45	19.06	32.97	5.82	65.26	40.22	62.63	10.75	31.37	48.44
Tm169	12.78	3.14	13.1	13.34	1.112	4.43	3.16	3.17	8.56	0.846	15.81	9.88	15.91	2.041	5.17	11.99
Yb172	137.11	32.76	138.96	148.11	9.98	34.04	26.48	24.84	94.02	6.4	165.21	105.79	177.32	17.92	41.46	129.66
Lu175	34.4	8.03	33.89	36.48	2.101	6.26	5.54	4.61	24.43	1.178	40.06	26.47	45.97	3.67	7.66	32.07
Total (ppm)	272	78	287	290	41	159	100	118	184	27	339	212	340	52	146	258
Lu_N/Sm_N	557.1	119.1	218.7	527.8	16.3	10.7	19.1	10.7	551.6	34.7	378.7	507.6	1038.1	59.0	34.5	475.8
Dy_N/Sm_N	32.6	14.7	15.5	29.9	6.9	6.3	7.2	6.5	29.1	21.7	27.4	31.7	47.9	13.6	14.3	29.0
Lu_N/Dy_N	17.11	8.10	14.07	17.63	2.38	1.69	2.65	1.64	18.94	1.60	13.84	15.99	21.65	4.35	2.40	16.41
Eu/Eu*	0.71	0.99	0.78	0.65	0.92	0.92	0.96	1.01	0.69	0.93	0.78	0.78	0.64	1.02	1.08	0.69
Ce/Ce*	79.9	11.4	25.3	42.8	6.6	36.4	/	19.6	36.4	3.9	69.3	/	/	/	/	53.3

ANNEXE 3: supplementary materials of Chapter 5

Table S1: LA-ICPMS material-analytical techniques

Laboratory & Sample Preparation	
Laboratory name	Laboratoire Magmas & Volcans, Univ. Clermont-Auvergne, France
Sample type/mineral	Monazite
Sample preparation	Thin section
Imaging	CL, FEI QUANTA 450w, 15 kV, 19mm working distance, Univ. Bourgogne-Franche Comté
Laser ablation system	
Make, Model & type	Resonetics/M-50E 193nm, Excimer
Ablation cell & volume	Laurin Cell ® two volumes cell, Laurin Technic Ltd., volume ca. 1-2 cm^3
Laser wavelength	193 nm
Pulse width	< 4 ns
Fluence	3.5 J.cm^{-2}
Repetition rate	1 Hz
Spot size	15 µm
Sampling mode / pattern	Single spot
Carrier gas	100% He, Ar make-up gas and N$_2$ combined using the Squid® device from RESOlution Instruments.
Background collection	30 secs
Ablation duration	60 secs
Wash-out delay	30 secs
Cell carrier gas flow	0.75 l/min
ICP-MS Instrument	
Make, Model & type	Agilent 7500cs, Q-ICP-MS
Sample introduction	Via conventional tubing
RF power	1350W
Make-up gas flow	0.87 l/min Ar
Detection system	Single collector secondary electron multiplier
Masses measured	204, 206, 207, 208, 232, 238
Integration time per peak	10 ms
Total integration time per reading	130 ms *(should represent the time resolution of the data)*
Sensitvity / Efficiency	20000 cps/ppm ^{238}U (44µm, 10Hz)
Dead time	35 ns
Data Processing	
Gas blank	30 second on-peak
Calibration strategy	Trebilcock used as primary reference material, Bananeira used as secondary reference material (Quality Control)
Reference Material info	Trebilcock (Tomascak et al., 1996) Bananeira (Gonçalves et al., 2016)
Data processing package used / Correction for LIEF	GLITTER ® (van Achterbergh et al., 2001)
Mass discrimination	Standard-sample bracketing with ^{207}Pb/^{206}Pb and ^{206}Pb/^{238}U normalized to reference material Trebilcock

Common-Pb correction, composition and uncertainty	No common-Pb correction.
Uncertainty level & propagation	Ages are quoted at 2sigma absolute, propagation is by quadratic addition according to Horstwood et al. (2003). Reproducibility and age uncertainty of reference material are propagated.
Quality control / Validation	Bananeira: lower intecept = 508 ± 12 Ma (2SD, MSWD = 0.41; N = 16)
Other information	For detailed method description see Paquette and Tiepolo (2007), Paquette et al. (2014) and Hurai et al. (2010).

Table S2: U-Pb data. Mz: monazite; Bt: biotite; Ms : muscovite ; Std : Staurolite ; Pl : plagioclase. a: data are corrected for U-Pb fractionation and for instrumental mass bias but uncorrected for commun Pb. b: % conc = percentage of concordance ((^{206}*Pb/*^{238}*U)age / (*^{207}*Pb/*^{235}*)age) x 100*

			Contents (ppm)				Corrected Ratios (a)					Age (Ma)				(b)
			Pb	Th	U								±		±	%
Texture	#	#Mz	ppm	ppm	ppm	Th/U	^{207}Pb/^{235}U	± 2σ	^{206}Pb/^{238}U	± 2σ	Rho	^{207}Pb/^{235}U	2σ	^{206}Pb/^{238}U	2σ	Con
Emosson Micaschist (AR14)																
Bt-Ms	1	Mz1/1	1899	56485	3318	17.0	0.406	0.019	0.0498	0.0019	0.81	346	14	313	12	90
Bt-Ms	2	Mz1/2	1877	58868	3016	19.5	0.424	0.019	0.0498	0.0019	0.85	359	14	313	12	87
Bt-Ms	3	Mz2/1	1636	47417	2998	15.8	0.461	0.020	0.0505	0.0020	0.87	385	14	317	12	83
Bt-Ms	4	Mz3/1	1743	52233	3339	15.6	0.416	0.019	0.0497	0.0019	0.83	353	14	313	12	89
Bt-Ms	5	Mz4/1	1660	50243	2886	17.4	0.461	0.022	0.0508	0.0020	0.80	385	16	320	12	83
Bt-Ms	6	Mz5/1	2019	62614	3270	19.1	0.405	0.020	0.0502	0.0020	0.80	345	14	316	12	91
Bt-Ms	7	Mz5/2	1938	59713	3229	18.5	0.411	0.021	0.0509	0.0020	0.78	350	15	320	12	92
Bt-Ms	8	Mz6/1	1771	55279	2351	23.5	0.577	0.028	0.0526	0.0021	0.81	462	18	331	13	71
Bt-Ms	9	Mz7/1	2079	62612	3043	20.6	0.441	0.021	0.0526	0.0021	0.81	371	15	331	13	89
Bt-Ms	10	Mz9/1	1668	51049	2446	20.9	0.491	0.024	0.0517	0.0020	0.81	405	16	325	12	80
Bt-Ms	11	Mz10/1	1815	54870	2450	22.4	0.464	0.023	0.0526	0.0021	0.80	387	16	331	13	85
Bt-Ms	12	Mz11/1	1771	52428	2781	18.8	0.439	0.021	0.0523	0.0020	0.83	369	14	329	13	89
Bt-Ms	13	Mz12/1	1401	43975	2218	19.8	0.531	0.029	0.0533	0.0021	0.72	433	20	335	13	77
Bt-Ms	14	Mz13/1	1775	53898	2986	18.0	0.420	0.021	0.0515	0.0020	0.79	356	15	324	13	91
Bt-Ms	15	Mz14/1	1985	61510	3051	20.2	0.427	0.021	0.0513	0.0020	0.82	361	15	322	12	89
Bt-Ms	16	Mz15/1	2002	61416	3925	15.6	0.419	0.020	0.0499	0.0020	0.83	355	14	314	12	88
Bt-Ms	17	Mz16/1	1891	58420	3599	16.2	0.390	0.020	0.0497	0.0020	0.79	334	14	312	12	93
Bt-Ms	18	Mz17/1	1414	38220	2999	12.7	0.529	0.027	0.0527	0.0021	0.78	431	18	331	13	77
Bt-Ms	19	Mz17/2	1883	55640	3797	14.7	0.427	0.020	0.0501	0.0020	0.83	361	15	315	12	87
Bt-Ms	20	Mz18/1	1609	50754	2376	21.4	0.423	0.022	0.0507	0.0020	0.76	358	16	319	12	89
Bt-Ms	21	Mz19/1	1463	45309	2257	20.1	0.607	0.031	0.0541	0.0022	0.80	482	19	340	13	71
Bt-Ms	22	Mz21/1	1805	51604	4064	12.7	0.430	0.021	0.0501	0.0020	0.83	363	15	315	12	87
Bt-Ms	23	Mz21/2	1874	53144	4388	12.1	0.414	0.021	0.0498	0.0020	0.81	352	15	313	12	89
Bt-Ms	24	Mz20/1	1754	53109	2652	20.0	0.537	0.027	0.0539	0.0022	0.80	436	18	339	13	78
Bt-Ms	25	Mz22/1	1597	41513	3856	10.8	0.465	0.025	0.0525	0.0021	0.74	388	18	330	13	85
Bt-Ms	26	Mz22/2	1568	40894	4286	9.5	0.398	0.020	0.0496	0.0020	0.79	340	15	312	12	92
Bt-Ms	27	Mz23/1	1907	56581	3525	16.1	0.427	0.023	0.0503	0.0020	0.75	361	16	316	13	88

Bellachat Micaschist (AR736)																
Bt-Ms	1	Mz1/1	303	7856	863	9.1	0.607	0.034	0.0496	0.0020	0.71	482	22	312	12	**65**
Bt-Ms	2	Mz2/1	1905	50651	4783	10.6	0.442	0.021	0.0493	0.0019	0.84	371	14	310	12	83
Std	3	Mz3/1	2059	54117	5093	10.6	0.438	0.020	0.0499	0.0020	0.85	369	14	314	12	85
Std	4	Mz3/2	1908	50896	5047	10.1	0.393	0.018	0.0491	0.0019	0.86	336	13	309	12	92
Std	5	Mz3/3	1776	40207	6253	6.4	0.420	0.019	0.0493	0.0019	0.86	356	14	310	12	87
Bt-Ms	6	Mz4/1	1978	54994	4685	11.7	0.395	0.019	0.0495	0.0019	0.82	338	14	312	12	92
Bt-Ms	7	Mz5/1	2164	47830	6107	7.8	0.875	0.037	0.0527	0.0020	0.90	638	20	331	13	**52**
Bt-Ms	8	Mz5/2	1921	47998	5828	8.2	0.389	0.017	0.0493	0.0019	0.88	333	13	310	12	93
Bt-Ms	9	Mz6/1	1275	29876	3729	8.0	0.486	0.024	0.0534	0.0021	0.79	402	17	**335**	**13**	**83**
Bt-Ms	10	Mz7/1	1402	34606	4174	8.3	0.419	0.019	0.0497	0.0020	0.88	355	13	312	12	88
Bt	11	Mz8/1	1547	36784	5249	7.0	0.393	0.016	0.0493	0.0018	0.90	337	12	310	11	92
Pl	12	Mz11/2	1569	37023	4469	8.3	0.473	0.021	0.0516	0.0019	0.84	393	14	324	12	83
Pl	13	Mz12/1	1777	43555	4898	8.9	0.394	0.018	0.0496	0.0019	0.84	337	13	312	11	93
Pl	14	Mz12/2	1787	45311	4349	10.4	0.416	0.019	0.0516	0.0020	0.84	353	13	324	12	92
Std	15	Mz14/1	1757	44933	4612	9.7	0.396	0.018	0.0493	0.0019	0.85	339	13	310	11	92
Std	16	Mz15/1	1521	36171	3825	9.5	0.452	0.020	0.0544	0.0021	0.86	378	14	342	13	90
Std	17	Mz15/2	1595	38060	4310	8.8	0.414	0.019	0.0523	0.0020	0.83	352	14	328	12	93
Std	18	Mz16/1	1772	39551	5331	7.4	0.402	0.017	0.0521	0.0020	0.89	343	12	327	12	95
Std	19	Mz16/2	1515	35996	3919	9.2	0.467	0.022	0.0533	0.0020	0.83	389	15	334	12	86
Pl	20	Mz18/1	1738	45345	4498	10.1	0.412	0.019	0.0525	0.0020	0.83	350	14	330	12	94
Bt-Ms	21	Mz17/1	1989	54253	4879	11.1	0.395	0.017	0.0494	0.0019	0.87	338	13	311	12	92
Bt-Ms	22	Mz17/2	1843	45563	5550	8.2	0.397	0.017	0.0494	0.0019	0.87	339	13	311	12	92

ANNEXE 4: supplementary materials of Chapter 6

Table S1.1: Operating conditions and instrument settings for U-Pb analyses of the sample AR37

Laboratory & Sample Preparation	
Laboratory name	Laboratoire Magmas & Volcans, Clermont-Ferrand, France
Sample type/mineral	Magmatic zircon
Sample preparation	Conventional mineral separation, 1 inch resin mount, 0.25μm polish to finish (Université Montpellier
Imaging	CL, FEI QUANTA 450w, 15 kV, 19mm working distance (Université Bourgogne-Franche Comté)
Laser ablation system	
Make, Model & type	Resonetics/M-50E 193nm, Excimer
Ablation cell & volume	Laurin Cell ® two volumes cell, Laurin Technic Ltd., volume ca. 1-2 cm^3
Laser wavelength	193 nm
Pulse width	< 4 ns
Fluence	3.5 J.cm^{-2}
Repetition rate	3 Hz
Spot size	27 μm
Sampling mode / pattern	Single spot
Carrier gas	100% He, Ar make-up gas and N$_2$ combined using the Squid® device from RESOlution Instruments.
Background collection	30 secs
Ablation duration	60 secs
Wash-out delay	30 secs
Cell carrier gas flow	0.75 l/min
ICP-MS Instrument	
Make, Model & type	Agilent 7500cs, Q-ICP-MS
Sample introduction	Via conventional tubing
RF power	1350W
Make-up gas flow	0.87 l/min Ar
Detection system	Single collector secondary electron multiplier
Masses measured	204, 206, 207, 208, 232, 238
Integration time per peak	10 ms
Total integration time per reading	130 ms *(should represent the time resolution of the data)*
Sensitvity / Efficiency	20000 cps/ppm ^{238}U (44μm, 10Hz)
Dead time	35 ns
Data Processing	
Gas blank	30 second on-peak
Calibration strategy	GJ-1 used as primary reference material, 91500 used as secondary reference material (Quality Control)
Reference Material info	91500 (Wiedenbeck et al., 1995) GJ1 (Jackson et al., 2004)
Data processing package used / Correction for LIEF	GLITTER ® (van Achterbergh et al., 2001)
Mass discrimination	Standard-sample bracketing with ^{207}Pb/^{206}Pb and ^{206}Pb/^{238}U normalized to reference material GJ-1
Common-Pb correction, composition and uncertainty	No common-Pb correction. Analyses discarded when discordance >10%

Uncertainty level & propagation	Ages are quoted at 2sigma absolute, propagation is by quadratic addition according to Horstwood et al. (2003). Reproducibility and age uncertainty of reference material are propagated.
Quality control / Validation	91500: Concordia age = 1064 ± 5 Ma (2SD, $MSWD_{(C+E)}$ = 0.2; *N=39*)
Other information	For detailed method description see Tiepolo (2003), Paquette and Tiepolo (2007) and Hurai et al. (2010) For detailed laser technical description see Müller et al. (2009).

Table S1.2 : Operating conditions and instrument settings for U-Pb analyses of all samples, with the exception of AR 37

Laboratory & Sample Preparation		
Laboratory name	Laboratoire Magmas & Volcans, Clermont-Ferrand, France	
Sample type/mineral	Magmatic zircon and monazite	
Sample preparation	Conventional mineral separation: heavy liquids, Frantz magnetic separator, handpicking under binocular microscope 1 inch Epotek® resin mount, 0.25um polish to finish (Université Montpellier)	
Imaging	CL, FEI QUANTA 450w, 15 kV, 19mm working distance (Université Bourgogne-Franche Comté)	
Laser ablation system		
Make, Model & type	Resonetics/M-50E 193nm, Excimer	
Ablation cell & volume	Laurin Cell ® two volumes cell, Laurin Technic Ltd., volume ca. $1cm^3$	
Laser wavelength	193 nm	
Pulse width	< 4 ns	
Fluence	*Zircon* 2.5 $J.cm^{-2}$ and 2.0 $J.cm^{-2}$	*Monazite* 2.0 $J.cm^{-2}$
Repetition rate	3 Hz	3 Hz
Spot size	27 µm	12 µm
Sampling mode / pattern	Single spot	
Carrier gas	100% He, Ar make-up gas and N_2 combined using the Squid® device from RESOlution Instruments.	
Background collection	30 secs	
Ablation duration	60 secs	
Wash-out delay	30 secs	
Cell carrier gas flow	0.70 l/min He	
ICP-MS Instrument		
Make, Model & type	Element XR SF-ICP-MS	
Sample introduction	Via conventional tubing	
RF power	1200W	
Make-up gas flow	0.98 l/min Ar	
Detection system	Single collector secondary electron multiplier (Faraday cup)	
Masses measured	204, 206, 207, 208, 232, 238	
Integration time per peak	20 ms	
Sensitvity / Efficiency	150 000 cps/ppm ^{238}U (47µm, 10Hz, 3.5J/cm^2)	
Dead time	6 ns	
Data Processing		
Gas blank	30 second on-peak	
Calibration strategy	*Zircon:* GJ-1 used as primary reference material, 91500 used as secondary reference material (Quality Control) Monazite: Trebilcock used as primary reference material, Bananeira used as secondary reference material (Quality Control)	

Reference Material info	*Zircon:* 91500 (Wiedenbeck et al., 1995) GJ1 (Jackson et al., 2004) *Monazite:* Trebilcock (Tomascak, 1996) Bananeira (Gonçalves et al., 2016)
Data processing package used / Correction for LIEF	GLITTER ® (van Achterbergh et al., 2001)
Mass discrimination	Standard-sample bracketing with ^{207}Pb/^{206}Pb and ^{206}Pb/^{238}U normalized to primary reference material
Common-Pb correction, composition and uncertainty	No common-Pb correction. Analyses discarded of the age calculation when discordance >20%
Uncertainty level & propagation	Ages are quoted at 2sigma absolute, propagation is by quadratic addition according to Horstwood et al. (2003). Reproducibility and age uncertainty of reference material are propagated.
Quality control / Validation	91500: Concordia age = 1066.4 ± 2.1 Ma (2SD, MSWD$_{(C+E)}$ = 0.57, *N* = 61) Concordia age = 1064.4 ± 4.8 Ma (2SD, MSWD$_{(C+E)}$ = 0.56, *N* = 27) Bananeira: Concordia age = 507.8 ± 5.4 Ma (2SD, MSWD$_{(C+E)}$ = 0.12, *N* = 4)
Other information	For detailed method description see Hurai et al. (2010). For detailed laser technical description see Müller et al. (2009).

Table S2.1: U-Pb LA-ICPMS results on zircon

		content (ppm)				Raw Ratios					Age (Ma)	
#	#Zr	Pb	Th	U	Th/U	^{207}Pb/^{235}U	± 2σ	^{206}Pb/^{238}U	± 2σ	Rho	^{206}Pb/^{238}U	± 2σ
AR801 - Pormenaz granite												
1	Zr1 rim	63	458	1816	0.25	0.2684	0.0088	0.03393	0.00093	0.83	215.1	5.8
2	Zr2 core	28	27	572	0.05	0.4016	0.0128	0.05277	0.00144	0.86	331.5	8.8
3	Zr2 rim	44	130	930	0.14	0.3681	0.0114	0.04851	0.00132	0.88	305.4	8.1
4	Zr3 core	52	222	1036	0.21	0.3688	0.0114	0.05015	0.00135	0.87	315.4	8.3
5	Zr3 rim	39	483	578	0.84	0.3993	0.0127	0.05362	0.00147	0.86	336.7	8.9
6	Zr4 zoned core	23	195	385	0.51	0.3944	0.0132	0.05373	0.00147	0.82	337.4	9.0
7	Zr5 rim	64	265	1498	0.18	0.3319	0.0109	0.04312	0.00117	0.82	272.2	7.3
8	Zr6 bright rim	20	120	478	0.25	0.3403	0.0115	0.04044	0.00111	0.81	255.5	6.8
9	Zr7 dark rim	61	361	1631	0.22	0.3142	0.0096	0.03785	0.00102	0.88	239.5	6.4
10	Zr8 core	24	36	230	0.16	0.9065	0.0317	0.10452	0.00285	0.78	640.9	16.7
11	Zr8 rim	24	400	605	0.66	0.3025	0.0109	0.03237	0.00090	0.77	205.3	5.6
12	Zr9 core	23	216	424	0.51	0.3792	0.0146	0.04969	0.00138	0.72	312.6	8.4
13	Zr10 tip 1	25	154	444	0.35	0.3997	0.0136	0.05352	0.00144	0.79	336.1	8.9
14	Zr11 tip 2	45	156	863	0.18	0.4041	0.0132	0.05358	0.00144	0.82	336.5	8.9
15	Zr12 rim	29	99	618	0.16	0.3567	0.0125	0.04747	0.00129	0.77	299.0	8.0
16	Zr13 zoned rim	72	336	1897	0.18	0.2910	0.0085	0.03876	0.00105	0.93	245.1	6.5
17	Zr13 bright core	34	91	715	0.13	0.3677	0.0113	0.04973	0.00135	0.88	312.8	8.2
18	Zr15 bright rim	22	163	422	0.39	0.3627	0.0121	0.04785	0.00129	0.81	301.3	8.0
19	Zr16 zoned tip	32	156	574	0.27	0.3886	0.0125	0.05396	0.00144	0.83	338.8	8.9
20	Zr17 zoned core	27	187	465	0.40	0.4015	0.0131	0.05415	0.00147	0.84	339.9	8.9

21	Zr17 bright rim	24	77	531	0.14	0.3649	0.0116	0.04612	0.00123	0.84	290.7	7.7
22	Zr18 dark core	56	124	1304	0.09	0.3392	0.0103	0.04580	0.00123	0.89	288.7	7.6
23	Zr19 zoned rim	38	67	736	0.09	0.3902	0.0123	0.05380	0.00144	0.85	337.8	8.9
24	Zr20 zoned rim	63	361	1415	0.25	0.3359	0.0099	0.04329	0.00117	0.92	273.2	7.1
25	Zr22 core	69	605	1134	0.53	0.4026	0.0128	0.05355	0.00144	0.85	336.3	8.8
26	Zr23 zoned core	33	281	560	0.50	0.3909	0.0124	0.05348	0.00144	0.85	335.9	8.8
27	Zr26 zoned tip	25	117	464	0.25	0.4018	0.0140	0.05367	0.00144	0.77	337.0	8.9
28	Zr27 zoned core	20	16	396	0.04	0.4064	0.0135	0.05424	0.00147	0.81	340.5	8.9
29	Zr28 core	20	55	378	0.15	0.3958	0.0159	0.05371	0.00147	0.68	337.2	9.0
30	Zr28 zoned rim	55	297	1259	0.24	0.3327	0.0099	0.04305	0.00114	0.89	271.7	7.1
31	Zr29 zoned rim	53	351	1475	0.24	0.2776	0.0083	0.03614	0.00096	0.89	228.9	6.0
32	Zr30 zoned rim	63	365	1720	0.21	0.2885	0.0086	0.03685	0.00099	0.91	233.3	6.1
33	Zr31 zoned rim	59	270	1273	0.21	0.3559	0.0107	0.04671	0.00123	0.88	294.3	7.7
34	Zr31 core	32	210	793	0.27	0.3165	0.0113	0.03995	0.00108	0.76	252.5	6.7
35	Zr32 core	38	207	294	0.70	0.9077	0.0276	0.10634	0.00285	0.88	651.5	16.5
36	Zr32 zoned tip	60	289	1371	0.21	0.3343	0.0101	0.04353	0.00117	0.89	274.7	7.2
37	Zr33 core	8.7	59	150	0.39	0.3945	0.0157	0.05404	0.00147	0.69	339.3	9.0
38	Zr33 dark rim	46	177	1364	0.13	0.2629	0.0078	0.03405	0.00090	0.89	215.9	5.6
39	Zr34 core	23	125	419	0.30	0.3910	0.0128	0.05363	0.00144	0.82	336.8	8.8
40	Zr34 zoned rim	24	112	504	0.22	0.3520	0.0128	0.04741	0.00129	0.75	298.6	7.9
41	Zr35 zoned rim	59	350	1445	0.24	0.3231	0.0103	0.04124	0.00111	0.85	260.5	6.8
42	Zr37 tip	32	427	510	0.84	0.3722	0.0156	0.04946	0.00135	0.65	311.2	8.3
43	Zr38 zoned tip	62	360	1410	0.25	0.3321	0.0099	0.04328	0.00114	0.88	273.1	7.1
44	Zr39 zoned core	20	150	332	0.45	0.3885	0.0129	0.05340	0.00144	0.81	335.4	8.7
45	Zr40 zoned rim	43	151	998	0.15	0.3341	0.0106	0.04366	0.00117	0.85	275.5	7.2
46	Zr41 zoned rim	45	170	948	0.18	0.3666	0.0117	0.04853	0.00129	0.84	305.5	8.0
47	Zr42 zoned rim	50	321	1299	0.25	0.3013	0.0090	0.03832	0.00102	0.89	242.4	6.3
48	Zr43 zoned rim	60	306	1478	0.21	0.3181	0.0095	0.04067	0.00108	0.89	257.0	6.7
49	Zr44 zoned core	40	282	1011	0.28	0.3115	0.0104	0.03902	0.00105	0.81	246.7	6.5
50	Zr45 zoned core	13	59	238	0.25	0.4000	0.0145	0.05465	0.00147	0.74	343.0	9.0
51	Zr47 bright tip	17	142	351	0.40	0.3374	0.0130	0.04341	0.00117	0.70	274.0	7.3
52	Zr47 dark inner rim	71	395	1672	0.24	0.3265	0.0096	0.04170	0.00111	0.91	263.4	6.8
53	Zr48 zoned rim	56	329	1622	0.20	0.2739	0.0086	0.03412	0.00090	0.84	216.3	5.6
54	Zr49 zoned core	17	65	319	0.20	0.3956	0.0138	0.05371	0.00144	0.77	337.2	8.8
55	Zr50 core	13	61	240	0.25	0.3883	0.0146	0.05389	0.00144	0.71	338.4	8.9
56	Zr51 zoned core	21	170	353	0.48	0.3974	0.0135	0.05388	0.00144	0.79	338.3	8.8
57	Zr52 zoned core	23	92	424	0.22	0.3941	0.0131	0.05366	0.00144	0.81	336.9	8.7
58	Zr53 zoned rim	65	275	1396	0.20	0.3532	0.0105	0.04641	0.00123	0.89	292.4	7.5
59	Zr54 zoned rim	47	257	1080	0.24	0.3338	0.0103	0.04397	0.00117	0.87	277.4	7.2
60	Zr55 zoned rim	21	99	379	0.26	0.3993	0.0138	0.05411	0.00144	0.77	339.7	8.8
61	Zr56 core	19	142	319	0.44	0.3926	0.0139	0.05392	0.00144	0.75	338.5	8.8
62	Zr57 zoned core	60	238	1153	0.21	0.3908	0.0122	0.05285	0.00138	0.84	332.0	8.6
63	Zr58 zoned core	21	66	402	0.16	0.3972	0.0136	0.05395	0.00144	0.78	338.7	8.8
64	Zr59 bright rim	18	64	382	0.17	0.3711	0.0145	0.04887	0.00132	0.69	307.6	8.1

65	Zr60 zoned tip	37	275	751	0.37	0.3486	0.0136	0.04631	0.00126	0.70	291.8	7.7
66	Zr61 zoned core	23	81	425	0.19	0.4041	0.0134	0.05384	0.00141	0.79	338.0	8.7
67	Zr62 bright zoned rim	8.7	46	158	0.29	0.3982	0.0166	0.05363	0.00147	0.66	336.8	8.9
68	Zr63 zoned core	70	452	1526	0.30	0.3416	0.0102	0.04430	0.00117	0.89	279.5	7.2
69	Zr65 zoned core	39	155	723	0.21	0.4046	0.0129	0.05447	0.00144	0.83	341.9	8.8
70	Zr66 zoned core	30	121	553	0.22	0.3949	0.0151	0.05431	0.00147	0.71	341.0	8.9
71	Zr67 bright zoned core	22	179	372	0.48	0.3915	0.0138	0.05351	0.00141	0.75	336.0	8.7
72	Zr68 bright zoned core	20	128	356	0.36	0.3868	0.0136	0.05357	0.00141	0.75	336.4	8.7
73	Zr69 zoned dark rim	58	284	1329	0.21	0.3327	0.0107	0.04374	0.00114	0.81	276.0	7.1
74	Zr69 bright core	28	202	485	0.42	0.3995	0.0135	0.05304	0.00141	0.78	333.2	8.6
75	Zr70 zoned rim	75	415	2027	0.20	0.2962	0.0089	0.03669	0.00096	0.88	232.3	6.0
AR865 - Montées Pélissier granite												
1	Zr1 core	47	262	899	0.29	0.3959	0.0122	0.05221	0.00150	0.93	328.0	9.2
2	Zr2 rim	5.0	4.5	100	0.04	0.4050	0.0179	0.05332	0.00159	0.67	334.9	9.7
3	Zr3 core	35	527	806	0.65	0.2904	0.0095	0.03809	0.00108	0.87	241.0	6.8
4	Zr4 zoned rim	24	119	607	0.20	0.3278	0.0107	0.03968	0.00114	0.88	250.8	7.1
5	Zr5 zoned tip	44	261	990	0.26	0.3237	0.0101	0.04476	0.00129	0.92	282.3	7.9
6	Zr7 zoned core	28	97	526	0.18	0.4007	0.0129	0.05444	0.00156	0.89	341.7	9.5
7	Zr8 core	40	241	742	0.32	0.4005	0.0125	0.05321	0.00153	0.92	334.2	9.3
8	Zr9 zoned tip	28	89	540	0.16	0.3997	0.0129	0.05398	0.00156	0.89	338.9	9.5
9	Zr10 zoned tip	50	214	1006	0.21	0.3747	0.0115	0.05043	0.00144	0.93	317.1	8.8
10	Zr11 zoned tip	45	180	902	0.20	0.3824	0.0125	0.05049	0.00144	0.88	317.5	8.9
11	Zr13 zoned tip	44	224	952	0.24	0.3440	0.0108	0.04600	0.00132	0.91	289.9	8.1
12	Zr15 zoned tip	39	126	731	0.17	0.4028	0.0131	0.05439	0.00156	0.88	341.4	9.5
13	Zr17 tip	35	165	642	0.26	0.4052	0.0128	0.05346	0.00153	0.91	335.7	9.3
14	Zr18 tip	40	164	818	0.20	0.3748	0.0117	0.04986	0.00141	0.91	313.7	8.7
15	Zr19 zoned core	36	189	752	0.25	0.3555	0.0113	0.04752	0.00135	0.89	299.3	8.3
16	Zr21 rim	42	287	944	0.30	0.3328	0.0111	0.04381	0.00126	0.86	276.4	7.7
17	Zr22 tip	26	329	699	0.47	0.2797	0.0094	0.03433	0.00099	0.86	217.6	6.1
18	Zr23 zoned tip	49	326	1060	0.31	0.3471	0.0108	0.04646	0.00132	0.91	292.7	8.1
19	Zr25 zoned tip	43	265	911	0.29	0.3529	0.0115	0.04647	0.00132	0.87	292.8	8.2
20	Zr26 tip	53	232	1150	0.20	0.3504	0.0115	0.04701	0.00135	0.87	296.1	8.3
21	Zr27 tip	48	905	1350	0.67	0.2791	0.0086	0.03531	0.00099	0.91	223.7	6.2
22	Zr28 zoned tip	41	125	786	0.16	0.3991	0.0131	0.05424	0.00153	0.86	340.5	9.5
23	Zr30 core	33	253	727	0.35	0.3346	0.0112	0.04451	0.00126	0.85	280.7	7.8
24	Zr31 core	30	101	556	0.18	0.4031	0.0128	0.05443	0.00153	0.89	341.7	9.5
25	Zr32 tip	50	196	1118	0.18	0.3451	0.0119	0.04615	0.00132	0.83	290.8	8.1
26	Zr34 rim	27	120	577	0.21	0.3575	0.0119	0.04763	0.00135	0.85	299.9	8.3
27	Zr36 core	21	153	564	0.27	0.2980	0.0116	0.03870	0.00111	0.73	244.8	6.9
28	Zr37 tip	42	347	1079	0.32	0.3017	0.0095	0.03870	0.00108	0.89	244.7	6.8
29	Zr38 zoned rim	27	128	555	0.23	0.3587	0.0122	0.04879	0.00138	0.83	307.1	8.5
30	Zr40 zoned tip	30	120	637	0.19	0.3594	0.0117	0.04865	0.00138	0.87	306.2	8.5
31	Zr41 zoned core	39	1045	1025	1.02	0.2698	0.0085	0.03477	0.00099	0.90	220.3	6.1

32	Zr42 core	33	152	638	0.24	0.3919	0.0126	0.05249	0.00147	0.87	329.8	9.1
33	Zr43 zoned tip	34	177	738	0.24	0.3381	0.0108	0.04550	0.00129	0.89	286.8	7.9
34	Zr44 core	33	136	619	0.22	0.3997	0.0133	0.05340	0.00150	0.84	335.3	9.2
35	Zr45 tip sup	35	175	699	0.25	0.3671	0.0119	0.04973	0.00141	0.88	312.8	8.6
36	Zr50 core	41	216	954	0.23	0.3229	0.0103	0.04220	0.00120	0.89	266.5	7.4
37	Zr52 core	49	297	1043	0.29	0.3319	0.0103	0.04516	0.00129	0.92	284.8	7.9
38	Zr53 core	35	162	750	0.22	0.3511	0.0127	0.04650	0.00135	0.80	293.0	8.2
39	Zr54 core	33	173	797	0.22	0.3193	0.0115	0.04115	0.00117	0.79	259.9	7.3
40	Zr55 core	36	201	770	0.26	0.3469	0.0106	0.04662	0.00132	0.92	293.7	8.1
41	Zr56 zoned tip	34	145	750	0.19	0.3450	0.0120	0.04656	0.00132	0.81	293.4	8.2
42	A11-Zr1 tip	36	164	724	0.23	0.3687	0.0113	0.04935	0.00141	0.94	310.5	8.6
43	A11-Zr2 rim	64	270	1450	0.19	0.3493	0.0110	0.04284	0.00123	0.92	270.4	7.5

AR73 - Vallorcine granite

1	Zr1 core	21	76	353	0.22	0.4468	0.0211	0.05878	0.00228	0.82	368.2	13.8
2	Zr15 core	37	77	253	0.30	1.3145	0.0535	0.13931	0.00534	0.94	840.7	30.2
3	Zr3 core	32	101	409	0.25	0.6065	0.0258	0.07656	0.00294	0.90	475.6	17.6
4	Zr17 core	67	31	181	0.17	6.1464	0.2444	0.35535	0.01365	0.97	1960.1	64.9
5	Zr16 rim1	23	38	303	0.13	0.6075	0.0256	0.07788	0.00300	0.92	483.5	17.9
6	Zr16 rim2	19	24	263	0.09	0.6107	0.0259	0.07404	0.00285	0.91	460.5	17.1
7	Zr33 core	44	201	924	0.22	0.3467	0.0141	0.04801	0.00183	0.94	302.3	11.3
8	Zr33 rim	21	48	461	0.10	0.3615	0.0153	0.04849	0.00186	0.90	305.2	11.5
9	Zr20 rim	27	56	672	0.08	0.3111	0.0133	0.04248	0.00165	0.91	268.2	10.1
10	Zr20 core	18	11	274	0.04	0.5467	0.0244	0.07294	0.00282	0.87	453.8	17.0
11	Zr21 rim	19	30	414	0.07	0.3500	0.0163	0.04832	0.00186	0.83	304.2	11.5
12	Zr21 core	12	76	141	0.54	0.6112	0.0335	0.07761	0.00306	0.72	481.9	18.3
13	Zr19 core	12	61	225	0.27	0.3874	0.0184	0.05125	0.00198	0.81	322.2	12.2
14	Zr6 rim	18	23	380	0.06	0.3774	0.0167	0.05196	0.00201	0.88	326.6	12.3
15	Zr11 core	29	80	266	0.30	0.8840	0.0372	0.10558	0.00408	0.92	647.0	23.8
16	Zr10 rim	28	113	574	0.20	0.3609	0.0152	0.04836	0.00186	0.91	304.4	11.5
17	Zr27 rim	36	15	688	0.02	0.4301	0.0179	0.05747	0.00222	0.93	360.2	13.5
18	Zr27 core	52	183	691	0.26	0.5715	0.0241	0.07374	0.00285	0.92	458.6	17.1
19	Zr12 rim	65	16	1486	0.01	0.3487	0.0142	0.04822	0.00186	0.95	303.6	11.5
20	Zr12 core	31	86	272	0.32	0.9409	0.0395	0.10743	0.00417	0.93	657.8	24.2
21	Zr13 rim	44	12	1004	0.01	0.3571	0.0155	0.04811	0.00186	0.89	302.9	11.5
22	Zr13 core	21	82	264	0.31	0.5777	0.0255	0.07530	0.00294	0.88	468.0	17.6
23	Zr39 rim	17	29	364	0.08	0.3653	0.0172	0.04926	0.00192	0.83	310.0	11.8
24	Zr39 core	74	24	1184	0.02	0.5258	0.0217	0.06767	0.00261	0.94	422.1	15.8
25	Zr40 core	64	59	184	0.32	5.4721	0.2237	0.32610	0.01266	0.95	1819.4	61.6
26	Zr25 rim	20	70	428	0.16	0.3516	0.0164	0.04863	0.00189	0.83	306.1	11.7
27	Zr37 rim	31	90	670	0.13	0.3462	0.0150	0.04802	0.00186	0.89	302.3	11.5
28	Zr35 rim	22	48	678	0.07	0.2540	0.0116	0.03486	0.00135	0.84	220.9	8.5
29	Zr35 core	13	84	266	0.31	0.3541	0.0185	0.04871	0.00192	0.75	306.6	11.9

MB43 - Montenvers granite

1	Zr01 tip	43	6.4	673	0.01	0.5363	0.0170	0.06999	0.00198	0.90	436.1	11.9
2	Zr02 centre	57	86	1244	0.07	0.3567	0.0110	0.04921	0.00138	0.91	309.7	8.6
3	Zr03 tip	109	184	3175	0.06	0.2763	0.0083	0.03703	0.00105	0.94	234.4	6.5
4	Zr06 dark rim	213	30	5721	0.01	0.2978	0.0088	0.04115	0.00117	0.96	260.0	7.1
5	Zr07 clear rim	10	32	216	0.15	0.3586	0.0165	0.04882	0.00144	0.64	307.3	8.8
6	Zr08 tip	138	33	3782	0.01	0.2926	0.0089	0.04005	0.00111	0.92	253.2	7.0
7	Zr09 centre	77	207	159	1.30	5.6982	0.1750	0.33062	0.00936	0.92	1841	45
8	Zr09 zoned tip	107	89	2412	0.04	0.3479	0.0104	0.04801	0.00135	0.94	302.3	8.3
9	Zr10 zoned centre	38	116	368	0.32	0.8377	0.0265	0.10013	0.00282	0.89	615.2	16.5
10	Zr10 dark zoned tip	404	98	9763	0.01	0.3270	0.0096	0.04527	0.00126	0.95	285.4	7.8
11	Zr11 tip	67	56	1503	0.04	0.3498	0.0107	0.04840	0.00135	0.91	304.7	8.3
12	Zr12 centre	50	750	909	0.82	0.3361	0.0107	0.04444	0.00126	0.89	280.3	7.7
13	Zr13 centre	49	300	985	0.30	0.3541	0.0111	0.04885	0.00138	0.90	307.5	8.4
14	Zr14 centre	38	56	827	0.07	0.3490	0.0111	0.04842	0.00135	0.87	304.8	8.3
15	Zr15 centre	49	90	1086	0.08	0.3494	0.0109	0.04819	0.00135	0.90	303.4	8.3
16	Zr16 centre	17	187	447	0.42	0.2463	0.0096	0.03424	0.00096	0.72	217.0	6.1
17	Zr17 tip	5.0	41	98	0.42	0.3513	0.0171	0.04900	0.00144	0.60	308.4	8.8
18	Zr18 tip	142	1872	2673	0.70	0.3378	0.0101	0.04639	0.00129	0.93	292.3	8.0
19	Zr19 centre	16	109	138	0.79	0.7891	0.0285	0.09611	0.00273	0.79	591.6	16.0
20	Zr19 dark zoned rim	209	84	5476	0.02	0.3026	0.0090	0.04177	0.00117	0.94	263.8	7.2
21	Zr20 dark zoned rim	121	61	2758	0.02	0.3511	0.0111	0.04802	0.00135	0.89	302.3	8.2
22	Zr21 zoned side	77	45	1735	0.03	0.3451	0.0111	0.04807	0.00135	0.88	302.6	8.3
23	Zr22 dark zoned tip	120	254	3002	0.08	0.3127	0.0094	0.04278	0.00120	0.93	270.1	7.4
24	Zr24 dark zoned tip	168	178	4815	0.04	0.2791	0.0083	0.03782	0.00105	0.93	239.3	6.5
25	Zr25 centre	42	58	870	0.07	0.3963	0.0134	0.05162	0.00144	0.82	324.5	8.9
26	Zr25 clear zoned centre	8.9	37	187	0.20	0.3563	0.0143	0.04869	0.00138	0.71	306.4	8.5
27	Zr27 zoned centre	8.5	49	175	0.28	0.3587	0.0145	0.04854	0.00138	0.71	305.5	8.5
28	Zr28 dark zoned tip	142	467	3021	0.15	0.3528	0.0107	0.04838	0.00135	0.92	304.6	8.2
29	Zr29 clear zoned centre	15	32	215	0.15	0.5766	0.0206	0.07322	0.00204	0.78	455.5	12.3
30	Zr30 clear zoned centre	16	138	315	0.44	0.3659	0.0136	0.04838	0.00135	0.75	304.5	8.3
31	Zr30 dark zoned tip	257	21	6369	0.00	0.3251	0.0100	0.04415	0.00123	0.91	278.5	7.5
32	Zr31 dark tip	91	115	2199	0.05	0.3252	0.0100	0.04448	0.00123	0.90	280.5	7.6
33	Zr32 clear centre	27	271	505	0.54	0.3489	0.0123	0.04866	0.00135	0.79	306.3	8.3
34	Zr33 clear centre	3.3	34	60	0.58	0.3458	0.0199	0.04905	0.00147	0.52	308.7	9.0
35	Zr34 dark tip	233	385	7045	0.05	0.2578	0.0078	0.03537	0.00096	0.90	224.1	6.1
36	Zr35 tip	23	84	321	0.26	0.5598	0.0192	0.07157	0.00198	0.81	445.6	11.9
37	Zr36 dark tip	195	25	4814	0.01	0.3232	0.0099	0.04468	0.00123	0.90	281.8	7.6
38	Zr37 clear zoned centre	18	92	241	0.38	0.5721	0.0201	0.07343	0.00204	0.79	456.8	12.2
39	Zr38 dark zoned tip	59	71	1315	0.05	0.3504	0.0112	0.04842	0.00132	0.85	304.8	8.2
40	Zr39 dark tip	93	65	2087	0.03	0.3483	0.0109	0.04833	0.00132	0.87	304.3	8.2
41	Zr41 clear zoned centre	14	178	267	0.67	0.3742	0.0142	0.04801	0.00135	0.74	302.3	8.3
42	Zr42 dark zoned tip	254	5556	4302	1.29	0.3306	0.0101	0.04533	0.00123	0.88	285.8	7.7
43	Zr43 tip	25	29	380	0.08	0.5601	0.0188	0.07148	0.00198	0.83	445.1	11.9
44	Zr44 dark zoned side	72	869	1436	0.60	0.3359	0.0107	0.04576	0.00126	0.87	288.4	7.7

45	Zr45 dark zoned rim	82	241	1892	0.13	0.3321	0.0104	0.04563	0.00126	0.88	287.7	7.7
MB37 - Mont Blanc granite												
1	Zr1 clear centre	12	64	212	0.30	0.4028	0.0151	0.05319	0.00156	0.78	334.1	9.5
2	Zr2 zoned centre	6.9	69	131	0.53	0.3770	0.0157	0.04810	0.00141	0.71	302.8	8.8
3	Zr3 Zoned clear	6.6	70	126	0.55	0.3439	0.0152	0.04809	0.00144	0.68	302.8	8.8
4	Zr5 zoned centre	6.4	51	128	0.40	0.3595	0.0166	0.04821	0.00144	0.65	303.5	8.9
5	Zr6 clear zoned rim	5.9	46	118	0.39	0.3551	0.0163	0.04874	0.00144	0.64	306.8	8.9
6	Zr7centre	13	133	255	0.52	0.3544	0.0131	0.04834	0.00141	0.79	304.3	8.7
7	Zr8 zoned tip	18	159	354	0.45	0.3502	0.0125	0.04860	0.00141	0.82	305.9	8.7
8	Zr9 zoned centre	29	252	566	0.45	0.3440	0.0114	0.04804	0.00138	0.87	302.5	8.5
9	Zr10 clear zoned centre	15	118	289	0.41	0.3570	0.0129	0.04840	0.00141	0.80	304.7	8.6
10	Zr11 zoned tip	28	206	498	0.41	0.3872	0.0131	0.05348	0.00153	0.85	335.8	9.5
11	Zr12 clear zoned tip	9.4	79	185	0.43	0.3485	0.0155	0.04853	0.00144	0.67	305.5	8.9
12	Zr13 dark zoned side	17	75	350	0.21	0.3734	0.0135	0.04860	0.00141	0.80	305.9	8.7
13	Zr14 clear zoned centre	15	140	282	0.50	0.3531	0.0131	0.04837	0.00141	0.79	304.5	8.6
14	Zr15 dark zoned tip	57	250	1206	0.21	0.3502	0.0110	0.04816	0.00138	0.91	303.2	8.5
15	Zr16 clear zoned centre	9.0	39	113	0.34	0.6223	0.0242	0.07818	0.00228	0.75	485.2	13.7
16	Zr17 clear zoned tip	8.4	73	163	0.45	0.3547	0.0147	0.04869	0.00144	0.71	306.5	8.8
17	Zr18 clear zoned tip	14	120	280	0.43	0.3561	0.0132	0.04845	0.00141	0.78	305.0	8.6
18	Zr19 zoned tip	16	134	318	0.42	0.3486	0.0127	0.04819	0.00141	0.80	303.4	8.6
19	Zr20 zoned centre	16	115	324	0.36	0.3622	0.0147	0.04816	0.00141	0.72	303.2	8.7
20	Zr20 zoned tip	14	108	270	0.40	0.3560	0.0145	0.04871	0.00144	0.73	306.6	8.8
21	Zr21 zoned tip	13	91	260	0.35	0.3500	0.0147	0.04819	0.00141	0.70	303.4	8.7
22	Zr22 zoned centre	15	124	298	0.41	0.3555	0.0131	0.04807	0.00138	0.78	302.7	8.6
23	Zr23 clear zoned tip	4.2	32	83	0.38	0.3505	0.0204	0.04874	0.00150	0.53	306.8	9.2
24	Zr24 zoned centre	18	201	335	0.60	0.3561	0.0133	0.04805	0.00138	0.77	302.6	8.6
25	Zr26 clear zoned centre	9.3	83	181	0.46	0.3671	0.0174	0.04821	0.00144	0.63	303.5	8.9
26	Zr27 zoned centre	23	305	414	0.74	0.3536	0.0122	0.04803	0.00138	0.83	302.4	8.5
27	Zr28 dark zoned tip	55	291	1149	0.25	0.3566	0.0113	0.04837	0.00138	0.90	304.5	8.5
28	Zr29 zoned tip	35	159	733	0.22	0.3589	0.0117	0.04818	0.00138	0.88	303.3	8.5
29	Zr30 centre	31	178	638	0.28	0.3517	0.0121	0.04827	0.00138	0.83	303.9	8.5
30	Zr32 zoned centre	19	283	331	0.86	0.3718	0.0132	0.04799	0.00138	0.81	302.1	8.5
31	Zr33 zoned tip	7.4	58	148	0.39	0.3366	0.0155	0.04838	0.00144	0.65	304.6	8.8
32	Zr34 zoned centre	14	122	264	0.46	0.3548	0.0132	0.04895	0.00141	0.78	308.1	8.7
33	Zr35 zoned centre	21	195	406	0.48	0.3518	0.0135	0.04801	0.00138	0.75	302.3	8.6
34	Zr36 zoned centre	45	165	483	0.34	0.7390	0.0256	0.09052	0.00261	0.83	558.6	15.4
35	Zr37 dark zoned rim	57	254	1207	0.21	0.3508	0.0113	0.04793	0.00135	0.87	301.8	8.4
36	Zr38 zoned centre	10	107	198	0.54	0.3568	0.0155	0.04830	0.00141	0.67	304.1	8.7
37	Zr39 dark zoned rim	71	414	1868	0.22	0.2865	0.0091	0.03847	0.00108	0.88	243.3	6.8
38	Zr40 zoned centre	19	241	343	0.70	0.3550	0.0135	0.04867	0.00141	0.76	306.4	8.6
39	Zr41 dark zoned rim	39	164	826	0.20	0.3495	0.0120	0.04890	0.00141	0.84	307.8	8.6
40	Zr42 zoned tip	11	79	219	0.36	0.3425	0.0148	0.04823	0.00141	0.68	303.6	8.6
41	Zr43 zoned centre	8.0	70	158	0.44	0.3694	0.0171	0.04839	0.00144	0.64	304.6	8.8

42	Zr44 dark zoned rim	91	650	2618	0.25	0.2598	0.0083	0.03531	0.00099	0.88	223.7	6.2
43	Zr45 zoned rim	15	119	306	0.39	0.3653	0.0137	0.04885	0.00141	0.77	307.5	8.6
AR37 - Courtenay Orthogneiss												
1	Zr01 Rim	27	19	341	0.05	0.693	0.035	0.0842	0.0034	0.80	521	20
2	Zr01 Centre	19	12	264	0.05	0.601	0.031	0.0771	0.0031	0.78	479	18
3	Zr04 Rim	22	22	311	0.07	0.607	0.031	0.0769	0.0031	0.78	478	18
4	Zr04 Centre	26	84	328	0.26	0.606	0.031	0.0771	0.0031	0.78	479	18
5	Zr03 Centre	27	46	366	0.13	0.602	0.029	0.0780	0.0031	0.81	484	18
6	Zr05 Centre	27	137	350	0.39	0.561	0.028	0.0715	0.0029	0.80	445	17
7	Zr31 Rim	24	26	330	0.08	0.628	0.031	0.0783	0.0031	0.80	486	19
8	Z31 Centre	28	225	227	0.99	0.760	0.044	0.0947	0.0038	0.70	583	23
9	Z32 Rim	15	27	204	0.13	0.629	0.038	0.0776	0.0032	0.67	482	19
10	Zr32 Centre	20	96	181	0.53	0.794	0.042	0.0964	0.0038	0.76	593	23
11	Zr17 Rim	32	17	451	0.04	0.592	0.028	0.0774	0.0031	0.85	481	18
12	Zr17 Centre	21	35	189	0.18	0.974	0.048	0.1132	0.0045	0.81	691	26
13	Zr18 Rim	53	23	739	0.03	0.614	0.028	0.0772	0.0030	0.87	479	18
14	Zr34 Rim	19	17	260	0.06	0.608	0.031	0.0781	0.0031	0.79	485	19
15	Zr34 Centre	21	37	281	0.13	0.590	0.030	0.0771	0.0031	0.78	479	18
16	Zr37 Rim	17	25	224	0.11	0.599	0.031	0.0782	0.0031	0.76	486	19
17	Zr35 Rim	20	24	265	0.09	0.605	0.031	0.0783	0.0031	0.77	486	19
18	Zr35 Centre	13	96	100	0.96	0.839	0.050	0.0990	0.0040	0.69	609	24
19	Zr36 Rim	27	33	361	0.09	0.609	0.030	0.0779	0.0031	0.81	484	18
20	Zr36 Centre	18	132	151	0.87	0.754	0.045	0.0928	0.0038	0.67	572	22
21	Zr38 Rim	22	26	303	0.09	0.599	0.030	0.0768	0.0031	0.78	477	18
22	Zr41 Rim	32	10	451	0.02	0.591	0.029	0.0768	0.0030	0.81	477	18
23	Zr41 Centre	50	306	568	0.54	0.591	0.028	0.0771	0.0031	0.82	479	18
24	Zr25 Rim	59	8	919	0.01	0.579	0.027	0.0702	0.0028	0.85	438	17
25	Zr25 Centre	54	316	481	0.66	0.764	0.040	0.0937	0.0037	0.76	577	22
26	Zr40 Rim	14	12	191	0.06	0.615	0.034	0.0784	0.0032	0.72	486	19
27	Zr40 Centre	59	476	650	0.73	0.597	0.030	0.0770	0.0031	0.79	478	18
28	Zr26 Rim	24	24	333	0.07	0.598	0.030	0.0774	0.0031	0.78	481	18
AR1028 - Morcles granite												
1	Zr1 centre	4.4	16	52	0.31	0.8079	0.0463	0.07717	0.00243	0.55	479.2	14.5
2	Zr3 zoned core	36	86	350	0.25	0.8687	0.0282	0.10301	0.00291	0.87	632.0	17.1
3	Zr3 dark side	10	23	99	0.23	0.8834	0.0348	0.10383	0.00300	0.73	636.8	17.6
4	Zr4 centre	22	24	316	0.08	0.5844	0.0202	0.07531	0.00216	0.83	468.1	12.9
5	Zr6 zoned dark centre	61	731	2298	0.32	0.2184	0.0073	0.02608	0.00075	0.87	166.0	4.7
6	Zr7 dark side	98	381	1300	0.29	0.6230	0.0200	0.07484	0.00213	0.89	465.2	12.7
7	Zr9 zoned centre	64	185	694	0.27	0.7735	0.0246	0.09319	0.00264	0.89	574.4	15.5
8	Zr10 centre	118	169	809	0.21	2.1305	0.0661	0.14498	0.00408	0.91	872.7	23.0
9	Zr11 zoned centre	23	101	298	0.34	0.6040	0.0213	0.07441	0.00213	0.81	462.7	12.7
10	Zr11 zoned tip	19	52	266	0.19	0.5842	0.0211	0.07396	0.00210	0.79	460.0	12.7
11	Zr12 tip	33	58	456	0.13	0.5928	0.0199	0.07600	0.00216	0.85	472.2	12.9

12	Zr15 zoned side	15	83	134	0.62	0.8782	0.0314	0.10257	0.00291	0.79	629.5	17.1
13	Zr17 clear zoned tip	14	36	115	0.31	1.0396	0.0383	0.11993	0.00342	0.77	730.2	19.7
14	Zr 18 zoned centre	31	176	402	0.44	0.6481	0.0249	0.07099	0.00204	0.75	442.1	12.3
15	Zr20 zoned centre	49	146	534	0.27	0.7441	0.0245	0.09186	0.00258	0.85	566.6	15.3
16	Zr21 centre	11	44	140	0.32	0.5954	0.0241	0.07618	0.00219	0.71	473.3	13.1
17	Zr21 dark zoned rim	33	52	466	0.11	0.5942	0.0208	0.07409	0.00210	0.81	460.8	12.6
18	Zr22 zoned tip	22	28	321	0.09	0.5672	0.0210	0.07302	0.00207	0.77	454.4	12.5
19	Zr24 centre	93	256	828	0.31	0.9542	0.0314	0.11073	0.00312	0.86	677.0	18.1
20	Zr25 zoned tip	3.9	16	40	0.39	0.8416	0.0774	0.09549	0.00345	0.39	587.9	20.3
AR833 - Lac Cornu Pegmatite												
1	Zr01 Lower tip	45	52	679	0.08	0.545	0.016	0.0708	0.0020	0.94	441	12
2	Zr02 Core	23	51	264	0.19	0.727	0.022	0.0895	0.0025	0.93	553	15
3	Zr02 Rim	16	23	241	0.09	0.542	0.018	0.0699	0.0020	0.82	436	12
4	Zr03 Core	6	18	66	0.28	0.739	0.027	0.0900	0.0026	0.79	556	15
5	Zr03 Rim	24	15	383	0.04	0.516	0.017	0.0681	0.0019	0.84	425	11
6	Zr04 Lower tip	19	22	276	0.08	0.568	0.018	0.0739	0.0021	0.89	460	13
7	Zr05 Core	39	19	562	0.03	0.580	0.018	0.0747	0.0021	0.90	464	12
8	Zr06 Lower tip	40	35	603	0.06	0.548	0.016	0.0706	0.0020	0.94	440	12
9	Zr07 Centre	56	275	737	0.37	0.552	0.016	0.0717	0.0020	0.95	446	12
10	Zr07 Lower tip	25	18	378	0.05	0.552	0.017	0.0723	0.0020	0.92	450	12
11	Zr08 Lower zone	32	30	451	0.07	0.578	0.017	0.0745	0.0021	0.94	463	13
12	Zr08 Core	43	56	624	0.09	0.571	0.017	0.0734	0.0020	0.92	457	12
13	Zr09 Upper tip	25	65	356	0.18	0.555	0.018	0.0710	0.0020	0.89	442	12
14	Zr12 Lower zone	16	12	226	0.05	0.584	0.019	0.0746	0.0021	0.87	464	13
15	Zr12 Core	18	35	152	0.23	1.058	0.037	0.1172	0.0033	0.80	714	19
16	Zr13 Core	137	55	357	0.16	7.923	0.231	0.3656	0.0103	0.96	2009	48
17	Zr13 Lower rim	45	30	665	0.04	0.568	0.017	0.0740	0.0021	0.93	460	12
18	Zr14 Upper rim	27	34	416	0.08	0.543	0.017	0.0698	0.0020	0.87	435	12
19	Zr15 Lower rim	47	14	764	0.02	0.519	0.016	0.0675	0.0019	0.90	421	11
20	Zr16 Core	29	40	245	0.16	1.091	0.033	0.1210	0.0034	0.92	736	19
21	Zr16 Lower rim	35	29	503	0.06	0.566	0.017	0.0737	0.0021	0.93	458	12
22	Zr17 Core	89	261	1017	0.26	0.707	0.021	0.0861	0.0024	0.93	533	14
23	Zr17 Lower rim	32	43	479	0.09	0.559	0.017	0.0706	0.0020	0.91	440	12
24	Zr18 Lower zone	42	27	618	0.04	0.580	0.017	0.0740	0.0021	0.93	460	12
25	Zr19 Lower zone	38	24	566	0.04	0.573	0.017	0.0733	0.0020	0.92	456	12
26	Zr21 Core	36	192	441	0.44	0.576	0.018	0.0745	0.0021	0.91	463	12
27	Zr21 Lower rim	50	29	721	0.04	0.586	0.018	0.0747	0.0021	0.92	464	12
28	Zr22 Core	27	45	395	0.11	0.561	0.018	0.0716	0.0020	0.89	446	12
29	Zr22 Lower rim	61	20	918	0.02	0.560	0.017	0.0725	0.0020	0.92	451	12
30	Zr23 Upper tip	23	15	334	0.04	0.573	0.018	0.0741	0.0021	0.89	461	12
31	Zr24 Centre	14	9	208	0.05	0.581	0.019	0.0742	0.0021	0.85	461	12
32	Zr26 Clear zoned lower part	20	57	279	0.20	0.584	0.019	0.0730	0.0020	0.88	454	12
33	Zr27 Centre	39	14	583	0.02	0.574	0.018	0.0732	0.0020	0.89	456	12

34	Zr28 Core	26	64	286	0.22	0.722	0.023	0.0892	0.0025	0.88	551	15
35	Zr28 Clear rim	34	23	503	0.05	0.564	0.017	0.0728	0.0020	0.89	453	12
36	Zr30 Tip	18	73	172	0.42	0.859	0.031	0.0960	0.0027	0.78	591	16
37	Zr29 Core	15	14	142	0.10	1.363	0.049	0.1110	0.0031	0.78	679	18
38	Zr29 Rim	33	26	508	0.05	0.551	0.018	0.0675	0.0019	0.86	421	11
39	Zr31 Centre	18	32	257	0.12	0.581	0.019	0.0741	0.0020	0.86	461	12
40	Zr32 Centre	30	18	465	0.04	0.539	0.017	0.0690	0.0019	0.86	430	11
41	Zr32 Rim	33	21	482	0.04	0.563	0.017	0.0741	0.0020	0.88	461	12
42	Zr33 Centre	63	695	638	1.09	0.553	0.017	0.0726	0.0020	0.86	452	12
43	Zr33 Rim	22	16	310	0.05	0.580	0.019	0.0751	0.0020	0.82	467	12
44	Zr34 Centre	19	20	265	0.08	0.575	0.019	0.0748	0.0020	0.83	465	12
45	Zr35 Lower rim	46	11	980	0.01	0.379	0.012	0.0509	0.0014	0.83	320	8
46	Zr35 Core	40	67	334	0.20	1.041	0.033	0.1187	0.0035	0.92	723	20
47	Zr36 Core	31	21	449	0.05	0.585	0.019	0.0739	0.0022	0.89	460	13
48	Zr36 Rim	18	0.7	400	0.00	0.370	0.013	0.0499	0.0015	0.84	314	9
49	Zr37 Core	15	25	210	0.12	0.573	0.019	0.0737	0.0022	0.88	459	13
50	Zr37 Rim	26	13	410	0.03	0.522	0.017	0.0676	0.0020	0.91	422	12
51	Zr38 Core	40	22	579	0.04	0.594	0.019	0.0752	0.0022	0.93	468	13
52	Zr38 Upper rim	24	20	375	0.05	0.527	0.017	0.0683	0.0020	0.91	426	12
53	Zr39 Centre	20	24	278	0.09	0.583	0.020	0.0748	0.0022	0.86	465	13
54	Zr39 Upper tip	32	17	518	0.03	0.517	0.018	0.0670	0.0020	0.86	418	12
55	Zr40 Lower tip	17	21	257	0.08	0.550	0.018	0.0708	0.0021	0.88	441	12
56	Zr41 Lower tip	15	18	226	0.08	0.569	0.022	0.0722	0.0021	0.77	449	13
57	Zr42 Centre	47	82	655	0.12	0.578	0.018	0.0742	0.0021	0.92	461	13
58	Zr44 Centre	36	52	513	0.10	0.575	0.020	0.0741	0.0022	0.85	461	13
59	Zr45 Lower tip	24	45	335	0.13	0.586	0.019	0.0751	0.0022	0.89	467	13
60	Zr46 Core	24	22	347	0.06	0.570	0.019	0.0730	0.0021	0.88	454	13
61	Zr46 Upper tip	22	21	316	0.07	0.565	0.018	0.0737	0.0021	0.89	458	13
62	Zr47 Upper tip	27	63	408	0.15	0.553	0.019	0.0670	0.0020	0.84	418	12
63	Zr48 Centre	10	11	139	0.08	0.576	0.021	0.0742	0.0022	0.81	461	13

AR1020 - Lac Cornu Pegmatite

1	Zr6	2.6	9.4	39	0.24	0.515	0.043	0.0674	0.0023	0.40	420	14
2	Zr7 Zoned centre	10	79	153	0.51	0.453	0.019	0.0597	0.0017	0.70	374	10
3	Zr7 Convolute tip	17	144	199	0.72	0.572	0.021	0.0732	0.0021	0.76	456	12
4	Zr8 Centre	6.9	38	88	0.43	0.578	0.029	0.0745	0.0022	0.59	463	13
5	Zr13 Zoned centre	10	65	130	0.50	0.551	0.025	0.0720	0.0021	0.63	448	12
6	Zr13 Zoned tip	9.0	74	121	0.61	0.514	0.023	0.0677	0.0020	0.64	423	12
7	Zr14 Zoned centre	12	80	147	0.54	0.573	0.024	0.0729	0.0021	0.67	454	13
8	Zr15 Zoned centre	13	129	150	0.86	0.561	0.023	0.0732	0.0021	0.70	455	12
9	Zr16 Tip	25	217	297	0.73	0.575	0.021	0.0735	0.0020	0.77	457	12
10	Zr16 Clear zoned lower part	8.4	16	119	0.14	0.555	0.024	0.0734	0.0021	0.66	457	12
11	Zr16 Clear zoned upper part	6.4	23	88	0.26	0.566	0.026	0.0734	0.0021	0.62	457	13
12	Zr18 Clear centre	8.1	7.0	133	0.05	0.501	0.023	0.0651	0.0019	0.61	407	11

13	Zr19 Dark centre	39	451	438	1.03	0.562	0.019	0.0731	0.0020	0.80	455	12
14	Zr19 Dark tip	27	255	312	0.82	0.573	0.020	0.0739	0.0020	0.79	459	12
15	Zr20 Clear centre	3.4	7.4	47	0.16	0.570	0.034	0.0741	0.0022	0.50	461	13
16	Zr20 Clear tip	5.9	31	81	0.39	0.523	0.031	0.0697	0.0021	0.50	434	13
17	Zr22 Clear centre	9.5	71	132	0.54	0.519	0.022	0.0649	0.0018	0.66	406	11
18	Zr23 Clear zoned part	12	72	153	0.47	0.576	0.024	0.0734	0.0020	0.68	456	12
19	Zr23 Clear zoned part	9.5	35	131	0.27	0.571	0.024	0.0726	0.0020	0.66	452	12
AR1006 - Lacs Noirs Pegmatites												
1	Zr1 Zoned tip	16	30	234	0.13	0.564	0.020	0.0735	0.0021	0.79	457	12
2	Zr2 Zoned tip	18	41	194	0.21	0.787	0.027	0.0941	0.0026	0.81	580	16
3	Zr3 Centre	17	30	247	0.12	0.554	0.020	0.0726	0.0020	0.79	452	12
4	Zr4 Zoned tip	12	29	178	0.16	0.559	0.021	0.0727	0.0020	0.75	453	12
5	Zr5 Zoned tip	13	30	191	0.16	0.568	0.021	0.0724	0.0020	0.77	450	12
6	Zr6 Low Th convolute tip	13	0.8	140	0.01	0.856	0.031	0.1042	0.0029	0.77	639	17
7	Zr8 Zoned centre	12	38	93	0.41	1.137	0.043	0.1260	0.0036	0.75	765	20
8	Zr8 Zoned rim	16	13	227	0.06	0.607	0.022	0.0728	0.0020	0.78	453	12
9	Zr9 Clear tip	13	31	179	0.18	0.590	0.024	0.0737	0.0021	0.71	458	13
10	Zr10 Centre	45	109	257	0.43	1.663	0.054	0.1672	0.0047	0.86	997	26
11	Zr12 Zoned centre	18	33	252	0.13	0.573	0.027	0.0729	0.0021	0.62	454	13
12	Zr13 Tip	22	30	322	0.09	0.574	0.022	0.0733	0.0021	0.75	456	12
13	Zr14 Centre	54	309	631	0.49	0.674	0.023	0.0763	0.0021	0.83	474	13
14	Zr15 Zoned tip	33	60	546	0.11	0.505	0.017	0.0633	0.0018	0.81	396	11
15	Zr16 Zoned fragment	24	21	352	0.06	0.578	0.020	0.0732	0.0020	0.79	455	12
16	Zr17 Zoned part	28	24	414	0.06	0.571	0.020	0.0733	0.0020	0.79	456	12
17	Zr18 Zoned part	17	68	151	0.45	0.912	0.041	0.1038	0.0030	0.64	637	18
18	Zr19 Inner zoned part	39	70	538	0.13	0.702	0.025	0.0734	0.0021	0.80	457	12
19	Zr20 Zoned part	23	27	332	0.08	0.570	0.019	0.0732	0.0020	0.82	456	12
20	Zr21 Zoned part	23	93	199	0.46	0.956	0.038	0.1098	0.0031	0.71	672	18
21	Zr22 Dark zone	44	24	471	0.05	0.826	0.026	0.0995	0.0028	0.88	612	16
22	Zr23 Zoned part	15	89	198	0.45	0.558	0.023	0.0732	0.0021	0.69	455	12
23	Zr24 Zoned tip	33	19	486	0.04	0.570	0.021	0.0726	0.0020	0.78	452	12
24	Zr25 Dark centre	66	560	800	0.70	0.557	0.017	0.0728	0.0020	0.88	453	12
25	Zr26 Dark centre	16	33	224	0.15	0.571	0.025	0.0739	0.0021	0.66	460	13
26	Zr28 Dark centre	31	147	336	0.44	0.726	0.024	0.0866	0.0024	0.84	535	14
27	Zr29 Zoned tip	22	43	312	0.14	0.610	0.022	0.0736	0.0021	0.78	458	12
28	Zr30 Clear centre	15	37	161	0.23	0.795	0.033	0.0957	0.0027	0.69	589	16
29	Zr31 Zoned tip	23	34	328	0.10	0.601	0.022	0.0735	0.0020	0.77	457	12
30	Zr32 Zoned centre	18	124	230	0.54	0.562	0.021	0.0731	0.0020	0.74	455	12
31	Zr33 Zoned centre	43	111	292	0.38	1.351	0.043	0.1390	0.0038	0.87	839	22
32	Zr34 Zoned centre	20	60	276	0.22	0.588	0.026	0.0732	0.0021	0.64	455	13
33	Zr35 Centre	9.2	18	130	0.14	0.579	0.025	0.0739	0.0021	0.65	459	13
AR916 - Chéserys Aplite												
1	Zr1 Zoned centre	97	756	2120	0.36	0.371	0.012	0.0460	0.0013	0.85	290	8

2	Zr3 Zoned centre	27	54	387	0.14	0.567	0.020	0.0734	0.0020	0.79	456	12
3	Zr4 Zoned tip	23	34	331	0.10	0.581	0.020	0.0740	0.0021	0.80	460	12
4	Zr6 Zoned centre	11	17	170	0.10	0.544	0.029	0.0700	0.0021	0.55	436	12
5	Zr7 Centre	12	99	140	0.71	0.580	0.023	0.0734	0.0021	0.71	456	12
6	Zr8 Centre	12	22	174	0.13	0.583	0.024	0.0729	0.0021	0.70	454	12
7	Zr9 Centre	37	45	534	0.08	0.577	0.020	0.0735	0.0020	0.82	457	12
8	Zr11 Zoned centre	17	44	226	0.20	0.644	0.026	0.0740	0.0021	0.69	460	13
9	Zr13 Zoned centre	19	108	245	0.44	0.574	0.021	0.0738	0.0020	0.76	459	12
10	Zr15 Zoned tip	23	27	338	0.08	0.559	0.020	0.0733	0.0020	0.79	456	12
11	Zr16 Zoned centre	39	417	440	0.95	0.582	0.020	0.0726	0.0020	0.81	452	12
12	Zr17 Zoned tip	20	36	287	0.13	0.564	0.021	0.0731	0.0020	0.74	455	12
13	Zr18 Zoned centre	61	346	675	0.51	0.717	0.024	0.0838	0.0023	0.82	519	14
14	Zr20 Zoned centre	31	273	367	0.74	0.580	0.021	0.0730	0.0020	0.76	454	12
15	Zr21 Zoned tip	51	44	774	0.06	0.559	0.021	0.0709	0.0020	0.76	442	12
16	Zr22 Zoned tip	13	26	189	0.14	0.595	0.024	0.0739	0.0021	0.68	459	13
17	Zr23 Centre	22	105	423	0.25	0.456	0.018	0.0569	0.0017	0.73	357	10
18	Zr24 Zoned tip	12	33	169	0.20	0.576	0.023	0.0735	0.0021	0.74	457	13
19	Zr25 Zoned tip	32	67	506	0.13	0.563	0.019	0.0682	0.0020	0.86	426	12
20	Zr26 Zoned tip	21	22	398	0.06	0.464	0.022	0.0579	0.0017	0.62	363	10
21	Zr27 Zoned tip	19	23	281	0.08	0.568	0.020	0.0735	0.0021	0.80	457	13
22	Zr28 Zoned centre	28	102	181	0.57	1.322	0.045	0.1390	0.0040	0.84	839	22
23	Zr28 Zoned tip	11	32	160	0.20	0.528	0.027	0.0688	0.0020	0.59	429	12
24	Zr29 Centre	35	439	444	0.99	0.514	0.019	0.0633	0.0018	0.77	396	11
25	Zr31 Zoned tip	20	27	288	0.09	0.560	0.020	0.0725	0.0020	0.79	451	12
26	Zr32 Zoned tip	25	35	386	0.09	0.555	0.022	0.0699	0.0020	0.71	435	12
27	Zr33 Zoned tip	10	17	151	0.11	0.522	0.026	0.0674	0.0020	0.59	421	12
28	Zr34 Zoned part	21	18	307	0.06	0.572	0.022	0.0733	0.0021	0.74	456	12
29	Zr35 Zoned tip	29	18	415	0.04	0.587	0.022	0.0755	0.0021	0.75	469	13
30	Zr37 Zoned part	12	18	190	0.09	0.531	0.027	0.0681	0.0020	0.57	425	12
31	Zr38 Clear zoned tip	10	92	198	0.46	0.366	0.016	0.0475	0.0014	0.67	299	8
32	Zr39 Clear zoned tip	6.5	33	85	0.39	0.565	0.026	0.0739	0.0021	0.62	460	13
33	Zr40 Zoned centre	42	40	618	0.06	0.568	0.019	0.0732	0.0020	0.81	456	12

Table S2.2: U-Pb LA-ICPMS results on monazite

		Concentration (ppm)				Raw ratios					Apparent age (Ma)	
#	# Mnz	Pb	Th	U	Th/U	^{208}Pb/^{232}Th	±2σ	^{206}Pb/^{238}U	±2σ	Rho	^{208}Pb/^{232}Th	±2σ
AR1028 - Morcles granite												
1	Mz1 Dark part	3345	110748	4232	26.2	0.01545	0.0005	0.04951	0.00144	0.1	309.9	9.0
2	Mz2 Zoned part	4569	151108	5322	28.4	0.01568	0.0005	0.04966	0.00144	0.1	314.6	9.2
3	Mz3 Dark centre	3679	119125	5037	23.7	0.01577	0.0005	0.04990	0.00144	0.1	316.3	9.2
4	Mz3 Clear tip	4931	164366	6151	26.7	0.01560	0.0005	0.04964	0.00144	0.1	313.0	9.2
5	Mz4 Centre	2691	89633	3671	24.4	0.01537	0.0005	0.04997	0.00147	0.1	308.3	9.0

6	Mz5 Tip	4017	131017	5633	23.3	0.01566	0.0005	0.04950	0.00144	0.1	314.1	9.2
7	Mz6 Centre	3040	98361	3969	24.8	0.01602	0.0005	0.05016	0.00147	0.1	321.2	9.5
8	Mz6 Centre	3410	112801	4730	23.9	0.01556	0.0005	0.04942	0.00144	0.1	312.1	9.2
9	Mz7 Clear centre	3644	122233	4854	25.2	0.01547	0.0005	0.04956	0.00144	0.1	310.2	9.2
10	Mz7 Dark part	2606	86740	3469	25.0	0.01558	0.0005	0.04997	0.00147	0.1	312.6	9.2
11	Mz8 Centre	1999	51485	3351	15.4	0.01830	0.0005	0.05407	0.00156	0.1	366.5	10.8
12	Mz8 Dark part	1920	62292	2912	21.4	0.01516	0.0005	0.05020	0.00147	0.1	304.2	9.0
13	Mz8 Zoned tip	2842	92970	3825	24.3	0.01543	0.0005	0.05006	0.00147	0.1	309.5	9.2
14	Mz8 Zoned side	2749	85001	4650	18.3	0.01561	0.0005	0.04963	0.00144	0.1	313.0	9.3
15	Mz9/1	1626	41410	4760	8.7	0.01569	0.0005	0.04944	0.00144	0.1	314.7	9.4
16	Mz9/2	1493	40028	4093	9.8	0.01531	0.0005	0.05008	0.00147	0.1	307.0	9.2

ANNEXE 5: supplementary materials of Chapter 7

Table S1: Operating conditions and instrument settings for U-Pb analyses

Laboratory & Sample Preparation	
Laboratory name	Laboratoire Magmas & Volcans, Clermont-Ferrand, France
Sample type/mineral	Zircon: grain mounts
Sample preparation	Conventional mineral separation: heavy liquids, Frantz magnetic separator, handpicking under binocular microscope 1 inch Epotek® resin mount, 0.25um polish to finish (Université Montpellier). Thin section (Université Bourgogne-Franche Comté)
Imaging	CL, FEI QUANTA 450w, 15 kV, 19mm working distance (Université Bourgogne-Franche Comté)
Laser ablation system	
Make, Model & type	Resonetics/M-50E 193nm, Excimer
Ablation cell & volume	Laurin Cell ® two volumes cell, Laurin Technic Ltd., volume ca. $1cm^3$
Laser wavelength	193 nm
Pulse width	< 4 ns
Fluence	$2.5 J.cm^{-2}$
Repetition rate	3 Hz
Spot size	33 µm
Sampling mode / pattern	Single spot
Carrier gas	100% He, Ar make-up gas and N_2 combined using the Squid® device from Resolution Instruments.
Background collection	30 secs
Ablation duration	60 secs
Wash-out delay	30 secs
Cell carrier gas flow	0.70 l/min He
ICP-MS Instrument	
Make, Model & type	Element XR SF-ICP-MS
Sample introduction	Via conventional tubing
RF power	1200W
Make-up gas flow	0.98 l/min Ar
Detection system	Single collector secondary electron multiplier (Faraday cup)
Masses measured	204, 206, 207, 208, 232, 238
Integration time per peak	20 ms
Sensitvity / Efficiency	150 000 cps/ppm ^{238}U (47µm, 10Hz, $3.5J/cm^2$)
Dead time	6 ns
Data Processing	
Gas blank	30 second on-peak
Calibration strategy	GJ-1 used as primary reference material, 91500 used as secondary reference material (Quality Control)
Reference Material info	91500 (Wiedenbeck et al., 1995) GJ-1 (Jackson et al., 2004)
Data processing package used / Correction for LIEF	GLITTER ® (van Achterbergh et al., 2001)
Mass discrimination	Standard-sample bracketing with ^{207}Pb/^{206}Pb and ^{206}Pb/^{238}U normalized to reference material GJ-1
Common-Pb correction, composition and uncertainty	No common-Pb correction. Analyses discarded of the age calculation when discordance >20%

Uncertainty level & propagation	Ages are quoted at 2sigma absolute, propagation is by quadratic addition according to Horstwood et al. (2003). Reproducibility and age uncertainty of reference material are propagated.
Quality control / Validation	91500: Concordia age = 1066.4 ± 2.1 Ma (2SD, MSWD$_{(C+E)}$ = 0.57, N = 61)
Other information	For detailed method description see Hurai et al. (2010). For detailed laser technical description see Müller et al. (2009).

Table S2.1: U-Pb LA-ICPMS results on zircon of AR476

#	#zircon	Pb	Th	U	Th/U	^{207}Pb/^{235}U	± 2σ	^{206}Pb/^{238}U	± 2σ	Rho	^{206}Pb/^{238}U age	± 2σ	Conc. age	± 2σ
Microconglomerate (AR476)														
1	Z01 dark rim	62	248	743	0.33	0.6320	0.0189	0.07971	0.00225	0.94	494.4	13.5	499	12
2	Z02 core	11	29	129	0.22	0.6549	0.0229	0.08228	0.00237	0.82	509.7	14.0	511	13
3	Z03 core	27	131	233	0.56	0.8149	0.0283	0.09910	0.00285	0.83	609.1	16.7	607	15
4	Z03 rim	29	205	230	0.89	0.8122	0.0256	0.09816	0.00279	0.90	603.6	16.4	604	14
5	Z04 zoned rim	24	72	286	0.25	0.6602	0.0208	0.08258	0.00234	0.90	511.5	14.0	515	13
6	Z05 rim	12	29	155	0.19	0.5872	0.0202	0.07556	0.00216	0.83	469.6	13.0	469	12
7	Z06 dark rim	19	37	433	0.09	0.3504	0.0111	0.04832	0.00138	0.90	304.2	8.4	304.6	8.2
8	Z08 rim	5.5	15	80	0.19	0.5927	0.0251	0.07156	0.00210	0.69	445.5	12.6	/	
9	Z09 zoned rim	22	93	263	0.35	0.6009	0.0192	0.07743	0.00219	0.88	480.7	13.2	478	12
10	Z10 core	24	71	328	0.22	0.5719	0.0227	0.06947	0.00201	0.73	432.9	12.2	/	
11	Z14 zoned tip	15	16	204	0.08	0.6130	0.0201	0.07536	0.00216	0.87	468.4	12.9	/	
12	Z11 core	14	29	147	0.20	0.7691	0.0255	0.09385	0.00267	0.86	578.3	15.8	579	14
13	Z12 core	26	61	146	0.42	1.5902	0.0501	0.15945	0.00453	0.90	953.7	25.2	972	19
14	Z 13 core	30	71	387	0.18	0.6141	0.0203	0.07849	0.00222	0.86	487.1	13.4	486	13
15	Z16 dark tip	57	124	1122	0.11	0.3907	0.0117	0.05327	0.00150	0.94	334.5	9.2	334.9	8.6
16	Z20 core	14	35	188	0.18	0.6144	0.0206	0.07605	0.00216	0.85	472.5	13.0	/	
17	Z20 rim	8.5	10	117	0.09	0.6284	0.0225	0.07634	0.00219	0.80	474.2	13.1	/	
18	Z18 zoned core	47	152	639	0.24	0.5634	0.0170	0.07231	0.00204	0.93	450.0	12.3	454	11
19	Z19 core	16	89	291	0.30	0.3830	0.0128	0.05325	0.00153	0.86	334.4	9.3	331.9	9
20	Z17 zoned core	16	51	173	0.30	0.7381	0.0249	0.09194	0.00261	0.84	567.0	15.5	563	14
21	Z21 zoned core	4.9	12	54	0.22	0.7401	0.0305	0.09149	0.00267	0.71	564.4	15.7	564	15
22	Z22 dark rim	32	157	388	0.40	0.6036	0.0193	0.07724	0.00219	0.89	479.6	13.1	480	12
23	Z23 zoned core	15	52	151	0.34	0.7716	0.0258	0.09465	0.00270	0.85	583.0	15.9	581	15
24	Z24 zoned tip	36	21	782	0.03	0.3754	0.0126	0.05016	0.00144	0.86	315.5	8.8	/	
25	Z25 tip	24	57	181	0.32	1.0866	0.0343	0.12477	0.00354	0.90	758.0	20.3	744	17
26	Z26 core	13	45	186	0.24	0.5497	0.0185	0.07049	0.00201	0.85	439.1	12.1	442	12
27	Z28 core	9	20	94	0.21	0.7549	0.0266	0.09207	0.00264	0.82	567.8	15.5	570	15
28	Z29 zoned rim	27	74	545	0.14	0.3777	0.0119	0.05197	0.00147	0.90	326.6	9.0	325.8	8.6
29	Z30 zoned core	7.7	20	87	0.23	0.7224	0.0371	0.08705	0.00264	0.59	538.1	15.6	540	15
30	Z32 core	35	81	692	0.12	0.3894	0.0121	0.05355	0.00150	0.90	336.3	9.3	334.6	8.8
31	Z33 core	36	140	496	0.28	0.5735	0.0180	0.07067	0.00201	0.90	440.2	12.0	/	
32	Z34 zoned core	12	39	120	0.32	0.7513	0.0260	0.09240	0.00264	0.82	569.7	15.6	569	15
33	Z35 core	22	195	341	0.57	0.4460	0.0148	0.05745	0.00162	0.85	360.1	10.0	/	

34	Z35 zoned rim	28	60	490	0.12	0.4522	0.0143	0.06012	0.00171	0.90	376.4	10.4	378.1	9.9
35	Z36 zoned core	10	31	107	0.29	0.7389	0.0262	0.09229	0.00264	0.81	569.1	15.6	565	15
36	Z37 zoned core	16	53	170	0.31	0.7516	0.0249	0.09066	0.00258	0.86	559.5	15.2	566	14
37	Z38 zoned core	18	34	120	0.28	1.3640	0.0444	0.14291	0.00405	0.87	861.1	22.9	875	19
38	Z39 zoned core	30	55	677	0.08	0.3441	0.0119	0.04689	0.00132	0.81	295.4	8.2	296.5	8
39	Z42 core	5.8	18	71	0.26	0.6689	0.0380	0.07974	0.00246	0.54	494.6	14.6	496	15
40	Z43 zoned tip	130	15	400	0.04	5.6390	0.1679	0.33273	0.00939	0.95	1851.6	45.4	/	
41	Z44 dark core	53	236	556	0.42	0.7023	0.0215	0.08779	0.00249	0.93	542.4	14.7	539	13
42	Z47 core	5	13	58	0.21	0.7640	0.0302	0.09324	0.00270	0.73	574.7	15.9	575	15
43	Z49 tip	24	29	363	0.08	0.5340	0.0186	0.06854	0.00195	0.82	427.4	11.8	430	11
44	Z50 core	40	14	632	0.02	0.5359	0.0166	0.06991	0.00198	0.92	435.6	11.9	436	11
45	Z51 zoned tip	13	31	122	0.25	0.9229	0.0314	0.10708	0.00306	0.84	655.8	17.8	661	16
46	Z52 tip	10	21	138	0.15	0.6254	0.0221	0.07552	0.00216	0.81	469.3	12.9	/	
47	Z53 core	18	68	254	0.27	0.5561	0.0184	0.07172	0.00204	0.86	446.5	12.2	448	12
48	Z54 core	22	69	217	0.32	0.7942	0.0259	0.09649	0.00273	0.87	593.8	16.1	594	15
49	Z55 rim	3.1	5.0	42	0.12	0.6163	0.0287	0.07594	0.00225	0.64	471.8	13.4	474	13
50	Z56 core	17	47	231	0.20	0.5985	0.0199	0.07375	0.00210	0.86	458.7	12.5	/	
51	Z56 dark tip	55	9.4	1210	0.01	0.3641	0.0116	0.04957	0.00141	0.89	311.9	8.6	313.5	8.4
52	Z57 core	77	320	991	0.32	0.5943	0.0180	0.07345	0.00207	0.93	456.9	12.4	/	
53	Z60 tip	38	131	418	0.31	0.7111	0.0223	0.08729	0.00246	0.90	539.5	14.6	545	13
54	P11/Z01 tip	96	43	503	0.09	2.9462	0.0892	0.18880	0.00534	0.93	1114.9	28.9	/	
55	P11/Z02 rim	59	155	738	0.21	0.6893	0.0217	0.08118	0.00231	0.90	503.2	13.7	/	
56	P11/Z03 tip	19	6	370	0.02	0.4092	0.0136	0.05498	0.00156	0.85	345.0	9.5	346.3	9.3
57	P11/Z04 core	10	24	104	0.23	0.7651	0.0278	0.09291	0.00267	0.79	572.7	15.7	575	15
58	P11/Z05 rim	37	31	422	0.07	0.7446	0.0236	0.09166	0.00258	0.89	565.4	15.3	565	14
59	P11/Z06 tip	20	36	219	0.17	0.7852	0.0262	0.09538	0.00270	0.85	587.3	15.9	588	15
60	P11/Z07 tip	10	19	113	0.17	0.7738	0.0282	0.09351	0.00267	0.78	576.2	15.8	579	15
61	P11/Z08 tip	41	92	484	0.19	0.7176	0.0251	0.08614	0.00246	0.82	532.7	14.6	/	
62	P11/Z10 tip	15	28	321	0.09	0.3657	0.0131	0.04918	0.00141	0.80	309.5	8.6	310.9	8.6

Table S2.2: U-Pb LA-ICPMS results on zircon of AR982

#	#zircon	Pb	Th	U	Th/U	^{207}Pb/^{235}U	± 2σ	^{206}Pb/^{238}U	± 2σ	Rho	^{206}Pb/^{238}U age	± 2σ
Metavolcano-sedimentary rocks (AR982)												
1	Zr1 Dark zoned centre	75	288	969	0.30	0.6035	0.0186	0.07634	0.00216	0.92	474.3	12.9
2	Zr2 Zoned tip	47	515	1301	0.40	0.2865	0.0091	0.03458	0.00096	0.88	219.1	6.1
3	Zr3 Zoned tip	54	209	918	0.23	0.4801	0.0150	0.06034	0.00171	0.91	377.7	10.3
4	Zr4 Zoned tip	71	357	1265	0.28	0.4520	0.0144	0.05685	0.00159	0.88	356.5	9.8
5	Zr5 Zoned tip	29	129	378	0.34	0.6088	0.0207	0.07590	0.00213	0.83	471.6	12.8
6	Zr6 Zoned tip	71	385	1549	0.25	0.3756	0.0116	0.04580	0.00129	0.91	288.7	7.9
7	Zr7 Centre	57	280	728	0.38	0.6053	0.0189	0.07532	0.00210	0.89	468.1	12.6
8	Zr8 Zoned tip	40	183	665	0.28	0.4871	0.0169	0.06019	0.00168	0.80	376.8	10.3
9	Zr10 Dark zoned tip	46	162	651	0.25	0.5667	0.0182	0.07154	0.00198	0.86	445.4	12.0

10	Zr11 Dark zoned tip	32	106	419	0.25	0.6125	0.0207	0.07757	0.00216	0.82	481.6	13.0
11	Zr12 Dark zoned tip	34	124	440	0.28	0.6159	0.0201	0.07620	0.00213	0.86	473.4	12.7
12	Zr13 Zoned tip	39	8.7	786	0.01	0.4053	0.0131	0.05458	0.00150	0.85	342.5	9.2
13	Zr14 Centre	38	123	505	0.24	0.6016	0.0201	0.07559	0.00210	0.83	469.7	12.6
14	Zr14 Zoned tip	36	105	731	0.14	0.4041	0.0137	0.04937	0.00138	0.83	310.6	8.4
15	Zr15 Side	15	2.6	288	0.01	0.4378	0.0158	0.05683	0.00159	0.77	356.3	9.7
16	Zr16 Dark zoned tip	77	780	2127	0.37	0.2930	0.0094	0.03513	0.00096	0.85	222.6	6.0
17	Zr17 Centre	72	361	920	0.39	0.6000	0.0197	0.07588	0.00210	0.84	471.5	12.5
18	Zr17 Tip	22	3.8	437	0.01	0.4171	0.0141	0.05634	0.00156	0.82	353.3	9.5
19	Zr18 Zoned tip	28	95	359	0.26	0.6399	0.0272	0.07599	0.00216	0.67	472.1	12.9
20	Zr19 Zoned centre	38	156	484	0.32	0.6217	0.0209	0.07817	0.00216	0.82	485.2	12.9
21	Zr20 Centre	65	321	829	0.39	0.5943	0.0188	0.07583	0.00207	0.86	471.2	12.4
22	Zr21 Centre	44	206	710	0.29	0.4872	0.0165	0.06115	0.00168	0.81	382.6	10.2
23	Zr22 Dark zoned centre	71	267	1351	0.20	0.4238	0.0138	0.05336	0.00144	0.83	335.1	8.9
24	Zr23 Zoned centre	37	158	663	0.24	0.4427	0.0172	0.05554	0.00153	0.71	348.5	9.4
25	Zr24 Centre	53	582	1223	0.48	0.3442	0.0111	0.04231	0.00114	0.84	267.1	7.1
26	Zr24 Convolute tip	33	5.1	683	0.01	0.3939	0.0133	0.05284	0.00144	0.81	331.9	8.8
27	Zr25 Zoned tip	51	383	1213	0.32	0.3432	0.0122	0.04153	0.00114	0.78	262.3	7.0
28	Zr26 Centre	63	593	1584	0.37	0.3276	0.0109	0.03927	0.00108	0.83	248.3	6.6
29	Zr26 Convolute tip	23	4.0	444	0.01	0.4189	0.0149	0.05605	0.00153	0.77	351.6	9.3
30	Zr27 Zoned centre	48	37	760	0.05	0.5250	0.0172	0.06791	0.00183	0.82	423.6	11.1
31	Zr27 clear tip	12	30	179	0.17	0.5427	0.0278	0.06926	0.00198	0.56	431.7	12.0
32	Zr28 Low Th side	41	8.6	820	0.01	0.4043	0.0135	0.05483	0.00147	0.80	344.1	9.0
33	Zr30 Zoned tip	40	270	896	0.30	0.3818	0.0136	0.04464	0.00120	0.76	281.5	7.5
34	Zr31 Zoned tip	49	232	745	0.31	0.5142	0.0172	0.06474	0.00186	0.86	404.4	11.3
35	Zr33 Zoned side	104	800	1811	0.44	0.4457	0.0150	0.05403	0.00156	0.86	339.2	9.5
36	Zr34 Zoned tip	46	210	578	0.36	0.5992	0.0194	0.07747	0.00222	0.89	481.0	13.2
37	Zr35 Low Th Dark tip	29	4.2	582	0.01	0.4116	0.0137	0.05530	0.00159	0.86	347.0	9.7
38	Zr38 Zoned centre	54	312	896	0.35	0.4732	0.0162	0.05841	0.00165	0.82	365.9	10.1
39	Zr38 Low Th Dark rim	23	1.9	451	0.00	0.4251	0.0146	0.05689	0.00162	0.83	356.7	9.9
40	Zr39 Centre	29	134	366	0.37	0.6245	0.0209	0.07554	0.00213	0.84	469.4	12.8
41	Zr40 Low Th convolute tip	21	3.6	398	0.01	0.4149	0.0147	0.05627	0.00159	0.80	352.9	9.8
42	Zr41 Centre	14	54	182	0.30	0.5809	0.0222	0.07520	0.00216	0.75	467.4	12.9
43	Zr42 Zoned centre	40	168	505	0.33	0.6084	0.0206	0.07721	0.00219	0.84	479.5	13.1
44	Zr43 Low Th tip	25	3.9	483	0.01	0.4491	0.0161	0.05536	0.00156	0.79	347.4	9.6
45	Zr44 Centre	23	106	296	0.36	0.5975	0.0205	0.07624	0.00216	0.82	473.7	12.9
46	Zr44 Low Th dark zoned tip	42	6.3	802	0.01	0.4224	0.0136	0.05716	0.00159	0.87	358.3	9.8
47	Zr46 Zoned centre	92	20	2009	0.01	0.3784	0.0118	0.05076	0.00141	0.89	319.2	8.7

ANNEXE 6: supplementary materials of Chapter 9

Table S1: References for the HP metamorphism

Massif	**Localisation**	**Etudes**
W-FCM	***Limousin***	*Berger et al., 2010* *Bellot and Roig, 2007*
E-FCM	***Lyonnais***	*Lardeaux et al., 2001* *Dufour, 1985*
	Najac	*Benmammar et al., 2020* *Lotout et al., 2018* *Delor et al., 1986*
	Lévézou	*Lotout et al., 2020* *Bouchardon, 1987*
	Haut-Allier	*de Hoÿm de marien et al., 2020* *de Hoÿm de Marien, 2019* *Ducrot et al., 1983*
	Artense	*Mercier et al., 1989*
	Marvejols	*Briand et al., 1988* *Pin and Lancelot, 1982*
	Maclas	*Gardien and Lardeaux, 1991*
	Vivarais	*Gardien, 1993*
	Bessenoits	*Paquette et al., 1995*
Montagne Noire	***Inner***	*Whitney et al., 2015* *Pitra et al., 2021* *Whitney et al., 2020* *Faure et al., 2014b*
	Outer	*Whitney et al., 2020*
Corsica - Sardinia	***Corsica***	*Cruciani et al., 2021* *Massonne et al., 2018* *Li et al., 2014* *Giacomini et al., 2008*
	North Sardinia	*Cortesogno et al., 2004* *Cruciani et al., 2012* *Cruciani et al., 2011* *Cruciani et al., 2015a* *Giacomini et al., 2005* *Di Vicenzo et al., 2004* *Palmeri et al., 2004*
	Middle Sardinia	*Cortesogno et al., 2004* *Cruciani et al., 2013* *Scodina et al., 2021*
	Gothard	*Biino, 1994* *Abrecht and Biino, 1994*

External Crystalline massifs	***Aiguilles-Rouges***	*Schulz and von Raumer, 1993* *Schulz and von Raumer, 2011* *Liégeois and Duchesne, 1981* *Bussy et al., 2011* *Vanardois et al., in review*
	Belledonne	*Jacob et al., 2021*
	Argentera	*Latouche and Bogdanoff, 1987* *Ferrando et al., 2008* *Rubatto et al., 2010* *Jouffray et al., 2020*
Vosges - Schwwarzwald	***Vosges granulite unit***	*Altherr, 2021* *Altherr and Kalt, 1996* *Altherr and Soder, 2018*
	Schwarzwald	*Kalt et al., 1994* *Alterr et al., 2021* *Marschall et al., 2003*

Table S2: References for the Carboniferous magmatism

Massif	Localisation	Study
FCM	**Velay Complex**	*Laurent et al,, 2017* *Couzinié et al,, 2014* *Barbarin et al,, 2012* *Didier et al,, 2013* *Mougeot et al., 1997* *Chelle-Michou et al., 2017* *Couzinié et al., 2021*
	Vivarais	*Briand et al., 2002*
	Cévennes	*Laurent et al,, 2017* *Monié et Al, 2000* *Brichau et al,, 2007*
	Margeride	*Laurent et al,, 2017* *Pin, 1979* *Lafon and Respaut, 1988* *Pin and Lancelot, 1982*
	Decazeville basin	*Bruguier et al,, 1998*
	Brévennes	*Laurent et al,, 2017*
	Livradois	*Laurent et al,, 2017* *Gardien et al., 2011*
	Plateau des Dômes	*Pin and Paquette, 2002*
	Haut-Allier	*Laurent et al,, 2017*
	W-FCM	*Lafon and Respaut, 1988* *Pin and Paquette, 2002* *Alexandrov et al,, 2000*

		Cartanaz et al., 2007
		Gébelin et al,, 2009
		Thiery et al,, 2009
		Thiery, 2010
		Rolin et al., 2008
		Cartanaz et al., 2008
		Rolin et al., 2006
	Bosmoreau basin	*Bruguier et al,, 1998*
		Roger et al., 2020
		Roger et al., 2015
		Trap et al., 2017
	Montagne Noire Dome	*Poilvet et al., 2011*
		Poujol et al., 2017
		Franke et al., 2011
		Faure et al., 2010
	Vosges	*Tabaud et al., 2015*
		Guillot et al., 2020
		Schaltegger et al., 1999
		Schaltegger et al., 1996
		Schulmann et al., 2002
		Kratinova et al., 2007
Corsica - Sardinia	**Corsica**	*Li et al., 2014*
		Paquette et al., 2003
		Renna et al., 2007
		Cocherie et al., 2005
		Di Rosa et al., 2020
		Poitrasson et al., 1998
	Sardinia	*Giacomini et al., 2008*
		Casini et al., 2012
		Rossi et al., 2009
		Padovano et al., 2014
		Oggiano et al., 2007
		Oggiano et al., 2005
ECMs	**Aiguilles-Rouges**	*This study*
		Bussy et al., 2000
		Capuzzo and Bussy, 2000
		Bussien Grosjean et al., 2017
	Mont-Blanc	*Bussy and von Raumer, 1993*
		Capuzzo and Bussy, 2000
		in Debon and Lemmet, 1999
		Bussy and von Raumer, 1994
	Aar	*Olsen et al., 2000*
		Schaltegger and Corfu, 1992
		Schaltegger, 1993
		Schaltegger and Corfu, 1995

		Schaltegger and von Quadt, 1990
		Sergeev et al., 1995
	Gothard	*in Debon and Lemmet, 1999*
		Bossart et al., 1986
		Debon et al., 1994
		Debon et al., 1998
	Belledonne	*in Debon and Lemmet, 1999*
		Fréville et al., 2018
		Fréville, 2016
	Grandes-Rousses	*Fréville, 2016*
		in Debon and Lemmet, 1999
	Pelvoux	*Guerrot and Debon, 2000*
		Fréville, 2016
	Argentera	*in Debon and Lemmet, 1999*
		Rubatto et al., 2001
MT	**Maures**	*Moussavou, 1998, in Bellot (2005)*
		Duchesne et al., 2013
	Tanneron	*Demoux et al., 2008*
NPZ	**Trois-Seigneurs**	*Vacherat et al., 2017*
	Arize	*Vacherat et al., 2017*
		Vacherat et al., 2017
	Ursuya	*Lemirre, 2016*
		Vielzeuf et al., 2021
	Treilles	*Vielzeuf & Pin, 1991*
		This study
		Olivier et al., 2008
		Olivier et al., 2004
	Agly	*Postaire, 1982*
		Tournaire Guille et al., 2019
		Odlum et al., 2019
		Respaut and Lancelot, 1983
PAZ	**Aya pluton**	*Denèle et al., 2012*
	Eaux-Chaudes	*Ternet et al., 2004*
	Crêtes-Blanches	*Ternet et al., 2004*
		Denèle, 2007
	Cauterets	*Guerrot, 1998*
		Denèle et al., 2014
	Bordères-Louron	*Gleizes et al., 2006*
	Bossost	*Mezger & Gerdes, 2016*
		Lopez-Sanchez et al., 2018
		Mezger & Gerdes, 2016
		Denèle, 2007
	Aston	*Denèle et al., 2014*
		Lemirre, 2016
		Schnapperelle et al., 2020

	Hospitalet	*Schnapperelle et al., 2020*
	Mont-Louis	*Denèle et al., 2014*
		Maurel, 2003; Maurel et al., 2004
	Canigou	*Denèle et al., 2014*
	Maladetta	*Pereira et al., 2014*
	Andorra	*Pereira et al., 2014*
	Saint-Laurent	*Maurel, 2003*
		Aguilar et al., 2013
	Bassiès	*Paquette et al., 1997*
		Poitrenaud et al., 2020
	Quérigut	*Roberts et al., 2000*
	Albères	*Laumonier et al., 2013*
	Lesponne-Chiroulet-Neouville	*Lemirre et al., 2019*
	Lys-Caillaouas	*Esteban et al., 2015*
		Lopez-Sanchez et al., 2018
	Sallent Basin	*Rodríguez-Méndez et al., 2014*
	Aguilla	*Kilzi et al., 2016*
	Troumouse	*Kilzi et al., 2016*
CRR	**Guilleries**	*Martinez et al., 2008*
	Montnegre	*Martinez et al., 2015*
	Priorat	*Martinez et al., 2015*

Table S3: References for the partial melting events

Massif	**Localisation**	**Etudes**
E-FCM	***Velay dome***	*review in Barbey et al., 2015*
	Lyonnais	*Duthou et al., 1994*
	Whole E-FCM	*review in Vanderhaeghe et al., 2020*
	Najac	*Benmammar et al., 2020*
W-FCM	***Limousin***	*review in Faure et al., 2008*
		Gébelin et al., 2009
Whole FCM		*review in Vanderhaeghe et al., 2020*
Montagne Noire		*Trap et al., 2017*
NPZ	***Agly***	*review in Vanardois et al., in prep*
		Siron et al., 2020
	Castillon - Ursuya - St-Barthélémy	*Lemirre, 2016*
	All NPZ	*review in Cochelin et al., 2021*
PAZ	***Aston dome***	*Mezger and Gerdes, 2016*
		Denèle et al., 2014
	All PAZ	*review in Cochelin et al., 2021*
ECMs	***Aiguilles-Rouges - Mont-Blanc***	*Bussy et al., 2000*
		review in Vanardois et al., in prep

	Belledonne - Pelvoux	*review in Fréville et al., 2018, in review, in prep; Fréville, 2016*
	Argentera	*Rubatto et al., 2001, 2010*
Maures-Tanneron		*review in Schneider et al., 2014; Oliot et al., 2015*
Corsica - Sardinia	***Corsica***	*Giacomini et al., 2008* *Li et al., 2014* *Review in Faure et al., 2014a*
		Cruciani et al., 2021
	Sardinia	*review in Cruciani et al., 2015b* *Cruciani et al., 2001* *Fancello et al., 2018*
Vosges	***central Vosges***	*Skrzypek et al., 2012* *Review in Skrzypek et al., 2014*

ÉCOLE DOCTORALE
PRES | Bourgogne | Franche-Comté
Environnements - Santé

Titre : Fusion partielle, transfert de magma et partitionnement de la déformation au cours de l'orogénèse Varisque. Exemple des massifs des Aiguilles-Rouges (Alpes) et de l'Agly (Pyrénées).

Mots clés : Fusion partielle, partitionnement de la déformation, transfert de magmas, orogénèse Varisque.

Résumé : A l'échelle des orogénèses, la déformation et la rhéologie de la lithosphère continentale sont fortement contrôlées par les processus de migmatisation et les phénomènes magmatiques au cours de l'évolution des grandes chaines continentales. La déformation de la croûte moyenne assistée par les mécanismes de fusion partielle et la présence de liquides silicatés joue un rôle majeur dans l'accommodation de grands déplacements horizontaux et verticaux au sein de l'orogenèse en construction. Ces fluages de la croûte partiellement fondue sont décrits dans les grands systèmes orogéniques actuels (e.g. Himalaya-Tibet et Andes) et anciens (Chaîne Varisque). Dans le détail, la déformation syn-orogénique, les processus de ségrégation des liquides silicatés et leur migration dans la croûte orogénique sont des phénomènes inter-opérant de manière complexe, à plusieurs échelles de temps et d'espace.

Par l'étude structurale, pétrologique et géochronologique des massifs Varisques de l'Agly (Zone Nord Pyrénéenne) et des Aiguilles-Rouges (Alpes occidentales), nous abordons cette problématique scientifique en ciblant la question des interactions entre partitionnement de la déformation et fusion partielle dans une croûte orogénique en déséquilibre à haute-température. En parallèle, nous proposons de repositionner ces massifs dans leur cadre tectonique Varisque afin d'améliorer la compréhension des processus de fluage à l'origine de leur construction et leur structuration.

La synthèse de nos résultats nous permet de proposer une évolution géodynamique des ECMs s'intégrant dans l'évolution de la chaîne Varisque Européenne et nous conduisent à présenter une nouvelle reconstitution paléogéographique de la branche Sud-Est Varisque à la fin du Carbonifère. Cette nouvelle vision du positionnement des ECMs, et la comparaison avec le massif de l'Agly nous permettent de discuter de l'évolution spatiale et temporelle du fluage de la croûte partiellement fondue au cours du Carbonifère.

Title : Partial melting, magmas migration and partitioning of the deformation during the Variscan orogeny. Examples of the Aiguilles-Rouges (Alps) and Agly (Pyrenees) massifs

Keywords : Partial melting, partitioning of the deformation, magmas migration, Variscan orogeny.

Abstract : During late orogenic evolution, deformation of the continental lithosphere is highly influenced by partial melting and magmatic processes. Melt-assisted deformation of the partially-molten middle crust plays a major role in the accommodation of large horizontal and vertical displacements of molten crustal domains during the building of the orogenic plateaus as described in actual and ancient orogenic systems (e.g. Himalayan-Tibetan, Andean and Variscan belts). In detail, syn-orogenic deformation, melts segregation and melt migration in the orogenic crust are complex phenomena, which interact at several time and space scales.

Through structural, petrological and geochronological studies of the Variscan Agly and Aiguilles-Rouges massifs (North Pyrenean Zone and Western Alps, respectively), the interplay between deformation partitioning, partial melting and magmatic processes in the hot orogenic crust is investigated. Meanwhile, the geodynamic setting and evolution of these massifs are replaced in the global Variscan tectonic framework in order to improve the understanding of late-orogenic crustal flow.

Our results allow to propose a tectonic model of the ECMs that fits in the bulk evolution of the European Variscan belt. We also present a reappraisal of the paleogeographic location of the ECMs in the Variscan belt during Carboniferous time. This new vision of the position of the ECMs and the comparison with the Agly massif allow to discuss and to propose a new spatial and temporal evolution of the flow of the partially molten crust during the Variscan late-orogenic evolution.

UBFC
UNIVERSITE
BOURGOGNE FRANCHE-COMTE

Université Bourgogne Franche-Comté
32, avenue de l'Observatoire
25000 Besancon